Université Lille 1 - Sciences et Technologies

Ecole Doctorale : Sciences de La Matière, du Rayonnement et de l'Environnement

THESE

presentée par

Danilo OLIVEIRA DE SOUZA

Pour l'obtention du grade de

DOCTEUR DE L'UNIVERSITE LILLE 1

Spécialité : Molécules et Matière Condensée

QUICK-EXAFS AND HYDROTREATING CATALYSTS: CHEMOMETRIC CONTRIBUTIONS

Thèse dirigée par Sylvain CRISTOL

Soutenue le 15 de juillet de 2015 devant le jury composée de :

Rapporteurs	Mme **Valérie BRIOIS**, (Directrice de Recherche) CNRS / Synchrotron SOLEIL
Rapporteurs	M **Arnaud TRAVERT**, (Maître de Conférences) LCS-Université de Caen
Examinateur	Mme **Virginie MOIZAN-BASLE**, (Ingénieur de Recherche) IFP-Energie Nouvelles
Président du Jury	M **Hervé VEZIN**, (Directeur de Recherche) CNRS / LASIR-Université Lille 1
Directeur de thèse	M **Sylvain CRISTOL**, (Professeur) UCCS-Université Lille 1
Co-encadrante	Mme **Christine LANCELOT**, (Maître de Conférences) UCCS-Université Lille 1

Université Lille 1 - Sciences et Technologies

Ecole Doctorale : Sciences de La Matière, du Rayonnement et de l'Environnement

THESE

presentée par

Danilo OLIVEIRA DE SOUZA

Pour l'obtention du grade de

DOCTEUR DE L'UNIVERSITE LILLE 1

Spécialité : Molécules et Matière Condensée

QUICK-EXAFS AND HYDROTREATING CATALYSTS: CHEMOMETRIC CONTRIBUTIONS

Thèse dirigée par Sylvain CRISTOL

Soutenue le 15 de juillet de 2015 devant le jury composée de :

Rapporteurs	Mme **Valérie BRIOIS**, (Directrice de Recherche) CNRS / Synchrotron SOLEIL
Rapporteurs	M **Arnaud TRAVERT**, (Maître de Conférences) LCS-Université de Caen
Examinateur	Mme **Virginie MOIZAN-BASLE**, (Ingénieur de Recherche) IFP-Energie Nouvelles
Président du Jury	M **Hervé VEZIN**, (Directeur de Recherche) CNRS / LASIR-Université Lille 1
Directeur de thèse	M **Sylvain CRISTOL**, (Professeur) UCCS-Université Lille 1
Co-encadrante	Mme **Christine LANCELOT**, (Maître de Conférences) UCCS-Université Lille 1

"Carry on, you will always remember
Carry on, nothing equals the splendor
Now your life's no longer empty
Surely heaven waits for you
Carry on my wayward son,
there'll be peace when you are done"

(Kansas, 1976)

Remerciements

Ce travail est été réalisé au sein du l'UCCS (l'Unité de Catalyse et Chimie du Solide) sur la direction du Professeur Sylvain CRISTOL. Mes sincères remerciements s'adressent donc tout d'abord à Sylvain CRISTOL qui m'a fait confiance en tant que thésard en acceptant d'encadrer ce travail doctorat. Au cours de ces années de thèse, le Sylvain CRISTOL m'a appris à être un chercheur plus autonome et critique sur mon travail. Merci beaucoup, Sylvain, pour tes multiples conseils, ton immense savoir et ta grande disponibilité. J'ai été extrêmement sensible à ses qualités humaines d'écoute, d'encouragements et de compréhension au long de ces années doctorales. Je ne pouvais pas imaginer avoir un meilleur mentor pour mon étude de doctorat.

Je souhaiterais exprimer ma gratitude à madame Christine LANCELOT, coencadrante de thèse, pour m'avoir accueilli dans le groupe « Énergie » de l'UCCS, pour tout son apprentissage au niveau laboratoire, notamment tout au début de ma thèse. Madame Lancelot a beaucoup contribué pour ma formation scientifique, en étant toujours respectueuse, méticuleuse et très organisée, un vrai exemple à suivre. Pour tout ça, je vous en remercie !

Le travail aurait été beaucoup plus difficile sans la présence d'Asma TOUGERTI. Le savoir, la patience, l'enthousiasme vivant et la bonne humeur m'ont donné de l'énergie supplémentaire pour les moments difficiles bien aussi que pour faire du travail une activité plus agréable. C'était vraiment le bonheur d'avoir toi comme collège/maître pendant ces bonnes années. Tu as été une voix très importante pour absolument tout pendant le travail de thèse. Un chaleureux merci !

J'adresse mes grands remerciements à madame Valérie BRIOIS, pour toute la disponibilité (notamment sur la ligne SAMBA au le Synchrotron SOLEIL), l'enthousiasme, les discussions et conseils précieux. Tout ça, tes efforts, ta patience, et ton savoir scientifique sont un exemple et une grande inspiration personnelle. J'apprends beaucoup à tes côtés et je t'en remercie énormément !

Je remercie également à tous les membres du jury, madame Virginie MOIZAN, monsieur Arnaud TRAVERT et monsieur Hervé VEZIN, pour les commentaires et questions sur mon manuscrit qui me donnent un point de vue différents sur mon travail et moi-même. Cela me donne motivation pour grandir comme chercheur en regardant ces perspectives.

Au cours de ces années de thèse, j'ai eu l'occasion d'être entouré de personnes qui ont été proche de moi soit sur le plan professionnel, soit sur le plan personnel (soit les deux !). La liste est longue. Certaines personnes sont toujours à l'UCCS, d'autres sont déjà reparties. Donc, sans prétention d'épuiser la liste, j'associe à ces remerciements tous les membres (et ex-membres) d'UCCS et des laboratoires voisins, avec qui j'ai pu travailler, discuter, jouer au tarot ou tout simplement rigoler un peu, boire du café tôt le

matin ou simplement passer des bons moments. Notamment, Edmond PAYEN et Lionel MONTAGNE, Jean-François « chef » PAUL, Jean-Seb GIRARDON, Anne-So MAMEDE, Carole LAMONIER, Jean-Charle MORIN, Elise BERRIER, Mickael CAPRON, Christophe DUJARDIN, Franck DUMEIGNIL, Jean-φ DACQUIN, Martine TRENTESAUX, Olivier GARDOL, le secrétariat (David, Barbara, Sandrine, Virginie). Ils m'ont donné l'opportunité de m'intégrer et de faire partie du C3 et sans leur précieux support il n'aurait pas été possible de mener cette recherche. Du côté des « labmates », je souhaite remercier : les latins (Manuel, Alexia, Andres et Jhon), Aline Bueno, Jérémy Faye, Diego, Silvia Fazzini, Georgette, Rémy, Guillaume, Jesus, Cyril, les jeunes (Hao, Lucie, Charlotte, Parnian et Hélori « easy »), Anita, Marie, Mireille et tous les autres thésards et post-doc pour l'amitié, le soutient et les bavardages. Et bien sur, pour le meilleur et plus sympa pot de thèse que quelqu'un pourrait avoir.

Mes remerciements vont aussi à ma famille et mes amis qui, avec cette question récurrente, « quand est-ce que tu la soutiens cette thèse ? », bien qu'angoissante en période fréquente de doutes, m'ont permis de ne jamais dévier de mon objectif final. Merci « meu pai e minha mãe » pour tout le support, l'affections même de très loin, la confiance, la sérénité dans le moment le plus durs de toute ma vie et pour la compréhension dans les moments d'absence. Également, mes frères Gabriel, PH et tous ceux qui m'ont beaucoup soutenu. Merci à ma deuxième « famille » (les brésiliens et les étrangers) que Lille m'a donnée, les moments durs et de solitude auraient été invivable sans vous. Les plaisir de vous avoir à mes côtés c'était déjà du bonheur. Je garderai pour toute ma vie les innombrables instants de joie, les soirées, les discussions, les voyages… Finalement, j'aimerais de dédier ce travail à la personne qui a soutenu sans restriction mon choix de partir loin pour pouvoir construire mon rêve, pour les encouragements et pour faire partie de ce chemin avec moi. Sans toi je n'y serais jamais arrivé, cela c'est notre succès, merci, mon cœur ! Merci, « meu amorequinho » !

Ces années de thèse ont été superbe personnellement et professionnellement, j'ai beaucoup grandi en France. J'ai appris à aimer encore plus le pays, sa culture et son peuple, spécialement la ville de Lille et, en particulier, l'équipe UCCS du C3. Je pense qu'il m'a fallu du temps pour observer, comprendre le fonctionnement du *modus operandi* de la société dans lequel j'étais incéré, pourtant, c'était le temps nécessaire pour consolider m'admiration pour vous. Je garderai toutes les mémoires de ce très beau passage dans mon cœur franco-brésilien !

Summary

General Introduction

The *International Energy Outlook 2013* (IEO2013) made by the U.S. Energy Information Administration (EIA) projects that world energy consumption will grow 56 percent between 2010 and 2040 [1]. Despite of the renewable energy and nuclear power are the world's fastest-growing energy sources, fossil fuel continue to supply almost 80 percent of world energy use through 2040. Particularly, liquid fuels (mostly petroleum-based) remain the largest source of energy. World using of petroleum and other liquid fuels grows from 87 million barrels per day in 2010 to 97 million barrels per day in 2020 and 115 million barrels per day in 2040. Much of this fuel consumption comes from transportation sector (63 percent of total increase in liquid fuel use from 2010 to 2040) and although advances in non-liquids transportations technologies are anticipated, they are not enough to offset the rising demand for transportation service worldwide, so liquid fuels continue to provide most of energy consumed.

The latest European Union directive published in 2012 [2], which is one of several policies designed to improve vehicle efficiency and increase the use of clean transportation fuels, requires the decreasing of sulfur levels on fuels on light-duty and heavy-duty vehicles in addition to the levels of pollutants such as nitrogen oxides, hydrocarbons, carbon monoxide, among others. European emission standards define acceptable limits for exhaust emissions of new vehicles. The current standard stage (namely, Euro 5) impose the availability of "sulfur-free" diesel and gasoline fuels, with sulfur levels < 10 ppm from 2009 [3].

The raise awareness of the impact of environmental pollution by cars shifted responsibility for control of pollutants also to the side of the oil refining industry. Thus, the set of Hydrotreating (HDT) processes represents the main issues for this sector. HDT process consists in treating oil feedstock in order to remove undesirable elements such as sulfur (called hydrodesulfurization process, HDS) or nitrogen (hydrodenitrogenation, HDN). In crude oil, sulfur is found in many different forms, namely, thiol, thiophene and benzothiophenic compounds. Beyond being a source of environment pollution (the combustion products, SO_X, are the origin of acid rain), these compounds poison the catalysts used in latter stages of petroleum refining. Furthermore, the elimination of such impurities is required for the improvement of the properties of the final products issued from refining (color, smell, stability…) and for the valorization of heavy feedstock, resulting in a major economic issue to the oil refining industry.

As any other heterogeneous catalytic process, in HDT, reactants in either gas or liquid phase are catalyzed on the surface of a solid material. On the microscopic level, the heterogeneous catalyzed process proceeds by a series of elementary steps, including the adsorption of reactants on the active surface of the catalyst material, breaking or weakening of adsorbate bonds, adsorbate diffusion and reaction to form products, followed by desorption to regenerate the active site on the surface. The keyword in understanding heterogeneous catalysis is the surface of the catalyst material since the chemical transformations takes place there. The properties of active surface sites depend among others on the type and number of surrounding atoms at the surface, the supporting material and the presence of

reactants and products. The reactivity of an heterogeneous catalyst scales directly with the number of exposed active sites on the surface, usually, these active sites are nanometer-sized particles onto highly porous oxide supports with high surface area (typically, 100-500 m^2/g). Often, the actual size and shape of the nanoparticles also determine the reactivity of the materials. This structural complexity of the materials combined with extreme reaction conditions reaching temperatures of several hundred degrees Celsius and pressures up to hundred bars are factors limiting the possibility of achieving a detailed structural characterization, explaining why catalyst development has primarily been based on empirical experimentation.

In many respects, heterogeneous catalysts have been treated as black boxes only characterized by their qualities in terms of reactivity, selectivity and stability with a poor understanding of the underlying mechanisms. In order to understand the macroscopic behavior of catalysts it is necessary to focus on the detailed atomic structure and fundamental microscopic processes of catalysis. The ultimate goal of rational catalyst development is to achieve full understanding and control of constituents at the molecular and atomic level. With this ability, it will be possible to construct tailor-made, high-performance catalysts for even highly specialized chemical reactions.

Hydrotreating catalyst, and especially HDS catalyst, is an excellent example of how the emergence of improved *in situ* catalyst characterization tools has led to a dramatic increase in performance. However, the traditional catalyst characterization techniques which have provided this insight seem to have reached a limit in terms of obtaining the desired insight into the atomic-scale structure of HDT catalysts. Due to the very complex atomic composition and structure of the catalysts the challenge to elucidate the fundamental operation-mode of HDT catalysts at the atomic scale presents big issues, once in previous studies important aspects of morphology, atomic-scale structure and position of active sites have only been suggested indirectly, simply due to the lack of appropriate characterization tools. Only by using highly specialized techniques new insights has been attained.

A considerable effort has been aimed at relating fundamental macroscopic properties such as catalyst activity and selectivity to microscopic properties, i.e. catalyst composition, electronic structure and geometric structure. Especially, *in situ* X-ray Absorption Fine Structure (XAFS) studies of the catalysts have given information on the composition, the average local coordination and interatomic distances of individual types of atoms in the catalyst particles. Taking into account the high penetrating power of x-rays used in XAFS, the x-ray absorption spectroscopy (XAS) is a suitable technique to perform *in situ* characterization once high energy x-rays weakly interact with reaction medium; nowadays one say XAS has become a workhorse technique to this kind of study.

With the advent of third generation synchrotron facilities allowing a high time framing in the description of the catalytic reaction, scientists could access to a deep and more accurate temporal description of the chemical species involved in the processes. Dedicated x-ray absorption beamlines worldwide provide

infrastructure and tools for handling catalysts in real and sometimes harsh conditions [4], tracking the relationship existing between the local order around the active element of the catalyst and its catalytic activity. Furthermore, high brilliance third generation synchrotron sources allied to the recent improvements of monochromator and x-rays detection systems have allowed the development of a new time-resolved XAS analysis mode. Quick-EXAFS (QEXAFS) reduces the time acquisition in several orders of magnitude when compared to conventional step-by-step acquisition mode.

Parallel to the development of the atomic-scale probe techniques for catalytic studies, the new specifications for sulfur levels contained in transport fuels imposed by recent legislation in European Union have encouraged scientist to research new routes of preparation for HDS catalysts. Technologically, the preparation of the HDS catalyst is a major issue, and the actual technique has decisive influence on the ultimate performance [5]. Usually, the catalyst support is impregnated with specially selected Mo-oxide compounds and whole range of additives, and subsequently sulfided inside the reactor into the nano-scaled particle structure, the active phase. The actual model for the Mo-based catalyst active phase consists of MoS_2 particles (molybdenite). MoS_2 is a layered compound consisting of S-Mo-S slabs held together by weak van der Waals force. Each slab consists of a tri-layer with two close-packed hexagonal (0001) planes of S atoms and an intermediate plane of Mo atoms, which are coordinated in a trigonal prismatic fashion to the six surroundings S atoms.

Upon adding Co in preparation of the MoS_2-based catalysts, a considerably more efficient catalyst is obtained. Since it has been established that small amounts of Co can dramatically change the reactivity of the catalysts, the Co is considered to be a *promoter* rather than a catalyst in its own right. There is a general agreement on the discussions about the promoted structure and it seems to have converged to the so-called CoMoS model, which was originally proposed by Topsøe, Clausen and coworkers [6].

CoMoS clusters are described as being essentially MoS_2-like, but with additional Co atoms embedded into the MoS_2 lattice at the perimeter of the cluster. It is proposed that Co atoms located at edge positions create new and more reactive sites. The promoting role of Co is, however, still extensively discussed, and the exact location of Co has not been identified [7]. A prerequisite for a thorough elucidation of this seems to be a better understanding of the morphology and atomic-scale structure of CoMoS clusters.

As important as the understanding of active phase structure is the role played by the support on catalytic activity. Since it is responsible in dispersion and stabilization of the active phase, the support may also interact directly with the cluster and this may influence the intrinsic activity of the active site in the Co-Mo-S structure [8]. In this picture, anatase TiO_2 was proposed recently to be a relevant support for HDS catalysts. Despite lower surface area of anatase compared to that of widest-used alumina γ-Al_2O_3, TiO_2-supported non-promoted MoS_2 catalysts were found to yield higher HDS activity than alumina-supported catalysts with an equivalent molybdenum loading per square nanometer [9]. However, for the

promoted system, the synergetic effect of cobalt and molybdenum is less efficient on TiO_2 than on alumina, and support interaction may be one reason for this behavior [10].

The catalytic properties of a material are determined by its composition and structure. These properties then define its physical and electronic structure. It is clear that both the physical and electronic properties may change when the catalyst is in the working state. Thus, the ideal characterization of a catalyst involves measurement of these properties during the catalytic reaction. One goal of catalyst characterization is then to measure these properties as the catalyst works and to relate these properties to the catalytic activity and selectivity. If these properties are measured, and their relationship with catalytic activity is understood, then knowledge will be obtained that should allow the researcher to design these properties into the catalyst. In other words, if the structure of the working catalyst is probed by using some physical or chemical technique and some physical property of the catalyst is found to change or scale directly with catalyst performance, then insight is gained about the active site. The next step then is to understand that specific physical property, and the factors that control it. Once these pieces of information are known, it should then be possible to design the desired properties into the material, and thereby develop an improved version of the catalyst, a new catalyst for a new process, or whatever the research objective calls for.

It is clear that the present picture of the working HDS catalyst is incomplete and that a gap exists between the insights obtained with the traditional catalyst characterization tools and the atomic-scale information essential for a deeper understanding. This twofold thesis is inserted in this picture, firstly, to get new insights in how different preparation routes may reflect in catalytic activity and, especially, how the distinct atomic-scale structures reflect in the catalytic performance for equivalents catalysts prepared by different routes. For that, we propose in this work a new one-pot sol-gel preparation route for CoMo-based catalysts supported on TiO_2 anatase. Furthermore, the major interest in our study is to take advantage of the dedicated beamline SAMBA, at Synchrotron SOLEIL, to record QEXAFS spectra during activation stage of HDS catalysts in order to get a full and fine description of the sulfuration kinetics at the atomic scale, particularly, to describe deeply the mechanisms that lead to the active phase formation of CoMo-based catalysts. Finally, since these so brand new techniques and dedicated machines give us a huge volume of data, in this study we have worked out a basic further tool as a user-friendly data analysis package in order to provide to the users a fully treated data in a short time-scale. We have applied the so-called *chemometrics* tools, such as Principal Component Analysis (PCA) and Multivariate Curve Resolution with Alternating Least Squares (MCR-ALS) on our *in situ* data provided by XAS experiments.

The Chapter I is dedicated to a presentation of the state-of-the-art in CoMo-based catalysts and its characterization tools. We shall present a review on HDS catalyst family and, particularly, those works in which was used the same techniques to describe its properties that we have used, namely, x-ray

photoelectron spectroscopy (XPS), transmission electron microscopy (TEM), low-energy ion scattering (LEIS) and Raman spectroscopy. We will also give special attention to XAS and *in situ* XAS analysis, since it is the workhorse of this thesis.

A crucial aspect of this work is concerned data treatment. Hence, a dedicated chapter was made in order to review this subject, to present an outline on motivation and application of fundamental *chemometrics* as well as a detailed description of the PCA and MCR-ALS methods, used to treat huge amount of data as the one obtained from time-resoled experiments. This is the topic of Chapter II.

In Chapter III we detail the tools, the techniques and experimental methods used to characterize our catalysts, both the classic techniques as well as synchrotron one. We present the fundamental of XPS, LEIS and XAS spectroscopy and focus the discussion in important aspects for our work. It is also described the routines for MCR-ALS calculation and details on EXAFS analysis of the data.

A scientific article related to the preparation and characterization of high-loaded CoMo-based catalysts supported on titania-TiO_2 entitled "*One-Pot Sol-Gel Preparation for Efficient Cobalt-Molybdenum-Titania Hydrotreating Catalysts*" and published at **ChemCatChem**, *vol. 4 (2012), p. 2112-2120* (DOI: 10.1002/cctc.201200165) is presented. This contribution is fully included in this thesis as a chapter itself, the Chapter IV. Therein are included the preparation routes, the experimental conditions for Raman and XPS spectroscopy, the results for these two techniques and the catalytic test.

Chapter V is devoted to the results of our measurements and to discuss them. It is included on it complementary characterization of the oxide-phase catalytic precursors such as Raman, LEIS and XPS measurements. Further, we present classical (*ex situ*) XAS analysis for dried and calcined oxide-phase, after Temperature Programmed Reduction (TPR) with H_2 and after activation reaction under H_2/H_2S treatment.

Chapter VI contains the calculations and results obtained from MCR-ALS analysis for all *in situ* XAS experiments performed in both series of catalysts.

Finally, on the last chapter we conclude the work and point out the perspectives both on scientific and technical level for basic characterization and structural study of the new one-pot sol-gel route of preparation of CoMo-based HDS catalysts

References

[1] U.S. Energy Information Administration, "International Energy Outlook 2013," July 2013. [Online]. Available: http://www.eia.gov/forecasts/ieo/pdf/0484(2013).pdf. [Accessed March 2014].

[2] E. Commission, "Road transport: Reducing CO2 emissions from vehicles," [Online]. Available: http://ec.europa.eu/clima/policies/transport/vehicles/index_en.htm. [Accessed March 2014].

[3] DieselNet, "Emissions Standards, European Union: Cars and light trucks," July 2013. [Online]. Available: http://www.dieselnet.com/standards/eu/ld.php. [Accessed March 2014].

[4] J. D. Grunwald and A. I. Frenkel, "Synchrotron Studies of Catalysts: From XAFS to QEXQFS and Beyond," *Synchrotron Radiation News*, vol. 22, pp. 2-4, 2009.

[5] D. D. Whitehurst, T. Isoda and I. Mochida, "Present State of the Art and Future Challegens in the Hydrodesulfuruzation of Polyaromatic Sulfur Compounds," *Advances in Catalysis*, vol. 42, p. 345, 1998.

[6] H. Topsøe, B. S. Clausen, R. Candia, C. Wivel and S. Mørup, "In situ Mössbauer emission spectroscopy studies of unsupported and supported sulfided Co-Mo hydrodesulfurization catalysts: evidences for and nature of a Co-Mo-S phase," *Journal of Catalysis*, vol. 68, p. 433, 1981.

[7] J. Lauritsen, S. Helveg, E. Lægsgaard, I. Stensgaard, B. Clausen, H. Topsøe and F. Basenbacher, "Atomic-Scale Structure of Co–Mo–S Nanoclusters in Hydrotreating Catalysts," *Journal of Catalysis*, vol. 197, no. 1, pp. 1-5, 2001.

[8] H. Topsøe, B. S. Clausen and F. E. Massoth, Hydrotreating Catalysis - Science and Technology, vol. 11, M. B. J. R. Anderson, Ed., Berlin, 1996.

[9] J. Ramirez, S. Fuentes, G. Diaz, M. Vrinat, M. Breysse and M. Lacroix, *Applied Catalysis*, vol. 52, p. 211, 1989.

[10] D. Costa, C. Arrouvel, M. Breysse, H. Toulhoat and P. Raybaud, "Edge wetting effects of γ-Al2O3 and anatase-TiO2 supports by MoS2 and CoMoS active phases: a DFT study," *Journal of Ccatalysis*, vol. 246, pp. 325-343, 2007.

Chapter I: Review of Literature

Table of Contents

Hydrotreating refers to a variety of catalytic hydrogenation processes which saturate unsaturated hydrocarbons and remove S, N, O and metals from different petroleum streams in a refinery. These processes represent some of the most important catalytic processes, being responsible for a big fraction of the total world market for catalysts.

Historically, hydrotreating processes have developed from cracking and hydrogenation processes introduced in the 1930. Before it, the Nobel-prize French scientist Paul Sabatier discovered the fixation of hydrogen on hydrocarbon double bonds using nickel containing catalysts. Later, BASF researches in Germany identified transition metal sulphides as catalysts for coal hydro-liquefaction and since 1924 one used molybdenum sulphide in process, they realized that active catalysts could be prepared from natural ores molybdenites (MoS_2) and wolframites (WS_2), which were then regarded as strategic materials. Then, after Second World War, hydrotreatment processes involving mixed molybdenum and cobalt sulphides supported on alumina were developed in USA. The discovery of the promoter effects of Co or Ni when added to MoS_2 or WS_2 can be credited to exploratory research by the oil refining industry [1]. Since that time, the refining industry has utilized this combination of sulphides and has developed new associations of supported sulphides for more specific applications. For a long time, the most important hydrotreating reaction has been the removal of sulfur from fuel fractions. Consequently, hydrotreating catalysts are also commonly referred to as hydrodesulfurization catalysts.

Up to the middle of the 1970's the hydrotreating processes were considered as relatively primitive. The catalysts used were not very elaborate. At that time there was just progress for dispersion of the active species and the porosity design in particular. One decade later, it became part of the awareness by scientists that the catalytic science which would have to show its innovative ability. Therefore, it started to rise greater concern on discovering new catalysts, on precise analysis of the reaction mechanism and on the developing novel and more adequate kinetic models.

Later, in the beginning of the 1980's, the role played by promoters elements started to be clarified regardless of the synergy effect on HDS activity has been known for some years before. It was to Pecoraro and Chianelli [2] the credit for having published the first careful systematic and almost exhaustive comparison of unsupported Transition Metal Sulphide (TMS) catalysts for their activity in the hydrodesulfurization of dibenzothiophene, a model of reaction relevant for the HDS of gas oils or even heavier feedstock, which are key processes for producing clean fuels from petroleum. Various theories or hypotheses were proposed in order to explain it [3]. Mainly two of them were subject of large debate in the literature: (i) the remote control theory [4] in which it is assumed that the phase made of sulfided promoter is necessary to produce spillover hydrogen which then migrates to the MoS_2 (or WS_2) phase where it can react with the organic substrate or create new catalytic centers; (ii) the model based on the so-called mixed CoMoS (or NiMoS) phase, first proposed by Ratnasamy and Silvanskar [5], and with first experimental evidences found by Topsøe and coworkers [6] [7]. Although neither of the two

theories has succeeded in convincing the scientific community up to now, the later has attracted more and more supporters nowadays, for that we will discuss it later in a specific topic.

Remote control theory is based on the proposal that the activity and selectivity of the optimized solid are related to the presence of two distinct phases, and that a contact synergy between these two separate phases occurs during catalytic reaction. A remote control of the active phase located on the hexagonal MoS_2 crystallite is exerted by the second phase (Co_9S_8) which is able to activate hydrogen. The activating hydrogen solid, called donor phase produces hydrogen 'H_{SO}' that 'spills over' onto the acceptor. The main role of this activated hydrogen is not to participate directly to the hydrogenation (HYD) reaction, but to create or modify the catalytic active site. The spilled over hydrogen then partially reduces the molybdenum sulphide phase (Figure I.1). This theory was supported by XPS measurements of non-supported Co-Mo catalysts that showed that the maximum of the catalytic activity corresponded to the decrease of the oxidation state of the Mo species. It was interpreted as to be that the binding energy of the Mo corresponds to a lower value of the Mo^{+4} cation, as reviewed by Grange and Vanhaeren [8]. The remote control theory assumes that, depending on the reduction state of the molybdenum cation, two kinds of activated species are promoted by fine-tuning of the coordination state of the acceptor phase. If sulfur atoms are removed, a triple unsaturated coordination site (CUS) is created which is a HYD center. Upon more sever reduction, a MoSH group neighboring the triple unsaturated atom is created. This center could be responsible for the HDS activity.

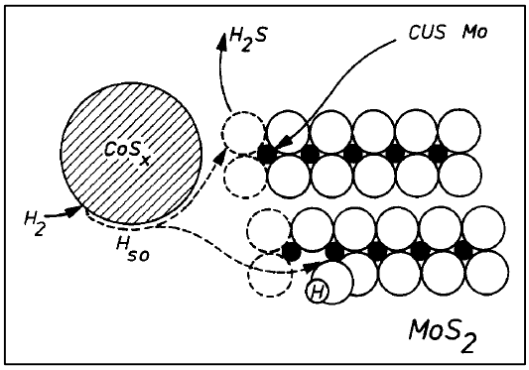

Figure I.1 - Schematic representation of the remote control model: formation of hydrogenation centers (CUS Mo) and of hydrogenolysis carbon-heteroatom bands (MoSH neighboring a CUS Mo) by action of hydrogen spillover (H_{SO} on the edges of MoS_2 *[8]*.

Nevertheless, one may advance that the CoMoS model was based on a specific Co-signal in a Mössbauer Emission Spectroscopy (MES) experiment attributed to CoMoS phase and a linear correlation between the amount of Co in this so-postulated CoMoS phase and thiophene HDS activity. However, Crajé *et al* [9] [10] showed that the same Co-signal in MES could be observed in Co/C and Co/Al_2O_3 systems and that there is no simple relationship between MES signal and HDS activity, thus this Mössbauer signal is not necessarily caused by the presence of a unique CoMoS phase. However, again, despite of all these

discussions, recent experimental and theoretical studies have pointed to an actual CoMoS phase and so, there is a general agreement on the CoMoS phase being the active phase for HDS catalysts.

A combination of the two models, the remote control theory and CoMoS 'theory', was also proposed to explain the gain in activity obtained by mixing for instance Co_9S_8 with a NiMoS sample [11]. The mixed phase model was interpreted as an illustration of the Sabatier principle by supposing that the promoter donate electrons to the main constituent and leads to a weakening of the metal-sulfur bond down to the optimum required for the HDS activity [12]. This interpretation was recently updated on the basis of *ab initio* calculations using the Density Functional Theory (DFT) and a new metal-sulfur bond energy model was proposed [13]. In fact, DFT *ab initio* calculated chemical descriptors directly linked to intrinsic properties of catalysts came to clarify the origin of volcano curves, which are usually used to correlate catalytic activity with intrinsic properties of catalysts such as its ability to form chemical bonds with reactants, products or intermediates.

Together with these studies, a greater attention begun to be pointed out to the molecular-scale reactivity and structure of active phase [14]. It became clear that the identification of the active phase through different physico-chemical techniques, the proposal of a model aiming at correlating all the experimental data and in some cases to predict new and unexpected behaviors, and a better understanding of the dynamics of the modification of the catalysts on-stream are some key parameters to improve the catalyst.

As regards heterogeneous catalysis, nowadays Sabatier's first principle formulation may be phrased as follows: for a target reaction, the optimal solid catalyst should provide a surface interacting neither too weakly nor too strongly with the reaction partners on the rate determining step [15]. If the interaction is too weak, the reactants may be not activated. If it is too strong, the surface is blocked (poisoned). Among the vast number of potential active TMS phases explored so far, the so-called Co(Ni)MoS and NiWS mixed phases were empirically found to be the most active or at least the ones with the more reasonable costs of the constitutive metallic elements. Industrially, this active phase is supported on high specific surface area porous materials in order to increase their dispersion and the number of exposed active sites.

TMS catalysts are used because of their ability to perform a myriad of important reactions in the presence of sulfur and because they remain stable. The second and third row TMS such as RuS_2 and Rh_2S_3 are the most active and stable TMS catalysts. They are, however, very expensive and as a result have not found wide commercial application, though still retaining a great potential. Because of the cost and scarcity of the noble metals Mo and W based catalysts are preferred and used in every refinery in the world for hydrotreating reactions involving hydrogenation (HYD), sulfur (HDS) and nitrogen (HDN) removal to meet environmental standards. When the promoter metal (Co or Ni) is in a optimal ratio with respect to the base metal (W or Mo) a significant increase in activity is achieved. The increase in activity varies according to details of preparation, materials and other factors, but generally can vary up to factors

of 10 to 12 times the un-promoted activity. This is called the *synergic effect* implying that the two components, promoter and base metal act together.

Several explanations have been proposed to explain the origin of the *synergic effect*, as discussed early. But the fact is that in view of the Sabatier's principle and its representation in a volcano curve could be improved by DFT calculations to predict (or confirm) the optimal synergy effect for CoMoS HDS catalyst. The experimental result for mixed CoMoS reported by Chianelli *et al.* [16] falls exactly on the maximum of volcano curve when the average energy descriptor (energy per metal-sulfur bond) between Co_9S_8 and MoS_2 is assigned to this synergetic ternary [17].

Fifty years ago, researchers in catalysis had very limited access to atomic-scale information about the state of the catalysts while the catalysis was taking place. This situation was related to the fact that very few techniques were available at the time that both allowed studies of the catalyst under reaction conditions and at the same time could provide detailed chemical and structural information. Thus, the reactor itself was often treated as a "black box" and catalysis research was largely built on post-mortem *ex situ* analysis of the catalysts and deductions based on different types of separate kinetic experiments. This gave ample room for interpretations and speculations, which often led to situations where many conflicting models were proposed for the same reaction over the same catalyst. A key problem was the lack of surface-sensitive techniques that could provide spectroscopic information at pressures relevant to the catalysis. Another problem was the difficulty of providing detailed structural insight into the complex nanostructures often present in heterogeneous catalysts. The many advances which occurred in surface science did not solve these problems, since surface science experiments were typically performed on single-crystal materials and under ultrahigh-vacuum (UHV) conditions. These difficulties have been termed the "materials gap" and the "pressure gap" in catalysis and significant efforts have been devoted to bridging these gaps.

The situation in catalyst characterization has changed dramatically and today researchers have a large variety of techniques available that may provide detailed atomic-scale structural and chemical insight into complex heterogeneous catalysts exposed to controlled environments. This type of investigations have been termed in situ studies. The term *in situ* is used very broadly and may have many different meanings. It has, for example, been used to describe studies of individual adsorption/desorption processes, studies of catalysts in a controlled environment after quenching of the reaction, or studies performed during catalysis under high pressure. In order to highlight the last type of *in situ* studies, they have been termed *in situ* on-line catalysis studies or *operando* studies. It is evident that such *operando* studies are especially important since they provide direct insight into the active state of a catalyst. Nevertheless, many other types of *in situ* experiments may provide very important insights. Some major developments have been the introduction of in situ methodologies for performing infrared spectroscopy,

Raman spectroscopy, X-ray diffraction, X-ray absorption spectroscopy, Mössbauer spectroscopy, nuclear magnetic resonance, and high-resolution electron microscopy (see, e.g., [18] [19] [20]).

X-ray diffraction (XRD) is the most widely used technique for obtaining structural information in catalysis research [20]. Beside the normal angle-dispersive mode, the energy-dispersive mode (EDXRD) can also be used and this mode has certain advantages for characterizing small particles and *in situ* studies. It is, however, important to note that XRD is not sensitive to structures where the length scale is less than about 2 nm. This presents a serious limitation since one of the goals in heterogeneous catalysis research often lies in the preparation of highly dispersed nanostructures with dimensions less than this value. Thus, one of the important developments in the past 50 years was the use of extended X-ray absorption fine structure (EXAFS), which unlike XRD does not require long-range order and can provide local structural insight (interatomic distances and coordination numbers) into complex nanostructures in heterogeneous catalysts. EXAFS has become the key technique for providing *in situ* structural insight into nanostructures in heterogeneous catalysts, the local structural information from EXAFS, however, does not allow direct determination of the 3D structure. Thus, many details of the structure of heterogeneous catalysts have remained ambiguous.

For heterogeneous catalysts, it is difficult to apply STM or other scanning probe techniques and high-resolution transmission electron microscopy (HRTEM) is the preferred technique. However, it is not trivial to perform such measurements *in situ*, since the gas at high pressure will interact with the electrons and decrease the possibility of achieving high-resolution images. In 1972, Baker and Harris [21] pioneered *in situ* microscopy and they achieved a resolution of about 2 nm. This allowed in subsequent studies the observation of many phenomena of importance to catalysis. A significant advance was made five years ago by Gai and Boyes, who demonstrated a resolution of about 0.23 nm [22]. However, in order to get detailed structural information on important metals in heterogeneous catalysis like Fe, Cu, and Ni, a resolution of at least 0.18 nm is required. Recently, this goal was reached [23]. Specifically, some year ago, it was demonstrated that it is possible to use *in situ* HTREM to resolve 0.14-nm lattice fringes, while the catalyst was exposed to reaction gases at elevated temperatures [23].

In catalysis research, it is often difficult to establish whether adsorbed species are reaction intermediates involved in the catalytic reaction or whether they are just spectator species occupying sites on the surface. Heterogeneous catalysts are nonequilibrium solids and their structures depend critically on the choice of preparation and activation parameters. *In situ* studies can be advantageously used to obtain information about such parameters.

Hydrodesulfurization catalysts have been, especially in the period preceding the mid-1980s, one of the most controversial group of catalysts (see, e.g., [3], [19]). In retrospect, the controversies can be related to the lack of adequate in situ characterization tools that could provide insight into the very complex structures under relevant sulfiding conditions. The catalytic behavior of Co-Mo/Al_2O_3 catalysts may be

very complex (Figure I.2) and catalysts with similar overall composition may exhibit very different promotional behaviors. Beside the models proposed to explain such behaviors and the origin of promotion, they remained speculative in the absence of direct *in situ* insight. By performing quantitative in situ MES phase analysis of many catalysts with different activities, it was revealed that the HDS activity is dominated by the fraction of the promoter atoms present in a structure called Co–Mo–S (Figure I.2). Thus, the *in situ* insight allows the establishment of important fundamental structure–activity relationships.

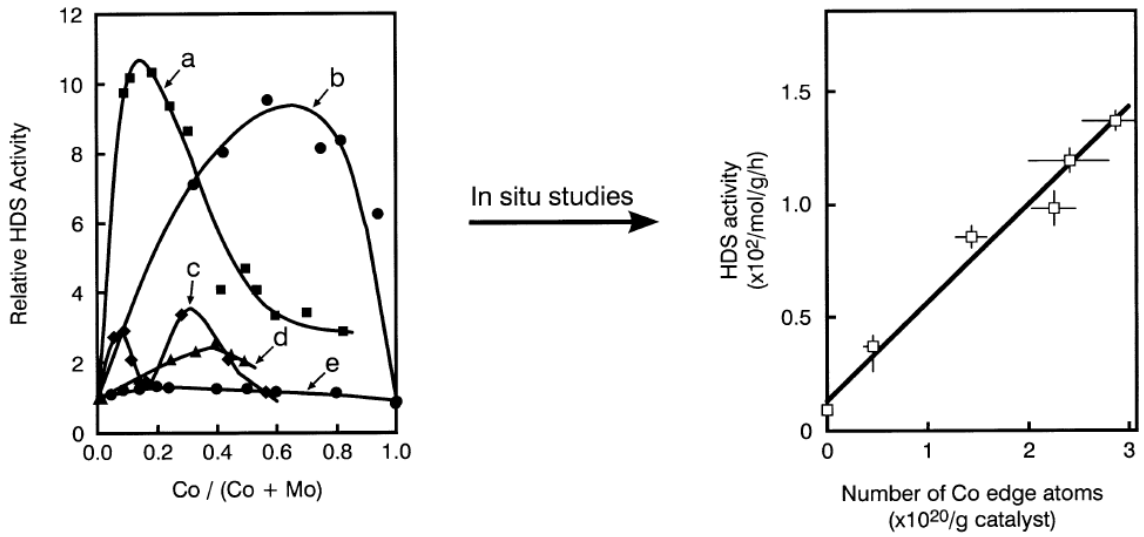

Figure I.2 - Illustration of the complex promotional behaviors encountered in Co–Mo/Al_2O_3 hydrodesulfurization catalysts (left panel) and the simple fundamental structure-activity relationships (right panel) which have resulted from the *in situ* studies (adapted from *[3]* and *[7]*)

Furthermore, the *in situ* studies revealed that the reason why catalysts with similar overall composition may have very different catalytic activities is related to the fact that not all the promoter atoms after activation may end up in the desired Co–Mo–S structures. In fact, the phase composition of such catalysts is very dependent on the choice of preparation and activation parameters and the in situ studies have allowed detailed insight into these very important parameters.

The *in situ* insight into the nature of the active structures and the preparation parameters leading to their formation has had a large impact on the developments of improved industrial hydrotreating catalysts [24]. Before the application of such techniques, catalyst developments in this field were done mainly by trial-and-error approaches and around 1980, the catalyst manufacturers and the refining industry regarded these catalysts as nearly optimized (Figure I.3). This has turned out not to be the case; the fundamental insight obtained from the application of *in situ* techniques has resulted in several novel molecular design strategies and many improved catalysts have been introduced to the industry (Figure I.3).

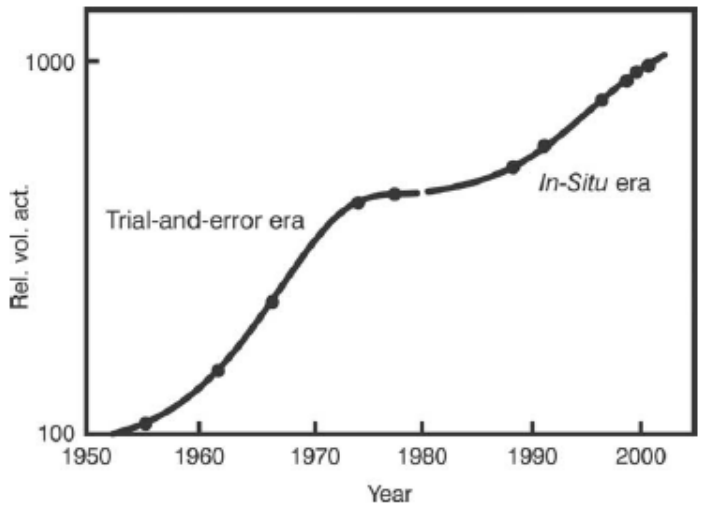

Figure I.3 - Developments in the catalytic activity of industrial HDS catalysts during the past 50 years. The figure illustrates how the in situ insight has resulted in improved catalysts based on new molecular design strategies (from *[24]*).

The *in situ* studies show that the catalytic activity is related to the presence of the Co–Mo–S edge structures in promoted catalysts and to the MoS_2 edge structures in unpromoted catalysts. In order to understand why these structure are important, more detailed atomic-scale insight into the structures has been sought after. This has been difficult to obtain experimentally since, for example, the important in situ structural technique EXAFS does not provide a unique 3D structure. In fact this limitation has led to different interpretations and proposals for the detailed structure of the Co–Mo–S and MoS2 nanoclusters (see, e.g., [3] [25]).

By the discussion above we like to stress and illustrate how the introduction of *in situ* techniques and *operando* studies has completely revolutionized research in heterogeneous catalysis. Over a few decades, we have seen a change from a situation where virtually no direct insight was available for the active catalysts to a situation today where a large variety of techniques may provide fundamental atomic-scale information under relevant conditions. The fact that the *in situ* insight can be obtained for complex heterogeneous catalyst systems under reaction conditions (i.e., operando studies) is very important since it has facilitated the establishment of direct links to the catalysis. *Operando* studies with simultaneous recording of catalytic activities have been especially useful in this connection.

Furthermore, in order to understand deeply catalysis, it is desirable to employ a combination of several *in situ* techniques and, in addition, to combine these studies with theoretical calculations as well as surface science experiments on model systems [26]. In view of the rapid advancement occurring in these fields, multidisciplinary approaches are expected to play an increasingly important role in the future.

1. On the Active Phase: from MoS_2 to CoMoS Model

In heterogeneous catalysis, the special properties of the surface atoms facilitate conversion of reactants into products at active surface sites. The properties of the active surface sites depend among others on the type and number of the surrounding atoms at the surface, the supporting material and the presence of reactants and products. A detailed description of the nanoparticle structure and reactivity is therefore of outmost importance in order to establish rational catalyst design strategies.

Although nanoparticles may be in some cases synthesized with predefined shapes and hence surface sites, there is no guarantee that the as-synthesized nanoparticles remain stable when subjected to the reaction conditions. The realization that the catalyst surface structures and therefore catalytic properties depend on the reaction conditions has spurred a tremendous interest in obtaining atomic-scale information about the structural and chemical state of catalysts during exposure to reaction conditions. The development of new experimental techniques combined with miniaturized reactors for the study of supported nanoparticle catalysts under *in situ* and *operando* conditions has resulted in a significant improvement of the fundamental understanding of the influence of particle size, particle shape, alloying, and aggregation on the activity, selectivity, and deactivation of the catalysts. The main drivers for the improved understanding are new experimental advancements in the fields of e.g. electron microscopy, X-ray and, synchrotron-based techniques as well as optical spectroscopy in combination with activity measurements.

Despite of the enormous amount of research, the structure of the active phase has been a matter of great debate. Although the presence of MoS_2 slabs has been generally accepted, the function and location of the promoter atoms (such as Co) are the main issues. A considerable effort has been aimed at relating fundamental macroscopic properties such as catalytic activity and selectivity to microscopic activities, i.e., catalytic composition, electronic structure and geometric structure. Especially, *in-situ* extended x-ray absorption fine-structure spectroscopy (EXAFS) studies of the catalysts have given information on the composition, the average local coordination and interatomic distances of individual types of atoms in the catalyst particles. As a starting point to understand the structure, *unpromoted* MoS_2 clusters are normally considered the initial guess for models of the catalyst. Therefore, on the next topics, we review works that finely describe the structure of promoted/unpromoted or supported/unsupported active phase.

1.1. Unpromoted Structure and Reactivity

Molybdenum-based HDT catalysts possess an active phase constituted by molybdenum disulfide. This phase is formed in the activation stage that transforms the initial oxide into a sulfide, MoS_2.

MoS_2 is a layered compound consisting of S–Mo–S slabs held together by weak van der Waals forces. The Mo-S bonds are strong, but the interaction between the sulfur atoms at the top and bottom of separate sandwich-like tri-layers is weak. A unit cell of MoS_2 is illustrated in Figure I.*4*(a)-(b). Each slab consists of a tri-layer with two close-packed hexagonal (0001) planes of S atoms and an intermediary hexagonal plane of Mo atoms, which are coordinated in a trigonal prismatic fashion to the six surrounding S atoms. In nature, pure MoS_2 (molybdenite) is normally encountered as the allotrope 2H-MoS_2 [27], which is a lamellar compound with the unit cell containing two S–Mo–S slabs stacked in an alternating fashion as illustrated in Figure I.*4*(c).

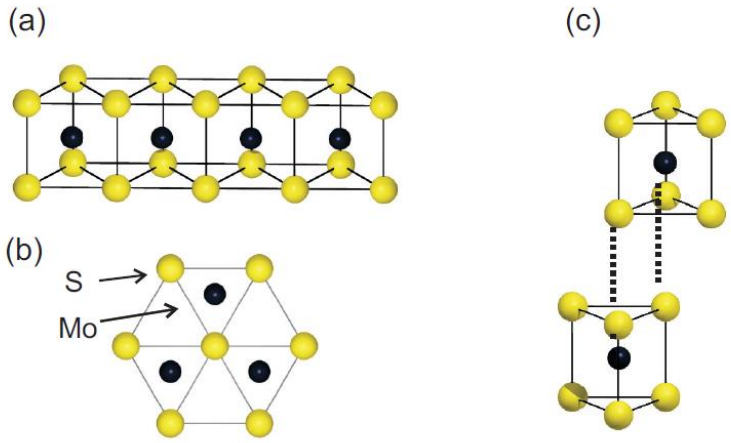

Figure I.4 - The crystal structure of MoS_2. (a) Side view of a single layer S–Mo–S slab of MoS_2. The Mo atoms (dark) are coordinated to six sulfur (yellow), in a trigonal prismatic coordination. (b) Within each layer, the S lattice (and Mo) is hexagonally arranged with in-plane interatomic distances $d_{S\text{-}S}$ or $d_{Mo\text{-}Mo}$ equal to 3.15 Å *[35]*. (c) Illustration of 2H-MoS_2 stacking sequence of successive layers in bulk MoS_2. The distance between the Mo layers is 6.15 Å.

In the catalysts, the MoS_2 crystallites are believed to grow as slabs with relatively large dimensions parallel to the (0111) basal plane compared to the height perpendicular to the basal plane [3]. The traditional catalyst consists primarily of non-stacked two-dimensional (i.e. single-layer) structures. Stacked crystallites structures are however, also observed in the catalysts at elevated sulfidation temperatures. These MoS_2 nanolayers can be viewed as single sheet of finite size (around 30-40 Å) dispersed over the surface of the support. The precise characterization of this phase raises crucial questions and has been subject of numerous studies in order to draw comparisons with the promoted systems.

When attempting to construct a simple molecular model for MoS_2 single sheet of finite size from the bulk MoS_2, the first question concerns the nature of the atomic edges terminating the MoS_2 sheet and which are stable under HDT conditions. Based on the crystallographic rules, an infinite number of edges driven by the crystallographic orientations can be present. In practice, two energetically competing edges are stable, as it will be discussed soon.

Concerning the reactivity of this active phase, it has been realized that basal plane of MoS_2 is catalytically very inactive, and hence that the activity in the HDS process is somehow associated with the edge terminating the clusters [3]. A popular model of the reactivity of this catalyst considers the differential reactivity of distinct exposed planes toward reactants, the so-called “rim-edge” model proposed by Daage and Chianelli [29]. They used chemical etching of microcrystals to create new catalytic sites, which are responsible for the DBT (dibenzothiophene) hydrogenation reaction. Average stacking heights of poorly crystalline MoS_2 powders were estimated by X-ray crystallography and for the first time correlated with the selectivity of the catalyst for hydrogenation versus HDS (hydrodesulfurization). They developed a simple two-site physical model where the catalyst particle were described as a stack of several discs. However, the two site were distinguished by their location on the edge. One site exists at the edge of exterior layers with adjacent basal planes exposed to the reacting environment. These are the “rim sites” on which both hydrogenation and desulfurization occur. The second site occurs on the interior layers that have no exposed basal plane surfaces, the discs "sandwiched" between the top and bottom discs. These are “edge sites” and only the desulfurization reaction occurs on them (Figure I.5).

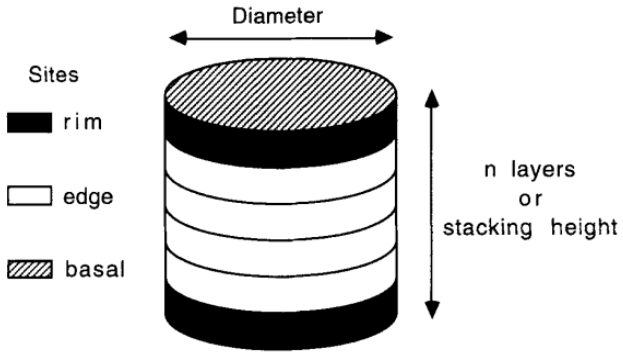

Figure I.5 - The "rim-edge" model **Source spécifiée non valide.**.

At a local point of view, coordinatively unsaturated sites along the edges of the catalyst particles are believed to provide the active sites, where molecules can adsorb and undergo further reaction. Since the morphology of the cluster ultimately determines the nature of the exposed edge, the shape is a very important aspect in understanding the reactivity of the catalysts. However, due to the amorphous and non-planar nature of the supports used in catalysis and the small size of the clusters, a detailed characterization is beyond the reach of some basic techniques, such as High Resolution Transmission Electron Microscopy (HRTEM) [30]. Hence, little knowledge of the detailed cluster morphology exists.

In early structural studies, there was no direct observation of the MoS_2 structures and it was typically assumed that the edge structures of MoS_2 were similar to those expected from cleaving a bulk MoS_2 crystal, i.e. a molybdenum edge, or Mo $(10\bar{1}0)$, and S $(\bar{1}010)$-edge, the sulfur edge (Figure I.6). For many years it was difficult to test this assumption, but after DFT [31] calculations and *in-situ* Scanning

Tunneling Microscopy (STM) [32] studies, it has been possible to observe directly the nanostructures and reveal how the important edges differs dramatically from an expected bulk structure. The studies showed that the shape of the catalyst pellets might be a dynamical function of the reaction conditions. It means that the 2D-morphology may fluctuate between a triangle, a hexagon or a deformed hexagon depending on the relative energy of the two edges. At same time, the (001) basal plane, capping the two-dimensional structures, is also stabilized. This plane is generated by "cutting" the van der Waals interactions ensuring the cohesion of the stacked layers in the bulk structure.

Nevertheless, it must be realized that the typical conditions of the STM experiments (also in the DFT calculation) are very different regarding pressure and temperature from those encountered in industry or in other *in-situ* or *operando* experiments. Indeed, technical issues in STM and computational costs in DFT are critic. Therefore, the major of relevant studies using these two techniques are performed, for instance, in systems that have either a weak influence (gold supported catalysts) or no influence of the support, so we can say they work with model catalysts. Thus, it has remained to be addressed whether information from the model studies indeed can be related to the industrial catalysts. This problem has been referred to as "the materials gap" in the field of catalysis.

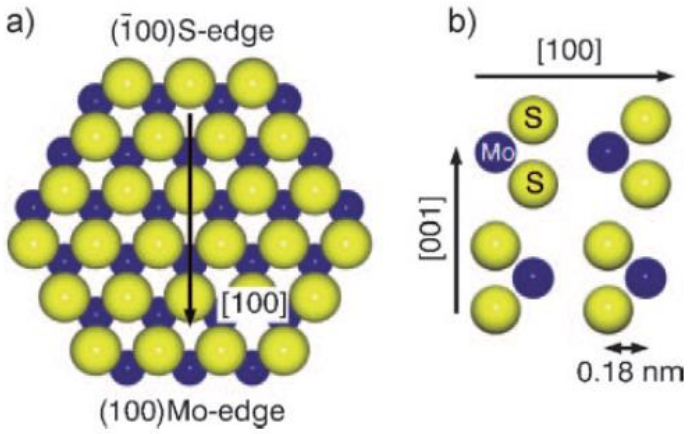

Figure I.6 - (a) A ball model of single-layer MoS_2 nanocrystal viewed along (001) projection. The hexagonally arranged Mo atoms (blue balls) are trigonal prismatically coordinated to S atoms (yellow balls) in two adjacent layers. The bulk-truncated nanocrystal exposes a Mo- and S-edge termination. (b) The 2H stacking sequence of two successive, single-layer MoS_2 slabs viewed along the <110> direction. The Mo planes are separated by 0.615 nm along the [001] direction and are rotated and translated so in-plane positions of S atoms in one layer coincide with the positions of the Mo atoms in the other layer and vice versa. The projected distance between neighboring Mo and S columns in a single layer along the <100> direction is 0.18 nm (from *[33]*).

On the efforts to get insights into morphology of supported MoS_2 structures, many structures have been considered [3], but most models have assumed hexagonal geometry. At this point, it is interesting to note that the first theoretical study of the 2D-morphology effects of MoS_2-based catalysts was provided by S. Kasztelan *et al.* [34] in the mid-80s, resulting in to so called "Geometrical Model". They showed

that the proportion of edges sites (over the total Mo atoms) is directly connected to the morphology of the MoS_2 nanoparticles, and it exhibits a maximum for triangles and hexagons Figure I.*7*. In addition, the position of this maximum also depends on the morphology.

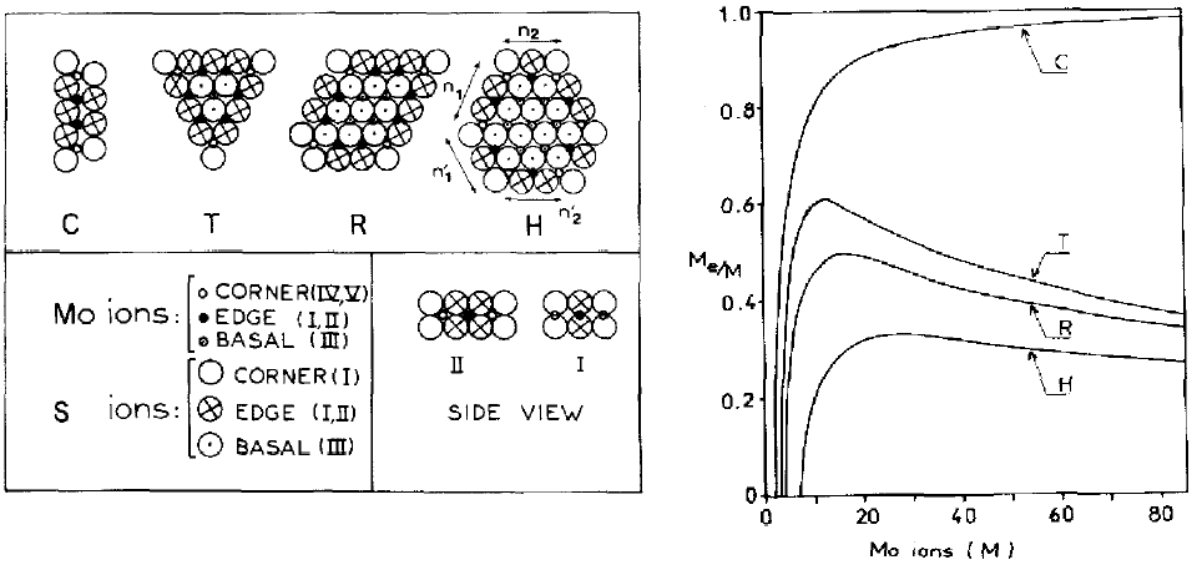

Figure I.7 - The geometrical model. Effect of the 2D-shape and size of MoS_2 nanocrystallites on the ratio of edge metal atoms (M_{edge})/total metal (M) atoms. C = chain like model, T = triangle, R = rhombohedron, H = hexagon or deformed hexagon *[34]*.

Early DFT calculations [31] for pure MoS_2 with 0.1-1 nm in diameter pointed out a strong tendency for Mo-terminated edges in active phase, while for CoMoS systems S-terminated edges are exposed because vacancies are easily formed on the latter. Based on the insight that DFT calculations have provided [35], one is able to predict how structures may change with changes in composition of the gas.

Recent advances in technology of microscopy have helped to elucidate morphology aspects of industrial-style MoS_2 nanocatalysts, particularly, crystallographic information on the edge structure [36]. By High Resolution (Scanning) Transmission Electron Microscopy (HRSTEM), images of nanocrystals of wet-impregnated MoS_2 synthesized on a high surface area graphitic support show particles with a slightly truncated triangular shape and a hexagonally arranged spots at the 0.27 nm and 0.16 nm lattice distances, corresponding to the MoS_2 (100) and (110) lattice planes, respectively. From Figure I.*8* we can see atomic arrangement in such a nanocrystal; it is a close-up of a MoS_2 nanoparticle. In this particular kind of image (high-angle annular dark-field, HAADF), it is dominated by the so-called Z-contrast, i.e., bright contrast coincides with atomic column positions and the intensity maxima scales with the total atomic number Z of the column [37].

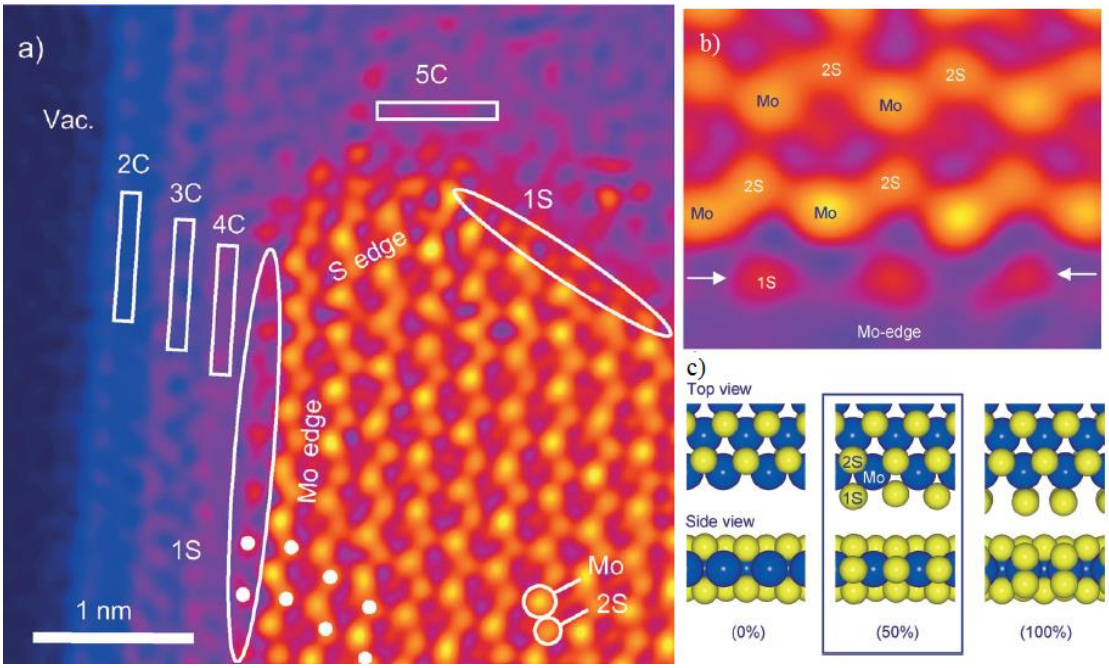

Figure I.8 - a) High Resolution STEM image of a single-layer MoS_2 nanocrystal on a graphite support oriented with the MoS_2 <001> direction along the electron beam. The image is colorized to further improve the visibility of the different intensity levels. White dots superimposed the image denotes sulfur sublattice position of the MoS_2 basal planes and Mo edge. b) Detailed atomic structure analysis of part of a single-layer nanocrystal such as in (a). The arrows point to single sulfur atoms that terminate the Mo edge as designated by an intensity analysis (from *[36]*). c) Ball models (top and side view, respectively) of different S coverage levels at the Mo edge (0%, 50%, 100%), adapted from *[38]*.

Thus, in Figure I.*8*a it is pointed the intensity levels relative to the vacuum level that can be attributed to a graphite flake with thickness of two (2C), three (3C) and four (4C) layers of carbon. The interior pattern of the MoS_2 consists of a hexagonal arrangement with a separation of 0.18 nm (<001> planes along the electron beam direction) that corresponds to either a single Mo atom (Mo, Z = 42) or two S atoms (2S, Z = 2 x 16). Based on that identification, the longer edges can be assigned as (100) Mo edges and the shorter edges as ($\bar{1}$00) S edges. A close examination along Mo-edge (Figure I.*8*b) indicates that it terminates by single sulfur atoms, which indicates that this edge in the industrial-style catalysts is not just a simple truncation of the bulk MoS_2 structure. Instead, it matches a 50% sulfur covered Mo edge termination structure Figure I.*8*c as predicted by experimental STM and theoretical DFT studies [35] [39] [38].

These results show that is indeed possible to obtain direct atomic structure information about the catalytically important edges of industrially relevant MoS_2 nanocatalysts, which is not available from STM. Moreover, the observed low-indexed are not only consistent with the previous experimental and theoretical model studies but also reveal the presence of corners and kink sites on the hexagonally shaped nanostructures. Although the reactivity of the corners considered in model studies [40], the role of kink sites has not previously been considered. As the kinks represents joints between Mo and S edges with a concave geometry, such sites may provide a favorable bonding geometry to mediate the dual

functionality of the adjacent edges [41] toward a combined hydrogenation and desulfurization reaction step.

The combined STM-DFT studies have also provided important information in the electronic structure of the nanocrystals, which plays a key role in catalysis. Figure I.9 shows that the small sulfided nanocrystal may have unique sites at the edge with a metallic-like character [32]. These spatially localized brim sites differ from the semi-conducting character of the bulk MoS_2 sites and appear due the crystal truncation. Recently, it was found that the metallic-like brim sites are important for HDS reactivity. Combined STM and DFT studies [42] have shown that the brim sites due their metallic character may bind sulfur-containing reactants such as thiophene test molecules. The observation of this key role played by brim sites in catalysis is novel, since sulfur vacancies were previously assumed to be the first step for hydrotreating reactions, thus, the active sites [6]. In fact, this insight was important in the development of new a generation of improved catalysts for the production of clean fuels. The *in-situ* studies of adsorbed intermediates open vast perspective for new types of *in situ* studies giving important insight into the reaction and inhibitions occurring in catalysis. Again, in such studies besides all the gain in approach it needs to be kept in mind that the conditions for the STM studies (both with respect to the substrate and gaseous surrounding) are far away from realistic reaction conditions. And in order to achieve new insights close to realistic conditions an approach by XAFS is the most reliable, flexible and the one that offers conditions to provide structural and reactivity information, for so it must to be considered.

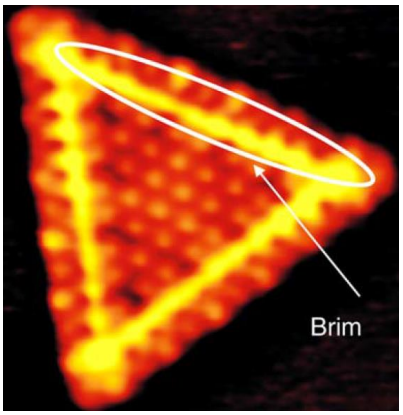

Figure I.9 - A STM image of a single-layer MoS_2 nanocrystal containing sites with metallic-like character, the so-called brim sites at the Mo-edge termination (from *[32]*).

It should be stressed that the STM studies reported so far in literature were performed mostly on Au supported MoS_2 model systems and although Au is expected to be rather inert, it has been questioned whether such triangular structures may also be observed for MoS_2 structures on more industrially relevant supports [43]. Recent microscopy investigations have investigated this issue and shown that the structures in the model catalysts may indeed also be observed in alumina-supported catalysts [26].

1.2. Promoted Catalyst Structure: The CoMoS Model

Upon adding Co in the preparation of the MoS_2-based HDS catalysts, a considerably more reactive catalyst is obtained, typically, one observes more than an order of magnitude higher when compared to unpromoted MoS_2. The origin of the effect of Co in the catalyst has been subject of an extensive debate, a fact that is related to the previously mentioned difficulties in obtaining direct atomic-scale information on the catalyst structure. Since it was established that small amounts of Co could dramatically change the reactivity of the catalysts, the Co is considered to be a *promoter* rather than a catalyst in its own right. In spite of various models have been proposed for the promoted structure, nowadays the enhanced activity has been attributed to the formation of bimetallic sulfided Co-Mo structures [14]. The discussion around this structure converged to the so-called CoMoS model. It should be noted that the Co–Mo–S structures were quite different from those proposed in the many models which existed at the time, and for many years, the Co–Mo–S model remained quite controversial.

At low Co/Mo ratio, Co atoms decorate the edges of MoS_2 nanoparticles, while small Co-sulfide particles are present at high ratios. For commercial catalysts, the Co/Mo ratio lies between the two extreme cases, hence usually a distribution of Co sulfide particles with different particle size and ordering co-exists in the catalyst during operation. Figure I.10 shows that the CoMoS phase is not the only species present on commercial $CoMo/Al_2O_3$ catalysts [3]. The figure point out that besides the active phase, i.e., the CoMoS phase, Co atoms are dissolved in the alumina support; the bulk of the thermodynamically stable cobalt sulfide, Co_9S_8, is also presented and unpromoted MoS_2 particles are likely present, indicating that the characterization of such catalyst is not straightforward.

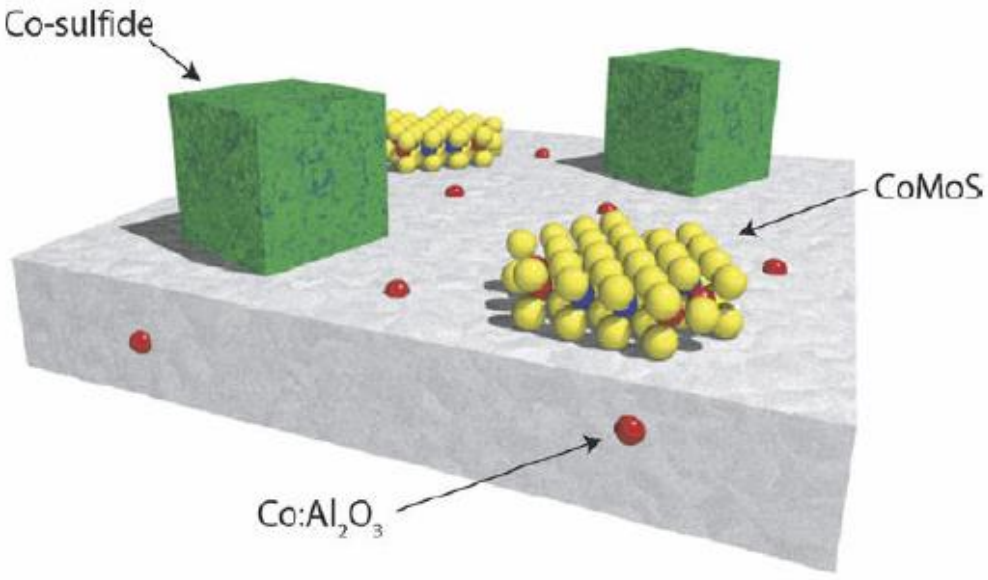

Figure I.10 - Schematic representation of the different phases present in typical alumina-supported catalysts: yellow, blue and red balls represent, respectively, sulfur, molybdenum and cobalt atoms *[51]*.

Of all these phases, only CoMoS structures are associated with an appreciable catalytic activity, and is therefore the structure of prime interest. Kasztelan *et al.* [34] confronted several geometrical models with experimental data to elaborate a geometric model that describes the promoted crystallites structure according to the "CoMoS" phase theory Figure I.11. In this model, promoter atoms substitute molybdenum atoms located on the edge planes.

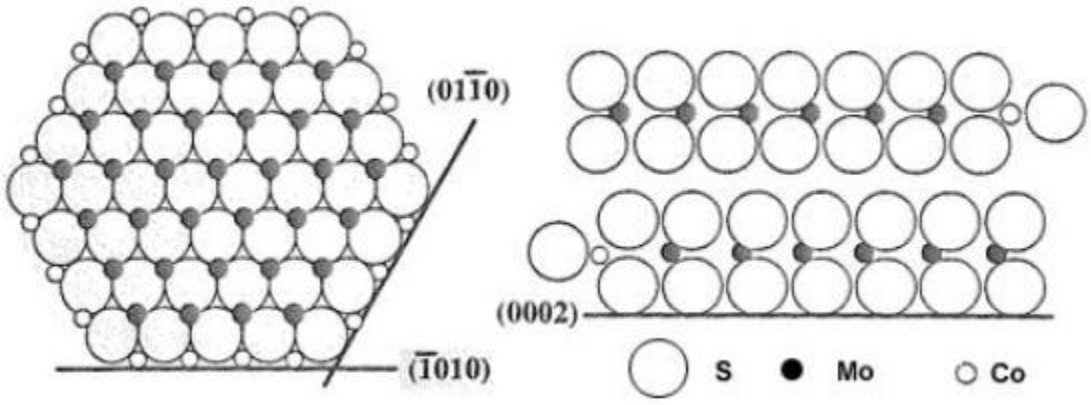

Figure I.11 - Geometric Model for decorated MoS_2 proposed by Kasztelan *et al [34]*.

In fact, there are several possible locations for the Co atoms in the structure: intercalation, pseudo-intercalation (either octahedral or tetrahedral position), bulk substitution, edge substitution, and edge addition were initially investigated by Raybaud *et al.* [45] by DFT, including the effect of the chemical potential on sulfur coverage at the edge. They demonstrated that the most stable models are those where Co (or Ni) substitutes Mo at the S- or Mo-edge. The optimized Co-Mo and Co-S distances for these two most stable configurations are fully compatible with EXAFS analysis.

In bulk MoS_2, which usually serves like a first model for EXAFS treatment of promoted catalysts, each molybdenum in the core of a slab is surrounding by 6 sulfur atoms at 2.42 Å and 6 molybdenum atoms at 3.16 Å. Early studies in promoted catalysts showed that the molybdenum atoms had a coordination number in sulfur around 6 with interatomic distances close to the ones present in crystalline MoS_2. However, the coordination number in molybdenum (regarded the second coordination shell) was smaller in this system. It is noteworthy that an atom on the edge of the slab presents a different corrdination compared to a core atom. As long as EXAFS is a technique that probes the average number among all MoS_2 particles, this decreasing in the molybdenum coordination number regarding the molybdenum, said N(Mo-Mo), may suggest an increasing of the ratio between edge-atoms and core-atoms.

This decreasing of the coordination number may corresponds to smaller MoS_2 crystallites and distant enough from each other neighbor crystallite such that Mo atoms from distinct particles do not influence for the coordination number of another particle. Thus, a decreasing in N(Mo-Mo) may suggest a better dispersion of particles on the support [46] [47].

Early XAS studies on Mo K-edge of CoMo-based catalysts supported on alumina suggested that besides the presence of the promoter the coordination number remains unchanged and near the one from the MoS_2 unpromoted structure; N(Mo-Mo) about 6 [46]. Nevertheless, studies on promoter (Co) K-edge showed the existence of a mixed phase by a second shell pic contribution, a Mo-Co bound of 2.77 Å [48]. This same work attributed a coordination number equals to 5 for Co regarding the sulfur on the first coordination shell and a bound distance *d*(Co-S) equals to 2.23 Å. Furthermore, since the air exposition of a CoMoS catalyst change to lower values this distance and since the first Co coordination shell suggest the presence of oxygen, it seems that Co are placed on the surface or on the edge of the active phase. A summary of some distances found on literature for the promoted active phase of CoMoS catalysts are listed on Table 1.

Table 1 - Main interatomic distances available on literature for CoMo catalysts.

Bound	d_{Mo-S}	d_{Mo-Mo}	d_{Co-S}	d_{Co-Co}	d_{Co-Mo}
Distance (Å)	2.39 - 2.41	3.12 - 3.20	2.18 - 2.33	2.42	2.7 - 2.9
Reference	[53] [54]	[53] [54]	[55]	[56]	[54] [55]

One relevant question concerns the effect of the promoter content on the stability of the edges of the CoMoS nanocrstallite. When considered high chemical potential of the sulfur, Co reveals a similar affinity for both S- and Mo-edge [50]. It suggests that a highly sulfiding regime (high partial pressure H_2S/H_2) tends to stabilize the promoter on both edges. In contrast, the decrease in the partial pressure of H_2S or an increase in temperature enhances the affinity of Co for the S-edge with respect to the Mo-edge. The typical HDS conditions follow this behavior with stability of Co atoms located at the S-edge.

In addition, it was observed a partial promoter decoration of the Mo-edge (corresponding to 50% Co) brings the edge energy close to the S-edge values. For the S-edge value, the 50% Co content becomes energetically more favorable. This result have significant consequences for the morphology and the reactivity of the active sites at the edges of the CoMoS phase.

From a structural point of view, several configurations are possible. For high $p(H_2S)/p(H_2)$, the Mo-edge exhibits 100% Co stabilized with 50 % S (Figure I.*12*a). For low partial pressure, the 50% Co partial occupation with the Mo-edge covered by 25% S is stable. It is remarkable that –Co–Mo–Co–Mo– (Figure I.*12*c) and the paired configuration –Co–Co–Mo–Mo– (Figure I.*12*d) are close in energy. For the S-edge, the most stable structure under HDS conditions, contains 100% Co and 50% S (Figure I.*12*b), where Co atoms are in a tetrahedral environment. In all cases (including mixed Co–Mo sites), the optimized local Co–Mo distances are comprised between 2.74 and 2.84 Å for the Mo-edge and are around 2.97 Å for the S-edge, which remains consistent with EXAFS data [51].

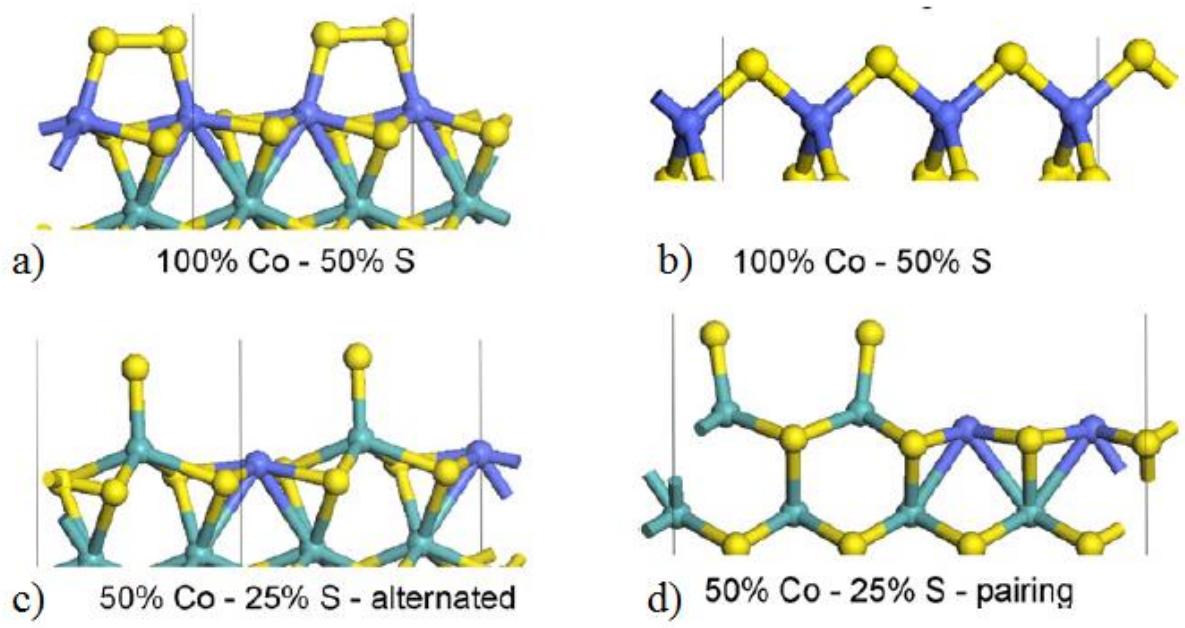

Figure I.12 - Local edge structures geometry optimization of the two CoMoS edges (yellow balls: sulfur, green balls: molybdenum, blues balls: cobalt).

Many studies point to a catalytic activity that depends on morphology of the Mo sulfide. There still doubts on the application of the "rim-edge" model to Co-promoted MoS_2 catalysts used in industrial HDS process, as long initial model was developed for a simple "unpromoted" MoS_2 system. The dispersion, the stacking and length of the fringes and the mode of the metal sulfide bonding to the support surface, which might be by either the edge or basal planes, are of importance. Obviously, the promoter might considerably alter all these properties, if it is already present in the initial oxide precursor. Indeed, the influence of the promoters, such as Co or Ni, on the MoS_2 dispersion was even suggested as one of the explanations of the promoting effect [52]. For some authors, on titania support, the higher affinity of Ni or Co for MoS_2 edge would result in the substitution of Ti decoration and then suppress Ti-promoting effect observed in MoS_2/TiO_2 [53].

Recently, modern techniques such as scanning tunneling microscopy (STM) and Density functional theory (DFT) have been applied to improve the description of "CoMoS" phase (e.g., [54]). On the basis of the detailed atomic-scale information provided by the STM images, a structural model of the CoMoS nanoclusters is proposed in which Co atoms have substituted Mo atoms along the S edges of hexagonally truncated nanoclusters.

As depicted in the ball model in Figure I.13 (a) and (c), a *tetrahedral* environment of the Co atoms is produced if the outermost protrusions are assumed to be S monomers. The proposed CoMoS model [55] is thus seen to have intrinsic under-coordinated sites at the S edge, and from a catalytic perspective this may be an attractive situation enabling adsorption of sulfur containing reactants.

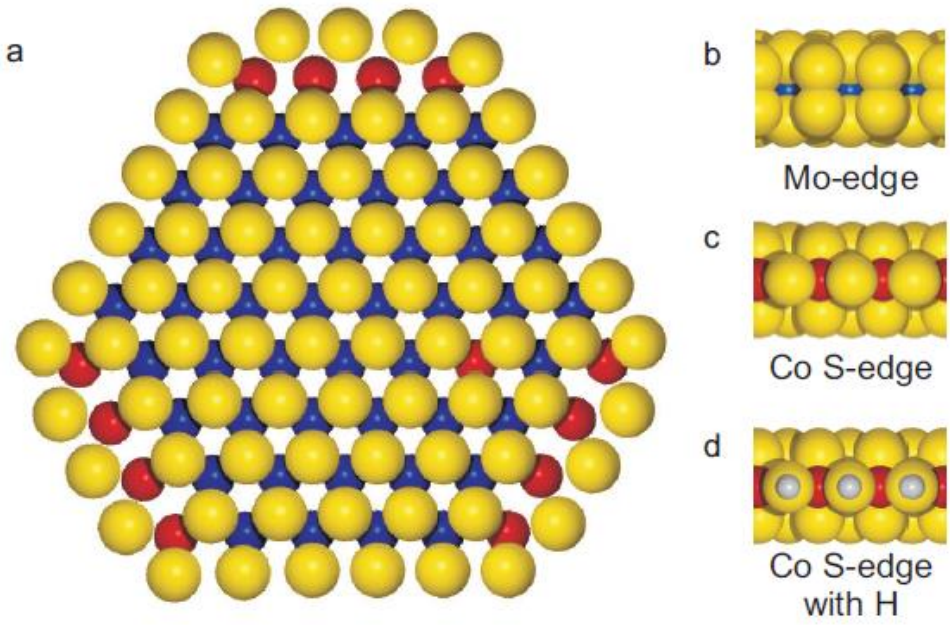

Figure I.13 - (a) Ball model of the proposed CoMoS structure. The CoMoS cluster is shown in top view exposing the unpromoted Mo edge and a Co-promoted S edge (Mo: blue, S: yellow, Co: red). Also shown on the basal plane is a single Co inclusion. (b) The Mo edge (shown in side view) is unaffected by Co and is covered with S dimers. (c) Co fully substitutes Mo on the S edge. S monomers adsorbed on the edge produce a tetrahedral coordination of each Co. (d) The existence of hydrogen adsorbed on the Co S edge is tentatively suggested from the experiments. The ball model shows a possible adsorption site of H (gray) on the Co-substituted S edge (side view).

The possibility of Co having only substituted a fraction of the Mo atoms at the S edge seems unlikely. At no instance were CoMoS clusters imaged with a periodicity larger than one lattice constant along the S edge, indicating a complete substitution with Co along the edges. The present model for CoMoS agrees well with previously published spectroscopic results on supported CoMoS catalysts.

From *in situ* EXAFS measurements, the local environment of substituted Co atoms has been inferred, and it is shown that the average distances from Co to the nearest atoms are $d_{Co\text{-}S} \approx 2.2$ Å and $d_{Co\text{-}Mo} \approx 2.9$ Å. Furthermore, the average coordination was found to be $N_{Co\text{-}S} = 5 \pm 1$ and $N_{Co\text{-}Mo} \approx 2$. These coordination numbers are consistent with the fully substituted S edge model shown in Figure I.13. In comparison of carbon-supported Co-Mo-S structure with XAFS results, the spectra of the catalysts with those of Co_9S_8 and CoS_2 model compounds shows that the Co atoms have a distorted 5- to 6-fold S coordination and that on average, every Co atom is in contact with 2 Co atoms at a distance of 2.80 Å. The compilation of some distances are summarized on Table 2 ([56] and references there in).

Table 2 - Coordination number and interatomic distances for Co in Co-Mo-S.

	$N_{Co\text{-}S}$	$d_{Co\text{-}S}$ (Å)	$N_{Co\text{-}Co}$	$d_{Co\text{-}Co}$ (Å)
STM/DFT	4.5 - 5.3	2.10	1.3 - 1.7	3.22
EXAFS	4.9 - 5.5	2.20 - 2.26	0.6 - 1.2	2.6 - 2.9

Concerning the morphology of the promoted structure, The main impact of Co on the MoS_2 based clusters viewed by STM [56] is to change the shape of the single-layer cluster from triangular to hexagonally truncated. Neither the stacking nor the orientation of the clusters on the substrate seem to be affected. The shape of the CoMoS clusters is determined by a preference for Co to be located on the S edges only and the morphological influence may be explained by a stabilization of the S edge by Co substitution relative to the Mo edges, thus effectively causing the cluster to expose both types of edges. Evidently, the actual shape of each cluster is dependent on a number of factors, such as the total amount of Co substituted on the edges and possible finite size effects on the Mo edges (even/uneven number of dimers). Furthermore, with respect to size, the CoMoS clusters are generally larger than their unpromoted counterparts synthesized at the same conditions.

The fact that the clusters exhibit shapes with varying degree of truncation, suggests that the growth of CoMoS clusters is not limited in the same way as the MoS_2 particles, to the growth mode of which only permits an even number of S dimers. The CoMoS clusters can grow with an arbitrary amount of Mo only limited by normal kinetic effects of ripening and the amount of Mo and Co locally present for the synthesis, and the morphology thus becomes less homogeneous in the experiment.

1.3. Influence of the Co/Mo Ratio on the Formation of Sulfided Phase

One of the challenging questions was initially to identify the role of the CoMoS (and NiMoS) phases and also to propose a better rationalization of the so-called synergy effect, that increase significantly (by several orders of magnitude) the hydrodesulfurization or hydrogenation activities. This activity increase is empirically known to be optimal for a Pr/(Pr + Mo) ratio close to 0.3 - 0.5 for Pr = Ni or Co, which corresponds to Pr/Mo ratio between 0.4 - 0.6 at fixed Mo loading [57].

In fact, γ-Al_2O_3 supported catalytic experiments performed with Co/Mo ratio varying in the range 0.1 - 0.7 were made in order to get new insights on the influence of promotion in the activity (for details, refer to [58] and references therein).

By deconvolution of XPS spectra, either of the molybdenum species as cobalt ones, it was observed the changes in species according to the atomic Co/Mo ratio. The Mo 3*d* spectra of sulfided catalysts were decomposed and three different oxidation degrees were found: VI (232.1 eV), V (230.1 eV) and IV (228.7 eV); they were attributed to the oxide, oxisulfide and sulfide phases, respectively. It was observed that different amounts of cobalt do not appear to influence the sulfurability of molybdenum: about 80% of the introduced molybdenum are sulfided into MoS_2 whereas just 10% for the lower Mo(V) and Mo(IV) each species, as one may see at Figure I.14a.

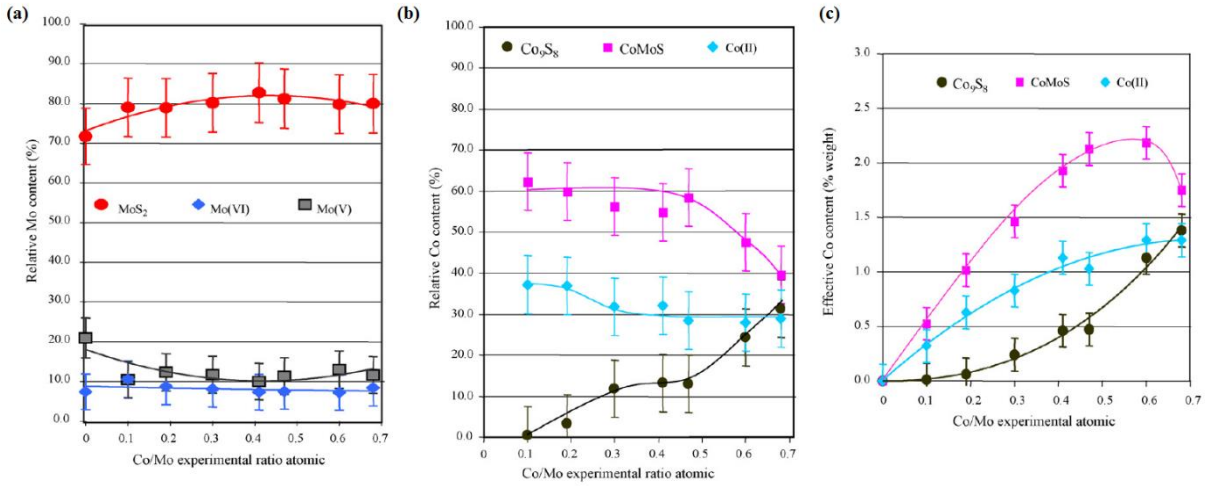

Figure I.14 - (a) Molybdenum speciation expressed as a relative % of the Mo content as a function of atomic ratio (evaluated by X-ray fluorescence) in the catalyst; red for MoS_2, blue for Mo(IV) and grey for Mo(V). (b) Cobalt speciation expressed as a relative % of the Co content as a function of atomic ratio in the catalyst; black for Co_9S_8, magenta for CoMoS and cyan for Co(II). (c) Evolution of effective content of the cobalt species to the atomic ratio Co/Mo for the sulfided catalysts *[59]*.

On the other hand, the trend for CoMoS species when we look at deconvolution of XPS Co 2p spectra for the same set of data. Indeed, on those catalysts with the ratio Co/Mo < 0.5, the proportion of cobalt engaged in the mixed phase CoMoS is stable regardless the Co/Mo ratio (Figure I.*14*b). The proportion of residual Co(II) decrease slightly whereas the proportion of sulfide Co_9S_8 cobalt increases gradually with the Co/Mo ratio. For Co/Mo > 0.5, the results show a clear decrease in the proportion of CoMoS phase in favor of the Co_9S_8 phase indicating that the additional cobalt added to reach the Co/Mo ratio of 0.6 and 0.7 does not allow the formation of an additional CoMoS phase, and generates Co_9S_8. The proportion of residual Co(II) oxide is relatively stable at 30% suggesting tht a non-negligible part of Co is difficult to sulfide.

Figure I.*14*c illustrates the change in the total content of cobalt species in the sulfided catalysts, expressed as a percentage weight of cobalt, as a function of atomic ration evaluated by X-ray fluorescence (XRF). The results confirm the trend observed for changes in relative contents; there is a maximum amount of active phase when Co/Mo ratio equals to 0.5. For a Co/Mo ratio of 0.6 and 0.7, the quantity of the CoMoS phase remains constant or decreases with respect to the Co_9S_8 species, whereas the oxide precursor contains a great amount of Co. Thus, an increase in the cobalt content led to an increase in the proportion of cobalt sulfide at the expense of the CoMoS phase. This result suggest that cobalt species may be difficult to sulfurize (low sulfurability) since it was found a high residual oxide content.

1.4. Activation and Genesis of the Active Phase by Sulfidation

Hydrotreating catalysts are generally available from manufacturers in oxide form (oxide precursors) and it is up to the refiners to convert them into the active sulfide phase. This sulfidation stage in generaly carried out at temperature range between 300 and 400 °C, under hydrogen pressure (0.2 up to 5 MPa), in the presence of sulfur compounds such as H_2S, dimethyl disulfide (DMDS), carbon disulfide (CS_2), etc. and optionally with the feedstock to be hydrotreated. Industrially, sulfidation is commonly carried out within the refinery using "*in situ*" methods.

It is acknowledged that the active CoMoS phase are obtained by sulfidation of the oxide entities which must be well dispersed on the surface of the support since the bulk oxide crystallites (such as $CoMoO_4$, MoO_3, Co_3O_4) are difficult to sulfide or give rise to phase segregation. This activation stage enabling the transition from the oxide precursor to the active catalyst is considered vital and it has a direct influence on the catalytic efficiency level and on their stability during the reaction. Therefore, obtaining catalysts with higher performances by controlling this stage requires a deep understanding of the transition from the oxide state to the sulfide state ([60] and references therein).

It is well stablished that over the range of temperature and sulfur partial pressure used in hydrotreating, the only stable phase in MoS_2. This is because MoS_3 is decomposed at around 300 °C and the Mo_2S_3 does not appear until above 600 °C. In fact, by extensive Temperature Programmed Sulfidation (TPS) studies, Moulijn and coworkers (see, for instance, [61] [62]) concluded that sulfidation initially takes place via an O–S exchange reaction on Mo^{VI}. This exchange is followed by reduction of Mo^{VI} by means of S elimination from the formed MoO_xS_y compounds. The formed elemental sulfur reacts with hydrogen toH_2S in the temperature region from 157 to 327 °C.

Regarding the promoters, it is the H_2S partial pressure relative to hydrogen that will determine the nature of the sulfide phases. Accordingly, in a pure H_2S atmosphere, CoS_2 will be obtained, while for H_2/H_2S mixtures containing increasingly smaller amounts of hydrogen sulfides, $Co_{1-x}S$ are observer and at the lowest H_2S concentrations Co_9S_8, the most commonly observed phases under hydrotreatment conditions, are obtained.

According to thermodynamics, sulfidation starting from transition metal oxides is favorable for the majority of them around 300 °C with the exception of the oxides of Ti, Zr, Nb, Hf and Ta, which require considerably higher temperatures.

In comparison with unsupported phases, dispersion of the supported oxide has an influence on sulfidation thermodynamics by approaching the (2D) surface thermodynamics that are more favorable to the formation of the CoMoS mixed phases identified on the catalyst. However, this matter phase is not stable at temperatures higher than 600 °C, from which segregation into Co_9S_8 and MoS_2 is observed.

Gas phase sulfidation is the method most commonly used in laboratories and thus is the subject matter of the majority of studies. The ratio H_2/H_2S partial pressure determines the composition of the sulfide phases and the morphology of the molybdenum disulfide crystallites (triangular or hexagonal slabs). In general, a mixed gas with 5-10% of H_2S in hydrogen is used. Results show that the first stage of sulfidation at γ-Al_2O_3 supported CoMo catalysts involves a rapid sulfur and oxygen atom exchange in the coordination sphere of Mo ([60] and references therein). Besides the temperature, pressure may also have an influence on the final organization of the catalyst, as on the nature or quantity of CoMoS phase formation.

It was thought that using the organic sulfiding agents normally used in liquid phase sulfidation for the provision of sulfur might also have an effect on the final catalyst activity [60]. Studies using these additives (such as, $CH_3 – S – CH_3$, $CH_3 – S – S – CH_3$) have shown a slightly gain on activity contrary to what is observed in liquid phase sulfidation. In comparison with H_2S, the use of dimethyl disulfide (DMDS) as activate agent on sulfidation of $CoMo/Al_2O_3$ catalysts, the catalytic performance in thiophene HDS seems to promote the stages involving C – S bond hydrogenolysis.

The formation of intermediary species during the sulfidation, as soon as reaction temperature starts to increase, of unpromoted Mo/Al_2O_3 is long known [63], as revealed by Raman spectroscopy in Figure I.15. The authors observed that Mo_3S_{13} based entities were initially formed and then converted into MoS_3 whereas oxysulfide entities were formed upon direct sulfidation of the hydrated oxididic precursors. These oxysulfides are then more rapidly converted in MoS_2, which showed that the presence of water improved catalyst sulfidation. The nature of the intermediates is thus dependent on the conditions prevailing during sulfidation, namely on the hydration state of the oxide precursor and the composition of the sulfidation atmosphere as well as activation conditions and state of precursors. Accordingly, two pathways were identified for this system, the oxysulfide pathway and MoS_3 one. MoS_3 is moreover the intermediate in the preparation, from thiosalts such as ammonium thiomolybdate of unsupported high specific surface area molybdenum.

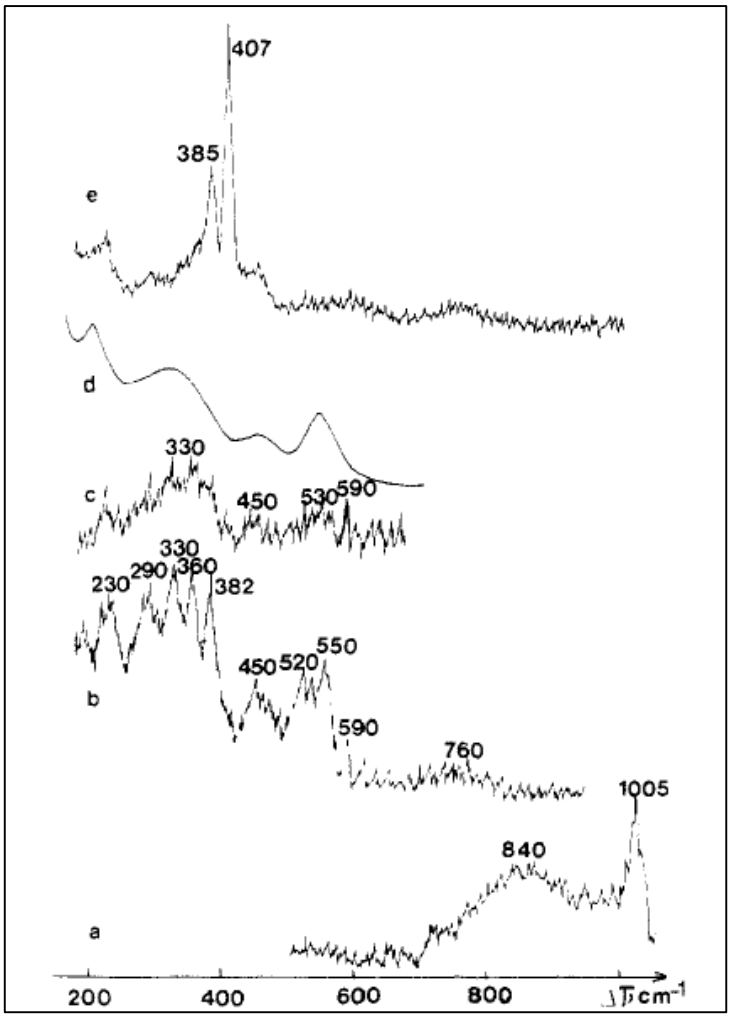

Figure I.15 - Raman spectrometric monitoring of the sulfidation of a dehydrated = 14% MoO_3 oxidic precursor with an H_2/H_2S mixture (90/10): a) oxidic precursor; b) 330 K, 5 min.; c) 470 K, 1 hour; d) MoS_3; e) 620 K, 3 hours *[63]*.

MoS_3 is an amorphous intermediate compound; stable at 200 °C, whose structure has been the subject of controversy. It is now admitted that it consists of a chain arrangement of molybdenum atoms, in trigonal prismatic coordination with six sulfur atoms as shown in Figure I.16. For every two alternate structural units there is an Mo – Mo pair with a shorter intermetallic distance and an S – S bond, this model corresponding to a formal charge: $Mo^{5+}(S_2^{2-})_{1/2}(S^{2-})_2$.

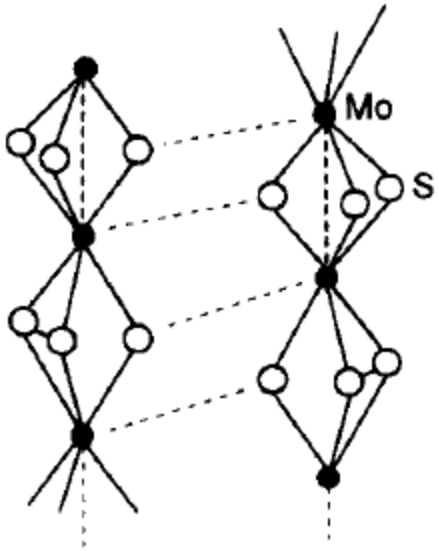

Figure I.16 – Crystalline structure of MoS_3 as proposed by Weber *et al. [64]*.

The production of hydrogen sulfide upon sulfidation of the oxide precursor is an argument in favor of this type of mechanism and it would seems to correspond to the second stage of the sulfidation reaction according to the equation:

$$MoS_3 + H_2 \rightarrow MoS_2 + H_2S$$

Such mechanism has been suggested by the observation by QEXAFS of Mo – S bonds, which are longer than in MoS_2 [65] [66].

The other mechanism involving oxysulfide intermediates (namely MoS_xO_y entities) was proposed by Schrader *et al.* [67], by de Jong *et al.* [68], by Muijsers *et al.* [69] and described in detail by Glasson in 1999. The latter evidenced, as in case of the MoS_3 hypothesis, the formation of intermediates containing S_2^{2-} groups, the formation of which being concomitant with the formation of Mo^{5+} species.

In the case of the promoted catalyst, the Co undergoes sulfidation in parallel to yield the active phase CoMos. However, the cobalt may also assume other form, such as Co_9S_8. Electron microscopy (TEM) has in some cases revealed the presence of isolated particles of Co_9S_8 even when crystallites of unsupported cobalt oxide were not detected on the oxide precursor. Furthermore, EDX technique (Energy-dispersive X-ray spectroscopy) has revealed the proximity of Co to the MoS_2 slabs.

With regard to the sulfidation of Co, QEXAFS monitoring at the K threshold of Co of the sulfidation of an industrial $CoMo/Al_2O_3$ catalyst shows that this sulfidation begins right from ambient temperature, unlike a Co/Al_2O_3 catalyst [70]. These kinetics are, however, highly dependent on the nature of the oxide supported species, their interactions and the presence of promoter or additives.

Whatever the type of sulfidation, the formation of MoS_2 crystallites is always observed. In general, aggregation of an assembly of sulfided polymolybdates will give rise to a MoS_2 particle decorated by

Co to form the well dispersed CoMoS phase on the surface of the support, as is confirmed by XPS studies.

TEM permits an exact quantification of the change in particle morphology during sulfidation. It can be observed that the average length of the crystallites, which can be observed and statistically analyzed from a sulfidation temperature of 376 K, increase continuously whereas the average stacking stabilizes at around 673 K [60].

The geometrical model [34] makes it possible to calculate the total number of atoms in a particle. By combining these TEM results with those obtained by XPS, bearing in mind that the particles observed are composed of Mo^{4+}, it is possible to deduce the density of crystallites per unit surface area and to monitor the variation in this parameter during sulfidation. As results, we note that the maximum number of particles is observed at around 200 °C, which means that the sulfidation of a CoMo catalyst may be described as a nucleation regime up to 200 °C followed by a MoS_2 particle growth regime at higher temperatures [60].

2. Support Effects

In hydrotreating catalysis, the active components are supported on a carrier. The carrier or support material usually provides high surface area in order to maximize active phase dispersion. The activity of HDS catalysts is strongly affected by the dispersion and morphology of the active phase. The interaction of the transition metal sulfide with the support has a large influence on the final dispersion and morphology of the active phase. Al_2O_3 is the most commonly used support in industry because of its strong interaction with the support, which results in a high dispersion and high stability of the active phase. This is highly stable, contains acid and basic sites, has a reasonably high surface area and porosity, can be easily formed into desired shapes, and is relatively inexpensive.

In fact, the support plays different roles that manifest spatial scales [71]:

- On a macroscopic scale, the shape of the catalyst pellet is derived from that of the support. The choice of size (ranging from a few tenths of a μm to a few mm) and shape (more or less spherical ball, cylindrical extrudate, polylobular extrudate, etc.) of a catalyst pellet is generally optimized depending on the application for which the catalyst is intended and the type of reactor. Furthermore, the mechanical properties of a catalyst are largely inherited from those of the support: in particular, the support must be sufficiently mechanically resistant to minimize fines formations (by crushing, for instance), which adversely affects the duration of the catalytic cycle;

- On a mesoscopic scale, the porosity of the catalyst it is also dictated by that of its support. The porosity of the support affects the genesis of the active phase (porous volume available to introduce the impregnation solution, diffusion of oxide precursors during impregnation and the support surface accessible to deposit the precursors) and catalyst performance. In fact, the average diameter of the pores (typically ranging from 100 nm to 1000 nm), their size distribution and connectivity will condition the intragranular diffusion of the reactants and the products of the catalytic reaction. Furthermore, changes in texture as the catalyst ages is one of the main causes of diminished catalyst activity or selectivity, which affects the duration of the cycle. The porosity of the support must therefore be suitable for the application in question in order to optimize the activity and selectivity of the catalyst;

- On an atomic scale, the nature, concentration and physicochemical properties (mainly acid-base) of the surface sites of the support are also crucial in terms of catalyst genesis. These sites will have a direct effect on the dispersion of the active phase and on its interaction with the support surface. Any change in the surface properties of a support is therefore an important lever for adjusting catalyst performance.

All these elements justify the fact that developing new supports is an industrial research field that it is at least as active as the development of new active phases. Besides alumina is the most common support used on industrial hydrotreatment processes, the modification or replacement of the alumina support has several different objectives, among them one points out [72]:

1. the improvement of dispersion of the active phase,
2. the modification of the reducibility of oxide precursor through change of the interaction between the active phase and the support,
3. decrease of concentration of the spinel phase, thereby increasing the useable Co content of the catalyst,
4. facilitate the metal recovery of spinel catalysts,
5. reduce the deactivation via coke formation.

One of the most striking experimental findings clearly illustrating the so-called effect of the support in catalysis by sulfides is the observation that the intrinsic thiophene HDS activity (when expressed per Mo site and thus ruling out any dispersion effect) was about 4.4 times higher for titania supported MoS_2 catalyst compared to the industrial used γ-alumina [73]. However, the expected synergy effect on adding the promoter was significantly weaker on titania compared to γ-alumina, which implies that preference is still given to the latter support for Co(Ni)MoS catalysts. In addition, γ-alumina is also preferred on an industrial scale due its optimal porous and acid properties. Nevertheless, on γ-alumina it is difficult to avoid formation of undesirable species such as $Co(Ni)MoO_4$ or $Co(Ni)Al_2O_4$ in the preparation of oxide precursors. As mentioned before, the species can lead to isolated sulfides of the Co_9S_8 type, which are

quasi-inactive in hydrotreating, or to poorly sulfided species of the Mo oxusulfide type or even to species which cannot be sulfided.

Encouraged by these results, a large number of new materials with high surface area and others properties suitable for support applications have been developed and tested. These include TiO_2, ZrO_2, MgO, carbon, SiO_2, zeolites, etc. [74] [75] [76] [77]. The properties of alternative supports for hydrotreating catalysts, as compared to conventional Al_2O_3, have been summarized by Luck [78] in Table 3. Although their use has long been limited by their small specific surface area, such supports (particularly, TiO_2) are now available and may in future rival with γ-alumina, with specific surface are reaching up to 300 m^2/g [79].

Differences in catalytic activities due to changes in support may arise because of variations in metal-support interactions, which, in turn, may influence the dispersion and morphology of active components. The formation of active phase of the catalyst and their dispersion on the support surface is deeply influenced by the interaction between the support and impregnated metal or metal salts. Strong interaction of the deposited of molybdate and cobalt ions with the support will retard their reducibility and sulfidability and lead to the formation of low active species [80]. Support interaction also play a key role on the degree of stacking of active phase structures. High resolution electron microscopy has provided valuable information on the degree of stacking in MoS_2 and CoMoS structures prepared with different supports [81]. Different size and stacking of MoS_2 slabs on various supports were proposed to be responsible for the better activity on TiO_2 and ZrO_2 [82]. For Ramirez *et al* the decoration of MoS_2 by Ti^{+3} species formed during sulfidation, affords very active unpromoted catalysts [73]. In a recent and very interesting study [83], STM was used to characterize titania (110)-supported MoS_2. It was evidenced that the shape of the slabs in flat contact with the metal oxide surface depended on surface structure of the TiO_2 substrate; they adopted the shape of uniform elongated platelets oriented along one of the high-symmetry direction of the two-fold symmetric TiO_2 support. The widths of the MoS_2 particles were originated from the optimized lattice matching distances of the MoS_2 lattice along either of the high symmetry directions of the TiO_2 (100), providing evidences that epitaxial relations are critical to determine both the size and orientation of the MoS_2 particles on the substrate. These epitaxial matches arise due the formation of either Mo-O-Ti or Mo-S-Ti chemical linkages at the particle edge [84].

Table 3 - Properties of alternative supports as compared to Al_2O_3 for HDT catalysts. HYD = hydrogenation, HCG = hydrocracking, HDN = hydrodenitrogenation, HDM = hydrodemetallisation.

Carrier	SiO_2/Al_2O_3	C	TiO_2	TiO_2MO_x	Ceramics	Clays
Surface Area per Unit Volume	>	>	<	>	<<	<<
Cost	>	=	>	>	>	<
Case of Forming	=	=	<	<	<<	>
Mechanical Strength	=	<	<	<	>	>
Cost of Preparation	=	>	=	=	>	>
Potential HDS Activity	<	>	>	>	<	<
Specific Advantage	HCG HDN	HYD	HCG HYD HDN	HCG HYD HDN	?	HDM
Regenerability	=	<<	<	<	=	=

In spite of many works dealing with the influence of the support, there are still many debates and contradictory results. The synergetic effect obtained on each support is highly dependent on the quantity and quality of the active phase, the dispersion, and the way of sulfidation. The role of the MoS_2 particles is to act as a secondary support merely to stabilize the highly dispersed Co-sulfide located on the edges. Stabilization of the MoS_2 slabs themselves is assumed to occur via Mo–O linkages to the support. The experimental evidence for the attachment of MoS_2 slabs to the support via Mo–O linkages is still not very convincing. For instance, Chiu *et al*. [85] attributed peaks in the Fourier transform of EXAFS data of a used $CoMo/Al_2O_3$ catalyst to two Mo–O contributions at 1.6 and 1.9 Å, respectively. However, it was ascribed that these Mo–O contributions to nonreducible oxygen atoms and did not link them to the proposed Mo–O linkages between support and MoS_2 particles.

Therefore, in order to evaluate correctly the support effect, it appeared very important to control carefully the formation and the quantity of the promoted active phase deposited in each support. In that sense, a systematic study was performed by Ninh *et al* [86] in NiMo system. The promotion of Ni atoms was made in already sulfided Mo supported catalysts. By doing so, the direct reaction between the promoter with MoS_2 edges minimize the interaction with the support and thus the loss of promoter in the support or isolated sulfided species is reduced while the promotion is optimized. As results, we point out the best dispersion of the sulfided phase with a lower stacking of MoS_2 slabs observed in TiO_2 and ZrO_2 compared to the others (γ-alumina and silica), besides the promotion was higher on alumina, as indicated by XPS quantification. Further, concerning the quality of the active phase, all the supports (except silica) do not seem to influence it. However, the variation in selectivity reflect an effect of the

support on the catalytic behavior of those sites, especially the sulfidation of titania and zirconia lead to more hydrogenating sites.

TiO_2 has a stronger interaction with Mo than Al_2O_3 and has proven to be a promising support for HDS catalyst (see e.g. [74]). On titanium oxide, MoS_2 slabs examined by TEM are generally shorter and less highly stacked than on other supports, but these dispersion effects, which are also present with promoted catalysts, cannot solely explain the greater activity of the non-promoted ones, as it was told early. On alumina, dissolution-precipitation phenomena at the surface of the support give rise to the formation of the Anderson-type heterpolyanion (HPA) $AlMo_6^{3-}$. This phenomenon is absent on TiO_2 where well-dispersed isopolymolybdates lead to smaller particles in the sulfide state, linked to a better intrinsic activity.

Concerning the modification carried by TiO_2 on the performance of the CoMo catalysts, Ramírez *et al.* [87] reviewed and summarized some important aspects about it:

1. The method of preparation of the support is of great importance to catalytic activity. It is not the total amount of Ti in the support that is relevant but rather the structures of the Ti oxide species on the surface. Isolated Ti oxide species do not increase significantly the HDS activity. To achieve high activity, the presence of reducible surface TiO_2-like structures is necessary.
2. The nature of the support modifies significantly the reactivity and properties of the supported Mo oxide phases.
3. TiO_2 is an electronic promoter in HDS catalysts. Under HDS reaction conditions Ti^{3+} species are formed in the reducing atmosphere prevailing and the electron ‘‘in excess’’ in each Ti^{3+} has the tendency to be transferred. Therefore, these Ti^{3+} species act in effect as electron donors. These electrons can be easily transferred, through the conduction band of the support, and be injected to the Mo 3*d* conduction band. This charge transfer effect is the requirement for MoS_2 promotion in HDS catalysts.
4. It is proposed that as a consequence of the charge transfer from Ti^{3+} centers to the HOMO (highest occupied molecular orbital) of Mo, occupying antibonding orbitals, the metal-sulfur bond in MoS_2 is weakened and the number of coordinatively unsaturated sites (CUS) per Mo atom in the sulfided catalyst increases with Ti content. This latter effect has been corroborated experimentally.
5. The electronic promotion of Mo by Ti has a limit, or a maximum according to the Sabatier principle, because excessive weakening of the metal sulfur bonds in MoS_2 would lead to an inappropriate interaction between the sulfur compounds and the active phase.
6. In the case of mixed Al-Ti oxides with low Ti content prepared by co-precipitation or sol–gel, where Ti ions are isolated, the electronic promotional effect is not effective because when Ti ions are surrounded by Al ions through Al–O–Ti bonds, the Ti^{3+} centers formed under reduction are stabilized, and therefore, the transfer of charge does not occur as easy as for Ti–O–Ti bonds.

7. The increased reducibility and sulfurability of oxide precursors in Ti-containing catalysts is related to the fact that the redox processes of the Mo phases are facilitated by the semiconductor character of TiO_2 in contrast to the insulating one presented by Al_2O_3.
8. TiO_2-containing catalysts seem well suited for HDS because the formation of a greater number of CUS in the MoS2 active phase, which favors the hydrogenation-hydrodesulfurization transformation route.

Mo K-edge EXAFS experiments also have helped to get insights in particle-support interaction. In two close papers, Leliveld *at al.* prepared CoMo-based catalysts samples in order to study the effect of the support and to obtain variations in the metal–sulfide support interaction both Mo/Al_2O_3 and Mo/TiO_2 catalysts [88] [89]. Additionally, the pretreatment of the catalysts prior to sulfidation was varied (noncalcined and calcined samples, sequential impregnation of Co and one-step MoCo impregnation) to create extra variations in the active phase–support interaction. As most catalysts contain Co as promoter, the influence of Co on the structure of MoS_2 and its attachment to the support was tested in these works.

Thus, analysis of the second shell of Mo/Al_2O_3(cal) results in a $N_{Mo–Mo}$ of 2.4. According to the authors, the coordination number of the second shell can be used as a direct measure of the two-dimensional size of the particle. With the use of a simple hexagonal model it corresponds to approximately four Mo atoms per slab. Further, the most obvious explanation for stabilization of these small particles is the linkage of the MoS_2 particles to the support via Mo-O-*X* bonds. For both the calcined TiO_2 and Al_2O_3 catalysts, a Mo–O contribution at 2.0 Å is observed in the Fourier transform of the sulfided catalysts (in agreement with the predicted value of 1.85 Å for the Mo-O-Al bond obtained by molecular modeling), which could well be ascribed to such a Mo-O-*X* linkage. These Mo-O-*X* linkages originate from the oxide catalysts and partly remain throughout all stages of the sulfidation process.

The authors also discuss about the influence of the orientation of the slab on the surface of the support (as it will be discussed soon). Their results indicate that $N_{Mo–S}$ increases with increasing particle size ($N_{Mo–Mo}$). If the slabs were bonded to the support through their basal plane the average sulfur coordination of the Mo-atoms would not change with increasing slab size. In edge-bonded slabs, however, where only the Mo atoms near the edge are in contact with the support the average sulfur coordination rises with increasing $N_{Mo–Mo}$. Although the molybdenum oxide species are more dispersed on Al_2O_3 the MoS_2 particles formed are smaller on TiO_2. Probably the “match” of the MoS_2 edge plane onto the surface of the support is better for titania than alumina. This might result in the growth of the MoS_2 particles on TiO_2 in the direction along the surface while on Al_2O_3 particle growth takes place in all directions.

The addition of Co to the Mo/Al_2O_3 catalysts does not cause a significant increase in $N_{Mo–Mo}$, with no formation of larger sulfide particles (as might be expected from the larger molybdenum oxide particles

present in the Co promoted catalysts relative to the unpromoted catalyst [88]). Whereas in titania supported Mo catalysts the addition of Co leads to much more pronounced results: the $N_{Mo–Mo}$ increases from 1.1 to an average value of 3.5 for the promoted catalysts. Evidently Co disturbs the interaction between the MoS_2 particles and the support, which causes the particles to grow. Moreover, the lower in the sulfidation rate for titania supported catalysts compared to alumina supported might be related to smaller molybdenum oxide particles in the promoted catalyst. Smaller particles are better stabilized by the titania surface and less susceptible to sulfidation (although the particle size for both particles is not that far, N_{Mo-Mo} of 2.5 versus 1.8). Another important speculation is the formation of $CoMoO_4$, from their discussion, the interaction between molybdenum oxide or its precursor and the titania surface is rather poor for Mo/TiO_2. This could favor the interaction of Mo with Co leading to $CoMoO_4$, which is known to sulfide at higher temperatures than MoO_3, in agreement with their own results [89].

3. On the Preparation of HDS Catalysts

On this topic, we describe the fundamentals of the techniques used to prepare our series of catalysts, named Wet Impregnation and One-Pot Sol-Gel routes, and review some interesting points on the advances of each one of them through the years.

3.1. The Classical Insipient Wetness Impregnation

In general words, incipient wetness impregnation (IW or IWI), also called capillary impregnation or dry impregnation, is a commonly used technique for the synthesis of heterogeneous catalysts. Typically, the active metal precursor is dissolved in an aqueous or organic solution. Then the metal-containing solution is added to a catalyst support containing the same pore volume as the volume of the solution that was added. Capillary action draws the solution into the pores. Solution added in excess of the support pore volume causes the solution transport to change from a capillary action process to a diffusion process, which is much slower. The catalyst can then be dried and calcined to drive off the volatile components within the solution, depositing the metal on the catalyst surface. The maximum loading is limited by the solubility of the precursor in the solution. The concentration profile of the impregnated compound depends on the mass transfer conditions within the pores during impregnation and drying [90].

The classic common steps to prepare supported CoMo catalysts include the incipient wetness impregnation of a shaped support (extrudates) by a solution containing molybdenum and cobalt. The

standard preparation method is historically based on solutions containing ammonium heptamolybdate ($Mo_7O_{24}(NH_4)_6$) (AHM) and cobalt nitrate. The impregnated solution volume is equal to the support pore volume to be impregnated. In practice, it is assumed that the pore volume to be filled is substantially identical to the volume of water which can be impregnated onto this support until incipient wetness is obtained on the surface of the extrudates, giving the Water Uptake Volume (WUV). In practice, WUV is generally slightly larger than the pore volume determined by mercury porosimetry, for example. This impregnation step is followed by a maturation step, where the catalyst is stored at room temperature in a water-saturated atmosphere for 24 hours. This step allows a good repartition of the precursors throughout the extrudates body. The next step consists in a drying step in order to remove the impregnation solvent and avoid steaming and thus sintering during the calcination step. The calcination step is subsequently carried out at temperatures ranging from 300 to 500 °C. A high temperature is indeed necessary to make sure that all counter ions, such as ammonium or nitrates are removed. Simultaneously, thermal treatments (drying and calcination) modify the structure of metal oxide precursors. The activation step may be carried out under gas phase (H_2S/H_2 mixture) or using spiked feeds containing a sulfiding agent such as for instance dimethyldisulfide.

The oxide state of the catalyst prior to sulfidation has been largely studied since the 60's [91]. Its morphology, structure and dispersion on the support have indeed a dramatic impact on the active phase characteristics and performances.

Generally, studies into the impregnation of an alumina support with an ammonium heptamolybdate solution only consider the phenomenon of adsorption on the surface of the support, but depending on the pH, molybdenum occurs in various forms in the impregnation solution, particularly a monomeric species (MoO_4^{2-}) at a basic pH and then, polymeric species when pH falls.

At low MoO_3 loadings, up to 6 wt% for an alumina with a specific surface area of 270 m²/g, molybdenum is mainly in monomolybdate form: MoO_4^{2-}. In the 6 to 14 wt% range, heptamolybdates species $Mo_7O_{24}^{6-}$ may be found. MoO_3 is formed when the alumina surface is saturated by polymolybdates species. These species adsorption is preferential because they strongly interact with alumina. According to Bachelier *et al.* [92] the saturation of adsorbed Mo occurs at higher MoO_3 loadings and after this a higher amount of Mo will precipitate into large bulky islands (refractory to sulfidation), blocking to some extend the sulfidation of alumina-bonded Mo by steric hindrance. At high molybdenum loadings (MoO_3 ~ 18 wt%), sulfide CoMo catalysts may thus present bulky islands of unsulfided MoO_x (x = 2 or 3 depending of the extent of the reduction performed during the activation stage), as well as MoS_2 slabs. Therefore, all the introduced molybdenum is unfortunately not active for HDS. Limitations thus arise from molybdenum species solubility (precipitation) and poor dispersion of the active phase on the support, which may lead to sintering.

In terms of promoter loading, the ideal amount for HDS is a function of the VI-B group metal loading according to the promoter/metal atomic ratio. It is difficult to say exactly an optimum atomic ratio for the HDS bimetallic catalysts, the change of this ratio is usually accompanied by the change of the bimetallic particle sizes, it has a direct influence on dispersion of the active phase on the support and, therefore, in the catalytic activity. Furthermore, depending on the method of preparation and the support it seems to find a particular optimum ratio (e.g., [93] [94] [95]). For instance, the ideal ratio is around 0.3 for the toluene hydrogenation case, which may not be generalized for all HDS reactions [96].

Improvements have been made on each preparation step to reach more active catalysts with higher loadings. In order to increase dispersion and loading of the active phase, new impregnation solutions have been used. Improvements in activation procedures have also been made in order to efficiently sulfide ever more loaded catalysts.

Recently, the Chiyoda Corporation has successfully developed a novel method for preparing mesoporous TiO_2 with higher surface areas than usual one. It is based on an aqueous precipitation method called “pH swing”. This opens new opportunities for the development of highly active catalysts for the deep hydrodesulfurization of gasoils, since the textural limitation could be overcome.

This method was tested in the impregnation of Mo catalysts for Dzwigaj *et al.* and both the oxide and sulfide phase were characterized [97]. It was proved that the textural limitation of the lower surface area of titania compared to alumina was overcome thanks to the preparation of a titania support with high surface area. The authors claimed that this new method of preparation of mesoporous TiO_2 by “pH swing” is a new opportunities for developing highly active catalysts for desulfurization, taking advantage of the higher reactivity of the molybdenum sulfide phase when it is dispersed on this oxide phase compared to conventional alumina support.

3.2. Sol-Gel method for support or catalysts preparation

Sol-gel methods have been recognized as interesting procedures to prepare catalysts. The versatility of the sol-gel techniques allows control of the texture, composition, homogeneity and structural properties of solids, and makes possible production of tailored materials such as dispersed metals, oxidic catalysts and chemically modified supports. The interest in catalyst preparation via sol-gel route dates back to early 80’s and have growing since then, especially since the middle of 90’s. The number and properties of the active sites and the reaction kinetics depend on several factors that can be controlled to some extend by the sol-gel methods of solid synthesis [98]. These factors include:

a) high specific surfaces area;
b) controlled pore size distribution;

c) textural stability under the preparation and reaction conditions;
d) for supported catalysts;
   i. the active phase must be at the surface, and not homogeneously distributed into the solid, and
   ii. must present a good and homogeneous dispersion;
e) structural properties must be controlled in order to get the desired crystalline variety or an amorphous structure if preferred;
f) purity of the catalyst components would be as high as possible (contaminants use to concentrate at the surface of solids and small content of impurities on a weight basis can lead to high surface impurities concentration);
g) easily controlled composition, especially for the preparation of multicomponent catalysts, or catalysts promoted by small concentrations of an additive;
h) mechanical properties must accomplish the requirements of the operation conditions; and
i) the catalysts should be active for as long as possible without severe deactivation due to chemical or physical blocking of active sites.

Thus, the early exploration on sol-gel preparation for catalysis, and particularly in HDS processes, was related to alumina support. As review by Cauqui and Rodríguez-Izquierdo [99]. For instance, two sol-gel methods to prepare HDS catalysts have been compared. In the first one, aluminum isopropoxide (AIP) is hydrolyzed in a large amount of water forming a fibrillar aluminium hydroxide; the gel is peptized with a HNO_3 solution giving a clear sol. $(NH_4)_6Mo_7O_{24}\cdot 4H_2O$ and $Co(NO_3)_2\cdot 6H_2O$ are dissolved in 1,3-butanediol and stirred with the sol for 1 day. The solvent is evaporated at low pressure and the sample is finally calcined in air at 500°C. In the second case, AIP is dissolved in 1-butanol and Mo and Co precursors are added to the solution. Water is further added and a gel is formed which is further dried and calcined at 500°C. The activity of the first catalyst showed to be about ten times higher than that of the second for the thiophene HDS reaction. Auger spectroscopy measurements on both catalysts can provide an explanation for this difference in behavior. The deep profiling method demonstrates that, in the first case, Mo and Co oxides are both at the surface, while in the second case significant amounts of cobalt are incorporated into the alumina matrix. In fact, cobalt atoms can easily substitute to aluminum ions in tetrahedral positions of the $A1_2O_3$ network, thus decreasing the synergic effect between surface cobalt and molybdenum. The first catalyst gives levels of activity similar to commercial HDS catalysts.

Another example, Dumeignil *et al.* [100] conduced a great work on CoMo-based HDS catalysts supported on sol-gel prepared γ-Al_2O_3. They pointed out a remarkable increase (about 60 %) in the catalytic activity for HDS of thiophene compared with an industrial CoMo catalyst with the same formulation. In subsequent works [101] [102], this same group studied the effect of the hydrolysis ratio during the sol-gel synthesis on the properties of the prepared γ-AlO powders to optimize the preparation

parameters of the catalyst support for HDS applications, putting on evidence the promising feature on sol-gel preparation as method of support for catalysts and catalyst production.

Among the various composite oxide supports, great considerations are taken into account the combination of TiO_2 and Al_2O_3. It is because of the increased reducibility and sulfurability of Ti-containing catalysts, which are related to the fact that the redox processes of the active phases (Mo) are facilitated by the semiconductor character of TiO_2 compared with the pure insulating Al_2O_3. The modification of the surface of alumina with TiO_2 eliminates the most reactive surface hydroxyl groups and avoids the formation of tetrahedral Mo oxide species, resulting in an increase of octahedral Mo active species and thus leading to a higher HDS activity [103] [104]. Based on the catalytic performance results and catalyst characterization, it can be found [103] that the anatase TiO_2 makes it easier to form octahedral coordination, which facilitates the formation of the coordinatively unsaturated sites or sulfur vacancies that are favorable for hydrodesulfurization reaction. Many of the explanations pass by the particle-support interaction.

Titania appeared as a good support for HDS catalysts but the low thermal stability and specific surface area of TiO_2-anatase prevented its industrial use as support for HDS catalysts. The low surface area affects directly the Mo loading and thereby the specific catalytic activity. Because of this, many studies have been undertaken to obtain Ti-containing supports with textural and mechanical properties similar to alumina but with a surface chemistry close to TiO_2.

Regarding the preparation of anatase-TiO_2 for support purposes, the solution sol-gel process used for preparing titania includes the hydrolysis-condensation of titanium alkoxides $Ti(OR)_4$ (R = Pr^i, Bu^n, Pr^n, Bu^t) as precursors forming rapidly titanium oxooligomers of a general formula $Ti_xO_y(OR)_{4x-2y}$. These oligomeric titanium species are in turn chemically active and react to form titania nanoparticles. In order to observe *in situ* the process of titania nanoparticles formation Stötzel *at al.* [105] performed a QEXAFS study for monitoring the main stages involved in the titania nanoparticle formation from titanium tetraisopropoxide (TTIP) precursors, also referenced in literature as $Ti\{OCH(CH_3)_2\}_4$, $Ti(OPr^i)_4$, or tetraisopropyl titanate.

It was showed that the formation of titania nanoparticles from the reaction of TTIP with water involves the following four-stepped temporal evolution. The formation of titania nanoparticles occurs when the total hydrolysis ratio is ranged between 1.0 and 1.35, before any TiO_2 nanoparticles appear. The formation of TiO_2 during the subsequent stage is highly dependent on the speed of water solution addition. These findings strongly suggest that the formation of TiO_2 observed at the advanced stage of the kinetic monitoring, for t > 300 s, follows a first order kinetic with respect to the concentration of water. Consequently, the kinetic of the cluster-cluster growth process of titania nanoparticles can be quantitatively described by a linear time dependency as expected in the so-called reaction limited

regime. The average particle size, determined via Mie scattering theory, is linked to the fraction of titania in the solution during the aggregation processes.

TiO_2 nanoparticles were also prepared at room temperature by dropwise addition of the mixture of titanium tetraisopropoxide (TTIP) and isopropanol with the mole ratio of TTIP/isopropanol=1.6 into water by Won Koo So *et al.* [106]. Different amount of concentrated $HNO_3(H^+)$ was added into this precipitate solution. The mole ratio of HNO_3 to TTIP(H^+/TTIP) was varied in the range between 0.02 and 0.67. The the preparation condition such as the H^+/TTIP and H_2O/TTIP mole ratios seems to affect seriously the formation of seed crystalline phase at room temperature and in turn the phase transformation behavior upon the post heating at higher temperatures. The titania particles prepared at the H^+/TTIP mole ratio of 0.67, which contained the mixed phases of anatase, brookite, and rutile at room temperature, showed only rutile phase at 750◦C. Also, the phase transformation from brookite to anatase and then subsequently to rutile occurred with heating.

A similar conclusion was obtained by Mahshid *et al.* [107]. The solution used was composed by 5ml titanium isopropoxide, TTIP and 15 ml isopropanol. A 250 ml solution of distilled water with various pH was used as the hydrolysis catalyst. The desired pH value of the solution was adjusted by adding HNO_3 or NH_4OH. The dried powders were calcined at temperature ranging from 200 to 800 °C.

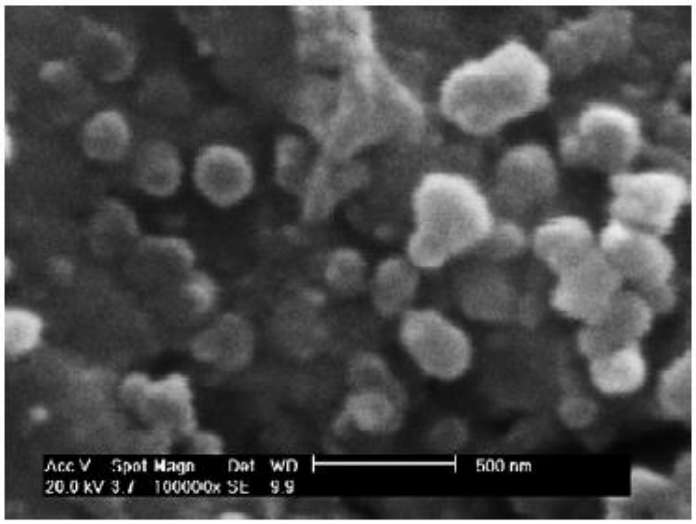

Figure I.17 - SEM micrographs of powder prepared at 400 °C in acid solution. The main characteristic are the spherical particles and the low agglomeration of anatase formation. *[107]*

According to the particle size obtained from Debye–Scherrer equation, the powder obtained from a solution at pH 2 consist of very fine anatase crystallites even at temperature lower than 100 °C. When the powder is treated thermally at 400 °C, the diameter of nanoparticles is approximately 28 nm and still consists of pure anatase phase Figure I.*17*. As the calcinations temperature is increased, the particle size increases. Rutile phase is formed at calcinations temperatures below 600 °C and grows slightly when

heated up to 800 °C. Powder morphology in these criteria is almost spherical which is due to acidic condition that prevents agglomeration.

In conclusion, hydrotreatment catalysts are designed according to feedstock and required product specifications. For middle distillate hydrotreatment, the active phase consists in "CoMoS" phase dispersed on a high surface area support. Historically, CoMo-based catalysts were prepared using heptamolybdate and cobalt nitrate. Increasing active phase loading was difficult, due to the low solubility of these species, and the active phase dispersion was poor, which led to sintering and thus decreased the yield in active "CoMoS" phase. Many improvements have been carried out regarding alternative routes of preparation, different supports or impregnation solutions with the introduction of HPA species. These advances in preparation drive to species with higher solubility and lead to high dispersion of the active phase. Higher active phase loading were thus reach and it was shown that further increases in activity were still possible. This promising and advanced preparation method consists in a one-pot sol-gel route for HDS catalysts and is described in a following chapter.

4. Characterization studies in CoMo-based Catalysts

Numerous cutting-edge experimental techniques have been used in order to deeply and clearly characterize the CoMoS (or also the well-studied NiMoS catalyst) catalytically active phase. An extensive set of experimental data has been thus available before any relevant theoretical insights. The non-exhaustive list of experimental techniques involved in this tremendous characterization task over the years consists of , X-ray photoelectron spectroscopy (XPS), Low-Energy Ion Scattering (LEIS, also called Ion-Scattering Spectroscopy, ISS), Transmission Electron Microscopy (TEM), Mössbauer spectroscopy, laser Raman spectroscopy, Extended X-ray Absorption Fine Structure (EXAFS) and Infrared (IR) spectroscopy.

All these characterization techniques provide details on the local structure of the active CoMoS phase although they cannot unambiguously determine the precise nature of the active site. For that reason, theoretical chemistry approaches have been more and more undertaken to give an even finer atomistic description of the CoMoS phase. Together with innovative surface science, one intends to overcome the limitations encountered by standard characterization techniques, which cannot unambiguously solve crucial questions such as:

- Nature of the active sites;
- Location of the Co (or Ni) promoters;

- Two-dimensional (2D) morphology of the active phase layer;
- Effect of the reaction conditions on the morphology and nature of the sites.

Initially answering these questions and making link with HDS activity will help us to understand the origin of the synergy effect. Thus, on this topic, far away of describe all great experiments done on this subject, we intend just to discuss and review some interesting points of view coming from typical techniques used to study HDS catalysts and over all that ones we also perform on this work, mainly, XPS and LEIS. Raman spectroscopy and TEM usually come with complementary technique in catalyst studies and since there are not the focus on these papers, we will not dedicate a whole section for it. However, we recognize the great contribution as characterization technique and, thus, when appropriate, we will cite the contribution of each. It is noteworthy that literature on promoted Mo/TiO_2 is still scarce no matter the technique referred. Most authors report on the sulfidation and the HDS activity of Mo/TiO_2, however structural information, the sulfidation and the influence on the HDS activity of the promoters are often neglected.

One important observation came with XPS study made by Gandubert and collaborators, which have combined theoretical analysis provided by DFT, XPS and TEM results (see, e.g. [59]). They could confirm the morphology evaluation and provide insight into the optimal atomistic decoration of the nanocrystallites. First, as predicted by DFT calculations [108], the cobalt-to-molybdenum atomic ratio from XPS results do not exceed 0.5 and the optimum ratio was to be 0.47. A further increase in promoter loading only results in a decrease in the decoration ration of the nanoparticle's edges. These results are compatible with two geometric models obeying this criterion: either hexagonal model $n_M = n_S = 5$ or a slightly deformed hexagonal model with $n_M = 6$ and $n_S = 4$. Hence, it is difficult to make a choice without the help of DFT modeling. Indeed, both models fit according to TEM and XPS and the only DFT criterion in favor of the truncated triangle model is the higher thermodynamic stability of the crystallites with 60-65% of M-edge under hydrotreating conditions.

Based on these two possibilities morphologies, it is possible to calculate the number of mixed Co-Mo sites at the M-edge normalized per molybdenum atom present in the MoS_2 sheet. The optimal number regarding the cobalt as promoter was to be Co/Mo = 0.3, which is consistent with the variation observed in hydrogenation activity for this value. These results have shown that the presence of Co at the edges directly influences upon the sulfur-metal bond energy at the edge, thus, on the morphology of the active phase.

Two others XPS contributions from Coulier *et al.* [53] [109] also show interesting insights in $CoMo/TiO_2$ systems. First of all, the Mo 3*d* XPS spectra of the unpromoted and promoted Mo/Al_2O_3 or Mo/TiO_2 are identical, from which we can conclude that the presence of Co has no influence on the sulfidation behavior of Mo. However, the XPS results show that the presence of Mo did influence the sulfidation of Co and Ni significantly for both Al_2O_3 and TiO_2. Compared to the sulfidation of e.g. Co

in Co/Al_2O_3, the presence of Mo facilitates the sulfidation of Co and Ni. They conclude that promoted Mo/TiO_2 catalysts show great similarity with Al_2O_3-supported catalysts. The sulfidation degree of the calcined CoMo catalyst is 75%, whereas the sulfidation degree of calcined Co/Al_2O_3, 45%. Calcination of the promoted catalysts in TiO_2 leads to incomplete sulfidation although the degree of sulfidation is higher compared to Al_2O_3 (81% for $CoMo/TiO_2$). Regarding Co $2p_{3/2}$, they observed differences in binding energy between sulfided Co in Co/TiO_2 (779.0 eV), which consists mainly of bulk Co-sulfide, and in CoMo catalysts (779.3 eV). They conclude that the difference in binding energy represents the difference of Co in bulk sulfide and in the active phase.

Few LEIS studies have focused on CoMo-based supported catalysts. Nevertheless, some fruitful insights can be get from it. It will serve also as illustrative cases in order to know the powerful and capabilities of this technique. One can say that LEIS is a absolute surface sensitivity technique, i.e., it can probe the outermost atomic monolayer of the material (we will give a full description of the technique in a subsequent chapter). In that sense, Helfensteyn *et al.* performed electron microscopy and LEIS analysis on both fresh and cokes-contaminated commercial $CoO\text{-}MoO_3(Al_2O_3)$ catalysts [110]. The catalyst pellets were investigated in three different conditions: fresh, partly contaminated and heavily cokes-contaminated after use in the industrial hydrotreatment processes for naphtha.

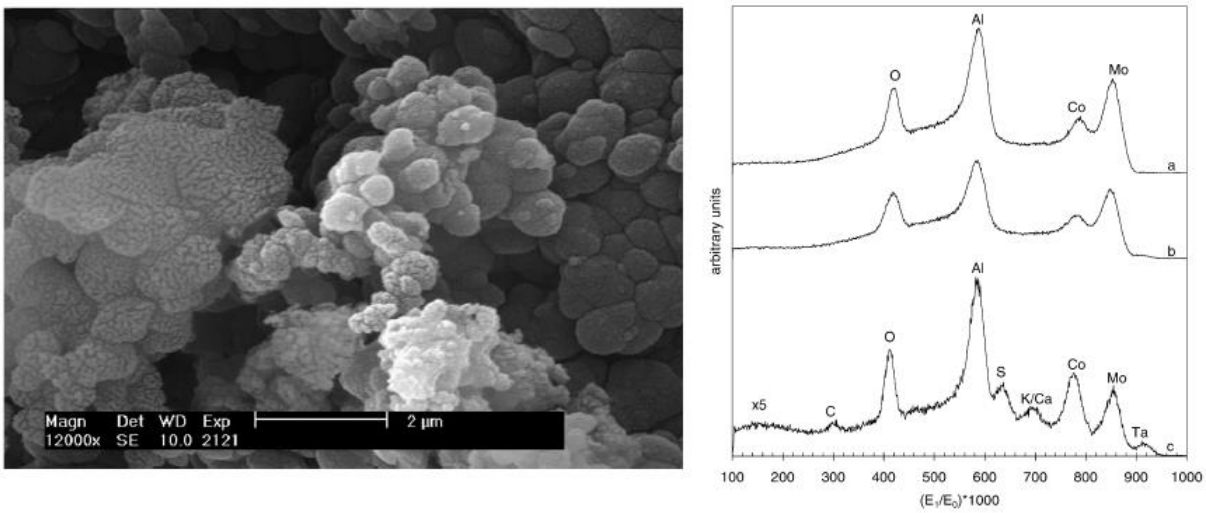

Figure I.18 - Left: SEM picture of a microscopic cauliflower of the contaminated catalyst. Right: LEIS spectra of the $CoO\text{-}MoO_3(Al_2O_3)$ oxide catalyst: (a) fresh, (b) heat-treated contaminated (regenerated), (c) contaminated pellets surface.

The SEM/EDX/LEIS-investigation shows a clear distinction between fresh and cokes-contaminated pellets. The LEIS-spectra (Figure I.*18* right) suggest a preferential C-deposition (coke impurity) on the Mo- and Al-atoms. Even gradations in cokes-contamination, which cannot be detected by visual inspection, can be distinguished with LEIS. The contaminated catalysts can be regenerated by a heat-treatment at 450 ◦C under air in a furnace. The contaminated pellets are apparently restored to their original state. These results clearly demonstrate that LEIS, by its surface sensitivity and despite the

extreme roughness (SEM images, Figure I.*18* left) of the studied surfaces, can give clear-cut information on the condition of commercial sulfided oxide catalysts.

A combination of LEIS and XPS analysis on Mo/TiO_2 with different Mo loadings was performed by Rondon *et al.* [111]. The idea were to correlate the surface coverage to the catalytic activity. Since each technique for surface coverage measurement (CO_2 chemisorption, low-temperature CO adsorption, XPS, IR-spectroscopy, Raman spectroscopy and LEIS) has its own limitation, by using three of them the validation of the method by the others is more reliable.

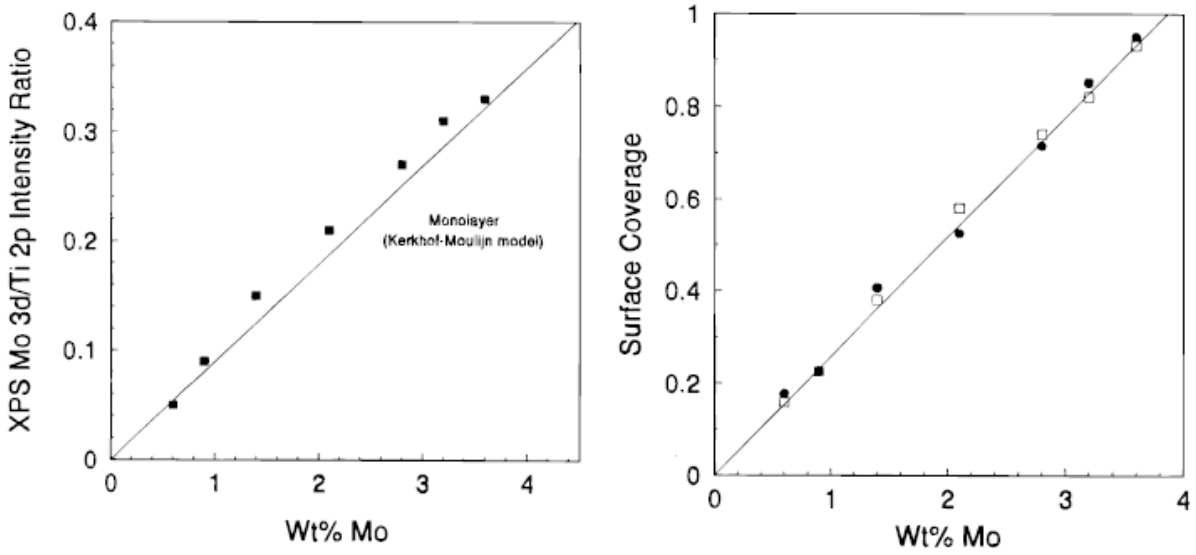

Figure I.19 – Left: Variation of XPS Mo 3*d*/Ti 2*p* intensity ratio as function of Mo loading for Mo/TiO_2 catalysts (the solid line referee the predicted monolayer). Right: Surface coverage for the same catalysts as function of Mo loading as determined by (●) LEIS, (□) CO_2 chemisorption. Again, the solid line represents the coverage predicted for monolayer dispersion *[111]*.

Thus, Raman spectroscopy was used to verify if there was any bulk molybdenum compound such as MoO_3. XPS spectroscopy indicates uniform dispersion of the Mo phase over the surface of titania for all the analyzed simples, as it can be seen by Mo 3*d*/Ti 2*p* intensity ratio Figure I.*19* (left) (the linear increase with intercept at the origin). The coverage values estimated above from the CO_2 chemisorption method agree with those obtained by LEIS (Figure I.*19*, right). Furthermore, these "experimental" coverages are consistent with the predicted values for monolayer dispersion. LEIS surface coverage rate was evaluated by taking Mo/Ti experimental intensity ratios.

A "pure" Raman contribution is worth mentioning, Lamonier *et al.* studied the dispersion limit of $Ni(Co)Mo/TiO_2$ and compared with $Ni(Co)Mo/Al_2O_3$ HDS oxide precursors [112]. The main objective were to get insights on the genesis of oxide precursors in impregnation process and the formation of Anderson-type structures, a fact well stablished on alumina support. The catalysts were prepared from a ammonium heptamolybdate and cobalt (nickel) nitrate solution. The detected Raman signals of CoMo-oxyhydroxide and $AlMo_6$ on dried solids are in accord to the formation of $CoMoO_4$ and MoO_3 phases

upon calcination. On the other hand, in titania supported CoMo solids no heteropolyanionic phase $Co^{II}Mo6$ is formed, isopolymolydate phase being well dispersed on CoMo solids. According to the authors, for improvement of catalytic performances the use of impregnation solution without ammonium is a better try as well as the use of a cobalt salt of $[Co_2Mo_{10}H_4O_{38}]^{6-}$.

5. In Situ XAS Studies Review

X-ray absorption spectroscopy is a powerful method for probing the average local electronic and geometric structures of catalysts in the working state. Element-specific data can be obtained over a wide range of temperatures (room temperature to >1000 K), and pressures (from sub ambient to well more than 100 bar). Because the specimen can be investigated under such a wide range of conditions, XAS has become one of the most frequently applied techniques for structural characterization of working catalysts. Often there is no other way to obtain the structural information provided by this technique that allows one to develop specific structure-activity relationships in catalysis. XAS is applicable to a broad range of elemental concentrations (from tens of ppm to wt. % levels), and therefore is used to characterize both high-surface-area supported catalysts and bulk catalysts (e.g., oxides). Although XAS has been used for almost 40 years to characterize catalysts in the working state, methodology, equipment, and applications are still being advanced.

Many methods can be used to probe a catalyst's structure under reaction conditions. XAFS spectroscopy[1] provides element-specific information about the local chemistry and physical structure of the element under investigation. XANES provides information about the chemical state of the element, including the oxidation state, and sometimes the local geometry (via selection rules), and EXAFS provides quantitative information about the distance from the absorbing atom to neighboring atoms and the coordination number and type of the neighboring atoms.

A major reason why XAFS spectroscopy has become a useful probe of catalyst structure is the fact that it is easily adapted to characterization of samples in reactive atmospheres. The X-ray photons are sufficiently penetrating that absorption by the reaction medium is minimal. Moreover, the use of X-ray-transparent windows on the catalytic reaction cell allows the structure of the catalyst to be probed at reaction temperature and pressure. For example, the catalyst may be in a reaction cell, with feed flowing over it, and normal online analytical tools (gas chromatography, residual gas analysis, Fourier transform (FT) infrared spectroscopy, or others) can be used to monitor the products. At the same time the

[1] For a full description of XAS spectroscopy and its variants (named, XANES and EXAFS), please refer to its dedicated Chapter.

interaction of the X-rays with the sample can be used to determine critical information about the electronic and geometric structure of the catalyst.

Among the techniques that can be used to reveal mixed phase of the CoMoS type (such as Mössbauer, IR or XPS), EXAFS is the only one that can provide structural information about the mixed phase under *in situ* conditions and its conversion from the oxide phase to the sulfide phase in the course of activation. It is thus the tool of choice for understanding this type of catalyst. XAS was, in fact, the first technique to reveal the presence of particles of MoS_2. A first review of the application of XAS spectroscopy to sulfide catalysts was published in 1986 by Konigsberger and Prins [113], a second one in 1996 by Clausen and Topsøe [114].

It was in the early 80s that XAS spectroscopy was applied to HDT catalysts and demonstrated the existence of an active phase in the form of nanoparticles of MoS_2 [46]. For the first time, through investigation of the Mo K-edge, this technique was able to demonstrate unambiguously, as a result of the concordance of structural parameters, that the active phase of a HDS catalyst comprise small particles of MoS_2, as illustrated in Figure I.*20* (left).

Later on, TEM technique confirmed this lamellar structure, which is characteristic of MoS_2 slabs. However, there was a contradiction between the length of the slabs observed by TEM (typically 2 to 3 nm) and that deduced from the number of neighbors N(Mo) obtained by EXAFS, which suggested sizes of 1 nm. This ambiguity was removed only in 1998 by Calais *et al*. [115]and then Shido and Prins [116] who explained this difference through local disorder in the vicinity of the slabs, which introduces a contribution to the static disorder affecting the number of Mo–Mo neighbors. In their excellent wotk, Shido and Prins suggested a new correlation for the correspondence between slab length and N(Mo) that in more realistic than the one produced by a simple geometrical model (Figure I.20, right). It is noteworthy that on TEM images, curved slabs are frequently observed and these curvatures also might contribute to the static disorder and consequently reduces the estimated particle sizes estimated by EXAFS.

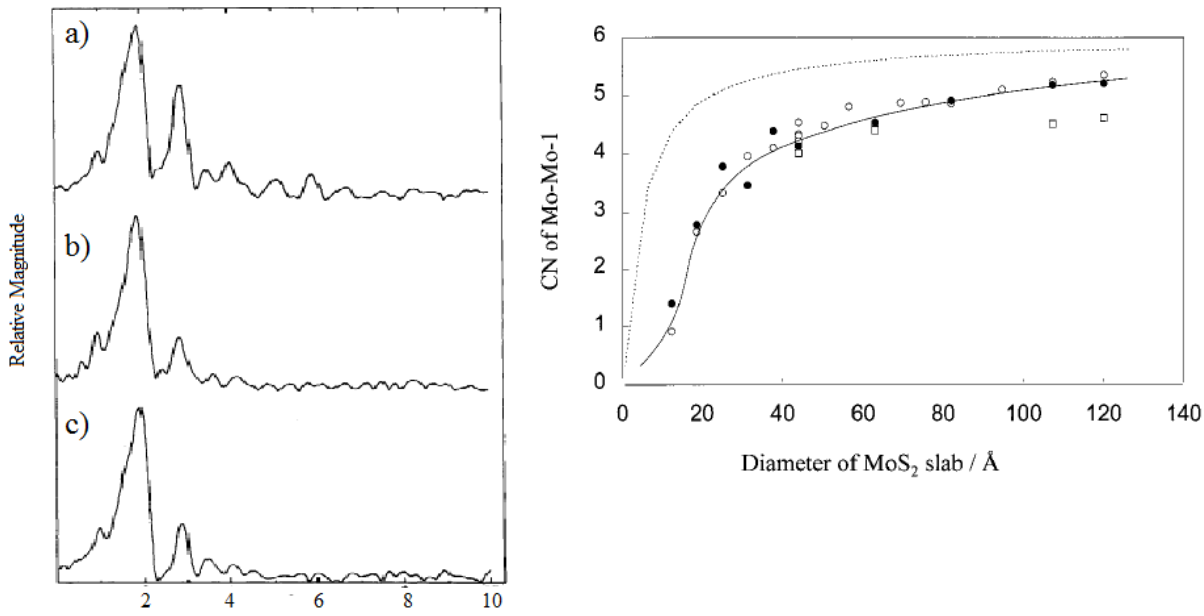

Figure I.20 - Left: Fourier Transform of XAS for (a) well-crystallized MoS_2; (b) sulfided Mo/Al_2O_3 and (c) sulfided $Co\text{-}Mo/Al_2O_3$ catalyst *[53]*. Right: Variation of coordination number N(Mo-Mo) with MoS_2 particle size: geometric model (dotted line) and model including structural disorder (full line). Circles and squares represent experimental data *[116]*.

Another important result of XAS spectroscopy applied to HDS catalysis is that has supported the CoMoS model suggested based on Mössbauer spectroscopy. Thus, among several evidences for the lamellar structure, Claussen *et al.* [46] were the first to observe the presence of a Co-Mo contribution located at 2.75-2.85 Å in the coordination sphere of Co beyond sulfur. CoMoS of type I and II were also proposed with the support of XAS [117].

5.1. Characterization of the Precursor State

The precursor state is one of the most difficult to define structurally because the environment of the atoms in the oxide state is very often very complex, particularly in octahedral environments (up to 5 distinct distances in the first Mo-O coordination sphere), and because of the several possible types of Mo environment in a given compound (see Table 4). EXAFS is unable to solve such environmental complexity; however, starting with perfectly characterized precursors it is always possible to follow the progress of impregnation, for example, or heat treatment (drying, calcination) and observe the local structural changes. As far as the preparation of HDS catalysts is concerned, it has been shown that alumina is not an inert support but takes part in the creation of oxide species with, for instance, the formation of heteropolyanions.

Table 4 - Mo-O distances of the first coordination distribution of some Mo-oxide reference compounds *[149]*.

Compound	MoO_3		$CoMoO_4$		$Mo_7O_{24}^{2-}$	
Mo-O Distances of the First Coordination Sphere	Mo-O(1)	1.67	Mo-O(1)	1.73 (x2)	Mo-O(1)	1.71 (x2)
		1.72		1.89		1.949
		1.94 (x2)		1.98		2.148
		2.25		2.31		1.991
		2.34	Mo-O(2)	1.72 (x2)		2.279
				1.93 (x2)	Mo-O(2)	1.99
				2.33 (x2)		1.96
						1.71 (x2)
						1.94
						2.18
						2.24
					Mo-O(3)	1.95
						2.17
						1.72
						1.71
						1.89
						2.51
					Mo-O(4)	2.26
						1.74
						1.89

XAS has been successfully used to distinguish different types of oxide precursors in catalytic preparation. For example, XANES gives a clear signature of the presence of Co^{3+} in $CoMo_6$ ammonium HPA and as counter anions in $AlMo_6$ or $CoMo_6$, as illustrated in Figure I.21 [119].

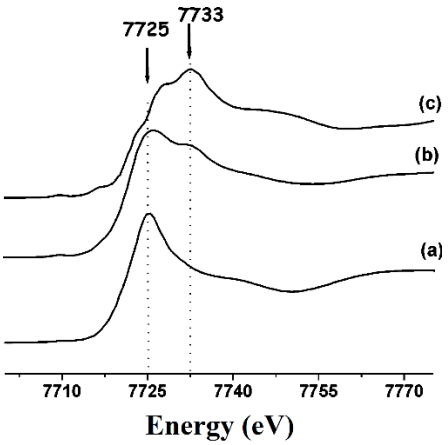

Figure I.21 - XANES at Co K-edge a) $AlMo_6Co$; b) $CoMo_6Co$; c) $CoMo_6$-Am (a non-refereed Anderson ammonium salt) *[119]*.

A systematic XAS study on CoMo-based catalysts was performed by Rochet in 2011 [120]. Impregnated catalysts with Co/Mo = 0.5 were prepared on alumina and studied by time-resolved XAS at Synchrotron SOLEIL. In order to well identify the oxide precursors and be able to distinguish contributions between

the HPA $CoMo_6$ and Co_2Mo_{10}, she performed EXAFS measurements on both Mo and Co K-edges. The EXAFS parameters corresponded to these two structures used on the work are listed on Table 5.

Table 5 - EXAFS Parameters at both Mo and Co K-edges of the two HPA *[120]*.

Mo K-edge				
	$CoMo_6$		**Co_2Mo_{10}**	
	N	**R (Å)**	**N**	**R (Å)**
Mo-O	2.4	1.71	2	1.70
Mo-O	2.0	1.95	2	1.93
Mo-O	2.2	2.30	2	2.30
Mo-Co	1.3	3.31	0.4	3.21
Mo-Mo	2.5	3.32	2	3.31

Co K-edge				
	$CoMo_6$		**Co_2Mo_{10}**	
	N	**R (Å)**	**N**	**R (Å)**
		Co^{3+}		
Co-O	6	1.91	6	1.90
Co-Co	-	-	1	2.77
Co-Mo	-	-	2	3.02
Co-Mo	6	3.29	5	3.27
		Co^{2+}		
Co-O	2	2.04	6	2.08
Co-O	4	2.21	-	-
Co-Mo	1	3.77	-	-

References like those presented on the table are important because as we can see that for both HPA the distances regarding Mo K-edge are quite similar. However, if we take into account the Co K-edge, one can look for contributions around 2.77 Å, since it is only present for Co_2Mo_{10} species. This contribution allows us to identify surely this compound, but it shall not exclude the presence of $CoMo_6$.

Thereby, Rochet could successfully describe the local atomic picture for the oxide precursors (dry and calcined) of impregnated CoMo-based catalysts in terms of HPA formed and their interactions with the Al_2O_3 support. It is noteworthy that this interaction happens via Mo-Al bound (2.63 Å) and also Co-Al (3.93 Å).

In summary, no matter the oxide precursor, they might be transformed or not in preparation step and XAS can provide evidence of these modifications.

5.2. Catalytic Reactors and Cells

The successful design of a catalytic reactor that also serves as a cell for XAS is critical for obtaining XAFS data of catalysts in the functioning state. There are no commercially available cells for such applications. Therefore, each research group has fabricated their own cells, often specifically designed for a particular catalyst or catalytic reaction.

Each cell design has its own set of advantages and disadvantages, and the information content desired from the experiment drives the designs of the cell. There are two broad classifications of the cells: (1) those that approximate plug-flow reactors—these are attempts to mimic the flow conditions in a true catalytic reactor and (2) cells that are not plug-flow reactors, and often include a pressed wafer of catalyst with substantial gas by-passing.

The overall purpose of the reactor cell is to protect the environment surrounding the catalyst such that the catalyst can be characterized in a well-controlled state, whether it is that of some precursor or that of the working catalyst. To accomplish the desired goals, the XAFS spectroscopy cells have been designed to allow a flow of reactants over, or through, the catalyst sample while the reactor is brought to a given temperature and pressure.

Different cells have been proposed to study catalysts in working conditions, one of the first designs of a cell for XAFS spectrosc opy of catalysts in reactive atmospheres was published by Lytle et al. in 1979 [121]. Following the pioneering investigations of Lytle et al., the 1980's saw several other groups using XAFS spectroscopy for characterization of catalysts in reactive atmospheres. In 1981, the Haldor Topsøe group reported an investigation of cobalt-molybdenum hydrodesulfurization catalysts [46]. A nice review, with detailed information and designs of reactors and cells for XAS measurements in work conditions can be found in the paper written by Bare and Ressler [122].

Particularly, a new cell for heterogeneous catalysis was developed on SAMBA beamline in Synchrotron SOLEIL [123]. This cell is also suitable for combination with Raman spectroscopy providing valuable complementary information on the state of the catalyst in working conditions. Furthermore, an on-line product analysis can be obtained either by mass spectrometry or Raman spectroscopy providing a full description of the activity of the catalyst[2]. In order to test the workability of the full set-up and to illustrate its possibilities, La Fontaine *et al*., the designers of such cell, performed a study of a bimetallic nickel-molybdenum catalyst supported on alumina during the calcination of a HDS catalyst. Spectra during calcination was recorded from room temperature (RT) up to 450 °C with a 2 °C/min ramp, in a mixture of O_2 and N_2 flux at atmospheric pressure. The records of Mo and Ni-edges as well as Raman signals obtained during the heating ramp of the calcination of the catalyst are exhibited in Figure I.*22*. By the evolution on the XANES pre-edge feature of Mo K-edge and by the shape of its white line, the authors pointed out a depolymerisation of the initial polymolybdates into a tetrahedral species MoO_4^{2-} upon calcination.

[2] A full description of SAMBA beamline, the Quick-EXAFS monochromator and the reaction cell (which were the same that was used on our work) are described on specific topic in the Methods Chapter.

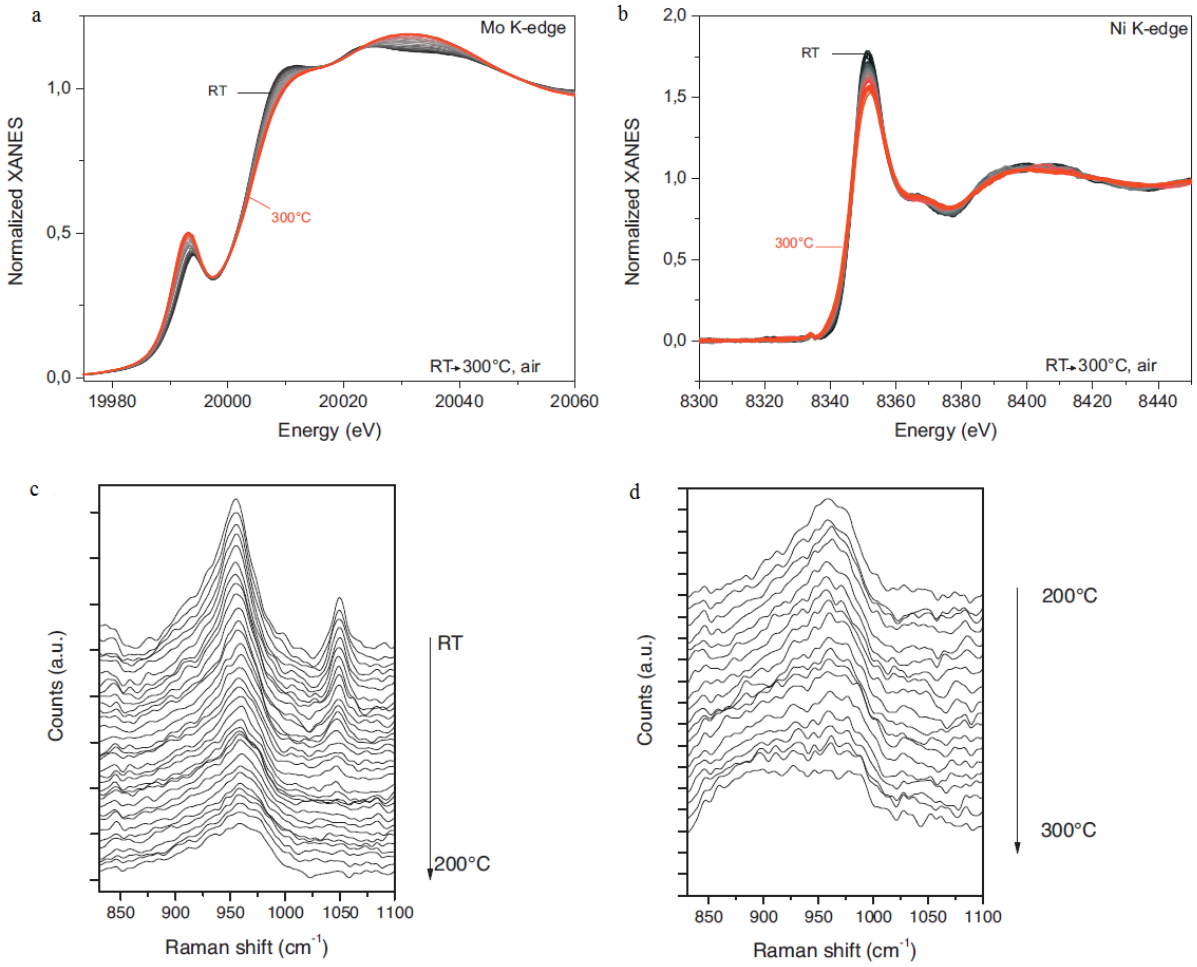

Figure I.22 - Mo (a) and Ni (b) Quick-XANES spectra obtained during the calcination of the hydrodesulphurization NiMo catalyst. Evolution of Raman signal obtained during the calcination of the hydrodesulphurization NiMo catalyst (c: from RT to 200 °C and d: from 200 to 300 °C) (from *[123]*).

Quantitative information was also obtained by EXAFS. At 300 °C the structure exhibits a single coordination shell of 3.6 ± 0.4 oxygen atoms at an average distance of 1.74 ± 0.02 Å. The Raman spectra helps to fix the points of dehydration and start of depolymerisation of the Mo species towards MoO_4^{2-} species. Raman also brings additional information with the monitoring of the decomposition of nitrate nickel species. The combination of these two techniques was used to speculate the XANES fingerprint of the totally denitrated and de-hydrated supported nickel species as to be the spectrum recorded at 156 °C. Such additional information is very convenient because this XANES spectrum presents only slight differences in white line shape and intensity from the one of the as-prepared catalyst. The authors highlighted that without the combination of XAS spectroscopy helped by Raman spectroscopy it would be very difficult to do the proposition of the spectrum recorded at ∼156 ◦C as the one associated to the de-nitrated Ni supported species.

In the same line of research, the SAMBA beamline group have published some recent works in Fisher-Tropsch catalysts using on purpose cell for *in situ* and *operando* experiments [124] [125]. Thanks to

new equipments of 3rd generation Synchrotron Radiation facilities and to the development of these new *in situ* systems as exampled above, it is possible to use time-resolved *operando* structural analysis under realistic conditions (such as, reaction temperature of 250 °C and pressure of 18-20 bar) in order to greatly improve the knowledge on catalytic property-structure relationship. All these recent developments give us the validation necessary on the set-up and show us how promising are these new *in-situ* experiments applied to structural evolution of catalysts during a reaction.

5.3. Reactivity Under H_2, Activation and QEXAFS

The activation of the catalyst is a particular important step because it leads to formation of the CoMoS active phase. In addition, since 1984, investigations with a view to understand this stage in the genesis of the catalyst have been carried out [126], showing that Mo/Al_2O_3 catalyst sulfide at 100 °C and below do not form MoS_2. Rather a Mo-S distance longer than the one observed in MoS_2 was observed and attributed to Mo-S-H or polysulfide. At higher sulfiding temperature (200 °C and above), Mo-Mo scatterings were observed. XAS has been used to compare sulfidation process of Mo and CoMo systems on titania and alumina [89]. From EXAFS analysis performed at various sulfiding temperatures, it was concluded that on alumina oxygen-sulfur exchange starts at a temperature just above room temperature resulting in the formation of monomer and dimer species molybdenum sulfide species containing disulfide ligands. Between 175 and 250 °C, the disulfide ligands are reduced with hydrogen and only molybdenum sulfide dimer species with a Mo-Mo distance of 2.77 Å remain. Above 250 °C, these dimers aggregate to larger MoS_2 particles. In contrast, on titania molybdenum oxide is sulfided to yield isolated molybdenum sulfide monomers at 250 °C, which similarly aggregate to MoS_2 particles between 250 and 350 °C. On both alumina and titania, it is suggested all intermediates are anchored to the support via Mo-O links with a bond length of 2.0 Å.

In the case of doped HDS catalysts, in which the active phase is of the CoMoS type, simultaneous investigation of X-ray absorption spectra at the edges of each metal element gave supplementary insights into the structure of the sulfide phase. Study of samples activated at different temperatures (or *in situ* studies) makes it possible to access the mechanism of formation of the sulfide phase and intermediaries present in these catalysts. When a HDS catalyst is heated *in situ* in a XAS cell with H_2, a clear change is observed in the Co-S coordination number. Such behavior can be attributed either to the formation of a vacancy or a change of the Co environment by formation of an S bridge [118].

The activation of a HDS catalyst is a major stage in the genesis of the active phase, which take place through a series of temperature rises and plateaus with the help of a sulfiding agent (mostly H_2S/H_2 mixture of variable concentration, actual or model feed). It is clear that intermediate states in sulfideing have been identified by different techniques. However, the use of rapid monochromator rotation in XAS

experiments makes it possible to benefit from a time resolution of a few seconds to a few msec and therefore to follow chemical reactions dynamically.

The first example of the use of quick EXAFS for characterizing the sulfidation of Mo in a HDS catalyst dynamically was achieved by Claussen [127]. This technique was used to follow the change in the conversion of the Mo oxide into sulfide and the creation of Mo slabs with the formation of Mo-Mo bonds in the plane of the slabs. QEXAFS was also useful to clarify the kinetics during sulfidation of Co species on the bimetallic catalysts. Geantet *at al.* [70] by looking at the first EXAFS peak, they showed that for $CoMo/Al_2O_3$ the first neighbor distance rapidly rises up to the value of Co–S distance, whereas for Co alone a temperature of 473 K is needed to perform the sulfidation.

A nice work on activation step (under H_2/H_2S) of CoMo-based HDS catalysts using QEXAFS was done by Rochet [120]. By probing both Co and Mo K-edges (Figure I.23a), this technique allowed her to describe at atomic level the local transformations on the structure from oxide phase until the active phase. It occurs in a 4-steps process if the catalyst is just dry and in a 3-steps process if the catalyst is calcined. The method chosen for derive the changes in structure from the data set was to consider changes in the isosbestic points during the reaction. Since it is just for illustration purposes, it is not worthy to talk about both the dry and the calcined catalyst activation results. Similar treatment, problems and results were obtained for the cases.

Regarding Mo K-edge, the first intermediary compound it was identified as a partial depolymerization of the oxide phase, there were some contributions from the second shell when one looks to the Fourier Transform (FT) of the EXAFS signal as well as the interaction with the support via Mo-Al (Figure I.23b). For the second intermediary compound, two models were taken to EXAFS analysis, MoS_3 and $\{MoOS_2\}$ compounds. The presence of a short distance contribution above the intense peak in the FT suggest the presence of an oxygen contribution and that was the model considered in the end. The final state was identified as MoS_2 with 6.1 S near neighbors (at 2.41 Å) and 3.9 Mo next neighbors (at 3.17 Å). Taken the reconstruction of each experimental spectrum of the reaction by linear combination of these four previous described, it was possible to make a concentration profile for the whole activation reaction.

Regarding the Co K-edge, some technical issues prevent a deeply analysis of the reaction. Particularly, such problems caused loss in efficiency of the system and, then, the EXAFS data could not be recorder at ideal conditions. Even so, as in the Mo K-edge case, it was possible to recognize a similar evolution of XANES spectra for the reaction. For the final state identification, an intense peak was simulated as to be a Co-S contribution with 4.6 neighbors at 2.22 Å. A second peak was present on FT of this final state, but neither the Co-Co contribution due to the expected phase Co_9S_8 at 2.5 Å for a Co-Mo contribution at 2.8 Å as suggested by others authors [117] [49] could make the refinement better, which do not exclude the presence of those species.

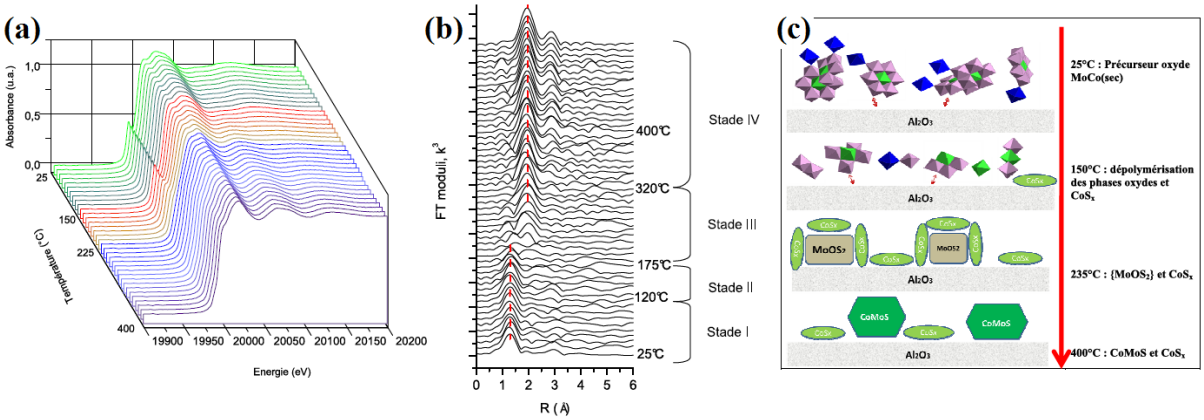

Figure I.23 – (a) XANES evolution of Mo K-edge of dried CoMo catalyst during activation under H_2/H_2S flux, different colors are related with phase changes. (b) Corresponded Fourier Transform Moduli from the EXAFS signal of dried CoMo catalyst. (c) Illustration of structural evolution during activation.

Finally, by taking into account the structural evolution in both Mo and Co K-edges a full description of the whole process during activation step was designed, as shown in Figure I.23c.

These examples illustrate the great benefit of using QEXAFS for understanding catalyst activation.

5.4. Application of Chemometrics in XAS studies

The use of chemometrics associated to spectroscopy data is not new [128]. Principal Component Analysis (PCA) is one of the most basic and widely used chemometric tools devoted to find the number and direction of the relevant sources of variation in a bilinear data set[3]. Taking into account its use (or methods directly derived from PCA, such as Evolving Factor Analysis, EFA) in XAS data analysis, one can find, for instance, interesting studies on this technique in order to provide an method to interpret complex XANES spectra and to obtain a quantitative distribution of the chemical species contributing to those spectra [129] [130] [131].

In fact, for a long time, principal component analysis (PCA) and factor analysis (FA) have been used to determine the rank of the matrix, generally assumed as the number of chemical species of the system, but PCA acts on the whole matrix returning its full rank. In the case of dynamic systems, we can apply a local PCA analysis to find the local rank of the data, such as evolving factor analysis (EFA),

One of the earlier studies associating XAFS and PCA for application in supported HDS catalysts was performed by Fay *et al.* in 1992 [132]. In this study, the goal of PCA application was to help to decide if there were 2, 3 or 4 spectral components on experimental both normalized and non-normalized χ (k)

[3] Conceptual presentation and formalism of Chemometrics method are on dedicated chapter.

spectra from XAFS measurements of Mo/TiO_2 catalysts with different Mo loadings. The reconstruction of the data matrix could be done for all the three possibilities Figure I.*24*.

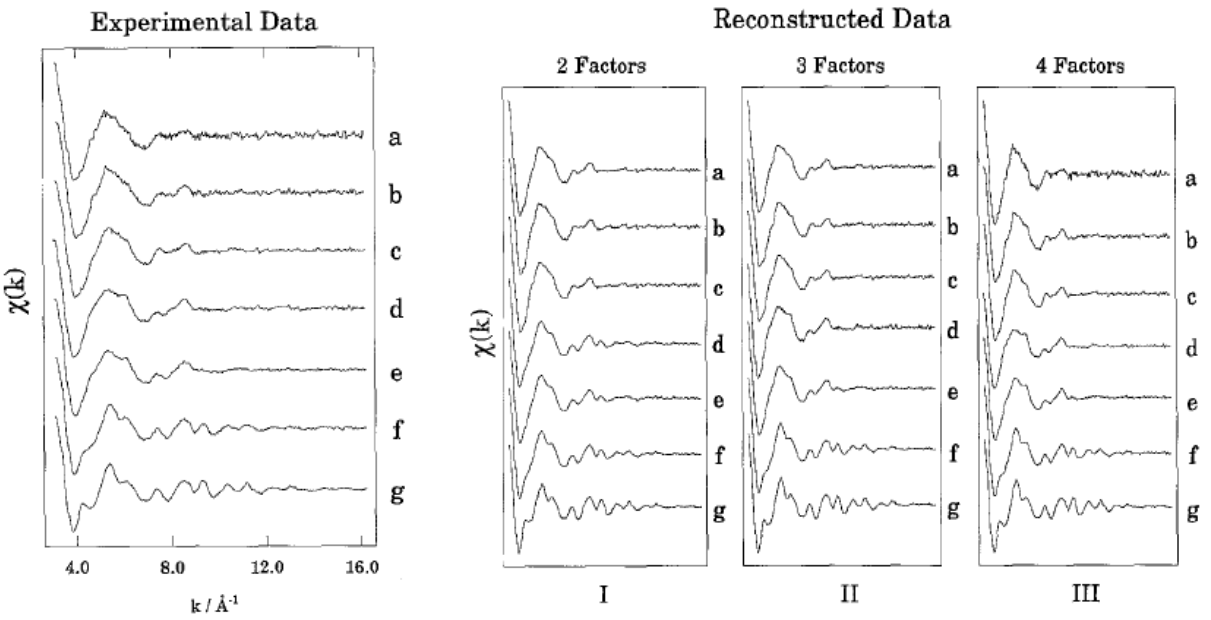

Figure I.24 – Experimental χ (k) data spectra of Mo/TiO2 catalysts used in PCA for different Mo loadings (0.5-13.5 wt. % MoO_3) and their reconstruction based on PCA results.

This figure provides a visual justification for the presence of 3 factors. Although 2 components reconstruct the original data matrix quite well, there is clearly some mismatch particularly between experimental spectrum *d* and reconstructed spectrum *d*(I). This difference is taken into account in spectrum (II) which uses 3 components. While using more components will always improve the agreement between the experimental data and the reconstructed data, addition of the fourth component slightly modifies spectrum d but also simply adds noise to spectrum a. Thus adding the fourth component appears to provide little additional information about the signal.

Thus, results from the principal component analysis indicated that three Mo species exist on the catalysts. One of these species was assigned to MoO_3, which was detected by Raman for the highest loading catalysts. The remaining two were attributed to structurally different octahedral "surface Mo species". Comparison of the PCA from several different analysis ranges indicated that PCA can be carried out on χ (k) spectra over a relatively small region of k-space. This could be useful in situations where spectral interferences limit the analysis range of EXAFS data. In addition, use of PCA can provide better justification for EXAFS curve fitting results since the maximum number of shells required to fit a spectrum is known from the prior PCA analysis.

When one takes into account a deeper chemometric analysis of the data, such as Multivariate Curve Resolution (MCR), the number of paper associating this technique to XAFS is still low. Just a few dozen articles are found when we associate MCR and XAS words on typical academic database and search

engines (particularly, up to the redaction of this manuscript, about 20 academic articles are found on ScienceDirect®).

A recent work performed by Conti *et al.* [133] illustrates the last trends in application of MCR in XAS data analysis. There, a chemometric approach has been applied to study the (XANES) evolution during *in situ* scanning of the $Cu_{0.1}V_2O_5$ xerogel/Li ions battery. Among the more common techniques, the fixed size windows evolving factor analysis (FSWEFA) permits the number of species involved in the experiment to be determined and the range of existence of each of them. This results combined with the constraints of the invariance of the total concentration and non-negativity of both concentrations and spectra, enabled the authors to obtain the spectra of the pure components using a multivariate curve resolution refined by an alternate least squares fitting procedure. This allowed the normalized concentration profile to be understood.

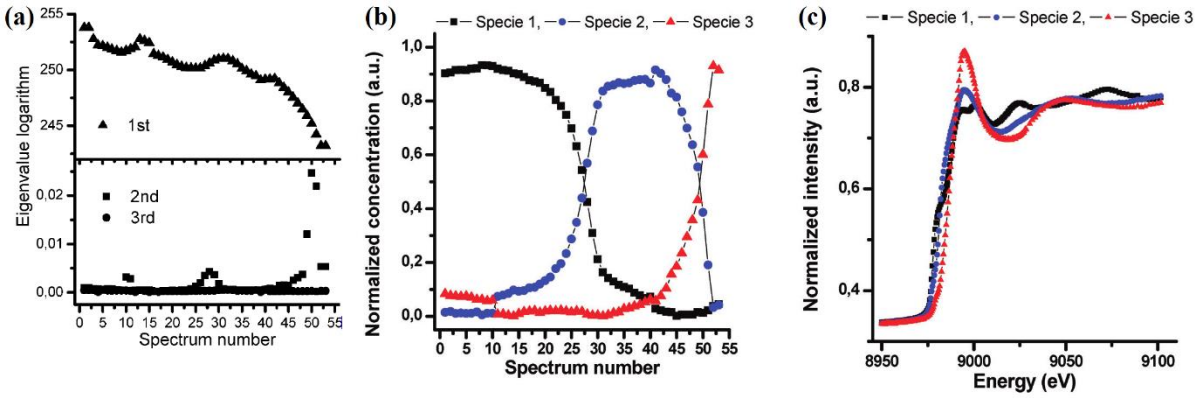

Figure I.25 – (a) Graph of the eigenvalue logarithm versus the central point of the FSWEFA window. Computed concentration profiles (b) obtained with the MCR data treatment and the corresponding pure spectra (c).

They described the procedure as follow: The output of the FSWEFA is represented as a graph of the log transform of the eigenvalues versus the evolution parameter. The obtained curves are peak-shaped; the peaks are located at the equivalence point of two superimposing species (Figure I.25a). This means that they can use the peak position as a first approximation of the boundary point between the range of existence of different species. In this hypothesis, one species exists before the peak and another one after it. In a first attempt, they have hypothesized four non-superimposing species, and the optimizing algorithm has converged to three species only. Then, applying MCR calculations, they were able to calculate the concentration profile (Figure I.25b) and the corresponding pure spectra (Figure I.25c). With this method the local coordination environment of the "new" detected species number 2 could be identified by EXAFS analysis, by using one of the EXAFS spectrum in the 32-40 range of recorded spectra, because, in them, the single chemical phase is certain (Figure I.25b). The pure spectra have been obtained and compared to the experimental ones, with very good agreement.

More generally, these examples show the potentiality of the joined chemometric-dynamic XAS approach to study the local structural dynamics of atomic species that undergo some structural modifications. In particular, the chemometric approach permits a quicker data interpretation that would be very time consuming and very challenging if a mixed phase could have been present and if only EXAFS was relied on.

References

[1] A. C. Byrns and L. W. Moore, "Catalytic Desulfurization of Gasolines by Cobalt Molybdate Process," *Industrial and Engineering Chemistry*, vol. 35, p. 1160, 1943.

[2] T. A. Pecoraro and R. R. Chianeli, "Hydrodesulfurization Catalysis by Transition Metal Sulfides," *Journal of Catalysis*, vol. 67, p. 430, 1981.

[3] H. Topsøe, B. S. Clausen and F. E. Massoth, Hydrotreating Catalysis - Science and Technology, vol. 11, M. B. J. R. Anderson, Ed., Berlin, 1996.

[4] B. Delmon, "New technical challenges and recent advances in hydrotreatment catalysis. A critical updating review," *Catalysis Letters*, vol. 22, p. 1, 1993.

[5] P. Ratnasamy and S. Sivasanker, "Structural Chemistry of Co-Mo-Alumnina Catalysts," *Catalysis Review: Science and Engineering*, vol. 22, p. 401, 1980.

[6] H. Topsøe, B. S. Claussen, R. Candia, C. Wivel and S. Mørup, "In situ Mössbauer emission spectroscopy studies of unsupported and supported sulfided CoMo hydrodesulfurization catalysts: Evidence for and nature of a CoMoS phase," *Journal of Catalysis*, vol. 68, p. 433, 1981.

[7] C. Wivel, R. Candia, B. S. Claussen, S. Mørup and H. Topsøe, "On the catalytic significance of a CoMoS phase in CoMo Al2O3 hydrodesulfurization catalysts: Combined in situ Mössbauer emission spectroscopy and activity studies," *Journal of Catalysis*, vol. 68, p. 453, 1981.

[8] P. Grange and X. Vanhaeren, "Hydrotreating catalysts, an old story with new challenges," *CAtalysis Today*, vol. 36, p. 375, 1997.

[9] M. W. J. Craje, V. H. J. Debeer, J. A. R. Vanveen and A. M. Vanderkraan, "Sulfidation of Co/Al2O3 and CoMo/Al2O3 Catalysts Studied by Mössbauer Emission Spectroscopy," *Journal of Catalysis*, vol. 143, p. 601, 1993.

[10] M. W. J. Crajé, V. H. J. d. Beer, J. .. R. v. Veen and A. M. v. d. Kraan, "Sulfidation and activity of Co/C catalysts having extremely low cobalt-loading: a mössbauer emission spectroscopy and thiophene hydrodesulphurization study," *Applied Catalysis A*, vol. 100, p. 97, 1993.

[11] M. Karroua, H. MAtralis, P. Grange and B. Delmon, "Synergy between "NiMoS" and Co9S8 in the Hydrogenation of Cyclohexane and Hydrodesulfurization of Thiophene," *Journal of Catalysis*, vol. 139, p. 371, 1993.

[12] S. Harris and R. R. Chianelli, "Catalysis by transition metal sulfides: A theoretical and experimental study of the relation between the synergic systems and the binary transition metal sulfides," *Journal of Catalysis*, vol. 98, p. 17, 1986.

[13] R. R. Chianelli, G. Berhault, P. Raybaud, S. Kasztelan, J. Hafner and H. Toulhoat, "Periodic trends in hydrodesulfurization: in support of the Sabatier principle," *Applied Catalysis A: General*, vol. 227, p. 83, 2002.

[14] H. Topsøe, Henrik, B. S. Claussen and S. Bjernes, "Importance of Co-MoS Type Structure in hydresulfurization," *Catalysis Reviews,* vol. 26, p. 395, 1984.

[15] R. I. Masel, Principles of Adsorption qnd Reaction on Solid Surfaces, 2nd ed., New york: Wiley, 1996.

[16] R. R. Chianelli, T. A. Pecoraro, T. R. Halbert, W. H. Pan and E. I. Stiefel, "Transition Metal Sulfide Catalysis: Relation of the Synergic Systems to the Periodic Trends in Hydrodesulfurization," *Journal of Catalysis,* vol. 86, p. 226, 1984.

[17] H. Toulhoat and P. Raybaud, "Kinetic interpretation of catalytic activity patterns based on theoretical chemical descriptors," *Journal of Catalysis,* vol. 216, p. 63, 2003.

[18] W. N. Delgass, G. L. Haller, R. Kellerman and J. H. Lunsford, Spectroscopy in Heterogeneous Catalysis, New York: Academic Press, 1979.

[19] G. Ertl, H. Knözinger and J. Weitkamp, Handbook of Heterogeneous Catalysis, Weinheim: VCH, 1997.

[20] J. W. Niemantsverdriet, Spectroscopy in Catalysis, 2nd ed., Weinheim: Wiley-VHC, 2000.

[21] R. T. K. Baker and P. S. Harris, "Controlled atmosphere electron microscopy," *Journal of Physics E: Scientific Instruments,* vol. 5, p. 793, 1972.

[22] E. D. Boyes and P. L. Gai, "Environmental high resolution electron microscopy and applications to chemical science," *Ultramicroscopy,* vol. 67, p. 219, 1997.

[23] P. L. Hansen, J. B. Wagner, S. Helveg, J. R. Rostrup-Nielsen, B. S. Clausen and H. Topsøe, "Atom-Resolved Imaging of Dynamic Shape Changes in Supported Copper Nanocrystals," *Science,* vol. 295, p. 2053, 2002.

[24] B. M. Moyse, "HDS Catalysts Have the Edge," *World Refining,* vol. January/February, p. 20, 2001.

[25] R. Prins, in *Handbook of Heterogeneous Catalysis*, Weinheim, VCH, 1997, p. 1908.

[26] H. Topsøe, "Developments in operando studies and in situ characterization of heterogeneous catalysts," *Journal of Catalysis,* vol. 216, p. 155, 2003.

[27] J. A. Wilson and A. D. Yoffe, "Transition Metal Dichalcogenides," *Advances in Physics,* vol. 18, p. 193, 1969.

[28] R. Dickinson and L. Pauling, "The Crystal Structure of Molybdenite," *Journal of American Chemical Society,* vol. 45, p. 1466, 1923.

[29] M. Daage and R. R. Chianelli, "Structure-Function Relations in Molybdenum Sulfide Catalysts: The "Rim-Edge" Model," *Journal of Catalysis,* vol. 149, p. 414, 1994.

[30] T. Hayden and J. Dumesic, "Studies of the Structure of Molybdenum Oxide and Sulfided Supported on Thin Films of Alumina," *Journal of Catalysis,* vol. 103, p. 366, 1987.

[31] L. S. Byskov, J. K. Nørskov, B. S. Clausen and H. Topsøe, "Edge termination of MoS2 and CoMoS catalyst particles," *Catalysis Letters,* vol. 64, p. 95, 2000.

[32] S. Helveg, J. V. Lauritsen, E. Lægsgaard, I. Stensgaard, J. K. Nørskov, B. S. Clausen, H. Topsøe and F. Besenbacher, "Atomic-Scale Structure of Single-Layer MoS2 Nanoclusters," *Physical Review Letters*, vol. 84, p. 951, 2000.

[33] C. Kisielowski, Q. Ramasse, L. Hansen, M. Brorson, A. Carlsson, A. Molenbroek, H. Topsøe and S. Helveg, "Imaging MoS2 Nanocatalysts with Single-Atom Sensitivity," *Angewandte Chemie International Edition*, vol. 49, p. 2708, 2010.

[34] S. Kasztelan, H. Toulhoat, J. Grimblot and J. P. Bonnelle, "A geometrical model of the active phase of hydrotreating catalysts," *Applied Catlysis*, vol. 13, p. 127, 1984.

[35] J. V. Lauritsen, M. V. Bollinger, E. Lægsgaard, K. W. Jacobsen, J. K. Nørskov, B. S. Clausen, H. Topsøe and F. Besenbacher, "Atomic-scale insight into structure and morphology changes of MoS2 nanoclusters in hydrotreating catalysts," *Journal of Catalysis*, vol. 221, p. 510, 2004.

[36] L. P. Hansen, Q. M. Ramasse, C. Kisielowski, M. Brorson, E. Johnson, H. Topsøe and S. Helveg, "Atomic-Scale Edge Structures on Industrial-Style MoS2 Nanocatalysts," *Angewandte Chemie International Edition*, vol. 50, p. 10153, 2011.

[37] P. Hartel, H. Rose and C. Dinges, "Conditions and reasons for incoherent imaging in STEM," *Ultramicroscopy*, vol. 63, p. 93, 1996.

[38] L. S. Byskov, J. K. Nørskov, B. S. Clausen and H. Topsøe, "DFT Calculations of Unpromoted and Promoted MoS2-Based Hydrodesulfurization Catalysts," *Journal of Catalysis*, vol. 187, p. 109, 1999.

[39] S. Cristol, J. F. Paul, E. Payen, D. Bougeard, S. Clémendot and F. Hutschka, "Theoretical Study of the MoS2 (100) Surface: A Chemical Potential Analysis of Sulfur and Hydrogen Coverage," *Journal of Physical Chemistry B*, vol. 104, p. 11220, 2000.

[40] A. Tuxen, J. Kibsgaard, H. Gøbel, E. Lægsgaard, H. Topsøe, J. V. Lauritsen and F. Besenbacher, "Size Threshold in the Dibenzothiophene Adsorption on MoS2 Nanoclusters," *ACS Nano*, vol. 4, p. 4677, 2010.

[41] P. G. Moses, B. Hinnemann, H. Topsøe and J. K. Nørskov, "The hydrogenation and direct desulfurization reaction pathway in thiophene hydrodesulfurization over MoS2 catalysts at realistic conditions: A density functional study," *Journal of Catalysis*, vol. 248, p. 188, 2007.

[42] J. V. Lauritsen, M. Nyberg, J. K. Nørskov, B. S. Clausen, H. Topsøe, E. Lægsgaard and F. Besenbacher, "Hydrodesulfurization reaction pathways on MoS2 nanoclusters revealed by scanning tunneling microscopy," *Journal of Catalysis*, vol. 224, p. 94, 2004.

[43] M. Jacoby, "Desulfurization Catalysis," *Chemical & Engineering News*, vol. 79, p. 8, 2001.

[44] H. Topsøe, "The role of Co–Mo–S type structures in hydrotreating catalysts," *Applied Catalysis A*, vol. 322, p. 3, 2007.

[45] P. Raybaud, J. Hafner, G. Kresse, S. Kasztelan and H. Toulhoat, "Structure, Energetics, and Electronic Properties of the Surface of a Promoted MoS2 Catalyst: An ab Initio Local Density Functional Study," *Journal of Catalysis*, vol. 190, p. 128, 2000.

[46] B. S. Clausen, H. Topsoe, R. Candia, J. Villadsen, B. Lengeler, J. Als-Nielsen and F. Christensen, "Extended x-ray absorption fine structure study of the cobalt-molybdenum hydrodesulfurization catalysts," *Journal of Physical Chemistry*, vol. 85, p. 3868, 1981.

[47] S. M. A. M. Bouwens, R. Prins, V. H. J. d. Beer and D. C. Koningsberger, "Structure of the Molybdenum Sulfide Phase in Carbon-Supported Mo and Co-Mo Sulfide Catalysts As Studied by Extended X-ray Absorption Fine Structure Spectroscopy," *Journal of Physical Chemistry*, vol. 94, p. 3711, 1990.

[48] S. M. A. M. Bouwens, J. A. R. v. Veen, D. C. Koningsberger, V. H. J. d. Beer and R. Prins, "Extended X-ray Absorption Fine Structure Determination of the Structure of Cobalt In Carbon-Supported Co and Co-Mo Sulfide Hydrodesulfurization Catalysts," *Journal of Physical Chemistry*, vol. 95, p. 123, 1991.

[49] B. R. G. Leliveld, J. A. J. v. Dillen, J. W. Geus and D. C. Koningsberger, "Structure and Nature of the Active Sites in CoMo Hydrotreating Catalysts. An EXAFS Study of the Reaction with Selenophene," *Journal of Physical Chelistry B*, vol. 101, p. 11160, 1997.

[50] E. Krebs, B. Silvi and P. Raybaud, "Mixed sites and promoter segregation: A DFT study of the manifestation of Le Chatelier's principle for the Co(Ni)MoS active phase in reaction conditions," *Catalysis Today*, vol. 130, p. 160, 2008.

[51] H. Topsøe, B. S. Clausen, N.-Y. Topsøe, E. Pedersen, W. Niemann, A. Müller, H. Bögge and B. Lengeler, "Inorganic cluster compounds as models for the structure of active sites in promoted hydrodesulphurization catalysts," *Journal of the Chemical Society, Faraday Transactions 1*, vol. 83, p. 2157, 1987.

[52] K. Inamura and R. Prins, "The Role of Co in Unsupported Co-Mo Sulfides in the Hydrodesulfurization of Thiophene," *Journal of Catalysis*, vol. 147, p. 515, 1994.

[53] L. Coulier, J. A. R. v. Veen and J. W. Niemantsverdriet, "TiO2-Supported Mo Model Catalysts: Ti as Promoter for Thiophene HDS?," *Catalysis Letters*, vol. 79, p. 149, 2002.

[54] F. Besenbacher, M. Brorson, B. S. Clausen, S. Helveg, B. Hinnemann, J. Kibsgaard, J. V. Lauritsen, P. G. Moses, J. K. Nørskov and H. Topsøe, "Recent STM, DFT and HAADF-STEM studies of sulfide-based hydrotreating catalysts: Insight into mechanistic, structural and particle size effect," *Catalysis Today*, vol. 130, p. 86, 2008.

[55] J. V. Lauritsen, S. Helveg, E. Lægsgaard, I. Stensgaard, B. S. Clausen, H. Topsøe and F. Besenbacher, "Atomic-Scale Structure of Co–Mo–S Nanoclusters in Hydrotreating Catalysts," *Journal of Catalysis*, vol. 197, p. 1, 2001.

[56] J. V. Lauritsen, J. Kibsgaard, G. H. Olesen, P. G. Moses, B. Hinnemann, S. Helveg, J. K. Nørskov, B. S. Clausen, H. Topsøe, E. Lægsgaard and F. Besenbacher, "Location and coordination of promoter atoms in Co- and Ni-promoted MoS2-based hydrotreating catalysts," *Journal of Catalysis*, vol. 249, p. 220, 2007.

[57] P. Grange, "Catalytic Hydrodesulfurization," *Catalysis Reviews Science and Engineering*, vol. 21, p. 135, 1980.

[58] C. Legens and P. Raybaud, "Activation and Genesis of the Active Phase by Sulfidation," in *Catalysis by Transition Metal Sulphides*, P. R. Hervé Toulhoat, Ed., Paris, Technip, 2013, p. 259.

[59] A. D. Gandubert, E. Krebs, C. Legens, D. Costa, D. Guillaume and P. Raybaud, "Optimal promoter edge decoration of CoMoS catalysts: A combined theoretical and experimental study," *Catalysis Today*, vol. 130, p. 149, 2008.

[60] C. Geantet and E. Payen, "Activation and Genesis of the Active Phase by Sulphidation," in *Catalysis by Transition Metal Sulphides*, P. R. Hervé Toulhoat, Ed., Paris, Technip, 2013, p. 274.

[61] P. Arnoldy, J. A. M. v. d. Heijkant, G. D. d. Bok and J. A. Moulijn, "Temperature-programmed sulfiding of MoO3/Al2O3 catalysts," *Journal of Catalysis*, vol. 92, p. 35, 1985.

[62] P. J. Mangnus, E. K. Poels and J. A. Moulijn, "Temperature programmed sulfiding of commercial cobalt oxide-molybdenum oxide (CoO-MoO3)/alumina catalysts," *Industrial & Engineering Chemistry Research*, vol. 32, p. 1818, 1993.

[63] E. Payen, S. Kasztelan, R. Szymanski, S. Houssenbay and J. Grimbolt, "Genesis and Characteriaztion by LRS and HREM of ALumina Supported MoS2," *Journal of Physical Chemistry*, vol. 93, p. 6501, 1989.

[64] T. Weber, J. C. Masers and J. W. Niemantsverdriet, "Structure of Amorphous MoS3," *Journal of Physical Chemistry*, vol. 99, p. 9194, 1995.

[65] R. Cattaneo, F. Rota and R. Prins, "An XAFS Study of the Different Influence of Chelating Ligands on the HDN and HDS of y-Al2O3-Supported NiMo Catalysts," *Journal of Catalysis*, vol. 199, p. 318, 2001.

[66] D. Nicosia and R. Prins, "The effect of phosphate and glycol on the sulfidation mechanism of CoMo/Al2O3 hydrotreating catalysts: an in situ QEXAFS study," *Journal of Catalysis*, vol. 231, p. 259, 2005.

[67] G. L. Schrader and C. P. Cheng, "In Situ Laser Raman Spectroscopy of the Sulfiding of Mo-Al2O3 Catalysts," *Journal of Catalysis*, vol. 80, p. 369, 1983.

[68] A. M. d. Jong, H. J. Borg, L. J. v. Ijzendoorn, V. G. F. M. Soudant, V. H. J. d. Beer, J. A. R. v. Veen and J. W. Niemantsverdriet, "Sulfidation Mechanism by Molybdenum Catalysts Supported on Silica/Silicon(100) Model Suport Studied by Surface Spectroscopy," *Journal of Physical Chemistry*, vol. 97, p. 6477, 1993.

[69] J. C. Muijsers, T. Weber, R. M. Vanhardeveld, H. W. Zandbergen and J. W. Niemantsverdriet, "Sulfidation Study of Molybdenum Oxide Using MoO3/SiO2/Si(100) Model Catalysts and Mo-IV3-Sulfur Cluster Compounds," *Journal of Catalysis*, vol. 157, p. 698, 1995.

[70] C. Geantet, Y. Soldo, C. Glasson, N. Matsubayashi, M. Lacroix, O. Proux, O. Ulrich and J.-L. Hazemann, "In situ QEXAFS investigation at Co K-edge of the sulfidation of a CoMo/Al2O3 hydrotreating catalyst," *Catalysis Letters*, vol. 73, p. 95, 2001.

[71] M. Digne, "Principles involved in the preparation of hydrotreatment catalysts," in *Catalysis by Transition Metal Sulphides - From Molecular Theory to Industrial Application*, P. R. Hervé Toulhoat, Ed., Paris, Technip, 2013, p. 117.

[72] P. Grange and X. Vanhaeren, "Hydrotreating catalysts, an old story with new challenges," *Catalysis Today*, vol. 36, p. 375, 1997.

[73] J. Ramirez, L. Cedeño and G. Busca, "The Role of Titania Support in Mo-Based Hydrodesulfurization Catalysts," *Journal of Catalysis,* vol. 184, p. 59, 1999.

[74] M. Breysse, P. Afanasiev, C. Geantet and M. Vrinat, "Overview of support effects in hydrotreating catalysts," *Catalysis Today,* vol. 86, p. 5, 2003.

[75] G. Muralidhar, B. N. Srinivas, M. S. Rana, M. Kumar and S. K. Maity, "Mixed Oxide Supported Hydrodesulfurization Catalysts - A Review," *Catalysis Today,* vol. 84, p. 45, 2003.

[76] J. Ramirez and F. Sánchez-Minero, "Support effects in the hydrotreatment of model molecules," *Catalysis Today,* vol. 130, p. 267, 2008.

[77] F. E. Massoth, G. Muralidhar and J. Shabtai, "Catalytic functionalities of supported sulfides. 2. Effect of support on Mo dispersion," *Journal of Catalysis,* vol. 85, p. 44, 1985.

[78] F. Luck, "A Review of Support Effects on the Activity and Selectivity of Hydrotreating Catalysts," *Bulletin des Sociétés Chimiques Belges,* vol. 100, p. 781, 1991.

[79] S. Dzwigaj, C. Louis, M. Breysse, M. Cattenot, V. Bellière, C. Geantet, M. Vrinat, P. Blanchard, E. Payen, S. Inoue, H. Kudo and Y. Yoshimura, "New generation of titanium dioxide support for hydrodesulfurization," *Applied Catalysis B: Environmental,* vol. 41, p. 181, 2003.

[80] M. J. Vissenberg, Y. V. d. Meer, E. J. M. Hensen, V. R. J. d. Beer, A. M. V. d. Kraan, R. A. v. Santen and J. A. R. V. Veen, "The effect of support interaction on the sulfidability of Al2O3 and TiO2 supported CoW and NiW hydrodesulfurization catalysts," *Journal of Catalysis,* vol. 198, p. 151, 2001.

[81] S. Eijsbouts, J. J. L. Heinerman and H. J. W. Elzerman, "MoS2 structures in higha-activity hydrotreating catalysts. I. Semi-quantitative method for evaluation of transmission electron microscopy results. Correlations between hydrodesulfurization and hydrodenitrogenation activities and MoS2 dispersion," *Applied Catalysis A,* vol. 105, p. 53, 1993.

[82] Y. Sakashita, Y. Araki, K. Honna and H. Shimada, "Orientation and morphology of molybdenum sulfide catalysts supported on titania particles, observed by using high-resolution electron microscopy," *Applied Catalysis A,* vol. 197, p. 247, 2000.

[83] J. Kibsgaard, B. S. Clausen, H. Topsøe, E. Lægsgaard, J. V. Lauritsen and F. Besenbacher, "Scanning tunneling microscopy studies of TiO2-supported hydrotreating catalysts: Anisotropic particle shapes by edge-specific MoS2–support bonding," *Journal of Catalysis,* vol. 263, p. 98, 2009.

[84] C. Arrouvel, M. Breysse, H. Toulhoat and P. Raybaud, "A density functional theory comparison of anatase (TiO2)- and γ-Al2O3-supported MoS2 catalysts," *Journal of Catalysis,* vol. 232, p. 161, 2005.

[85] N.-S. Chiu, S. H. Bauer and M. F. L. Johnson, "Co/Mo/Al203 catalyst structure determination by EXAFS: II. Mo K-edge of the sulfided state," *Journal of Catalysis,* vol. 98, p. 32, 1986.

[86] T. K. T. Ninh, L. Massin, D. Laurenti and M. Vrinat, "A new approach in the evaluation of the support effect for NiMo hydrodesulfurization catalysts," *Applied Catalysis A,* vol. 407, p. 29, 2011.

[87] J. Ramirez, G. Macias, L. Cedeño, A. Gutiérrez-Alejandre, R. Cuevas and P. Castillo, "The role of titania in supported Mo, CoMo, NiMo, and NiW hydrodesulfurization catalysts: analysis of past and new evidences," *Catalysis Today*, vol. 98, p. 19, 2004.

[88] R. G. Leliveld, A. J. v. Dillen, J. W. Geus and D. C. Koningsberger, "A Mo–K Edge XAFS Study of the Metal Sulfide-Support Interaction in (Co)Mo Supported Alumina and Titania Catalysts," *Journal of Catalysis*, vol. 165, p. 184, 1997.

[89] R. G. Leliveld, A. J. v. Dillen, J. W. Geus and D. C. Koningsberger, "The Sulfidation of γ-Alumina and Titania Supported (Cobalt)Molybdenum Oxide Catalysts Monitored by EXAFS," *Journal of Catalysis*, vol. 171, p. 115, 1997.

[90] K. P. d. Jong, Synthesis of solid catalysts, Weinheim: Wiley-VCH, 2009.

[91] F. Boccuzzi, L. Marchese and G. Martra, "Physical-chemistry at the cross-road of advanced," *Physical Chemistry Chemical Physics*, vol. 15, p. 13236, 2013.

[92] J. Bachelier, M. J. Tilliette, J. C. Duchet and D. Cornet, "Surface properties of sulfided MoAl2O3 catalysts," *Journal of Catalysis*, vol. 76, p. 300, 1982.

[93] X. Duana, G. Qian, X. Zhou, D. Chen and W. Yuan, "MCM-41 supported Co-Mo bimetallic catalysts for enhanced hydrogen production by ammonia decomposition," *Chemical Engineering Journal*, Vols. 207-208, p. 103, 2012.

[94] M. Hussain, S.-K. Song, J.-H. Lee and S.-K. Ihm, "Characteristics of CoMo Catalysts Supported on Modified MCM-41 and MCM-48 Materials for Thiophene Hydrodesulfurization," *Industrial & Engineering Chemistry Research*, vol. 45, p. 536, 2006.

[95] L. Chuan, S. Bin, C. Min, S. Hong-yan and Q. Guo-he, "Application of Co-Mo/CNT catalyst in hydro-crackingof Gudao vacuum residue," *Journal of Fuel Chemistry and Technology*, vol. 35, p. 407, 2007.

[96] P. Leprince, La Raffinage du Pétrole: Procédés de Transformation - IFP, Paris: Editions Technip, 1998.

[97] S. Dzwigaj, C. Louis, M. Breysse, M. Cattenot, V. Bellière, C. Geantet, M. Vrinat, P. Blanchard, E. Payen, S. Inoue, H. Kudo and Y. Yoshimura, "New generation of titanium dioxide support for hydrodesulfurization," *Applied Catalysis B: Environmental*, vol. 41, p. 18, 2003.

[98] J. B. Miller and E. I. Ko, "Control of mixed oxide textural and acidic properties by the sol-gel method," *Catalysis Today*, vol. 35, p. 269, 1997.

[99] J. M. Rodriguez-Izquierdo and M. Cauqui, "Application of the sol-gel methods to catalyst preparation," *Journal of Non-Crystalline Solids*, vol. 147&148, p. 724, 1992.

[100] F. Dumeignil and J. Grimblot, "Synthesis, characterization and HDS activity of CoMo/Al2O3 catalysts prepared by two ways (impregnation of a sol-gel alumina and complete sol-gel synthesis)," *Studies in Surface Science and Catalysis*, vol. 127, p. 357, 1999.

[101] F. Dumeignil, K. Sato, M. Imamura, N. Matsubayashi and E. Payen, "Modification of structural and acidic properties of sol–gel-prepared alumina powders by changing the hydrolysis ratio," *Applied Catalysis A: General*, vol. 241, p. 319, 2003.

[102] F. Dumeignil, K. Sato, M. Imamura, N. Matsubayashi, E. Payen and H. Shimada, "Characterization and hydrodesulfurization activity of CoMo catalysts supported on sol–gel prepared Al2O3," *Applied Catalysis A: General*, vol. 287, p. 135, 2005.

[103] W. Huang, A. Duan, Z. Zhao, G. Wan, G. Jiang, T. Dou, K. H. Chung and J. Liu, "Ti-modified alumina supports prepared by sol–gel method used for deep HDS catalysts," *Catalysis Today*, vol. 131, p. 314, 2008.

[104] I. R. Galindo, T. Viveros and D. Chadwick, "Ignacio R. Galindo,†,‡ Tomas Viveros,*,† and David Chadwick Oxides Prepared by the Sol-Gel Method and Their Activity in 2-Propanol Dehydration," *Industrial & Engineering Chemistry Research*, vol. 46, p. 1138, 2007.

[105] J. Stötzel, D. Lützenkirchen-Hecht, R. Frahm, C. V. Santilli, S. H. Pulcinelli, R. Kaminski, E. Fonda, F. Villain and V. Briois, "QEXAFS and UV/Vis Simultaneous Monitoring of the TiO2-Nanoparticles Formation by Hydrolytic Sol-Gel Route," *Journal of Physical Chemistry*, vol. 114, p. 6228, 2010.

[106] W. W. So, S. B. Park, K. J. Kim, C. H. Shin and S. J. Moon, "The crystalline phase stability of titania particles prepared at room temperatureby the sol-gel method," *Journal of Materials Science*, vol. 36, p. 4299, 2001.

[107] S. Mahshid, M. Askari and M. S. Ghamsari, "Synthesis of TiO2 nanoparticles by hydrolysis and peptization of titanium isopropoxide solution," *Journal of Materials Processing Technology*, vol. 189, p. 296, 2007.

[108] E. Krebs, A. Daudin and P. Raybaud, "A DFT Study of CoMoS and NiMoS Catalysts: from Nano-Crystallite Morphology to Selective Hydrodesulfurization," *Oil & Gas Science and Technology – Rev. IFP*, vol. 64, p. 707, 2009.

[109] L. Coulier, G. Kishan, J. A. R. v. Veen and J. W. Niemantsverdriet, "Surface science models for CoMo hydrodesulfurization catalysts: Influence of the support on hydrodesulfurization activity," *Journal of Vaccum Science & Technology A*, vol. 19, p. 1510, 2001.

[110] S. Helfensteyn, H. Tollet, J. Degrève and C. Creemers, "LEIS-surface analysis of commercial sulfided oxide catalysts," *Applied Catalysis A: General*, vol. 239, p. 221, 2003.

[111] S. Rondon, M. Houalla and D. M. Hercules, "Determination of the Surface Coverage of Mo/TiO2 Catalysts by ISS and CO2 Chemisorption," *Surface and Interface Analysis*, vol. 26, p. 329, 1998.

[112] C. Lamonier, D. Soogund, J. Mazurelle, P. Blanchard, D. Guillaume and E. Payen, "Origin of the dispersion limit in the preparation of Ni(Co)Mo/Al2O3 and Ni(Co)Mo/TiO2 HDS oxidic precursors," *Studies in Surface Science and Catalysis*, vol. 162, p. 713, 2006.

[113] D. C. K. a. R. Prins, Ed., X-Ray Absorption - Principles, Applications, techniques of EXAFS, SEXAFS and XANES, Chichester: John Willey and Sons, 1988.

[114] H. Topsøe and B. S. Clausen, "Sulfide Catalysts," in *X-ray Absorption fine Structure for Catalysts and Surfaces*, Y. Iwasawa, Ed., Singapore, World Scientific, 1996, p. 235.

[115] C. Calais, N. Matsubayashi, C. Geantet, Y. Yoshimura, H. Shimada, A. Nishijima, M. Lacroix and M. Breysse, "Crystallite Size Determination of Highly Dispersed Unsupported MoS2Catalysts," *Journal of Catalysis*, vol. 174, p. 130, 1998.

[116] T. Shido and R. Prins, "Why EXAFS Underestimated the Size of Small Supported MoS2 Particles," *Journal of Physical Chemistry B,* vol. 102, p. 8426, 1998.

[117] S. M. A. M. Bouwens, F. B. M. Vanzon, M. P. Vandijk, A. M. Vanderkraan, V. H. J. Debeer, J. A. R. Vanveen and D. C. Koningsberger, "On the Structural Differences Between Alumina-Supported Comos Type I and Alumina-, Silica-, and Carbon-Supported Comos Type II Phases Studied by XAFS, MES, and XPS," *Journal of Catalysis,* vol. 146, p. 375, 1994.

[118] C. Geantet and C. Pichon, "X-Ray Absorption - EXAFS, XANES," in *Catalysis by Transition Metal Sulfides - From Molecular Theory to Industrial Applications*, P. R. Hervé Toulhoat, Ed., Paris, Technip, 2013, p. 453.

[119] C. Martin, C. Lamonier, M. Fournier, O. Mentre, V. Harle, D. Guillaume and E. Payen, "Preparation and Characterization of 6-Molybdocobaltate and 6-Molybdoaluminate Cobalt Salts. Evidence of a New Heteropolymolybdate Structure," *Inorganic Chemistry,* vol. 43, p. 4636, 2004.

[120] A. Rochet, *Charactéristique Structurale de Catalyseurs Hétérogènes en Conditions de Fonctionnement par Spectroscopie d'Absroption des Rayons X Résolue dans le Temps,* Université Paris Sud, 2011.

[121] F. W. Lytle, P. S. P. Wei, R. B. Greegor, G. H. Via and J. H. Sinfelt, "Effect of chemical environment on magnitude of x-ray absorption resonance at L I I I edges. Studies on metallic elements, compounds, and catalysts," *Journal of Chemical Physics,* vol. 70, p. 4849, 1979.

[122] S. R. Bare and T. Ressler, "Characterization of Catalysts in Reactive Atmospheres by X-ray Absorption Spectroscopy," *Advances in Catalysis,* vol. 52, p. 339, 2009.

[123] C. L. Fontaine, L. Barthe, A. Rochet and V. Briois, "X-ray absorption spectroscopy and heterogeneous catalysis: Performances at the SOLEIL's SAMBA beamline," *Catalysis Today,* vol. 205, p. 148, 2013.

[124] A. Rochet, V. Moizan, F. Diehl, C. Pichon and V. Briois, "Quick-XAS and Raman operando characterisation of a cobalt alumina-supported catalyst under realistic Fischer–Tropsch reaction conditions," *Catalysis Today,* vol. 205, p. 94, 2013.

[125] A. Rochet, V. Moizan, C. Pichon, F. Diehl, A. Berliet and V. Briois, "In situ and operando structural characterisation of a Fischer–Tropsch supported cobalt catalyst," *Catalysis Today,* vol. 171, p. 186, 2011.

[126] T. G. Parham and R. P. Merrill, "An EXAFS study of the structure of supported cobalt molybdate catalysts as a function of sulfiding temperature," *Journal of Catalysis,* vol. 85, p. 295, 1984.

[127] B. S. Claussen, G. Steffensen, T. B. Zunic and H. Topsoe, "Hasylab Annual Repport DESY," 1994.

[128] A. d. Juan and R. Tauler, "Chemometrics applied to unravel multicomponent processes and mixtures Revisiting latest trends in multivariate resolution," *Analytica Chimica Acta,* vol. 500, p. 195, 2003.

[129] C. Marquez-Alvarez, I. Rodriguez-Ramos, A. Guerrero-Ruiz, G. L. Haller and M. Fernandez-Garcia, "Selective Reduction of NOx with Propene under Oxidative Conditions: Nature of the

Active Sites on Copper-Based Catalysts," *Journal of the American Chemical Society*, vol. 119, p. 2905, 1997.

[130] S. R. Wasserman, P. G. Allen, D. K. Shuh, J. J. Bucher and N. M. Edelstein, "EXAFS and principal component analysis: a new shell game," *Journal of Synchrotron Radiation*, vol. 6, p. 284, 1999.

[131] Q. Wang, J. C. Hanson and A. I. Frenkel, "Solving the structure of reaction intermediates by time-resolved synchrotron x-ray absorption spectroscopy," *journal of Chemical Physics*, vol. 129, p. 234502, 2008.

[132] M. J. Fay, A. Proctor, D. P. Hoffmann, M. Houalla and D. M. Hercules, "Determination of the Mo Surface Environment of Mo/TiO2 Catalysts by EXAFS, XANES and PCA," *Mikrochimica Acta*, vol. 109, p. 281, 1992.

[133] P. Conti, S. Zamponi, M. Giorgetti, M. Berrettoni and W. H. Smyrl, "Multivariate Curve Resolution Analysis for Interpretation of Dynamic Cu K-Edge X-ray Absorption Spectroscopy Spectra for a Cu Doped V2O5 Lithium Battery," *Analytical Chemistry*, vol. 82, p. 3629, 2010.

[134] H. Topsøe, "In situ characterization of catalysts," in *Studies in Surface Science and Catalysis*, 2000.

[135] C. Martin, "Catalyseurs d'hydrodesulfuration préparés à partir d'heteropolyanions de type Anderson," Lille, 2003.

[136] R. R. Chianelli, "Periodic Trends Transition Metal Sulfide Catalysis: Intuition and Theory," *Oil & Gas Science and Technology – Rev. IFP*, vol. 61, p. 503, 2006.

[137] A. Stanislaus, A. Marafi and M. S. Rana, "Recent advances in the science and technology of ultra low sulfur diesel (ULSD) production," *Catalysis Today*, vol. 153, p. 1, 2010.

[138] A. Travert, H. Nakamura, R. A. v. Santen, S. Cristol, J.-F. Paul and E. Payen, "Hydrogen Activation on Mo-Based Sulfide Catalysts, a Periodic DFT study," *journal of the American Chemical Society*, vol. 124, p. 7084, 2002.

[139] B. Pawelec, R. Mariscal, J. L. G. Fierro, A. Greenwood and P. T. Vasudevan, "Carbon-supported tungsten and nickel catalysts for hydrodesulfurization and hydrogenation reactions," *Applied Catalysis A: General*, vol. 206, p. 295, 2001.

[140] B. S. Clausen, H. Topsøe and R. Frahm, "Application of Combined X-Ray Diffraction and Absorption Techniques for in Situ Catalyst Characterization," *Advances in Catalysis*, vol. 42, p. 315, 1998.

[141] B. S. Clausen, J. Schiøtz, L. Gråbæk, C. V. Ovesen, K. W. Jacobsen, J. K. Nørskov and H. Topsøe, "Wetting/ non-wetting phenomena during catalysis: Evidence from in situ on-line EXAFS studies of Cu-based catalysts," *Topics in Catalysis*, vol. 1, p. 367, 1994.

[142] B. Hinnemann, J. K. Nørskov and H. Topsøe, "A Density Functional Study of the Chemical Differences between Type I and Type II MoS2-Based Structures in Hydrotreating Catalysts," *The Journal of Physical Chemistry B*, vol. 109, p. 2245, 2005.

[143] C. V. Ovesen, B. S. Clausen, J. Schiøtz, P. Stoltze, H. Topsøe and J. K. Nørskov, "Kinetic Implications of Dynamical Changes in Catalyst Morphology during Methanol Synthesis over Cu/ZnO Catalysts," *Journal of Catalysis*, vol. 168, p. 133, 1997.

[144] C. Lamonier and E. Payen, "Progress in the preparation of new catalysts," in *Catalysis by transition metal sulphides - From molecular theory to industrial appplications*, Paris, Technip, 2013, p. 151.

[145] C. I. Cabello, F. M. Cabrerizo, A. Alvarez and H. J. Thomas, "Decamolybdodicobaltate(III) heteropolyanion: structural, spectroscopical, thermal and hydrotreating catalytic properties," *Journal of Molecular Catalysis A: Chemical*, vol. 186, p. 89, 2002.

[146] C. I. Cabello, I. L. Botto and H. J. Thomas, "Anderson type heteropolyoxomolybdates in catalysis:: 1. (NH4)3[CoMo6O24H6]·7H2O/γ-Al2O3 as alternative of Co-Mo/γ-Al2O3 hydrotreating catalysts," *Applied Catalysis A: General*, vol. 197, p. 79, 2000.

[147] D. Costa, C. Arrouvel, M. Breysse, H. Toulhoat and P. Raybaud, "Edge wetting effects of γ - Al2O3 and anatase-TiO2 supports by MoS2 and CoMoS active phases: A DFT study," *Journal of Catalysis*, vol. 246, p. 325, 2007.

[148] D. Wang, W. Qian, A. Ishihara and T. Kabe, "Elucidation of Sulfidation State and Hydrodesulfurization Mechanism on TiO2 Catalysts Using 35S Radioisotope Tracer Methods," *Journal of Catalysis*, vol. 203, p. 322, 2001.

[149] I. V. Babich and J. A. Moulijn, "Science and technology of novel processes for deep desulfurization of oil refinery streams: a review," *Fuel*, vol. 82, p. 607, 2003.

[150] J. A. R. v. Veen, E. Gerkema, A. M. v. d. Kraan and A. Knoester, "A real support effect on the activity of fully sulphided CoMoS for the hydrodesulphurization of thiophene," *Journal of the Chemical Society, Chemical Communications*, vol. 22, p. 1684, 1987.

[151] J.-D. Grunwaldt, A. M. Molenbroek, N.-Y. Topsøe, H. Topsøe and B. S. Clausen, "In Situ Investigations of Structural Changes in Cu/ZnO Catalysts," *journal of Catalysis*, vol. 194, p. 452, 2000.

[152] J. Mazurelle, C. Lamonier, C. Lancelot, E. Payen, C. Pichon and D. Guillaume, "Use of the cobalt salt of the heteropolyanion [Co2Mo10O38H4]6- for the preparation of CoMo HDS catalysts supported on Al2O3, TiO2 and ZrO2," *Catalysis Today*, vol. 130, p. 41, 2008.

[153] J. Mazurelle, C. Lamonier, C. Lancelot, E. Payen, C. Pichon and D. Guillaume, "Use of the cobalt salt of the heteropolyanion [Co2Mo10O38H4]6- for the preparation of CoMo HDS catalysts supported on Al2O3, TiO2 and ZrO2," *Catalysis Today*, vol. 130, p. 41, 2008.

[154] M. Breysse, B. A. Bennett, D. Chadwick and M. Vrinat, "Structure and HDS Activity of Co-Mo Catalysts: A Comparison Of Alumina and Carbon Supports," *Bulletin des Sociétés Chimiques Belges*, vol. 90, p. 1271, 1981.

[155] M. Sugioka, F. Sado, T. Kurosaka and X. Wang, "Hydrodesulfurization over noble metals supported on ZSM-5 zeolites," *Catalysis Today*, vol. 45, p. 327, 1998.

[156] M. P. D. l. Rosa, S. Texier, G. Berhault, A. Camacho, M. J. Yácaman, A. Mehta, S. Fuentes, J. A. Montoya, F. Murrieta and R. R. Chianelli, "Structural studies of catalytically stabilized model

and industrial-supported hydrodesulfurization catalysts," *Journal of Catalysis,* vol. 225, p. 288, 2004.

[157] P. Raybaud and H. Toulhoat, "Atomic Scale Description of the Interaction Between the Support and the Sulohide Nona-crystallites," in *Catalysis by Transition Metal Sulphides*, P. R. Hervé Toulhoat, Ed., Paris, Technip, 2013, p. 101.

[158] R. Candia, B. S. Clausen and H. Topsøe, in *Proceedings of the Ninth Iberoamerican Symposium on Catalysis*, Lisbon (Portugal), 1984.

[159] R. Candia, O. Sørensen, J. Villadsen, N.-Y. Topsøe, B. S. Clausen and H. Topsøe, "Effect of Sulfiding Temperature on Activity and Structures of CO-MO/AL2O3 Catalysts. ii," *Bulletin des Sociétés Chimiques Belges,* vol. 93, p. 763, 1984.

[160] S. Eijsbouts, L. C. A. v. d. Oetelaar and R. R. v. Puijenbroek, "MoS2 morphology and promoter segregation in commercial Type 2 Ni–Mo/Al2O3 and Co–Mo/Al2O3 hydroprocessing catalysts," *Journal of Catalysis,* vol. 229, p. 352, 2005.

[161] S. Brunet, D. Mey, G. Pérot, C. Bouchy and F. Diehl, "On the hydrodesulfurization of FCC gasoline: a review," *Applied Catalysis A: General,* vol. 278, p. 143, 2005.

[162] T. Fujikawa, K. Idei, K. Ohki, H. Mizuguchi and K. Usui, "Kinetic behavior of hydrogenation of aromatics in diesel fuel over silica–alumina-supported bimetallic Pt–Pd catalyst," *Applied Catalysis A: General,* vol. 205, p. 71, 2001.

[163] V. L. Barrio, P. L. Arias, J. F. Cambra, M. B. Güemez, B. Pawelec and J. L. G. Fierro, "Hydrodesulfurization and hydrogenation of model compounds on silica–alumina supported bimetallic systems," *Fuel,* vol. 82, p. 501, 2003.

[164] X. Carrier, J. F. Lambert and M. Che, "Ligand-Promoted Alumina Dissolution in the Preparation of MoOX/γ-Al2O3 Catalysts: Evidence for the Formation and Deposition of an Anderson-type Alumino Heteropolymolybdate," *Journal of the American Chemical Society,* vol. 119, p. 10137, 1997.

Chapter II: Chemometrics, from PCA to MCR-ALS

Table of Contents

1. Introduction

This chapter is a compilation of fundamental concepts in chemometrics found in the literature. These concepts are very clear and well-explained in such references and we will reproduce some of them highlighting the ones we judge important for this thesis.

Today's laboratory instruments produce a plethora of data. It is not uncommon for processes to have hundreds or thousands of measured variables. Some analytical instruments measure tens of thousands of variables. For instance, in a typical FTIR spectrometer, the absorbance is measured at over 10,000 frequencies. Chemical processes are becoming more heavily instrumented and the data are recorded more frequently [1]. The authors say ([1]): "*This increase in instrumentation is creating a data overload, and the result is that a good deal of the data are "wasted"; that is, no useful information is obtained from them. The problem is one of both compression and extraction. Generally, there is a great deal of correlated or redundant information in laboratory and process measurements. This information must be compressed in a manner that retains the essential information and is more easily displayed than each of the variables individually. In addition, essential information often lies not in any individual variable but in how the variables change with respect to one another; that is, how they co-vary. In this case, the information must be extracted from the data.*"

Furthermore, in the presence of large amounts of noise, it would be desirable to take advantage of some sort of signal averaging. The mathematical manipulation of experimental data is a basic operation associated with all modern instrumental analytical techniques. Computerization is ubiquitous and the range of computer software available to spectroscopists can appear overwhelming. Whether the final result is the determination of the composition of a sample or the qualitative identification of some species present, it is necessary for analysts to appreciate how their data are obtained and how they can be subsequently modified and transformed to generate useful information. It is important to broadly define the concept of a component as any entity giving a distinct and real, pure response. In this picture lies *chemometrics*.

Adams wrote in his book [2]: "*The term chemometrics was proposed more than 30 years ago (by Svante Wold and Bruce R. Kowalski in the early 1970s) to describe the techniques and operations associated with the mathematical manipulation and interpretation of chemical data. It is within the past 20 years, however, that chemometrics has come to the fore, and become generally recognized as a subject to be studied and researched by all chemists employing numerical data [3]. This is particularly true in analytical science. In a modern instrumentation laboratory, the analytical chemist may be faced with a seemingly overwhelming amount of numerical and graphical data. The identification, classification and interpretation of these data can be a limiting factor in the efficient and effective operation of the*

laboratory. Increasingly, sophisticated analytical instrumentation is also being employed out of the laboratory, for direct on-line or in-line process monitoring. This trend places severe demands on data manipulation, and can benefit from computerized decision-making." This is especially true when dealing with *in situ* experiments.

He continue: "*Chemometrics is complementary to laboratory automation. Just as automation is largely concerned with the tools with which to handle the mechanics and chemistry of laboratory manipulations and processes, so chemometrics seeks to apply mathematical and statistical operations to aid data handling.*"

Many of the methods employed in chemometrics are based on the concept of soft modeling, which contrary to the hard modeling do not need to know a kinetic model linked to the reaction studied. It is worthy to note that soft modeling provides a more realistic framework for many of the chemometric methods than the traditional modeling derived from first principles (hard models) in chemistry. A hard model usually describes the system in terms of traditional chemical and physical relationships using just one or a very few variables at the same time and its goal is to extract the basic parameters of the process, i.e., the kinetic rate constants or equilibrium constants from the measurements. Because most interesting chemical systems or processes are complex, the applications of hard modeling have been limited to the simple systems. However, soft model is used to describe the variation and correlation between the dependent variables and the latent variables, which are linear combinations of the measured variables in the covariance matrix of data. In particular, soft modeling approaches attempt to describe a system without a priori information or any kind of model assumption.

Garrido *et al.* wrote [4]: "*Hard-modelling methods usually provide trustworthy solutions for systems where a reliable reaction model can be postulated. However, in many cases an explicit reaction model cannot be postulated. De Juan et al. [5] have described that the main drawback of the hard-modelling methods lies in correctly stating the kinetic model. The correct choice, when in-depth chemical knowledge of the system is not available, depends on tedious trial-and-error procedures. Another disadvantage is that hard modelling methods do not work in the presence of non-modelled noise or spectral artifacts, such as baseline drift.*"

From [6]: "*In a 1997 nonmathematical paper, Steve Brown and Barry Lavine state, 'Chemometrics is not a subfield of Statistics. Although statistical methods are employed in Chemometrics, they are not the primary vehicles for data analysis'. On the one hand, one has to recognize the fact that many users of chemometric techniques are not aware of the statistical backgrounds of the techniques and indeed, maybe even the developers of those techniques may also not be aware of, or at least, give the statistical considerations their proper weight. This situation means that nobody is paying the attention that would eventually lead to the condition being corrected, which would result in a better theoretical*

understanding of the techniques themselves, with a concomitant improvement in their reliability and definition of their range of applicability."

Questions currently plaguing us, such as "How many PCA factors should I use in my model?" may never be answered in a completely rigorous and satisfactory fashion, but certainly improvements in the current state of knowledge should be attainable, with attendant improvements in the answers to such questions. New questions may arise which only fundamental statistical considerations may answer; one that has recently come to our attention is, "What is the best way to create a qualitative (i.e., identification) model, if there may be errors in the classifications of the samples used for training the algorithm?"

Still from [6] : "*Part of the problem, of course, is that the statistical questions involved are very difficult, and have not yet been solved completely and rigorously even by statisticians. Thus of necessity we push on and muddle through in the face of not always having a completely firm, mathematically rigorous foundation on which to base our use of the techniques we deal with. Therefore, we use these techniques anyway because otherwise we would have nothing: if we waited for complete rigor before we did anything, we would likely be waiting a long, long time, maybe indefinitely, for a solution that might never appear, and in the meanwhile be helpless in the face of the real (and real-world) problems that confront us [7].*"

In that picture, we introduce Principal Component Analysis (PCA), which is a favorite tool of chemometricians for data compression and information extraction, its formalism and possibilities concerning the range of application in science problems, particularly when related to x-ray absorption spectroscopy and *in situ* experiments. We extend our discussion to another factor-based tool for data analysis that is related to PCA, namely Evolving Factor Analysis (EFA), and we will show how it is used to make an initial guess for MCR analysis. Then, we will develop the concept and the formalism of Multivariate Curve Resolution with Alternating Least Squares (MCR-ALS) and we will show how this data treatment is been used nowadays in *is situ* experiments, particularly, applied to time-resolved x-ray absorption spectroscopy.

2. Principal Component Analysis (PCA)

The central idea of principal component analysis (PCA) is to reduce the dimensionality of a data set consisting of a large number of interrelated variables, while retaining as much as possible of the variation present in the data set. This is achieved by transforming to a new set of variables, the principal components (PCs), which are uncorrelated, and which are ordered so that the first *few* retain most of the variation present in *all* of the original variables.

Many analytical measures cannot be represented as a time-series in the form of a spectrum, but are composed of discrete measurements, e.g. compositional or trace analysis. Data reduction can still play an important role in such cases. The interpretation of many multivariate problems can be simplified by considering not only the original variables but also linear combinations of them. That is, a new set of variables can be constructed each of which contains a sum of the original variables each suitably weighted. These linear combinations can be derived on an *ad hoc* basis or more formally using established mathematical techniques. Whatever the method used, the aim is to reduce the number of variables considered in subsequent analysis and obtain an improved representation of the original data. The number of variables measured is not reduced.

"*The aims of performing a principal components analysis on multivariate data are basically two-fold. Firstly, PCA involves rotating and transforming the original, n, axes each representing an original variable into new axes. This transformation is performed in a way so that the new axes lie along the directions of maximum variance of the data with the constraint that the axes are orthogonal, i.e. the new variables are uncorrelated. It is usually the case that the number of new variables, p, needed to describe most of the sample data variance is less than n. Thus, PCA affords a method and a technique to reduce the dimensionality of the parameter space. Secondly, PCA can reveal those variables, or combinations of variables that describe some inherent structure in the data and these may be interpreted in chemical or physico-chemical terms.*" (in Molecular and Analytical Spectroscopy, by Dr. N. P. Sharma, New Delhi, 2001)

PCA finds combinations of variables, or *components* (or *factors*), which describe major trends in the data. If **X** is a data matrix with *m* rows and *n* columns, and with each variable being a column and each sample a row, PCA decomposes **X** as the sum of *r* $\mathbf{t}_i$ and $\mathbf{p}_i$, where *r* is the rank[4] of the matrix **X**:

$$\boldsymbol{X} = \boldsymbol{t}_1\boldsymbol{p}_1^T + \boldsymbol{t}_2\boldsymbol{p}_2^T + \cdots + \boldsymbol{t}_k\boldsymbol{p}_k^T + \cdots + \boldsymbol{t}_r\boldsymbol{p}_r^T \quad (1)$$

Here *r* must be less than or equal to the smaller dimension of **X**, *i.e.*, $r \leq \min\{m,n\}$. The $\mathbf{t}_i$, $\mathbf{p}_i$ pairs are ordered by the amount of variance captured. The $\mathbf{t}_i$ vectors are known as *scores* and contain information on how the *samples* relate to each other (each spectrum, in our particular case). The $\mathbf{p}_i$ vectors are known as *loadings* and contain information on how the *variables* (a single energy value) relate to each other. Generally, the PCA model is truncated after *k* components and the remaining small variance factors are consolidated into a residual matrix E:

$$\boldsymbol{X} = \boldsymbol{t}_1\boldsymbol{p}_1^T + \boldsymbol{t}_2\boldsymbol{p}_2^T + \cdots + \boldsymbol{t}_k\boldsymbol{p}_k^T + \boldsymbol{E} \quad (2)$$

While the form of Equation (2) may at first seem foreign, there are chemical systems that can be modeled with exactly the same equation. For example, if **X** were a number of absorbance spectra of mixtures

[4] There is multiple definitions for the term, but we can state that the rank of a given matrix is maximal number of linearly independent column vectors (or, equivalently, row vectors) in this matrix.

which followed Beer's law (linear additively), then the $\mathbf{t}_i$ could be replaced with concentrations and the $\mathbf{p}_i$ could be replaced with pure component spectra. In fact, that is the conventional approach used in spectroscopy experiments treated with PCA method.

Mathematically, PCA relies upon the singular value decomposition (SVD) algorithm [8] in linear algebra, which is briefly described as follows.

$$\begin{bmatrix} x_{11} & x_{12}\dots & x_{1n} \\ a_{21} & a_{22}\dots & a_{2n} \\ n_{31} & n_{32}\dots & n_{3n} \\ e_{41} & e_{42}\dots & e_{4n} \\ \vdots & \vdots & \vdots \\ s_{m1} & s_{m2}\dots & s_{mn} \end{bmatrix} = \begin{bmatrix} E_{11} & E_{12}\dots & E_{1n} \\ i_{21} & i_{22}\dots & i_{2n} \\ g_{31} & g_{32}\dots & g_{3n} \\ \mathrm{e}_{41} & \mathrm{e}_{42}\dots & \mathrm{e}_{4n} \\ \vdots & \vdots & \vdots \\ \mathrm{n}_{m1} & \mathrm{n}_{m2}\dots & \mathrm{n}_{mn} \end{bmatrix} \times \begin{bmatrix} v_{11} & \cdots & 0 \\ \vdots & \ddots & \vdots \\ 0 & \cdots & v_{nn} \end{bmatrix} \times \begin{bmatrix} w_{11} & \cdots & w_{1n} \\ \vdots & \ddots & \vdots \\ w_{n1} & \cdots & w_{nn} \end{bmatrix}$$

$$[A] = [E] \times [V] \times [w]^T \qquad (3)$$

The SVD method is based on the theorem that any $m \times n$ matrix **A**, whose number of rows m is greater than or equal to its number of columns n, can be written as the product of an $m \times n$ column-orthogonal matrix **E**, an $n \times n$ diagonal matrix **V** with positive or zero elements, and the transpose of an $n \times n$ orthogonal matrix **w** [9]. The columns of the **E** matrix are the eigenvectors, and the diagonal elements of the **V** matrix are the corresponding eigenvalues.

Thus, SVD constructs an orthonormal basis set given as column vectors of the **E** matrix in equation (3) from the vector subspace spanned by the input column vectors of the **A** matrix. In practice, and particularly, in the analysis of a set of XANES spectra arising from mixtures (superimpositions) of spectra from two or more different reference compounds, therefore, column vector (x_{1j}, a_{2j}, n_{3j}, e_{4j}... s_{mj}) in matrix **A** represents an experimental XANES spectrum of the j^{th} unknown mixture, and there are n such unknown spectra in the data set to be analyzed, each with m data points. The output matrix **E** has, therefore, a dimension n, which is the number of columns in the input matrix **A**. Oftentimes, however, eigenvalues v_{ii} equal to zero indicate that the subspace spanned by the input vectors was not, in fact, n-dimensional. The columns of **E** that correspond to zero, v_{ii}, should then be discarded from the orthonormal basis set.

$$\begin{bmatrix} E_{11} & E_{12}\dots & E_{1n} \\ i_{21} & i_{22}\dots & i_{2n} \\ g_{31} & g_{32}\dots & g_{3n} \\ \mathrm{e}_{41} & \mathrm{e}_{42}\dots & \mathrm{e}_{4n} \\ \vdots & \vdots & \vdots \\ \mathrm{n}_{m1} & \mathrm{n}_{m2}\dots & \mathrm{n}_{mn} \end{bmatrix} \times \begin{bmatrix} v_{11} & 0 & 0 & 0 \\ 0 & v_{22} & 0 & 0 \\ 0 & 0 & 0_{jj} & 0 \\ 0 & 0 & 0 & 0_{nn} \end{bmatrix} \times \begin{bmatrix} w_{11} & \cdots & w_{1n} \\ \vdots & \ddots & \vdots \\ w_{n1} & \cdots & w_{nn} \end{bmatrix} = \begin{bmatrix} x_{11} & x_{12}\dots & x_{1n} \\ a_{21} & a_{22}\dots & a_{2n} \\ n_{31} & n_{32}\dots & n_{3n} \\ e_{41} & e_{42}\dots & e_{4n} \\ \vdots & \vdots & \vdots \\ s_{m1} & s_{m2}\dots & s_{mn} \end{bmatrix}$$

$$[E]^{PCA} \times [V]^{PCA} \times [w]^t = [A^*]^{PCA} \qquad (4)$$

PCA can be employed to determine the number of reference model spectra needed to simulate the experimental data. In addition, given a set of spectra of suitable reference model compounds, PCA in combination with target transformation can be utilized to identify those model compounds that constitute

probable components in the original set of unknown XANES spectra. It must be noted that the number of compounds present in the measured XANES spectra of unknowns has to be equal or smaller than the number of spectra.

The above PCA procedure used to determine the minimum number species contained in an unknown sample has been applied to XAFS analysis by Fay *et al.* [10] and reiterated in detail later by Wasserman [11].

To use the above-described SVD algorithm, a column matrix **A** has to be constructed containing the experimental XANES spectra interpolated onto the same energy grid. From the eigenvalues in the SVD output matrix **V**, it can be determined how many eigenvectors are sufficient to reproduce the experimental XANES spectra; hence, the number of principal components present in the experimental data set. In equation (4), for instance, if two out of the *n* eigenvectors in equation (5) are needed to generate a column matrix **A*** containing the *n* PCA-calculated XANES spectra and if the columns in **A*** and **A** are identical within experimental errors, then the experimental XANES spectra in matrix **A** indeed consist of only two principal components.

The output of SVD can be utilized to determine whether a particular vector *T* lies within the vector subspace spanned by the orthonormal basis vectors, i.e., the eigenvectors or principal components. This procedure is known as *target transformation*. With respect to the case discussed in the preceding paragraph and provided the vector *T* has been interpolated onto the same grid as the number of rows *m* of the *A* matrix, a target transformation consists of a multiplication of a column matrix **E** containing the eigenvectors, the transpose of this matrix, and the vector *T* as shown in equation (5). If *T** and *T* are identical within experimental errors, the vector *T* is indeed included in the vector subspace and is a principal component of the input vector set given in the column vectors of matrix **A**.

$$\begin{pmatrix} T_1^* \\ e_2^* \\ s_3^* \\ t_4^* \\ . \\ . \\ . \\ v_m^* \end{pmatrix} = \begin{bmatrix} E_{11} & E_{12} \\ i_{21} & i_{22} \\ g_{31} & g_{32} \\ e_{41} & e_{42} \\ . & . \\ . & . \\ . & . \\ n_{m1} & n_{m2} \end{bmatrix} \times \begin{bmatrix} E_{11} & i_{21} & g_{31} & e_{41} & . & . & . & n_{m1} \\ E_{12} & i_{21} & g_{32} & e_{42} & . & . & . & n_{m2} \end{bmatrix} \times \begin{pmatrix} T_1 \\ e_2 \\ s_3 \\ t_4 \\ . \\ . \\ . \\ v_m \end{pmatrix}$$

$$(T^*) \quad = \quad [E] \quad \times \quad [E]^t \quad \times \quad (T) \qquad (5)$$

Finally, to utilize target transformation, an XANES spectrum of a pure reference compounds after interpolation onto the same energy grid as the unknown spectra may be multiplied with the eigenvector column matrix according to eq. (5). A good agreement (direct superimposition, with a residual <1.0%, for example) of the reference spectrum (*T* in eq. 5) and the resulting vector (*T** in eq. 5) indicates that this particular reference compound is a probable species in the unknown mixture.

We are interested in linear combinations of variables, with the goal of determining that combination that best summarizes the *n*-dimensional distribution of data. We are seeking the linear combination with the largest variance, with normalized coefficients applied to the variables used in the linear combinations. This axis is the so-called first principal axis or first principal component. Once this is determined, then the search proceeds to find a second normalized linear combination that has most of the remaining variance and is uncorrelated with the first principal component. The procedure is continued, usually until all the principal components have been calculated. In this case, $p = n$ and a selected subset of the principal components is then used for further analysis and for interpretation.

We can summarize the goals of PCA as to be:

(1) Extract the most important information from the data table,

(2) Compress the size of the data set by keeping only this important information,

(3) Simplify the description of the data set, and

(4) Analyze the structure of the observations and the variables.

Often, only the important information needs to be extracted from a data matrix. In this case, the problem is to figure out how many components need to be considered. A first procedure is to plot the eigenvalues according to their size, the so called "scree", and to see if there is a point in this graph (often called an 'elbow') such that the slope of the graph goes from "steep" to "flat" and to keep only the components which are before the elbow. This procedure, somewhat subjective, is called the *scree* or *elbow* test. Another standard tradition is to keep only the components whose eigenvalue is larger than the average. However, this procedure can lead to ignoring important information. Unfortunately, a foolproof method for automating the choice has yet to be discovered. Instead, the choice must be made based upon a few rules of thumb and the user's knowledge of the data.

The main goal of any factor analysis, i.e., the recovery of the underlying "true" factor causing the observed variance in the data, is identical to the main goal of curve-resolution methods. Another way to look the PCA question is that in factor analysis, "abstract" factors are clearly distinguished from "true" factors, and the key operation is to find a transformation from abstract factors to the true factors using rotation methods. PCA produces an orthogonal bilinear matrix decomposition, where components or factors are obtained in a sequential way to explain maximum variance. Using these constraints plus normalization during the bilinear matrix decomposition, PCA produces unique solutions. These "abstract" unique and orthogonal (independent) solutions are very helpful in deducing the number of different sources of variation present in the data. However, these solutions are "abstract" solutions in the sense that they are not the "true" underlying factors causing the data variation, but orthogonal linear combination of them. On the other hand, in curve-resolution methods, the goal is to unravel the "true" underlying sources of data variation. It is not only a question of how many different sources are present

and how they can be interpreted, but to find out how they are in reality. The price to pay is that unique solution are not usually obtained by means of curve-resolution methods unless external information is provided during the matrix decomposition [12].

PCA is perhaps the most commonly used factor analysis technique; however, it is not the only one. In the following, additional factor-based techniques are considered that are useful for extracting information from a data set. While techniques such as PCA calculate factors based on mathematical properties such as capturing maximum variance and orthogonality, the factors are often difficult to interpret because they are generally not directly related to chemical properties. For example, PCA loadings of a data set of measured spectra generally are not pure component spectra. Instead, the loadings are typically linear combinations of pure analyte spectra that have positive and negative intensities. Factor analysis techniques discussed below are aimed at estimating factors that have desirable properties from a chemical point of view and are easier to interpret.

We will discuss a particular technique, the evolving factor analysis (EFA), but there exist other similar ones such as evolving window factor analysis (EWFA) or fixed-size moving window evolving factor analysis (FSMW-EFA). These techniques are appropriate for data that are naturally ordered or have continuity, and can be used to find an initial estimate of the range of existence of analytes in an evolving system. This discussion is followed by a section on multivariate curve resolution (MCR). MCR examples utilize EFA results to initialize the algorithm for an evolving data set. MCR is also known as self-modeling curve resolution (SMCR). The MCR section introduces the mathematical model for the technique as well as the constrained alternating least squares algorithm (ALS). Although ALS is not the only algorithm used in MCR, it is one of the most common. It is one of several algorithms available that solve the objective function in a constrained least squares sense.

Like PCA, EFA can be used to determine how many "factors" are present in a data set; that is, how many independent sources of variation exist. Additionally, EFA can be used to determine where in a data set the factors first appear and where they disappear.

2.1. Evolving Factor Analysis (EFA)

According to Wise *et al.* in [1]: "*The fundamental idea of EFA is to follow the singular values of a data matrix as rows (samples) are added. Given a data matrix* ***X*** *(usually not mean-centered when performing EFA) with m samples and n variables, the singular value of the first row (sample) is determined. Next, the singular values for the first two rows are calculated, followed by the first three rows, and so on until all m samples have been considered. Since the number of samples considered, and thus the number of factors, evolves as the method proceeds, the technique is known as EFA. Of course, the number of non-zero singular values can never be greater than the lesser of the number of rows and columns in the sub-*

matrix considered. It is also customary to do EFA in the reverse direction, i.e., determine the singular values starting from the last row in the matrix and working upwards until all rows have been considered.

Once the singular values have been determined, they (or their logarithms, since they usually span many orders of magnitude) can be plotted versus the ordered variable (e.g., time). As new factors enter the data, new significant singular values will rise from the baseline of small singular values associated with noise in the data. Working in the reverse direction, significant singular values will rise from the baseline when factors disappear from the data matrix (see discussion on following paragraphs and an example in Figure II.1)."

Both EFA and FSMW-EFA are local-rank analysis methods. The former is more process oriented and rely on the sequential evolution of the components as a function of time or any other variable in the data set. The second can be applied to process and mixtures. In EFA, the evolution of a chemical system is gradually measured by recording a new response vector at each stage of the process under study. Mimicking the experimental protocol, EFA performs principal component analysis on submatrices of gradually increasing size in the process direction, enlarged by adding a row (response), one at a time. This procedure is performed from top to bottom of the data set (forward EFA) and from bottom to top (backward EFA) in order to investigate the emergence and the decay of the process contributions, respectively. Figure II.1 displays the information provided by EFA for an example (a particular chromatography data set, in this case) and how to interpret the results.

Each time a new row is added to the expanded submatrix (Figure II.1 down), a PCA model is computed and the corresponding singular values or eigenvalues are saved. The forward EFA curves (thin solid line) are produced by plotting the saved singular values or log (eigenvalues) obtained from PCA analysis of submatrix expanding in the forward direction. The backward EFA curves (thin dashed line) are produced by plotting the singular values or log (eigenvalues) obtained from PCA analysis of the sub matrix expanding in the backward direction. The lines connecting corresponding singular values (s.v.), i.e., all of the first s.v., the second s.v., the i^{th} s.v., indicate the evolution of the singular values along the process and, as consequence, the variation of the components. Emergence of a new singular value above the noise level delineated by the pool of nonsignificant singular values indicates the emergence of a new component (forward EFA) or the disappearance of a component (backward EFA) in the process.

Figure II.1 (down) also shows how to build initial estimates of concentration profiles from the overlapped forward and backward EFA curves as long as the process evolves in a sequential way (the thick line in the figure). For a system with *n* significant components, the profile of the first component is obtained combining the curve represent the first s.v. of the forward EFA plot and the curve representing the n^{th} s.v. of the backward EFA plot. Note that the n^{th} s.v. in the backward EFA is related to the disappearance of the firs component in the forward EFA plot. The profile of the second component is splicing the curve representing the second s.v. in the forward EFA plot to the curve representing the

$(n - 1)^{th}$ s.v.–from the backward EFA plot, and so forth. Combining the two profiles into one profile is easily accomplished in a computer program by selecting the minimum value from the two s.v. lines to be combined. It can see that the resulting four profiles obtained by EFA are good approximations of the real profile shown in Figure II.1 (up).

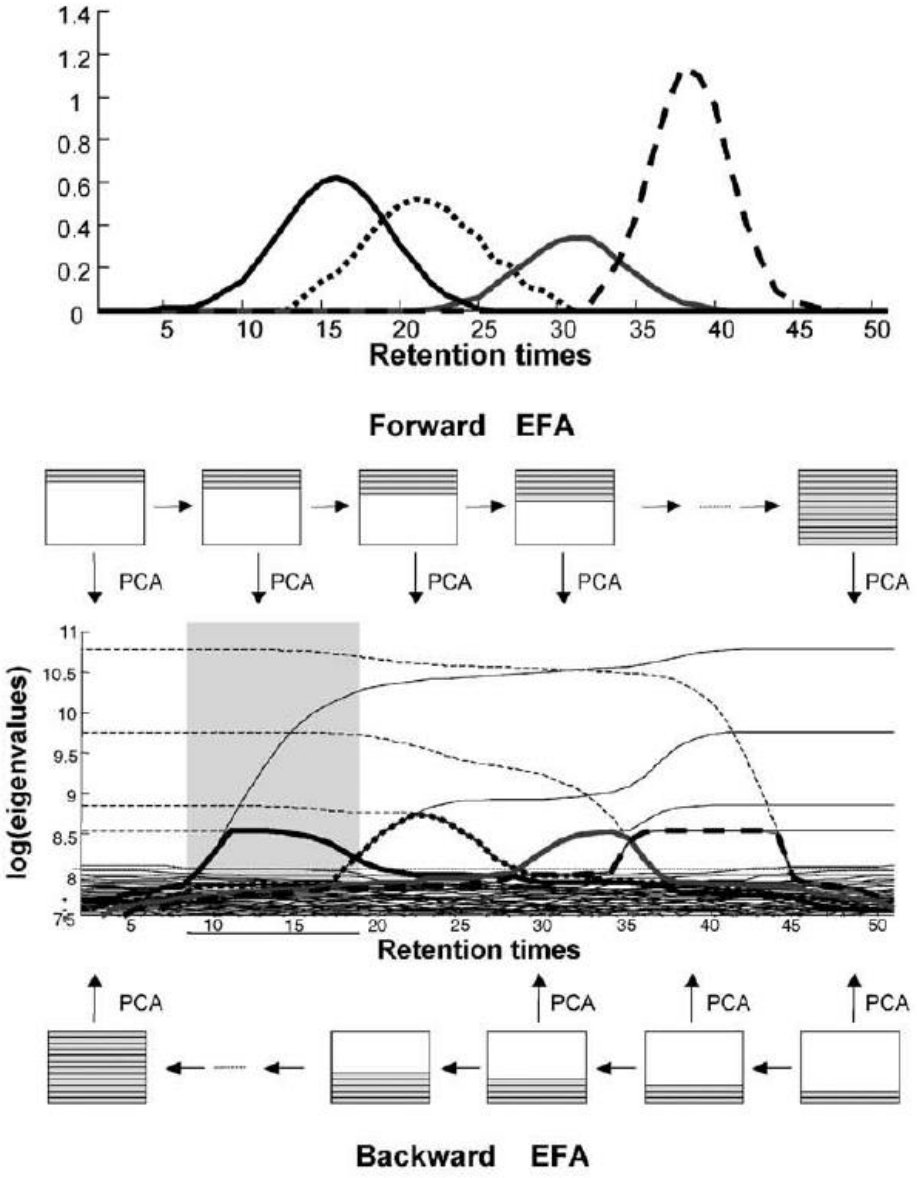

Figure II.1 - (Up) Concentration profiles of an HPLC-DAD (a chromatography evolution) data set. (Down) Information derived from the data set in (upper figure) by Evolving Factor Analysis (EFA): scheme of PCA runs performed. Combined forward EFA (solid black lines) and backward EFA (dashed black lines) plot. The thick lines with different line styles are the derived concentration estimates. The shaded zone marks the concentration window for the first eluting compound. The rest of the elution range is the zero-concentration window ([13]).

The information provided by the EFA plots can be used for the detection and location of the emergence and the decay of the compounds in an evolving process. Therefore, the concentration window and the zero-concentration region for each component in the system are easily determined for any process that

evolves such that the emergence and decay of each component occurs sequentially. For instance, the concentration window of the first component elute is shown as a shaded zone in Figure II.1 (down).

3. Multivariate Curve Resolution with Alternating Last Squares (MCR-ALS)

The common goal for all the resolution techniques is to recover pure contributions due to the individual species in the system from the multivariate experimental instrumental response (the measured spectra signals) [14]. Self-modeling multivariate curve resolution (SMCR) methods are often applied to resolve such multivariate spectroscopic data. Such techniques address one of the most difficult problems in analytical spectroscopy, the qualitative and quantitative characterization of mixtures containing unknown amounts of an unknown number of unknown components. SMCR does not need any spectra libraries or any *a priori* information on the number of components or concentration profiles.

In principle, with any MCR technique you can resolve the pure component spectra. The assumptions might involve Beer's law or a certain bilinear model for the data. In 1960, Wallace developed a method to find the number of components in a multi-component system [15]. It was perhaps the first member of the MCR family. The starting point of the new term MCR is in 1971 when Lawton and Sylvester discussed a method based on factor analysis to resolve a two-component system [16].

The starting point of MCR goes back to the realization that the number of chemical components in a mixture might be determined by the matrix rank of the data matrix if each component has a different spectrum and corresponding concentration profile. Lawton and Sylvester first introduced MCR to resolve two-component mixture spectra in 1971. Their approach was based on principal component analysis and non-negativity constraints on both the spectral estimates and their corresponding concentrations.

Iterative resolution methods, such as MCR-ALS, obtain the resolved concentration and response matrices through the one-at-a-time refinement or simultaneous refinement of the profiles in $\mathbf{C}$, in $\mathbf{S}^T$, or in both matrices at each cycle of the optimization process. The profiles in $\mathbf{C}$ or $\mathbf{S}^T$ are "tailored" according to the chemical properties and the mathematical features of each particular data set. The iterative process stops when a convergence criterion (e.g., a preset number of iterative cycles is exceeded or the lack of fit goes below a certain value) is fulfilled.

Prior knowledge about the data set (chemical or related to mathematical features) can be used in the optimization process, but it is not strictly necessary. The main complaint about iterative resolution methods has often been the longer calculation times required to obtain optimal results; however, improved fast algorithms and more powerful PCs have overcome this historical limitation.

3.1. MCR Method: General Definition and Limitations

As developed by de Juan and Tauler (in [13]): "*All resolution methods decompose mathematically a global mixed instrumental response into the pure contributions due to each of the components in the system* [13]. *This global response is organized in a matrix* ***D*** *containing raw information about all the components present in the data set. Resolution methods allow for the decomposition of the initial mixture data matrix* ***D*** *into the product of two data matrices* ***C*** *and* $\boldsymbol{S}^T$*, each of them including the pure response profiles of the n mixture or process components associated with the row and the column direction of the initial data matrix, respectively (see Figure II.2). In matrix notation, the expression valid for all resolution methods is:*

$$\boldsymbol{D} = \boldsymbol{C}\,\boldsymbol{S}^T + \boldsymbol{E} \tag{6}$$

where $\boldsymbol{D}(r \times c)$ *is the original data matrix,* $\boldsymbol{C}(r \times n)$ *and* $\boldsymbol{S}^T(n \times c)$ *are the matrices containing the pure response profiles related to the data variation in the row direction and in the column direction, respectively.* $\boldsymbol{E}(r \times c)$ *is the error matrix, i.e. the residual variation of the data set that is not related to any chemical contribution. Parameters r and c are the number of rows and the number of columns of the original data matrix, respectively, and n is the number of chemical components in the mixture or process.* ***C*** *and* $\boldsymbol{S}^T$ *often refer to concentration profiles and spectra (hence their names), although resolution methods are proven to work in many other diverse problems* [13].

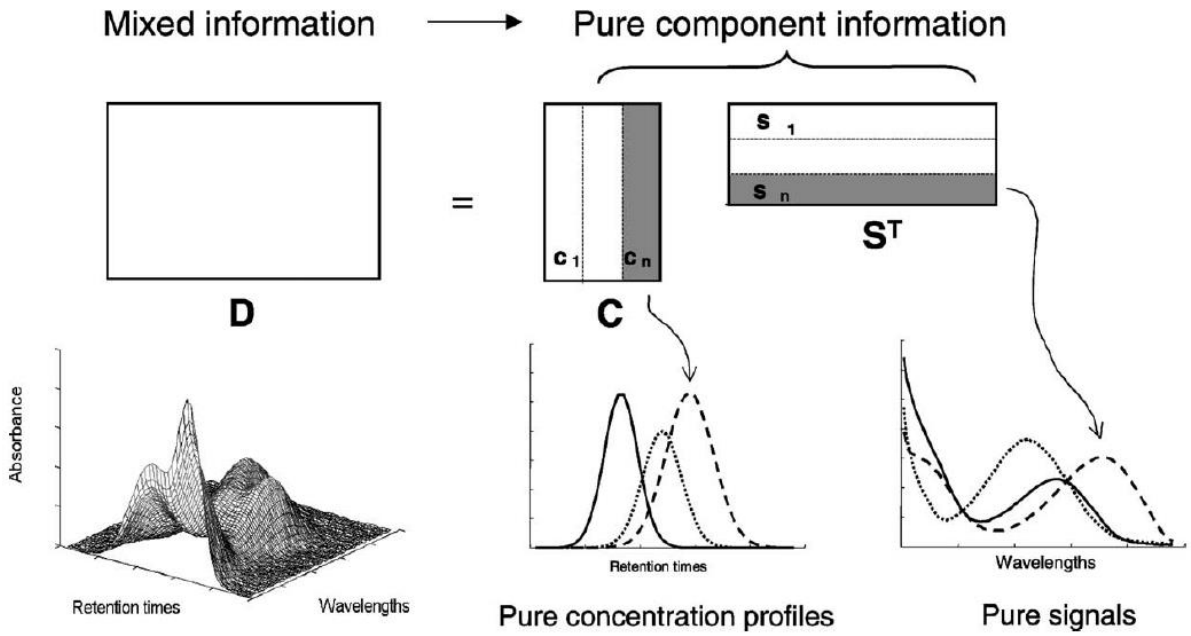

Figure II.2 - Data set decomposition provided by resolution methods and graphical representation of the information obtained for a chromatography example.

From the early days in resolution research, the mathematical decomposition of a single data matrix, no matter the method used, is known to be subject to ambiguities. This means that many sets of paired ***C***

and $\boldsymbol{S}^T$-type matrices can reproduce the original data set with the same fit quality. In plain words, the correct reproduction of the original data matrix can be achieved by using response profiles differing in shape (rotational ambiguity) or in magnitude (intensity ambiguity) from the sought (true) ones [17].

These two kinds of ambiguities can be easily explained. The basic equation associated with resolution methods, $\boldsymbol{D} = C\,S^T$, can be transformed as follows:

$$\boldsymbol{D} = C\,(T\,T^{-1})\,S^T \tag{7}$$

$$\boldsymbol{D} = (CT)\,(T^{-1}\,S^T) \tag{8}$$

$$\boldsymbol{D} = C'\,S'^T \tag{9}$$

*Where $\boldsymbol{C'} = CT$ and $\boldsymbol{S'^T} = (T^{-1}S^T)$ describes the **D** matrix as correctly as the true **C** and $\boldsymbol{S}^T$ matrices do, though $\boldsymbol{C'}$ and $\boldsymbol{S'}^T$ are not the sought solutions. The rotational ambiguity problem indicates that a resolution method can potentially provide as many solutions as **T** matrices can exist, i.e. infinite, unless **C** and **S** are forced to obey certain conditions. In a hypothetical case with no rotational ambiguity, the basic resolution model could still be rewritten as shown below:*

$$\boldsymbol{D} = \sum_{i=1}^{n}\left(\frac{1}{k_i}c_i\right)\left(k_i s_i^T\right) \tag{10}$$

$$\boldsymbol{D} = C'\,S'^T \tag{11}$$

*Where k_i are scalars. The concentration profiles of the new $\boldsymbol{C'}$ matrix would have the same shape as the real ones, but being k_i times smaller, whereas the spectra of the new $\boldsymbol{S'}$ matrix would be shaped like the **S** spectra, though k_i times more intense.*

How seriously ambiguity problems can affect resolution results has a different answer in each data set. In different manners, the main purpose of past and current investigation is finding ways to suppress, when feasible, or minimize this source of uncertainty in resolution results and to assess the effect on the quality of the profiles recovered."

Starting with the results of the EFA it is possible to obtain an initial estimate of the concentration profiles, or at least, the range of existence in the data set of each component. These concentration profiles are used as initial estimates in the constrained and alternating least squares optimization. At each iteration of the optimization, a new estimate of the spectra matrix **S** and of the concentration profiles **C** is obtained.

It is also possible to combine data sets from different process runs (or analytical runs) simply by augmented matrices as follows:

$$\boldsymbol{D} = \begin{bmatrix} \boldsymbol{D}_1 \\ \boldsymbol{D}_2 \\ \vdots \\ \boldsymbol{D}_p \end{bmatrix} = \begin{bmatrix} \boldsymbol{C}_1 \\ \boldsymbol{C}_2 \\ \vdots \\ \boldsymbol{C}_p \end{bmatrix} S^T + \begin{bmatrix} \boldsymbol{E}_1 \\ \boldsymbol{E}_2 \\ \vdots \\ \boldsymbol{E}_p \end{bmatrix} \quad (13)$$

where $\mathbf{D_p}$ are the ordered data for each of the p =1,…, P process runs and the $\mathbf{C_p}$ are the associated contribution profiles from the runs. Combining data from different runs, and/or measured standards, may also contribute to the stability of the solutions obtained. Augmented matrices of standard analytes can be included to improve selectivity and allow MCR to be used for quantification [13][18][17].

3.2. The Role of Constraints

According to de Jaun and Tauler ([13]): "*Although resolution does not require previous knowledge about the chemical system under study, additional knowledge, when existing, can be used to improve the results obtained and to tailor the sought pure profiles according to certain known features. The working procedure of the different resolution methods is very diverse but many of them start with initial estimates of* ***C*** *or* ***S*** *and work by optimizing iteratively the concentration and/or response profiles using the available information about the system* [17][18][19]. *The introduction of this information is carried out through the implementation of constraints. A constraint can be defined as any mathematical or chemical property systematically fulfilled by the whole system or by some of its pure contributions* [20]. *Constraints are translated into mathematical language and force the iterative optimization process to model the profiles respecting the conditions desired.*

Although generally accepted nowadays, there is still a certain controversy related to the application of constraints, due presumably to misuses and rudimentary implementations of these conditions in the past. The application of constraints should be always prudent and soundly grounded and they should only be set when there is an absolute certainty about the validity of the constraint. Even a potentially applicable constraint can play a negative role in the resolution process when factors like experimental noise or instrumental problems distort the related profile so as it is no longer obeyed or when the profile is modified so roughly that the convergence of the optimization process is seriously damaged. When well implemented and fulfilled by the data set, constraints can be seen as driving force of the iterative process to the right solution and, often, they are found not to be active in the last part of the optimization process. Resolution methods have progressed through the new formulation and better implementation of constraints."

There are several ways to classify constraints: the main ones related either to the nature of the constraints or to the way they are implemented. In terms of nature, constraints can be based on either chemical or mathematical feature of the data set. In term of implementation, we can distinguish between equality constrains or inequality constrains. The former sets the elements in a profile to be equal to a certain

value, whereas inequality constraint forces the element in a profile to be unequal (higher or lower) than a certain value. Figure II.3 shows the effect of some of these constraints on the correction of a profile.

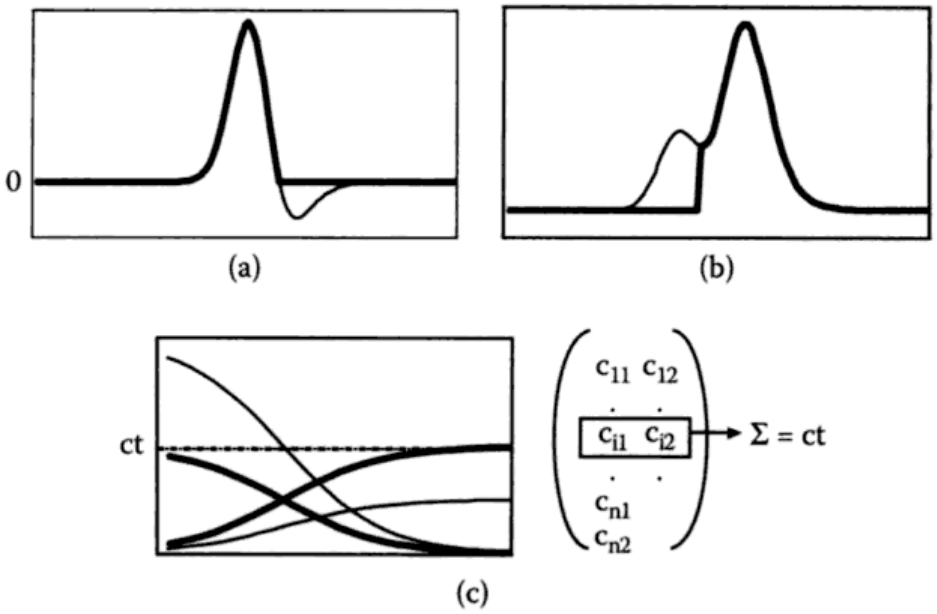

Figure II.3 - Effects of some constraints on the shape of resolved profiles. The thin and the thick line represent the profile before and after being constrained, respectively. Constrains shown are (a) nonnegativity, (b) unimodality and (c) closure.

Most of the constraints firstly implemented were directly linked to chemical properties fulfilled by the pure concentration or response profiles.

3.2.1.Nonnegativity

The nonnegativity constraint is applied when it can be assumed that the measured values in a experiment will always be positive. For exemple, it can be applied to concentrations and to many instrumental signals, such as UV absorbances and fluorescence intensities [17][18][19]. This constraint forces the value in a profile to be equal or greater than zero. It is an example of an inequality constraint (Figure II.3a).

3.2.2.Unimodality

Unimodality allows the presence of only one maximum per profile (Figure II.3b). It was useful in many concentration profiles related to processes, like reaction profiles or peaks in a chromatographic elution process [17][19]. It is important to note that this constraint does not only apply to peaks, but to profiles that have a constant maximum (plateau) or a decreasing tendency.

3.2.3.Closure

The closure constraint is applied to closed reaction systems, where the principle of mass balance is fulfilled. With this constraint, the sum of concentrations of all of the species involved in the reaction (the suitable elements in each row of the **C** matrix) is forced to be equal to a constant value (the total concentration) at each stage in the reaction. This is an example of inequality constraint (Figure II.3c). Closure (or mass balance) was valid in many reaction systems as well [17][18].

3.2.4.Other Sorts of Constraints

De Juan and Tauler say (in [13]): "*The most recent progress in chemical-related constraints refers to the implementation of a physicochemical model into the resolution process. Such a strategy has reconciled the separate worlds of hard- and soft-modelling and has allowed for the resolution of chemical systems unable to be tackled successfully by any of these two pure methodologies. In resolution methods where hard- and soft-modelling coexist, advantages from both aspects can be taken. Thus, the strictness of the hard model constraint decreases dramatically the ambiguity of the related profiles and provides fitted parameters of physicochemical and analytical interest, such as equilibrium and kinetic constants or total analyte concentrations. The soft part of the algorithms allows for the modelling of complex systems, where the central reaction system evolves in the presence of absorbing interferential.*

Chemical information associated with the knowledge of pure spectra or pure concentration profiles can also be introduced in the optimization as an additional equality constraint. The known profiles may be set to be invariant along the iterative process. Following this concept, the knowledge of a profile does not need to be complete to be used. When some elements are known, they can also be fixed. This has opened the possibility to use two-way resolution methods for quantitative purposes. Thus, some data sets analogous to those used in multivariate calibration, formed by the signals recorded in a series of calibration and unknown samples, can be analyzed. The quantitative information is obtained by resolving the system using an additional constraint that fixes the known concentration values of the analytic(s) in the calibration samples in the related concentration profile(s) [21]. *This approach provides also the qualitative information related to resolution methods in the form of pure signal profiles associated with the analytic and interferential and has proven to be as powerful as classical multivariate methods in examples where the net signal of the analytic is not very minor.*

Other constraints are related to mathematical features and can be applied to all data sets regardless of their chemical nature. These constraints are associated with the concept of local rank, i.e. how the number and distribution of components vary locally along the data set. The key constraint within this family is selectivity. It holds for concentration and spectral windows where only one component is present and suppresses completely the ambiguity linked to some of the profiles in the system. The strong effect of this constraint and the easy link with the analogous chemical concept explain its early and wide application in resolution problems [17][18]. *Not so common, but equally recommended is the use of other local rank constraints in iterative resolution methods. Setting which components are absent in data set windows with a number of components smaller than the total rank always contribute to the correct resolution of profiles and can be particularly helpful in multicomponent systems like spectroscopic images or mixtures, where more process-related constraints (unimodality, closure, etc.) are not applicable.*"

3.3. Quality Assessment of Results

They highlight ([13]): "*until recently, research in resolution was mainly focused on the design and improvement of the algorithms used and not much in providing procedures to assess the quality of the results obtained. The main sources of uncertainty associated with the resolution results are the ambiguity of the recovered profiles and the experimental noise of the data. Providing methodologies to quantify this uncertainty is not only a topic of interest in the current research, but a necessary step to introduce the use of resolution methods in standard analytical procedures.*

The possible existence of ambiguity in resolution is known since the earliest research in this area [3]. *After years of experience, it has been possible to set resolution theorems that indicate clearly the conditions needed to recover uniquely the pure concentration and signal profiles of a compound in a data set. These conditions depend mainly on the degree of overlap among the region of occurrence of the compound and the rest of constituents and on the general distribution of the different compound windows along the data set. Therefore, in the same system, some profiles can be recovered uniquely and some others will be necessarily affected by a certain ambiguity.*

Even in the absence of ambiguity, the experimental error contained in real data can propagate in the resolution results. This source of uncertainty affects the results of all kinds of data analysis methods and, in simpler approaches, like multivariate or univariate calibration, is easily quantified with the use of well-established and generally accepted figures of merit. Although some figures of merit have been proposed for higher order calibration methods, finding analytical expressions to assess the error associated with resolution results is an extremely complex problem because of the huge number of non-linear parameters that are calculated, as many as elements in all the pure profiles resolved."

Although ambiguity and noise are two distinct sources of uncertainty in resolution, their effect on the resolution results cannot be considered completely independent.

References

[1] B. M. Wise, N. L. Ricker, D. J. Veltkamp, and B. R. Kowalski, "A Theoretical Basis for the Use of Principal Components Models for Monitoring Multivariate Processes," *Process Control and Quality*, vol. 1, p. 41, 1990.

[2] M. J. Adams, *Chemometrics in Analytical Spectroscopy*. Cambridge: Royal Society of Chemistry, 2004.

[3] S. Wold, "Chemometrics; what do we mean with it, and what do we want from it?," *Chemometrics and Intelligent Laboratory Systems*, vol. 30, no. 1, pp. 109–115, Nov. 1995.

[4] M. Garrido, F. X. Rius, and M. S. Larrechi, "Multivariate curve resolution-alternating least squares (MCR-ALS) applied to spectroscopic data from monitoring chemical reactions processes.," *Analytical and bioanalytical chemistry*, vol. 390, no. 8, pp. 2059–66, Apr. 2008.

[5] A. de Juan, M. Maeder, M. Martínez, and R. Tauler, "Combining hard- and soft-modelling to solve kinetic problems," *Chemometrics and Intelligent Laboratory Systems*, vol. 54, no. 2, pp. 123–141, Dec. 2000.

[6] B. K. Lavine and S. D. Brown, "Chemometrics Brightens the Future of Spectroscopy," *Today's Chemist at Work*, vol. 6, no. 9, p. 28, 1997.

[7] H. Mark and J. W. Jr., *Chemometrics in Spectroscopy*, 1st ed. London, UK: Academic Press, 2007.

[8] E. R. Malinowski, *Factor Analysis in Chemistry*, 2nd ed. New York, 1991.

[9] J. Stoer and R. Bulirsch, *Introduction to Numerical Analysis*. New York, 1980.

[10] M. Fay, A. Proctor, and D. Hoffmann, "Determination of the Mo surface environment of Mo/TiO2 catalysts by EXAFS, XANES and PCA," *Microchimica Acta*, vol. 293, pp. 281–293, 1992.

[11] S. R. Wasserman, "The Analysis of Mixtures: Application of Principal Component Analysis to XAS Spectra," *Journal de Physique IV*, vol. C2, p. 203, 1977.

[12] P. Gemperline, *Practical Guide To Chemometrics*, 2nd ed. Boca Raton: CRC Press, 2006.

[13] a. de Juan and R. Tauler, "Chemometrics applied to unravel multicomponent processes and mixtures," *Analytica Chimica Acta*, vol. 500, no. 1–2, pp. 195–210, Dec. 2003.

[14] S. D. Brown, "Information and data handling in chemistry and chemical engineering: the state of the field from the perspective of chemometrics," *Computers & Chemical Engineering*, vol. 23, no. 2, pp. 203–216, Dec. 1998.

[15] R. M. Wallace, "Analysis of Absorption Spectra of Multicomponent Systems," *The Journal of Physical Chemistry*, vol. 64, no. 7, pp. 899–901, Jul. 1960.

[16] W. H. Lawton and E. A. Sylvestre, "Self Modeling Curve Resolution," *Technometrics*, vol. 13, no. 3, pp. 617–633, Aug. 1971.

[17] R. Tauler, A. Smilde, and B. Kowalski, "Selectivity, local rank, three-way data analysis and ambiguity in multivariate curve resolution," *Journal of Chemometrics*, vol. 9, no. 1, pp. 31–58, Jan. 1995.

[18] R. Tauler, "Multivariate curve resolution applied to second order data," *Chemometrics and Intelligent Laboratory Systems*, vol. 30, no. 1, pp. 133–146, Nov. 1995.

[19] B. G. M. Vandeginste, W. Derks, and G. Kateman, "Multicomponent self-modelling curve resolution in high-performance liquid chromatography by iterative target transformation analysis," *Analytica Chimica Acta*, vol. 173, pp. 253–264, Jan. 1985.

[20] A. de Juan, Y. Vander Heyden, R. Tauler, and D. . Massart, "Assessment of new constraints applied to the alternating least squares method," *Analytica Chimica Acta*, vol. 346, no. 3, pp. 307–318, Jul. 1997.

[21] M. C. Antunes, J. E. J. Simão, A. C. Duarte, and R. Tauler, "Multivariate curve resolution of overlapping voltammetric peaks: quantitative analysis of binary and quaternary metal mixtures," *The Analyst*, vol. 127, no. 6, pp. 809–817, May 2002.

Chapter III: Experimental Methods

Table of Contents

1. Introduction

In this chapter we are not intend to be fully described the techniques used the work. Instead, the main goal is provide a description of the important aspects as well as some particular issues that we may found when dealing with supported catalysts. For instance, XPS and Raman spectroscopy are well-known and widely used techniques in catalysis. While for the former we spent some pages for relatively important discussion, the latter is totally described on the next chapter, which contains the full contain of the article published in peer review journal. The same was done for preparation method. Thus, we do not take into account in the present chapter the set-up description for neither XPS nor Raman techniques, since it is reported on the next chapter.

However, techniques such as Low-Energy Ion Scattering (LEIS) and X-ray Absorption Spectroscopy (XAS) deserve special attention, either because they are relatively new for catalysis studies (particularly, LEIS) or because the interpretation and technical aspects are in a certain sense not "obvious" (the data treatment and interpretation of XAS data). For these cases, we try to be more detailed in the description of the technique.

We also reserved a especial section for the routine followed in MCR treatment of the data.

2. Surface Analysis: XPS and LEIS

Modern methods of surface analysis stand in contrast to the so-called classical methods. Classical methods include adsorption isotherms, which give surface areas and pore-size distribution, measurements of surface roughness, photoelectric work function, thickness measurements, reflectivity, and microscopy to obtain surface topography. The information obtained by the classical methods can be characterized as "descriptive". This means that they provide an index to qualitative surface features such as roughness, topography, etc., but little quantitative or "chemical" information.

Modern methods of surface analysis are spectroscopic methods. They can provide chemical information that the classical methods cannot. For example, one can obtain elemental analyses, information about oxidation states and organic functional groups, quantitative analyses as either elemental ratios or oxidation state ratios, and distributions of materials either across the surface or from the surface inward toward the bulk.

Quantitation of results from surface spectroscopic methods is still a matter of research and debate. Nevertheless, the ability to acquire chemical information about surfaces has placed surface analysis in the forefront of modern analytical chemistry. In the next two sections, we present the two fundamental techniques used in this work, namely x-Ray Photoelectron Spectroscopy (XPS) and Low-Energy Ion Scattering (LEIS).

2.1. XPS

For the development of new catalytic systems, it is extremely important to investigate the changes of the surface electronic, chemical and structural properties during a particular process. Analytical techniques, such as X-ray photoelectron spectroscopy (XPS), based on the detection of ejected electrons, are the most suitable methods for the analysis of surfaces because they probe a limited depth of the sample [1]. In the following, the information obtained by this technique relevant to the field of catalysis will be outlined.

2.1.1. General Background

XPS is based on the photoelectric effect arising when high energy photons (usually in the keV range) hit a material with the consequent emission of electrons (photoelectrons). Einstein's law gives the photoelectron kinetic energy, E_k, which is the measured quantity in the experiment: $E_k = h\nu - E_b$. Here, $h\nu$ is the energy of the incident radiation and E_b the binding energy of the electron in a particular level [2].

Photoelectron peaks are labelled according to the quantum numbers of the level from which the electron originates (Figure III.*1*). The electron is characterized by a total momentum number $j = l + s$, where l is the orbital momentum number and s the spin momentum number which is equal to ± ½. Therefore, whenever $l > 0$, the peak is split into a doublet, with an energy difference called *spin-orbit splitting* which increases with Z roughly as Z^5 [2].

The XPS technique provides quantitative and qualitative information. Quantitative information arises from the element specificity of the binding energies and the relation between the intensity of the photoelectron peaks and the element concentration (as it will be discussed on the next subsection). Qualitative information are obtained from the energy position of a photoelectron peak with respect to the energy position of the same level in a reference compound (chemical shift).

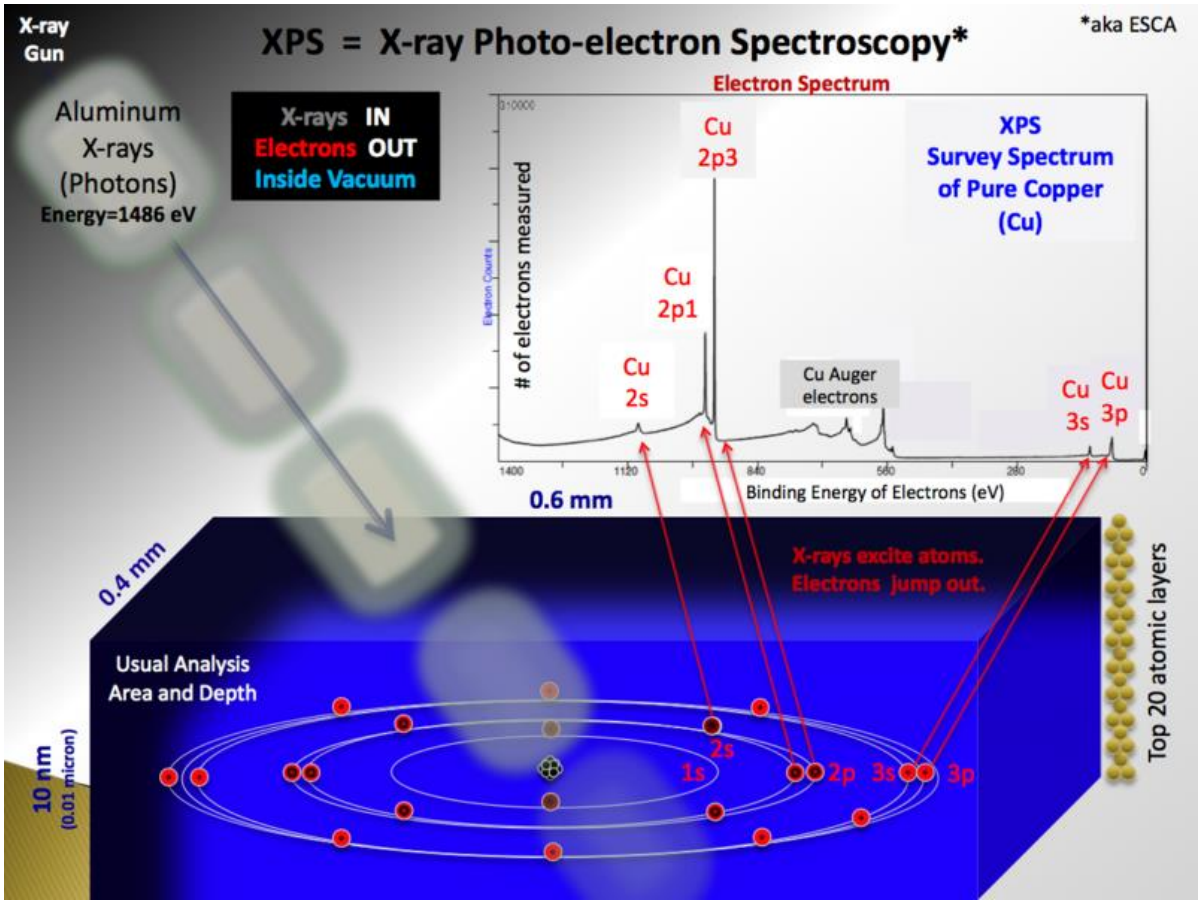

Figure III.1 - Rough schematic picture of XPS process. The inset shows a typical graphic obtained for XPS analysis ["XPS PHYSICS" by Bvcrist. Licensed under Public].

Chemical shifts of binding energies of a certain element level are due to different oxidation states and different chemical environments. They are interpreted in terms of a simple electrostatic theory, called "charge potential model" [3]. According to the model, the energy of the atom is divided into two terms, one associated with the net charge on the probe atom and the other term associated with the charge distribution of the surrounding atoms. Both terms are considered as "initial state effect" since they refer only to the electrostatic potential experienced by the core electron in the ground state before ionization. A more realistic theory takes into account the relaxation effects involved in the redistribution of the electronic charge during ionization, and referred to as "final state effect". The binding energy chemical shift of a level of the atom *i* in a molecule with respect to a reference can then be expressed as:

$$\Delta E_b = \frac{\Delta q_i}{r_V} - \frac{\sum \Delta q_i}{r_{ij}} - \Delta R \qquad (1)$$

The first term on the right represents the electrostatic potential due to the valence charge on atom *i* with an average valence orbital radius r_v. The summation term is the sum of the potentials at atom *i* due to the surrounding atoms *j* considered as point charges and located at r_{ij}. ΔR is the relaxation term.

The use of the technique for sample composition analysis is based on the linear relation between the intensity of the signal I_A from element A and its atomic concentration C_A. Thus, for a surface layer:

$$I_A = F \cdot k \cdot S \cdot \sigma_A \cdot C_A \cdot L(\theta) \tag{2}$$

F is the intensity of the incident photons, k is an instrumental factor and S is the sample-analyzed area. All three parameters are constant for a given instrumental configuration. The parameter σ_A is the cross-section for the emission of the photoelectron. $L(\theta)$ is the angular asymmetry factor, depending on the angle θ between the direction of propagation of the photons and the direction of the outgoing electrons, which describes the intensity distribution of the photoelectrons. When thick materials are probed, the inelastic mean free path (IMFP) of the electrons, indicated by λ, and representing the distance that the electrons can travel inside the solid without suffering inelastic collision, should be considered. Eq. (2) is corrected by an attenuation factor taking into account the angle of the electron detection with respect to the surface (take-off angle φ). Then, the XPS peak intensity I_d from a layer of material of thickness d is given by the following equation:

$$I_d = I_\infty\left(1 - e^{-d/sin\emptyset}\right) \tag{3}$$

I_∞ is the intensity from an "infinitely' thick layer for electrons of IMFP = λ and λ sin φ is referred to as "effective escape depth".

Because of its surface enhanced sensitivity, XPS represents a valid tool for particle size determination. Indeed XPS intensity ratios of particle related peaks I_p and support related peaks I_s are strongly dependent on the catalyst dispersion. Qualitatively, catalysts with the same loading of metal over the same support exhibit high I_p/I_s values in the case of small particles as compared to large particles. The estimate of size from XPS data is not simple and modelling of the supported catalyst is needed.

Several approaches exist which take into account the morphology of the supports in terms of surface area and porosity. Maybe the most known model for high area supports was the one proposed by Kerkhof and Moulijn [4][5] who considered the catalysts as a series of slabs with cubic particles of sizes c in between. The thickness t of the slabs are estimated from the density ρ and the specific surface area S_0 of the support, according to

$$t = \frac{2}{\rho} S_0 \tag{4}$$

The model assumes that the electrons leave the sample in a direction perpendicular to the surface.

The relation between the experimental intensity ratio of metal over support photoelectron peaks I_p/I_s and the monolayer intensity ratio (for details, see e.g. [6]) is given by

$$\frac{\left(I_p/I_s\right)_{crystallite}}{\left(I_p/I_s\right)_{monolayer}} = \frac{1-e^{-\alpha}}{\alpha} \quad (5)$$

By plotting this relation for different value of α, an estimate of the crystallite sizes is obtained. Reliable values of the sizes are dependent on cross-section values, on electron IMFPs and on support surface areas.

The chemical information implicit in the X-ray-induced photoelectron spectrum is a very important feature of the XPS technique. For almost all elements, the binding energy of the photoelectron peak shows small perturbations that reflect the chemical environment of the element under consideration. The most important source of chemical state information in XPS comes actually directly from the energy position of the photoelectron core level peaks. Although the core levels are not directly involved in the chemical bonding process, their binding energy depends on the chemical environment. In a simplified picture, this effect, which is called the "chemical shift", originates from the change in electrostatic potential inside the orbitals of the valence electrons (i.e., at the location of the core electrons).

Large variations in chemical shifts are expected for different oxidation states but can also arise from difference in lattice site and molecular environment. In an accurate model, the electron orbitals cannot be assumed to remain frozen during photoemission and the electron-density around the atom relaxes in response to the creation of the positively charged core hole. This reduces the kinetic energy of the outgoing photoelectron and thereby increases the derived electron-binding energy. Such level shifts are well documented in handbooks and databases and are widely used to get chemical state information. However, in some cases, the change in potential is insignificant although the valence electrons are changed considerably due to different chemical bonds.

When dealing particularly with supported catalysts, such as CoMo/TiO_2, one has to take into account that this type of system is characterized by the possible presence of more than one oxidation state for the transition metal, and in fact the identification of the surface species has been one of the main problems tackled with XPS [7]. The progress in data acquisition and in data treatment techniques has permitted remarkable achievements in the peak resolution and attribution, often supported by different techniques. In arriving at the distribution of the various oxidation states, it was generally assumed that the concentration of the species was proportional to the relevant peak intensity, disregarding morphological differences in the partition of the species, at least in the first instance. In several treatments, the Kerkhof-Moulijn model is adopted. One must remind that this model assumed a homogeneous "promoter" particle distribution, sometimes not supported by the XPS results, nor by those from different techniques. At least for Mo/TiO_2 systems, experiments showed a good agreement for Kerkhof-Moulijn model and XPS measurements [8].

2.1.2. Quantification Analysis

As discussed above, XPS is a quantitative technique in the sense that the number of electrons recorded for a given transition is proportional to the number of atoms at the surface. In practice, however, to produce accurate atomic concentrations from XPS spectra is not straightforward. The precision of the intensities measured using XPS is not in doubt; that is intensities measured from similar samples are repeatable to good precision. What may be doubtful are results reporting to be atomic concentrations for the elements at the surface. An accuracy of 10% is typically quoted for routinely performed XPS atomic concentrations. Since many problems involve monitoring changes in samples, the precision of XPS makes the technique very powerful.

The first issue involved with quantifying XPS spectra is identifying those electrons belonging to a given transition. The standard approach is to define an approximation to the background signal. The background in XPS is non-trivial in nature and results from all those electrons with initial energy greater than the measurement energy for which scattering events cause energy losses prior to emission from the sample. The zero-loss electrons constituting the photoelectric peak are considered to be the signal above the background approximation. A variety of background algorithms are used to measure the peak area; none of the practical algorithms are correct and therefore represent a source for uncertainty when computing the peak area. Usually the background is a linear or Shirley type [9]. Peak areas computed from the background subtracted data form the basis for most elemental quantification results from XPS.

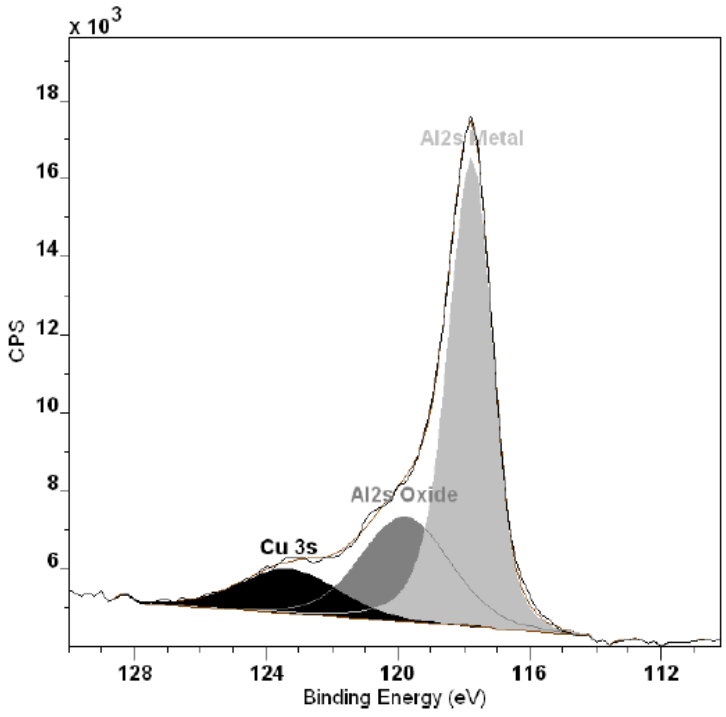

Figure III.2 - Typical XPS survey spectrum taken from a compound sample.

The data in Figure III.*2* illustrates an XPS spectrum measured from a typical sample encountered in practice. The inset tile within Figure III.*2* shows the range of energies associated with the Cu 2*s* and Al 2*s* photoelectric lines. Since these two transitions include multiple overlapping peaks, there is a need to apportion the electrons to the Cu 2*s* or the Al 2*s* transitions using a synthetic peak model fitted to the data (usually, Gaussian or Lorentzian functions, representing contributions from different chemical species). The degree of correlation between the peaks in the model influences the precision and therefore the accuracy of the peak area computation.

2.2. LEIS

Low-Energy Ion Scattering (LEIS), also called Ion Scattering Spectroscopy (ISS), is a unique tool in surface analysis, since it provides the atomic composition of the outer atomic layer. To take full advantage of this feature, it is important that the results can be quantified, which can be a nontrivial problem.

The outer surface atoms dominate many processes such as adhesion, catalysis, electron emission, growth and wetting. It is, therefore, not surprising that in 80-90% of the challenges facing chemical and electronic industry relate to surfaces. In the case of poor adhesion, they relate to the surfaces that are exposed after failure. While for other surface analytic techniques, the composition analysis is an average over a few or generally, even over many atomic layers, for LEIS the analysis is selective for the outer atoms. All kinds of materials are studied, including metals, semiconductors, ceramics, organics and polymers. The only major restriction being, similar to the other beam techniques in surface analysis, which need vacuum, that the materials vapor pressure is low enough to sustain the vacuum.

2.2.1. Fundamentals of LEIS Technique and Composition Analysis

In LEIS a sample (target) is bombarded with noble gas ions (He^+, Ne^+ or Ar^+) with energies (E_0) typically between 0.5 and 10 keV. The incident ion beam is directed towards the surface at an angle α with respect to the surface normal; typically, α is smaller than 60°. Only projectiles that are backscattered into a certain solid angle element $d\Omega$ (at a scattering angle θ; typically 140°) are analyzed (Figure *III.3*).

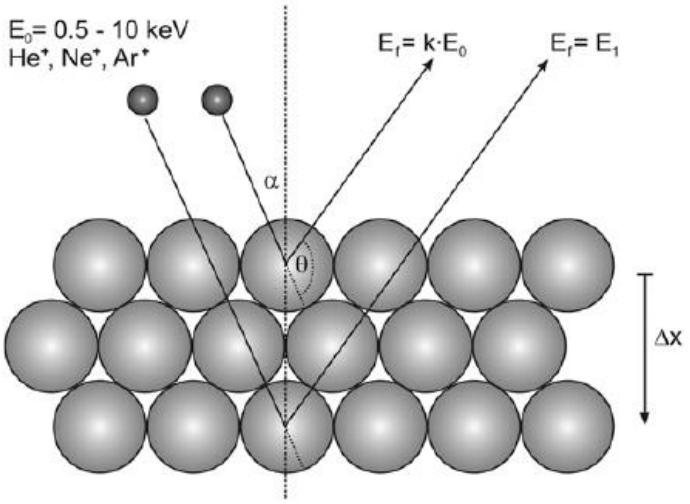

Figure III.3 - Schematic of experimental conditions in LEIS [10].

For quantitative surface analysis, only the signal of scattered ions, S^+, is analyzed. There is also the possibility to analyze the signal of backscattered neutrals, S^0.

In this regime, projectiles are scattered from surface atoms almost exclusively by binary collisions, with an energy $E_f = k\,E_0$ ($k < 1$, see equation (6). Ions that have penetrated the target up to a depth Δx will leave the surface with an energy $E_1 < k\,E_0$.

In an elastic binary collision of a projectile of mass m_1 and primary energy E_0 with a target atom of mass m_2 at rest, the energy transfer only depends on the scattering angle θ. The kinematic factor k, which is defined as the ratio E_f/E_0, can be calculated from energy and momentum conservation and yields:

$$E_f = k \cdot E_0 = \left(\frac{\cos\theta \pm \sqrt{\left(\frac{m_2}{m_1}\right)^2 - \sin^2\theta}}{1 + \frac{m_2}{m_1}} \right)^2 \cdot E_0 \qquad (6)$$

Where the positive sign applies to $m_2/m_1 \geq 1$ while both positive and negative signs are solutions if $1 \geq m_2/m_1 \geq |\sin\theta|$.

From Eq. (6), it becomes obvious that for scattering angles above 90° E_f is a unique function of m_2. It is seen that backscattering ($\theta > 90°$) for a mass ratio $q = m_2/m_1 < 1$ is not possible. Consequently, hydrogen is the only element that cannot be directly detected in backscattering. Mass separation deteriorates rapidly for small scattering angles and for $q > 10$. It is also influenced by other factors like energy spread of the primary ions, energy resolution of the analyzer, thermal vibrations of the target atoms and finite acceptance angle of the analyzer. In practice, values of $q > 2$ are preferred, since for $q < 2$ the final energy of the projectile is very low and neutralization so efficient that detection becomes difficult.

A typical LEIS spectrum for 3 keV He^+ ions scattered by a pure Al target is given in Figure *III.4* (θ = 142°, α = 0°). The (binary collision or surface) peak is due to He^+ ions that are backscattered in a single collision from an Al atom at the surface of the target. The signal at higher energies originates from double and multiple scattering of He^+ ions. The background at energies lower than that of the elastic peak (the "low-energy tail") is a result from backscattering in deeper layers. Its intensity is mainly due to a reionization process. This tail provides non-destructive in-depth information. The onset of the tail gives the reionization threshold. For a multi-component sample the masses of the different target atoms can be derived from the positions of the binary collision peaks; the intensities of these surface peaks are a measure for the atomic surface concentrations.

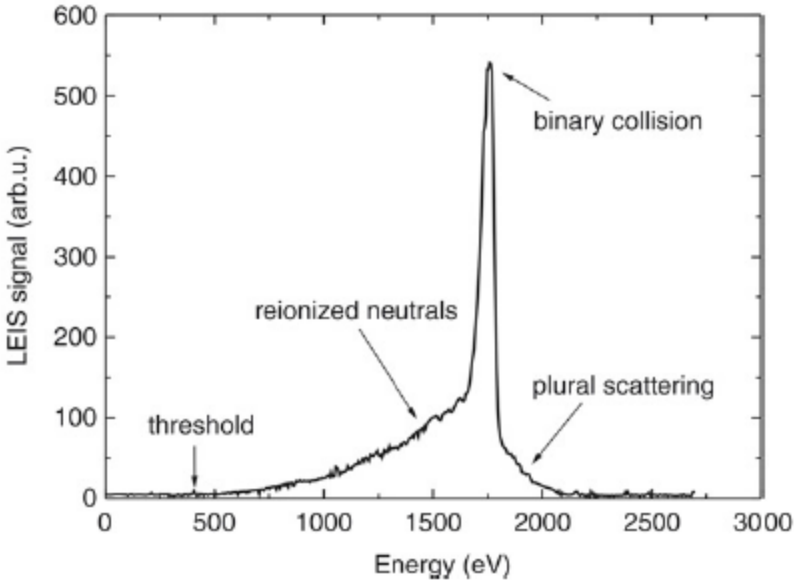

Figure III.4 - LEIS spectrum of 3 keV He+ scattered over 142° polycrystalline aluminum [10].

For a quantitative analysis of the surface composition one can relate the signal (the yield of ions) S_i, i.e. the measured number of backscattered ions from a surface atom of mass m_1 detected for a primary ion current I_p, to the surface concentration N_i of element i (atoms per surface area) via:

$$S_i = \frac{I_p}{e} \cdot t \cdot \xi \cdot R \cdot S_t F_i \cdot \eta_i \cdot N_i \tag{7}$$

With e the elementary charge, t the acquisition time, ξ the instrumental factor (including detector solid angle, detector efficiency and analyzer transmission), R a factor that takes into account the surface roughness and η_i is the elemental sensitivity factor. $S_t F_i$ is a steric factor taking into account the shielding by neighboring atoms ($S_t F_i$ = 1 for atoms in the outer surface). The elemental sensitivity η_i is given by:

$$\eta_i = P_i^+ \cdot \frac{d\sigma_i}{d\Omega} \tag{8}$$

Here, the ion fraction $P_i^+ = S_i^+ / (S_i^+ + S_i^0)$ and the derivative represents the differential cross section. For rough surfaces, such as encountered for powders, also a roughness factor should be included.

In the regime of high energy ion backscattering (Rutherford backscattering, RBS) the Coulomb repulsion between two nuclei $V_C(r)$ is a reasonable choice for the scattering potential. In the LEIS regime, screening of the nuclear charges by electrons bound to the target atom and to the ion becomes important.

In principle, either the peak area or height can be used as LEIS signal for surface composition analysis, but the peak area is the more appropriate physical quantity. Quantitative surface composition analysis is based on Eq. (7). However, the elemental sensitivity factor is only known for a few combinations of elements, incident ions, ion energies and scattering angles [11]. Therefore, quantitative analysis is often based on calibration against reference samples with known surface concentrations.

The surface sensitivity of LEIS is largely due to the fact that only scattered ions are analyzed. In general, most of the incoming ions are neutralized upon impact. Thus, knowledge about neutralization is a necessary requirement for the understanding of the sensitivity factor. Neutralization introduces interesting physics and insight into this physics helps in choosing experimental conditions which allow for quantitative analysis of the surface composition with LEIS.

In the case that the sensitivity η_i for a given element does not depend on the presence and identity of its neighboring atoms ("the matrix"), quantification of the surface composition is possible by using a reference sample of known surface density N_i^{ref} via

$$S_i = S_i^{ref} \cdot \frac{N_i}{N_i^{ref}} \tag{9}$$

For the total signal, the fraction ζ_i of the surface covered by atoms *i* is given by:

$$\zeta_i = \frac{N_i}{N_i^{ref}} \tag{10}$$

When pure elemental samples are used as reference materials, $\zeta_i^{ref} = 1$. For binary compounds consisting of elements *i* and *j*, the applicability of Eq. (9) can easily be checked by studying the signals of the elements for targets of differing atomic compositions. The elements *i* and *j* should cover the full surface:

$$\zeta_i + \zeta_j = 1 \tag{11}$$

This equation implicitly assumes that there is no net change in the total number of atoms per unit area when elements *i* and *j* are mixed. In fact, this assumption for surfaces is analogous to Vegard's law[5] for the volume of an alloy. Combination of Eq. (9) and (11) gives:

$$S_i = S_i^{ref} - S_i \cdot \frac{S_i^{ref}}{S_j^{ref}} \tag{12}$$

Thus, if matrix effects are absent and Vegard's law holds for the surface, one expects a linear decrease of the signal for element *i* with increasing content of element *j*.

The surface atomic fraction x_i^{surf} of a binary alloy consisting of elements *i* and *j* is:

$$x_i^{surf} = \frac{N_i}{N_i + N_j} = \frac{\frac{S_i}{S_j}}{\frac{S_i}{S_j} + \frac{N_j^{ref} \cdot S_i^{ref}}{N_i^{ref} \cdot S_j^{ref}}} \tag{13}$$

Thus, to determine the surface atomic fractions we need to know the ratio of the surface densities of the reference samples as well as the LEIS signal ratios of the elements *i* and *j* in the binary target and in the reference targets. Analogous to Eq. (13) for binary compounds, one can write an equation for multicomponent samples containing j_{max} elements in the surface:

$$x_i^{surf} = \left[\sum_{j=1}^{j_{max}} \frac{S_j}{S_i} \frac{S_i^{ref}}{S_j^{ref}} \frac{N_j^{ref}}{N_i^{ref}} \right]^{-1} \tag{14}$$

Alternatively, Wheeler [12] has outlined a simple empirical approach to quantitative analysis using ISS. He has calculated relative scattering cross sections (σ_r) for a series of metal oxides, relative to oxygen ($\sigma_r^{\,0} = 1$) as shown in Table 6.

Table 6 - Metal-to-Oxygen Peak Height Ratios for Selected Oxides for ^{4}He (adapted from [12]).

Oxide	Metal/Oxygen Peak Height Ratio	$\sigma_r^{\,0}$ Calculated (σ_0 = 1.00)
TiO_2	2.4	4.8
Al_2O_3	1.4	2.0
CoO	8.0	8.0
MoO_3	2.7	8.2
Fe_3O_4	4.9	6.6

[5] **Vegard's law** is an approximate empirical rule that holds that a linear relation exists, at constant temperature, between the crystal lattice parameter of an alloy and the concentrations of the constituent elements [46].

These data are valid only for a given probe gas and for a given incident ion energy. The values for σ_r, in Table 6 were obtained assuming σ_r does not vary with the matrix. Then

$$\sigma_r^m = \frac{I^m}{I^0}\left(\frac{C^0}{C^m}\right) \tag{15}$$

Where I^0 and I^m are peak-height intensity of oxygen and the metal, respectively; and C^0 and C^m, the concentrations (atomic fraction) of oxygen and metal, respectively. Wheeler also assumed the surface stoichiometry is that of the bulk. The relationship between σ_r and atomic number Z was found to be $\sigma_r = 0.04\ Z^{1.57}$.

The utility of this approach can he shown by a simple example. Assume an unknown surface oxide on iron gave LEIS peak ratios for Fe and O of $I^{Fe}/I^O = 4.9$. From eq. (15) one can write

$$\frac{C^O}{C^{Fe}} = \frac{\sigma^{Fe}}{\sigma^O} \times \frac{I^O}{I^{Fe}} = 6.6 \times \left(\frac{1}{4.9}\right) = 1.35$$

Thus the atomic O/Fe ratio on the oxide surface is 1.35**,** essentially that for Fe_3O_4. One must be cautious in applying σ_r, values to other than oxide systems. For example, application to LEIS data for FeS_2 gave an empirical formula of $FeS_{1.9}$.However, when applied to MoS_2 the results were $MoS_{1.2}$. It is not clear whether this error is due to the surface composition being different from that of the interior or an error in the approach.

2.2.2. Features of LEIS Spectra

Composition analysis in LEIS is based on the principle that only ions that have been backscattered by a single binary collision (single scattering: SS) contribute to the peaks in the spectrum. Since noble gas ions are used for the analysis, effective neutralization strongly reduces the contributions from double (DS) and multiple (MS) scattering processes. However, depending on the scattering conditions, DS and MS can still be important and even dominate a LEIS spectrum. In general, the scattered ion energies for DS and MS differ significantly from that of SS. For a reliable composition analysis, it is thus important to recognize the DS and MS contributions and preferably select conditions where these processes are negligible. An important feature of LEIS is its surface sensitivity. A critical issue is how far the second and deeper layers may contribute to the LEIS signal and what is really meant by the “outer” atomic layer.

Eq. (6) shows how the kinematic factor k depends on the scattering angle θ and the masses of the projectile and target atom. In a LEIS experiment, a number of parameters will contribute to the width of the SS peak. According to Eq. (6), both the spread in the energy of the primary ions, E_0, and in the

scattering angle (angular spread in the primary beam and in the acceptance of the analyzer) will contribute.

Since the target atom is not a free atom and inelastic processes may occur, some deviations from Eq. (6) are observed. The coupling of the target atom with the lattice of the sample will have some effect. For the energies used in LEIS the actual scattering process, during which the momentum and energy of the projectile change significantly, is much shorter than a characteristic vibration time. At primary energies of 100 eV or more the effective mass of the target atom is, therefore, still that of a free atom. A non-zero motion of the target atom will induce, however, a Doppler broadening in the final energy of the scattered ion, typically about 5 eV [13]. Another effect that affect a LEIS spectrum is that inelastic processes give a peak shift to lower energies in the order of few dozens of eV in low ion beam range of energy [10].

At higher energies, various inelastic processes may take place, which leads to an increase in the widths of the LEIS peaks. This makes it impossible to separate elastic and inelastic processes. The SS peak in LEIS will thus contain both processes. The shift of the maximum of the peak is a good indication of the importance of inelastic effects. Mikhailov *et al.* [14] reported for 1 keV He^+ scattering by different elements that the maximum of the SS peak was 19-35 eV lower than expected on the basis of a binary collision (Eq. (6)). The shift was largest for elements where reionization is important. For even higher energies and other noble gas ions, the contribution of inelastic processes can become even larger.

The tail in a LEIS spectrum is the background signal at energies that start just below the elastic binary collision peak and extends to a low-energy threshold (see Figure III.*4*). The values for the thresholds is controversial for the most of elements, especially for He^+ [10].

The tail is generally ascribed to primary ions that penetrated into the solid, suffered multiple collisions (nuclear stopping) and inelastic losses (electronic stopping) and were finally emitted from the target into the direction of the analyzer. Due to the statistical nature of these processes, the tails have a very smooth structure. On average, the larger the energy loss the longer the path through the solid. To be analyzed and detected in an electrostatic analyzer (ESA) the scattered particle must be in an ionized state. This could mean either that the ion has survived neutralization during its passage through the solid or that after neutralization the noble gas atom is reionized. Different models have been presented to describe the physics that determines the ion fraction after passage through the solid and thus the intensity and shape of the tail. This subject is still a matter of debate.

The intensity and shape of the tail is determined by backscattering in the deeper layers, the straggling through these layers and the ion fraction of the backscattered particles. Whenever the scattering and reionization probabilities are high and neutralization unlikely, the tails can dominate the LEIS spectrum.

The main contribution to a high ion fraction is due to reionization. At projectile energies greater than the threshold energy, also for collisions with smaller scattering angles reionization is possible. This leads to the observation that usually the intensity of the tail increases with increasing energy.

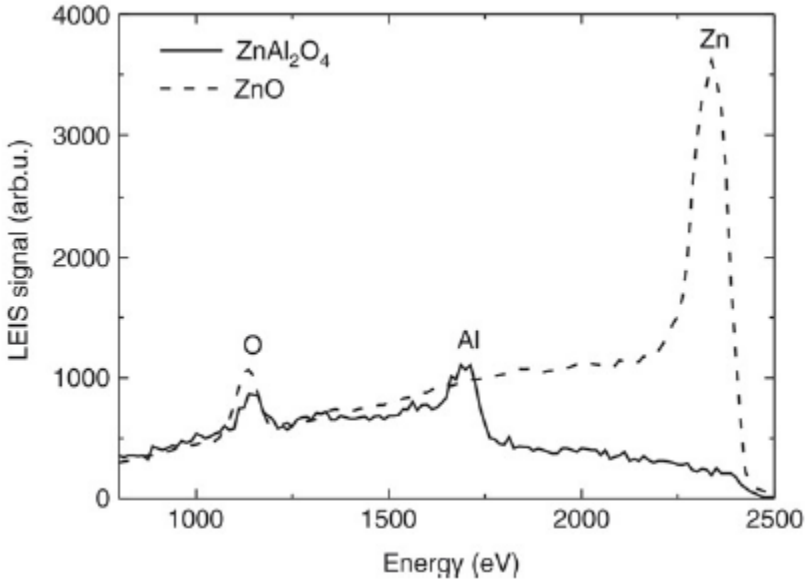

Figure III.5 - Energy spectra of 3 keV He+ backscattered from $ZnAl_2O_4$ (solid line) and ZnO (dashed line). In $ZnAl_2O_4$ there is no surface peak for Zn, since the Zn cations are below the surface. The onset of the tail agrees with ZnO, indicating that Zn is present in the 2nd and deeper layers.

For complex systems, high intensity tails are thus quite common, since it is likely that one of the surface components will provide the reionization. Figure III.5 [15] gives the LEIS spectrum for $ZnAl_2O_4$ as a characteristic example of a mixed oxide. Since only the surface peaks of Al and O show up, the Zn atoms must be located below the outer surface. The fact that there is a background in the spectrum extending from low energies up to the expected energy for Zn shows that the presence of Zn extends from deeper layers to just below the surface. The helium ions that are detected in LEIS were first neutralized when entering the solid, backscattered by a Zn atom below the surface and made "visible" in LEIS by reionization during an interaction with an oxygen atom when leaving the solid.

This example illustrates the strength of the LEIS technique: the peaks can be used to selectively analyze atomic composition of the outer surface. These are the atoms that can be chemically active. The shapes of the tails provide information on the in-depth distribution of the elements.

The tail intensity observed in an experiment depends on the primary energy and the type of analyzer used. The tails should not be included in the signal used for the surface composition analysis. This means that in quantitative analysis background subtraction is important [16].

2.2.3. Analysis of "Real" Surfaces

The choice of which type of noble gas ions at which primary energy are used as projectiles influences mass separation and elemental sensitivity. The analysis of low mass elements requires the use of He^+ ions in order to obtain a higher elemental sensitivity for the lowest masses. With increasing mass one may have to switch from He^+ to Ne^+ ions if one wants to resolve LEIS peaks of different elements in the surface.

Eq. (6) shows that for different masses the corresponding peaks are separated in energy by an amount $\Delta E = \Delta k\, E_0$ that increases linearly with the primary energy E_0. However, the peak width also broadens with increasing energy due to elastic and inelastic effects. The choice of energy is of minor importance if the broadening due to elastic effects dominates. Then, peak separation and elastic effects both scale linearly with energy. If, however, inelastic effects are dominant, the peak also broadens with velocity, i.e. the square root of the energy. In this case, a higher energy results in a higher resolving power.

Most oxides and polymers are insulators. To prevent them from charging by the incident ion beam the surfaces have to be flooded with low-energy electrons. In the case of inhomogeneous charging (extremely rough surfaces), LEIS peaks are broadened. Proper charge compensation can avoid this. However, when using charge compensation, one also has to consider the possible modification of the surface due to the electron impact.

Catalysts are generally very good insulators, especially when they are highly dispersed and (inhomogeneous) charging of the surface is difficult to avoid. Insufficient neutralization, due to a too low electron current causes a positive charging voltage, and consequently an energy dependent shift of the LEIS spectrum towards higher energies. In the extreme case, this charging prevents the ions from reaching the sample and they are reflected with their primary energy E_0.

An important feature of LEIS is its sensitivity for the outermost layer. Thus, a monolayer of impurities will have a dramatic effect on the result. For example, H cannot be detected directly when analyzing energy spectra of backscattered projectiles. The effect of H in LEIS is demonstrated in Figure III.6a. The solid curve in the LEIS spectrum is obtained for a clean Pd surface, whereas the dashed curve shows the LEIS spectrum for a Pd surface that is saturated with H. Obviously, the Pd surface peak has completely disappeared due to the presence of H. The ions that scatter from Pd atoms are neutralized when they pass close to an H atom, thereby completely suppressing the binary collision peak.

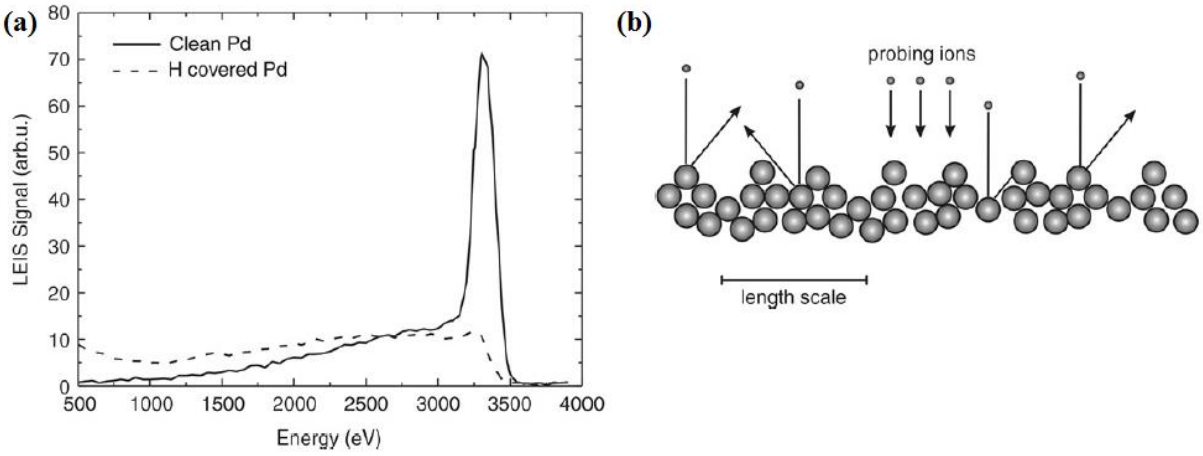

Figure III.6 - (a) LEIS spectra measured on Pd demonstrating the influence of H on LEIS signal. (b) Illustration how shadowing and blocking reduce the LEIS signal for a rough surface consisting of spherical particles.

When a sample is introduced from the ambient atmosphere into the analysis chamber, it is generally contaminated to some degree by water or organic molecules. As one is mostly interested in the underlying surface, cleaning procedures have become an essential part of LEIS measurements. Commonly used cleaning procedures include sputtering, heating and chemical treatment.

Surface roughness is often considered as one of the important parameters that influences the LEIS signal. This is especially relevant, when samples with different roughness are used for quantification. In Figure *III.6*b it is illustrated how roughness affects the scattered ion signal. Shadowing will prevent part of the incoming ions to reach all atoms from which they could be scattered, while blocking along the outgoing trajectory can prevent them from reaching the analyzer. This shielding (shadowing + blocking) results not only from scattering but also from neutralization. These effects both reduce the number of backscattered particles into the analyzer. Surface roughness can also lead to a higher effective density of the surface atoms and thus to an increase in the LEIS signal. Due to the monolayer sensitivity of LEIS, the influence of shielding will be more severe in a surface analysis by LEIS than in an analysis using surface techniques that probe deeper.

In fact, many applications involve extreme surface roughness. In heterogeneous catalysis, for instance, where the important chemical conversions are restricted to the surface, specific surface areas of 100-1000 m^2/g are quite normal. Studies have shown that in some cases surfaces with highest roughness give the smallest signal reduction [17]. As pointed out by the author, however, the reduction (shadowing by neighboring atoms) is determined by the slope (4.8°and 21°, respectively) of the surface rather than the roughness itself. Thus, the local tilt of the surface is important for the signal reduction.

In another study of influence of roughness in the LEIS signal, Jansen *et al.* [18] pressed the silica powders to pellets. This is believed to be important to obtain reliable and reproducible results. Jansen *et al*. obtained the same Si and O signals for pressures between 2 and 2000 MPa (20-20 000 kg/cm^2). One could expect that the influence of compaction be more pronounced for inhomogeneous samples. Therefore, the influence of compaction was also studied for highly dispersed silica that had been impregnated with a sub-monolayer of Ta_2O_5. It was found that up to 300 MPa the compaction had no influence on the Si, O and Ta signals.

Although the precise value of the compaction was not important, a minimum value (< 1 MPa) is required to ensure that the characteristic length scale of the roughness of the powder is smaller than the diameter of the ion beam.

Such experiments as the ones performed by Jensen *et al.* [18] indicate that it is not the specific surface area (roughness) but the surface slopes that determine the shielding/blocking. The signal reduction is thus a measure for the surface roughness at an atomic scale for particular systems [19].

2.2.4. Experimental Conditions

LEIS measurements were performed at the Regional Platform of Surface Analysis, an annex of UCCS, with a high sensitive Ion ToF Qtac100 instrument.

Monoenergetic $^4He^+$ ions were produced to give a beam of 3 keV and ion beam current of 5.5 nA. Pressure main set was 1 x 10^{-10} mbar. The setup utilize a mass filter in order to guarantee homogeneity and free ion impurities. The Double Toroidal Analyzer (DTA) gives a sensibility 3000 higher than conventional LEIS machines. Data were collected with an acquisition time about 120 seconds, and the primary gun ion dose is about 4 x 10^{12} ions/cm^2. Dried samples were pressed into pellets and mounted on a probe for insertion into the spectrometer. Seven scans were taken for each sample. Surface charging during analysis has been effectively eliminated by flooding the surface with low-energy electrons.

This setup allows to work in “quasi-static” mode, i.e., with ion energies and current densities that are low enough to leave the surface virtually unchanged. In practice, at the end of a measure, our beam damage (sputter) about 0.05 of a monolayer in one scan. LEIS energy range used was 700.0 - 2800.0 eV, which were enough to observe the characteristic peaks from all elements present in our samples.

Peak fitting was performed with dedicated software in order to relatively quantify the elements. The LEIS peak is proportional to the amount of scattering surface atoms. Thus, the quantification is straightforward, backgrounds are subtracted from peaks, the peaks are integrated and areas are proportional to the surface fraction of the atoms. The model for quantification of ISS data takes into account the influence of isotopic distribution on elemental peak shape, ion neutralization, background

due to inelastic scattering, and other factors that influence mass resolution such as width of the scattering angle and spread in primary ion beam energy.

3. X-Ray Absorption Spectroscopy

X-ray absorption fine structure (XAFS) spectroscopy is one of the most powerful tools we have for mapping local structure. In this technique, one probes a sample with x-rays that are tuned to the energy of a core electron shell in the element we wish to study. One may monitor how many x-rays are absorbed as a function of their energy. If taken with sufficient accuracy, the spectrum exhibits small oscillations that are the result of the local environment's influence on the target element's basic absorption probability. This turns out to be a unique signature of a given material; it also depends on the detailed atomic structure and electronic and vibrational properties of the material. From the spectrum, one can extract the distances between the absorber and its near-neighbor atoms, the number and type of those atoms, and the oxidation state of the absorbing element—all parameters that determine local structure. By selecting a different x-ray energy, one can obtain this information for any element in the sample, called atomic selectivity.

For this reason, XAFS is a very important probe of materials, since knowledge of local atomic structure, i.e., the species of atoms present and their locations, is essential to progress in many scientific fields, whether for biology, chemistry, electronics, geophysics, metallurgy, or materials science. However, extracting this information with precision in the often complicated, aperiodic materials of importance in modern science and technology is not easy, even with the subtle and refined experimental techniques currently available.

XAFS spectroscopy began to emerge as a practical experimental tool in the early 1970s, after Dale Sayer, Edward Stern, and Farrel Lytle [20][21][22] demonstrated that a Fourier transform could be used to analyze the absorption spectra. Their work coincided with the development of synchrotron x-ray sources that emit enough x-ray photons in the right spectral range to enable rapid, highly accurate absorption measurements. With the subsequent availability of inexpensive computing power to analyze the data and implement the increasingly accurate theoretical models, XAFS flourished.

The present section brings a discussion on the fundamental theory and the experimental aspects that are important in our study, such as synchrotron light, the setup for *in situ* analysis and the data treatment.

3.1. Physical Principles and EXAFS Equation

X-rays are ionizing radiation and thus, by definition, have sufficient energy to eject a core election from an atom. Each core shell has a distinct binding energy, and thus if one plots x-ray absorption as a function of energy, the spectrum for any atom resembles typically the spectrum of the Figure III.*7*.

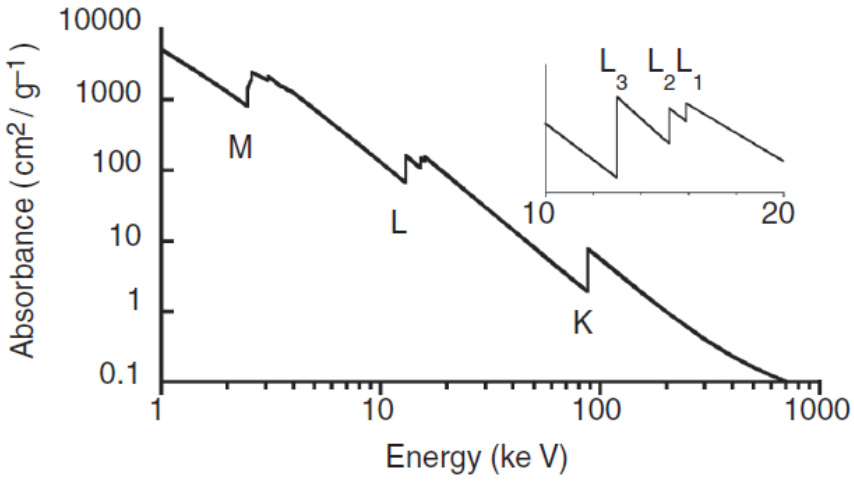

Figure III.7 - A typical XAS spectrum. Particularly, a low-resolution x-ray absorption spectrum for Pb. Three major transitions are seen (K, L, and M edges), corresponding to excitation of an electron from *n* = 1, 2, and 3 shells, respectively. At higher resolution (inset) both the L and the M edges are split (see text for details)

When the X-ray energy is scanned through the binding energy of a core shell, there is an abrupt increase in absorption cross-section. This gives rise to a so-called absorption edge, with each edge representing a different core-electron binding energy. The edges are named according to the principal quantum number of the electron that is excited: K for *n* = 1, L for *n* = 2, M for *n* = 3, etc.

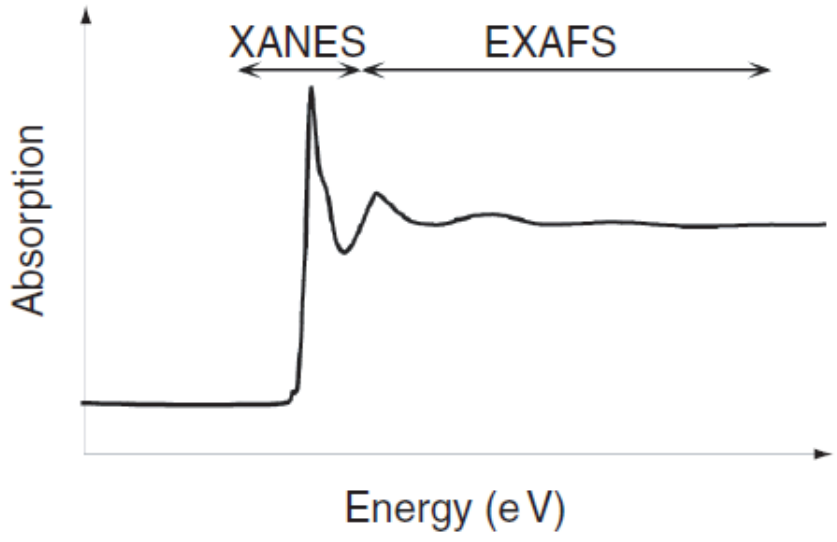

Figure III.8 - Schematic illustration of an X-ray absorption spectrum with the XANES and EXAFS division region.

An absorption edge by itself is of little value beyond elemental identification. However, if one examines any of the edges in Figure III.*7* in more detail, they are found to contain a wealth of information. This is illustrated by the schematic absorption edge shown in Figure III.*8*. The absorption edge is not simply a discontinuous increase in absorption, as suggested by Figure III.*7*, but in fact shows significant structure both in the immediate vicinity of the edge jump and well above the edge. The structure in the vicinity of the edge is referred to as X-ray absorption near-edge structure (XANES). The oscillations above the edge, which can extend for 1000 eV or more, are referred to as extended X-ray absorption fine structure (EXAFS). The distinction between XANES and EXAFS is arbitrary, since the same fundamental physical principles govern photo-absorption over the entire XAS region and there is no unambiguous definition that distinguishes between "near-edge" and "extended" structure. In an attempt to emphasize the essential similarity of these regions, the term has gained some currency as a reference to the entire structured absorption region. Nevertheless, the terms EXAFS and XANES remain the most widely used, with some justification, since the XANES and EXAFS regions are generally analyzed differently. The XANES region is sensitive to oxidation state and geometry, but is not, in most cases, analyzed quantitatively. The EXAFS region is sensitive to the radial distribution of electron density around the absorbing atom and is used for quantitative determination of bond length and coordination number. A fourth acronym, which is popular in the soft X-ray and surface science communities, is NEXAFS, standing for near-edge X-ray absorption fine structure. This acronym is redundant, since NEXAFS and XANES are used to refer to the same features, and is potentially confusing, given its similarity to EXAFS.

When a beam of X-ray photons passes through a material, the incident intensity I will be decreased by an amount that is determined by the absorption characteristics of the material being irradiated. For a path length dx of the radiation through the material the decrease dI is given by

$$dI = -\mu(E) I \, dx \tag{16}$$

with the linear absorption coefficient $\mu(E)$ a function of the photon energy. Integrating equation (16) over the total thickness x yields Lambert's law,

$$I_t = I_0 e^{-\mu(E)x} \tag{17}$$

At the absorption edge, E_{edge}, the kinetic energy of the electron (E_k) is defined to be equal to E_0, often referred to as the zero-point energy or "inner potential". For any energy above this, the photoelectron kinetic energy is given by

$$E_k = h\nu - E_{binding} \tag{18}$$

Quantum mechanically the outgoing photoelectron can be represented as a spherical wave with wavelength λ ($\lambda = 2\pi/k$) defined as

$$k = \sqrt{\left(\frac{8\pi^2 m}{h^2}\right)\left(h\nu + E_0 + E_{edge}\right)} \tag{19}$$

With k being the wave-vector, m the mass of the electron and h the Planck's constant.

The linear absorption coefficient $\mu(E)$ is proportional to the transition probability of the photoelectric event. According to Fermi's Golden Rule the transition probability is (within the dipole approximation) a function of the initial state and final-state wave functions [23]:

$$\mu(E) = C\left|\langle\psi_f|\hat{e}r|\psi_i\rangle\right|^2 \delta(E_f - E_i - h\nu) \tag{20}$$

Here $\hat{e}$ is the electric field polarization vector of the photon, and r the coordinate vector of the electron. The dipole approximation is only valid when the wavelength of the photons is larger than the size of the absorbing atom. The final state wave function ψ_f consists of two main parts, namely the outgoing electron wave and a backscattered electron wave

$$\psi_f = \psi_{outgoing} + \psi_{backscattered} \tag{21}$$

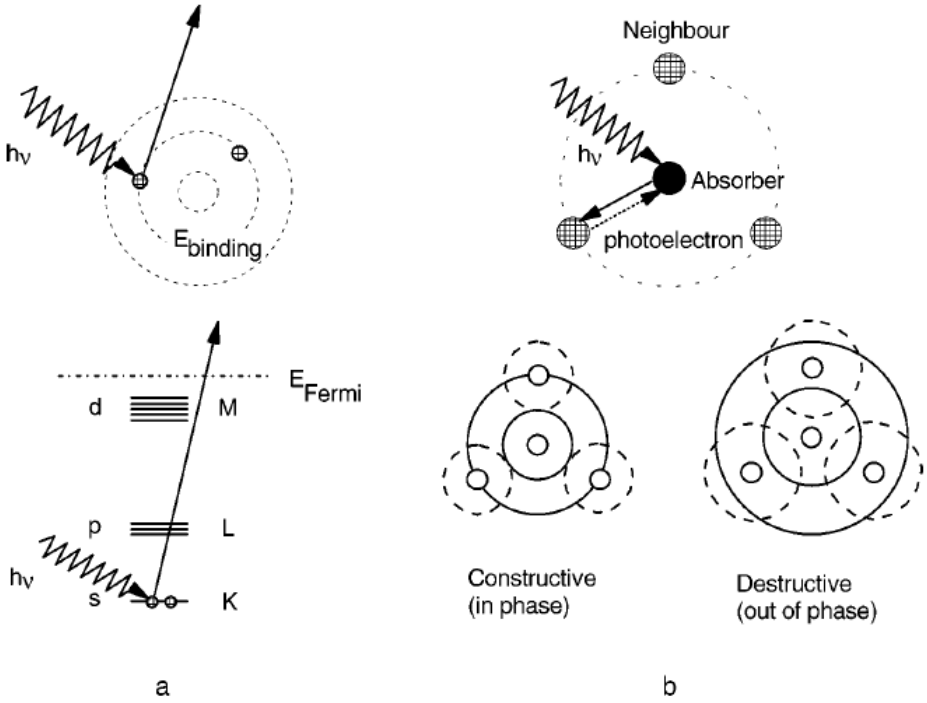

Figure III.9 - (a) Schematic illustration of the photoelectric effect in terms of excitation of the different orbital (top) or different energy levels (bottom), (b) illustration of neighboring shells of atoms about the absorber (top) and constructive (in phase) or destructive (out of phase) interference between outgoing photoelectron wave and backscattered off this shell of neighboring atoms (bottom).

Interference between these two final-state wave functions causes the observed fine structure in X-ray absorption spectra. Figure III.9a shows a schematic representation of the photoelectric effect, that is, the interaction of an X-ray photon with matter producing a photoelectron with a kinetic energy given by (18). Figure III.9b makes clear that the outgoing electron can be viewed as a spherical wave that scatters off neighboring atoms (e.g., electron density), producing a backscattered wave. The outgoing and backscattered waves interfere, causing an interference pattern varying between total construction (the two waves are fully in phase) or total destruction (the two waves are exactly out of phase). Since the path lengths of both waves define their final phase, it can be seen that the distance to the neighboring atoms determines the interference pattern. Equation (20) shows that the absorption coefficient is proportional to the transition probability defined by the matrix element.

The absorption coefficient exhibits a fine structure because the final wave state function is modulated due to the interference pattern. As a result, the absorption coefficient above the absorption edge is defined as

$$\mu_{Total} = \mu_0[1 + \chi_{EX}] \tag{22}$$

with μ_0 representing the atomic background. χ_{EX} forms the oscillatory part of the total absorption, describing the scattering of the outgoing electron against the neighboring atoms. It is called the EXAFS function. Since the oscillatory part is created by the interference between the outgoing and backscattered waves, χ_{EX} contains information about the local structure around the absorber atom. The fact that a specific photon energy is needed to excite electrons makes X-ray absorption spectroscopy an element specific technique.

The main point in dealing with XAFS measurements is to get atomic structural information. A beautiful theory was developed to treat the EXAFS part of a XAS spectrum and it has shown work very well with a great sort of systems (e.g., [24]). The way it is used nowadays for this task is the so-called EXAFS equation. Since it is a quantum complex system, the derivation of the equation carry some approximations, which pass from the dipole-electron approximation, the scattering potential (the Muffin-tin approximation is the most known), relativistic effects, many-body effects, and so on ([25]). Thus, the EXAFS equation is written as:

$$\chi(E) = \sum_R S_0^2 N_R \frac{|f(k)|}{kR^2} \times sin(2kR + 2\delta_c + \Phi)\, e^{-2R/\lambda(k)} e^{-2\sigma^2 k^2} \tag{23}$$

Here the structural parameters are the interatomic distances R, the coordination number (or number of equivalent scatters) N_R, and the temperature dependent *rms* fluctuation in bond length σ, which should also include effects due to structural disorder. In addition, $f(k) = |f(k)|e^{i\Phi(k)}$ is the backscattering amplitude, δ_c is central-atom partial-wave phase shift of the final state, and $\lambda(k)$ is the energy-dependent

XAFS mean free path. Although the overall amplitude factor S_0^2 did not appear in the original formula, one has added it here for completeness, since it takes into account many-body theory, provided the terms are appropriately renormalized. Moreover, although the original EXAFS formula referred only to single-scattering contributions from neighboring shells of atoms, the same formula can be generalized ([26]) to represent the contribution from N_R equivalent multiple-scattering contributions of path length *R/2*.

3.2. Synchrotron Source: SOLEIL

The features of interest in XAFS spectra consist of small variations in the absorption coefficient $\mu(E)$, which can be determined directly in a transmission experiment. Sometimes useful information, such as edge shifts, can be obtained from XANES spectra that are noisy, but in general, very good signal to noise ratio (S/N) is required for EXAFS analysis and detailed XANES analysis. For EXAFS measurements, one requires S/N ratios better than 10^3 in order to determine the spectra accurately enough in the region ≈ 600 - 1000 eV above the absorption edge. It is generally necessary to measure spectra at least this far above the edge in order to get adequate spatial resolution. The EXAFS signal may damp out quickly above the edge because of disorder and/or low-Z scatters, rapidly plunging the signal into the noise, unless the noise level is kept very low [27].

An intense beam is required to obtain good data in a reasonable time frame (minutes to hours): on the order 10^{10} photons/sec or better within the required energy bandwidth of an eV or so. For this reason, synchrotron radiation sources are by far the preferred sources of X-rays for XAFS experiments. The X-ray beam should have an energy bandwidth of approximately 1 eV or less in order to resolve the XANES features, or at most a few eV, in order to resolve the XAFS right above the edge. It is not difficult to produce such a narrow bandwidth using crystal monochromators, but in addition, it is necessary to accurately and stably scan the energy of the incident beam over a range of approximately 1 keV above the edge.

Synchrotron radiation takes its name from a specific type of particle accelerator. However, synchrotron radiation has become a generic term to describe radiation from charged particles travelling at relativistic speeds in applied magnetic fields, which force them to travel along curved paths. Besides synchrotrons themselves, synchrotron radiation is produced in storage rings where electrons are kept circulating at constant energy. In a storage ring the synchrotron radiation is produced either in the bending magnets needed to keep the electrons in a closed orbit, or in insertion devices such as wigglers or undulators situated in the straight sections of the storage ring.

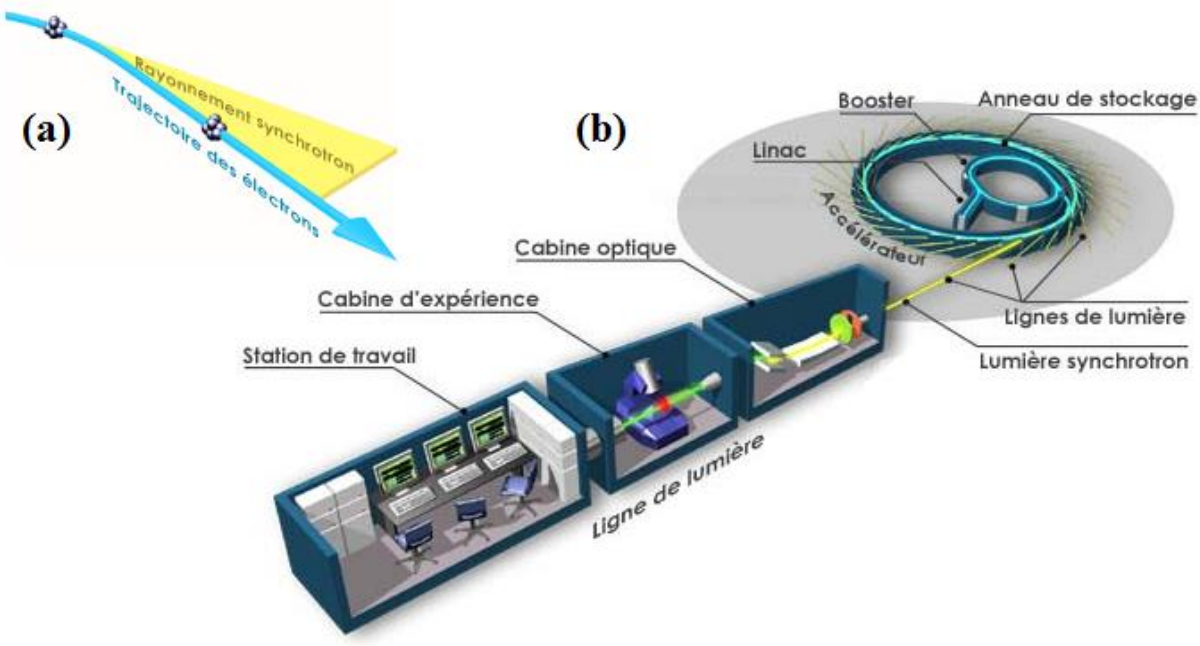

Figure III.10 - (a) Schematic picture of relativistic electrons being deflected by magnets to produce synchrotron light. (b) A typical synchrotron source and its main features (source: http://www.synchrotron-soleil.fr/).

A schematic scheme of a third generation Synchrotron source, such as SOLEIL, and its operation is illustrated in Figure III.*10*b. Electrons are generated in an electron gun, very like the cathode ray tubes found in old television sets. They are then fired out into the machine, where they are accelerated up to very high speeds through a series of three particle accelerators. These are called the linear accelerator, or linac, the booster synchrotron and the large storage ring. The linac and the booster synchrotron both work to accelerate the electrons so that they are travelling at nearly the speed of light.

The storage ring is what gives the Synchrotron source its iconic doughnut shape. The storage ring is not a true circle, but a type of polygon, made of dozen straight sections angled together with bending magnets, and this magnetism is used to steer the electrons around the ring. When the path of the electron beam is bent by its powerful magnets, the electrons lose energy in the form of light Figure III.*10*a. This light can then be channeled out of the storage ring and into the experimental stations, called beamlines. It is inside these beamlines that scientists carry out their experiments. The beamline contains three different sections; the optics hutch, where the light is filtered and focused; the experimental hutch, where the sample sits and the experiment is carried out; and the control cabin, where the scientists control the experiment.

3.2.1. SAMBA Beamline

SAMBA (**S**pectroscopy **A**pplied to **M**aterial **B**ased on **A**bsorption) is a hard x-ray absorption spectroscopy (XAS) beamline [28] from synchrotron SOLEIL, in which the XAFS experiments of this

work were performed. The design of SAMBA optics is optimized in order to be very versatile and to cover the 4.5-43 keV energy range with a high flux of photons and stability and optimum energy resolution. Three detection modes are available: transmission, fluorescence and total electron yield. At the time of the experiments in our work step-by-step acquisition mode as well as Quick-EXAFS one were available. However, since middle 2014 the latter spectrometer monochromator is placed in a new dedicated beamline, named ROCK (**R**ocking **O**ptics for **C**hemical **K**inetics).

A more detailed description of some components of SAMBA beamline are present in the following, particularly, the transmission mode, the monochromator, the Quick-EXAFS device and the reaction cell.

i. Transmission Mode

EXAFS beam-line works commonly in transmission. Transmission mode is the most straightforward: it simply involves measuring the X-ray flux before and after the beam passing through a uniform sample Figure III.*11*a. Under these conditions, the transmitted flux I is related to the incident flux I_0 by $I/I_0 = \exp(-\mu(E)\cdot x)$, or $\mu(E)\cdot x = \ln(I_0/I)$.

It is common for experimenters to informally use the terms I_0 and I to refer to the ionization chamber signals, rather than the beam fluxes. This imprecision is of no consequence for transmission experiments, but it does matter for fluorescence and electron yield. If the detectors are linear, the detector signal will be proportional to the flux; however, the output will be multiplied by an energy-dependent detector sensitivity that is a consequence of the declining fill gas absorption as a function of energy. The measured absorption coefficient also will have contributions from the air and windows that are in the beam path between the two detectors. Since a logarithm of the detector signals is taken, the log transforms the multiplicative energy dependent detector sensitivity factor into an additive slowly varying function of energy that can be readily subtracted out. The normal XAFS data reduction methods automatically take care of such “background.”

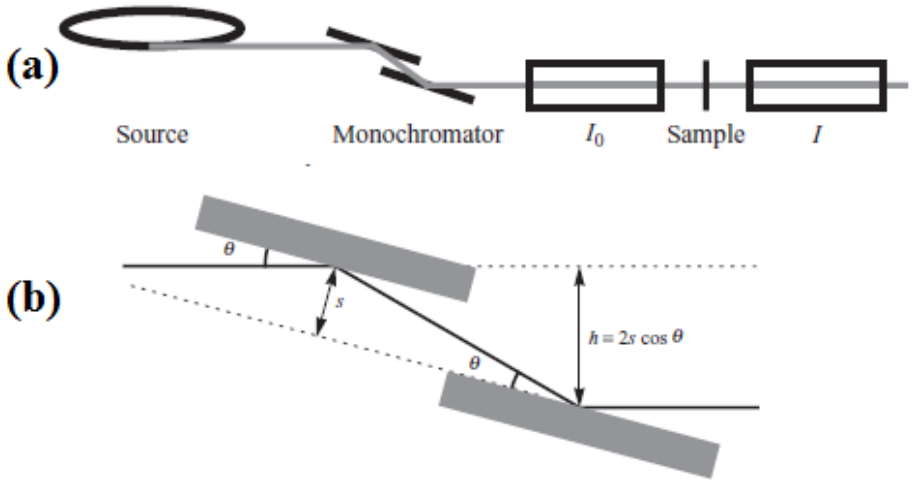

Figure III.11 – (a) Shematic representation of the transmission acquisition mode. (b) Schematic of a downward reflecting double-crystal monochromator [27].

ii. Monochromator

Monochromators are essential for XAFS experiments because an X-ray beam of approximately 1 eV bandwidth FWHM[6] is needed, and synchrotron sources generally produce beams with bandwidths of tens to hundreds of eV (undulators), or thousands of eV (bending magnets and wigglers). Approximately 1 eV bandwidth is needed so that near-edge (XANES) features and the EXAFS modulations right above the edge can be resolved. Ideally, the monochromator resolution width will be several times smaller than the intrinsic lifetime broadening of the absorption edge under consideration, so the data quality is not limited by the monochromator.

Double crystal monochromators are most commonly used in XAFS spectroscopy. The precise rotational motions are carried out by a precision goniometer or rotation stage that keeps the diffracting surface of the first crystal fixed. Usually the crystals are contained within a stainless steel vacuum chamber a meter or so in size. Vacuum enclosures are preferred for the following reason: if the polychromatic "white" beam passes through air, ozone is produced, which may damage the optics. Furthermore, air scatters and absorbs the beam, degrading the beam brilliance.

The incident beam from the synchrotron has a very wide range of wavelengths in it. Although the lower-energy photons usually are absorbed by the beamline windows, or filters specifically inserted for that purpose, the beam falling on the first monochromator crystal can carry significant (e.g. tens of kilowatts) power that must be handled. The beam at the desired energy is diffracted because it meets the Bragg condition $n\lambda = 2d \sin\theta_B$, or equivalently $E = (hc/2d_{hkl})(1/\sin\theta_B)$, see Figure III.*11*b. Multiples of that energy ("harmonics") generally will also be diffracted. Photons of other energies are absorbed, which

[6] FWHM = Full Width Half Maximum (of the resolution function).

deliver a substantial amount of heat to the crystal. This is removed directly by passing coolant through channels in the crystal, or indirectly by conduction to a cooled heat sink (typically a water-cooled copper block), or other means.

SAMBA beamline uses a sagittal focusing double-crystal monochromator. A first one, located 16m from the source, DCM1, equipped with a first water-cooled Si(111) crystal permits horizontal focusing in the 4–40 keV energy range. A second monochromator, DCM2, located after DCM1 at 18m from the source, dedicated to Quick-EXAFS and step-by-step acquisition mode in the domain 5 to 40 keV without focusing. It is equipped with channel-cut Si(220) and Si(311) crystals, both are water-cooled. This setup satisfy the permanent access to the 4-40 keV energy range, the sagittal focusing and the Quick-EXAFS acquisition mode.

The energy of the beam is selected by setting the angle of incidence of the beam onto a crystal. Silicon (occasionally germanium) is commonly used for energies above approximately 2 KeV (Bragg's law cannot be satisfied at energies lower than 1.977 KeV for Si) because it has suitable diffraction and thermal properties, and extremely high quality crystals are readily available from the semiconductor industry. The silicon is cut so that specific diffraction planes (e.g. *hkl* = 111, 220, 311, 400) are parallel to the crystal surface; these are called symmetric "Si(111)" etc. crystals.

iii. Quick-EXAFS device

With the advent of bright synchrotron radiation sources and the resulting potential reduction in data collection time, huge opportunities for in situ time-resolved EXAFS investigations have emerged in the field of the *in situ* and *operando* studies.

Quick-EXAFS (QEXAFS) stands for all EXAFS experiments where the X-ray monochromator is mechanically moved continuously and data are collected on the fly ([29]). This definition encompasses a very broad range of time scales and nowadays authors talk about QEXAFS for time frames in the order of several milliseconds, such in QEXAFS apparatus present on SAMBA beamline at Synchrotron SOLEIL ([30]).

To perform QEXAFS it is necessary to quickly change the Bragg angle of the monochromator crystal between two values corresponding to the extremes of the desired absorption spectrum and repeat this movement repeatedly. In SAMBA QEXAFS [31], the implementation was done following Frahm *et al.* concept ([32]), i.e., to separate the Bragg movement into two parts: one goniometer is used to move the Bragg angle over a large range and another one is used to move faster over a small amplitude. The monochromator is modular: a channel-cut crystal is mounted on a first stage that is capable of fast oscillations with an adjustable amplitude and that carries the water-cooling pipes and the heat exchanger. This part is then mounted on a larger goniometer that moves the crystal to the desired Bragg angle.

Finally, the goniometer is mounted on a Z stage to align the crystal and keep it on the X-ray beam when the Bragg angle is changed over a large interval (Figure III.*12*a).

The monochromator consists of two channel cut crystals, Si(311) and Si(111). Each channel cut crystal is mounted on a cam driven tilt table allowing periodic oscillations with a user selectable amplitude $\Delta\theta$ around an average fixed Bragg angle, θ_B. This amplitude can be tuned from 0.1° to 4° by an original SOLEIL in vacuum variable cam design. The θ_B Bragg angle is selected by one of the two goniometers holding the oscillating tilt tables and can be varied from 6° to 30°. The Si(111) channel-cut is used in the 4 -17 keV energy range whereas the Si(311) channel-cut is used in the 8-37 keV energy range.

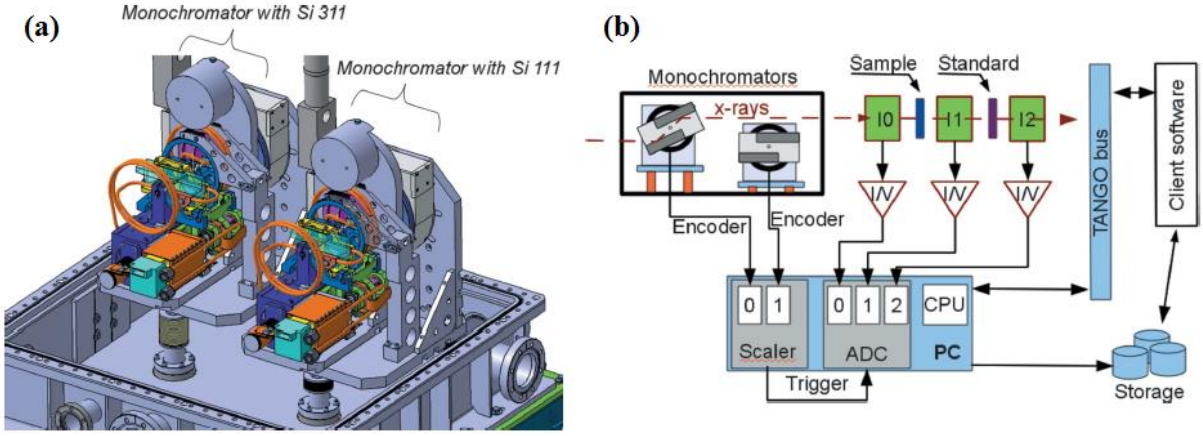

Figure III.12 - (a) View of the QEXAFS monochromator: two distinct sub-units, each one being an independent QEXAFS monochromator itself, are installed along the X-ray beam path. (b) Scheme of the hardware/software system used to acquire data with the QEXAFS monochromator ([31]).

Maximum performance of the Quick-EXAFS mechanics in terms of oscillation frequency of the channel-cut is 40 Hz for two recorded spectra: one with the Bragg angle collection in the downward direction and the other with the Bragg angle collection in the upward direction. Nevertheless, due to the photon flux available at the sample position at the SAMBA beamline in Quick-EXAFS configuration (flux ~10^{11} ph/s at 8 keV) the optimal time resolution of experiments on real samples is around 100 ms, although the SAMBA users work at speeds close to 1 Hz (time resolution 500 ms) [33]. The wide Bragg oscillation range up to 4° allows the recording of EXAFS data up to 1000 eV or more at any edge covered by the beamline (from the Ti to the Cs K-edges).

A unique feature of the SAMBA QEXAFS is its ability to move from one edge to another even when two different monochromators are needed, called “edge-jumping”. The high degree of automation of the beamline permits adjustment of the amplifier gains and the gaseous content of the ionization chambers while changing the monochromator conditions, as in the case of HDS bimetallic catalysts [31].

“Edge jumping” provided unique knowledge of the order of occurrence of sulfidation processes for both metallic species with complementary techniques (absorption/diffraction), as verified by Rochet *et al.*

[34] for Fisher-Tropsch catalysts: EXAFS spectra was acquired at the Co edge with Si(111), while Si(311) was used to acquire diffraction images at a fixed energy around the Mo K-edge.

Electronics and software developed to operate data acquisition with the QEXAFS monochromator follow the "continuous scan" scheme of Synchrotron SOLEIL described by Renaud et al. ([35]). Scaler and analog-to-digital converter (ADC) are triggered at a user-selectable frequency which is provided by the scaler itself. A scheme of the system is represented in Figure III.*12*b. Several ADC cards or scalers can be chained to increase the number of measured quantities: avalanche photodiodes, fluorescence detectors, other encoders or thermocouples [31].

iv. Catalytic Reaction Cell

At the SAMBA beamline, special efforts were done to offer to the scientific community a user-friendly Quick-EXAFS set-up made of two permanently installed Quick-EXAFS monochromators and a complete set-up dedicated for the study of catalysts in working conditions [31].

Actually the pre-treatment (drying, calcination, etc.), activation and reaction of heterogeneous catalysts span a wide range of temperatures, pressures and chemical environments (oxidizing or reducing gas, poisonous gases like CO or H_2S…). A single environment is not suitable for fulfilling all these conditions. In this framework, the strategy adopted at SAMBA was to develop catalytic cells (suitable for transmission and/or fluorescence) and other optimized for some specific reactions in harsh reaction conditions [33]. The cells were designed to mimic closely the catalytic reactions with powders gently pressed into a cavity, under atmospheric pressure and at temperatures up to 600 °C. Schematic views of one of these cells are presented in Figure III.*13*a. It is made of a sample holder, a heated block and a cell body.

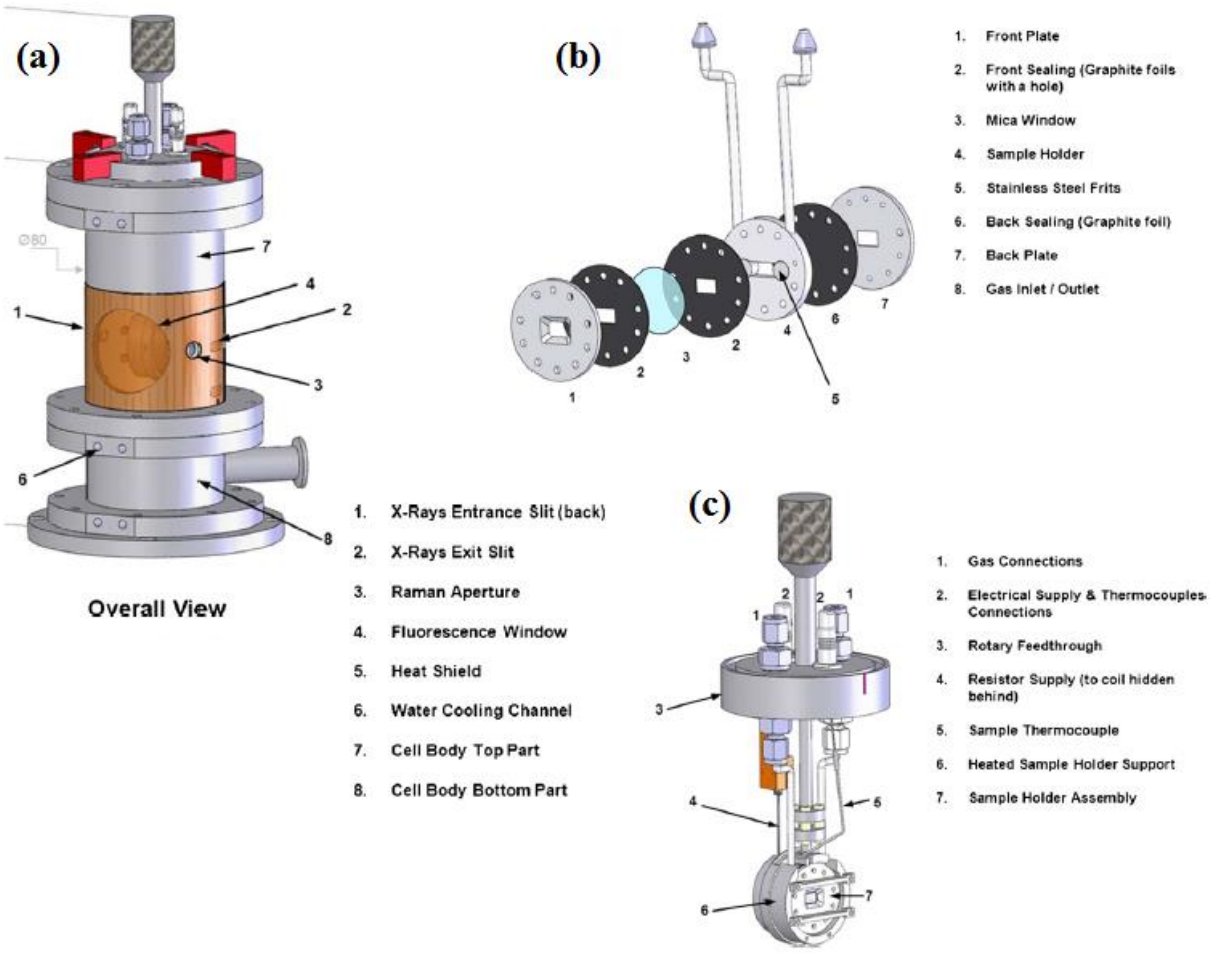

Figure III.13 - (a) Overall view of the reaction cell for QEXAFS. (b) Exploded view of the sample holder. (c) Schematic view when connected to the rotary feed through and assembled into the heated block [33].

The sample holder consists of an assembly of different elements, as presented in Figure III.*13*b. It includes a central element (the so-called "sample holder"), front and back plates, graphite foils (usually 500 µm thick) used as seals and a mica window (muscovite, 25 µm thick) for Raman coupling. Assembling these different elements allows the powder to be confined in the central cavity of the sample holder (cavity aperture: 5 mm (V) × 8 mm (H)).

To ensure a homogeneous and smooth distribution of the gases through the powder, two sintered stainless steel cylinders are set at the gas inlet and outlet of the sample holder cavity. These devices limit the formation of preferential gas paths through the powder. In addition, the use of graphite foils and 10 tightened screws to maintain the assembly, prevent from any gas leaks at this level. The gas connections between the sample holder assembly and the gas supply stainless steel tubes are ensured by two tube fittings, with ferrules, also made of stainless steel.

The sample holder assembly fits into a heated block, as shown in Figure III.*13*c. A resistor with a coil shape is mounted at the back of the heated block. The heat is transferred first by contact between the resistor and the block, then through all to the block by conduction, and finally to the sample holder by

contact through its back plate. To maximize the thermal transfer, the sample holder assembly is maintained into the heated block by two clamps, which allows the full surfaces to remain in contact during the temperature regulation.

3.3. Data Analysis

The analysis of EXAFS data can be divided into two stages: reduction of the measured absorption spectra to EXAFS (i.e., application of EXAFS Equation, (22)) and analysis of the χ(k) data to obtain structural parameters (N_R, σ and R). These parameters are usually obtained simulating the experimental signal using Eq. (23). This is done by an automatic computer-based minimization procedure. Data reduction involves both normalization and conversion to *k* space (Equation (19)). Data analysis is, at least in principle, a relatively straightforward problem of optimizing the variable parameters in Equation (23) so as to give the best fit to the observed data using some sort of non-linear least-squares fitting procedure.

In order to fit EXAFS data, it is first necessary to determine the parameters that define the scattering (f(k), S_0^2, Φ and λ(k)). This can be done using *ab initio* calculations or from model compounds of known structure. CIF files (*Crystallographic Information File*) are largely used for initial reference to build a model. In recent years, the available theoretical methods for quickly and accurately calculating these parameters have improved dramatically. *Ab initio* calculations are now relatively straightforward, one of the program widest used is FEFF [36].

Using carefully calibrated parameters to determine S_0^2 and E_0, it is possible to obtain excellent accuracy for EXAFS bond length determinations. Typical values, determined by measuring data for structurally defined complexes, are 0.01-0.02 Å for nearest-neighbor distances and somewhat worse for longer distance interactions. The precision of bond-length determinations is even better, with experimentally determined reproducibility as good as 0.004 Å. Coordination number is less well defined, due in part to correlation between N and σ^2 (see Equation (23)). In many cases, EXAFS coordination numbers cannot be determined to better than ±1. As noted above, EXAFS has only weak sensitivity to atomic type. Typically, it is only possible to determine the atomic number of the scattering atom to ±10. Despite these limitations, the ability to provide structural information, particularly highly accurate bond lengths, for non-crystalline systems, has made EXAFS an extremely important tool in coordination chemistry [24].

3.3.1. Data Reduction

Structural parameters determination follows several steps, which are summarized in Figure III.*14*. Before μ_0 can be determined in eq. (22), the pre-edge (X-ray absorption before the actual absorption

edge occurs) has to be subtracted. The pre-edge is usually approximated by a modified Victoreen function and calculated by extrapolation of the pre-edge region in the data.

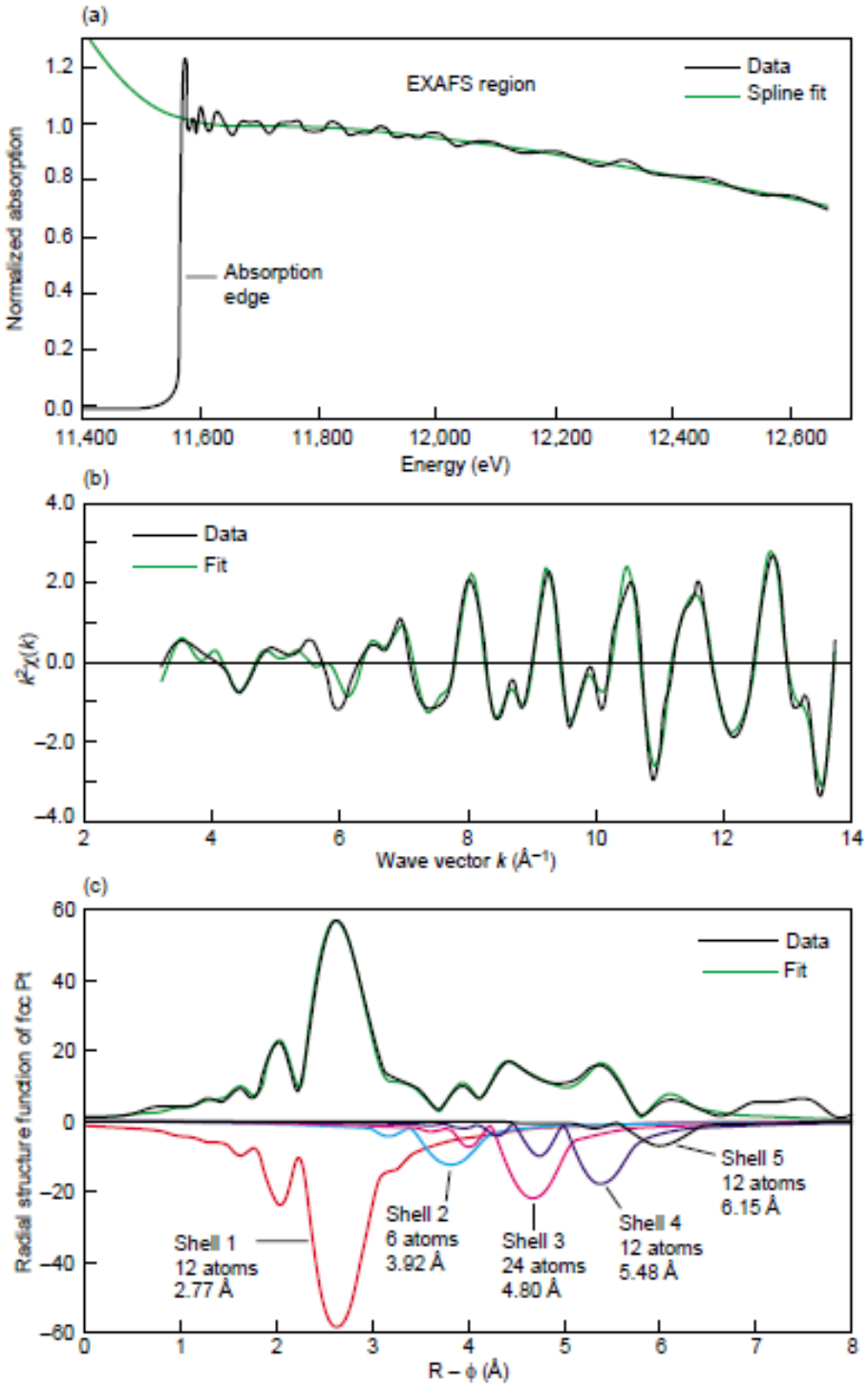

Figure III.14 - The different steps for extraction of the oscillatory part of an X-ray absorption spectrum, shown here at the L_3 edge for platinum foil (from [37]): (a) Normalization after pre- and post-edge background removal, edge position (E_0) determination (typically chosen at the inflection point) and free-atom absorption coefficient μ_0 adjustment (usually by a polynomial spline). (b) Transformation of the EXAFS spectrum to k scale through equation (19) and curve fitting of experimental data to a theory function such as eq. (23) in order to obtain the structural parameters. (c) Fourier transformed data to create a pseudo-radial distribution function $\chi(R)$ that helps illuminate a "shell structure".

After the pre-edge subtraction, the absorption edge energy (E_0) has to be defined; a rather arbitrary choice [24]. The inflection point (i.e., the maximum in the first derivative of the absorption edge) is generally considered as a systematic choice. The atomic background (μ_0) after the absorption edge has to be determined (Figure III.*14*a), normally using a cubic spline.

Before $\chi(k)$ can be obtained, the total absorption as obtained from experiment has to be normalized per absorber atom. Generally, spectra are normalized by division of the absorption data by the edge-step at 50 eV after the absorption edge (Figure III.*14*a). Finally, $\chi(k)$ is calculated according to (22) (Figure III.*14*b).

3.3.2. Fourier Transform

From Sayers *et al.* work [38] we know that Fourier Transformation (FT) of $\chi(k)$ results in a radial distribution function defined in *R*-space (Figure III.*14*c). The distance found in the Fourier transformation is about 0.2-0.5 Å shorter than the actual distance due to the energy dependence of the phase factors in the sine function (because the phase shift of sine function in eq. (23)).

Since the Fourier transform is a complex function, both real and imaginary parts are obtained. Figure III.*14*c show the absolute part of the FT for the Pt foil. The absolute part is determined mainly by the number of neighbors and disorder. The imaginary part is very useful in the analysis of EXAFS data for an accurate determination of the absorber-scatterer distance and for the discovery of unknown contributions when analyzing EXAFS data.

The FT is useful for obtaining a qualitative understanding of a system. However, Fourier transforms are subject to several potential artifacts and cannot be used for quantitative data analysis. Depending on the resolution of the data, multiple shells of scatterers do not necessarily give rise to multiple peaks in the FT. Perhaps more important, two peaks may appear to be well-resolved despite the fact that they have substantial overlap. This phenomenon is due to the fact that the FT is a complex function, including both real and imaginary components. Usually, what is plotted is the modulus of the Fourier transform, thus losing all phase information.

3.3.3. Curve Fitting and Limitations of EXAFS

Typically, absorber-scatterer interactions are grouped into “shells” (formally, it is a pseudo-radial distribution profile). A shell is a group of similar scatterers at approximately the same distance from the absorber (Figure III.*14*c). A nonlinear least-squares fitting algorithm is then used to model the observed data using equation (23). The least squares fitting can be done in either *k*-space or in *R*-space.

The difference between fitting in *k*-space and *R*-space is rather subtle, but very important, and the advantages lie with the *R*-space fitting [39]. In *k*-space one has to reverse Fourier transform the experimental $\chi(k)$ over the chosen ΔR region in the Fourier filtering process. This introduces truncation errors at the outer regions of the data as discussed above, thereby reducing the reliable Δk-range. Taking the Fourier transform in either direction (forward or reverse) introduces truncation errors, but this truncation effect is not a problem in *R*-space fitting, because the chosen ΔR region is much smaller than the total *R* range anyway. Secondly, the noise build up problem is minimized in *R*-space fitting, since the model function has no noise in it. However, in *k*-space fitting, one has to forward, and then reverse the Fourier transform process on the experimental data. Although this eliminates the high-frequency noise and higher shells, it can increase the relative magnitude of the low-frequency noise. Thirdly, and perhaps most important, in *k*-space fitting the variance defined in expression for independent parameters (N_{indp}, see below) has many maxima and minima. This is because the $\chi(k)$ function is an oscillatory function so that if the wavelength of the model and experimental χ are not very similar, the two functions go in and out of phase, introducing many hills and valley in the variance function.

The number of independent data points in an EXAFS spectrum is not equal to the number of measured data points. In most cases, EXAFS spectra are significantly oversampled, so that $N_{indp} << N$. The limitation in N_{indp} results from the fact that EXAFS spectra are "band-limited" and thus do not contain contributions from all possible frequencies. N_{indp} can be estimated as $N_{indp} = (2\Delta k\, \Delta R)/\pi$.

Since k_{min} is approximately 2 $Å^{-1}$, k_{max} is often 12-14 $Å^{-1}$ or less, and the *R* range over which EXAFS signals are seen is approximately 1-4 Å, N_{indp} can be 20 or less, although larger values are possible. For filtered data, N_{indp} is often much smaller; for $\Delta R \leq 0.8$ Å, N_{indp} may be as small as 6-8. In such cases, it may be impossible to obtain meaningful fits using two shells of scatterers. If three parameters (*R*, σ^2 and *N*) are refined per shell, then for two shells there may be no free parameters. Although the fit may reproduce the data perfectly, the refined structural parameters could not be physically meaningful [40].

The ability to determine accurate structures for non-crystalline samples has made EXAFS extremely useful in coordination chemistry. However, there are several practical limitations to the ability of EXAFS to probe structure. One involves the ability of EXAFS to resolve contributions from two different scatterers. The best resolution that can be achieved is given $\Delta R \geq \pi/2\Delta k$. This gives $\Delta R \geq 0.13$ Å for data to $k_{max} = 12$ $Å^{-1}$. However, this estimate is generally too optimistic, mainly because the Debye-Waller factor (σ^2 in eq. (23)) can mimic the damping that is caused by the presence of two shells of scatterers. This illustrates the fact that although the resolution limit of EXAFS is much better than those of most crystallography, it is nevertheless sufficiently poor that it is often not possible to resolve the contributions from different nearest neighbors, even when they are known chemically to be present at different distances.

4. Chemometrics Routine

Chemometrics routines used in our work were totally based on the toolbox MATLAB® package created by Jaumont *et al.* [41]. In MATLAB we can find some algorithms for MCR-ALS purposes, however they have the drawback of how the selected constraints are input in the execution of the MATLAB routine. This process can be troublesome and difficult in complex cases where several data matrices are simultaneously analyzed and/or different constraints are applied to each of them for an optimal resolution. Based on this issue an improved MCR-ALS toolbox with a user-friendly graphical interface was created by the authors and will be presented in the following subsections.

4.1. Algorithm

A description of the MCR-ALS method was presented in the last chapter. It is based on a bilinear model given by the equation above:

$$\boldsymbol{D} = \boldsymbol{C}\boldsymbol{S}^{\boldsymbol{T}} + \boldsymbol{E} \tag{24}$$

The goal of MCR-ALS is the bilinear decomposition of the data matrix **D** into the "true" pure response profiles associated with the variation of each contribution in the row and the column directions, represented by matrices **C** and $\mathbf{S}^{\mathbf{T}}$, respectively, which are responsible for the observed data variance.

In spectroscopic measurements, the rows of matrix **D** are the spectra measured during the experiment, the column profiles of matrix **C** and the row profiles of $\mathbf{S}^{\mathbf{T}}$ are associated respectively with the concentration and pure spectra profiles of the resolved components. The superscript *T* means the transpose of matrix **S**, where pure spectra are column profiles. **E** is the matrix of residuals not explained by the model and ideally should be close to the experimental error. Eq. (24) is the multiwavelength extension of Lambert–Beer's law in matrix form. It is noteworthy that the term "pure components" denotes a group of features that varies with a unique pattern, compared to other responses coming from the sample. It does not necessarily have to be a chemically pure component but could represent, e.g., a mixture of chemically pure components as long as they behave together (kinetically) in the same manner.

MCR-ALS solves iteratively Eq. (24) by an Alternating Least Squares algorithm, which calculates concentration **C** and pure spectra $\mathbf{S}^{\mathbf{T}}$ matrices optimally fitting the experimental data matrix **D**. This optimization is carried out for a proposed number of components and using initial estimates of either **C** or $\mathbf{S}^{\mathbf{T}}$. Initial estimates of **C** or $\mathbf{S}^{\mathbf{T}}$ can be obtained either using Evolving Factor Analysis [42] or SIMPLISMA [43] derived methods. Convergence is achieved when in two consecutive iterative cycles, relative differences in standard deviations of the residuals between experimental and ALS calculated

data values are less than a previously selected value. The user may modify this value, depending on the stage of the optimization. Usually at the beginning of the study a higher value is used (i.e. 1%) for exploratory purposes. In contrast, once a good model has been found, lower values are attempted to see whether there is any appreciable improvement in **C** and $\mathbf{S}^T$ solutions, both in qualitative and quantitative terms.

Figures of merit of the optimization procedure are the percent of lack of fit, the percent of variance explained and the standard deviation of residuals respect experimental data.

Lack of fit is defined as the difference among the input data **D** and the data reproduced from the $\mathbf{CS}^T$ product obtained by MCR-ALS. This value is calculated according to the expression:

$$lack\ of\ fit\ (\%) = 100\sqrt{\left(\frac{\sum_{ij} e_{ij}^2}{\sum_{ij} d_{ij}^2}\right)} \tag{25}$$

where d_{ij} designs an element of the input data matrix **D** and e_{ij} is the related residual obtained from the difference between the input element and the MCR-ALS reproduction.

Two different lack of fit values are calculated, differing on the definition of the input data matrix **D** (either the raw experimental data matrix or the PCA reproduced data matrix using the same number of components as in the MCR-ALS model). These two lack of fit values are evaluated and shown at the end of each iterative cycle, when all constraints have been already applied and finally given in the results of the optimization. These values are useful to understand whether experimental data were well fitted and also to evaluate whether the ALS optimization fit approached PCA fit.

Percent of variance explained (Eq. (26)) and standard deviation of residuals respect experimental data (Eq. (27)) are calculated according to the following expressions where d_{ij} and e_{ij} are the same as above and n_{rows} and $n_{columns}$ are the number of rows and columns in the **D** matrix.

$$R^2 = \frac{\sum_{ij} d_{ij}^2 - \sum_{ij} e_{ij}^2}{\sum_{ij} d_{ij}^2} \tag{26}$$

$$\sigma = \sqrt{\frac{\sum_{ij} e_{ij}^2}{n_{rows} n_{columns}}} \tag{27}$$

Simultaneous MCR-ALS analysis of multiple independent experiments run under different experimental conditions is a useful and powerful strategy in resolution. Eq. (24) can be extended to allow for the MCR-ALS simultaneous analysis of several experiments followed by the same spectroscopic technique (a three-way bilinear system). This data arrangement gives rise to a column-wise augmented matrix,

where the resolved pure spectra are common to all experiments and the concentration profiles can be different from experiment to experiment. Eq. (28) shows the model for a two-experiment system, giving data matrices $\mathbf{D^1}$ and $\mathbf{D^2}$, a common pure spectra matrix $\mathbf{S^T}$ and submatrices $\mathbf{C^1}$ and $\mathbf{C^2}$ with the concentration profiles related to $\mathbf{D^1}$ and $\mathbf{D^2}$, respectively.

$$\begin{bmatrix} \boldsymbol{D^1} \\ \boldsymbol{D^2} \end{bmatrix} = \begin{bmatrix} \boldsymbol{C^1} \\ \boldsymbol{C^2} \end{bmatrix} \boldsymbol{S^T} + \begin{bmatrix} \boldsymbol{E^1} \\ \boldsymbol{E^2} \end{bmatrix} \quad (28)$$

4.2. Operating Procedures

MCR-ALS optimization with a user-friendly interface works following the classical scheme of the alternating least squares procedures, i.e., the iterative optimization of the resolved concentration profiles and spectra subject to selected constraints. The dialog boxes that appear during the MCRALS execution are mainly related to: a) input of initial information, b) selection of constraints and selection of optimization parameters, and c) display of resolution results.

4.2.1. Input of Initial Information

The first step is data selection, the matrix **D** that contains the spectra evolution previously recorded on MATLAB. Once data is selected, one can perform either PCA (via single value decomposition) in order to estimate the number of components present on the dataset or entry the number of components manually. It is noteworthy that a deeper PCA analysis, which includes rank-analysis via eigenvalues explanation, scree plots and score plots, are strongly encouraged. After all, a 100% precisely unambiguous answer is hardly obtained by any of these tools. Indeed, they are able to give us just the most likely number of PC's inside our system. Usually, one stablishes a narrow window of possibilities and MCR-ALS calculations are performed and compared with different numbers of PC's.

The next step is to make the initial guess. Three option are available for that: SIMPLISMA method, which can either return pure spectra or profile concentration; determination of profile concentration by Evolving Factor Analysis (EFA) or manually entry a matrix that contains either pure spectra or a matrix with the concentration profile calculated by whatever alternative method. This entire step is illustrated in the Figure III.*15*.

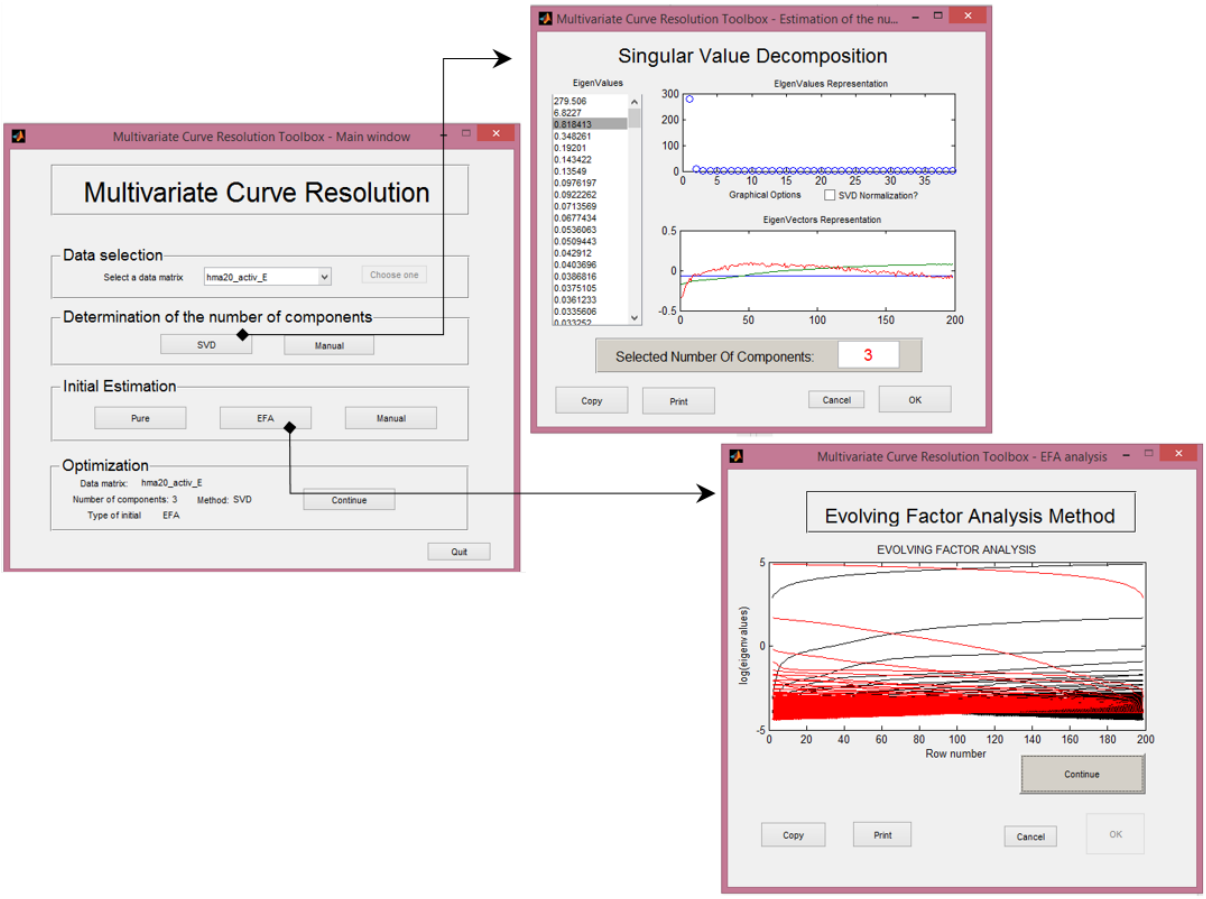

Figure III.15 - Initial step in MCR calculation procedure: data selection, determination of number of components and initial guess by EFA.

Then, the initial MCR graphic input window can be launched (Figure III.*16*). In this window, the user has to select: a) the matrix **D** to be analyzed (the matrix variable in this case), b) the initial estimates of either concentration or spectra profiles (**C** or $\mathbf{S}^{\mathbf{T}}$) (e.g., concentration profile calculated by EFA in Figure III.*16*), and c) the number of sub matrices simultaneously analyzed in the augmented data matrix **D** (if necessary). This value is defined by the number of experiments performed at different conditions and/or monitored by different spectroscopic techniques. In our particular case, we had opportunity to perform activation and reduction reactions for the same of our samples (but not for all samples), so, we have the choice of using an augmented matrix with two sub matrices for those ones.

Figure III.16 - Selection of data set main window. The user have to select the data set (in this example the activation for impregnated catalyst with 20% in Mo loading), the initial guess (concentration profile as determined by EFA) and the number of matrices. The plots show information about the system as described in the text.

Once these matrices have been selected, six different plots are obtained completing the graphical representation of the initial known information about the system under study. The top plots of Figure III.*16* display the columns of the raw data set showing the process evolution at each wavelength (left plot) and the rows of the raw data set, i.e., the experimental spectra acquired along the evolution of the process (right plot). Left and right in the middle of Figure III.*16*, the plots display the initial estimates of the concentration profile **C** matrix and the species spectra $\mathbf{S}^{\mathbf{T}}$ matrix estimated by linear least squares from these concentration initial estimates **C** and data matrix **D**. Finally, at the bottom of Figure III.*16*, Principal Component Analysis results of matrix **D** are obtained i.e. plot of scores and loadings matrices, for the preselected number of components in the system.

4.2.2. Selection of ALS Constrains and Selection of Optimization Parameters

Figure III.*17* shows the simplest dialog box, when only a single experiment is analyzed. When dealing an augmented matrix, there is an intermediary step before constraint selection that will not be treat here (for further details, refer to original paper [41]). Initially, when the Selection of ALS Constraints window in Figure III.*17* is loaded, the only active buttons are those to select which constraints should be applied. When one particular constraint and the matching checkbox button are selected, new options are gradually activated in the graphical interface to give details on *where* and *how* the constraint should come into play in the resolution process.

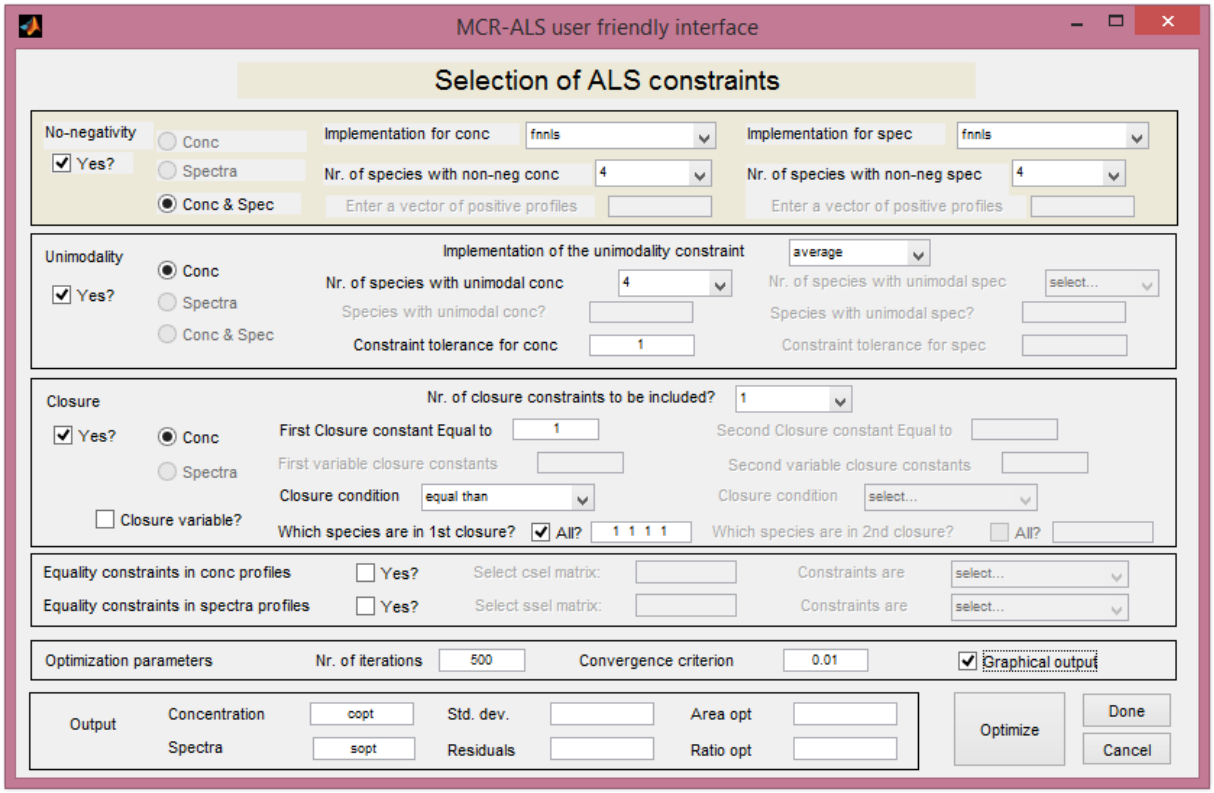

Figure III.17 - Selection of the ALS constraints window in the case of a single experiment analysis. See text for a detailed explanation about the constraints selection and implementation.

The first thing to be decided is the direction of application of the constraint (concentration and/or spectral). To do so, the suitable radio buttons can be clicked at the left hand side of the constraints that allow for this option. Once the direction(s) of application are selected, the user must answer how many and which components (species) in the **C** and/or $\mathbf{S}^T$ matrix should be constrained.

The application of the non-negativity constraint can be carried out according to different least squares approaches, the classical non-negative least squares, *nnls* and the more recent fast non-negative least squares, *fnnls* [44].

For the unimodality constraint, the options "average" implementation (the smoothest one) is preferred. The secondary maxima are corrected taking averages similarly as in unimodal least squares algorithms [45]. A constraint tolerance can be selected to allow for some local departures of the unimodality condition. For instance, 1.5 means that 50% of local departure of the unimodal condition is allowed, i.e. that in the decreasing slopes of the main peak a particular point can increase a maximum of 50% of the previous value before the unimodality constraint is applied. Values between 1.0 (no departures from the unimodal condition allowed) and 1.1 are usual in systems with low to medium noise levels.

Closure in the concentration direction is related to mass balance equations in closed reaction systems. The total concentration of the system (closure constant) can be fixed to a single value or to a variable (changing) value. The program allows for the introduction of two closure conditions (two mass balance equations); however, the application of this option is not recommended when common species are shared by both mass balances. Closure can be implemented as an equality constraint (the closure constant is exactly equal to some preselected value) or as a smoother inequality constraint. In the latter case, the mass balance should "*equal or be lower than*" the preselected value for the closure constant.

Other features are present when several data matrices are simultaneously analyzed, either from several different experiments and/or from several different spectroscopic techniques. The identification and correspondence of species between different matrices is one of them. Since the main goal of this section is to present an overview of the software, we believe it is not worth to detail all these option here and for further interest, we claim to refer the original paper.

Once the constraints are selected, the choice of the optimization parameters and the information needed to present the output of the resolution method are carried out in the same way for single and augmented matrices.

The bottom part in Figure III.*17* concerns the parameters used to control the end of the optimization process like the maximum number of iterations allowed and the convergence criterion. It is done in percentage of change of standard deviation of residuals between two consecutive iterations, i.e., 0.01 means that convergence is achieved when the change in the standard deviation of the residuals is lower or equal to 0.01% between two consecutive iterations.

4.2.3. Display of the Results

Once convergence is achieved or after the maximum number of iterations is exceeded or in case of divergence, the optimal resolution results are shown, as exampled in Figure III.*18*.

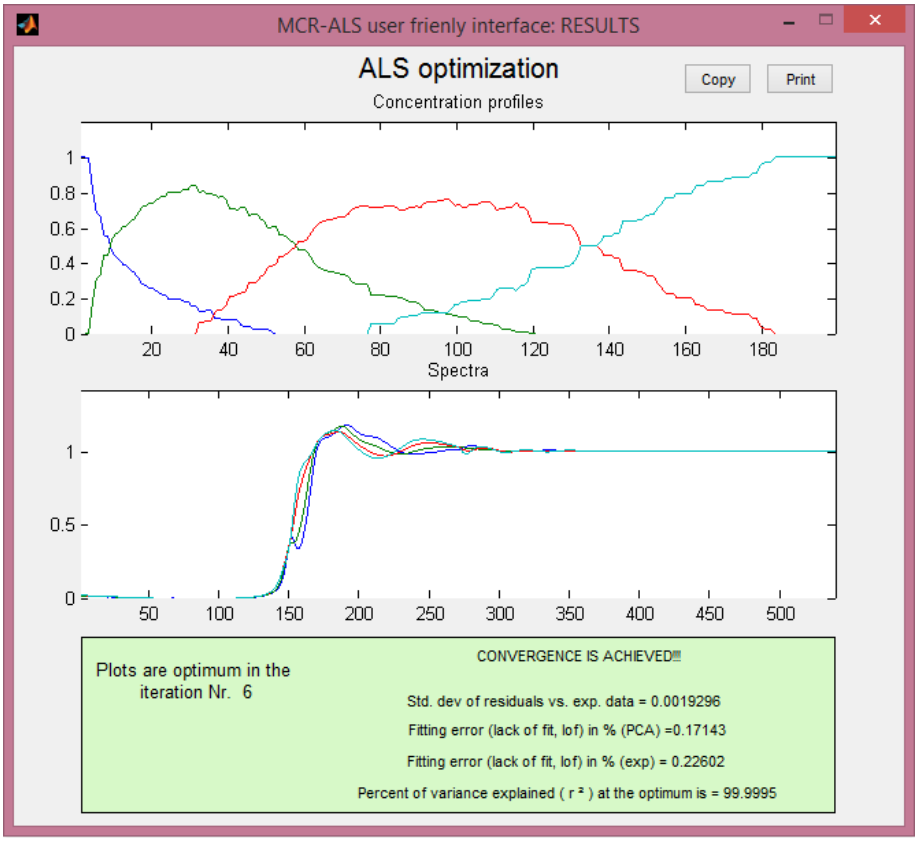

Figure III.18 - ALS optimization results window. In this window, a representation of resolved concentration and spectra with other optimization (percentage of variance explained, lack of fit). These results correspond to the analysis runs with the constraints selected in Figure III.17.

In this window, a plot of the resolved concentration and spectra profiles is given, as well as figures of merit related to the optimization results. The window correspond to the results obtained in the analysis of one of our sample, namely, an impregnated catalyst with 20% of Mo loading during the activation reaction (HMA-20_act). Data corresponding to the final results, Concentration Profile and Pure Spectra, are stored in exportable stables in MATLAB. Particularly, pure spectra are considered to perform fine XAFS analysis with dedicated software.

References

[1] J. W. Neimantsverdriet, *Spectroscopy in Catalysis*. Wheinheim: VCH, 1993.

[2] T. A. Carlson, *Photoelectron and Auger Spectroscopy*. New York: Plenum Press, 1975.

[3] D. M. Hercules and S. H. Hercules, "Analytical chemistry of surfaces. Part II. Electron spectroscopy," *Journal of Chemical Education*, vol. 61, no. 6, p. 483, Jun. 1984.

[4] F. P. J. M. Kerkhof and A. M. Moulijn, "Quantitative Analysis of XPS Intensities for Supported Catalysts," *Journal of Physical Chemistry*, vol. 83, no. 7, pp. 1612–1619, 1979.

[5] V. León, "A simplified Kerkhof-Moulijn model for dispersion quantification from XPS atomic concentrations," *Surface Science*, vol. 339. pp. L931–L934, 1995.

[6] A. M. Venezia, "X-ray photoelectron spectroscopy (XPS) for catalysts characterization," *Catalysis Today*, vol. 77, no. 4, pp. 359–370, Jan. 2003.

[7] A. Cimino, D. Gazzoli, and M. Valigi, "XPS quantitative analysis and models of supported oxide catalysts," *Journal of Electron Spectroscopy and Related Phenomena*, vol. 104, no. 1–3, pp. 1–29, Jul. 1999.

[8] S. Rondon, M. Houalla, and D. M. Hercules, "Determination of the Surface Coverage of Mo / TiO Catalysts by ISS and CO Chemisorption," *Surface and Interface Analysis*, vol. 26, no. June 1996, pp. 329–334, 1998.

[9] J. Végh, "The Shirley background revised," *Journal of Electron Spectroscopy and Related Phenomena*, vol. 151, no. 3, pp. 159–164, May 2006.

[10] H. Brongersma, M. Draxler, M. Deridder, and P. Bauer, "Surface composition analysis by low-energy ion scattering," *Surface Science Reports*, vol. 62, no. 3, pp. 63–109, Mar. 2007.

[11] H. H. Brongersma, M. Carrere-Fontaine, R. Cortenraad, A. W. Denier van der Gon, P. J. Scanlon, I. Spolveri, B. Cortigiani, U. Bardi, E. Taglauer, S. Reiter, S. Labich, P. Bertrand, L. Houssiau, S. Speller, S. Parascandola, H. Ünlü-Lachnitt, and W. Heiland, "A round robin experiment of elemental sensitivity factors in low-energy ion scattering," *Nuclear Instruments and Methods in Physics Research Section B: Beam Interactions with Materials and Atoms*, vol. 142, no. 3, pp. 377–386, Jul. 1998.

[12] M. A. Wheeler, "Analysis of surface composition by ion scattering spectrometry," *Analytical Chemistry*, vol. 47, no. 1, pp. 146–148, Jan. 1975.

[13] J. B. Theeten and H. H. Brongersma, "Rétrodiffusion d'ions de gaz rares de faible énergie par la surface d'un solide : mécanismes fondamentaux et application à la détermination des structures cristallines de surface," *Revue de Physique Appliquée*, vol. 11, no. 1, pp. 57–63, Jan. 1976.

[14] S. N. Mikhailov, R. J. M. Elfrink, J.-P. Jacobs, L. C. A. van den Oetelaar, P. J. Scanlon, and H. H. Brongersma, "Quantification in low-energy ion scattering: elemental sensitivity factors and

charge exchange processes," *Nuclear Instruments and Methods in Physics Research Section B: Beam Interactions with Materials and Atoms*, vol. 93, no. 2, pp. 149–155, Jul. 1994.

[15] H. H. Brongersma and J.-P. Jacobs, "Application of low-energy ion scattering to studies of growth," *Applied Surface Science*, vol. 75, no. 1–4, pp. 133–138, Jan. 1994.

[16] J. T. Grant, "Background subtraction techniques in surface analysis," *Journal of Vacuum Science & Technology A: Vacuum, Surfaces, and Films*, vol. 2, no. 2, p. 1135, 1984.

[17] G. C. Nelson, "Influence of surface roughness on the intensity of elastically scattered low-energy noble- gas ions," *Journal of Applied Physics*, vol. 47, no. 4, pp. 1253–1255, Apr. 1976.

[18] W. P. a. Jansen, A. Knoester, a. J. H. Maas, P. Schmit, A. Kytökivi, a. W. Denier v.d. Gon, and H. H. Brongersma, "Influence of compaction and surface roughness on low-energy ion scattering signals," *Surface and Interface Analysis*, vol. 36, no. 11, pp. 1469–1478, Nov. 2004.

[19] R. Cortenraad, S. N. Ermolov, B. Moest, A. W. Denier van der Gon, V. G. Glebovsky, and H. H. Brongersma, "Crystal-face dependence of low-energy ion scattering signals," *Nuclear Instruments and Methods in Physics Research Section B: Beam Interactions with Materials and Atoms*, vol. 174, no. 1–2, pp. 173–180, Mar. 2001.

[20] E. Stern, "Theory of the extended x-ray-absorption fine structure," *Physical Review B*, vol. 10, no. 8, pp. 3027–3037, Oct. 1974.

[21] F. Lytle, D. Sayers, and E. Stern, "Extended x-ray-absorption fine-structure technique. II. Experimental practice and selected results," *Physical Review B*, vol. 11, no. 12, pp. 4825–4835, Jun. 1975.

[22] E. Stern, D. Sayers, and F. Lytle, "Extended x-ray-absorption fine-structure technique. III. Determination of physical parameters," *Physical Review B*, vol. 11, no. 12, pp. 4836–4846, Jun. 1975.

[23] A. Messiah, *Quantum Mechanics*. New York: Dover Publications, 1999.

[24] P. Lee, P. Citrin, P. Eisenberger, and B. Kincaid, "Extended x-ray absorption fine structure—its strengths and limitations as a structural tool," *Reviews of Modern Physics*, vol. 53, no. 4, pp. 769–806, Oct. 1981.

[25] J. J. Rehr, "Theoretical approaches to x-ray absorption fine structure," *Reviews of Modern Physics*, vol. 72, no. 3, pp. 621–654, Jul. 2000.

[26] J. Rehr and R. Albers, "Scattering-matrix formulation of curved-wave multiple-scattering theory: Application to x-ray-absorption fine structure," *Physical Review B*, vol. 41, no. 12, pp. 8139–8149, Apr. 1990.

[27] G. Bunker, *Introduction to XAFS*. Cambridgr: Cambridge University Press, 2010.

[28] S. Belin, V. Briois, A. Traverse, M. Idir, T. Moreno, and M. Ribbens, "SAMBA a New Beamline at SOLEIL for XRay Absorption Spectroscopy in the 440keV Energy Range," *Physica Scripta*, vol. T115. p. 980, 2005.

[29] R. Frahm, "New method for time dependent x-ray absorption studies," *Review of Scientific Instruments*, vol. 60, no. 7, p. 2515, Jul. 1989.

[30] V. Briois, E. Fonda, S. Belin, L. Barthe, C. La Fontaine, F. Langlois, M. Ribbens, and F. Villain, "SAMBA: The 4–40 keV X-ray absorption spectroscopy beamline at SOLEIL," in *UVX 2010 - 10e Colloque sur les Sources Cohérentes et Incohérentes UV, VUV et X ; Applications et Développements Récents*, 2011, pp. 41–47.

[31] E. Fonda, A. Rochet, M. Ribbens, L. Barthe, S. Belin, and V. Briois, "The SAMBA quick-EXAFS monochromator: XAS with edge jumping.," *Journal of Synchrotron Radiationotron*, vol. 19, no. Pt 3, pp. 417–24, May 2012.

[32] R. Frahm, M. Richwin, and D. LtzenkirchenHecht, "Recent Advances and New Applications of TimeResolved Xray Absorption Spectroscopy," *Physica Scripta*, vol. 2005, no. T115, p. 974, 2005.

[33] C. La Fontaine, L. Barthe, A. Rochet, and V. Briois, "X-ray absorption spectroscopy and heterogeneous catalysis: Performances at the SOLEIL's SAMBA beamline," *Catalysis Today*, vol. 205, pp. 148–158, Apr. 2013.

[34] A. Rochet, "Caractérisation Structurale de Catalyserus Hétérogènes en Condition de Fonctionnement par Spectroscopie d'Absorption des Rayons X Résolue dans le Temp," Paris Sud, 2011.

[35] G. Renaud, G. Abeille, E. Elkaim, E. Fonda, F. Langlois, and J. Malik, "Continous Scan at Synchrotron SOLEIL," in *Proceedings of the International Conference on Accelerators and Large Experimental Physics Control Systems*, 2009.

[36] J. J. Rehr, J. J. Kas, M. P. Prange, A. P. Sorini, Y. Takimoto, and F. Vila, "Ab initio theory and calculations of X-ray spectra," *Comptes Rendus Physique*, vol. 10, no. 6, pp. 548–559, Jul. 2009.

[37] S. D. Conradson, "Application of X-ray Absorption Fine Structure Spectroscopy to Materials and Environmental Science," *Applied Spectroscopy*, vol. 52, no. 7, p. 252A–279A, Jul. 1998.

[38] D. Sayers, E. Stern, and F. Lytle, "New Technique for Investigating Noncrystalline Structures: Fourier Analysis of the Extended X-Ray—Absorption Fine Structure," *Physical Review Letters*, vol. 27, no. 18, pp. 1204–1207, Nov. 1971.

[39] D. Koningsberger and B. Mojet, "XAFS spectroscopy; fundamental principles and data analysis," *Topics in catalysis*, vol. 10, pp. 143–155, 2000.

[40] A. Michalowicz, K. Provost, S. Laruelle, A. Mimouni, and G. Vlaic, "F-test in EXAFS fitting of structural models," *Journal of Synchrotron Radiation*, vol. 6, no. 3, pp. 233–235, 1999.

[41] J. Jaumot, R. Gargallo, A. de Juan, and R. Tauler, "A graphical user-friendly interface for MCR-ALS: a new tool for multivariate curve resolution in MATLAB," *Chemometrics and Intelligent Laboratory Systems*, vol. 76, no. 1, pp. 101–110, Mar. 2005.

[42] M. Maeder, "Evolving factor analysis for the resolution of overlapping chromatographic peaks," *Analytical Chemistry*, vol. 134, no. 6, pp. 527–530, 1987.

[43] W. Windig and J. Guilment, "Interactive self-modeling mixture analysis," *Analytical Chemistry*, vol. 63, no. 14, pp. 1425–1432, Jul. 1991.

[44] R. Bro and S. De Jong, "A fast non-negativity-constrained least squares algorithm," *Journal of Chemometrics*, vol. 11, no. 5, pp. 393–401, Sep. 1997.

[45] R. Bro and N. D. Sidiropoulos, "Least squares algorithms under unimodality and non-negativity constraints," *Journal of Chemometrics*, vol. 12, no. 4, pp. 223–247, Jul. 1998.

[46] A. Denton and N. Ashcroft, "Vegard's law," *Physical Review A*, vol. 43, no. 6, pp. 3161–3164, Mar. 1991.

Chapter IV: One-Pot Sol-Gel Preparation for Efficient Cobalt-Molybdenum-Titania Hydrotreating Catalysts

Table of Contents

1. Introduction

This chapter is dedicated to present our first results on the characterization of TiO_2-supported CoMo-based HDS catalysts prepared via one-pot sol-gel method. Such results were published under original paper format at ChemCatChem[7] journal.

Sol-gel route of preparation of oxide materials with controlled textural properties is already known for catalytic supports, but it was the first time that such method was reported for titania-based materials. Titania has appeared as relevant catalytic support to HDS and its use is into the context of the search of alternative and more efficient catalysts that fulfill the global demand of clean fuel.

In this picture, this work focused on the synthesis of oxide precursors of the active phase and their characterization by X-ray powder diffraction (XRD), N_2 porosimetry, X-ray photoelectron spectroscopy (XPS) and transmission electron microscopy (TEM). Further, we used Raman spectroscopy to check molybdenum dispersion. Some of these techniques were used to characterize the sulfided form of the solids and the catalytic performance were evaluated for the thiophene HDS model reaction.

A series with increasing Mo loading was synthetized. We vary the weight percentage of MoO_3 to the total mass (wt%) of the solid keeping Co/Mo atomic ratio equals to 0.5. The goal of the oxide precursors characterization is twofold. By one hand, we can verify how textural properties and dispersion of the oxide on the support evolve with increasing the Mo loading. We recall that in such one-pot method, solution for oxide precursor is mixed with the solution for support, thus, increasing the Mo loading should change support properties, which should have influence also on active phase and its dispersion on the support. This influence should be, thus, reflected on the catalytic activity and data from classical catalytic method of preparation (incipient wetness impregnation, IWI) is considered for comparison purposes.

2. Full Published Article

Above, we present the full paper as it was published in ChemCatChem journal.

CHEMCATCHEM

ChemPubSoc Europe

DOI: 10.1002/cctc.201200165

One-Pot Sol–Gel Preparation for Efficient Cobalt–Molybdenum–Titania Hydrotreating Catalysts

D. L. Nguyen,[a] S. Gillot,[a] D. O. Souza,[a] P. Blanchard,[a] C. Lamonier,[a] E. Berrier,[a] T. V. Kotbagi,[b] M. K. Dongare,[b] S. B. Umbarkar,[b] S. Cristol,[a] E. Payen,[a] and C. Lancelot*[a]

Titania-based hydrodesulfurization catalysts were prepared by using a one-pot sol–gel method with the titanium peroxo complex as titanium precursor and molybdenum and cobalt precursors dissolved in the aqueous hydrogen peroxide solution used during synthesis. Catalysts with MoO_3 loadings varying from 5 to 40 wt% and a Co/Mo atomic ratio of 0.5 were prepared. Solids with molybdenum loadings below 20 wt% MoO_3 demonstrated poor hydrodesulfurization activity for the model compound thiophene. This was attributed to the presence of a large amount of embedded cobalt and molybdenum species in the titania matrix. A significant increase in the catalytic activity was observed for solids containing 20 and 25 wt% of MoO_3 on which active species appeared to be accessible on the titania surface. Furthermore, the highest conversion obtained on these sol–gel solids was superior to the highest conversion obtained on reference catalysts prepared through the impregnation of ammonium heptamolybdate and cobalt nitrate on commercial titania.

Introduction

The active phase of conventional hydrodesulfurization (HDS) catalysts consists in well-dispersed nanosized MoS_2 crystallites dispersed onto the support γ-Al_2O_3 and promoted with cobalt or nickel atoms. These active phases are classically obtained by the sulfidation of an oxidic precursor $CoMo/Al_2O_3$, or $NiMo/Al_2O_3$, which is prepared through incipient wetness impregnation (IWI) of alumina with an aqueous solution of ammonium heptamolybdate and cobalt nitrate. The textural properties of the support and, more precisely, its pore volume govern the amount of ammonium heptamolybdate solution, which is brought into contact with the surface through IWI and is, thus, a strong limiting factor for molybdenum loading.[1] The above mentioned limitation is especially severe when considering low-porosity supports such as anatase TiO_2. However, anatase TiO_2 was proposed recently to be a relevant alternative. Despite of the lower surface area of anatase TiO_2 compared to that of alumina, TiO_2-supported MoS_2 catalysts were found to yield three times higher HDS and hydrogenation activities than alumina-supported catalysts with an equivalent molybdenum loading per square nanometer. However for the promoted system, the synergetic effect of cobalt and molybdenum is less efficient on TiO_2 than on alumina.[2] Arrouvel et al. proposed that smaller MoS_2 crystallites are stabilized on TiO_2,[3] and Costa et al. explained that cobalt promotion could rather be the same on alumina and TiO_2 but the efficiency of the CoMoS sites would be inferior on TiO_2 because of a different linkage on the support.[4]

Oxide materials with controlled textural properties can be afforded by using the sol–gel method. This preparation method has been used extensively for preparing supports with interesting textural properties, and many studies report on the sol–gel synthesis of alumina,[5,6] titania,[7] silica,[8] and various mixed oxides such as alumina–titania,[9–12] alumina–silica,[13] alumina–zirconia,[14] titania–silica,[15] and titania–zirconia.[16–19] Another advantage of the sol–gel method is that it makes it possible to introduce the precursors of the active phase to the precursors of the support in one single step of preparation. As a consequence, the active phase loading is not restricted by the solubility of the precursors in the volume of water corresponding to the pore volume of the support. Le Bihan et al. prepared MoO_3/Al_2O_3 catalysts in which the MoO_3 loading is higher than the one that can be afforded by using the IWI technique and the oxomolybdate phase is still well dispersed.[20] A markedly higher catalytic activity for thiophene HDS was obtained by adding the ammonium heptamolybdate salt to aluminum alkoxide before hydrolysis. Similar results were obtained on addition of ammonium tetrathiomolybdate with enhanced activity in conversion of dibenzothiophene.[21] Cobalt-promoted molybdenum catalysts were also prepared by using the same protocol.[22] Unlike molybdenum-based catalysts, the best performance of thiophene HDS was obtained by using impregnated CoMo catalysts on the sol–gel alumina because of the presence of weakly sulfidable oxides MoO_3 and $CoMoO_4$ on the one-pot sample. The introduction of phosphorus and the modification of the acidobasic character of alumina during the one-pot sol–gel synthesis of, respectively, NiMo– and CoMo–

[a] D. L. Nguyen, S. Gillot, D. O. Souza, Dr. P. Blanchard, Prof. C. Lamonier, Dr. E. Berrier, Prof. S. Cristol, Prof. E. Payen, Dr. C. Lancelot
Unité de Catalyse et de Chimie du Solide, UMR CNRS 8181
Université Lille Nord de France
59655 Villeneuve d'Ascq (France)
Fax: (+33) 3-20-43-65-61
E-mail: christine.lancelot@univ-lille1.fr

[b] T. V. Kotbagi, Dr. M. K. Dongare, Dr. S. B. Umbarkar
National Chemical Laboratory
Pune, Maharashtra 411 008 (India)

alumina catalysts have also been reported.[23–27] Minato et al. prepared monometallic cobalt–silica-based catalysts in one step by mixing cobalt chloride and water glass solutions and attributed the higher thiophene HDS activity of the sol–gel catalysts to the presence of more exposed cobalt species in the sol–gel solids.[28] In addition, the authors pointed out differences in activation energy attributable to a difference in nature of active species between the sol–gel and conventional catalysts. Venezia et al. used a total sol–gel route to prepare SiO_2-supported CoMo catalysts by adding methanol and $Si(OMe)_4$ to an aqueous solution of ammonium heptamolybdate and cobalt nitrate.[8] It is proposed that the sol–gel synthesis enables an improved dispersion of the supported elements. Contrarily, as active species can be embedded into the silica matrix, the technique can cause a decrease in the number of available active sites. Rivera-Muñoz et al. reported a one-pot preparation for molybdenum–silica-based catalysts, and molybdenum and promoter chlorides were dissolved in the ethanol and tetramethyl orthosilicate mixture prior to hydrolysis.[29,30] The authors suggested that better and more uniform dispersion of the active phase is obtained in the case of molybdenum–silica gel catalysts. They also observed that the catalyst obtained through the proposed method requires a lower quantity of the metal promoter for the same high catalytic activity than commercial catalysts, in spite of differences in the surface area. This was attributed to the highly uniform distribution of fine and catalytically active particles on the silica matrix.

To our knowledge, the studies devoted to one-pot HDS catalysts reported in the literature describe only the preparation of alumina- and silica-based materials. Nevertheless, of the available supports, titania appears as relevant for HDS. This work reports on a one-pot sol–gel synthesis of cobalt–molybdenum–titania-based materials through a peroxo route described previously by some of us for titania synthesis.[31] Molybdenum and cobalt salts were added to the titania precursor according to a one-pot preparation to yield high loading MoO_3–TiO_2 catalysts with expected original properties and enhanced catalytic activity. The as-synthesized solids were characterized in both the oxidic and sulfided forms by XRD, N_2 porosimetry, X-ray photoelectron spectroscopy (XPS), and transmission electron microscopy (TEM) analysis. Molybdenum dispersion was evaluated by using Raman spectroscopy. Catalytic performances of the CoMo catalysts were then evaluated for the thiophene HDS model reaction.

Results

Evolution of the physical properties of the calcined solids

The physical properties of the CoMo-based catalysts are listed in Table 1. Between 0 and 15 wt% MoO_3, no considerable variation in the surface area was noticed, with values between 63 and 83 $m^2 g^{-1}$. An increase in the surface area was then observed for CoMo17.5Ti and CoMo20Ti, with respective values of 90 and 126 $m^2 g^{-1}$. The surface area can be expressed in square meter of support instead of square meter of catalyst by removing the contribution of the weight gain consecutive to the introduction of the active phase. The exposed surface area values of titania were then found to be 109, 168, and 121 $m^2 g^{-1}$ for CoMo17.5Ti, CoMo20Ti, and CoMo25Ti, respectively. This indicates that, for these contents, the presence of molybdenum leads to the synthesis of titania with a high surface area. At a higher molybdenum content, the surface area showed a progressive decrease to 18 $m^2 g^{-1}$ for the highest molybdenum loading (40 wt%).

Table 1. The physical properties of the calcined oxidic precursors. The specific surface area (SSA), porous volume (V_p), and pore diameter (d_p) were determined by N_2 adsorption–desorption, and the titania crystal size (D) was determined by XRD and TEM).

Sample name	SSA [$m^2 g^{-1}$]	V_p [$cm^3 g^{-1}$]	d_p [nm]	D [nm][a]
TiO_2	65	0.22	5.2/14.7	30.0
CoMo5Ti	83	0.18	3.5/11.0	21.6
CoMo10Ti	63	0.08	3.6/8.0	n.d.
CoMo15Ti	64	0.06	3.9	15.4/12[b]
CoMo17.5Ti	90	0.11	3.6/5.3	n.d.
CoMo20Ti	126	0.21	5.5	10.6
CoMo25Ti	83	0.09	3.6	8.8/8[b]
CoMo35Ti	51	0.06	3.6	6
CoMo40Ti	18	n.d.	n.d.	n.d.

[a] Determined by XRD analysis. [b] Also determined by TEM analysis.

The N_2 adsorption–desorption isotherms and the pore size distributions are presented in Figures 1 and 2, respectively. For all solids, type IV isotherms with H_2-type hysteresis loop (IUPAC classification) were observed. A step increase in the nitrogen-adsorbed amount with a small pressure increase corresponds to capillary condensation. At the end of the capillary condensa-

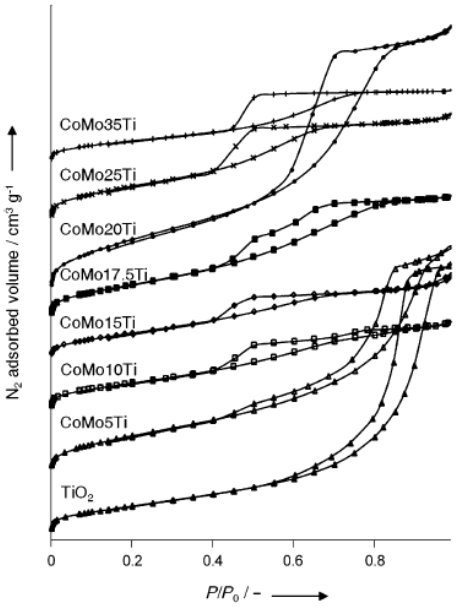

Figure 1. N_2 adsorption–desorption isotherms obtained on the calcined CoMoxTi solids, in which x = 0–35 wt% MoO_3.

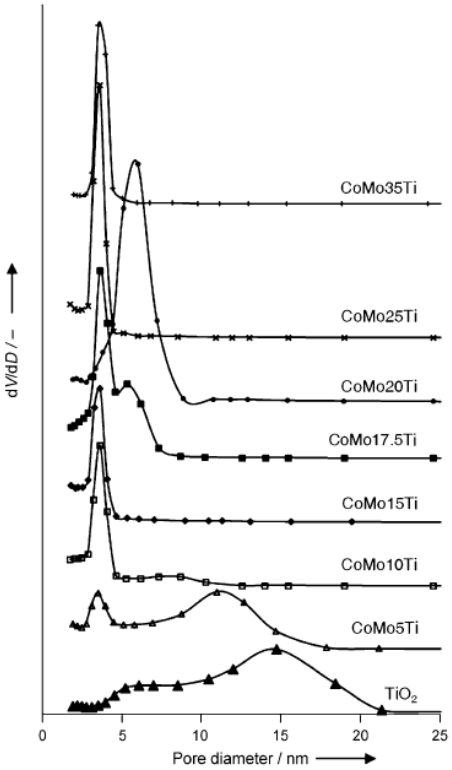

Figure 2. BJH pore size distribution obtained on the calcined CoMo*x*Ti solids, in which $x = 0$–35 wt% MoO_3.

tion step, a well-defined plateau (high P/P_0) is observed. All these evolutions are consistent with the formation of a mesoporous solid. However, solids with molybdenum loadings below and above 5 wt% demonstrate different behaviors. Pure TiO_2 and CoMo5Ti showed very similar isotherms, which corresponded to pore volumes of around 0.2 $cm^3 g^{-1}$. The pore size distribution was broad and bimodal for these solids, with mean pore diameters of 5.2 and 14.7 nm for TiO_2 and a slight shift toward lower values (3.5 and 11.0 nm) for CoMo5Ti. CoMo*x*Ti solids with molybdenum loadings above 5% presented a narrow monomodal distribution centered on a diameter between 3.6 and 3.9 nm (except for CoMo20Ti, for which the value was 5.5 nm, and CoMo17.5Ti, which showed both contributions). An intermediate situation was observed for CoMo10Ti with a small contribution of larger pores (8 nm).

As shown in Table 1, the porous volume initially decreased for molybdenum contents up to 15 wt% MoO_3, which can be related to the disappearance of the large pores present on pure titania. The further increase in the total pore volume for CoMo17.5Ti and CoMo20Ti solids corresponds to the increase in surface area. If expressed per gram of support, that is, if the contribution of the weight gain consecutive to the introduction of the active phase is removed, the pore volume of CoMo20Ti is slightly higher than that of pure TiO_2 (0.28 vs. 0.22 $cm^3 g^{-1}$ for pure TiO_2). The porous volume of the solids decreased again above 20 wt% MoO_3, which is in agreement with the evolution of the surface area.

These results showed the formation of titania with different porosity, depending on the molybdenum and cobalt content added during the synthesis: a broad and bimodal porosity observed at low loadings, with the contribution of only small mesopores with a much more narrow distribution at high molybdenum loadings.

The crystallographic structure of each sample was determined by using XRD. In all solids, the diffractograms shown in Figure 3 evidenced crystallized anatase, with the characteristic

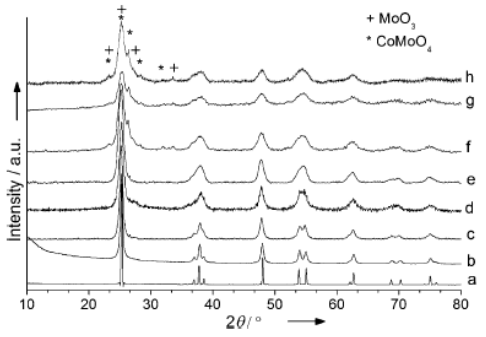

Figure 3. XRD diffractograms of the calcined CoMo*x*Ti solids with MoO_3 loadings (*x*) of a) 0, b) 5, c) 15, d) 20, e) 25, f) 30, g) 35, and h) 40 wt%.

main diffraction peaks at 25.3, 37.8, 48.1, 53.9, 55.1, and 62.7° (PDF 84-1286). Above 30 wt% of MoO_3, diffraction peaks at 23.6, 27.4, 33.6 and 23.3, 26.5, 28.4, 32.1 account for the presence of MoO_3 (PDF 85-2405) and $CoMoO_4$ (PDF 21-0868), respectively. When increasing the molybdenum loading, a broadening of the peaks corresponding to anatase was observed, which is related to a decrease in size of the titania crystallites. The average crystallite size of titania was then calculated with the Scherrer equation from the (101) peak for solids with molybdenum loadings below 30 wt% MoO_3, because above this value the overlapping of $CoMoO_4$, MoO_3, and TiO_2 diffraction peaks prevents an accurate determination of the crystallite size of anatase. The measurement of the crystallite size of anatase was also performed by using TEM, with a statistical determination of the particle diameter measured on 100 particles (see Table 1). Values calculated from XRD analysis and measured by using TEM were consistent, and the whole series showed a continuous decrease in the crystallite size if molybdenum was incorporated, from a diameter of 30 nm for pure TiO_2 down to 6 nm for CoMo35Ti solid. Note that the constant decrease in the titania particle size is not systematically associated with an increase in the surface area in relation with the modification of the porosity of the material. Between 0 and 15 wt% MoO_3, the surface area remained constant although the particle size decreased, which can be explained by the concomitant decrease in the porous volume. As regards the CoMo20Ti solid, both porous volume and particle size evolve in a way to increase the specific surface area. Above this loading, the surface area

decreases because of the loss of porous volume forming more dense material.

If the molybdenum content is increased, the evolution of the titania crystal size, surface area, and porosity is related to the presence of cobalt and molybdenum species that could prevent the growth of titanium peroxo chains, which then leads to smaller crystallites of titania with reorganized porosity in the final calcined catalyst.

Raman spectroscopy analysis of the dried and calcined solids

Dried solids were characterized by using Raman spectroscopy, and Figure 4 shows the corresponding spectra. An intense line at 518 cm^{-1} was observed together with two less intense lines at 280 and 905 cm^{-1} and a broad one in the region around

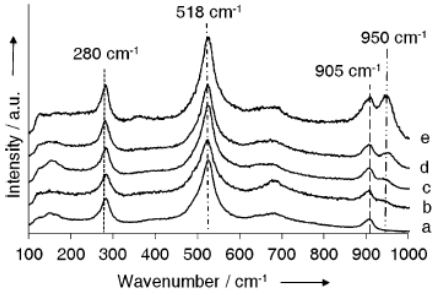

Figure 4. Raman spectra of the dried CoMo*x*Ti solids with MoO_3 loadings (*x*) of a) 0, b) 5, c) 10, d) 15, and e) 30 wt%.

660 cm^{-1}. The strong lines at 905 and 518 cm^{-1} were assigned to ν_{O-O} and ν_{Ti-O2} modes, respectively, of peroxy titanium complexes according to literature data.[32] The broad line at 660 cm^{-1} indicated the presence of a short-range order or the onset of anatase crystallization. The Raman line at 280 cm^{-1} was attributed to the lattice mode of metal octahedra.[32] If cobalt and molybdenum were present in the solids, a line appeared at 950 cm^{-1}, a characteristic of polymolybdate entities, relative intensity of which increased with the molybdenum content.

The calcined samples were also characterized by using Raman spectroscopy (see Figure 5). The presence of anatase was confirmed by the presence of the characteristic lines corresponding to the Raman-active fundamental modes at 144 cm^{-1} (E_g), 197 cm^{-1} (E_g), 399 cm^{-1} (B_{1g}), 513 cm^{-1} (A_{1g}), 519 cm^{-1} (B_{1g}), and 639 cm^{-1} (E_g) for all solids.[33,34] Raman spectra of all the oxidic catalysts demonstrate a broad line at 950 cm^{-1}, which was attributed to well-dispersed polymolybdate species.[35] From 30 wt% MoO_3, the features of bulk beta $CoMoO_4$ (338, 375, 938, and 945 cm^{-1}) were also observed. In addition to $CoMoO_4$, bulk alpha MoO_3 was identified on the CoMo40Ti sample (129, 290, 668, 819, and 994 cm^{-1}). The formation of these compounds is detrimental to the good dispersion of the molybdenum and cobalt entities and subsequently to the catalytic activity.[36,37]

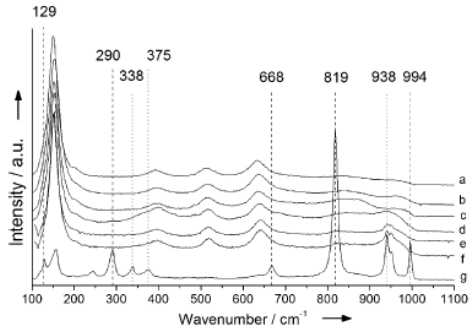

Figure 5. Raman spectra of calcined CoMo*x*Ti oxidic precursors with MoO_3 loadings (*x*) of a) 10, b) 15, c) 20, d) 25, e) 30, f) 35, and g) 40 wt%.

Characterization of the sulfided solids

TEM analysis was performed on pure TiO_2 and on sulfided samples CoMo*x*Ti ($x = 5$, 15, 25, and 35). Representative images are shown in Figure 6. On all solids, the crystalline structure of anatase was identified, with characteristic interplanar distances of 0.35 nm for the (1 0 1) family. Pure titania and CoMo5Ti demonstrated similar structures, which is in agreement with the gel formation observed during the synthesis of both solids. They showed irregularly shaped particles, with sizes between 20 and 30 nm for TiO_2 and between 10 and 20 nm for CoMo5Ti, which are in the order of magnitude of the values obtained from XRD results (see Figure 6a and b). A structure with holes can also be distinguished on these two solids. On solids with higher molybdenum content, these holes tend to disappear and smaller compact round crystalline particles were observed,

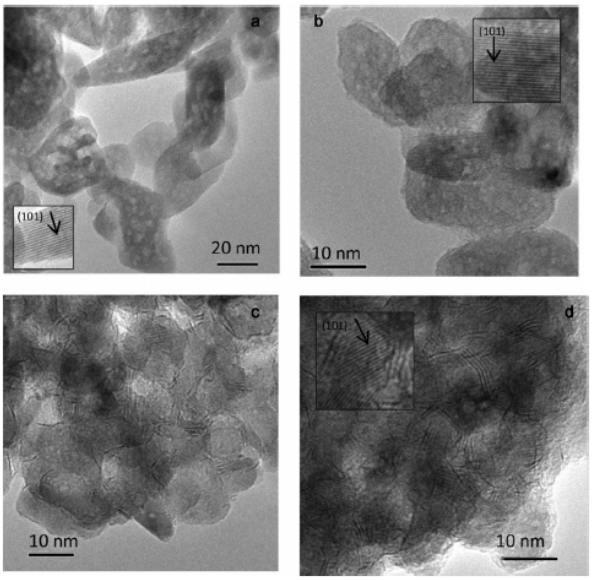

Figure 6. TEM images of pure titania and sulfided catalysts: a) TiO_2, b) CoMo5Ti, c) CoMo15Ti, and d) CoMo25Ti.

with mean diameter matching with that determined by using XRD.

The MoS_2 phase consists of a typical layered structure with a spacing of 0.6 nm between the slabs. On CoMo5Ti, no such structure could be observed by using TEM, which indicates that, on this solid, no molybdenum species were accessible for sulfidation or that the sulfided entities were too small to be detected by using this technique. On all other solids, the images revealed the presence of a layered MoS_2 phase (see Figure 6c and d). Statistics were then calculated on approximately 800 slabs to determine the distribution of size and stacking for each sample (Figures 7 and 8). The average length

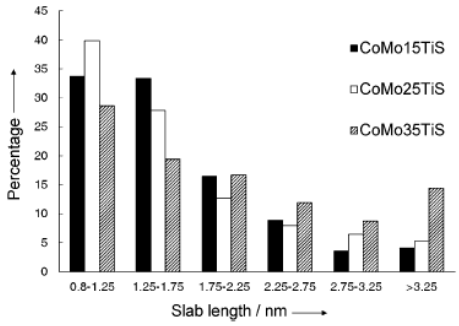

Figure 7. Distribution of MoS_2 slab lengths in the sulfided catalysts.

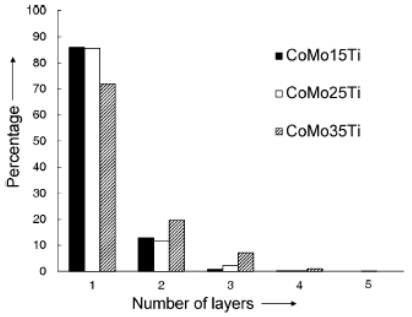

Figure 8. Stacking degree of MoS_2 slabs in the sulfided catalysts.

of the slabs (L) and the average number of layers in the slabs (N) are given in Table 2. CoMo15Ti and CoMo25Ti presented similar values for the morphology of the active phase ($L=1.7$ and 1.8 nm; $N=1.2$), whereas longer slabs with higher stacking are observed on CoMo35Ti ($L=2.2$ nm; $N=1.4$). Average stacking on TiO_2-supported catalysts was found by Mazurelle et al. to be lower than the one on alumina-supported catalysts regardless of the starting impregnated solutions,[38] which is in agreement with the dispersive properties of the titania surface.

XPS analysis of all the sulfided CoMo*x*Ti solids was performed. Regardless of the solid, the molybdenum spectra demonstrated a Mo $3d_{5/2}$ photopeak at 228.8 eV characteristic of MoS_2, as illustrated in Figure 9 on the CoMo20Ti catalyst. The I_{Mo3d}/I_{Ti2p} ratios in the sulfided solids are listed in Table 3 and

Table 2. Average length and stacking of the MoS_2 slabs in the sulfided catalysts as determined by TEM.

Sample	Average length [nm]	Average stacking
CoMo15Ti	1.7	1.2
CoMo25Ti	1.8	1.2
CoMo35Ti	2.2	1.4

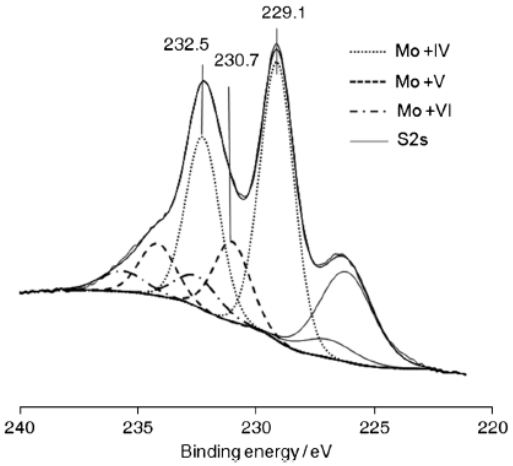

Figure 9. Example of decomposition of Mo 3d XPS spectra on sulfided CoMo20Ti.

Table 3. Atomic ratios Mo/Ti in the bulk solid and as calculated from XPS analysis in the sulfided catalysts.

Sample name	Mo/Ti (bulk)	Mo/Ti (XPS)
CoMo5Ti	0.03	0.02
CoMo15Ti	0.10	0.12
CoMo20Ti	0.15	0.16
CoMo25Ti	0.20	0.25
CoMo30Ti	0.35	0.47

compared with theoretical bulk atomic ratios. On CoMo5Ti, the Mo/Ti ratio determined from XPS analysis appears to be lower than the theoretical one, which points out the possible embedding of molybdenum species into the catalyst particles. On the solids with 15 wt% MoO_3 and above, the Mo/Ti ratio obtained by XPS analysis was always higher than the theoretical ratio, which indicates the presence of more and more molybdenum on the surface of the titania support, with the difference between the two ratios increasing with the molybdenum content.

The methodology implemented for the decomposition of the Mo 3d spectra has been described elsewhere.[39] The Mo 3d spectra were decomposed into three well-known contributions, respectively attributed to molybdenum(VI) oxide (Mo $3d_{5/2}$ BE = 233.0 eV), molybdenum(V) oxysulfide (Mo $3d_{5/2}$ BE = 230.5 eV), and molybdenum(IV) disulfide (Mo $3d_{5/2}$ BE = 228.8 eV). The decomposition of the Mo 3d spectra was per-

formed, which simulated each contribution with two peaks corresponding to the Mo $3d_{5/2}$ and Mo $3d_{3/2}$ core levels and taking into account that the binding energy difference BE(Mo $3d_{5/2}$)-BE(Mo $3d_{3/2}$) is equal to 3.15 eV, the Mo $3d_{5/2}$/Mo $3d_{3/2}$ peak area ratio is equal to 1.5, and the full-widths at half-maximum of the Mo $3d_{5/2}$ and Mo $3d_{3/2}$ peaks are almost the same. The S2s peaks that contribute to the total envelope of the Mo 3d spectra were simulated (with one peak for each sulfur type species, i.e., S^{2-} and S_2^{2-}) by taking as reference the S 2p peaks with respect to the following criteria: BE(S 2s)-BE(S 2p) = 64 eV. No peak characteristic of sulfates at 169.0 eV was observed, which is usually considered as the indication that no accidental exposure to air occurred during the transfer of the sulfided catalysts from the sulfiding reactor to the XPS machine.[39,40]

The performed decompositions enabled the determination of the sulfidation degree of molybdenum, the evolution of which, with respect to the molybdenum loading, is given in Table 4. CoMo5Ti presented a low percentage of sulfided MoS_2 together with a very high amount of oxysulfide species, which indicates that the molybdenum detected by XPS analysis is only partially sulfided. The percentage of molybdenum(V) decreased with respect to molybdenum(IV), with a maximum around 70% for CoMo20 and CoMo25Ti.

Table 4. Percentage of molybdenum(IV), molybdenum(V), and molybdenum(VI) in the sulfided catalysts as calculated from XPS.

Sample	Mo^{IV}	Mo^{V}	Mo^{VI}
CoMo5Ti	38.8	54.8	6.4
CoMo15Ti	62.3	23.2	14.5
CoMo20Ti	68.2	21.0	10.8
CoMo25Ti	68.3	22.3	9.4
CoMo30Ti	62.4	30.0	7.6

Catalytic activity

The performances of the CoMo*x*Ti catalysts were evaluated for thiophene HDS at 300 °C and atmospheric pressure after sulfidation of the oxidic precursor. These performances are to be compared with those of reference catalysts prepared by using the classical impregnation method. However, pure titania obtained through this sol–gel method showed very low water pore volume, which is the limiting parameter in the impregnation method that did not allow the impregnation of a significant amount of molybdenum. Hence, for comparison we selected in the literature catalytic performances in thiophene HDS of catalysts prepared through IWI on a commercial titania (NORPRO, with a surface area of 100 $m^2 g^{-1}$ and porous volume of 0.4 $cm^3 g^{-1}$), with molybdenum loadings varying from 2.8 to 15.0 wt% MoO_3.[38] Mazurelle et al. prepared these catalysts through simultaneous IWI of cobalt nitrate $Co(NO_3)_3 \cdot 9H_2O$ and ammonium heptamolybdate $(NH_4)_6Mo_7O_{24} \cdot 4H_2O$, with a Co/Mo atomic ratio adjusted to 0.5. The catalytic results of both sol–gel catalysts and impregnated catalysts from this reference are combined in Figure 10.

Regarding the impregnated solids, a typical evolution of the conversion versus the molybdenum loading was observed,

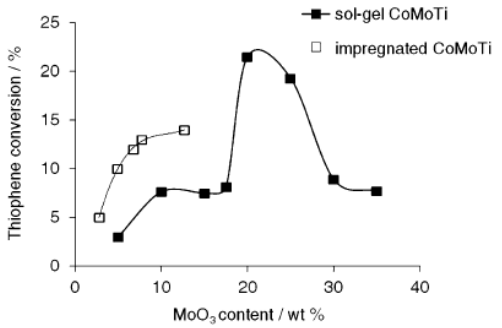

Figure 10. Thiophene hydrodesulfurization conversion versus MoO_3 content (wt%) for sol–gel CoMo*x*Ti catalysts and for impregnated catalysts.

with a gradual increase until a plateau was reached around 12 wt% MoO_3. This plateau corresponds to the dissolution limit of the starting materials inside the volume of water corresponding to the pore volume of the support considered. A further increase in molybdenum loading results in a decrease in conversion, which is associated with the formation of undesirable MoO_3 and $CoMoO_4$ species.[20,38] A very different trend was obtained with the sol–gel CoMo*x*Ti catalysts. A very low conversion of 3% is obtained on the CoMo5Ti catalyst. Between 5 and 17.5 wt% of MoO_3, the activity is slightly increased to 7–8% and remains in the same order of magnitude in this range of molybdenum loadings. A sharp increase in conversion is observed for the CoMo20Ti and CoMo25Ti catalysts, with values of 21.5 and 19.3%, respectively. If the molybdenum content was increased above 25 wt% of MoO_3, a sharp decrease down to 8.9 and 7.7%, respectively, was observed for the CoMo30Ti and CoMo35Ti catalysts.

Discussion

A series of cobalt–molybdenum–titania-based catalysts have been prepared with the titanium peroxo complex as the Ti precursor. The first step consists of the hydrolysis of $Ti(OR)_4$ with immediate precipitation of the hydrolyzed titanium species. The total contact time between the titanium precursor and water is an important parameter and has been limited to 10 min, which is presented as an optimum contact time by Van de Velde et al.[41] Balancing the hydrolysis time should result in $Ti(OH)_x(OR)_{4-x}$ ($1 \leq x \leq 3$). These partially hydrolyzed species can then be dissolved in an aqueous medium by adding hydrogen peroxide, which leads to a yellow solution, as observed in this work, which is characteristic of titanium peroxo species. Upon calcination, these species condense to form TiO_6 units in the hydrated form, which condense further to form crystalline TiO_2.[32] The rutile phase is characterized by linear chains of TiO_6 octahedra that share a pair of opposite edges, whereas in anatase each TiO_6 octahedron shares four edges with different octahedra, forming zigzag chains.[42] The pH of the starting solution determines the type of the titania phase: Zhang et al. observed that rutile was formed from pH 2 precursor solution, whereas anatase was formed from pH 4 to 9 precursor solution.[42] The presence of anatase as confirmed by XRD and

Raman analysis on the final calcined solids was then in agreement with the value of pH 4 of our starting solution.

A gradual evolution of the solution into a clear gel was observed over a period of 24 h. This viscosity increase could be explained through chain linking between the titanium peroxo species. The polymerization of these species is favored considerably because of the presence of partially hydrolyzed titanium alkoxides. For these species, good leaving groups in the form of butoxide chains are present and will drive the reaction equilibrium toward the side of polymerization species.[41] Drying of the gel led to an orange powder, which is characterized by the presence of titanium peroxo structures evidenced by Raman spectroscopy. After calcination, titania in the anatase phase was characterized by using XRD and Raman spectroscopy, which demonstrated a specific surface area of 65 $m^2 g^{-1}$, a porous volume of 0.22 $cm^3 g^{-1}$, and bimodal pore size distribution (5.2 and 14.7 nm).

During the synthesis of the CoMo5Ti solid, a clear orange solution leading to an orange gel was also observed if cobalt and molybdenum precursors were added to the H_2O_2 solution used for the dissolution of the titanium hydroxide precipitate. The corresponding calcined solid CoMo5Ti showed a bimodal pore size distribution and a N_2 adsorption–desorption isotherm similar to that of pure TiO_2. The added amount of molybdenum and cobalt does not seem to disrupt in a significant way the texture of TiO_2. However, a decrease in the titania crystal size was evidenced by XRD analysis even at this small loading, which suggests that the presence of cobalt and molybdenum species prevents the growth of titanium peroxo chains, leading then to smaller crystallites of titania in the final calcined catalyst. The poor catalytic performance of this solid in thiophene HDS (3% conversion) can be explained by a small amount of active phase on the surface of titania, as no MoS_2 slabs were evidenced by TEM analysis. Moreover, XPS analysis revealed a very low sulfidation rate of molybdenum (38.8%) together with a large proportion of oxysulfide species (54.8%). This suggests that the molybdenum species detected by using XPS are embedded into the titania matrix and are, thus, unavailable for further activation by sulfidation. This explanation is in good agreement with the values of the Mo/Ti ratio determined by using XPS, which appears to be lower than the bulk ratio. This hypothesis is also supported by the comparison of the respective catalytic performance of the sol–gel and impregnated catalysts (no bulk cobalt or molybdenum oxide or cobalt molybdate species were detected on both solids). On the impregnated catalyst with 5% MoO_3, all molybdenum is on the surface and can give potential active phase, which led to a conversion of 10% whereas only 3% conversion was obtained on the sol–gel CoMo5Ti with the same molybdenum loading.

Above 5 wt% MoO_3, a heterogeneous mixture was observed after dissolution of the titanium hydroxide precipitate by the hydrogen peroxide solution and no clear gel was obtained after maturation. Titanium peroxo species were also observed by Raman spectroscopy on the dried solids, together with polymolydate species. The texture of the calcined solids was modified as a narrow monomodal pore size distribution was observed. A continuous decrease in the crystal size was also observed. Between 5 and 20 wt% of MoO_3, the activity in thiophene HDS slightly increased to 7–8% and remained constant in this range of molybdenum loadings. If compared to the CoMo5Ti catalyst, the gain in activity can be related to a larger amount of accessible molybdenum and is in agreement with the evolution of the Mo/Ti ratio (calculated from XPS data), which is larger than the bulk ratio for this catalyst. Moreover, on the CoMo15Ti catalyst, molybdenum disulfide slabs were observed by using TEM and the molybdenum sulfidation degree reached 62%. However, as no increase in the conversion was observed on increasing the molybdenum content (in the absence of bulk cobalt, molybdenum oxide, or cobalt molybdate species as evidenced by using Raman spectroscopy), a part of molybdenum seems to be still trapped in the titania matrix in this molybdenum content range.

The best performance in thiophene HDS was obtained on the solids with 20 and 25 wt% of MoO_3 with conversions of around 20%. In contrast to the case of the impregnated catalyst, a good dispersion of the molybdate phase was evidenced by using Raman spectroscopy even at these loadings. The sulfidation degree and the morphological parameters of the active phase were similar to those on the CoMo15Ti catalyst that showed much lower conversion. This could be attributed to the availability of a large amount of total molybdenum on the surface of CoMo20Ti and CoMo25Ti solids. The exposed surface areas of the titania support were found to be 168 and 121 $m^2 g^{-1}$ for CoMo20Ti and CoMo25Ti, respectively, if expressed per gram of support. Owing to these high surface areas, a good dispersion of molybdenum and cobalt species is observed even at such significant molybdenum loadings. Moreover, the activities expressed per gram of molybdenum were similar for the optimum catalysts of both sol–gel and impregnated catalysts, with respective values of 74.7×10^{-7} and 76.6×10^{-7} $mol_{thiophene}\, s^{-1} g_{Mo}^{-1}$.

With a further increase in the molybdenum content above 25 wt% of MoO_3, a sharp decrease down to 8.9 and 7.7% was observed for the CoMo30Ti and CoMo35Ti catalysts, respectively, and could be attributed to the presence of undesirable MoO_3 and $CoMoO_4$ species, as evidenced by using XRD and Raman spectroscopy.

Conclusions

Cobalt–molybdenum–titania-based hydrodesulfurization (HDS) catalysts were prepared by using a one-pot sol–gel method with titanium peroxo complex as the Ti precursor. This new synthesis method enabled the preparation of catalysts with high molybdenum contents, as opposed to the classical impregnation method, in which the limiting parameter is the solubility of the active-phase precursors in the amount of water corresponding to the pore volume of the support. In addition, Raman analysis revealed that molybdenum and cobalt were present as well-dispersed species at molybdenum loadings as high as 20 wt%.

For molybdenum content below 5 wt.% MoO_3, a uniform gel was formed during synthesis, which suggests that molybdenum and cobalt species could be trapped and could remain

embedded in the titania matrix after calcination. This was corroborated by using XPS and TEM analysis and by the low conversion obtained for the corresponding solids in thiophene HDS.

Above MoO_3 loadings of 5 wt%, the presence of molybdenum species disrupted the gel formation and caused a rearrangement of the porous structure. Despite the increase in the sulfidation rate, the conversion remained constant in this range of loading, which indicated that probably a part of molybdenum species remained embedded.

At molybdenum content above 25 wt% MoO_3, the low values of thiophene conversion were attributed to the presence of MoO_3 and $CoMoO_4$ species.

The best performance in thiophene HDS was obtained on the solids with 20 and 25 wt% of MoO_3 with conversions of around 20%. As the sulfidation degree and morphological parameters of the active phase were similar to those of CoMo15Ti catalysts that showed much lower conversion, we propose that a large amount of total molybdenum became accessible on the surface of CoMo20Ti and CoMo25Ti solids. The exposed surface areas of the titania support increased to 168 and 121 $m^2 g^{-1}$ for CoMo20Ti and CoMo25Ti, respectively, which were high enough to allow good dispersion of molybdenum and cobalt species with no bulk MoO_3 or $CoMoO_4$ detected, even at these significant molybdenum loadings. The performance of these new catalysts was found to be superior to that of the best catalyst obtained by classical impregnation on commercial TiO_2 (≈12 wt% of MoO_3) with respective conversions of 22 and 14%. Indeed, the newly developed sol–gel-based method allows for a larger amount of well-dispersed molybdenum species to be deposited, while keeping the same activity per gram of molybdenum.

Experimental Section

Catalyst preparation

The catalysts were prepared according to the method proposed by Sonawane et al. for the synthesis of titania and modified to obtain cobalt- and molybdenum-based catalysts.[31] Titanium(IV) isopropoxide (4.8 g; Aldrich Chemicals) was hydrolyzed with deionized water (100 mL) and left under vigorous stirring for 10 min. The resulting titanium hydroxide precipitate was separated through decantation and washed thoroughly with water until the alcohol generated during the hydrolysis of titanium alkoxide was completely removed. The precipitate was dissolved in aqueous hydrogen peroxide (75 mL; 30% *v/v*, Qualigen), which resulted in an exothermic reaction. Addition of water (200 mL) was necessary to mitigate this reaction and to avoid the development of a highly viscous polymeric gel phase. A clear yellow solution, characteristic of a titanium peroxo complex, was obtained within 30 min. In the case of molybdenum- and cobalt-containing solids, MoO_3 and $CoCO_3$ were dissolved in the hydrogen peroxide solution; their quantities were adjusted to obtain the required MoO_3 loading together with a Co/Mo ratio of 0.5 on the calcined oxide precursor. After maturation for 5 days and drying of the gel at 100 °C, the resulting powders were calcined under air flow at 500 °C for 3 h (heating rate: 1 °C min^{-1}.

Note that the titanium peroxide solution evolves to form a very uniform yellow transparent gel; if molybdenum was added during synthesis, the gel homogeneity was maintained for molybdenum content below 5%. For molybdenum content above 5%, the apparition of denser flocks was observed during the maturation step in peroxide solution and even finely dispersed particles at high molybdenum loadings. The resulting mixtures were dried and calcined according to the protocol used for cobalt- and molybdenum-free gel.

All the catalysts were similarly activated through sulfidation under atmospheric pressure of the oxidic precursors at 400 °C for 2 h (heating rate: 6 °C min^{-1}) under a flow of 10 vol% H_2S in H_2 (flow rate: 60 mL min^{-1}).

The prepared solids were named CoMo*x*Ti, in which *x* is the molybdenum content expressed as wt% MoO_3 in the calcined solid.

Physical characterization

N_2 adsorption–desorption isotherms were recorded at −196 °C by using an automated ASAP2010 instrument from Micrometrics. Before each run, a known mass of sample (≈0.200 g) was heated at 350 °C for 3 h under vacuum. Specific surface areas were calculated from the linear part of the BET line. Pore size distributions were obtained by applying the BJH equation to the desorption branch of the isotherm. The total pore volume was estimated from the N_2 uptake at a $P/P_0 = 0.995$. On the CoMo40Ti sample, only the specific surface area was calculated by using the single-point BET method on a Micromeritics Flowsorb instrument after desorption at 200 °C for 30 min under a flow of 30% N_2 in helium.

Powder X-ray diffraction patterns of the samples were collected on a SIEMENS D5000 diffractometer equipped with a CuK_α anticathode ($\lambda = 1.5406$ Å). The diffractograms were recorded for 2θ between 10 and 80° by using a 0.1° step with an integration time of 4 s. Phase identification was performed by comparison with the JCPDS database.

To check the dispersion of the molybdate phase, the Raman spectra of the oxidic precursors were recorded at RT by using a Raman microprobe Infinity from Jobin–Yvon equipped with a N_2-cooled charge-coupled device detector. The exciting laser source was the 532 nm line of the Nd:YAG laser.

TEM was used to determine the morphology of the solids and to evaluate the repartition in size and stacking of the MoS_2 slabs present on the sulfided catalysts. The TEM pictures were taken on a TECNAI electron microscope operating at an accelerating voltage of 200 kV. Before analysis, the powders were ultrasonically dispersed in ethanol. Two drops of ethanol containing the solid were then deposited on a carbon–copper grid.

The solids in the sulfided form were characterized by using XPS. Preparation of XPS specimen was performed under argon atmosphere in a glove box to avoid any reoxidation of the solids. The powdered samples were pressed into an indium foil attached to the sample holder, which was introduced directly in the XPS spectrometer through the connection of the glove box to the XPS transfer chamber of the spectrometer. The XPS spectra were recorded by using a VG ESCALAB 220 XL spectrometer equipped with a monochromatic AlK_α ($E = 1486.6$ eV) X-ray source. The surface atomic ratios I_{Mo3d}/I_{Ti2p} were calculated by using the VG Eclipse software after subtracting the nonlinear Shirley background and the contribution of the S2s signal to the Mo3d signal. The Mo3d spectra were decomposed by using an interactive least-squares

program, and the fitting peaks of the experimental curves were defined by using a combination of Gaussian (70%) and Lorentzian (30%) distributions.[39]

Thiophene catalytic test

Thiophene is the simplest molecule representative of the aromatic sulfur compounds present in the feeds to be treated and the HDS of thiophene under atmospheric pressure of H_2 is used commonly as a reference HDS test to initially evaluate the potential of catalysts.[43]

The tests were performed at atmospheric pressure in a flow-type reactor packed with 0.2 g of the catalyst. Before reaction, the oxidic precursor was sulfided as described above. The reactor was then naturally cooled to the reaction temperature of 300 °C under the sulfidation mixture. Thiophene, which was previously purified by two successive vacuum distillations, was introduced in the reactor at a constant pressure of 6.65 kPa in a flow of hydrogen (total flow rate: 20 mL min^{-1}). Reactants and products (butane, but-1-ene, *trans*-but-2-ene, *cis*-but-2-ene) were analyzed by using a gas chromatograph equipped with a flame ionization detector and a PLOT alumina column. Taking into account the relative response factor for each compound, the conversion α was calculated by using Equation (1):

$$\alpha = \frac{\sum_{i=1}^{4} a_i/4}{(a_{thio}/3.4) + \sum_{i=1}^{4} a_i/4} \quad (1)$$

in which a_i is the peak area of product i and a_{thio} is the peak area of thiophene.

Conversion values are reported after 4 h of reaction; all catalysts show a stabilized activity after 3 h.

Acknowledgements

We gratefully acknowledge Mrs. L. Burylo, Mrs. M. Trentesaux, and Dr. M. A. Baurain who conducted XRD and XPS measurements, and Mr. Gérard Cambien of the ECL, Villeneuve d'Ascq, who kindly recorded the N_2 adsorption–desorption isotherms of our solids. The TEM facility in Lille, France, is supported by the Conseil Regional du Nord-Pas de Calais and the European Regional Development Fund. This work was performed as part of a collaboration under the International Associated Laboratory program between UCCS (CNRS) and NCL (CSIR).

Keywords: cobalt · heterogeneous catalysis · molybdenum · sol–gel process · titanium

[1] S. Dzwigaj, C. Louis, M. Breysse, M. Cattenot, V. Bellière, C. Geantet, M. Vrinat, P. Blanchard, E. Payen, S. Inoue, H. Kudod, Y. Yoshimura, *Appl. Catal. B* **2003**, *41*, 181–191.
[2] J. Ramirez, I. Ruiz-Ramirez, L. Cedeno, V. Harlé, M. Vrinat, M. Breysse, *Appl. Catal. A* **1993**, *93*, 163–180.
[3] C. Arrouvel, M. Breysse, H. Toulhoat, P. Raybaud, *J. Catal.* **2005**, *232*, 161–178.
[4] D. Costa, C. Arrouvel, M. Breysse, H. Toulhoat, P. Raybaud, *J. Catal.* **2007**, *246*, 325–343.
[5] N. Bejenaru, C. Lancelot, P. Blanchard, C. Lamonier, L. Rouleau, E. Payen, F. Dumeignil, S. Royer, *Chem. Mater.* **2009**, *21*, 522–533.
[6] F. Dumeignil, K. Sato, M. Imamura, N. Matsubayashi, E. Payen, H. Shimada, *Appl. Catal. A* **2005**, *287*, 135–145.
[7] L. Cedeño, R. Zanella, J. Ramírez, H. Mendoza, G. Hernández, P. Schacht, *Catal. Today* **2004**, *98*, 83–89.
[8] A. M. Venezia, V. La Parola, G. Deganello, D. Cauzzi, G. Leonardi, G. Predieri, *Appl. Catal. A* **2002**, *229*, 261–271.
[9] W. Huang, A. Duan, Z. Zhao, G. Wan, G. Jiang, T. Dou, K. H. Chung, J. Liu, *Catal. Today* **2008**, *131*, 314–321.
[10] A. Duan, R. Li, G. Jiang, J. Gao, Z. Zhao, G. Wan, D. Zhang, W. Huang, K. H. Chung, *Catal. Today* **2009**, *140*, 187–191.
[11] A. A. Cecílio, S. H. Pulcinelli, C. V. Santilli, Y. Maniette, V. Teixeira da Silva, *J. Sol-Gel Sci. Technol.* **2004**, *31*, 87–93.
[12] Y. Wang, H. Zhong, L. Jiang, *Petroleum Processing and Petrochemicals* **2008**, *39*, 11–15.
[13] V. La Parola, G. Deganello, A. M. Venezia, *Appl. Catal. A* **2004**, *260*, 237–247.
[14] S. Chen, L. Lao, X. Cheng, *Indian J. Chem. Technol.* **2009**, *16*, 272–277.
[15] Z. Zhang, Y. Zhou, S. Zhang, C. Xu, *Energy Fuels* **2006**, *20*, 2293–2298.
[16] S. K. Maity, M. S. Rana, S. K. Bej, J. Ancheyta-Juárez, G. Murali Dhar, T. R. S. Prasada Rao, *Catal. Lett.* **2001**, *72*, 115–119.
[17] M. C. Barrera, C. Marín, M. Viniegra, J. A. De Los Reyes, J. G. Pacheco, F. Murrieta, *Pet. Sci. Technol.* **2004**, *22*, 87–101.
[18] M. C. Barrera, M. Viniegra, J. Escobar, M. Vrinat, J. A. De Los Reyes, F. Murrieta, J. García, *Catal. Today* **2004**, *98*, 131–139.
[19] M. C. Barrera, J. Escobar, J. A. de los Reyes, M. A. Cortés, M. Viniegra, A. Hernández, *Catal. Today* **2006**, *116*, 498–504.
[20] L. Le Bihan, C. Mauchaussé, L. Duhamel, J. Grimblot, E. Payen, *J. Sol-Gel Sci. Technol.* **1994**, *2*, 837–842.
[21] L. Le Bihan, C. Mauchaussé, E. Payen, J. Grimblot, *Stud. Surf. Sci. Catal.* **1999**, *127*, 105–112.
[22] F. Dumeignil, J. Grimblot, *Stud. Surf. Sci. Catal.* **1999**, *127*, 357–360.
[23] R. Iwamoto, J. Grimblot, *Stud. Surf. Sci. Catal.* **1997**, *106*, 195–210.
[24] J. Quartararo, J. P. Amoureux, J. Grimblot, *J. Mol. Catal. A-Chem.* **2000**, *162*, 345–35.
[25] R. Iwamoto, J. Grimblot, *Stud. Surf. Sci. Catal.* **1999**, *127*, 169–176.
[26] R. Iwamoto, J. Grimblot, *Stud. Surf. Sci. Catal.* **1999**, *121*, 289–294.
[27] C. Flego, V. Arrigoni, M. Ferrari, R. Riva, L. Zanibelli, *Catal. Today* **2001**, *65*, 265–270.
[28] Y. Minato, K. Aoki, M. Shirai, M. Arai, *Appl. Catal. A* **2001**, *209*, 79–84.
[29] E. Rivera-Muñoz, D. Lardizabal, G. Alonso, A. Aguilar, M. H. Siadati, R. R. Chianelli, *Catal. Lett.* **2003**, *85*, 147–151.
[30] E. Rivera-Muñoz, G. Alonso, M. H. Siadati, R. R. Chianelli, *Catal. Lett.* **2004**, *94*, 199–204.
[31] R. S. Sonawane, S. G. Hegde, M. K. Dongare, *Mater. Chem. Phys.* **2003**, *77*, 744–750.
[32] S. I. Seok, M. Vithal, J. A. Chang, *J. Colloid Interface Sci.* **2010**, *346*, 66–71.
[33] J. Zou, J. Gao, F. Xie, *J. Alloys Compd.* **2010**, *497*, 420–427.
[34] K. Porkodi, S. D. Arokiamary, *Mater. Charact.* **2007**, *58*, 495–503.
[35] S. Kasztelan, J. Grimblot, J. P. Bonnelle, E. Payen, H. Toulhoat, Y. Jacquin, *Appl. Catal.* **1983**, *7*, 91–112.
[36] J. A. R. van Veen, E. Gerkema, A. M. van der Kraan, P. A. J. M. Hendriks, H. Beens, *J. Catal.* **1992**, *133*, 112–123.
[37] P. Mazoyer, C. Geantet, F. Diehl, S. Loridant, M. Lacroix, *Catal. Today* **2008**, *130*, 75–79.
[38] J. Mazurelle, C. Lamonier, C. Lancelot, E. Payen, C. Pichon, D. Guillaume, *Catal. Today* **2008**, *130*, 41–49.
[39] N. Frizi, P. Blanchard, E. Payen, P. Baranek, C. Lancelot, M. Rebeilleau, C. Dupuy, J. P. Dath, *Catal. Today* **2008**, *130*, 32–40.
[40] D.-Y. Yu, J.-A. Wang, J.-L. Ou Yang, *Thin Solid Films* **1997**, *293*, 1–5.
[41] N. Van de Velde, M. Arin, P. Lommens, D. Poelman, I. Van Driessche, *Thin Solid Films* **2011**, *519*, 3475–3479.
[42] W. Zhang, S. Chen, S. Yu, Y. Yin, *J. Cryst. Growth* **2007**, *308*, 122–129.
[43] M. J. Ledoux, C. P. Huu, F. Luck, *J. Catal.* **1990**, *121*, 70–76.

Received: March 21, 2012
Revised: May 22, 2012
Published online on September 27, 2012

3. Conclusion

One-pot sol-gel HDS anatase-supported catalysts were prepared with different Mo loading. This method allow us to avoid the recurrent problem of solubility in precursor solution found in classical insipient wetness impregnation, namely, the solubility of the active phase precursor solution in the amount of water corresponding to the pore volume of the support. Thus, the method allow us to prepare solids with higher molybdenum contents.

As expected, the Mo loading change the textural properties of the prepared solids. For instance, as we increase the loading, we increase the specific surface area, the pore volume, the diameter pore, etc. An optimal loading of 20% in wt.% MoO_3 is observed and higher loadings do not improve such properties, likely due to the presence of bulk MoO_3 and $CoMoO_4$ species detected by Raman spectroscopy and XRD. For the optimal 20% wt.% solid, surface specific area is equal to 168 m^2/g, the pore volume is 0.21 cm^3/g and the pore diameter is equals to 5.5 nm. Further, catalytic activity present a singular behavior with a peak of activity for 20% wt.% catalyst. The conversion values on activity for such sample were higher than conversion of equivalent catalysts prepared by classical insipient wetness impregnation supported on commercial titania with specific surface area of 100 m^2/g and pore volume of 0.4 cm^3/g.

Analysis of the active phase by TEM and XPS revealed very low degree of sulfidation in lower Mo loading catalysts, which corroborates with low catalytic activity for these samples. Such results suggest that in these solids, part of the Mo species are embedded in the support matrix. For 20% wt. MoO_3 catalyst, the degree of sulfidation (measured by the percentage of Mo^{IV} species) were higher, about 70%, and TEM revealed low stacking degree (about 1.0). In solids with higher Mo loading values, the poor catalytic activity was attributed to the presence of undesirable bulk MoO_3 and $CoMoO_4$ (that do not suffer sulfidation easily).

The one-pot sol-gel method proved to be suitable to produce HDS catalysts with large Mo loading and better activity. In the next chapter, we will show further results on the characterization of this series that complement results obtained so far, such as XPS studies of the oxide phase in Co and Mo region and low-energy ion spectroscopy (LEIS). Moreover, we describe X-ray absorption spectroscopy (XAS) ex situ and in situ results, which will allow us to describe finely the local atomic structure of the oxide precursors and the sulfided phase. Further, we compare the structure with impregnated catalyst supported on TiO_2 with higher specific surface area (200 m^2/g). As it will be detailed in the next chapter, such enhanced support serves to overcome the limit of Mo-species solubility imposed by pore volume of the support in order to achieve a large Mo loading.

Chapter V: From Oxide Precursor to Active Phase

Table of Contents

1. Introduction

In this chapter, we are interested firstly to present complementary results from oxide phase characterization of the catalysts that were not included in the previous chapter. Here we will deal with both HDS series of Co-promoted Mo-based catalysts supported on TiO_2, i.e., the one synthesized via sol-gel and the other one synthesized by classic impregnation method.

Since the two methods give us distinct catalytic behavior, a detailed description of oxide phase may reveal important clues that lead to deeper insight on the structure of active phase and thereafter, the catalytic activity. In this picture, for sol-gel and impregnated series, we consider XAFS measurements from oxide phase and we discuss the structural atomic arrangement and the differences among them.

As the main important part of this chapter, we present all *in situ* XAFS measurements of activation phase for both series of catalysts. At this point, our focus is fixed in a qualitative description of the activation process and a full description of the active phase of the catalysts, say a "classical" XAFS analysis of the problem. We let for the next chapter, where we deal with MCR-ALS calculations, the detailed depiction of the activation step itself and anything else that we can take from that analysis, such as concentration profiles and formation of intermediate compounds as well as the structural description of such compounds.

2. Catalytic Description and Complementary Characterization

The set of CoMo-based catalysts used in this work is reported on Table 7. Whatever the samples, its name carries a code related to its method of preparation. Thus, those prepared by one-pot sol-gel method received a SG before a number, while those prepared by impregnation received a HMA (due to the precursor salt used in the impregnation solution, the Ammonium Heptamolybdate). The number is related to the MoO_3 percentage in weight to the total catalytic mass. Thereby, we have two series of catalysts prepared with equivalent (and increasing) Mo loadings. This evolution in Mo loading will enable us to probe changes in structure (and, eventually, in a differentiation in start compound) due to this Mo increasing to the final structure. By knowing the dynamics of the structural genesis at atomic level, we may be able to tailor the active phase in order to improve the catalytic efficiency. In addition, we prepared two samples for the optimal Mo loading without the promotor, namely, SG-Mo20 and HMA-Mo20. They will be helpful in the structural study and may provide comparative information when dealing with the fine interpretation of the spectra (particularly, the XAFS ones). Eventually, we

will also display data for higher Mo loadings in sol-gel preparation, such as SG-25 and SG-30, respectively, catalysts prepared with 25 and 30 % in wt. of MoO_3. However, we stress that, since MoO_3 and $CoMoO_4$ bulk phases were identified in these samples, we consider that they do not represent a new structure compared to lower Mo loading and, thus, they will not bring novel information, particularly to atomic structural characterization.

Table 7 - Summary of samples used on this study.

Method of Preparation	**Precursors**	**Name**	**% wt. of MoO_3**	**XAFS *ex situ***	**XAFS *in situ***	
					Mo K-edge	Co K-edge
One-Pot Sol-Gel	MoO_3 + $CoCO_3$	SG-5	5	X[a]	X[b]	X
		SG-10	10	X	X	X
		SG-15	15	X[a]	X	X
		SG-20	20	X[a]	X[b]	X
		SG-25	25	-	-	-
		SG-30	30	-	-	-

Method of Preparation	**Precursors**	**Name**	**% wt. of MoO_3**	**XAFS *ex situ***	**XAFS *in situ***	
					Mo K-edge	Co K-edge
IWI	HMA + Co-Nitrate	HMA-5	5	X	X[b]	X
		HMA-10	10			
		HMA-15	15	X		
		HMA-20	20	X	X[b]	X

[a] - *It was recorded XAFS spectra for both dried and calcined samples.*
[b] - *In these samples, we also performed in situ Temperature Programed Reduction (TPR).*

As it was shown in the previous chapter, the performance of the catalysts were evaluated in HDS reaction of thiophene at 300 °C and atmospheric pressure after sulfidation of the oxide precursors (a general scheme is indicated in Figure V.*1*a, the experimental details are detailed in the previous chapter). The catalytic activity behavior is quite different depending on the method of preparation, as it was discussed is the previous chapter. Here, we present the same results with an additional test included, the one for impregnated CoMo catalysts prepared via simultaneous IWI supported in a commercial high specific surface area (SSA) TiO_2 (200 m^2/g) (green triangles in Figure V.*1*b).

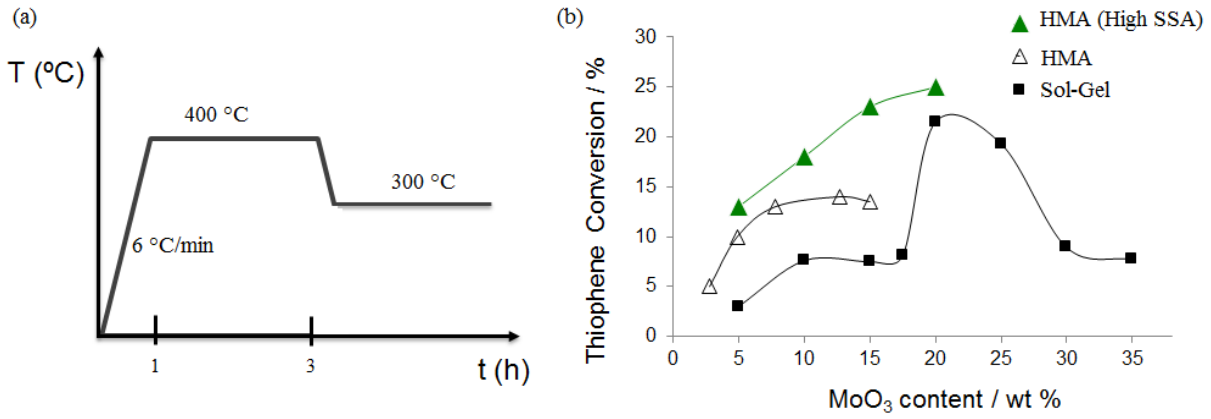

Figure V.1 - (a) General scheme for activation (at 400 °C, 1 atm) and sulfidation (at 300 °C, 1 atm) steps. (b) Catalytic activity for three series of catalysts as function of the Mo loading: green triangles, impregnated HMA catalysts supported in commercial TiO_2 with high SSA (200 m^2/g); white triangles, impregnated HMA catalysts in lower SSA TiO_2 (100 m2/g); black squares, one-pot sol-gel catalysts.

As previously discussed, for the impregnated catalysts one observes a behavior that first increase with the Mo loading and then stabilizes in a plateau from a certain Mo loading value. In fact, in the additional test, we observe a similar trend; at 20% in weight of MoO_3 the catalyst supported in TiO_2 with high SSA seems to achieve its maximum value in conversion. It is interesting to note that for the one-pot sol-gel catalysts the typical value for SSA measured by BET is 100 m^2/g except for the SG-20, which have a SSA of 168 m^2/g. Thus, we decided to take into account these catalysts in higher SSA support for reference purposes, first for overcoming limit of solubility imposed by pore volume of the support, secondly because regarding the catalytic activity (particularly for 20% of Mo loading), we believe that the atomic structure may be closer to such higher SSA catalysts.

2.1. Sol-gel Route and Impregnation Method

The steps used in the catalytic preparation via one-pot sol-gel method are described at the previous chapter. Even so, a general scheme of catalyst preparation via one-pot sol-gel is illustrated in Figure V.2. Since the main goal of this thesis is to describe the atomic structure evolution with the Mo loading, we will focus our attention up to where the point in catalytic activity is prominent, i.e., the catalysts with 20% wt. of MoO_3. After this limit, with a further increase in the molybdenum content the catalytic activity experiment a sharp decrease, which is attributed to the presence of bulk MoO_3 and $CoMoO_4$ species.

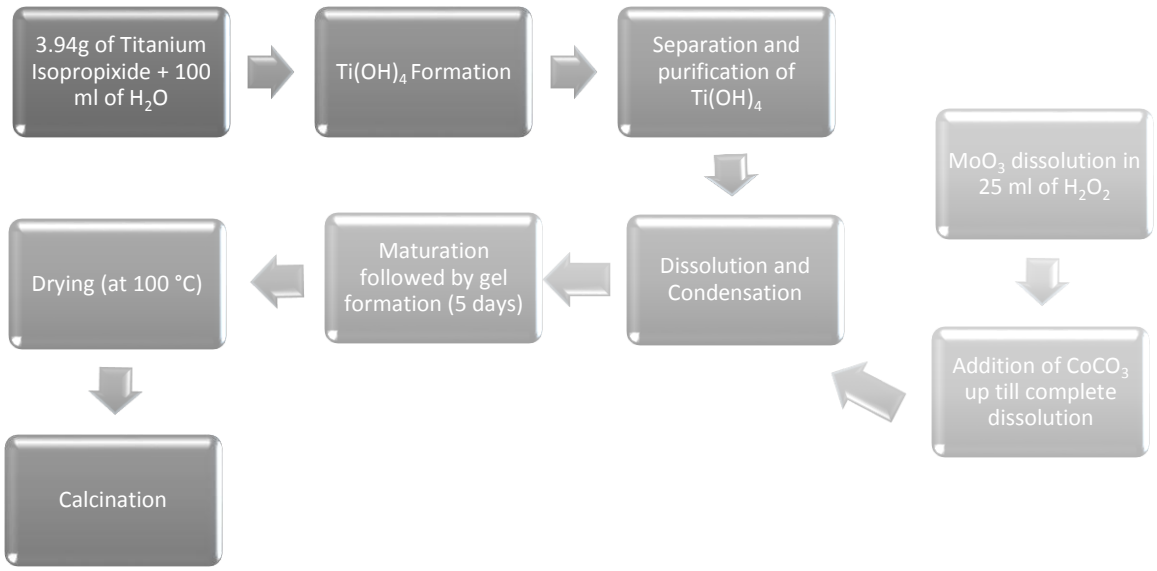

Figure V.2 - General scheme for catalyst preparation via one-pot sol-gel method.

As early stated, one can see distinct aspects in the solutions used in order to prepare one-pot sol-gel catalysts, while precursor solution for SG-5 forms an orange-yellow gel, just like the yellow gel formation after maturation of dissolution of the hydrolyzed titanium species in hydrogen peroxide, for SG-10 we observe a single "cloudy" phase (but not a gel) solution. For higher Mo loading precursor solutions a heterogeneous mixture is observed. Particularly, for higher Mo loadings (namely, SG-15 and SG-20), Raman spectroscopy of the "solid" part (the precipitate we find at the bottom of the maturation container) in the heterogeneous solution is dominated by Rutile-TiO_2 peaks. After calcination, this structure clearly evolves to pure anatase-TiO_2 (as pointed by XRD). As complementary data, we show the Raman spectrum for SG-5 sample after calcination (Figure V.3a). Similar features is observed as to the other samples from sol-gel series (see previous chapter); the spectrum is dominated by single phase Anatase-TiO_2 (with characteristic lines at 144, 197, 399, 513, 519 and 639 cm^{-1}). No bulk evidence of $CoMoO_4$ or MoO_3 was found.

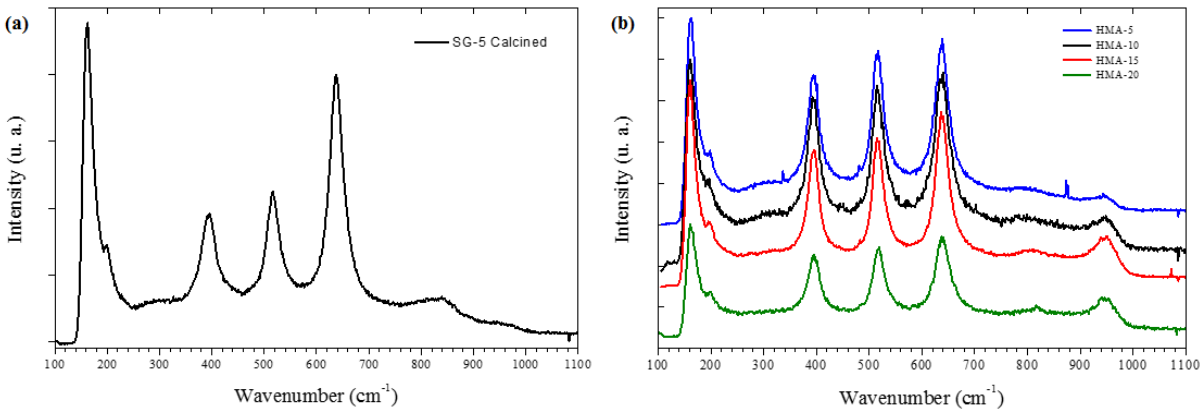

Figure V.3 - Raman spectrum for (a) SG-5 sample after calcination and (b) for impregnated series catalysts after calcination; blue (HMA-5), black (HMA-10), red (HMA-15), green (HMA-20).

In order to have a sort of "reference" (in atomic arrangement and catalytic activity) for the one-pot sol-gel catalysts we prepared impregnated catalysts by simultaneous Incipient Wetness Impregnation (IWI). A solution of Ammonium Hepatmolybdate Tetrahydrate (HMA, with linear formula $(NH_4)Mo_7O_{24}\cdot 4H_2O$, ≥ 99.0%, from Sigma-Aldrich®), Cobalt(II) Nitrate Hexahydrate (with linear formula $Co(NO_3)_2\cdot 6H2O$, ≥ 99.0%, from Fluka/Sigma-Aldrich®) and double distillated water was used to impregnate a commercial Titanium (IV) Oxide with specific surface area of 200 m^2/g. The solutions were made in order to keep the Co/Mo atomic ratio equals to 0.5. Since the former impregnated catalysts used for comparison features low SSA (and pore volume), this new series is closer to sol-gel series, or at least, gives us an upper range with respect to the physical characteristics.

All solids were dried in oven for one night at 100 °C and then, calcined inside a reactor cell in air flux at 500 °C with a ramp of 1 °C/min for 4h. The next step was the activation, where the oxide precursor becomes the active phase. For that, the sample is placed in a reactor and a mixed gas flow (9/1 ratio of H_2/H_2S) pass through it while the temperature increase in a fixed rate (see scheme in Figure V.*1*a).

Raman spectra after calcination step was recorded for HMA series (Figure V.*3*b). As for sol-gel series, the anatase-TiO_2 peaks are evident. Prominent peak around 950 cm^{-1} is characteristic of the preparation method and the oxide precursors [1], and the small and discrete feature in 819 cm^{-1} may indicate some MoO_3 bulk on the sample instead of well dispersed polymolybdate species.

2.2. Surface Characterization of the Catalysts: LEIS and XPS Spectroscopy

Surface analysis such XPS and LEIS can provide us useful information concern the oxide phase. While XPS is useful in order to differentiate chemical species (particularly useful in sulfided state), the high sensibility to first atomic layer of LEIS can, in theory, provide a more realistic coverage ratio of the sample. It is important to say that LEIS is still a developing technique, i.e., many aspects of quantification theory are still under discussion [2][3][4][5]. New machines with highest sensibility are now available and the influence (mainly) of analyzer, reionized ions contribution to total signal, matrix effects or scattering profile are some of the issues. Thus, LEIS and XPS results may strongly diverge, particularly if a well-planned experiment and careful data analysis was not taken into account. Furthermore, in spite of the fact that both techniques are related to the surface, there is an important conceptual difference between them, which is related to the depth analysis regarded by each one. They are not the same and this is a sufficient condition to produce differences in analysis. Thereby, we stress that our focus on LEIS results in this section is just to present the technique, show some first results and to discuss the possibilities and perspectives of using LEIS as a tool in catalysts studies. Additionally, selected XPS spectra sulfidation state are discussed for both series.

2.2.1. Low-Energy Ion Scattering

Dried sol-gel catalysts were submitted to LEIS in order to compare outmost layer features as function of Mo loading (Figure V.*4*). The peaks of oxygen, titanium and molybdenum are clearly resolved no matter the sample. These peaks are located at 1155 eV (O), 2100 eV (Ti) and 2455 eV (Mo). Co peak are expected at 2255 eV, but since it is located between two intense peaks (Ti and Mo) it is masked by them, and to evaluate its position (as well quantify it) becomes problematic.

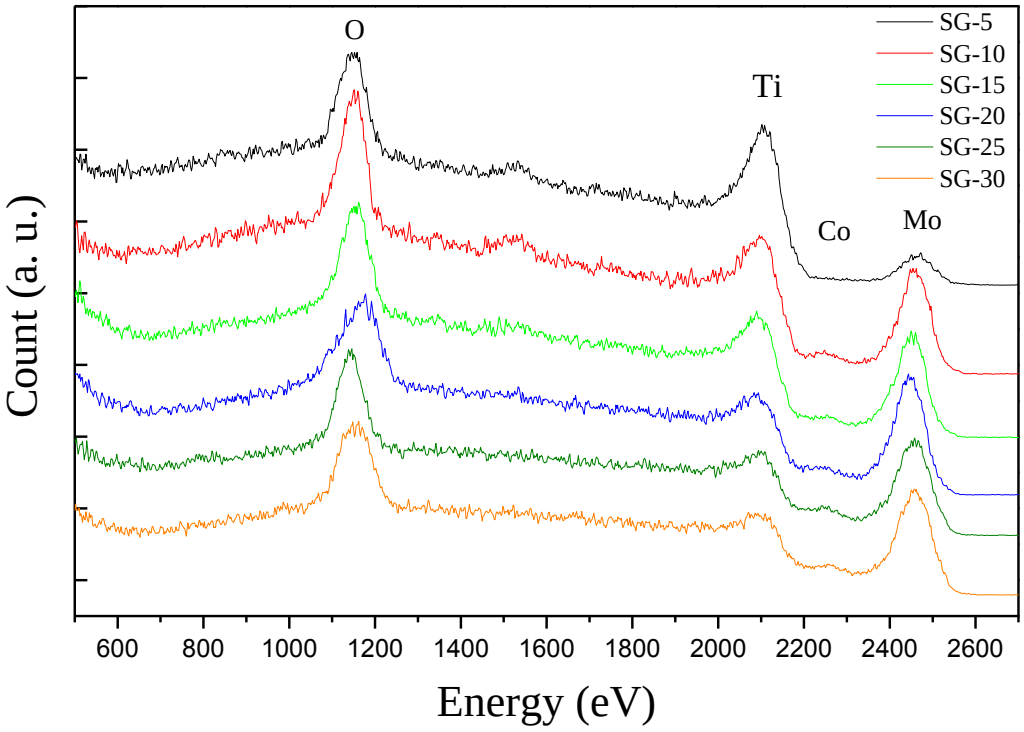

Figure V.4 - LEIS spectra for dried sol-gel catalysts supported in anatase-TiO_2 ($^4He^+$, primary energy 3 keV).

Four samples can be stored simultaneously on the carousel in the UHV-chamber (Figure V.5). This set up allows for analysis of different samples under identical experimental conditions. Consequently, normalization of the scattered intensity to that of the support is unnecessary. In the energy spectra, the peak height is taken as a measure for the scattered intensity. However, the final results are identical if peak areas are used instead. Whatever the case, background subtraction was performed.

Considering the doses yield by the beam ($5.6 \times 10^{-14}/cm^2$), a rough estimate of the surface erosion during analysis indicates that in this period only a small fraction of the outermost layer has been eroded, namely, 0.05 of one monolayer after the first scan.

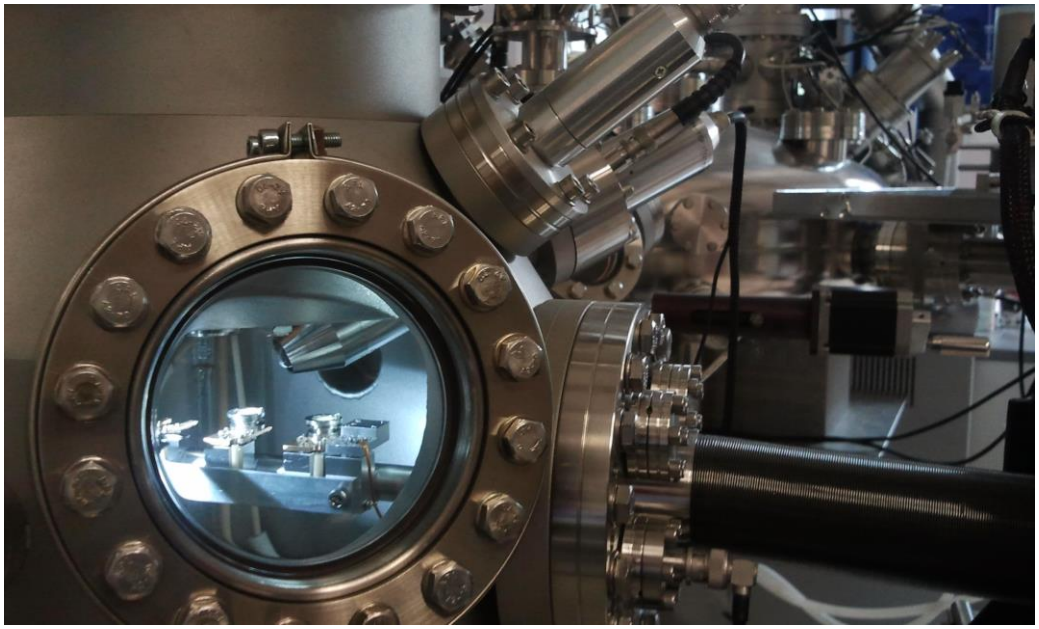

Figure V.5 - LEIS analysis chamber of the setup used in this work.

Usually in LEIS measurements more than one scan is taken for each sample. In our case, we recorded seven scans for each dried catalyst in both series. Analysis of the scans are twofold, at one hand if we consider the first one as more representative of the first atomic monolayer (as long it did not suffered the effects of ion dose degradation), it may contains external impurities that can be detected due high LEIS sensibility. At the other hand, the more we "clean" the surface sputtering it with the ionic beam, the more we cause surface erosion bombarding the surface with this beam. This evolving process for selected samples is showed in Figure V.*6*. At low ion doses, the Ti intensity constantly increases with time, while the Mo signal experiments a slight (but slower than Ti) increase in intensity for the first three scans and after that, it remains constant. The oxygen signal behaves similar as the Ti signal. This general trend is true for all the catalysts no matter the method of preparation, except for sol-gel 5, 10 and 15% of Mo loading, where the intensity of Mo peaks do not seem to change during all the experiment. For these low Mo loading sol-gel solids, it may indicates that a part of Mo species is inserted into the TiO_2 matrix, but a quantification of this statement is not possible.

Still concerning the time evolution of LEIS spectra, we can point out another remarkable feature that indicates great difference between the two preparation methods. We see clearly from Figure V.*6* that while for low Mo loading one sees the presence of Ti peak, for 20% catalysts this peak is null at the beginning. It is also true, however, that in SG-20 a little shoulder (black arrows on right column of the Figure V.*6*) in Ti peak at the first scan may indicate that the surface of the support is not entirely covered by the catalyst precursor. Finally, whatever the Mo-loading, intensity ratio Mo/Ti in impregnated catalysts are greater than in sol-gel samples, which highlight that in impregnated catalysts the presence of Mo species in surface is more evident compared to sol-gel solids.

In addition to that, in these sol-gel samples, a spurious peak around 1500 eV is found and it can be attributed to sodium atoms. Since the samples were analyzed before calcination, i.e., dried, this trace of sodium may come from the large amount of water used during preparation of the precursors (200 ml). Distilled water was used, but a better option could be the using of double deionized water.

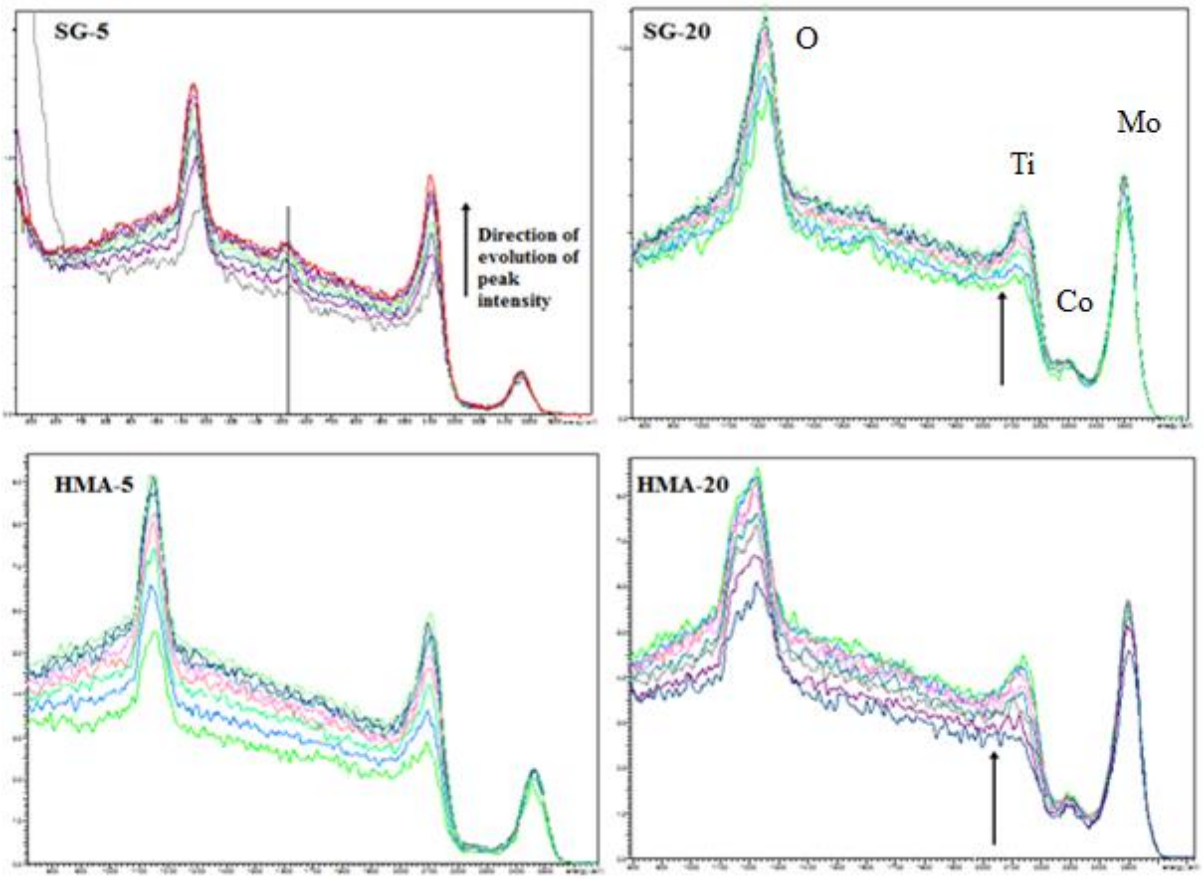

Figure V.6 - LEIS spectra scan evolution for selected samples. The first scan is lower in intensity and its evolution follows the direction of the arrow. For SG-5 it is marked the position of spurious peak.

The initial and progressive increase of the Ti and O peak intensities at Figure V.6 indicates that these atoms are initially partly shielded by some other elements. The removal of these elements proceeds very rapidly. We recall once again that LEIS spectra were recorded for dried samples thus, the presence of impurity is not surprising. It seems, therefore, reasonable to identify the shielding element as light species, such as carboneous species in which hydrogen terminations is also presented (usually in the form of hydroxides). In the energy spectra these elements cannot be observed, likely the background below oxygen peak masks them. Additionally, we can state (expect) that in contrast to molybdenum, titanium is more susceptible to be shielded by such carboneous species.

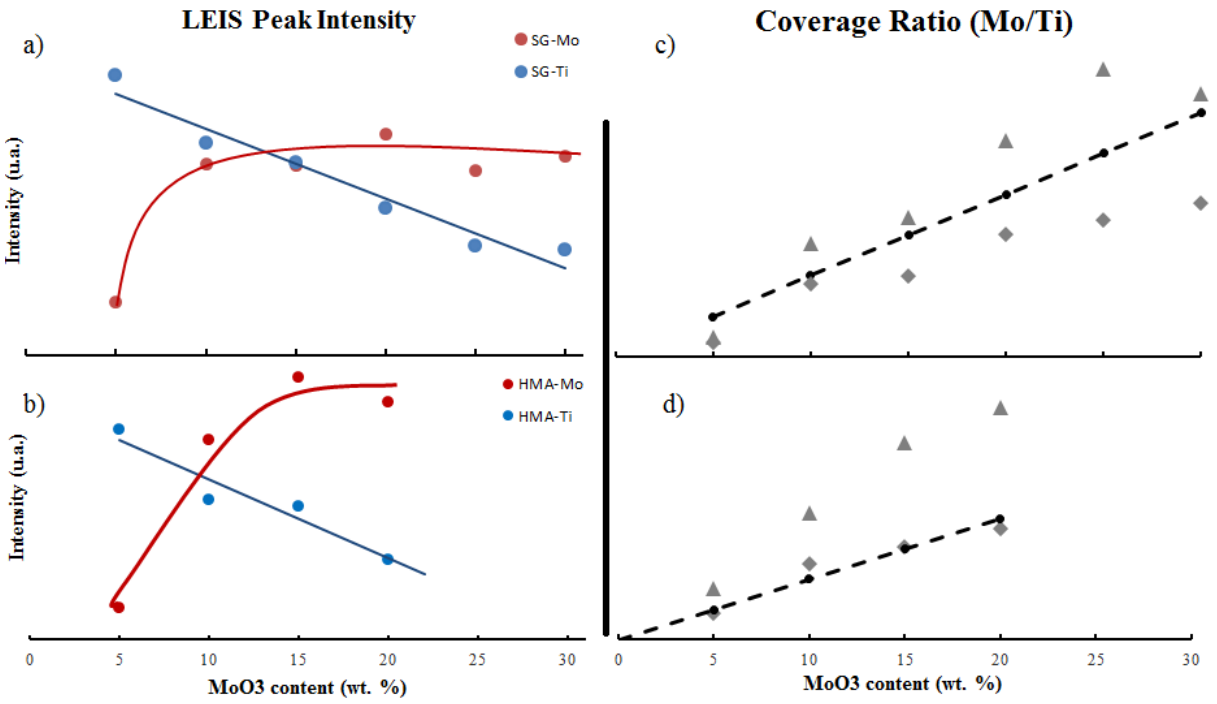

Figure V.7 - (Left panel) LEIS Mo (red dot) and Ti (blue dot) peak intensity (scan 7) as function of MoO_3 content for (a) sol-gel catalysts and (b) impregnated catalysts. (Right panel) Coverage ratio (Mo/Ti) for different LEIS scans (triangles and rhombi represent, respectively, first and seventh scan) for (c) sol-gel series and (d) impregnated series. Black dashed line is the ideal model (calculated) for monolayer coverage.

A variation in a specific LEIS signal on changing the loading may be originated, in principle, from several processes. Important factors that determine the signal intensity are the density of surface atoms and the neutralization probability. Regarding the latter, it is reported in literature that no matrix effects take place in Mo/TiO_2 system [6], which means that the neutralization process is insensitive to the chemical environment of a surface atom. So, neither changes in the surface composition nor changes in the surface morphology are assumed to influence the neutralization probability. An evidence for this assumption would be a linear dependence of the Mo and Ti signals on the Mo loading as observed in Figure V.7(a and b). On the other hand, a nonlinear relationship is expected when matrix effects are occurring. Clearly, Ti obeys the linear rule while Mo seems to escape from it. Further, since Co peak becomes non-negligible at higher Mo loadings and once it is very close to Mo peak, it may cause some interference in evaluation of Mo area. Moreover, since we are dealing with powder samples instead a film, contribution to deeper layers becomes more pronounced, which plays a major role in quantification process, as stated in Chapter III.

Figure V.7 (c) and (d) shows the results for atomic coverage, respectively, for sol-gel preparation and impregnated catalysts. A first issue in LEIS measurements is to define which scan is more representative of the real surface of the catalysts. In the figure, triangles represent the first scan recorded while rhombi represent the seventh one. By looking the impregnated catalysts, we observe clearly that the seventh scan is in good agreement with the predicted values for monolayer dispersion (the black solid line).

However, for sol-gel catalysts we observe a slight deviation from this model for greater values (first scan) or lower values (seventh scan). It is true that the major variance in data happens for 25 and 30% of Mo loading. This may be related to the fact that we observe a great bulk contribution from MoO_3 and $CoMoO_4$ (for details, see the previous chapter).

i. LEIS Partial Conclusions

LEIS is a suitable tool to detect element presence in surface of solids. A peak is attributed to each element present in our solids and its peak intensity (or area) is proportional to the amount of it on the surface. The results suggest that in sol-gel solids with low Mo loadings (particularly, SG-5, SG-10 and SG-15), part of Mo species are inserted in the TiO_2 matrix. The results present in two columns of the Figure V.*7* are complementary. From Figure V.*7a* and *b*, one sees that stabilization in Mo detection occurs from 20% of Mo loading in impregnated series and for 15% in sol-gel series. However, while in impregnated catalysts (Figure V.*7*d) the ratio Mo/Ti is such that obeys the ideal monolayer behavior, in sol-gel series (Figure V.*7*d) this ratio is dropped to lower values, indicating that Mo is observed less than expected. It reinforces the idea that part of Mo species in sol-gel series is "hidden" in the structure. Figure V.*7*d also reveals us that in first scan an important amount of Ti is not detected, which can be interpreted in views of impurities (probably, carboneous species) from a not clean surface, as expected for uncalcined samples. Thereby, the last scan seems to represent the actual catalytic surface.

Finally, considering the fitting issues particularly in Co peak, we decided to do not consider quantification of such element, thus Co/Mo atomic ratio values are not showed here.

2.2.2. X-Ray Photoelectron Spectroscopy

i. Oxide Solids

The surface exposure and type of species formed after precursor calcination was studied by XPS technique. The Mo $3d_{5/2}$, Co 2p and Ti 2p core-level spectra provided useful information about the chemical state of the elements and their relative proportions on the surface of the oxide catalysts. For all calcined samples, the values of Binding Energy (BE) corresponding to selected core levels of these elements are compiled in Table 8. All spectra were calibrated according to C 1s energy (= 284.9 eV).

Table 8 - Binding Energies for selected orbitals in Mo and Co XPS spectra for calcined catalysts.

Preparation Method	Name	Mo $3d_{5/2}$ (eV)	Co $2p_{3/2}$ (eV)	Mo 3d / Ti 2p	Co 2p / Mo 3d
One-Pot Sol-Gel	SG-5	232.5	780.3	0.05	0.4
	SG-10	232.8	780.9	0.09	0.4
	SG-15	232.9	780.7	0.12	0.4
	SG-20	233.1	781.0	0.24	0.6

Preparation Method	Name	Mo $3d_{5/2}$ (eV)	Co $2p_{3/2}$ (eV)	Mo 3d / Ti 2p	Co 2p / Mo 3d
IWI	HMA-5	231.7	780.9	0.08	0.4
	HMA-10	232.9	781.3	0.06	0.6
	HMA-15	232.7	781.3	0.17	0.7
	HMA-20	232.7	781.3	0.20	0.7

Whatever the method of preparation or Mo loading of the samples, the binding energy of Ti $2p_{3/2}$ core-level peak remained unchanged (464.6 ± 0.3 eV), confirming that there is no change in the Ti^{IV} oxidation state. Concerning the BE of Mo $3d_{5/2}$ energy level (232.9 ± 0.2 eV), we observe that for all the samples one has indication of Mo^{VI} species (as in the MoO_3); with average separation of 3.3 eV between both spin-orbit components (see a typical Mo 3d XPS spectrum in Figure V.*9*). A lower level for molybdenum in SG-5 (see Table 8) may indicate a different species or interaction with support [7]; however, since HMA-5 also present lower values compared to the other samples in its own series it is likely that the low Mo (and Co) loadings in these samples (and, thus, low signal-to-noise ratio) prevents a precise area value determination.

Coverage ratio (Mo/Ti) follows the expected behavior, i.e., it increases with Mo loading. This is true for both series. Concerning Co/Mo ratio, the nominal value is 0.5. Both series are in an acceptable according with it. HMA-5 has Co/Mo ratio equals to 0.4; this value increases to 0.6 for HMA-10 and stabilizes in 0.7 for higher Mo loadings (HMA-15 and HMA-20). In sol-gel series, except for SG-20 (Co/Mo = 0.6), the other solids have a ratio value equals to 0.4.

Figure V.*8* compares the Kerkhof-Moulijn ([8], [9]) model of monolayer dispersion with Mo/Ti atomic ratio from both series of catalysts (Table 8). One observes that for impregnated catalysts the predicted values and the linear fitting of data match almost perfectly. For sol-gel series, the model deviates slightly, but we can consider that monolayer distribution model is a good one for describing also sol-gel catalysts. Qualitatively comparing with LEIS equivalent plot (right panel in Figure V.*7*), one observes that a similar monolayer-like behavior for HMA series. For sol-gel series, instead, LEIS deviates largely from monolayer model. We tend to attribute this difference to the greater surface sensibility of LEIS, which *a priori* is more precise and sensitive the surface elemental quantification.

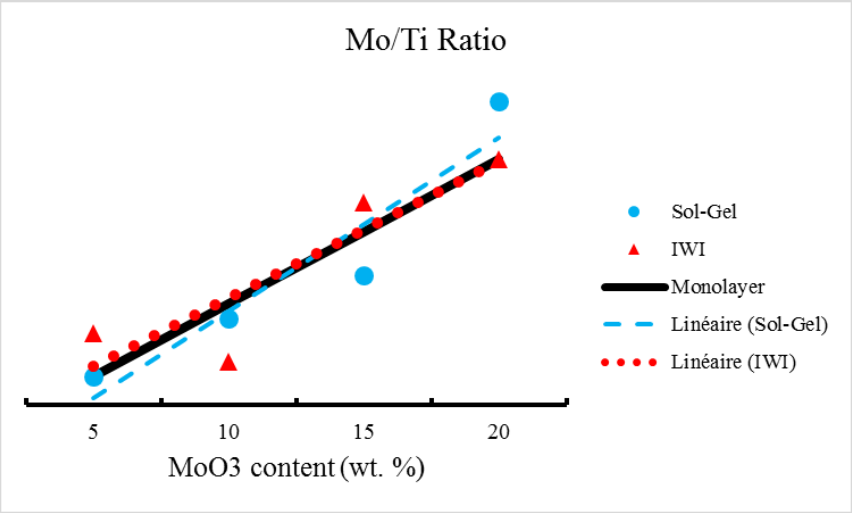

Figure V.8 - Mo/Ti atomic Ratio for both series of catalysts. The black line represents the ideal monolayer distribution according to Kerkhof-Moulijn model.

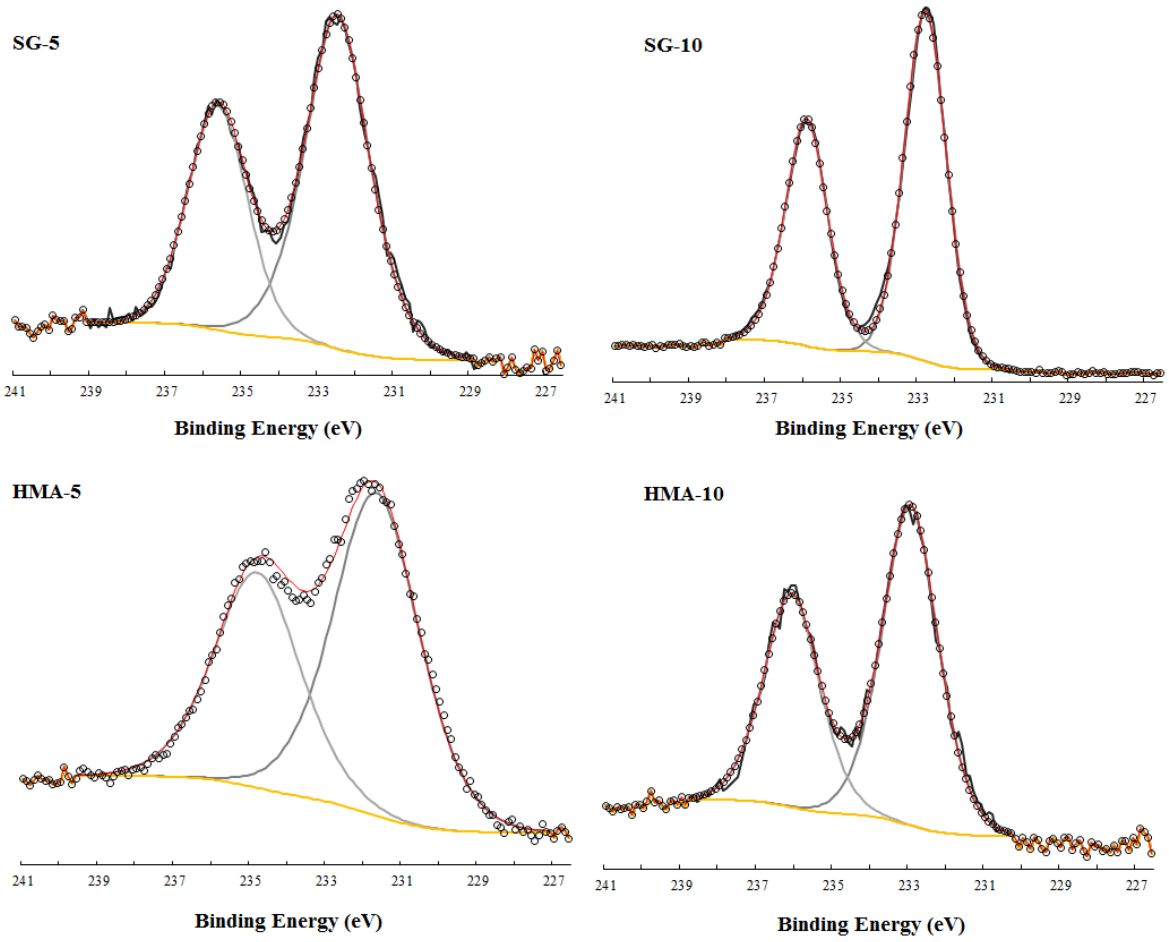

Figure V.9 - XPS spectra for lower Mo loadings (namely, 5 and 10%) in oxide state. The red line represents the fit to collected data (circles). The thin lines are components of the spectral deconvolution and yellow line is the Shirley background.

An interesting aspect in Mo 3d spectra region deserves some attention. We recall that in LEIS measurements a spurious peak was located in sol-gel series of dried catalysts (Figure V.*4*), which was attributed that to sodium atom. The presence of sodium at CoMo systems is known to play a direct role on Mo XPS spectra, particularly at Mo 3d peaks. Comparing sol-gel and impregnated spectra for lower Mo loadings, i.e., 5 and 10 % (Figure V.*9*), a better resolution of the Mo 3d doublet with the consequent narrowing of each component was found for the sol-gel samples. Such effect depends on the amount of sodium and its LEIS peak is no longer detected (or at least, is inconclusive) for others Mo loading in sol-gel series. According to previous study on CoMo catalysts supported on alumina [10], the presence of sodium in the support, by increasing the local pH, favors the adsorption of Mo via the monomeric species MoO_4^{2-} rather than polymeric species such as $Mo_7O_{24}^{6-}$. Moreover it has been shown that sodium would inhibit the formation of Mo(V) caused by the reducing action of NH_3 formed by decomposition of the ammonium salt deposited in the pores [10][11]. The combination of these two effects would result in narrower Mo 3d spectra for the sodium containing catalysts. The presence of sodium itself do not seem to influence catalytic activity [12], but it was shown that sodium ions drive the formation of β-$CoMoO_4$ oxide phase in amorphous aluminosilicate supported CoMo catalysts [13], which may not necessarily be the present case. For higher loadings, the shape of spectra are similar no matter preparation method.

Concerning cobalt XPS spectra, upon ionization, the 2p level splits into $2p_{1/2}$ and $2p_{3/2}$ peaks with the spin-orbit coupling ratio of 1:2. About 16 eV separates the former peak from the latter to higher energy. Considering that the difference in Co 2p binding energy between Co^{2+} and Co^{3+} is indistinguishable, the appearance of shake-up satellite peaks could be taken as an indication of the presence of Co^{2+} ions. This is because, contrary to the low spin Co^{III} compounds (Co_3O_4; in fact this compound has mixed Co^{II}-Co^{III} configuration), the high spin Co^{II} compounds (CoO) usually have intense satellite peaks associated to their 2p lines. Further, it is well known [14] that intense satellite structures, with separation about 5-6 eV above principal Co $2p_{3/2}$ and Co $2p_{1/2}$ lines, are observed in compounds with high-spin Co^{2+} (S = 3/2) configuration. The intensity of the satellites are larger in this high-spin Co^{2+} than in the low-spin Co^{2+} (S = 1/2) compounds and complexes. Co $2p_{3/2}$ - Co $2p_{1/2}$ peak separation increases with the number of unpaired electrons, thus, this separation for Co complexes with $S = 3/2 > S = 1/2 > S = 0$. Further, this separation was found to be 15.4 eV for low-spin Co^{2+} and 16.0 for high-spin Co^{2+} ions. Deconvolution of main $2p_{3/2}$ contributions required an extra small peak in order to account multiplet effects [15].

Figure V.*10* shows normalized Co-XPS spectra for oxide solids of both series. The first important fact is the (expected) very low signal for lowest Mo loadings; in SG-5, just a discreet feature is observed.

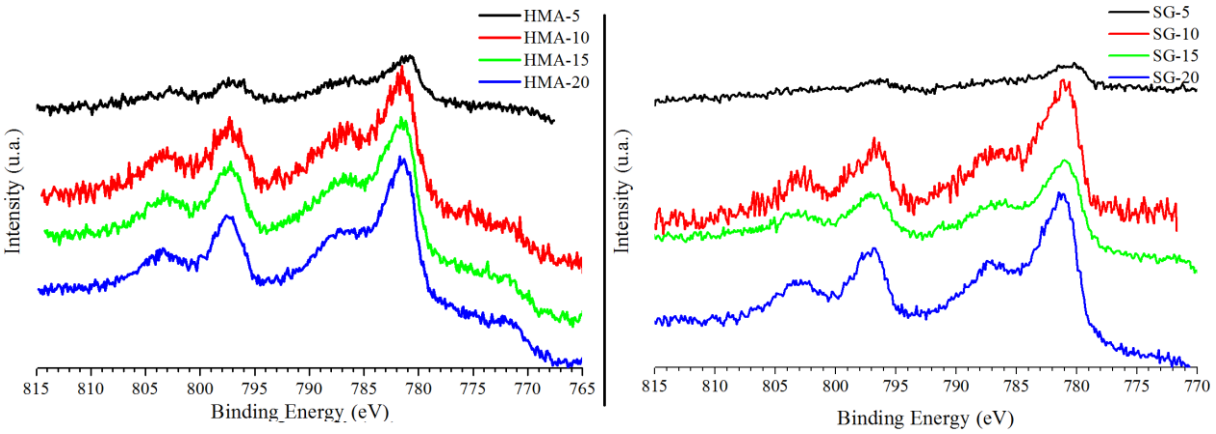

Figure V.10 - Cobalt XPS spectra for HMA and SG series.

Deconvolution of Co XPS spectra are showed in Figure V.*11*, main peaks are drawn with solid lines, while satellites are represented as dashed lines. Selected parameters obtained from modeling are presented in Table 9. The energy separation between main peaks lies in the range 16.10 - 16.35 eV. In our study, the satellites are shifted into the range of 5.3 - 5.8 eV, suggesting Co^{II} in a high spin configuration. Satellite separation in both sol-gel and impregnated series are virtually the same. For the former, the average value is equals to 5.55 (± 0.15) eV while in impregnated series this average value is equals to 5.37 (± 0.17) eV.

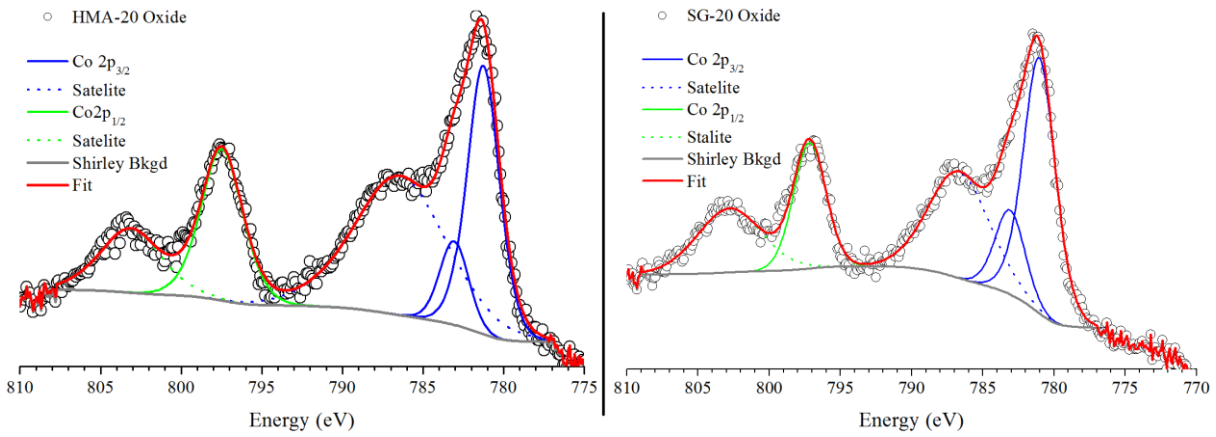

Figure V.11 - Co XPS deconvolution for HMA-20 (left) and SG-20 (right) spectra.

Further, the prominent satellite feature presents in sol-gel catalysts compared to impregnated solids (see Figure V.*11*) may indicate an octahedral symmetry for cobalt environment instead of tetrahedral symmetry in impregnated solids. This discussion is just to highlight the differences between the samples and we know that XPS is not the best way to resolve this symmetry issue. XANES data will address this point in a more detailed manner.

Table 9 - Physical parameters extracted from Co XPS modeling.

Preparation Method	Sample	Split $2p_{3/2}$ - $2p_{1/2}$	Intensity Ratio ($2p_{3/2}$ - $2p_{1/2}$)	Satellite Separation
Sol-Gel	SG-5	16.20	1:1.88	5.3
	SG-10	16.42	1:2.06	5.8
	SG-15	16.35	1:1.94	5.5
	SG-20	16.13	1:1.93	5.6
IWI	HMA-5	16.10	1:1.77	5.5
	HMA-10	16.08	1:1.75	5.6
	HMA-15	16.08	1:1.65	5.2
	HMA-20	16.21	1:1.72	5.2

ii. Sulfided Solids

Decomposition procedure for sulfided molybdenum 3d XPS spectrum is well stated in the previous chapter. Here the objective is to compare main differences between catalysts from two methods of preparation. Thus, we performed a finer XPS decomposition following constrained model for each individual contribution (see [17] and references there in). As consequence of such finer constrained model, Mo-component quantitative values may be slightly different from those presented in the previous chapter. Figure V.*12* shows Mo 3d XPS spectra for SG-20 and HMA-15 after sulfidation step. The first feature is the small peak centered at 227.3 eV necessary to fit due to S_2^{2-} species (usually attributed to MoO_xS_y) compound. Besides that, it is noticeable the different ratio in distribution of Mo species. While HMA-15 XPS is ruled by Mo^{IV} contribution (MoS_2), in SG-20 we observe large amount of Mo^{V} and Mo^{VI}. In the later, Mo^{IV} represents 50% of total Mo 3d contribution while in HMA-15 it is 82% (see Table 10).

Table 10 - Percentage of molybdenum species in sulfided catalysts as calculated from XPS.

Sample	*% of Mo^{IV}*	*% of Mo^{V}*	*% of Mo^{VI}*
HMA-15	81.9	6.0	12.1
SG-20	45.6	27.5	26.8

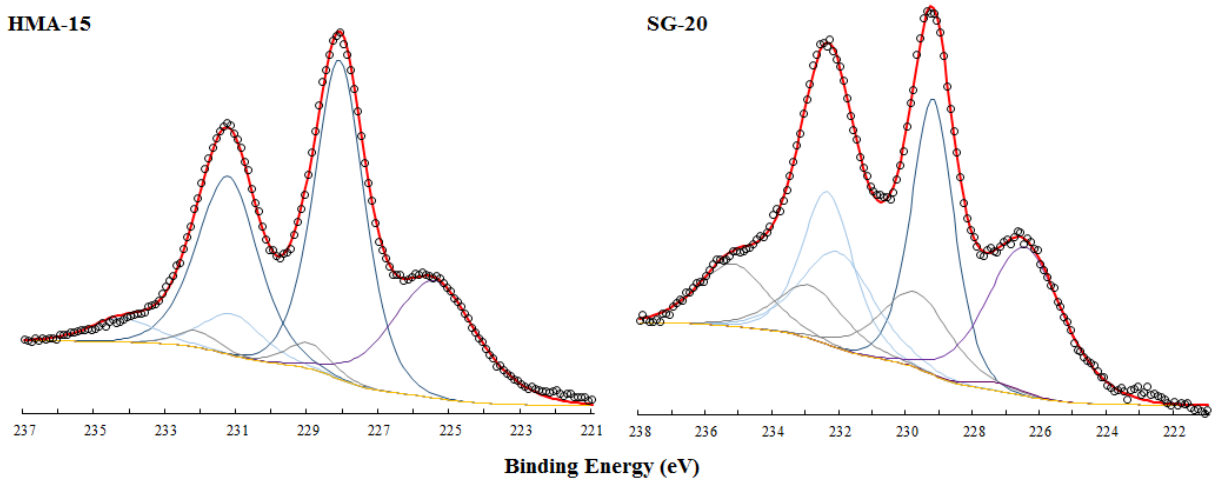

Figure V.12 - XPS spectra of Mo 3d level for selected samples after sulfuration. The red line represents the fit to collected data (circles). The thin lines are components of the spectral deconvolution and yellow line is the Shirley background.

The Co-oxide spectra contains the spin-orbit components Co $2p_{3/2}$ at 780.3 eV and the Co $2p_{1/2}$ at 796.2 eV. On the basis of the binding energies, spin-orbit coupling and satellites (shake-up), the peaks are attributed to Co^{2+} present as CoO or $CoMoO_4$ [16]. It is tricky to analyze changes in BEs observed (and if they are significant) among the samples listed on Table 8 because signal to noise ratio in certain samples, particularly for low Mo loadings.

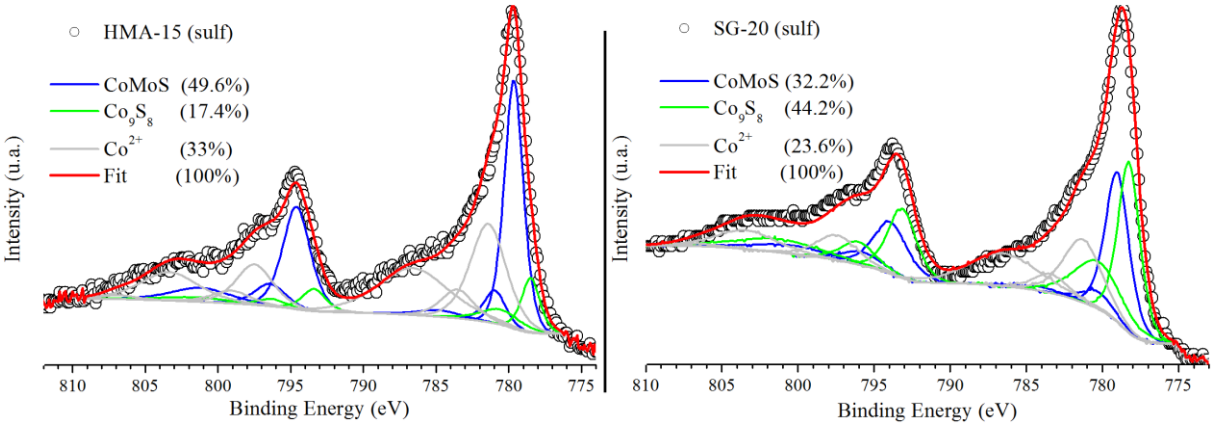

Figure V.13 - XPS spectra in Co region for selected sulfide samples. The red line represents the fit to collected data (circles). The colored lines are components of the spectral deconvolution, in parentheses their corresponding percentage to the total.

After H_2/H_2S activation, XPS Co 2p spectra are transformed as shown in Figure V.*13*. XPS model was built inspired on the work made by Gandubert *et al* [17]. Sharper Co 2p components, found at lower binding energies (777-778 eV) are attributed to sulfided cobalt species or to reduced cobalt Co^0, practically indistinguishable [18]. The sulfide species distribution is quite different between the two samples. In HMA-15 the Co-sulfide CoMoS specie (50%) gives equal contributions to total area with oxide specie (Co^{2+}), whereas in SG-20 the former is responsible for 32.2% and one observes just 23.6% of Co^{2+}; the main contribution is due to another sulfide specie, Co_9S_8 (44.2%). These results are in good

agreement with the results from Mo XPS (Table 10) for SG-20, in the sense that we found relatively the same amount of Mo oxide (26%) and Co oxide species (23%). In HMA-15, Co oxide species represent 33% whereas Mo oxide species represent just 12%.

The presence of sulfur after reaction is confirmed by the peaks of S 2p at 161.5 eV and S 2s at 225.6 eV in Figure V.*12*. The comparison of Co 2p/Mo 3d intensity ratio of the samples before and after reaction (for SG-20 are, respectively, 0.34 and 0.74, while for HMA-15 are 0.68 and 0.43), indicates that cobalt has tendency to segregate to the surface during sulfidation in sol-gel catalyst, this trend is less pronounced in impregnated catalyst. Once again, while in oxide state the spectra are quite similar, after sulfidation, the main peak characteristic to CoMoS phase (778 eV) is considerably sharper in HMA catalyst. 50% of all contribution in Co 2p region is due to this phase in HMA-15, whereas in SG-20, CoMoS phase contribute with 32.2% for the overall spectrum. We stress that the XPS-phase names are just a usual attribution for the peak, not necessarily is a confirmation or statement of such phase in the sample.

No changes in Ti 2p spectrum was observed when comparing oxide and sulfided samples in HMA-15 and SG-20, which means that titanium retains its Ti^{4+} formal oxidation state even after sulfidation. It was proposed by Ninh *et al.* [19] that regarding S 2p XPS region one could simulate TiS_x (S^{2-}) contribution at 161.0 eV and 162.0 eV that could indicate sulfidation of titanium. However, we could accurately simulate the S 2p region by using contributions from the two main specie of sulfides in each sample, S^{2-}, from MoS_2 (162.2 eV and 163.4 eV) and S_2^{2-}, from MoO_xS_y or MoS_3 (162.9 eV and 164.2 eV). If is that the case, for HMA-15 5% of S 2p area is due to S_2^{2-} specie, while in SG-20 this value is 13%.

Several groups proposed that, in the case of titania-supported CoMo catalysts, the sulfidation of the support could create Ti^{3+} species which would act as promoter for the MoS2 phase [20][21]. This promotion by Ti was recently contested according to thermochemical calculations as the calculated Gibbs free energy does not favour at all the formation of a TiMoS phase in HDS conditions [22]. We did not found any evidence of changes due titanium in our system and the results discussed into these two last paragraphes do not enable us to assert that titanium plays a promotion role in active phase of catalysts, as discussed by Coulier *et al.* [20]. In the present work, the sulfidation of the support was not detected by XPS thus, we believe that Ti acts exclusively as a support in our catalysts.

iii. XPS Conclusions

XPS analysis were performed in order to characterize the solids of both series of catalysts. Results in Table 8 for oxide solids indicate a good agreement of nominal Co/Mo atomic ratio (equals to 0.5), in sol-gel series such value is 0.4 for all samples except for SG-20 (equals to 0.6). In impregnated series,

the values are slightly large, except for HMA-5, where Co/Mo ratio is equal to 0.4. The coverage ratio, Mo/Ti, increase with Mo loading, as expected and predicted by the Kerkhof-Moulijn monolayer model (Figure V.*11*).

Particularly narrowed-peak Mo oxide XPS spectra were found for low Mo loading in sol-gel series compared to impregnated solids of equivalent loading. It may due to the presence of sodium in these samples, as indicated by LEIS. Co oxide XPS spectra indicates Co^{II} state with high spin configuration.

The presence of sulfided species was confirmed in both Co and Mo XPS spectra. Comparing sulfidation rate for the two elements for each sample, one observes equivalent rates in SG-20, i.e., we found about 26% of non-sulfided Mo species and 23% on non-sulfided Co species. In HMA-15, the respective values are 12% and 33%. It may suggest a stronger correlation between Mo and Co species in sol-gel preparation.

3. The Oxide Precursors Local Atomic Structure: *Classical* XAFS Analysis

In order to characterize the atomic structure of the phases(s) which form the oxide precursors, *ex situ* XAFS experiments were performed at the SAMBA beamline at the Mo K-edge for the set of prepared catalysts. As stated in Table 7, we recorded Mo K-edge XAFS spectra from calcined samples for both series of catalysts (prepared by one-pot sol-gel and by impregnation). Further, XAFS spectra under same conditions were recorded for dried (i.e., non-calcined, or fresh) sol-gel samples. Therefore, we will be able to check if any structural or phase changing occurred during the calcination step. In order to clarify the presentation of our study and better contrast the difference in structure between the two different methods of preparation, firstly we present individual feature of the samples separated by method. A topic dedicated to references related to our study anticipates the sample description; we make some considerations concerning the refinement method, some issues and limitations that guide the rest of this manuscript. After, we pass to impregnated series, because is a known system and it serves as basis for what expect in terms of final state and active structure, describing the individual structure of each sample. Then, we describe our one-pot sol-gel catalysts individual structures, the dried, calcined, reduced and active phases.

Data reduction of XAFS spectra were performed with Demeter Bruce Ravel's package [23]. ATHENA drives XAS data processing chores and pre-treatment, such as background removal, normalization, pre-edge definition, etc. The E_0 value was fixed (20,004 eV) after alignment of spectra by using Mo-metallic foil as reference. This well-known value is tabulated and it can be checked, for example, in French Absorption Spectroscopy (FAME) beamline's site from European Synchrotron Radiation Facility

(ESRF)[8]. Fourier Transform procedure was made with a Kaiser-Bessel window type. Least squares fitting of EXAFS spectra were carried with ARTHEMIS in R-space and CIF files from HMA, $CoMoO_4$ (for Mo-Co contrbutions) or $CoMo_6$ (whose structures are reported, respectively, on [24], [25] and [26]) were used for crystallographic data input for FEFF calculation. Once taken S_0^2 parameters from known bulk references, such as MoO_3, $CoMo_6$ or HMA (in fact, an average value), we could determine the EXAFS parameters, such as, *N*, *R*, σ and ΔE_0.

3.1. On the Reference Compounds, XAFS Fitting of Oxygen Sphere and its Limitations

In order to have a start point in structural comparison and initial model structure for bond lengths in fit of EXAFS, different reference compounds are recorded with distinct atomic environments. In this subsection, we briefly report the reference compounds registered in same conditions of the catalyst data and make a discussion about the limitation of EXAFS fitting of oxygen sphere, particularly in Mo-based compounds.

Concerning Mo K-edge, we performed XAS measurements of two oxide reference compounds: bulk ***MoO_3*** and bulk ammonium heptamolybdate, henceforth ***HMA*** and bulk ***MoO_2***. Additionally, we refined ***$CoMo_6O_{24}H_6$***, henceforth ***$CoMo_6$***, EXAFS (no XANES available) data to be used also as reference for bond distances. At Co K-edge, the reference compounds were ***CoO*** and ***Co_3O_4***. We have also recorded XAS data for ***MoS_2*** in Mo K-edge as reference for sulfided state. XANES spectra and its respective FT of EXAFS moduli are presented in Figure V.*14* to Figure V.*17*. Each EXAFS spectra was simulated from its own crystallographic data, a CIF file. Fitting parameters resulted from this simulation are presented in Table 11.

Fitting reference compounds of know structure (thus, *N* known for each contribution) allow us to use the principle of chemical transferability and use some parameters of these references in the fit of our samples, for instance, E_0, S_0^2 or any other parameter deemed convenient. We have used the average value of Mo references to fix our S_0^2 in the refinement of the catalytic structures. Taking into account all four Mo-reference compounds, such average is equal to 0.9. Besides, we use the references in qualitative analysis by comparing their XANES and EXAFS spectra with our data.

MoO_3 Fourier Transform of EXAFS moduli presents two main contributions around 1.7 Å and 3.2 Å (without phase correction), which may be well reproduced by 6 oxygen nearest-neighbors at 5 distinct distances in the range 1.68 - 2.36 Å and 3 Mo-O distances for the molybdenum next nearest-neighbors at 3.45 Å, 3.78 Å and 4.06 Å.

[8] http://www.esrf.eu/UsersAndScience/Experiments/CRG/BM30B

HMA, was simulated by using a large Mo-O and Mo-Mo bond distribution. The first coordination shell present four Mo-O distances in the 1.70 - 2.69 Å range and three Mo-Mo bond distances at 3.20 Å, 3.30 Å and 3.43 Å.

In ***MoS_2*** structure, molybdenum presents two intense contributions at FT of EXAFS spectra at 2.0 Å and 2.8 Å (without phase correction), which can be simulated considering 6 sulfur nearest-neighbors at 2.40 Å and 6 molybdenum next nearest-neighbors at 3.17 Å.

CoO, in which cobalt has a formal oxidation state Co^{II}, presents an intense white line and a little pre-edge peak, typical for octahedral species surrounded by oxygen atoms. The first coordination sphere is simulated with 6 oxygen nearest-neighbors at 2.10 Å and the second coordination sphere with 12 cobalt atoms at 3.01 Å.

Co_3O_4 has a spinel structure with two distinct cobalt sites: one tetrahedral (T_d) and another octahedral (O_h), each one with a particular occupancy ratio. Taking this fact into account, the pre-edge peak in XANES its spectrum is more intense when compared to a Co compound purely octahedral, such as CoO. Thereafter, white line has diminished its intensity. The EXAFS simulation for this structure is usually performed with 5 nearest-neighbors oxygen atoms at 1.89 Å (which represents the average distance and coordination number for the both sites) and 2 cobalt contributions relative to the next nearest-neighbors at 3.13 Å and 3.29 Å with, respectively, 4 and 12 atoms.

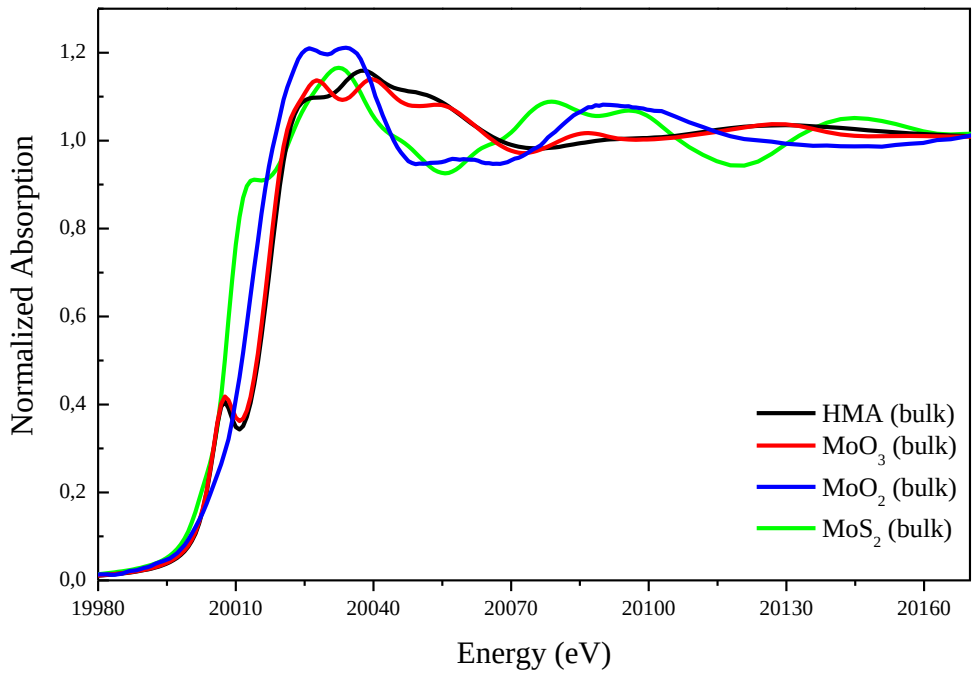

Figure V.14 - Mo K-edge XANES spectra of selected reference compounds: HMA, MoO_3, MoO_2 and MoS_2.

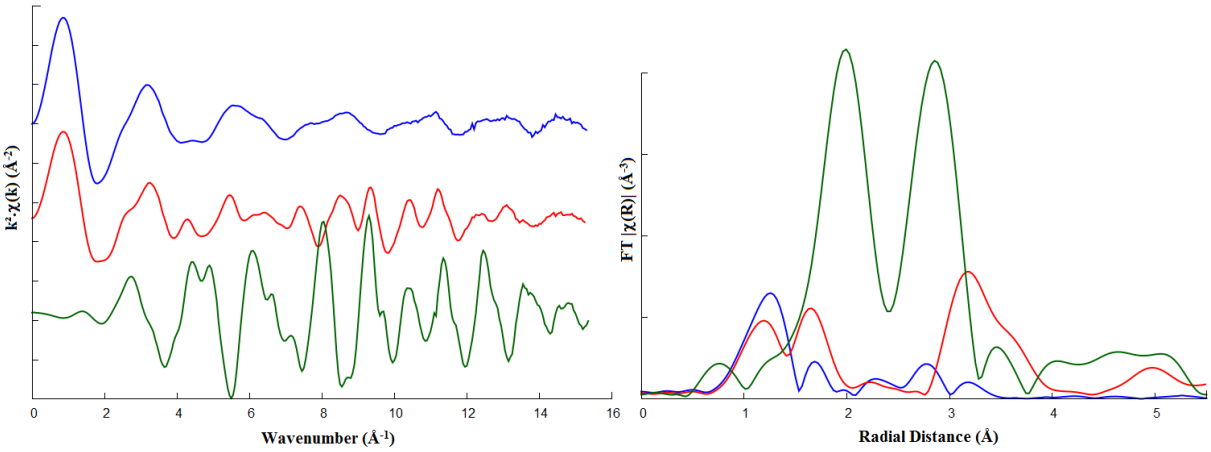

Figure V.15 - Mo K-edge EXAFS and its FT of selected reference compounds: HMA (blue), MoO_3 (red) and MoS_2 (green).

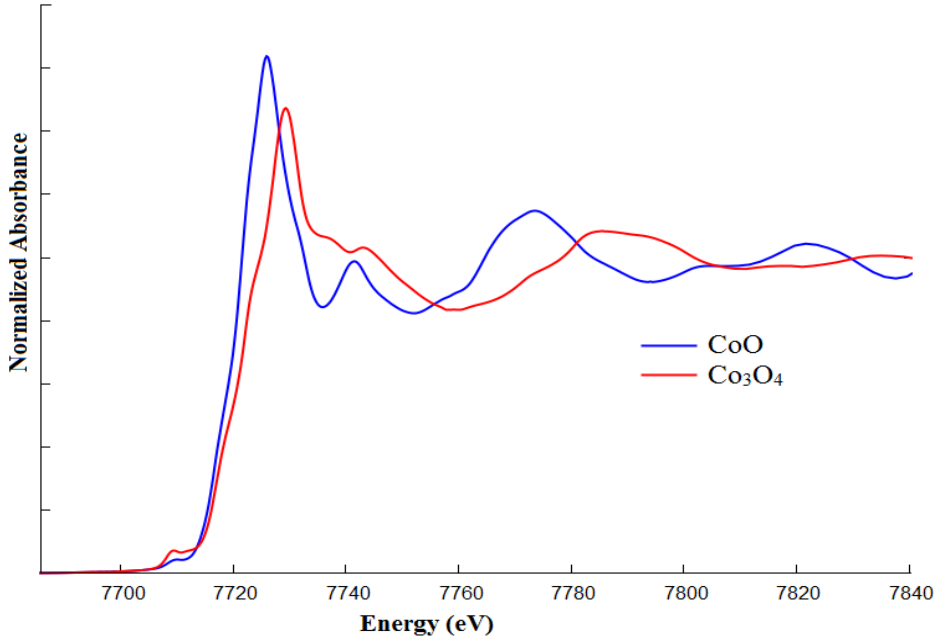

Figure V.16 - Co K-edge XANES spectra of selected reference compounds: CoO (blue), Co_3O_4 (red).

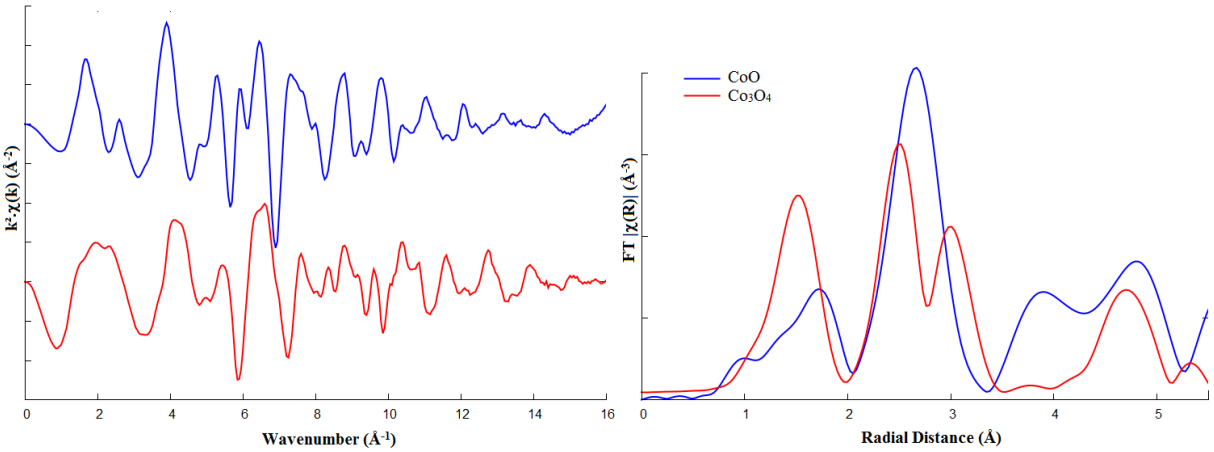

Figure V.17 - Co K-edge EXAFS and its FT of reference compounds: CoO (blue), Co_3O_4 (red).

Table 11 - Refinement of EXAFS parameters for reference compounds used in this work.

Reference Compound	Bond	*N*	*R* (Å)	σ^2 (Å²)	S_0^2	ΔE (eV)	R-factor
$CoMo_6$	Mo-O	2	1.73	0.001	0.81	3.7	0.01
	Mo-O	2	1.95	0.001			
	Mo-O	1	2.34	0.001			
	Mo-Co	2	3.26	0.002			
	Mo-Mo	1	3.31	0.002			
MoO_3	Mo-O	1	1.68	0.001	1.0	5.8	0.03
	Mo-O	1	1.81				
	Mo-O	2	1.98				
	Mo-O	1	2.19				
	Mo-O	1	2.36				
	Mo-Mo	2	3.45	0.005			
	Mo-Mo	2	3.78				
	Mo-Mo	1	4.06				
HMA	Mo-O	1	1.70	0.001	0.9	-2.3	0.005
	Mo-O	1	2.26	0.002			
	Mo-O	2	2.45	0.007			
	Mo-O	2	2.69				
	Mo-Mo	1	3.20	0.004			
	Mo-Mo	1	3.30				
	Mo-Mo	1	3.43				
MoO_2	Mo-O	1	1.91	0.001	0.85	-2.4	0.02
	Mo-O	3	1.98	0.001			
	Mo-O	2	2.04	0.001			
	Mo-Mo	1	2.52	0.003			
	Mo-Mo	1	3.09	0.004			
	Mo-Mo	8	3.70	0.004			
MoS_2	Mo-S	6	2.40	0.003	0.96	5.3	0.01
	Mo-Mo	6	3.17	0.002			
	Mo-S	6	4.01	0.003			
CoO	Co-O	6	2.10	0.01	0.87	3.2	0.007
	Co-Co	12	3.01	0.008			
Co_3O_4	Co-O	4	1.89	0.001	0.74	-0.7	0.02
	Co-Co	12	2.86	0.008			
	Co-Co	4	3.37	0.003			

The particular analysis of Mo environment insert in polyoxoanions by EXAFS has its own issue. It is well known that most of the polyoxoanions of Mo are made of edge-sharing octahedra with a cisdioxo structure (two short adjacent terminal Mo=O bonds) [27] with a spread in Mo-O distances, as it showed the results for our fit in Table 11 and Figure V.18. The many different distances make a thorough quantitative EXAFS analysis of the first Mo-O shell rather difficult [28]. It is not uncommon to find in the literature results in on supported Mo oxide compounds where a low oxygen coordination number was found or imperfect fits was done (for instance, respectively, [29] and [30]). It do not means that we must to reject or discard oxygen first coordination sphere, it just means that one must be careful in analysis and interpretation of results.

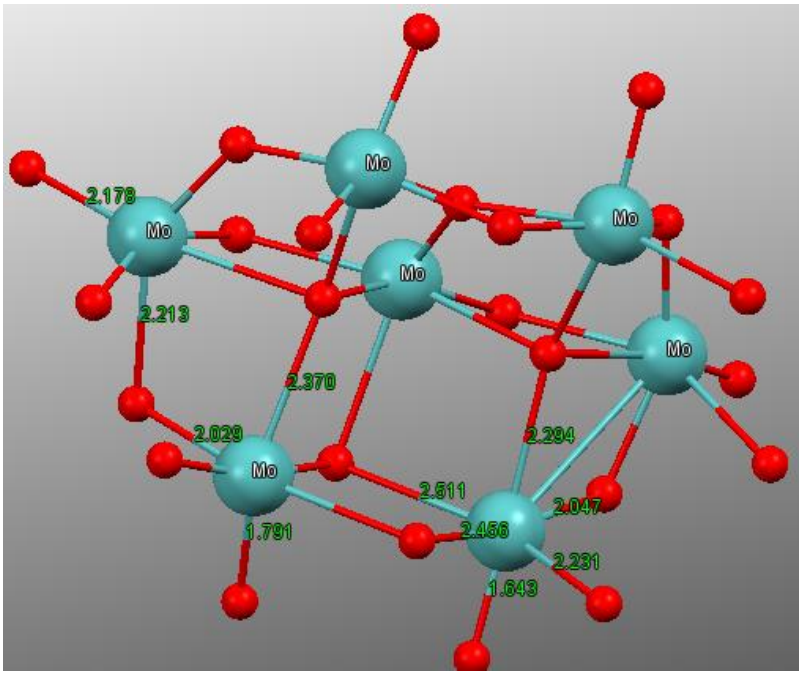

Figure V.18 - Asymmetric unit of Molybdenum Heptamolibdate molecule.

It should be stressed that for disordered systems, which is the case for MoO_6 octahedral environment in polyoxoanions, the true coordination number is not trivial to obtain. Contrary to well-ordered compounds where this parameter may be determined to an accuracy of about 10%, usually the uncertainty is much larger is distorted systems due the presence of non-Gaussian thermal as well as static disorder. Furthermore, since the Debye-Waller factor and the coordination number enter as a product in the EXAFS equation, a change in the apparent coordination number may also be due to a changing in the Debye-Waller factor.

The greatest issue concerning oxygen environment around Mo atoms in polyoxoanions is the limitation of the free independent parameters allowed in the fitting. The available data-range determines the number of free parameters that may be optimized according to the Nyquist theorem ([31], [32]):

$$N_{indp} \sim \frac{2\Delta k \Delta r}{\pi}$$

Here, Δk and Δr represent, respectively, the window width adopted in *k*-space and *r*-space, the range where EXAFS is defined. When fitting the full EXAFS spectrum, the maximum number of independent parameters indicated from equation above can be less than the number of parameters needed to fit the total structure. This is because one has to include all shells in the data analysis, as well as all multiple scattering paths. One can avoid this problem by analyzing only one or two particular peak distributions (i.e., choosing a small range of Δr where it is known that just certain kind of atoms contributes). Of course, the number of free parameters must be reduced when limiting Δr, however, the number of parameters required to fit just one or two shells is now also very much smaller.

In the present case, usually we have a short Δr range (say, 2 Å), due to the oxygen confined region, which leads, typically, 15 independent points. When dealing with an environment where each Mo-O contribution has to be considered individually with its own parameter, we face with insufficient number of variables to make reliable the fitting. It results in an instable and not perfect fit with high correlated parameters and high error bars, mainly concerning the coordination number, which is currently our case.

The determination of a unique set of coordination parameters for a particular contribution to an EXAFS spectrum is often difficult due to this such high correlation between the value of the coordination number *N* and the Debye-Waller factor σ^2 (i.e., different combinations of *N* and σ^2 can lead to similar quality fits). However, this set of combinations depends on the *k* weight factor, which has been used for the Fourier transform. It has been shown ([33] and references therein) that by simultaneous minimization of the variance in a k^1- and k^3-weighted Fourier transform, a unique set of parameters can be found, and further, that a good fit is required with both weightings before one can trust the final results. It is essential to use phase- and amplitude-corrected Fourier transforms when applying this method, because otherwise the asymmetry of the peaks will obscure the results. This absolutely is not a guarantee of getting the correct value for coordination number parameter (due to limitation discussed in previous paragraphs), but is essential to obtain stabilized fit, a good reason to adopt this protocol in our refinements.

By these arguments discussed, we stress that along our study we will not deserve much care on the oxygen distribution distances and coordination numbers. We will limit ourselves to describe a general trend concerning such environment.

3.2. Impregnated Catalysts Series

In this section, we describe the local atomic structure of the impregnated oxide precursor catalysts prepared with ammonium heptamolybdate and cobalt nitrate. The data were recorded as described in previous chapter. HMA samples that were performed XAFS experiments are listed in Table 7.

Since one of the main goals of this work is to describe the new one-pot sol-gel catalysts and their structural characterization, no XAS spectrum for dried sample was recorded for impregnated catalyst. The impregnated ammonium heptamolybdate-cobalt nitrate prepared catalysts are largely used in industry and widely studied. For that reason, it serves as a reference for catalytic performance and structural comparison

3.2.1.1. XAFS Analysis at Molybdenum K-Edge

XANES spectra for the catalysts prepared by IWI are presented in Figure V.*19*. Spectra for all solids can be superimposable and no visual differences can be remarked. The general shape is close to HMA reference with a characteristic pre peak typical for distorted octahedral systems. The oscillations are smooth and no prominent shoulder like in MoO_3 bulk is observed. This softness of the spectra is also correlated with the nanometric size of the particles, the lack of longer order arrangement implies in a loss in stronger XANES oscillation feature. HMA-20 presents a pre peak slightly more intense compared with other impregnated catalysts, indicating that Mo atoms in this sample are inserted in a more regular (or less distorted) octahedral environment compared to lower loadings.

The inset of Figure V.*19* shows the FT of EXAFS. The first peak is related to oxygen distribution around the central atom. All catalysts present the same first peak feature, closer to HMA than MoO_3 and, then, an octahedral symmetry environment with irregular Mo-O distances distribution is expected. In the second distribution region, one observes a wide distribution of low intense peaks. As showed in the last topic, in HMA reference these peaks correspond mainly to Mo-Mo bonds, but *ab initio* (FEFF) calculations indicate presence of long Mo-O (e.g., at 2.5 Å) and multiple scatterings. Disregarding the minor variations caused by eventual signal to noise ratio or data reduction, the FT of EXAFS for HMA-20 (and similarly, HMA-Mo20) presents a smoother shape comparing with lower Mo-loading impregnated catalysts.

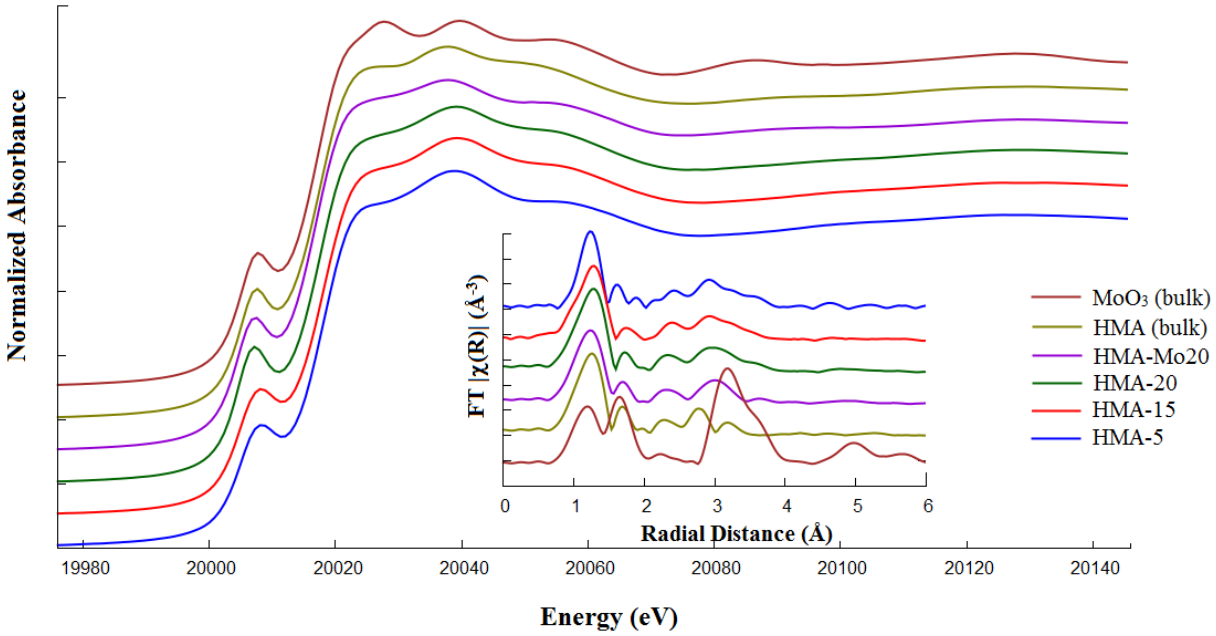

Figure V.19 - Mo K-edge XANES spectra for calcined catalysts prepared by IWI and the compounds used as reference (MoO_3 and HMA). The onset show the FT of EXAFS signal for these samples.

In order to quantify this analysis we resort to the Table 12. In general lines, all spectra can be simulated with two distinct Mo-O contributions in the first coordination sphere and two Mo-Mo contributions in

the second coordination one. We also have simulated (two) Mo-Co bounds (like the one found in $CoMoO_4$). The presence of these cobalt contributions improve the refinement, but the low N_{Co} values with high uncertainty numbers suggests that such atoms may be segregated. Alternatively, we have simulated a short range Mo-Mo contribution at 2.75 Å replacing the Mo-Co short bond. However, such contribution is found just in MoO_2, a structure far from our solids. Moreover, a short Mo-Mo bond in the refinements mess up any Mo-Co contribution, which implies in a lack of fit at the region around 3.8 Å. Energy troubles were find in energy ΔE_0 parameter for HMA-5. A steady fit was just achieved after fixing this value to the average value of the others solids of the series. Actually, after fixing ΔE_0 to 1.8 (the average, considering the other 3 solids), we performed fits varying ΔE_0 in a wide range (± 5.0) around this fixed value in order to guarantee the best choice.

All impregnated calcined solids have similar structure in terms of coordination number and bond distances. We found two Mo-O distances at 1.74 Å and 1.95 Å, respectively, 3.4 and 1.6 coordinated; two Mo-Mo contribution at 3.27 and 3.40 Å with coordination around 1.0 and, finally, two low coordinated Mo-Co bonds around 2.75 Å and 3.85 Å (except, obviously, for HMA-Mo20).

Table 12 - Refinement of Mo K-edge EXAFS parameters of calcined impregnated catalysts.

Preparation Method	Sample	Bond	N	R (Å)	σ² (Å²)	Δσ	ΔE₀ (eV)	Parameters
IWI Calcined	HMA-5	Mo-O	3.1	1.74	0.004	0.001	2.0 (fixed)	Δk = 5.1-13.7 ΔR = 1-4 N_{ind} = 16 χ^2_{Red} = 86 R_{factor} = 0.01
		Mo-O	1.6	1.94				
		Mo-Mo	1.0	3.27	0.003	0.006		
		Mo-Mo	1.0	3.40				
		Mo-Co	0.2	2.74	0.001	0.005		
		Mo-Co	0.2	3.83				
	HMA-15	Mo-O	4.0	1.75	0.006	0.001	1.2 (±2.8)	Δk = 5.1-13.3 ΔR = 1-4.1 N_{ind} = 15 χ^2_{Red} = 464 R_{factor} = 0.001
		Mo-O	1.6	1.96				
		Mo-Mo	1.3	3.27	0.004	0.006		
		Mo-Mo	1.3	3.40				
		Mo-Co	0.2	2.76	0.003	0.004		
		Mo-Co	0.2	3.86				
	HMA-20	Mo-O	3.4	1.74	0.005	0.001	2.0 (±2.9)	Δk = 5.1-13.6 ΔR = 1.1-3.9 N_{ind} = 16 χ^2_{Red} = 212 R_{factor} = 0.003
		Mo-O	1.7	1.96				
		Mo-Mo	1.2	3.27	0.003	0.005		
		Mo-Mo	1.2	3.41				
		Mo-Co	0.1	2.75	0.0007	0.005		
		Mo-Co	0.1	3.88				
	HMA-Mo20	Mo-O	3.0	1.72	0.004	0.001	2.1 (±3.4)	Δk = 5.1-13.1 ΔR = 1-4 N_{ind} = 15 χ^2_{Red} = 575 R_{factor} = 0.01
		Mo-O	1.6	1.95				
		Mo-Mo	1.5	3.28	0.004	0.004		
		Mo-Mo	1.5	3.41				
Uncertainty	HMA-5:	N_{Mo-O} = 0.6; $N_{Mo-Metal}$ = 0.8/0.2			* *R*-uncertainty are ~ 0.5% in average			
	HMA-15:	N_{Mo-O} = 0.5; $N_{Mo-Metal}$ = 0.9/0.2						
	HMA-20:	N_{Mo-O} = 0.5; $N_{Mo-Metal}$ = 0.8/0.1						
	HMA-Mo20:	N_{Mo-O} = 0.5; N_{Mo-Mo} = 0.8						

3.2.2.XAFS Analysis at Cobalt K-Edge

As in sol-gel series case, despite all information we can get from EXAFS study at Mo K-edge, by looking the same catalyst from another point of view and to regard XAS measurements at Co K-edge may help to get new insights on the precursor's structure. Thereby, we have performed also *ex situ* Co K-edge XAS experiments in our samples.

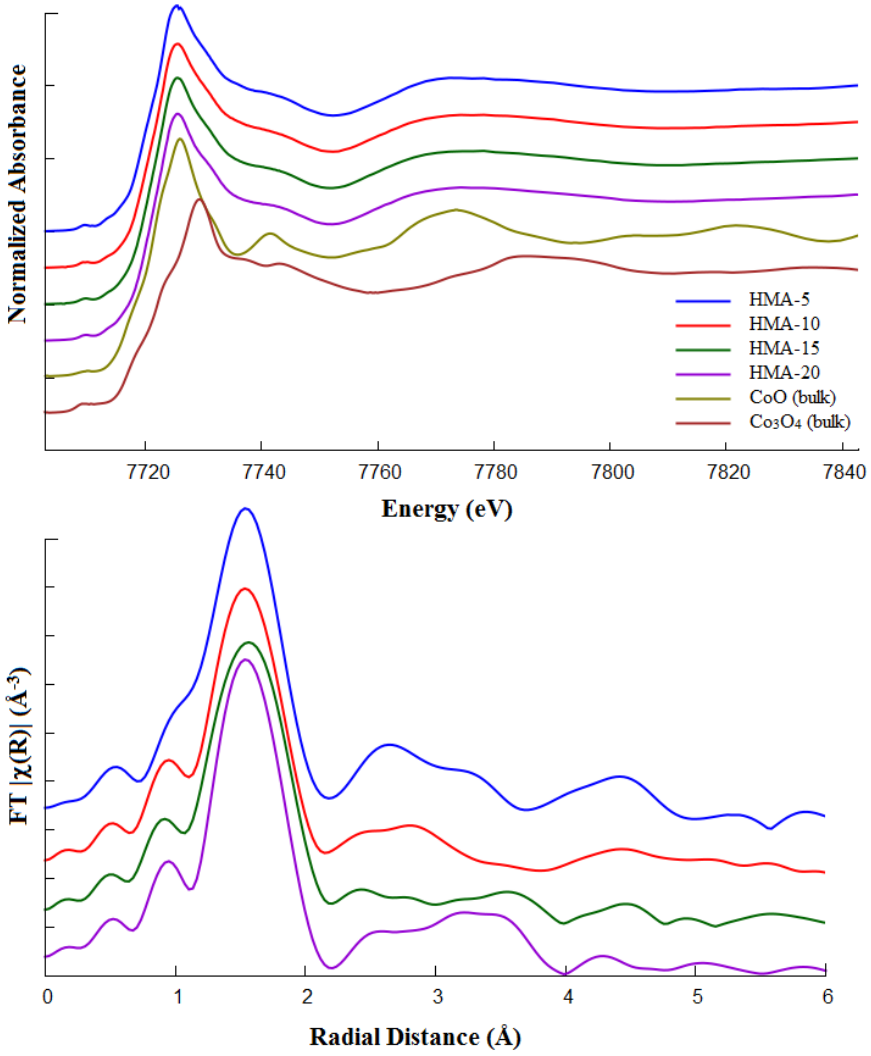

Figure V.20 - (Top) Co K-edge XANES spectra for calcined catalysts prepared by IWI and the compounds used as reference (CoO and Co_3O_4). (Bottom) FT of EXAFS signal for the impregnated catalysts.

In terms of XANES spectra (top, in Figure V.*20*), like in sol-gel catalysts, all HMA-spectra can be perfectly superimposable. In fact, HMA and sol-gel Co K-edge XANES spectra are all superimposable, which means that at least Co atoms are inserted in the same environment, in a symmetry matter.

FT of EXAFS moduli for HMA catalysts series are shown in Figure V.*20* (bottom). For the first radial distribution peak, the overall structure is the same as in sol-gel series, a major Co-O contribution around 1.5 Å (without phase correction) and a minor second coordination sphere, where the main contribution

to the signal comes from Co-metal bond distances. In such next-nearest distribution, one observes important differences between the two series, now one has a weaker but wider distribution that spreads up to 4.0 Å. It is a strong indication of very tiny Co-coordinated structures in this system. We observe also that in the second coordination sphere, the salient part of the peak moves when we move to higher Mo concentration. In HMA-5 one sees it centered at 2.6 Å (without phase correction), at HMA-10 it reduces its intensity, at HMA-15 it is roughly flat and low, and, finally, for HMA-20 it increase its intensity centered at 3.3 Å (without phase correction).

Table 13 shows the structural parameters after EXAFS fitting of HMA catalyst. For all the samples, the first coordination sphere can be simulated with a Co-O contribution around 2.04 Å and about 4 oxygen atoms. No Co-Co contribution could be simulated, which indicate good Co dispersion in structure or very segregated Co-coordinated structure.

Table 13 - Refinement of Co K-edge EXAFS parameters of calcined HMA catalysts.

Preparation Method	Sample	Bond	N	R (Å)	σ² (Å²)	Δσ	ΔE (eV)	Parameters
IWI Calcined	HMA-5	Co-O	4.1	2.02	0.007	0.002	-0.6 (±3.7)	Δk = 4.8-11 ΔR = 1-3.7 N_{ind} = 10 χ^2_{Red} = 18 R_{factor} = 0.01
		Co-Mo	2.8	3.18	0.010	0.009		
		Co-Mo	2.8	3.33	0.010	0.009		
	HMA-15	Co-O	4.3	2.05	0.009	0.002	1.2 (±3.4)	Δk = 4.8-11.1 ΔR = 1-3.9 N_{ind} = 11 χ^2_{Red} = 20 R_{factor} = 0.01
		Co-Mo	0.5	3.21	0.009	0.01		
		Co-Mo	1.0	3.87	0.009	0.01		
	HMA-20	Co-O	4.2	2.03	0.006	0.002	-1.8 (±3.4)	Δk = 4.8-11.4 ΔR = 1.1-3.9 N_{ind} = 12 χ^2_{Red} = 20 R_{factor} = 0.02
		Co-Mo	0.5	3.19	0.004	0.009		
		Co-Mo	0.9	3.85	0.004	0.009		
Uncertainty:	HMA-5	$N_{Co\text{-}O}$ = 1.0; $N_{Co\text{-}Mo}$ = 2.0				* *R*-uncertainty are < 0.5% in average		
	HMA-15	$N_{Co\text{-}O}$ = 1.0; $N_{Co\text{-}Mo}$ = 1.0						
	HMA-20	$N_{Co\text{-}O}$ = 0.9; $N_{Co\text{-}Mo}$ = 0.7						

3.3. One-Pot Sol-Gel Catalyst Series

Exceptionally in this section, we will adopt a variation in nomenclature of the samples in order to differentiate dried from calcined oxide precursors. Thus, for sol-gel series the samples will receive an additional indication in their names. Dried samples had a "(dry)" added after the code of the sample (according to Table 7), while calcined samples earn an additional "(calc)". In that sense, for instance,

calcined sol-gel catalyst with 5% wt. of MoO_3, will be named as SG-5(calc). The dried equivalent of this sample will receive the name SG-5(dry).

3.3.1. XAFS Analysis at Molybdenum K-Edge

Dried Solids: In order to characterize local atomic order, XAFS measurements were performed in dried and calcined samples at Mo K-edge. XANES usually is the first qualitative analysis because it can carry visual differences among spectra that may give us a first idea of the oxidation state, structural local symmetry and chemical composition. The current procedure is to compare visually data collected with known reference compounds. In order to check structural evolution of oxide precursors during calcination step, firstly we describe dried solids confronting XANES spectra of dried sol-gel catalysts with bulk MoO_3 and HMA, as showed in Figure V.*21*.

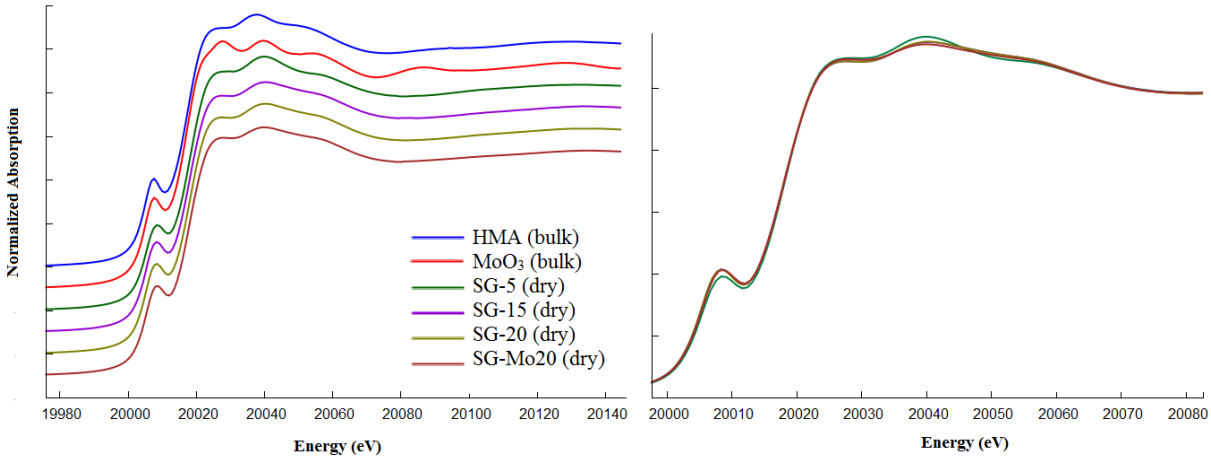

Figure V.21 - (Left) Mo K-edge XANES spectra for dried sol-gel catalysts and the compounds used as reference (MoO3 and HMA). (Right) Superposed dried catalysts, SG-5, SG-15, SG20 and SG-Mo20 (same legend as right panel).

One observes that whatever the prepared catalyst, the XANES spectra are overlapped (on the right panel of Figure V.*21*). It is quite remarkable that despite these sol-gel samples to be prepared with MoO_3, they seem do not retain its former structure, being closer to HMA reference compound, which is confirmed when one regards the Fourier Transform (FT) of EXAFS spectra for this same set of data (Figure V.*22*). SG-5 shows a slight lower pre-edge peak intensity and a more pronounced second XANES oscillation, which may indicate a more structured species, with well-defined and homogeneous distribution of Mo-Mo bonds, for instance. As long there is no shift in energy, all Mo species are in the same formal oxide state (Mo, as in MoO_3). The low intense pre-peak, with noticeable shoulder on first XANES oscillation and a strong second XANES oscillation is typical for a distorted octahedral symmetry, where six oxygen atoms surround each molybdenum.

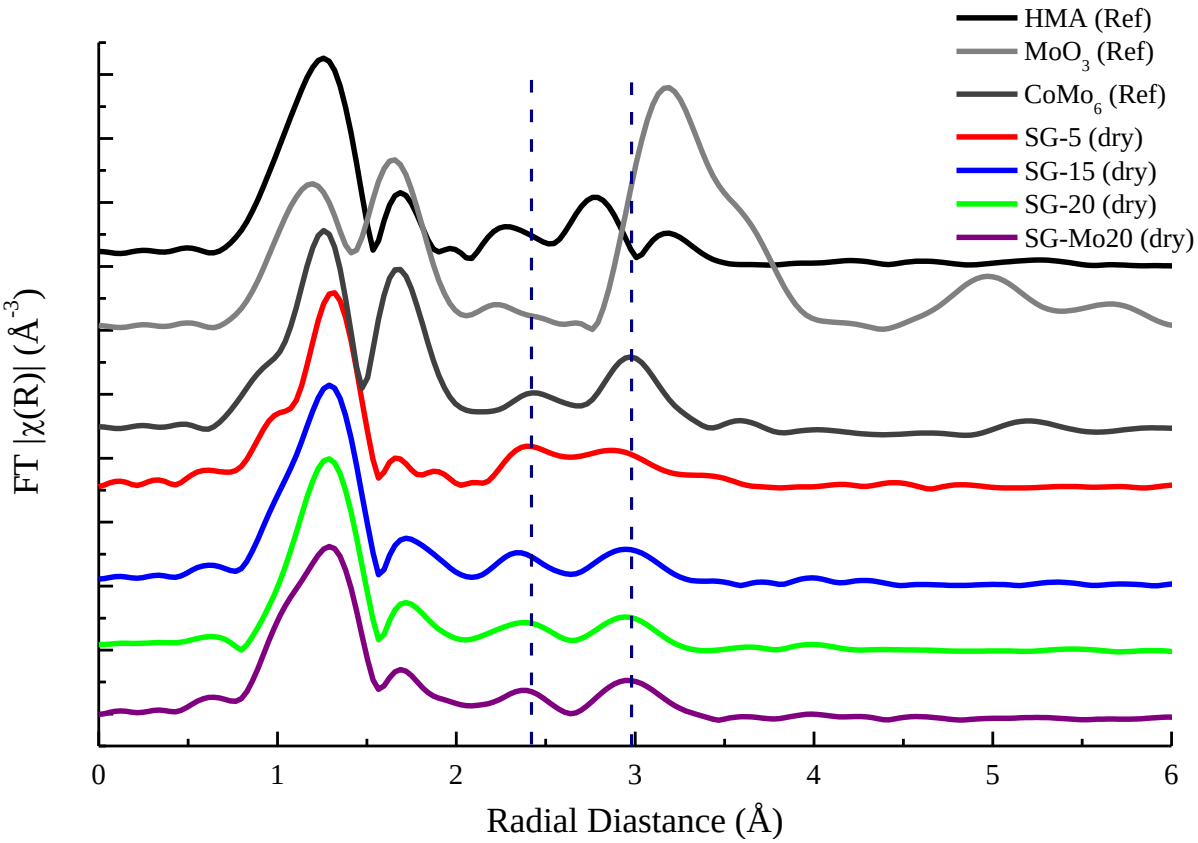

Figure V.22 - Fourier Transform moduli of the EXAFS spectra of the references compounds and dried catalysts in Mo K-edge.

The atomic structural similarities between reference (particularly, something related to HMA and $CoMo_6$) and dried sol-gel catalysts stay more evident when looking at FT of EXAFS[9] in the Figure V.*22*. One observes the first radial distribution (related to the Mo-O distance) is close to HMA, i.e., the first high peak at 1.2 - 1.3 Å and the small peak at 1.7 Å, which in part reflects other Mo-O distances related to octahedral distortion. Instead, the second nearest-neighbors distribution (the peaks ranged between 2 - 3.6 Å) is very close in position and intensity to $CoMo_6$ structure, particularly to highest Mo loadings, such as SG-15 and SG-20. In such reference compound, the signal from this last contribution arises, predominantly, from Mo-Mo and Mo-Co bonds (centered 2.9 Å) and multiple scattering (small peak centered on 2.4 Å), as predicted by FEFF *ab initio* calculations. Such coincidence with $CoMo_6$ peak positions do not imply, in any sense, the existence of the $CoMo_6$ structure in our solids. The radial distribution observed for our catalysts is the same we observe in usual supported polymolybdate catalysts, as for instance, our HMA-prepared catalysts (see 3.2.1.1) and XANES (Figure V.*21*) suggests similarities with HMA-reference structure.

A compilation of the structural parameters values obtained after EXAFS refining for all sol-gel catalysts are summarized in the Table 14. All solids have the same Mo-O and Mo-Mo distance distribution, i.e.,

[9] We recall that values refereed to FT graphs are presented without phase correction.

two oxygen nearest-neighbors at 1.71 Å and ~2.26 Å with coordination, respectively, 2.4 and 1.0 (except for SG-5, which is slightly lower coordinated). Second redial distribution region is similar for all solids, two low coordinated Mo-Mo bonds respectively around 2.59 Å and 3.27 Å. In SG-5, broader and slightly more intense peaks are noticed with a small extra contribution at 3.4 Å (without phase correction). These features can be viewed quantitatively in the Mo-Mo coordination numbers and the extra Mo-Mo distance (3.68 Å).

Table 14 - Mo K-edge EXAFS refining parameters for dried sol-gel catalysts.

Preparation Method	Sample	Bond	N	R (Å)*	σ² (Å²)	Δσ	ΔE (eV)	Parameters
Sol-Gel Dried	SG-5	Mo-O	2.2	1.71	0.003	0.001	-4.0 (±5.0)	Δk = 5.1-13.9 ΔR = 1-3.8 N_{ind} = 15 χ^2_{Red} = 857 R_{factor} = 0.02
		Mo-O	0.5	2.24				
		Mo-Mo	0.4	2.58	0.008	0.007		
		Mo-Mo	1.2	3.28				
		Mo-Mo	0.4	3.68				
	SG-15	Mo-O	2.5	1.71	0.004	0.001	-3.7 (±3.3)	Δk = 5.1-13.9 ΔR = 1-3.4 N_{ind} = 13 χ^2_{Red} = 976 R_{factor} = 0.006
		Mo-O	1.1	2.27				
		Mo-Mo	0.3	2.59	0.006	0.006		
		Mo-Mo	0.7	3.27				
	SG-20	Mo-O	2.4	1.72	0.003	0.001	-3.6 (±3.8)	Δk = 5.1-13.9 ΔR = 1-3.4 N_{ind} = 13 χ^2_{Red} = 2106 R_{factor} = 0.009
		Mo-O	1.0	2.23				
		Mo-Mo	0.4	2.59	0.007	0.007		
		Mo-Mo	0.8	3.27				
	SG-Mo20	Mo-O	2.4	1.70	0.003	0.001	-3.9 (±4.8)	Δk = 5.1-13.8 ΔR = 1-3.4 N_{ind} = 13 χ^2_{Red} = 2942 R_{factor} = 0.01
		Mo-O	1.1	2.29				
		Mo-Mo	0.2	2.60	0.004	0.007		
		Mo-Mo	0.5	3.27				
Uncertainty:	SG-5:	N_{Mo-O} = 0.4; N_{Mo-Mo} = 0.9			*All *R*-uncertainty are < 0.5% in average			
	SG-15:	N_{Mo-O} = 0.4; N_{Mo-Mo} = 0.5						
	SG-20:	N_{Mo-O} = 0.4; N_{Mo-Mo} = 0.5						
	SG-Mo20:	N_{Mo-O} = 0.5; N_{Mo-Mo} = 0.4						

Always keeping in mind the limitation based on discussion concern Mo-O contribution in EXAFS fitting, at least one can highlight some features on this first radial distribution. Comparing SG-20 and SG-Mo20, based on the results present in Table 14 and in the XANES features, cobalt addition seems to do not change the oxygen environment in the catalyst structure, i.e., distance distribution in SG-20 is as regular as in SG-Mo20. Further, similar number of Mo-O and Mo-Mo distances were used to describe both radial distributions. No Mo-Co is detected in any solid.

Calcined solids: Now we describe the calcined sol-gel solids so we can check if structural evolution has passed during calcination step. Refined parameters of the fitting are summarized in Table 15. The overall

features of the XANES spectra are similar, however, spectra of calcined solids are no longer superimposable; it means that there is a slight evolution in some of its aspects (Figure V.*23*). First, the pre-peak intensity increases when increasing Mo loading (the onset of Figure V.*23*). Qualitatively, this means that Mo atoms in SG-5 structure are inserted in an octahedral environment, while for the others Mo loadings, this neighborhood is more distorted. Further, one observes a considerable decreasing in the second XANES bump (20039 eV) as well as in the third one (around 20006 eV).

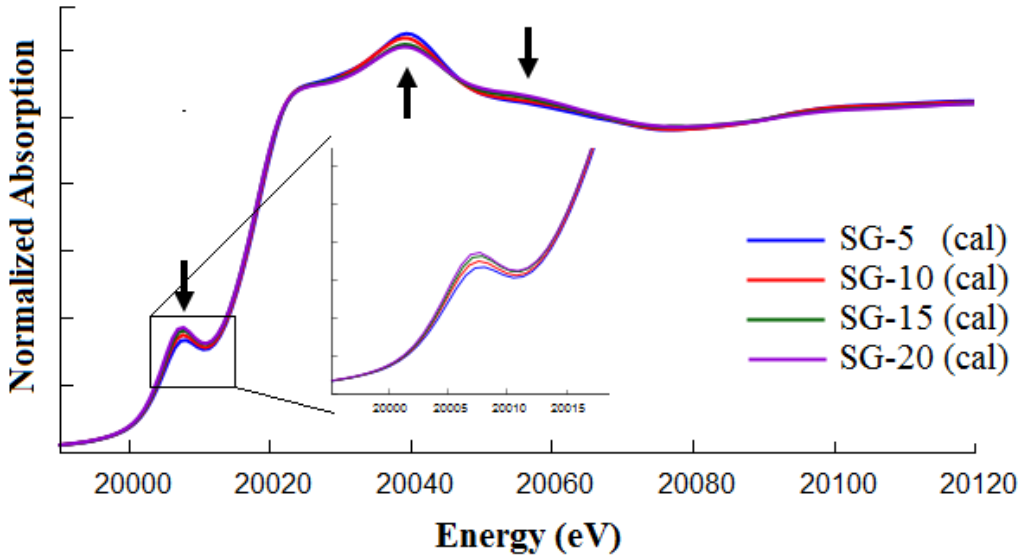

Figure V.23 - Mo K-edge XANES spectra of calcined sol-gel catalysts. The arrows point the noted structural evolution, illustrated by the onset.

A clear evidence of structural evolution with Mo loading is better noted when we look at EXAFS or its FT (Figure V.*24*). In a visual analysis, one sees that the major changes are in low *k* values, which concerns the oxygen atoms surrounding the Mo central atom. In a first glance, it seems that in the broad region between 5 - 6 $Å^{-1}$, no new oscillation is created. Instead, the two consecutive oscillations become closer and the intensity ratio between them stay less important. The two oscillations around 8 $Å^{-1}$ are strongly linked to heavy atoms, namely molybdenum and cobalt. Here, there is no shift among them along the Mo loading, just difference in intensity ratio. It may indicate a strong contribution in the number of neighbors. While SG-5 and SG-10 are similar, SG-15 and SG-20 form another "family" (i.e., they have the same overall features). This separation in families is clearer looking the FT of EXAFS (the onset of Figure V.*24*); both first and second radial distribution peaks support it. This first qualitative analysis indicates that, whatever the Mo loading, we have likely the same structure (the same chemical species) for the catalysts, with remarkable changes in oxygen distribution distances. Furthermore, we can interpret the trend in $N_{Mo}(N_{Co})$ ratio (viewed as increasing in amplitude contributions of FT EXAFS in the second coordination sphere peaks, onset in Figure V.*24*) due to different size of the particles.

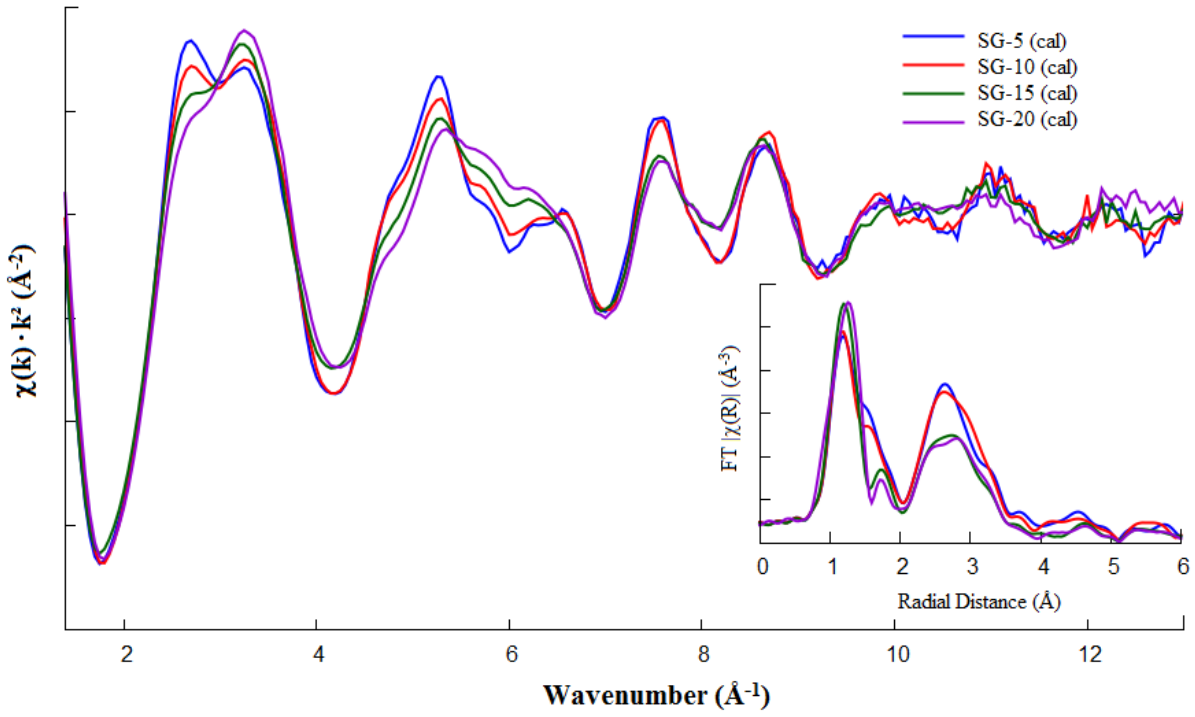

Figure V.24 - Mo K-edge EXAFS of calcined sol-gel catalysts and its Fourier Transform (onset).

Quantitative values of the calcined sol-gel catalysts are summarized in Table 15. The calcined structures are characterized by presence of both Mo-Mo and Mo-Co bonds. Such contributions were simulated taking into account distances from (FEFF) calculated $CoMoO_4$ structure. Concerning the first distribution (related to oxygen neighbors) all catalytic structures were simulated with two Mo-O distances, (around 1.74 Å and 1.95 Å). It seems to exist a trend when increasing Mo loading, a slight shortening in the first Mo-O distance (from 1.77 Å at SG-5 to 1.72 Å at SG-20 and SG-Mo20) and a slight enlargement of the second Mo-O distance (from 1.92 Å to 1.97 Å). Coordination number evolution is inconclusive due to large uncertainty (it seems to decrease with Mo loading); particularly, large N_O in SG-10 happens because large correlation (> 95%) between this parameter and Debye-Waller factor.

In second distribution region, relative to next-nearest neighbors, we have Co and Mo contributions. The same Mo-Mo distances, with higher coordination, are still found in calcined catalysts. A trend to increase coordination number with Mo loading is observed. Again, in SG-10 high correlation between parameters mess the final value, this phenomena is also present in SG-15 (high value for $N_{Mo\text{-}Co}$). For Mo-Co contributions one sees an inverse trend, a decrease in coordination with increasing Mo loading. The Mo-Mo(Co) distance values do not move along the series. In SG-Mo20, two extra Mo-Mo contributions could be simulated compared to the dried solid. The two longer Mo-Mo contributions in SG-Mo20 (3.22 Å and 3.34 Å) seem to appear like a single averaged Mo-Mo distance in SG-20 (3.27 Å).

Table 15 - Mo K-edge EXAFS refining parameters for calcined sol-gel catalysts.

Preparation Method	Sample	Bond	N	R (Å)*	σ² (Å²)	Δσ	ΔE (eV)	Parameters
Sol-Gel Calcined	SG-5	Mo-O	3.2	1.77	0.012	0.008	-6.8 (±3.4)	Δk = 4.8-13.6
		Mo-O	3.2	1.92				ΔR = 1-3.9
		Mo-Co	1.6	3.06	0.004	0.003		N_{ind} = 16
		Mo-Co	1.6	3.83				χ^2_{Red} = 219
		Mo-Mo	0.6	3.26	0.001	0.004		R_{factor} = 0.01
	SG-10	Mo-O	4.0	1.74	0.009	0.004	-6.1 (±3.2)	Δk = 5.2-12.7
		Mo-O	2.9	1.93				ΔR = 1-3.9
		Mo-Co	1.3	3.08	0.005	0.002		N_{ind} = 15
		Mo-Co	1.3	3.83				χ^2_{Red} = 1891
		Mo-Mo	2.0	3.27	0.01	0.01		R_{factor} = 0.009
	SG-15	Mo-O	2.6	1.74	0.006	0.003	-5.8 (±5.2)	Δk = 5.2-13.2
		Mo-O	1.7	1.93				ΔR = 1-3.9
		Mo-Co	0.7	3.03	0.004	0.008		N_{ind} = 15
		Mo-Co	0.7	3.82				χ^2_{Red} = 7129
		Mo-Mo	1.2	3.26	0.007	0.01		R_{factor} = 0.02
	SG-20	Mo-O	2.8	1.72	0.005	0.001	-7.8 (±3.0)	Δk = 5.2-13.6
		Mo-O	0.9	1.97				ΔR = 1-3.9
		Mo-Co	0.3	3.02	0.001	0.004		N_{ind} = 15
		Mo-Co	0.3	3.82				χ^2_{Red} = 1550
		Mo-Mo	1.5	3.27	0.007	0.005		R_{factor} = 0.004
	SG-Mo20	Mo-O	1.6	1.72	0.002	0.002	-3.1 (±5.5)	Δk = 5.2-13.8
		Mo-O	0.5	1.96				ΔR = 1.1-3.8
		Mo-Mo	0.1	2.57	0.002	0.004		N_{ind} = 14
		Mo-Mo	1.2	3.22				χ^2_{Red} = 2148
		Mo-Mo	1.2	3.34				R_{factor} = 0.02
Uncertainty:	SG-5:	$N_{Mo\text{-}O}$ = 1.7; $N_{Mo\text{-}Mo(Co)}$ = 0.7(0.7)					*R-uncertainties are < 0.5% in average	
	SG-10:	$N_{Mo\text{-}O}$ = 1.5; $N_{Mo\text{-}Mo(Co)}$ = 2.0(0.7)						
	SG-15:	$N_{Mo\text{-}O}$ = 1.0; $N_{Mo\text{-}Mo(Co)}$ = 1.0(1.0)						
	SG-20:	$N_{Mo\text{-}O}$ = 0.5; $N_{Mo\text{-}Mo(Co)}$ = 1.0(0.3)						
	SG-Mo20:	$N_{Mo\text{-}O}$ = 0.9/0.5; $N_{Mo\text{-}Mo}$ = 0.1/0.8						

After calcination, we lost the typical polymolybdate structure, as seen in FT of EXAFS, to a distribution with stronger Mo-Mo contributions and the arising of Mo-Co bonds. This effect is systematically observed for all calcined SG-solids, no matter the presence of cobalt (Figure V.*25*), thus is not the Co adding that mess up the original arrangement. Since this trend is not observed in impregnated catalysts (calcined HMA-samples hold the same polymolybdate-type peak distribution), and recalling that preparation method includes support and precursor all together, we can assume that the transformation of the support drives the changes in precursor structure.

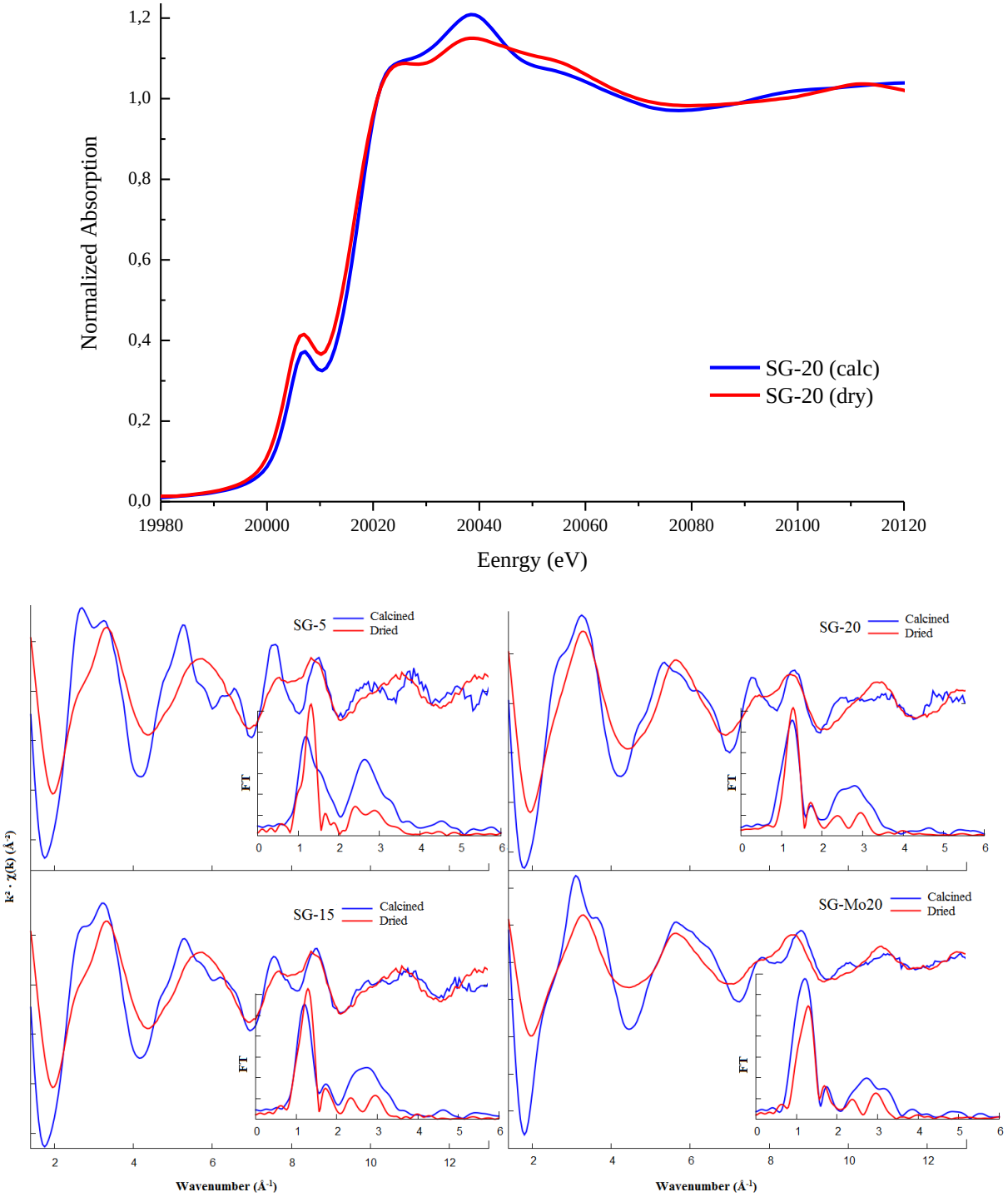

Figure V.25 - (Up) XANES comparison between dried and calcined SG-20 catalyst. (Down) Mo K-edge EXAFS signal and the Fourier Transform (onset) comparison between dried and calcined sol-gel catalysts.

In order to closely look to the differences before and after calcination, we referee to the upper panel of the Figure V.*25*, where one compares SG-20(dry) and SG-20(calc) XANES. A decrease in pre-peak intensity feature and a more pronounced second XANES bumps (around 20040 eV) are observed. Lower panel of the figure also shows comparison between EXAFS and its Fourier transform of dried and calcined sol-gel catalysts. Regarding EXAFS when increasing Mo loading, changes in dried solids are

not pronounced as in calcined solids (see Figure V.*24*). In other words, changes in calcined structure with Mo loading are more evident than in dried solids. Whatever the Mo loading, when comparing dried solid and its calcined structure, EXAFS changes tend to be always the same, a mismatch in low values of wavenumber, particularly around 5 $Å^{-1}$, no shift in oscillations for frequencies around 8 $Å^{-1}$ and a slight deviation in intensity ratio in region around 11 $Å^{-1}$. In FT EXAFS moduli, this behavior is rendered by a slight decreasing in Mo-O peak (in SG-5, also a broadening) as well as a considerable increase and shift to lower *R* position in the peak related to Mo-Mo(Co) bonds.

Quantitatively, one observes that the first Mo-O bond remains unchanged but with higher coordination after calcination. The second (weak and low-coordinated) Mo-O contribution (around 2.26 Å) in dried solids gives place to a short Mo-O distance around 1.95 Å in calcined catalysts. Further, after calcination, we lose the (first) short Mo-Mo bond and Mo-Co bonds arise. This first Mo-Mo contribution in dried samples are low-coordinated, and Mo-Co contributions in calcined solids are important (Figure V.*26*), which leads us to wonder if such Mo-Mo bond really voids or if it is masked by the Mo-Co peak. This trend is quantitatively observed for the other solids of the series, as it shows the results in Table 14 and Table 15.

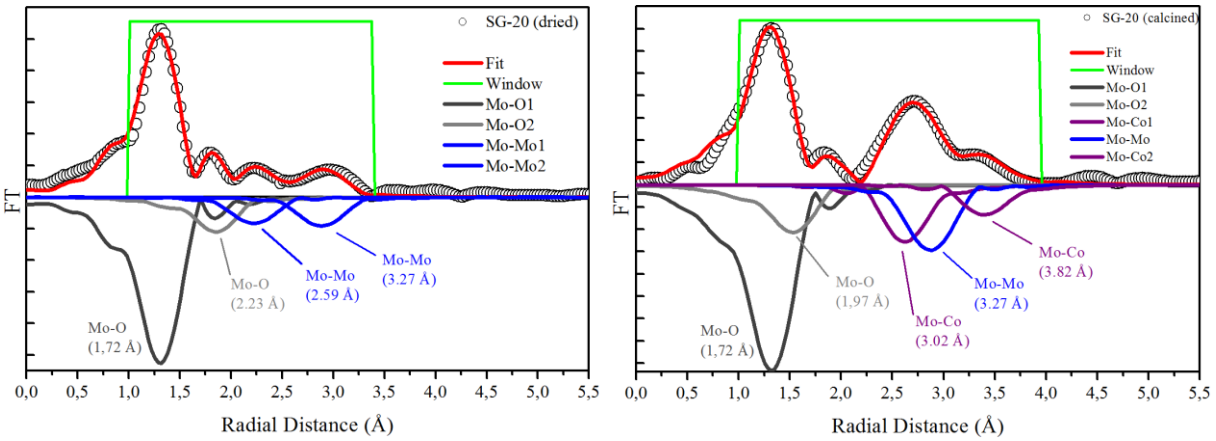

Figure V.26 - FT EXAFS fit comparison between SG-20 dried (left) and calcined (right) samples. In order to better visualization, it is indicated the individual contribution of coordination peaks.

3.3.2. XAFS Analysis at Cobalt K-Edge

It is not uncommon to face with data and experiments that not provide complete information about the structure. We must expect that the response from Mo K-edge to be different from Co K-edge. In that sense, Co K-edge analyses arise as a complementary information in order to solve ambiguous issues in structure of the catalysts.

XANES spectra of sol-gel oxide precursors are perfectly superimposable. They have a pronounced white line but less intense when compared to the CoO bulk reference (Figure V.*27* Top). The position and the

shape of the Co K absorption edge provide information about the charge and geometry of the Co species. The oxidation state of the sol-gel catalysts is clearly similar to the CoO (formally, Co^{2+}). However, there is no other similar feature comparing to this reference compound. Further, the XANES of our catalyst spectra are not a linear combination between the two references (namely, CoO and Co_3O_4), but looking at the shape of the spectra, we expect an octahedral environment such as in cobalt (II) oxide. Another important feature is the small protuberance pointed around 7730 eV, just after the white line. It usually indicates the presence of Co^{3+} ions, the nonbonded and antibonded levels of the Co^{3+} are less stabilized whereas the 1*s* level is more stabilized, leading to a higher transition energy. In anyway, our samples are dominated by Co^{2+} though it may not to be a "pure" Co^{2+} environment. The presence of two oxidation states in structure causes a broadening of the white line and its decreasing in intensity, as observed in Co_3O_4.

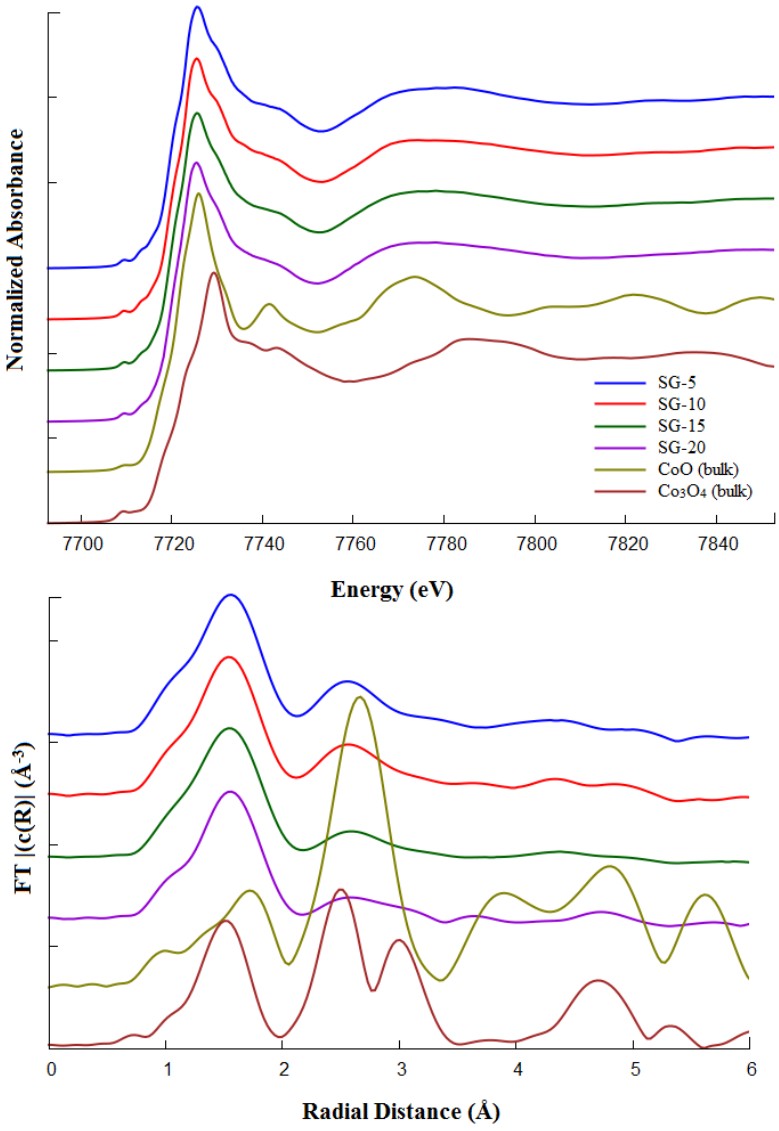

Figure V.27 - (Top) Co K-edge XANES spectra for sol-gel catalysts and bulk references. (Botton) FT of EXAFS signal. In order to better visual comparison, reference compounds had have its intensities lowed in FT figure (0.5 and 0.6, respectively for CoO and Co_3O_4).

At the bottom of Figure V.*27* we show the Fourier Transform of EXAFS signal for the sol-gel catalysts and the reference compounds. The shell structure is quite similar among the catalysts and without exceptions; they carry no major features of the references. Indeed, in a pure visual comparison, one would say that the spectra are strongly related to Anderson-type heteropolyanions (HPAs) (see [26]). In such structure, Co atoms are presented in two oxidation states. The Co^{2+} are coordinated with the heteropolyanion by oxygen bonds in Mo polyhedra surrounding the Co^{3+} octahedral, as draw in Figure V.*28*. They present strong Co-O contributions around 1.5 Å (without phase correction) but unlike the reference compounds, weak Co-Co intensities around 2.5 Å (without phase correction). The values for the EXAFS fits of the sol-gel catalysts are summarized in Table 16.

Table 16 - Refinement of Co K-edge EXAFS parameters of calcined sol-gel catalysts.

Preparation Method	Sample	Bond	N	R (Å)	σ² (Å²)	Δσ	ΔE (eV)	Parameters
Sol-Gel Calcined	SG-5	Co-O	4.6	2.01	0.006	0.002	-2.8 (±4.0)	Δk = 4.9-11.3 ΔR = 1.1-3.2 N_{ind} = 8 χ^2_{Red} = 88 R_{factor} = 0.006
		Co-Co	2.5	2.95	0.016	0.006		
	SG-10	Co-O	4.8	2.01	0.006	0.002	-3.8 (±4.4)	Δk = 4.8-11.2 ΔR = 1-3.3 N_{ind} = 9 χ^2_{Red} = 44 R_{factor} = 0.01
		Co-Co	1.4	2.94	0.013	0.005		
	SG-15	Co-O	4.4	2.02	0.006	0.002	-2.2 (fixed)	Δk = 4.8-11.2 ΔR = 1.2-3.5 N_{ind} = 9 χ^2_{Red} = 64 R_{factor} = 0.001
		Co-Co	1.3	2.93	0.011	0.006		
		Co-Mo	1.3	3.26	0.012	0.008		
	SG-20	Co-O	4.1	2.01	0.006	0.001	-2.9 (fixed)	Δk = 4.8-11.2 ΔR = 1.1-3.9 N_{ind} = 10 χ^2_{Red} = 86 R_{factor} = 0.01
		Co-Co	1.0	2.93	0.007	0.08		
		Co-Mo	1.0	3.27	0.007	0.007		
Uncertainty:	SG-5	$N_{Co\text{-}O}$ = 1.0; $N_{Co\text{-}Co}$ = 1.5						
	SG-10	$N_{Co\text{-}O}$ = 1.2; $N_{Co\text{-}Co}$ = 1.2						
	SG-15	$N_{Co\text{-}O}$ = 0.5; $N_{Co\text{-}Mo(Co)}$ = 0.8						
	SG-20	$N_{Co\text{-}O}$ = 0.7; $N_{Co\text{-}Mo(Co)}$ = 0.9						

For all solids, just one Co-O contribution was needed in simulation, at 2.01 Å. Oxygen coordination number decreases with increasing the Mo loading. In SG-5, 5 O atoms surround cobalt in average, whereas the coordination number in SG-20 is equal to 4.1. Regarding second pseudo-radial distribution peak, the visual differences are translated in number. SG-5 and SG-10 have similar structures, a well-defined peak centered in 2.6 Å corresponding to Co-Co bonds. The higher intensity in SG-5 means higher next-nearest Co neighbors, 2.5 and 1.4, respectively, for SG-5 and SG-10. SG-15 and SG-20

present a slightly distinct feature on this region. Second peak is wider than lower Mo loadings and less intense. For these two high loadings catalysts we needed to introduce a Co-Mo contributions. However, the low signal to noise ratio prevented a fine and unconstrained fit, as it can be seen by high uncertainty values for *N*. For SG15, we just obtained reliable values when doing $N_{Co\text{-}Co} = N_{Co\text{-}Mo}$ and then, fixing energy for an optimal value of -2.2 eV. We obtained this optimal number fixing the E_0 value and performed a fit for each value in a wide energy range (from -10 up to 10). For SG-20, besides E_0 optimization (fixed as -2.9 eV), we had to copy information from Co-Mo bond length from Mo K-edge. Co-Mo distance was set to have the same distance as Mo K-edge, i.e., 3.27 Å

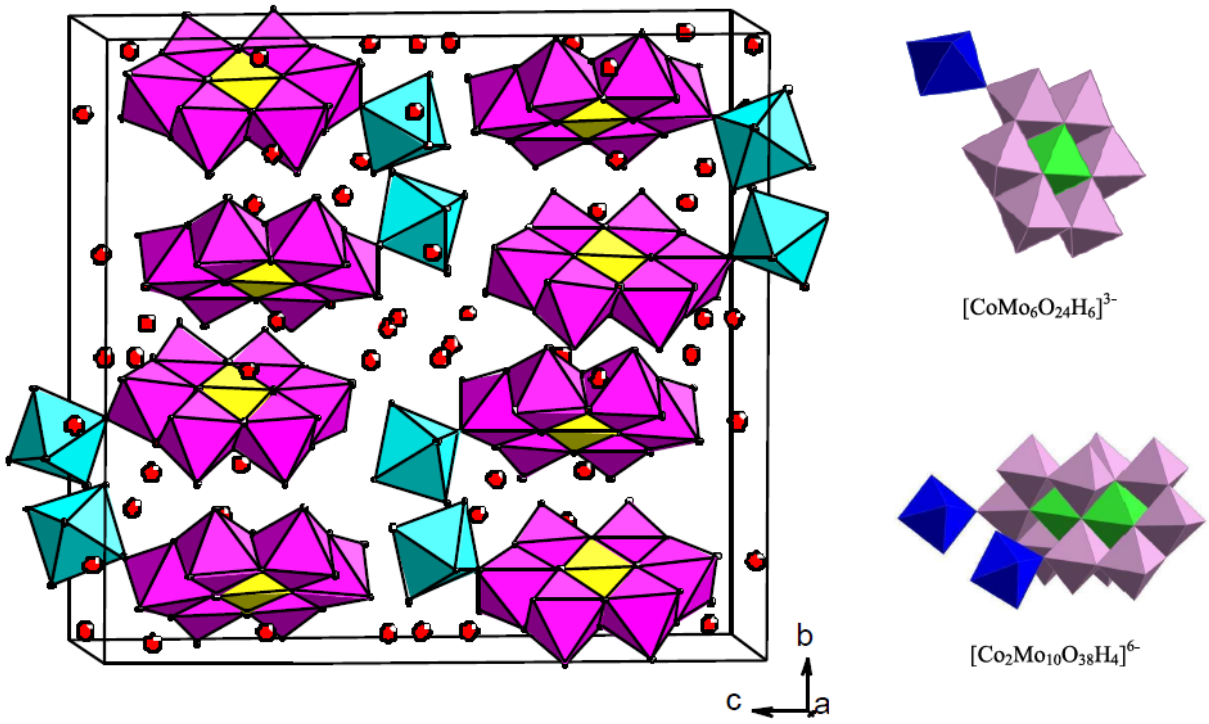

Figure V.28 - (Left) Crystal structure of a typical Anderson-type HPA such as $[CoMo_6O_{24}H_6]^{3-}$, or $CoMo_6$. Rose represents Mo octahedral, light blue Co^{2+} and yellow (green) Co^{3+} (adapted from [26]). (Right) Asymmetric unit of $CoMo_6$ (top) and its derivate Co_2Mo_{10} (bottom).

We can illustrate different Co environments based on scheme of an Anderson-type HPA (Figure V.*28*). The purpose here is just make a qualitative picture of different Co environments in the two preparation methods, regarding what we should expect as EXAFS response.

When looking at Mo atoms, its neighborhood is rich in Mo atoms compared to Co atoms. Thus, a very low (or even a null) signal from Co atoms is expected in Mo K-edge EXAFS; it is naturally quite difficult to fit a Mo-Co contribution. It is true for both sol-gel and impregnated solids (see Table 12 and Table 15). On the other hand, considering the environment like in the scheme above, at Co K-edge both Co-Co and Co-Mo bond distances may appear when and both contributions may be identified when fitting Co K-edge. The presence of only Co-Mo bonds in impregnated solids (Table 13) contrary to sol-gel that present both Co-Co and Co-Mo bonds (Table 16) suggests an environment where cobalt atoms are more

homogeneous in sol-gel solids compared to impregnated catalysts. In other words, in HMA solids, we can draw an environment where Co atoms are surrounded by Mo forming well-dispersed particles, far from each other. In sol-gel catalysts, either Co and Mo form particles that gather both atoms in a single particle with equal Co/Mo ratio, or the dispersion of the particles are not so good as in impregnated solids. Since we suspect that part of Mo are inserted into the support matrix (see results in Chapter IV), we can also imagine a scenario with the two contributions.

3.4. Partial Conclusions: Oxide Precursors

XAFS analysis revealed us the fine local structure of oxide precursors. Mo K-edge XANES spectra from impregnated catalysts are smooth with no strong oscillations and close to HMA-reference compound. Concerning Mo local structure, such catalysts present nearest neighbor number close to 5, which is in accord with the theoretical value ($N = 6$) for octahedral distribution (as in references, MoO_3 and HMA). The next-nearest neighbor region is formed by two Mo-Mo distances and (two) low coordinated Mo-Co contributions. Comparing HMA-20 and HMA-Mo20 (the equivalent catalyst with no cobalt), no large change in coordination number or bond length is observed in Mo K-edge. Co K-edge EXAFS refinement indicates the presence of weak coordinated Co-Mo bonds (in agreement with Mo K-edge) but no Co-Co bonds, suggesting the Co atoms play a small role in this structure or they are in a segregate phase.

For sol-gel series, XAFS records were performed for dried and calcined solids. Mo K-edge for dried sol-gel catalysts indicate similar structure no matter the Mo loading, two oxygen as nearest-neighbors in coordination number close to 3.5 (one short distance and another longer) and two low coordinated Mo-Mo distances (a remarkable short distance Mo-Mo bond at 2.59 Å is highlighted). No Mo-Co contributions could be simulated and no major differences is seen when comparing SG-20(dry) with SG-Mo20(dry), i.e., it seems that cobalt plays no role in dried sol-gel structure.

After calcination, one observes a slight evolution with the Mo loading, pointed out by XANES and FT EXAFS at Mo K-edge. Data suggests that SG-5 and SG-10 form a group with close structural similarities whereas SG-15 and SG-20 form another group. Quantitatively, EXAFS refinement at Mo K-edge points out to a slight trend of decreasing in coordination number of nearest-neighbors (oxygen). Further, calcined sol-gel solids exhibit two Mo-Co contributions with the same trend of oxygen "first shell", to decrease the coordination number with Mo loading. The short length Mo-Mo distance is absent (or masked by the Mo-Co one) and the longer Mo-Mo bond found in dried solids remains unchanged (slightly high coordinated). In Co K-edge EXAFS fit, distinctly to impregnated solids, we were able to well simulate both Co-Mo and Co-Co contributions (except for low Mo loadings, where just Co-Co contributions were simulated). The parameter values are in agreement with Mo K-edge. We can analyze the influence of cobalt in the structure by looking SG-20 and SG-Mo20. When no cobalt is present in

structure, the low coordinated Mo-Mo short distance (at 2.57 Å) can be simulated. Further, the single Mo-Mo contribution observed in SG-20 (3.27 Å) seems to be the average of the remaining two Mo-Mo contributions observed in SG-Mo20 (3.22 Å and 3.34 Å). It suggests that Co atoms in sol-gel structure plays an effective role in that case.

By all these aspects, one can state that do exist a strong structural evolution from dried to calcined sol-gel catalysts that is driven likely by support (or with the support) changes after calcination.

We can highlight some distinct aspects when comparing solids from both preparation methods. Maybe the most evident is how is arranged the neighborhood around Mo atoms. As pointed out by EXAFS at Mo K-edge, despite similarities in Mo-O distances, the impregnated solids has higher coordination number compared to sol-gel catalysts. HMA catalysts present two Mo-Mo contribution whereas in sol-gel samples we observe just one. Apart from the equivalent distance found in sol-gel solids at 3.27 Å (with nearly the same coordination number), impregnated catalysts exhibit one extra longer Mo-Mo contribution at 3.40 Å. Solids from both methods present two Mo-Co contributions. However, in impregnated series, we have one short (2.75 Å) and one long (3.88 Å) distance, both very low coordinated (around 0.1). In sol-gel catalysts, we have two slightly stronger distances, one at 3.02 Å and another at 3.82 Å.

Comparing the parameters extracted from Co K-edge for both preparation method, despite the same oxygen distribution distances and coordination number for both series, the atomic distribution on second coordination sphere is largely different. For high Mo loading samples of the HMA series have a Co-Mo bond length (around 3.20 Å), but at the same time no Co-Co contributions in these solids suggests a single Mo-surrounded Co structure that are well-distributed in the whole solid. In SG solids, instead, the important Co-Co bond observed indicate that cobalt are next to each other.

In anyway, it is harsh to speculate about the particular structure viewed from cobalt (and for sol-gel solids, in general) because in sol-gel preparation method precursor and support were mixed in one just step. This open wide possibilities, for instance, $CoMoO_4$-type structure, an Anderson-type environment, or just an ill-dispersion of Co atoms caused by no reaction with molybdenum oxide. In summary, it seems that in sol-gel solids, the cobalt atoms are more influent than in impregnated catalysts.

4. Activation Reaction Studied by *in situ* XAFS: The Active Phase

The prepared oxide catalysts, namely SG-*x* (*x* = 5, 10, 15, 20) and HMA-*y* (*y* = 5, 20) were characterized by QEXAFS during activation step at both, Co and Mo K-edges. We also performed QEXAFS

characterization during Temperature-Programming Reduction (TPR) under H_2 flow for the SG-5, SG-20, HMA-5 and HMA-20 samples at Mo K-edge. The analysis conditions are presented below

In this section, basically, we will make a qualitative description of the reactions in terms of the evolutions of the spectra. It is quite important to describe the trends in the evolution, the minor details of each reaction, and look at temperature changing steps and to compare evolution in terms of preparation method.

As quantitative contribution, we describe molecular structure of the final states either after sulfuration or after reduction (or both). Furthermore, we discuss in a comparative sense, the differences and similarities among the final state according to its preparation method.

In order to distinguish different states of the same sample, in this section we add on a suffix to the sample name according to the treatment that was carried. For instance, the final state of SG-5 after sulfuration process will be named SG-5(sulf). In the same way, after TPR, this same sample will be named SG-5(red).

4.1. Analysis Conditions of QEXAFS *In Situ*

EXAFS data were recorded in QEXAFS mode at SAMBA beamline at Synchrotron SOLEIL [34] with a 1 Hz frequency. This setup allow us to get at each second one spectrum at the increasing of the Bragg angle and one spectrum at the decreasing of the Bragg angle. However, in order to avoid any variation from the difference of mechanic movement of the monochromator, we take into account just the spectra at the increasing of the Bragg angle.

SAMBA beamline in QEXAFS mode is able to record (virtually) at the same time both Mo and Co K-edges. Nevertheless, we are using TiO_2 as catalytic support. Titanium interacts strongly with x-rays and it prevented us to use this feature of SAMBA beamline (recording both edges at the same time). This was especially true for low Mo-loading samples (such as SG-5 and HMA-5) where we did not achieve to setup the machine in order to give us an acceptable compromise between the edge-jump and low signal-to-noise ratio for the two edges at the same time. Thus, in order to keep the same experimental conditions for all samples whatever the Mo-loading, we performed separated experiments for each K-edge (Co and Mo), obviously, using different samples from the same catalyst. By doing so, we could maximize the acquisition conditions for both edges.

Further, in order to improve the signal-to-noise ratio the data used in the analysis were averaged in 30 seconds of the reaction, i.e., despite one spectrum per second, we average every 30 spectra to form one.

The treatment used in reaction cell to get the active phase was very similar to the other processes. The samples were heated up to 400 °C in a ramp of 6 °C/min under a flux of H_2/H_2S (15% H_2S). At the plateau, the samples stayed for 1h and then naturally cooled down to the room temperature under Helium flux, to record another set of spectra (Figure V.*29*). At the plateau and after cooling down, no longer reaction neither atomic-structural changes are expected, thus we averaged each 200 spectra to form a single one.

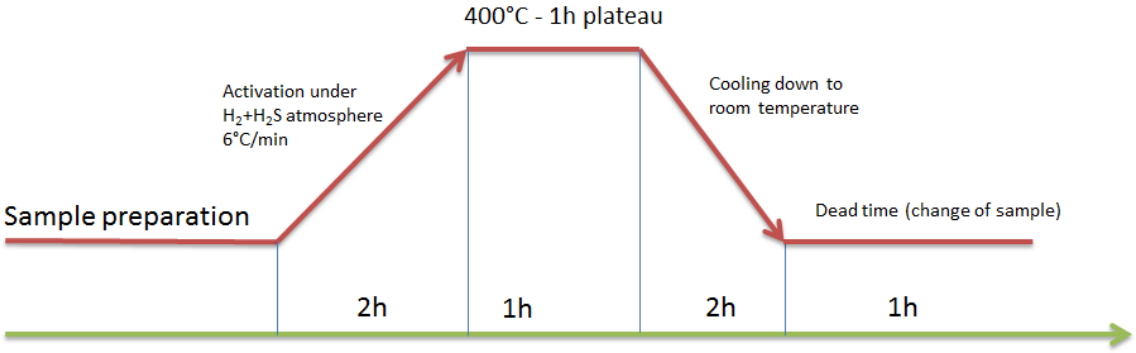

Figure V.29 - *In Situ* XAFS general scheme for a sample record during the activation reaction experiment.

The mass of each catalyst was chosen to optimize the edge-jump at the corresponding K-edge. In order to fill up the reaction cell cavity, the catalysts were eventually diluted with diamond powder.

4.2. Impregnated Series Activation and TPR

4.2.1. XAFS Analysis at Mo K-Edge

Activation: From data recorded in QEXAFS mode at the Mo K-edge on the calcined impregnated catalysts, we are able to probe spectral evolution during the solid activation. The first approach is to look how XANES evolves during the reaction, as illustrated in Figure V.*30* for HMA-20. One observes that the oxide precursor evolves rapidly when activation starts. Pre-edge feature vanishes in the first minutes after the beginning, suggesting that structural changes are present early in activation. One observes also changes in XANES oscillations feature, particularly, the third one disappears in the beginning of the reaction, but with a slower rate when compared with the pre-edge feature. On the course of the reaction, one observes the edge shift to lower energy values and the first XANES bump (typical for an HMA-like oxide) no longer exist from the half of the reaction on. The final state has a shoulder and one first broad XANES oscillation that is typical for a MoS_2 compound, as expected.

In order to illustrate another point of view, we chose to describe evolution in terms of Fourier transform of the EXAFS signal. MoS_2 has a typical clear and unique intense peak in the FT, which makes it easy to differentiate Mo-O and Mo-S contribution. Looking at the structural evolution by this point of view may be visually easy and instructive, as drawn in Figure V.*31*. In the foreground of the figure, we see the initial oxide state, the large peak related to oxygen distance distribution, or the first coordination sphere, is centered on 1.1 Å (without phase correction) as previously stated. As soon as the reaction starts, this oxygen contribution experiments a rapid intensity decreasing. After the first third of the reaction (about 120 °C), the oxygen peak is almost not noticed. From that moment, one observes the arising of the Mo-S distance peak (at 2.0 Å, without phase correction). In addition, from the middle of the reaction up to the end, one sees this peak rising strongly together with the appearance of the Mo-Mo contribution distance (at 3.5 Å, without phase correction). The latter becomes late evident and it becomes pronounced from the last quart of the reaction.

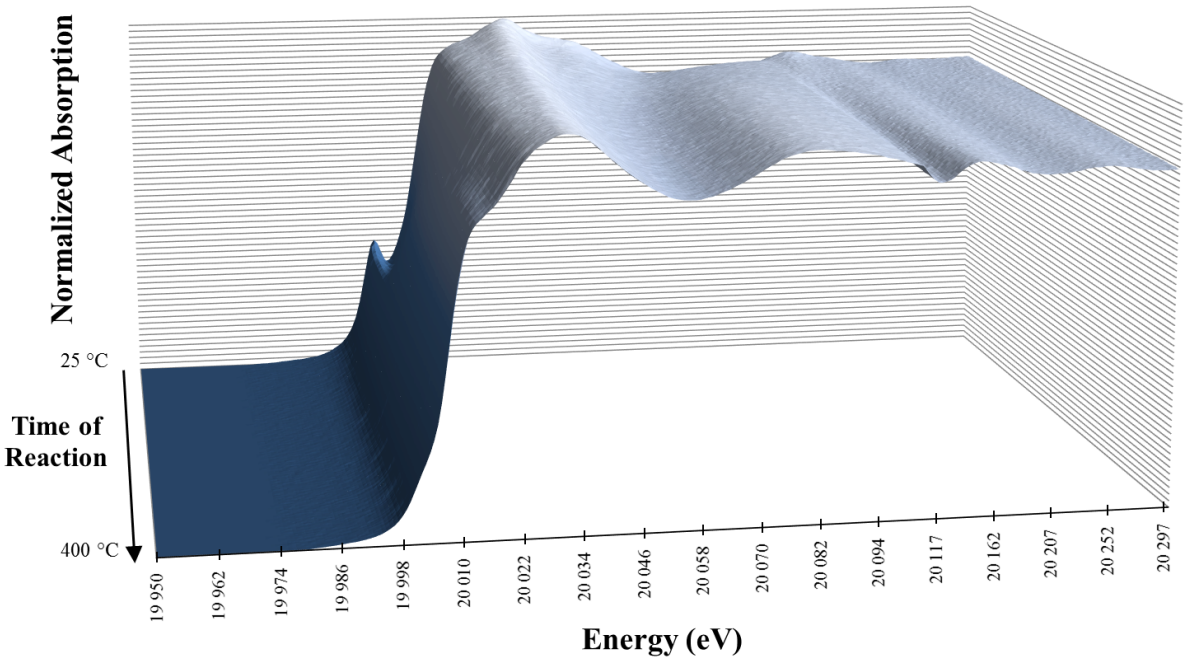

Figure V.30 - Mo K-edge XANES spectral evolution of HMA-20 during the activation reaction.

The inset of the Figure V.*31* shows as final state spectra for HMA-5 and HMA-20 together with the bulk MoS_2. One observe that the positions of the peaks perfectly match the positions of the reference, namely, Mo-S and Mo-Mo contributions, respectively at 2.0 Å and 2.8 Å (without phase correction). A second Mo-S contribution is expected around 3.4 Å (without phase correction), but we note that it is very small at HMA-20(sulf) and is virtually void at HMA-5(sulf). This observation is intimately relate to the size of the particles, since the ratio between the two main peaks in the ideal structure (around 1:1) is not nowhere near true for catalyst structures. In other words, in HMA-20 one has nanosized MoS_2 particles.

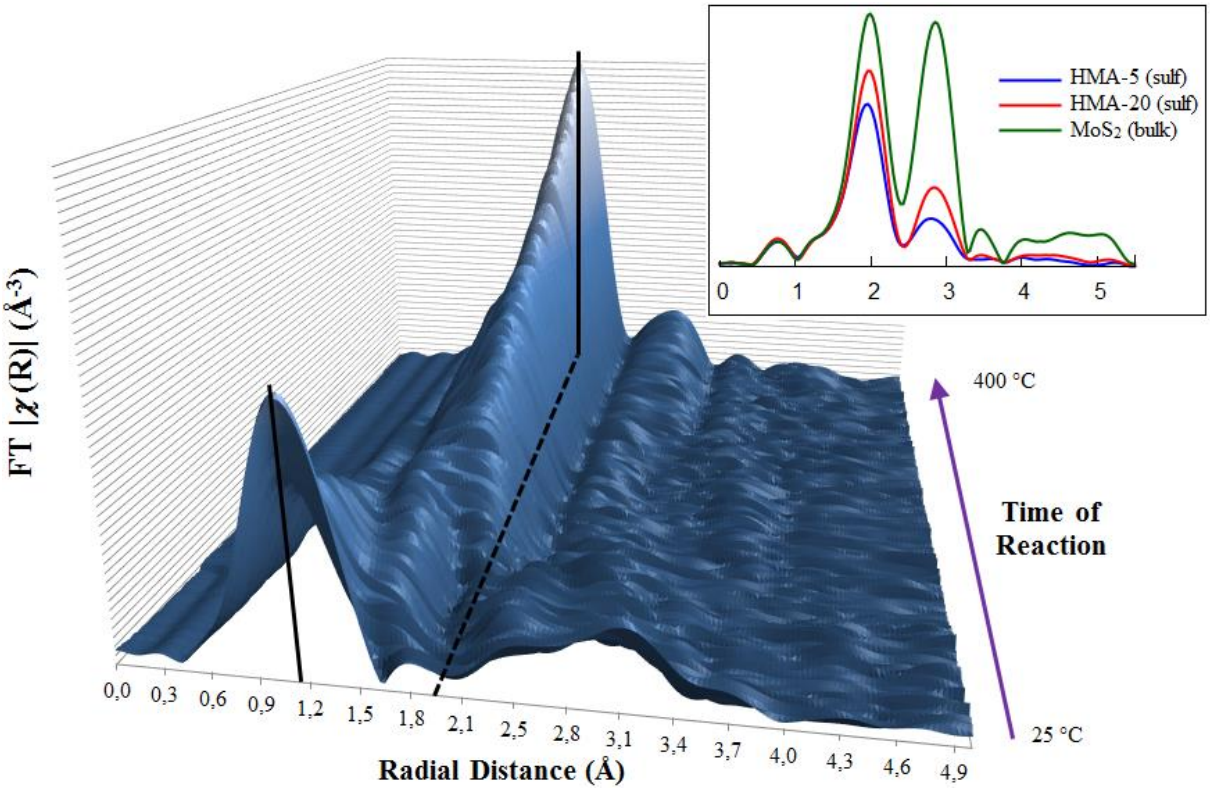

Figure V.31 - Mo K-edge FT EXAFS of HMA-20 during activation. The onset shows the final spectra for HMA-5 and HMA-20 compared to the MoS2 reference.

The structural parameters obtained from refinement of EXAFS of final state spectra after sulfuration reaction for impregnated catalysts can be read on the Table 17. All the distance types and values are in accordance with a MoS_2 model. Thus, we may say for sure that both catalysts totally transform into MoS_2. A slight enlargement in the second Mo-S distances in both samples is observed, likely due to nanometric size of the particles. We equally attribute to it the mismatch in the number of Mo-Mo contribution. It is noteworthy to say that such second Mo-Mo contribution is related to the 2-D structure (see Figure V.*32*a)

Table 17 - Refinement of Mo K-edge EXAFS parameters of the HMA catalysts after sulfuration.

Preparation Method	Sample	Bond	N	R (Å)	σ² (Å²)	Δσ	ΔE (eV)	Parameters
HMA Sulfided	HMA-5	Mo-S	5.3	2.40	0.0053	0.0006	3.2 (±0.9)	Δk = 4.6-13.7 ΔR = 1-4.1 N_{ind} = 16 χ^2_{Red} = 136 R_{factor} = 0.008
		Mo-Mo	2.9	3.16	0.007	0.001		
		Mo-S	0.7	4.10	0.0053	0.0006		
	HMA-20	Mo-S	5.6	2.40	0.0045	0.0005	6.5 (±0.7)	Δk = 4.7-13.5 ΔR = 1-4 N_{ind} = 16 χ^2_{Red} = 436 R_{factor} = 0.005
		Mo-Mo	3.5	3.17	0.005	0.001		
		Mo-S	0.7	4.10	0.0045	0.0005		
Uncertainty:	HMA-5: N_{Mo-S} = 0.3/0.7; N_{Mo-Mo} = 0.9 HMA-20: N_{Mo-S} = 0.3/0.6; N_{Mo-Mo} = 0.7					* *R*-uncertainty are < 0.5% in average		

As long all evidences clearly point to a MoS_2 pure phase formation and considering such impregnated routine a stablished well-known procedure to form such kind of active phase, we can regard HMA-20 as a reference for nanosized MoS_2 particle, as it was mentioned early in this text. Assuming that, for now on we will consider this compound as a suitable reference for a TiO_2-supported nanosized MoS_2 particle in XANES analysis (see Figure V.*32*b).

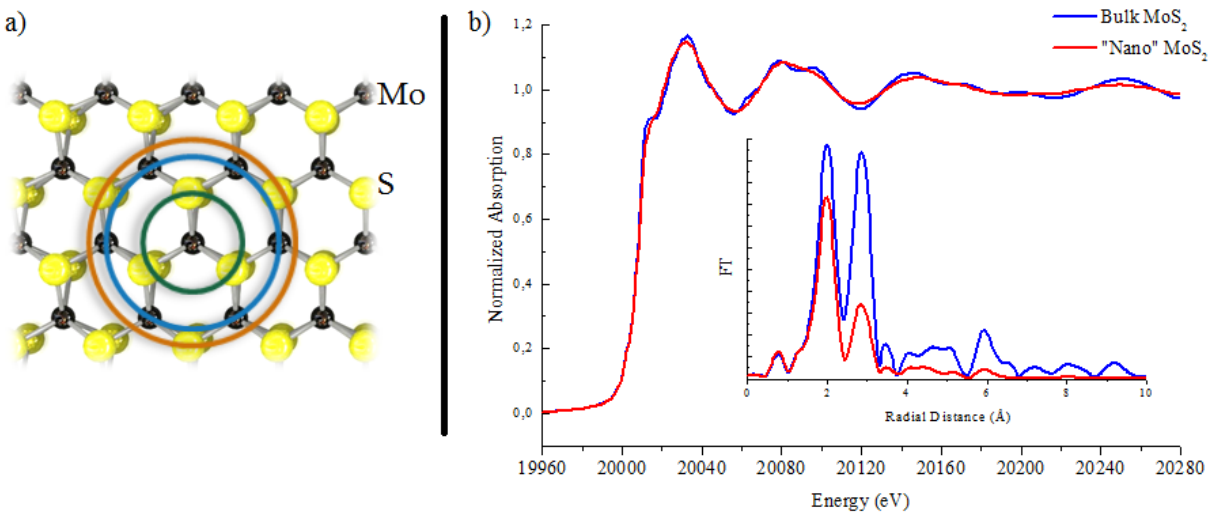

Figure V.32 - a) 2D ideal structure of MoS_2, each Mo atom (black) has 6 sulfur atoms (yellow) as nearest-neighbors (green circle), 6 Mo atoms as next-nearest-neighbors (blue circle) and 6 sulfur atoms on the 3rd coordination shell (orange circle). b) XANES and FT EXAFS (inset) comparison between experimental bulk MoS_2 (blue) and supported "nanosized" MoS_2 (red).

Reduction: Figure V.*33* shows XANES spectra of impregnated solids after TPR, HMA-5, HMA-20 and HMA-Mo20 are plotted with MoO_2, the reference. HMA-Mo20 spectra is quite similar to MoO_2. HMA-5 and HMA-20 are almost superimposed and both present a pre-edge feature that is absent in the MoO_2 reference, which may indicate that a complete reduction was not achieved. FT of EXAFS (inset of Figure V.*33*) confirms these similarities between HMA-Mo20 and the reference. By the differences observed between HMA-20 and HMA-Mo20, we can conclude that cobalt addition to the catalyst seems to modify strongly the structure, particularly, the second radial distribution region (the range in *R* between 2 - 4 Å).

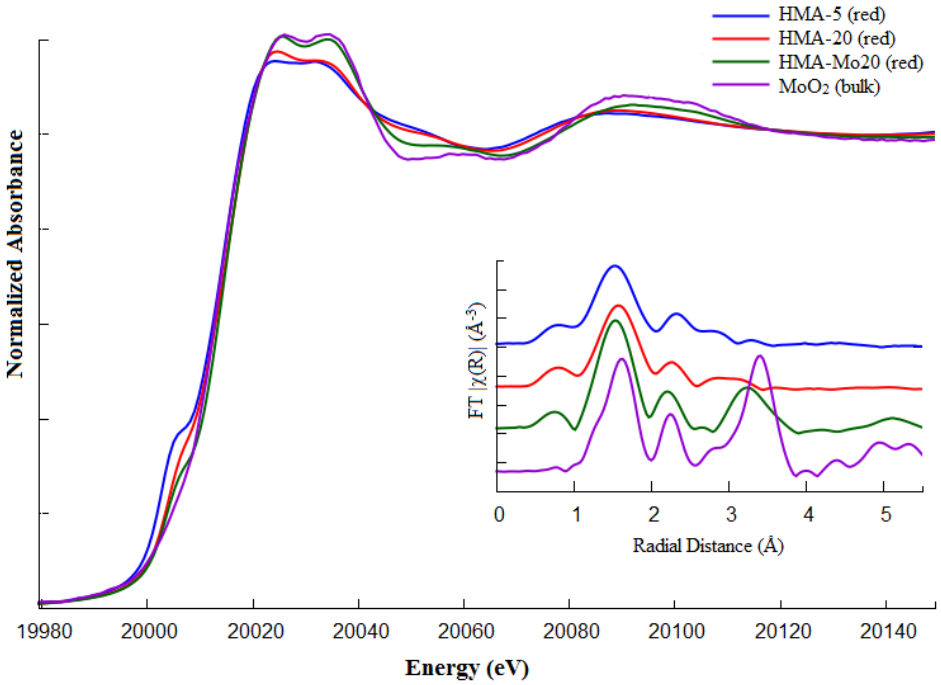

Figure V.33 - Mo K-edge XANES spectra for HMA catalysts after reduction compared to MoO_2refernce.

Structural parameters obtained from EXAFS fitting are listed in Table 18. As said before, cobalt insertion in structure drastically modifies the atomic arrangement (or the size of the particle). Comparing HMA-20 and HMA-Mo20, one observes that we save the same configuration for the oxygen sphere and the first Mo-neighbors, about 4 oxygen atoms at 2.00 Å and 0.5 Mo atoms at 2.57 Å. However, in HMA-Mo20, in average 2 extra Mo atoms are located in long distance, at 3.71 Å, whereas in HMA-20 we found 0.5 Mo atoms at 3.29 Å. In HMA-5, we were able to simulate just the first Mo-Mo bond and it has the similar values comparing to HMA-20.

Table 18 - Refinement of Mo K-edge EXAFS parameters of the HMA catalysts after TPR.

Preparation Method	Sample	Bond	N	R (Å)	σ² (Å²)	Δσ	ΔE (eV)	Parameters
HMA Reduced	HMA-5	Mo-O	3.6	2.01	0.004	0.003	-6.9 (±6.4)	Δk = 4.7-13.4 ΔR = 1.1-4 N_{ind} = 11 χ^2_{Red} = 237 R_{factor} = 0.09
		Mo-Mo	0.3	2.61	0.001	0.006		
	HMA-20	Mo-O	3.6	2.03	0.004	0.001	-3.4 (±3.5)	Δk = 4.5-13.6 ΔR = 1.1-3.9 N_{ind} = 16 χ^2_{Red} = 1835 R_{factor} = 0.05
		Mo-Mo	0.5	2.60	0.004	0.005		
		Mo-Mo	0.4	3.29				
	HMA-Mo20	Mo-O	4.0	2.00	0.004	0.001	-1.2 (±3.0)	Δk = 4.4-13.3 ΔR = 1-3.8 N_{ind} = 15 χ^2_{Red} = 520 R_{factor} = 0.04
		Mo-Mo	0.5	2.55	0.003	0.003		
		Mo-Mo	2.0	3.71				
Uncertainty:	HMA-5:	N_{Mo-O} = 1.3; N_{Mo-Mo} = 0.3						
	HMA-20:	N_{Mo-O} = 0.8; N_{Mo-Mo} = 0.3						
	HMA-Mo20:	N_{Mo-O} = 0.8; N_{Mo-Mo} = 0.3/1.0						

4.2.2. XANES Analysis at Co K-Edge

As previously stated, unfortunately, we were not able to record high definition data at Co K-edge during *in situ* experiments in order to perform EXAFS simulation analysis. Thus, for activation reaction at Co K-edge we count just with the XANES spectra for the catalysts in the final state, i.e., after activation reaction. Figure V.*34* shows the final state for both impregnated catalysts. HMA-20 clearly arrived in a complete sulfidation state, while HMA-5 seems to retain some spurious oxidic phase. A rough linear combination fit, using as reference HMA-20(sulf) and oxide HMA-5, results in 65% of sulfided phase. It is noteworthy to say that feature observed in XANES around 7760 eV is nothing but a glitch[10] and do not represent real behavior.

HMA-20(sulf) presents all features of a sulfided specie, although XANES is not perfectly similar to Co_9S_8 compound (see, for instance, [35], [36]). Bulk Co_9S_8 has a prominent pre-peak at 7710 eV and a characteristic shoulder around 7718 eV. Further, the first XANES peak (around 7730 eV) is slightly less intense than the second one (around 7740 eV). HMA-20(sulf) has low pre-peak, no shoulder and both XANES oscillations are equally intense. It can be either due to the nanoscale particle that loses characteristic intensities in the main feature peaks (analogously to HMA-20(sulf) at Mo K-edge

[10] A glitch is a localized disturbance (an artifact) caused by experimental problems (sometimes intrinsic) such as Bragg spot of the monochromator, sample inhomogeneity, monochromator instability, source instability, and a number of other problems.

compared to MoS_2), or because we do not have a Co_9S_8-type structure in our final state. There is no much reports in literature on Co K-edge for CoMo-based catalysts (particularly, TiO_2-supported), but similar mismatch was recorded in Al_2O_3-supported catalysts ([35], [36]).

EXAFS (the inset of Figure V.*34*) just presents a mismatch in the first oscillations, as expected for this situation. Low signal-to-noise ratio prevents further discussion on the high wavenumber values, so that it becomes impossible to describe fine differences in atomic environment of sulfided Co species.

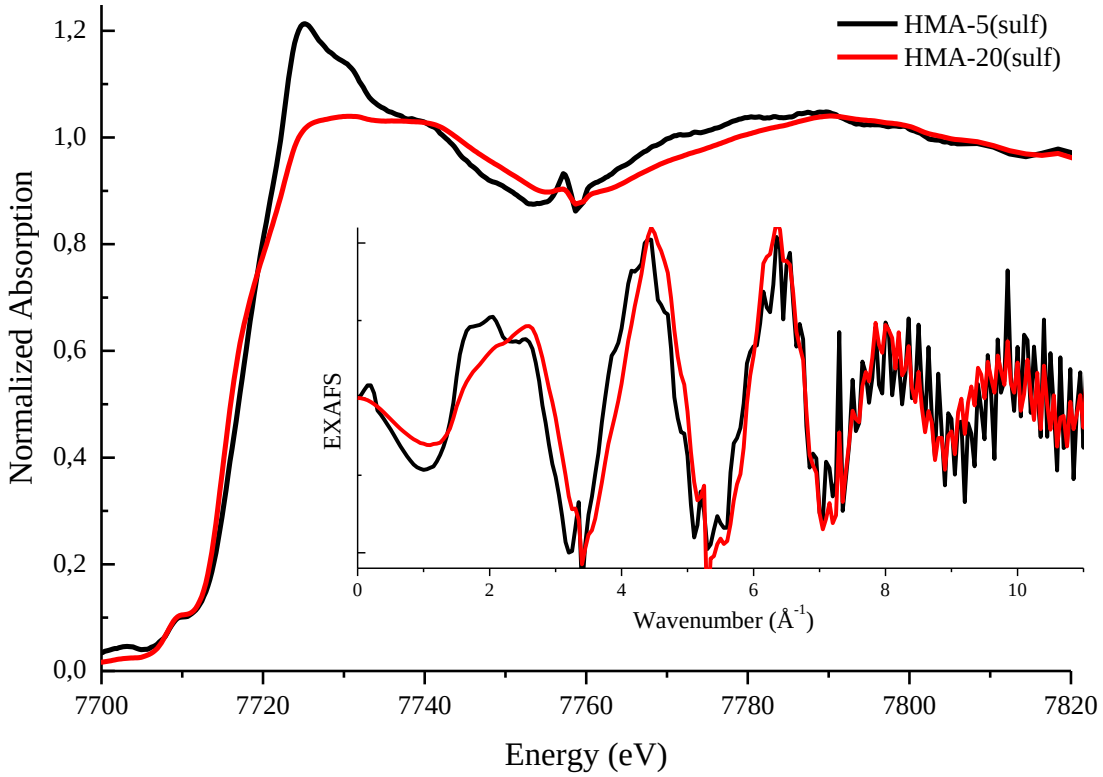

Figure V.34 - Co K-edge XANES for HMA catalyst with EXAFS on the inset of the figure.

Particularly, in the HMA-20 evolution (Figure V.*35*), a similar trend to SG-20 is observed. A very rapid transformation takes place even in room temperature, the withe line intensity downs suddenly. Then, a slowdown in the intensity decreasing is observed up to the middle of the reaction. The edge shift to low energy values takes place smoothly, but is more pronounced from the middle of the reaction on. Further, one observes a slight intensity increase of the small pre-peak at 7710 Å. The final state spectrum seems to stabilize on the last quarter of the activation and no greater changes is observed until the end. We recall that disturbances at 7760 eV and 7820 eV are nothing but glitches.

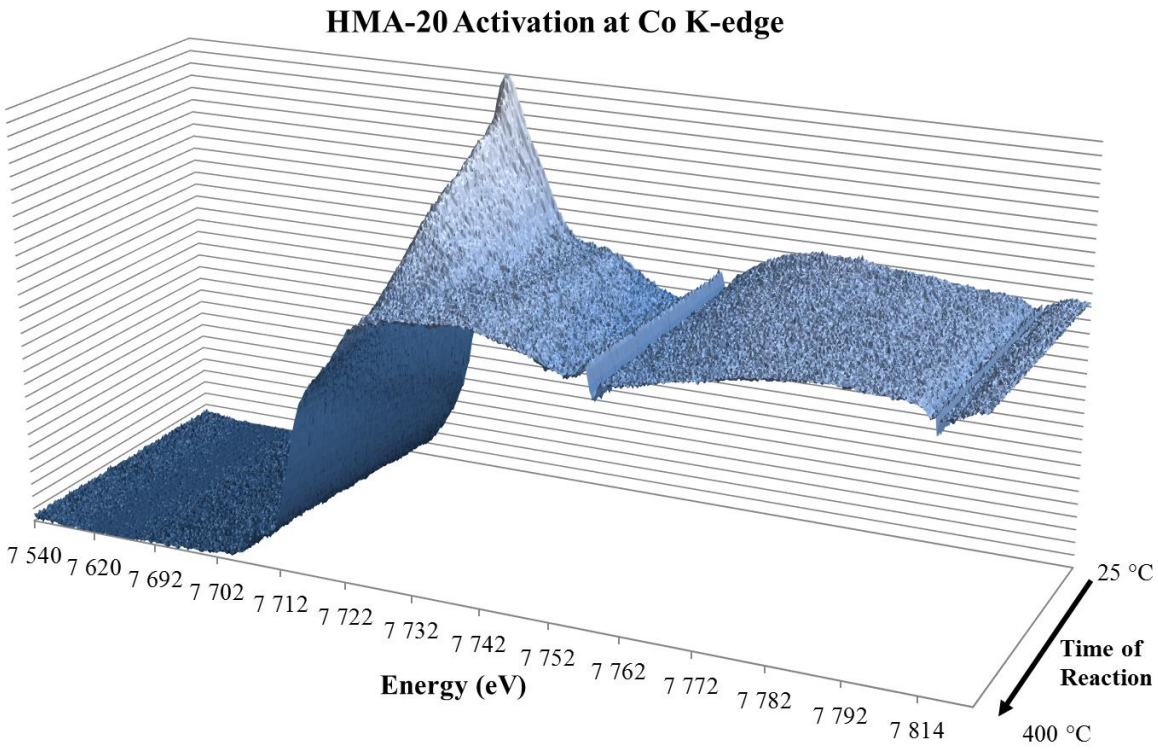

Figure V.35 - Co K-edge XANES evolution of HMA-20 during activation.

4.3. One-Pot Sol-Gel Series Activation and TPR

4.3.1. XAFS Analysis at Molybdenum K-Edge

Activation: From data recorded in QEXAFS mode at Mo K-edge on the calcined sol-gel catalysts, we are able to probe XANES spectral evolution during the activation step reaction, as it is observed in Figure V.*36* for the SG-20.

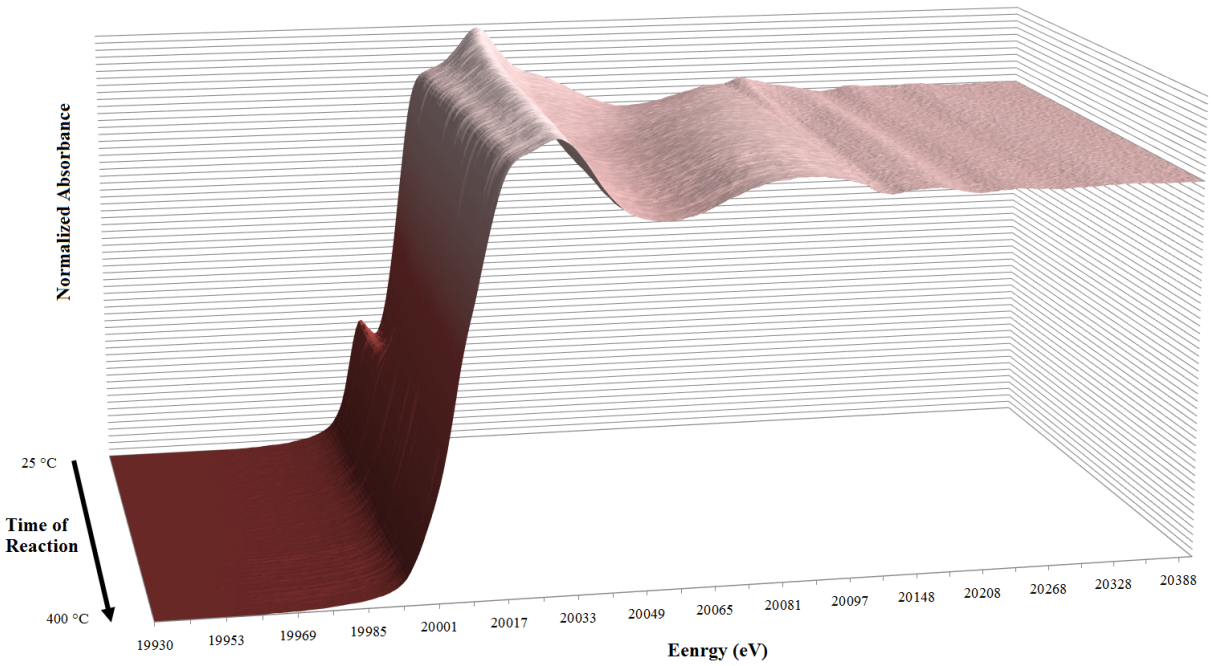

Figure V.36 - Mo K-edge XANES spectral evolution of SG-20 during the activation reaction.

One notes that the first structural changing happens early, when the pre-edge peak gradually disappears (around 100 °C). During this time interval, the first EXAFS oscillation move down in energy as well as the absorption edge. One observes that at the half of the reaction, the shape of the final state spectrum is already evident and dominant. We expect, thus, to achieve a sulfided condition in this region.

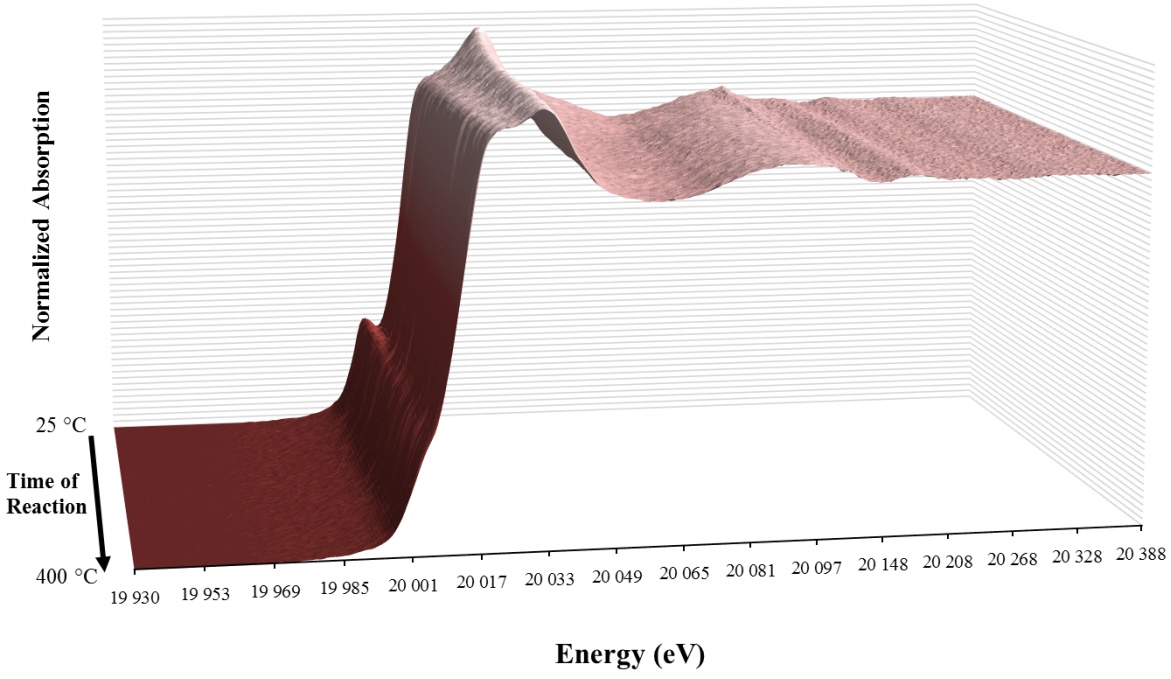

Figure V.37 - Mo K-edge XANES spectral evolution of SG-5 during the activation reaction.

In contrast to SG-20 evolution during the activation, when looking at the other extremity of the sol-gel series, SG-5 has a distinct behavior, as observed in Figure V.*37*. On observes that the oxide precursor do not evolve to a clear sulfided final state. The intensity of the pre-edge feature drops as fast as in SG-20, but a trace of it remains until the end of the process. Furthermore, no large edge shift to lower energy value is observed and the first XANES oscillation is still intense in the final state.

In Figure V.*38* (Top), the final state XANES spectrum of SG-20 is compared to the initial state spectrum and the MoS_2 bulk reference. It is clear that in the final state the catalysts does not present the MoS_2 structure, despite great similar features between SG-20(sulf) and MoS_2 such as oscillation frequency and XANES peak around 20033 eV. Evidences of partial sulfidation are the absence of the shoulder around 20013 eV in the SG-20(sulf) and the position of the absorption edge, between the initial state and MoS_2 final state.

The suspicions are readily confirmed when we observe the Fourier Transform of the EXAFS signal for SG-20(sulf) (the inset in Figure V.*38*). The Mo-S contribution at 2.0 Å (without phase correction) is present as well as the typical Mo-Mo contribution in MoS_2 environment around 2.8 Å (without phase correction). In fact, the latter is slightly shifted to lower values of *R* in SG-20(sulf) compared to the reference. However, there is still a considerable contribution centered on 1.3 Å (without phase correction) due to Mo-O bond. Such oxygen distance clearly is not the same as in oxide initial state, instead, usually such shift to higher energies is typical for a Mo-O bond in a reduced oxide, as shown in Figure V.*38*-top comparing oxygen peak in the precursor oxide and in MoO_2). That means that in the final state either we have a non-sulfured reduced mixed with MoS_2 phase or a single oxysulfide phase. EXAFS signal (Figure V.*38*, bottom) confirms that the overall structure is close to MoS_2 phase, thus, with sulfided state features. The oscillation frequency is in accordance to the MoS_2 EXAFS, and no remarkable outside oscillation is observed. Since they are not superimposed and taking into account the XANES spectra, we definitely can assure that SG-20(sulf) is not a pure MoS_2-type compound.

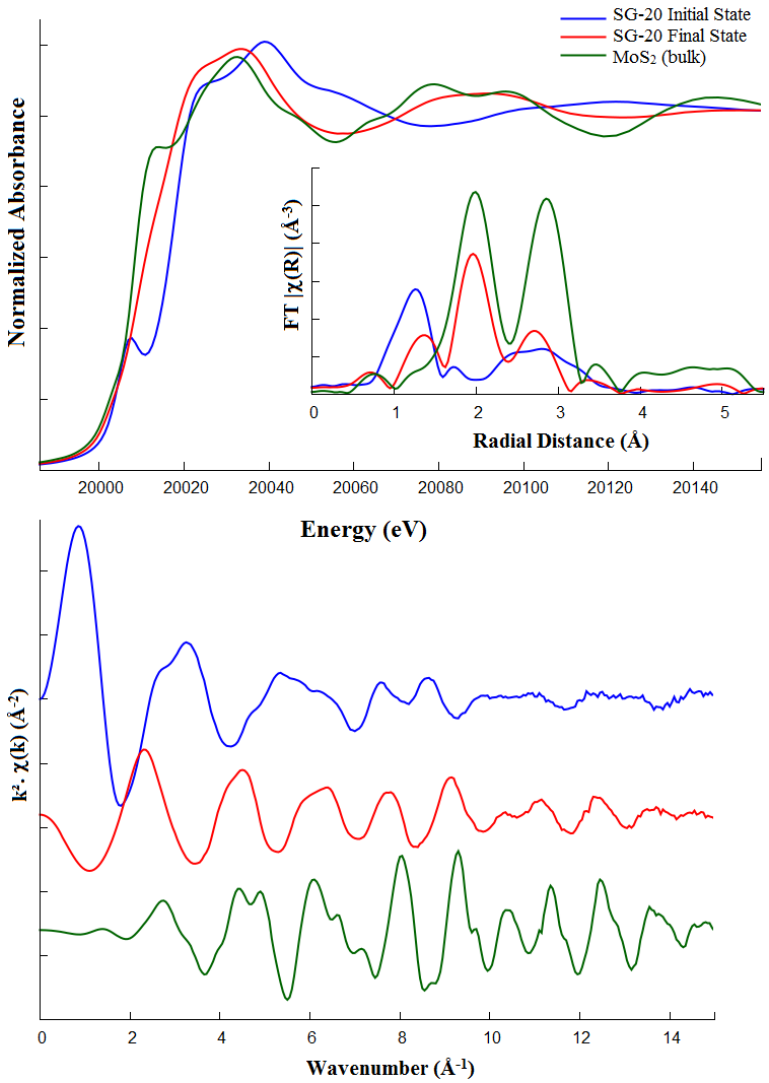

Figure V.38 - (Top) Mo K-edge XANES spectra comparison of initial state (blue), final state (red) and bulk MoS_2 (green). The onset represents the FT of EXAFS signal; MoS_2 was weighted by 0.5 in order to favor comparison. (Bottom) k^2-weighted EXAFS from initial state, final state and bulk MoS_2.

Given unique XANES properties such as atomic selectivity, oxidation state and local atomic symmetry sensitivity and so on, a first step of classical XAS analysis includes linear combination fit of references compounds to a certain state. Particularly, we are interested to know on the degree of sulfidation of the final state, in others words, we want to know how much of our final state corresponds to the active phase, MoS_2. The conventional procedure consists in take the XANES of bulk MoS_2 as reference and fit it to the final states of each sol-gel XANES.

As showed in Figure V.*38*(top), direct visual comparison tell us that SG-20(sulf) XANES is far from MoS_2 bulk reference. The FT indicates that a shifted Mo-O contribution (which suggests reduced specie) is present in this final state. This trend is observed for all solids of the series. Therefore, as reference to the linear combination of the final state, we take the MoS_2 and the spectrum corresponding to the final

state of the TPR[11]. As long we have TPR data just for SG-5 and SG-20, for SG-10 and SG-15 we performed two linear combination tests considering the following groups of reference: {MoS_2 + SG-5(red)} and {MoS_2 + SG-20(red)}, then, it was taken the best fit (the smallest residual). Here, instead of use MoS_2 bulk spectrum as reference, we adopted the sulfided spectrum of HMA-20 recorded at room temperature after the reaction as reference for a nanosized MoS_2 particle, as previously discussed. It is well-known that XANES spectra have their features modified with the size of the particle. Thus, it is no use to consider bulk structure to perform linear combination in our nanosized catalyst.

Results from the linear combination fit are displayed in Table 19, note that in spite of SG-5(sulf) appears as more sulfided than SG-10(sulf), its figure of merit is more than twice the reduced-χ^2 of SG-10(sulf). Furthermore, taking into account the uncertainty, both have the same "degree of sulfidation". Anyway, as we will show, in both SG-5(sulf) and SG-10(sulf) final state, none Mo-S contribution as found when analyzing EXAFS structural parameters.

Far of indicating the precise sulfidation degree, these results are concerned to the aspects revealed by XANES, i.e., they are related to properties such as local atomic symmetry, oxidation state, etc.

Table 19 - XANES Linear Combination fit* for Sol-Gel final sulfided states.

Sample	*% of MoS_2*	*% of Reduced Specie*	*Reduced-χ^2*
SG-5	20.1(6)	79.9(6)	61.8 x 10^{-6}
SG-10	19.5(4)	80.5(4)	28.7 x 10^{-6}
SG-15	42.5(6)	57.5(6)	33.0 x 10^{-6}
SG-20	50.8(2)	49.2(2)	9.1 x 10^{-6}
SG-Mo20	58.8(8)	41.2(8)	58.8 x 10^{-6}

* Linear combination fit by using least square method in the range of -20 eV < E_0 < 100 eV.

Looking deep in the structure, Figure V.*39* show us the Fourier Transform of EXAFs signal of sol-gel sulfided solids, references are also display in same figure. As indicated by linear combination fit, all samples present a Mo-O contribution, indicated by peak centered in 1.3 Å (without phase correction). This peak is more prominent in the two lower Mo loadings, namely, SG-5(sulf) and SG-10(sulf). SG-15(sulf), SG-20(sulf) and SG-Mo20(sulf) present the same shape, although SG-15(sulf) has less intense peaks. The peak centered in 2.0 Å is associated to Mo-S bond characteristic of MoS_2 phase. Such contribution is found in all solids, but in SG-5(sulf) lower Mo loadings it is slightly shifted to higher distances. Further, in SG-5(sulf) this peak is very low and merged with the neighbor peak, which biases an accurate evaluation of intensity of such contribution (particularly, the coordination number).

[11] Reduced final spectra will be discussed in details above in the text, here we just intend to present the procedure used to perform liner combination fit. Thus, here we give importance to the results of the fit, not the shape of reduced spectra to the active final state.

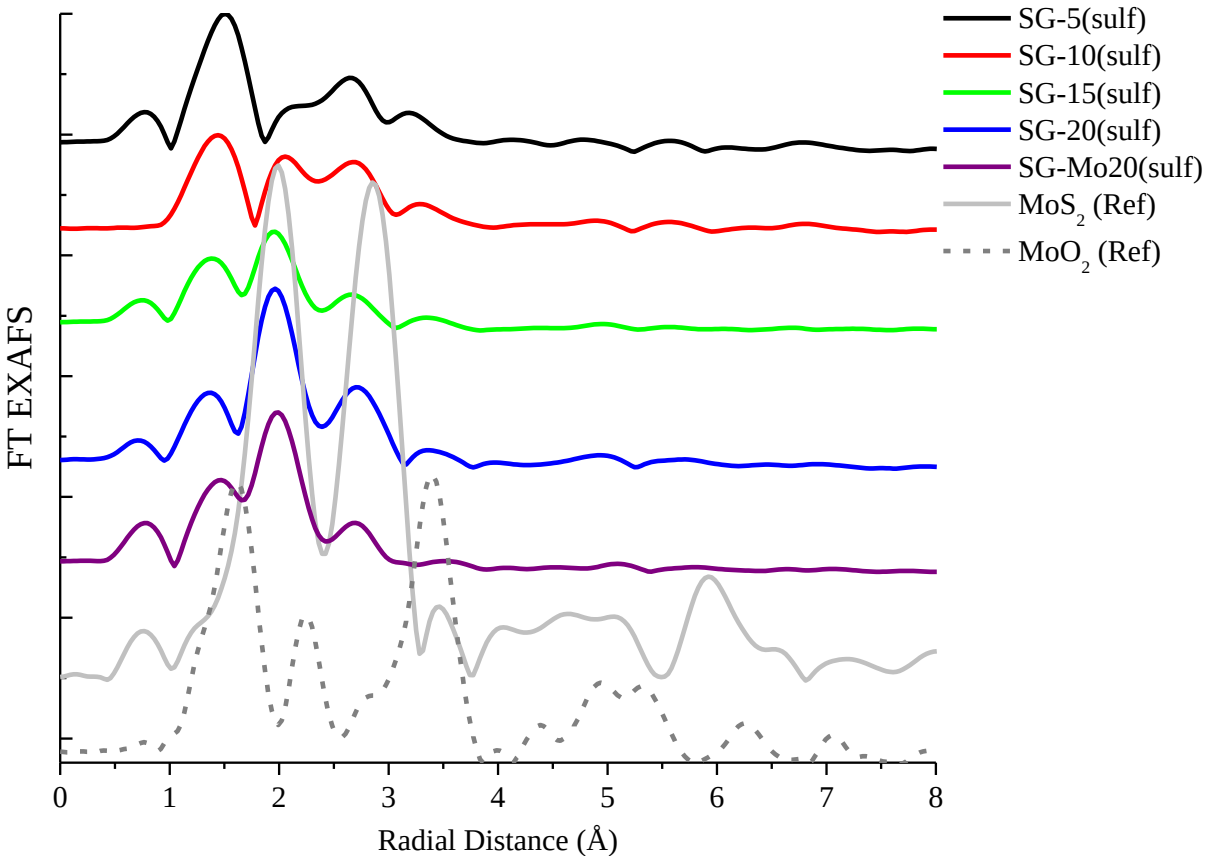

Figure V.39 - Fourier Transform of sulfided sol-gel EXAFS signal compared with references at Mo K-edge.

Detailed structural parameters obtained by EXAFS refinement for the sulfided sol-gel solids are summarized in Table 20. All solids present contributions from oxygen, sulfur and (two) molybdenum.

In spite of SG-5(sulf) could have been simulated with Mo-S contribution, in fact, it presents a very low (or even null) degree of sulfidation; coordination number is 0.6 with high relative uncertainty. This result is not surprising, since spectral evolution of such solids do not led to a sulfide state. Further, in this sample fit, we dealt with high parametric correlation (~ 94%) between coordination number and Debye-Waller factor, which prevent accuracy of such parameter values.

Comparing SG-20(sulf) and SG-Mo20(sulf) (the free-cobalt solid), the effect of cobalt insertion suggest a structuration of the particles, in the sense that one can see farther in the structure, as indicated the presence of a second Mo-Mo contribution (3.68 Å). Mo-O and Mo-S for all solids are equivalent, but a slight elongation is observed in Mo-O for lowest Mo loadings and in Mo-S bond in SG-10(sulf). In the latter, despite we find a Mo-S contribution, the other features, particularly the Mo-Mo contribution, make it closer to SG-5(sulf) than the highest Mo loadings.

Table 20 - Refinement of Mo K-edge EXAFS parameters of sol-gel catalysts after sulfuration.

Preparation Method	Sample	Bond	N	R (Å)	σ² (Å²)	Δσ	ΔE (eV)	Parameters
Sol-Gel Sulfided	SG-5	Mo-O	3.1	1.96	0.004	0.001	-6.0 (±2.1)	Δk = 4.6-12.9 ΔR = 1.1-3.8 N_{ind} = 14 χ^2_{Red} = 187 R_{factor} = 0.01
		Mo-S	0.6	2.78	0.009	0.005		
		Mo-Mo	1.9	3.20	0.009	0.002		
		Mo-Mo	1.9	3.69	0.009	0.002		
	SG-10	Mo-O	1.9	2.01	0.004	0.005	7.4 (±5.1)	Δk = 4.4-12.8 ΔR = 1-3.7 N_{ind} = 15 χ^2_{Red} = 369 R_{factor} = 0.04
		Mo-S	0.9	2.44	0.003	0.007		
		Mo-Mo	1.4	2.92	0.008	0.003		
		Mo-Mo	1.4	3.82	0.008	0.003		
	SG-15	Mo-O	1.5	1.97	0.005	0.005	-5.4 (±2.6)	Δk = 4.3-13.4 ΔR = 1-3.8 N_{ind} = 15 χ^2_{Red} = 1800 R_{factor} = 0.04
		Mo-S	2.0	2.40	0.007	0.004		
		Mo-Mo	1.5	3.23	0.009	0.005		
		Mo-Mo	1.5	3.62	0.009	0.005		
	SG-20	Mo-O	2.0	1.97	0.005	0.005	-5.3 (±3.0)	Δk = 4.3-13.2 ΔR = 1-4.2 N_{ind} = 12 χ^2_{Red} = 606 R_{factor} = 0.03
		Mo-S	2.7	2.40	0.004	0.002		
		Mo-Mo	2.1	3.19	0.006	0.002		
		Mo-Mo	1.1	3.68	0.006	0.002		
	SG-Mo20	Mo-O	1.6	1.99	0.004	0.006	6.4 (±1.9)	Δk = 4.7-13.4 ΔR = 1.1-4 N_{ind} = 9 χ^2_{Red} = 1265 R_{factor} = 0.02
		Mo-S	2.6	2.40	0.006	0.002		
		Mo-Mo	1.3	3.16	0.006	0.001		
Uncertainty:	SG-5:	N_{Mo-O} = 0.8; N_{Mo-S} = 0.6; N_{Mo-Mo} = 1.4						
	SG-10:	N_{Mo-O} = 1.0; N_{Mo-S} = 0.8; N_{Mo-Mo} = 1.0						
	SG-15:	N_{Mo-O} = 1.0; N_{Mo-S} = 0.8; N_{Mo-Mo} = 1.0						
	SG-20:	N_{Mo-O} = 1.4; N_{Mo-S} = 0.6; N_{Mo-Mo} = 0.9						
	SG-Mo20:	N_{Mo-O} = 0.3; N_{Mo-S} = 0.6; N_{Mo-Mo} = 0.9						

Reduction: We extend our analysis to *in situ* TPR experiments. XANES spectral evolution is illustrated in Figure V.*40* for SG-20. In tis sample, from the start structure, one notes that it passes a long time in the reaction without visual changes in XANES profile. Up to ¾ of the reaction (290 °C) we observe no changes in pre-edge peak intensity, neither edge shift position nor XANES peak profile changes. In the last quarter of the reaction, an abrupt diminishing in pre-edge peak intensity happens together with absorption edge shift to lower energies, indicating that reduction are in course. Further, XANES feature is drastically modified, a shoulder suddenly appears and the overall spectra assumes a shape that tends to the MoO_2 one (see Figure V.*35*, and see Table 11 for details in the structural parameters).

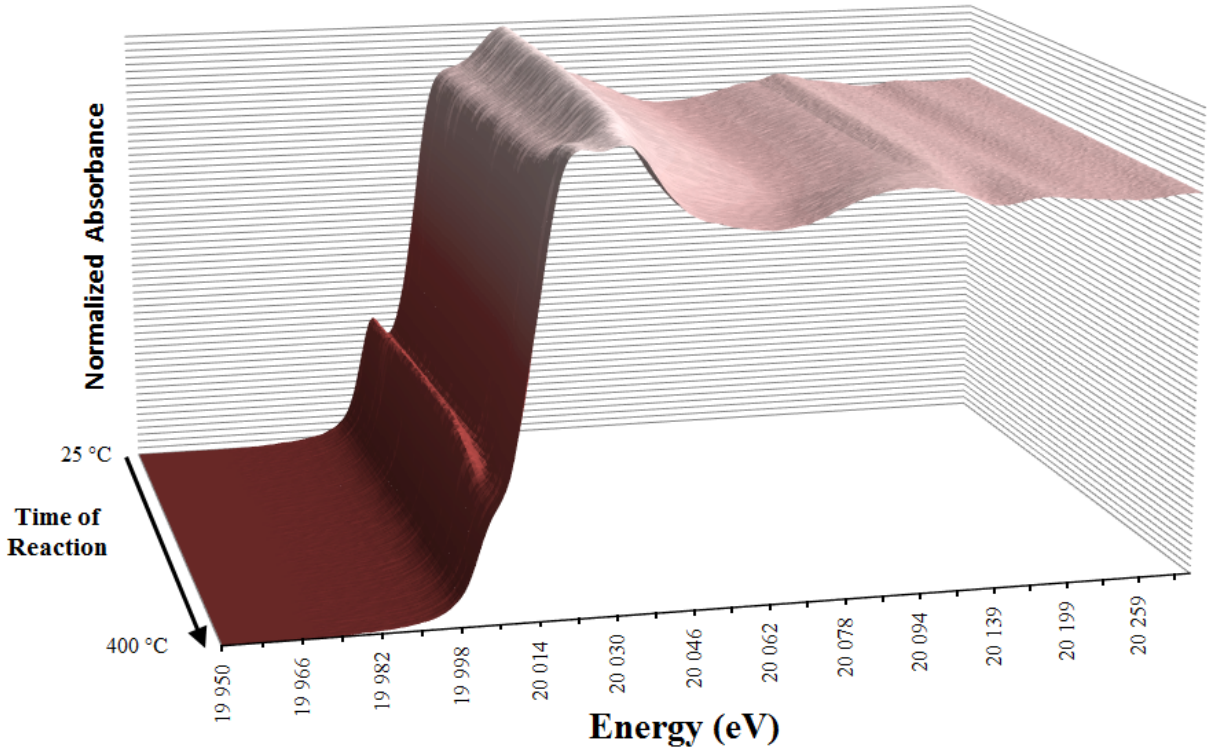

Figure V.40 - Mo K-edge XANES spectral evolution of SG-20 during the TPR reaction.

One can confront the final state XANES of the samples after the reduction in Figure V.*41*. All spectra have the same white line intensity. In spite of none of the spectra have the exactly shape of the reference (MoO_2), we note a smooth evolution from SG-5(red) to SG-20(red), the second XANES oscillation centered at 20035 Å have similar intensity at SG-5(red) and MoO_2. It is less intense when compared to the first XANES oscillation at 20025 Å in SG-5(red), whereas both intensities are comparable in MoO_2. Moving to SG-20(red) this ratio is reversed, the first oscillation amplitude is more intense than the second one, but the difference is even more pronounced in the SG-Mo20(red). However, we cannot find these same similarities when one looks the FT of the EXAFS (inset of Figure V.*41*). Except a low intense secondary peak centered at 2.2 Å (without phase corrections) in SG-20(red) and SG-Mo20(red), no feature is shared among them and the MoO_2 reference and catalysts spectra. FT of EXAFS in SG-5(red), instead, presents a broad and more intense peaks along the second radial distribution centered in 2.8 Å.

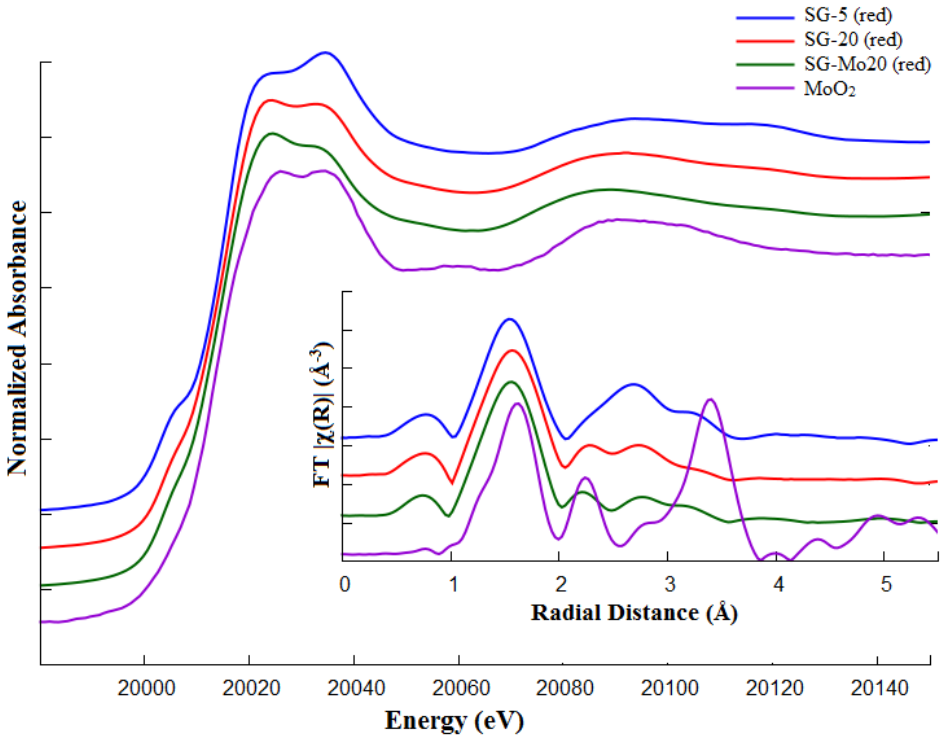

Figure V.41 - Mo K-edge XANES for SG catalysts after reduction compared against the bulk MoO_2. Onset: FT of EXAFS for the same date set.

The refinement of the structures was performed using mainly MoO_2 as model for bond lengths. *Ab initio* FEFF calculation indicates three Mo-O distinct distances (1.93 Å, 1.98 Å and 2.06 Å) for the first radial distribution peak. The other main contributions come from Mo-Mo bonds in 2.49 Å, 3.09 Å and 3.69 Å.

Figure V.*42* shows us the EXAFS signal for sol-gel reduced solids. As in XANES, we note large similarities between SG-20(red) and SG-Mo20(red), whereas SG-5(red) has its own feature. One observes that SG-5 has a more complex shape, clearly with distinct frequencies composing the total sign (the split feature of some bumps suggests that). Instead, except for small shoulders present at 5 $Å^{-1}$ and 7.5 $Å^{-1}$, SG-20 and SG-Mo20(red) seems to have one main frequency that domain the total signal. One observes that EXAFS of these two solids are very close to the EXAFS signal of HMA-20(red), our reference catalyst. Thus, we expect to see a similar behavior to our sol-gel catalysts. It is intriguing as the high value wavenumber region presents such low bump intensities. Since theses spectra were recorded after the cool down to the room temperature, we can discard temperature effects.

It is well known from EXAFS theory that each bond length corresponds to one oscillation weighted by corresponding atomic back-scattering function. For light atoms, such as oxygen, the back-scattering function has its maximum in lower wavenumber values, whereas for heavy atoms, the maximum is on high wavenumber values. Low intensity in higher wave number may indicate that Mo atoms have no Mo as neighbors or very tiny particles. Despite XANES similarities with the reference (MoO_2) indicate structured particles, we are interested in get more qualitative insights on fine structure. In order to know if more than one specie is present in our reduced solid, we use back-Fourier transform (BFT) to analyze

particular contributions. This operation can reduce the noise and make the analysis cleaner isolating important and meaningful oscillations. Filtering different regions and looking at the BFT, we confirm that small peaks in FT of SG-20(red) and SG-Mo-20(red) are due to Mo-Mo bond-lengths.

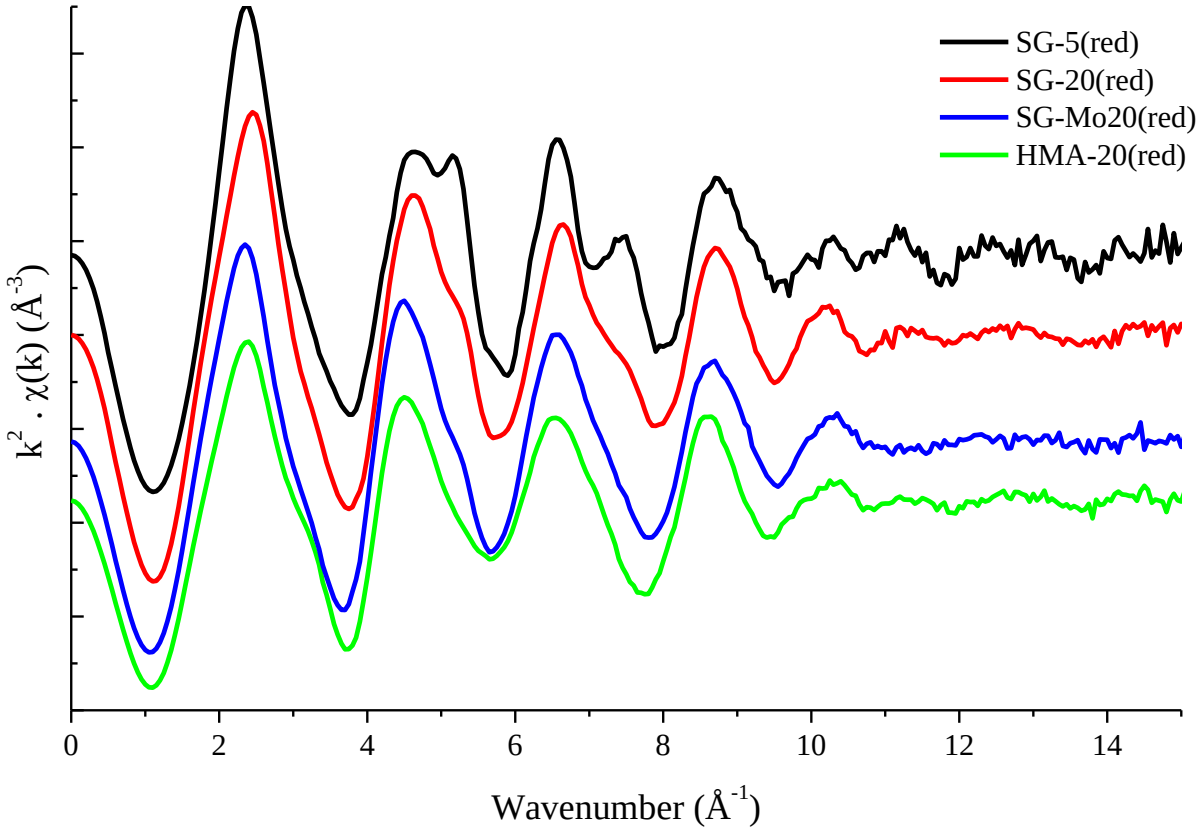

Figure V.42 –EXAFS signal for reduced sol-gel solids compared to HMA-20(red)

This distinction is important but do not change the fact that the main oscillation is due to oxygen in higher Mo loadings. It means that the Mo-Mo contribution in reduced solids, SG-20(red) and SG-Mo20(red), is very weak to the point of being hardly detectable. This causes deep impact in EXAFS simulations of these solids when regarding Mo-Mo bond. As discussed, one can see that effect on the difference in intensity when looking at the very small peaks between 2.1 - 4.0 Å in FT graph of the solids (inset of Figure V.*41*) compared to SG-5(red). Therefore, in reduced SG-20(red) and SG-Mo20(red), structural information suffers of large uncertainty and must be regarded with attention. The results are shown in Table 21.

Particularly, we notes that SG-5(sulf), where almost null sulfidation were observed, is very similar to SG-5(red). Thus, it might be interesting to compare both final processes in order to check how far it goes the reduction during activation. Figure V.*43* compares structural forms for SG-5(red) and SG-5(sulf), i.e., respectively, after reduction and after sulfidation process. In XANES the differences are subtle, with very little deviation in some oscillations, we would say that both are the same structure. Blue arrow indicates the main (if not, the only) difference between the two structures, in SG-5(red) we

observe a very small pre-peak feature that is absent in SG-5(sulf). It means that oxygen symmetry around the central atom in the former is slightly more deformed when compared to later. This difference is more sensitive looking at first radial distribution (the oxygen "sphere of coordination"), as confirms the first peak at FT (inset *B* in Figure V.*43*). This feature, even minimal, suggest slight differences in structure. We stress that it is not due to pre-treatment or extraction conditions, since the same parameters were set in both cases. Quantitatively, comparing data from EXAFS model fit for both structures (Table 20 and Table 21), one observes that oxygen distribution and coordination are equivalent (taking into account the error bars). However, we simulated a weak (i.e., low coordinated) Mo-S contribution for SG-5(sulf), which, obviously, is not presented in SG-5(red). Despite the low coordination level, the presence of such contribution can be noted by the presence of a shoulder when looking at the Fourier Transform graph (pointed by the blue arrow in the inset *B* of the Figure V.*43*). Such contribution can be also responsible for the slight difference in Mo-Mo bond length when comparing both structures, in SG-5(red) the two Mo-Mo bonds are slightly enlarged.

Table 21 - Refinement of Mo K-edge EXAFS parameters of sol-gel catalyst (SG-5) after TPR.

Preparation Method	Sample	Bond	N	R (Å)	σ² (Å²)	Δσ	ΔE (eV)	Parameters
Sol-Gel Reduced	SG-5	Mo-O	3.6	1.96	0.007	0.003	-8.0 (fixed)	Δk = 4.3-12.4 ΔR = 1-3.8 N_{ind} = 14 χ^2_{Red} = 795 R_{factor} = 0.07
		Mo-Mo	1.6	3.22	0.010	0.004		
		Mo-Mo	1.6	3.70				
	SG-20	Mo-O	2.1	1.96	0.0007	0.003	-2.1 (±4.1)	Δk = 4.5-13.6 ΔR = 1.1-3.5 N_{ind} = 13 χ^2_{Red} = 2049 R_{factor} = 0.03
		Mo-O	2.1	2.09				
		Mo-Mo	1.5	2.63	0.009	0.005		
		Mo-Mo	1.5	2.88				
		Mo-Mo	1.5	3.31				
	SG-Mo20	Mo-O	2.1	1.97	0.0003	0.002	2.5 (±3.3)	Δk = 4.5-13.6 ΔR = 1-3.5 N_{ind} = 13 χ^2_{Red} = 1440 R_{factor} = 0.02
		Mo-O	2.1	2.09				
		Mo-Mo	1.5	2.64	0.012	0.006		
		Mo-Mo	1.5	2.88				
		Mo-Mo	1.5	3.35				
Uncertainty:	SG-5:	N_{Mo-O} = 2.1; N_{Mo-Mo} = 1.6						
	SG-20:	N_{Mo-O} = 0.6; N_{Mo-Mo} = 1.2						
	SG-Mo20:	N_{Mo-O} = 1.0; N_{Mo-Mo} = 1.3						

It is noteworthy that, particularly for coordination number, good values were obtained and are in agreement with the fits performed in sulfided samples, but great correlation (~ 90%) between the parameter *N* (coordination number) and σ² (the Debye-Waller) had as consequence large uncertainty in the former (see Table 21). We stress, though, that this fact is inherent of the method (and theory) of EXAFS modeling and fitting.

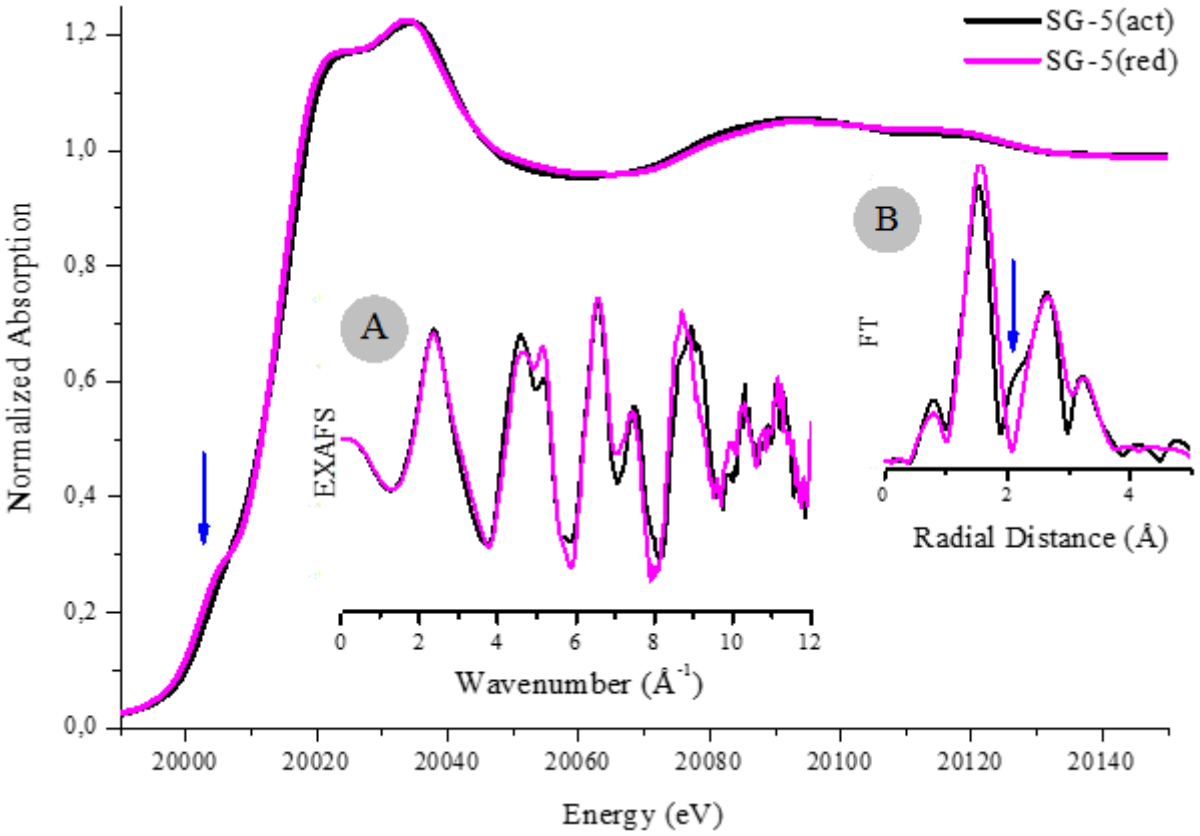

Figure V.43 - Structural comparison between XANES of the SG-5 after activation and reduction. Blue arrow indicate a pre-peak feature present on reduction and absent in "sulfided" SG-5. Inset *A* is EXAFS and inset *B* is the Fourier transform of EXAFS (blue arrow in inset *B* indicates the main visual difference concerning the two structures).

4.3.2. XANES Analysis at Cobalt K-Edge

For the same reasons discussed before, for Co K-edge we have to rely only the XANES spectra. Figure V.*44* compares the final state spectra for the sol-gel catalysts at XANES and EXAFS part. After sulfidation, XANES comparative analysis states that the Co environment is almost unchanged for SG-5 and SG-10 catalysts. SG-15 and SG-20 experiments a strong decreasing of the white line and a shift to lower energy, suggesting a higher degree of sulfidation. White line intensity at 7725 eV in Co K-edge arises from 1*s* transition of Co^{2+} atoms, while the protuberance at 7733 eV is due to Co^{+3} transitions [26]. Thereby, after sulfuration one finds that the ratio Co^{II}/Co^{III} is strongly affected in SG-20, while remains virtually untouchable in SG-5 and SG-10.

EXAFS (Figure V.*44*, inset) points out some interesting features. All the samples have similar behavior, in number of oscillations and amplitude. Nevertheless, as the Mo loading increases the position of the second oscillatory amplitude (in the 4.0 - 4.5 Å range) seems to move to higher values of wavenumber without, however, moving the amplitudes in higher wavenumber values. Due to low signal-to-noise ratio values, no greater discussion can be performed on EXAFS.

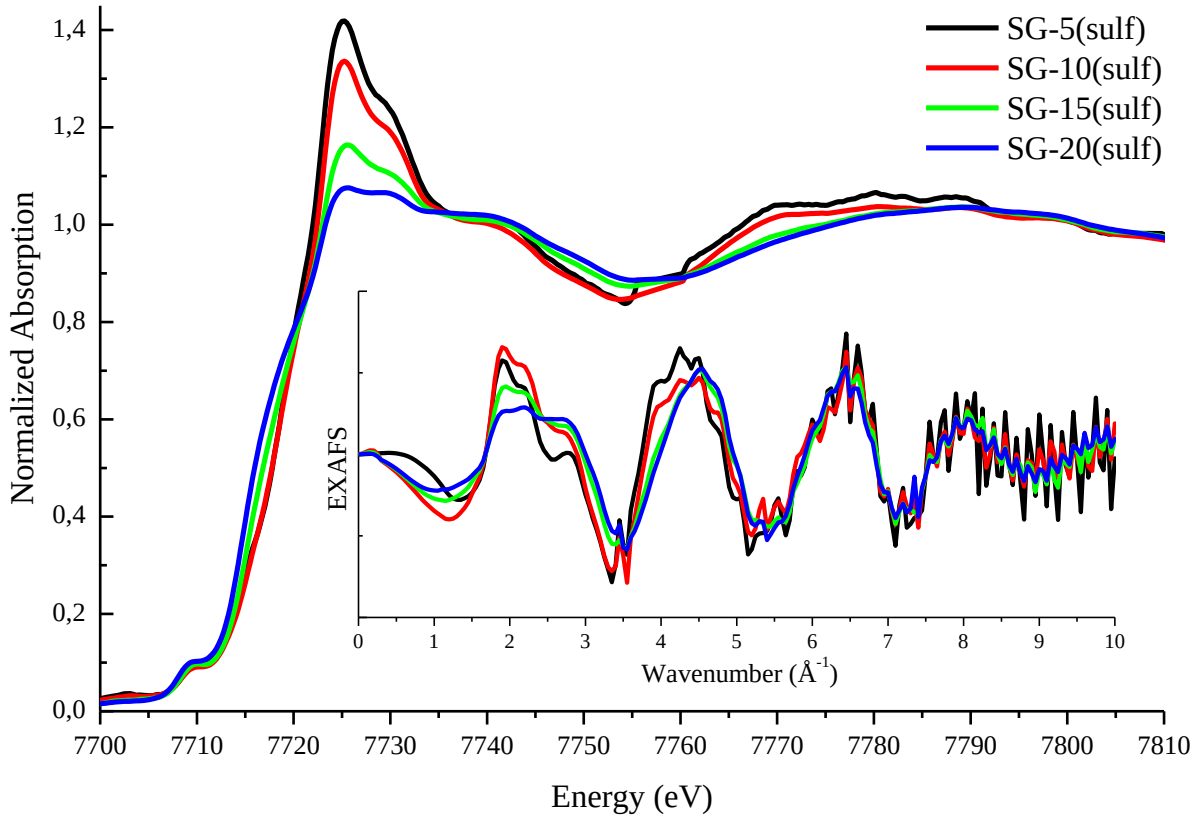

Figure V.44 - Co K-edge XANES for SG-series. (Inset) EXAFS signal for SG-series.

Particularly, looking at SG-20 evolution in Figure V.*45*, it is clear from rapid and early decrease of the white line intensity that Co-environment begins to transform at room temperature under H_2S/H_2 flow. In fact, the right to say is that, whatever the transformation (not necessarily a sulfidation), it begins at room temperature. After this rapid event (which takes just few minutes), decreasing of the white line with temperature is smooth and it is accompanied by a shift to lower energy values, characterizing the sulfidation of the species. The shift is stabilized after 50 minutes of the reaction, when temperature is about 170 °C, which shows clearly that Co sulfidation is a rapid process. However, in SG series, such process is not complete, since after the end of reaction one has a small feature of the white line. Further, SG-20 final state is not similar to HMA-20 final state (our reference).

The same trend is observed for SG-15, but obviously, with a different final state. In SG-10, no abrupt transformation is present at the very beginning of the reaction, just smooth and continuous decreasing in the white line until the end of the reaction. The slight decreasing in SG-5 white line is not significant, and very weak sulfidation is achieved in this sample.

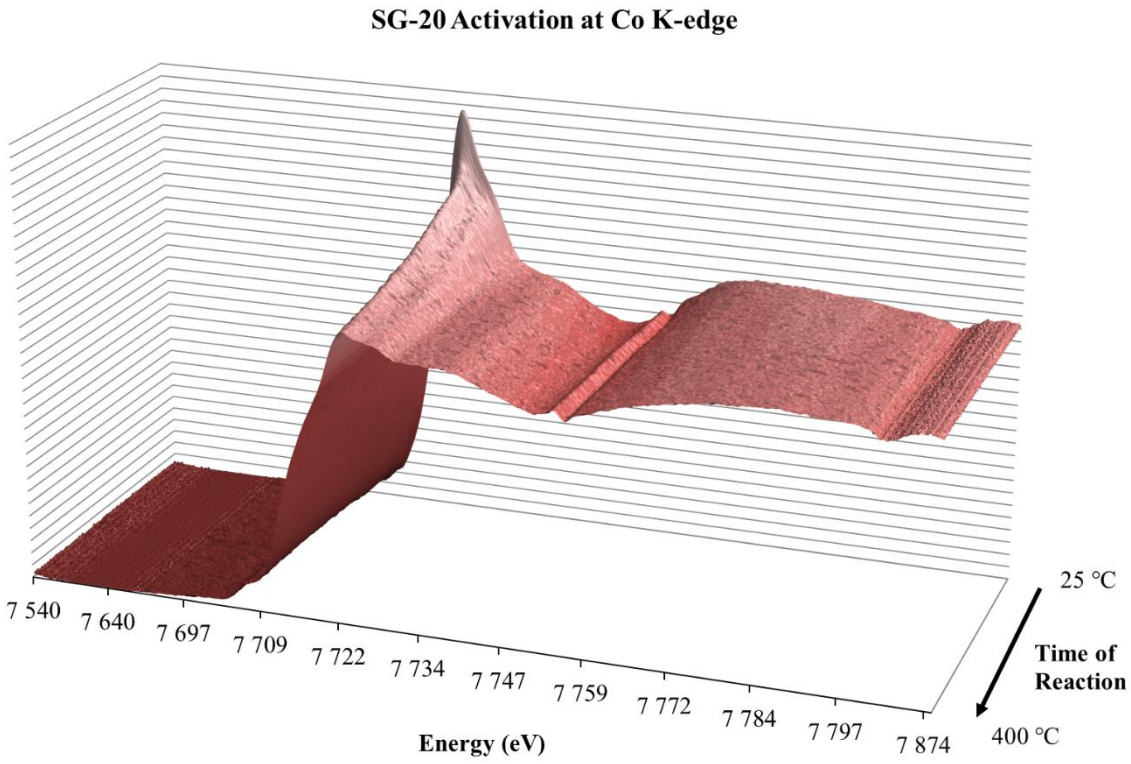

Figure V.45 - Co K-edge XANES evolution of SG-20 during activation. Glitches are observed at 7750 Å and 7800 eV.

Analogously to Mo K-edge, we take HMA-20(sulf) at Co K-edge as a model to a nanosized unique-phase sulfided species and take it as reference for XANES linear combination fit. At this point it is important to make a proviso, as shown in Co K-edge XANES for HMA catalysts (4.2.2), the HMA-20 final state do not correspond perfectly to a Co_9S_8 specie, and it is possibly because we have not a pure state at the end. The other reference for the fit is the respective initial oxide state and the results, i.e., for the SG-20(sulf) the reference is its own initial oxide spectrum. The results is associated to the "sulfidation degree" of each solid and it is showed in Table 22 (parenthesis indicates uncertainty in the last significant figure).

Table 22 - XANES Linear Combination fit* for Sol-Gel final sulfided states.

Sample	*% of Co-sulfided*	*% of Oxidic Specie*	*Reduced-χ^2*
SG-5	33.8(7)	66.2(7)	421.3 x10^{-6}
SG-10	42.0(8)	58.0(8)	532.4 x 10^{-6}
SG-15	73.5(5)	26.5(5)	150.3 x 10^{-6}
SG-20	90.0(3)	10.0(3)	84.2 x 10^{-6}

* Linear combination fit by using least square method in the range of -20 eV < E_0 < 100 eV.

As expected, higher degree of sulfuration is achieved for SG-20 with some oxide contribution. As decreasing Mo loading, the Co-sulfidation is lower. It is intriguing the fact the linear combination fit

give us 90% of sulfidation in Co species in SG-20 while the corresponding value for Mo species is about 50% (for MoS_2 species, see Table 19).

4.4. Partial Conclusion: Final State Structure

XAFS analysis revealed us that impregnated catalysts have a well behavior and, in a certain way, foreknowable evolution to the active final state. By this, we mean that, at least for the optimal Mo loading (HMA-20), the evolution of the precursor compounds led to sulfided states, which are assumed as the active phase. Molybdenum species evolves from the oxide precursor to the active phase, MoS_2, as confirmed by XANES and EXAFS fit at Mo K-edge. Such results allowed us to consider the XANES of HMA-20(sulf) as a model to a TiO_2-supported nanosized MoS_2 particle. HMA-5(sulf) also present a MoS_2 structure, as active phase, but the coordination number are lower, when compared to HMA-20(sulf). The reduction of both HMA-20 and HMA-5 precursor solids present equivalent structures at Mo K-edge. TPR XANES tends to MoO_2 (bulk), but pre-edge remaining feature suggests that a complete reduction was not achieved. EXAFS indicates simple structures, with oxygen atoms at the first coordinate distribution (~ 2.01 Å) and low coordinated Mo atoms at the second coordinate distribution. Co K-edge, however, is distinct when considering HMA-20(sulf) and HMA-5(sulf). Residual XANES white line in the later indicates that sulfidation was not completed. XANES in HMA-20(sulf) has no white line, which allows to state that Co species are (nearly) completed sulfided in a structure that do not seems to be a Co_9S_8. However, since no EXAFS is available, we are not able to fully describe the final state structure at Co K-edge.

Considering sol-gel series, at Mo K-edge, the activation is quite different when comparing lowest and highest Mo loadings. The sulfidation degree of SG-5(sulf) is minimal, as revealed by linear combination fit (Table 19), and EXAFS parameters (Table 20). SG-20(sulf) presents strong characteristics of sulfidation, but at the same time, an important contribution of a Mo-O bound remains at the final state (Figure V.39). Linear combination fit points to a degree of sulfidation of ~ 58%. At Co K-edge, despite the similar evolution compared to impregnated solids, all sol-gel catalysts have a remaining white line at the end of sulfidation. Reduction of sol-gel precursors results in structures that are more complex, when comparing with impregnated reduced solids. Except for SG-5(red), reduced sol-gel solids have two distinct oxygen distances in the first coordinate shell and three distinct molybdenum distances at the second one (Table 21).

5. Comments and Assessments

LEIS, as stated before, it is a technique in development. The interpretation and analysis are subtle as well as the planning of the experiments to be performed. Moreover, the equipment itself and the setup are quite recent in the UCCS and at that time we suffered by a sort of anxiety to get our own results in order to develop the possibilities of this technique in catalysis.

In that sense, as first attempt we performed LEIS measurements with some fresh non-calcined samples. After this long series of measurements, data analysis and deep reflection, we realize that more background on experimental planning and data analysis theory would be fundamental to obtain valuable quantitative information. We acknowledge the naïve planning of the experiments, the choice of the samples, particularly, the lack of reference compounds to calibration and quantitative interpretation.

The 3 keV of primary $^{4}He^{+}$ ionic beam is a first typical choice for the most of the LEIS experiments. However, for our system, this setup is twofold tricky. As long we have a powder catalyst, instead a film the contribution to the final spectrum of deeper layers of each element is strong when compared to thin film systems. Further, in these setup conditions, the proximity of Ti, Co and Mo characteristic peaks produces a tail overlap among them. For instance, the deep layer signal of Mo masks the first monolayer signal of Co atoms making tremendously tricky and difficult to separate individual atomic contributions and, therefore, quantitative analysis. In powder samples, the issue of the scan representativeness itself is an open question! Moreover, since we are studying structural changes when increasing Mo loading, simple (but not less important) reference measurements were not performed, such as, single support measurement, i.e., the support itself (anatase-TiO_2) with none charge, or MoO_3 powder without support. These references are fundamental for quantitative analysis and validation of system assumptions, such as no matrix effects.

In LEIS, the first obvious choice to gain separation resolution among peaks is to use a ^{20}Ne ion beam. Nevertheless, in our samples, this setup brought the Ti LEIS peak too close to the lower limit of the energy window, thereby, close to the background region. Furthermore, we lost oxygen peak, usually used as intensity normalizer.

These points do not invalidate LEIS measurements as promising tool in catalytic studies and characterization. A systematic and well-controlled study using known reference compounds must be adopted in order to enable quantitative results. A primary $^{4}He^{+}$ beam with higher energy is likely the best choice for peak separation. Simpler and known systems, namely TiO_2 and MoO_3 must be systematically measured in different setups (energy and type of the primary beam, charge compensation, dose yield, bombarding area, etc.) must be considered to find the best setup for CoMo-based supported catalysts.

XAFS was used to characterize the local structure of catalysts in calcined oxide precursor state, after sulfidation and after reduction.

At Mo K-edge, in impregnated-prepared calcined solids, XANES indicates similar structure for all solids of the series no matter the Mo loading. Such XANES features are similar to bulk ammonium heptamolybdate structure. The fine analysis of the structure indicates the presence of two oxygen distinct distances as nearest-neighbors and a mix of two pairs of molybdenum and cobalt as next nearest neighbors. While Mo neighbors present a reasonable coordination number (N_{Mo} slightly above 1.0), coordination number related to Co neighbors are very low (N_{Co} ~ 0.2), which suggest segregation of these two (Co and Mo) species. Such segregation is supported when considering Co K-edge analysis. No Co-Co bound were identified, which can be interpreted as if Co structures are formed (or located) distance from other Co structures. Thus, Co atoms see just molybdenum as next-nearest-neighbors and just Co-Mo are identified.

Considering the sol-gel series, XAFS was used to characterize dried and calcined solids. Dried samples have similar XANES structure. Fine structure refinement, however, indicates a slight difference for lowest Mo loading. It has a poorer oxygen environment and one extra longer Mo-Mo contribution. No Co neighbor was identified. After calcination, the structure undergoes great changes driven by support transformation. Co neighbors could be identified in both Co and Mo K-edges, suggesting that calcined sol-gel solids have a structure in which cobalt is insert more effectively into the structure when compared to impregnated calcined solids.

Besides all technical possibilities of SAMBA beamline, particularly as regards to the Quick-EXAFS monochromator, and the large know-how sustained by its team, an *in situ* catalytic experiment with the particular condition of using TiO_2 as support and different Mo loadings is still a fine and delicate running. Thus, we faced with many issues that are inherent when dealing with this kind of experiment. If by one hand, we were successful in performing measurements following our original planning, i.e., make *in situ* experiments in both Co and Mo K-edges, by the other hand, we could not record enough data in order to answer some fundamental questions. For instance, bad records on Co K-edge allowed us exploitation just XANES part of the absorption spectra spoiling a full description of the active state structure of the catalysts.

By the results obtained analyzed in this chapter, we see clearly that, while impregnated catalysts present well-behaved results (measured by the quality of the refinement and the expected final states after sulfidation, for instance). In sol-gel series, we faced with a structure somewhat predictable; in the sense that after activation we cannot recognize a structure similar what we expected, i.e., a MoS_2 in Mo K-edge as observed in HMA series, for instance.

In anyway, we accomplished the *in situ* experiments and characterization of activation and reduction of TiO_2-supported CoMo-based catalysts. By our data analysis, it is clear that one-pot sol-gel prepared-TiO_2 plays a significant role in the structure. However, unfortunately, the support plays a negative role for data analysis (e.g., significantly masking Raman and XRD interpretation, in LEIS and XAS data record, etc.), requiring extra attention in experiment planning.

References

[1] J. Mazurelle, C. Lamonier, C. Lancelot, E. Payen, C. Pichon, and D. Guillaume, "Use of the cobalt salt of the heteropolyanion [Co2Mo10O38H4]6− for the preparation of CoMo HDS catalysts supported on Al2O3, TiO2 and ZrO2," *Catalysis Today*, vol. 130, no. 1, pp. 41–49, Jan. 2008.

[2] D. Primetzhofer, S. N. Markin, J. I. Juaristi, E. Taglauer, and P. Bauer, "LEIS: A reliable tool for surface composition analysis?," *Nuclear Instruments and Methods in Physics Research Section B: Beam Interactions with Materials and Atoms*, vol. 267, no. 4, pp. 624–627, Feb. 2009.

[3] H. Brongersma, M. Draxler, M. Deridder, and P. Bauer, "Surface composition analysis by low-energy ion scattering," *Surface Science Reports*, vol. 62, no. 3, pp. 63–109, Mar. 2007.

[4] E. Taglauer, A. Kohl, W. Eckstein, and R. Beikler, "Aspects of analysing supported catalysts by low-energy ion scattering," *Journal of Molecular Catalysis A: Chemical*, vol. 162, no. 1–2, pp. 97–103, Nov. 2000.

[5] R. Cortenraad, A. W. D. Van Der Gon, and H. H. Brongersma, "Influence of analyser transmission and detection efficiency on the energy dependence of low-energy ion scattering signals," *Surface and Interface Analysis*, vol. 29, no. April, pp. 524–534, 2000.

[6] S. Rondon, M. Houalla, and D. M. Hercules, "Determination of the Surface Coverage of Mo / TiO Catalysts by ISS and CO Chemisorption," *Surface and Interface Analysis*, vol. 26, no. June 1996, pp. 329–334, 1998.

[7] T. Patterson, J. Carver, D. Leyden, and D. Hercules, "A surface study of cobalt-molybdena-alumina catalysts using X-ray photoelectron spectroscopy," *The Journal of Physical Chemistry*, vol. 80, no. 15, p. 1700, 1976.

[8] F. P. J. M. Kerkhof and A. M. Moulijn, "Quantitative Analysis of XPS Intensities for Supported Catalysts," *Journal of Physical Chemistry*, vol. 83, no. 7, pp. 1612–1619, 1979.

[9] V. León, "A simplified Kerkhof-Moulijn model for dispersion quantification from XPS atomic concentrations," *Surface Science*, vol. 339. pp. L931–L934, 1995.

[10] A. Lycourghiotis, C. Defosse, F. Delannay, and B. Delmon, "Effect of sodium on the CoMo/γ-Al2O3 system. Part 2.—Influence of sodium content and preparation methods on the state of dispersion and nature of molybdenum supported on γ-Al2O3," *Journal of the Chemical Society, Faraday Transactions 1: Physical Chemistry in Condensed Phases*, vol. 76, p. 2052, Jan. 1980.

[11] C. Thomazeau, V. Martin, and P. Afanasiev, "Effect of support on the thermal decomposition of (NH4)6Mo7O24·4H2O in the inert gas atmosphere," *Applied Catalysis A: General*, vol. 199, no. 1, pp. 61–72, 2000.

[12] a. . Venezia, V. La Parola, G. Deganello, D. Cauzzi, G. Leonardi, and G. Predieri, "Influence of the preparation method on the thiophene HDS activity of silica supported CoMo catalysts," *Applied Catalysis A: General*, vol. 229, no. 1–2, pp. 261–271, Apr. 2002.

[13] A. M. Venezia, F. Raimondi, V. La Parola, and G. Deganello, "Influence of Sodium on the Structure and HDS Activity of Co–Mo Catalysts Supported ON Silica and Aluminosilicate," *Journal of Catalysis*, vol. 194, no. 2, pp. 393–400, Sep. 2000.

[14] D. C. Frost, C. A. McDowell, and I. S. Woolsey, "X-ray photoelectron spectra of cobalt compounds," *Molecular Physics*, vol. 27, no. 6, pp. 1473–1489, Jun. 1974.

[15] A. P. Grosvenor, B. A. Kobe, M. C. Biesinger, and N. S. McIntyre, "Investigation of multiplet splitting of Fe 2p XPS spectra and bonding in iron compounds," *Surface and Interface Analysis*, vol. 36, no. 12, pp. 1564–1574, Dec. 2004.

[16] Y. Okamoto, T. Imanaka, and S. Ternishi, "Surface structure of CoO-MoO3/Al2O3 catalysts studied by X-ray photoelectron spectroscopy," *Journal of Catalysis*, vol. 65, no. 2, pp. 448–460, Oct. 1980.

[17] A. D. Gandubert, C. Legens, D. Guillaume, S. Rebours, and E. Payen, "X-ray Photoelectron Spectroscopy Surface Quantification of Sulfided CoMoP Catalysts Relation Between Activity and Promoted Sites Part I : Influence of the Co / Mo Ratio," vol. 62, no. 1, pp. 79–89, 2007.

[18] T. Koranyi, I. Manninger, and Z. Paal, "Sulfidation of Co□Mo catalysts by thiophene: Structure and activity," *Solid State Ionics*, vol. 32–33, pp. 1012–1018, Feb. 1989.

[19] T. K. T. Ninh, L. Massin, D. Laurenti, and M. Vrinat, "A new approach in the evaluation of the support effect for NiMo hydrodesulfurization catalysts," *Applied Catalysis A: General*, vol. 407, no. 1–2, pp. 29–39, Nov. 2011.

[20] L. Coulier, J. a R. van Veen, and J. W. Niemantsverdriet, "TiO2-Supported Mo Model Catalysts: Ti as Promoter for Thiophene HDS?," *Catalysis Letters*, vol. 79, no. April, pp. 149–155, 2002.

[21] D. Wang, X. Li, E. W. Qian, A. Ishihara, and T. Kabe, "Elucidation of promotion effect of cobalt and nickel on Mo / TiO 2 catalyst using a 35 S tracer method," *Applied Catalysis A: General*, vol. 238, pp. 109–117, 2003.

[22] C. Arrouvel, M. Breysse, H. Toulhoat, and P. Raybaud, "A density functional theory comparison of anatase (TiO2)- and γ-Al2O3-supported MoS2 catalysts," *Journal of Catalysis*, vol. 232, no. 1, pp. 161–178, May 2005.

[23] B. Ravel and M. Newville, "ATHENA, ARTEMIS, HEPHAESTUS: data analysis for X-ray absorption spectroscopy using IFEFFIT.," *Journal of synchrotron radiation*, vol. 12, no. Pt 4, pp. 537–41, Jul. 2005.

[24] E. Shimao, "Structure of the Mo7O6−24 Ion in a Crystal of Ammonium Heptamolybdate Tetrahydrate," *Nature*, vol. 214, no. 5084, pp. 170–171, Apr. 1967.

[25] C. Livage, A. Hynaux, J. Marrot, M. Nogues, and G. Férey, "Solution process for the synthesis of the 'high-pressure' phase CoMoO4 and X-ray single crystal resolution," *Journal of Materials Chemistry*, vol. 12, no. 5, pp. 1423–1425, Apr. 2002.

[26] C. Martin, C. Lamonier, M. Fournier, O. Mentré, V. Harlé, D. Guillaume, and E. Payen, "Preparation and characterization of 6-molybdocobaltate and 6-molybdoaluminate cobalt salts. Evidence of a new heteropolymolybdate structure.," *Inorganic chemistry*, vol. 43, no. 15, pp. 4636–44, Jul. 2004.

[27] M. Pope, *Heteropoly and Isopoly Oxometalates*. Berlin: Springer-Verlag, 1983.

[28] D. Koningsberger and R. Prins, Eds., "X-Ray Absorption: Principles, Applications, Techniques of EXAFS, SEXAFS and XANES," in *X-Ray Absorption: Principles, Applications, Techniques of EXAFS, SEXAFS and XANES*, New York: John Wiley, 1988, p. 321.

[29] B. S. Clausen, B. Lengeler, and H. Topsøe, "X-ray absorption spectroscopy studies of calcined Mo-Al2O3 and Co-Mo-Al2O3 hydrodesulfurization catalysts," *Polyhedron*, vol. 5, no. 1–2, pp. 199–202, Jan. 1986.

[30] R. Leliveld and A. Van Dillen, "A Mo–K Edge XAFS Study of the Metal Sulfide-Support Interaction in (Co) Mo Supported Alumina and Titania Catalysts," *Journal of catalysis*, vol. 196, pp. 184–196, 1997.

[31] E. A. Stern, "Number of relevant independent points in x-ray-absorption fine-structure spectra," *Physical Review B*, vol. 48, no. 13, pp. 9825–9827, Oct. 1993.

[32] G. Bunker, *Introduction to XAFS*. Cambridgr: Cambridge University Press, 2010.

[33] D. Koningsberger and B. Mojet, "XAFS spectroscopy; fundamental principles and data analysis," *Topics in catalysis*, vol. 10, pp. 143–155, 2000.

[34] E. Fonda, a Rochet, M. Ribbens, L. Barthe, S. Belin, and V. Briois, "The SAMBA quick-EXAFS monochromator: XAS with edge jumping.," *Journal of synchrotron radiation*, vol. 19, no. Pt 3, pp. 417–24, May 2012.

[35] T. Kubota, N. Hosomi, K. K. Bando, T. Matsui, and Y. Okamoto, "In situ fluorescence XAFS study for hydrodesulfurization catalystsPresented at the International Congress on Operando Spectroscopy, Lunteren, The Netherlands, March 2-6, 2003.," *Physical Chemistry Chemical Physics*, vol. 5, no. 20, p. 4510, Oct. 2003.

[36] Y. Okamoto, M. Kawano, and T. Kubota, "Fraction of the CoMoS phases accessible to NO in Co–Mo hydrodesulfurization catalysts," *Chemical Communications*, no. 9, pp. 1086–1087, Apr. 2003.

Chapter VI: Chemometrics Applied to *In situ* Activation XAFS Data

Table of Contents

1. Introduction

Great concern has been growing in structural characterization in order to depict the mechanisms of a chemical reaction in atomic level. Synchrotron Radiation Facilities have increased their instrumental performance enormously and nowadays they provide the physical structure and experimental conditions that allows the scientists go deep inside the matter and inspire new methods for reach specific description in atomic level. While recording a single spectrum used to take several tens of minutes, now it can be recorded in less than 10 s or even in the order of milliseconds. This has opened up the way to perform in situ and operando XAS experiments with the ambitious aim to shed light on transient structures. When dealing with nanometric-sized particles, the identification of the chemical species involved during the reaction is no longer straightforward by XAS due the lack of known spectral fingerprints for these species. Chemometrics is insert in this context, to process large data sets of *in situ* experiments in order to obtain pure constituent spectra. In this chapter, we present our results where we applied MCR-ALS calculations in *in situ* XAS experiments.

Recalling briefly the main points in the procedure, the very first step in MCR method is to determine the number of species that better describes the whole data set. In the chemometrics sense, it means to choose the suitable *k* rank for the matrix $\boldsymbol{C}$ (which contains the concentration profile of the compounds in the reaction) and $\boldsymbol{S}^T$ (the matrix with the pure spectra of each compound) in the relation $\boldsymbol{D} = \boldsymbol{C}*\boldsymbol{S}^T + \boldsymbol{E}$, where $\boldsymbol{D}$ is the experimental data set matrix and $\boldsymbol{E}$ is the residual. This can be done by PCA analysis of the data set matrix for Quick-EXAFS experiment. PCA should provide a mean to describe the data into linearly independent information and, thus, help to determine the rank of the data matrix. Such rank is closely related to the eigenvalues of the matrix calculated via PCA. In an ideal situation, the eigenvalues decrease with the number of the principal component until a certain PC number equals to *k*, from which, the subsequent eigenvalues are equals to zero. Then, we consider *k* as the rank of the matrix. In practical situations, however, the decrease of the eigenvalues is generally smooth and hardly falls to zero, leading to ambiguous rank estimation. Thus, scree (and log-scree) plot, evolving score and loading plots, 2D (3D) scatter plot of scores and residual are eventually considered to perform rank matrix analysis. For systems whose the assembling allows, namely, SG-5, SG-20, HMA-5 and HMA-20 systems, augmented column-wise matrix is used, i.e., data from two different experiments (TPR and activation) for the same sample is considered together for MCR analysis.

The use of augmented matrix is mainly a workaround on the rank-deficiency issue, which will be discussed further on this chapter. When using multivariate curve resolution methods, it is necessary to take into account the rank deficiency, which is not always present but is often found in experimental data obtained from a chemical reaction [1]. The rank of the experimental matrix, when there is no noise

or any other cause of variability, should be equal to the number of chemical species. In that case, the mathematical rank is equal to the chemical one. However, when the number of species in the data exceeds the number of transformations plus one, there is rank deficiency [2]. It is not unusual to encounter rank-deficient systems when dealing with data from spectroscopy measurements. Baseline offset, background introduce rank changes [3]. In mathematical terms, this phenomenon leads to an "apparent" rank that is higher than the chemical species in the system. It is important to stress that not always an augmented system is a full-ranked one so, even a three-way system resolution may be still rank-deficient (for instance, see [4]).

Since so far, no golden rules have been defined to obtain the correct number of significant components, in practice, trial-and-error approach based on different rank estimations is recommended. Besides that, the residuals should be carefully checked as well as the variance explained, the general shape of each resulted spectrum and concentration profile must be reliable and the critically prior knowledge of the system must be confronted with the results.

This chapter starts with a didactic part, where we explain in details the different fashions to deal with PCA and MCR issues. Doing so is twofold; first, we intend to make clear the logical reasoning adopted to deal with this kind of problem, second, by explaining this "step-by-step" dealing and handling to the problem one first time, we can skip intermediary steps for the further data sets. The intention is not overcharge this manuscript with redundant explanations and figures that justify equivalent arguments.

2. The Reference System: MCR-ALS applied on HMA-20 (Mo K-Edge)

Since Chemometrics is an in-developing technique, particularly when applied to time-resolved *in situ* XAS experiments, we must certify by our best the applicability of this tool to our system. In order to check the reliability of MCR method, we first consider the reaction of the HMA-20 catalyst, which in principle is a well-studied system. It means that we expect to obtain known results, i.e., at the end of the activation, the MoS_2 active phase and, likely, reduced and oxy-sulfided intermediates (see, for instance, results from Rochet work in a similar system at [5]). In other words, we expect to find an *n*-step reaction, with *n* meaning the total number of pure compound found in the reaction less one. In that sense, we have three matrix systems to consider, one formed by the TPR reaction, the second with H_2/H_2S activation data and, finally, the augmented column-wise matrix with TPR and activation gathered in a single data set. In the following, we discuss in details the PCA and MCR analysis.

XAS spectra were recorded as stated on previously chapters. Each row of the data set is an average of 30 spectra and corresponds to 30 seconds of the reaction. We followed the reaction from room temperature up to 400 °C with a ramp of 6 °C/min. After 1h at the plateau, the gas flux was turned to

He and the sample was naturally cooled to the room temperature, when another set of spectra was recorded.

2.1. PCA Analysis of HMA-20 Matrices at Mo Kedge

The HMA-20 TPR matrix (214,539) is formed by the evolving spectra disposed in 214 rows with 539 variables (energy values) each one, the columns. Some conventional XAFS data pre-processing, namely, normalization, background subtraction and edge position correction were considered. (About) The one hundred first variables correspond to the pre-peak XAS region and it represents, roughly, noise. In order to minimize this noise effect to the MCR-ALS calculations all this region was ignored. At the end we have a (214,425) matrix that describe XAS evolving spectra during the reduction reaction of HMA-20 oxide precursor under H_2 flow. Following the same argument, HMA-20 activation matrix is a (199,425) one and augmented column-wise HMA-20 system is a (413,425) matrix.

Singular Value Decomposition (SVD) was performed in each one of these matrices and the results are gathered in the table below. Table 23 shows for the eight first principal components their eigenvalue, variance explained and cumulative variance explained. First, one must to select a criterion in order to select the number of principal components for each data set. It should be noted that a variety of statistical stopping rules for defining such number exist (for example, [6]).

Table 23 - SVD analysis for the three HMA-20 matrices*.

	Reduction			*Activation*			*Augmented System*		
PC	**Eigenvalue**	**Var. Expl.**	**Cum. Var. Expl.**	**Eigenvalue**	**Var. Expl.**	**Cum. Var. Expl.**	**Eigenvalue**	**Var. Expl.**	**Cum. Var. Expl.**
1	288.810	95.70	95.70	279.503	95.96	95.96	401.812	94.00	94.00
2	7.33853	2.43	98.16	6.82244	2.34	98.30	12.8970	3.02	97.02
3	0.82408	0.27	98.43	0.81838	0.28	98.58	3.84998	0.90	97.92
4	0.56335	0.19	98.62	0.34820	0.12	98.70	0.95519	0.22	98.14
5	0.33626	0.11	98.73	0.19192	0.07	98.77	0.61645	0.14	98.29
6	0.19887	0.07	98.80	0.14329	0.05	98.81	0.43920	0.10	98.39
7	0.17744	0.06	98.86	0.13533	0.05	98.86	0.40567	0.09	98.48
8	0.15651	0.05	98.91	0.09746	0.03	98.89	0.22930	0.05	98.54
9	0.11256	0.04	98.95	0.09208	0.03	98.93	0.18404	0.04	98.58

** Values of Variance Explained and Cumulative Variance Explained are given in %.*

One way to regard the Table 23 in order to establish a number of components is to consider a threshold below which the explained variance assumes a negligible value. Say, for instance, 1% of variance

explained. It means that we take the rank of the matrix the number of PC's which variance explained is just above 1%. For instance, consider the variance explained values write in Table 23 for the reduction reaction. The first PC explain 95.7% of the data, the second PC explain 2.43% of the data (and the cumulative variance explained goes to 98.16%), the third PC explain 0.27% of the data (with 98.43% of cumulative variance explained). From third PC on, each new PC is responsible to explain a worthless part of the data, namely, less than 1% (see also the cumulative variance explained), and we may assume that 3 PC's is enough to describe the whole data set. In other words, following this criteria, we assume that 2 PC's is not enough to describe our data set, so we include the third one, but we exclude the forth PC on because they no add that much information to describe the data set (the yellow highlighted values in Table 23). If we adopt this criterion, all three systems, the reduction, activation and augmented column-wise matrix, would have three components, which should mean three pure species in each reaction. Another threshold that could be adopted is to consider the difference in magnitude of a certain eigenvalue and the next one. We consider the PC's until the difference between the *n*th PC and the $(n+1)^{th}$ PC tends to zero (the green highlighted values on Table 23). As an example, if we consider the eigenvalues of the reduction, one observes that from PC 1 up to PC 5 the difference between the eigenvalue and the next is not negligible (for instance, the difference between PC 5 and PC 4 is 0.23). From PC 6 on, this difference tends to zero (PC 6 - PC 7 = 0.19 - 0.17 = 0.02) and, thus, PC 6 is out of our criteria. In this scenario, reduction would have five pure compounds; activation, four pure compounds; and the augmented system, 7 (or even 8) pure compounds.

Alternatively, we may look at eigenvalues for a matrix data set by its scree plot, or log scree plot (Figure VI.*1*). The central idea is to consider as "good" PC number the "elbow" in this curve. Since the first eigenvalue is far larger than the following ones, we can either plot the logarithmic of the eigenvalues against the PC number or exclude the first PC from the ordinary plot. From the figure, while reduction and activation point to 3 PC's each, the augmented system point to at least 4 PC's. The analysis of logarithmic plot is subtle because the "elbow" is not obvious, but similar results as before can be considered.

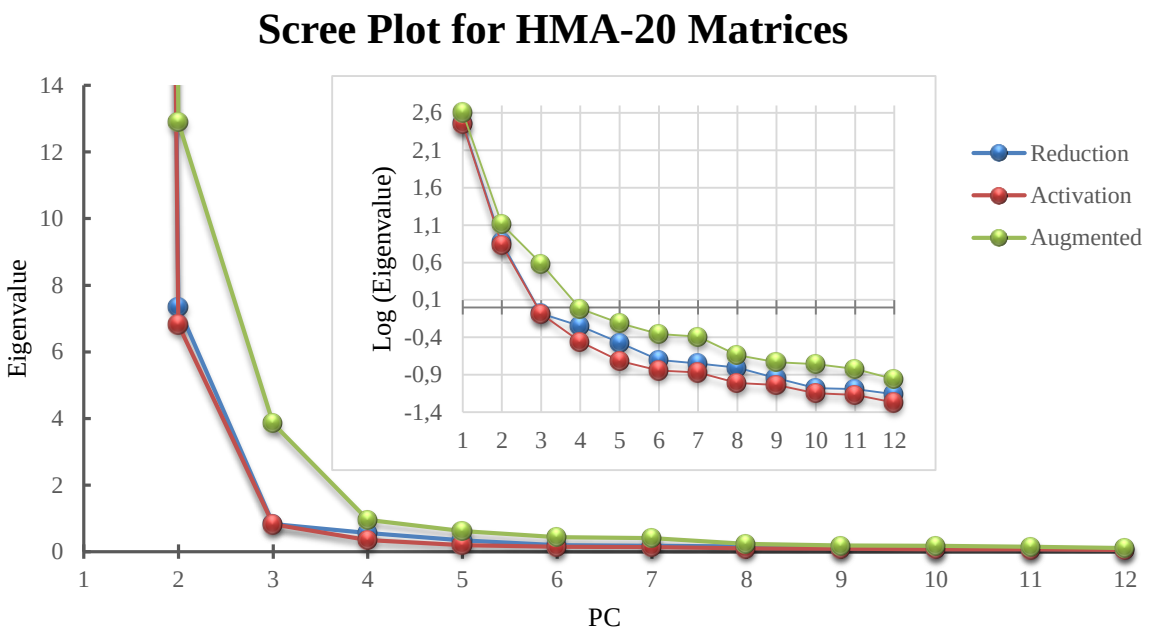

Figure VI.1 - Scree plot for HMA-20 system (from second PC onwards). The inset shows the log values scree plot.

As seen above, it is difficult to set a clear criterion to determine the "good" PC number. We must go deeper in data exploration in order to be more critical in number determination of significant components. Next, we present a series of graphical tools that may be helpful in principal component number.

2.1.1. Plot Analysis of the TPR of HMA-20

Particularly, the scores from PCA. One must to recall that scores describe the data structure in terms of a sample[12] pattern, and more generally show samples differences or similarities.

In the sense of the last paragraph, Figure VI.*2* presents two plots related to the scores: the evolving score plot and the scatter plot of the scores for the TPR of HMA-20. At left panel of Figure VI.*2*, the evolving score plot, we can regard each PC score in terms of a structured pattern. The first PC score is a straight line, it is an average data structure of the spectra; it means that each sample (i.e., each XAS spectrum in our data set) follows the same rough pattern, particularly, a typical XAS pattern: an edge jump followed by few strong oscillations smoothed along the "variable" axis. This "average" structure is almost the same no matter which spectrum we look at, and it is given by the PC 1 of the loading matrix (Figure

[12] We stress that here we use the PCA definition to "sample", which in our particular case means each row of the matrix (and each row represent one spectrum at a given time of the reaction). Each sample has a score on each PC. It reflects the sample location along that PC; it is the coordinate of the sample on the PC.

VI.4). Back to the score plot, as we move to higher PC orders we observe the loss of a "structure". One observes that in PC 3 a noisy, but still structured, curve is present. In the limit case, PC 6 has a completely random behavior, which means that this component is nothing but noise and surely do not represent a pure species. Surely, one has at least two pure compounds in the TPR reaction, corresponding to the initial oxide state and the final reduced state. One must to judge now if the others components (namely, PC 3, PC 4 and PC 5) represent pure compounds or if they are simply artifacts that appears due to any reason (noise, background, etc.) as previously discussed.

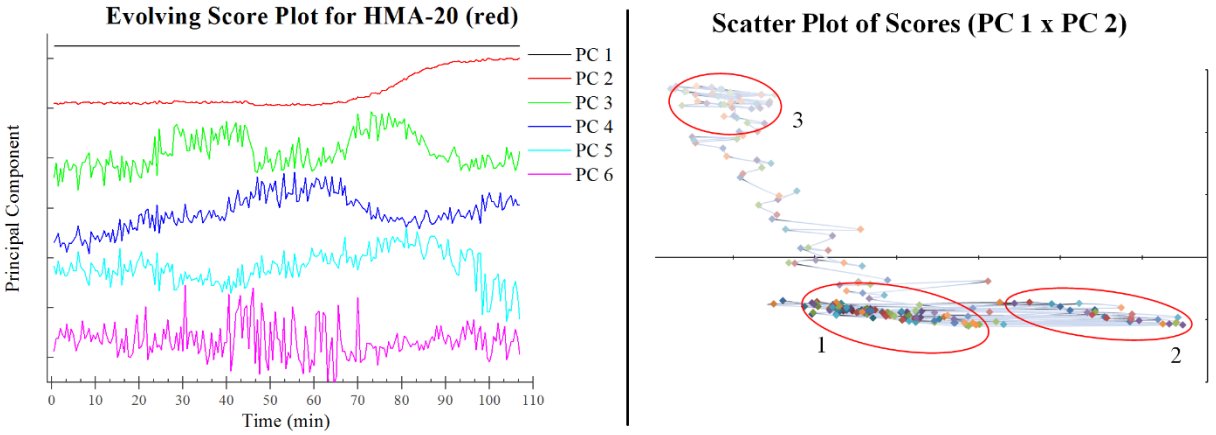

Figure VI.2 - (Left) Evolving Score Plot and (Right) Scatter Plot of Scores for the TPR of HMA-20, where each point represents one spectrum. The red circles highlight the different clusters.

The interesting aspect of a 2D-scatter plot of the scores (right panel in Figure VI.2) is the correlation among the samples. In such a kind of graph, similar samples are gathered in clusters. One clearly sees three well-defined clusters on the scatter plot, which means we have three pure compounds during the reaction. Furthermore, by looking at the one-by-one scatter plot (i.e., the sequence in which each point appears in the plot) one realizes that clusters are formed according the numbers in the circles that marks each cluster. In other words, it obeys a logical sense of the reaction. Since the first point of the reaction represents the first spectrum recorded during the experiments, such one-by-one scatter plot shows the first spectra been placed inside the cluster number 1, which means that during the beginning of the reaction no big changes in the structure happens. Sometime later, the cluster number 2 rises and for a moment, spectra are place alternately in either cluster 1 or cluster 2, indicating the formation of an intermediate and the co-existence of two species. The last spectra suddenly take a different path up to the region inside the circle 3, which is the last and lonely component of the reduction.

We have to remember that such scatter plot is just a 2D projection of a higher-ordered dimensional space. Thereby, we should look at a 3D scatter plot in order to check if any information is wasted when a lower dimensional projection is considered.

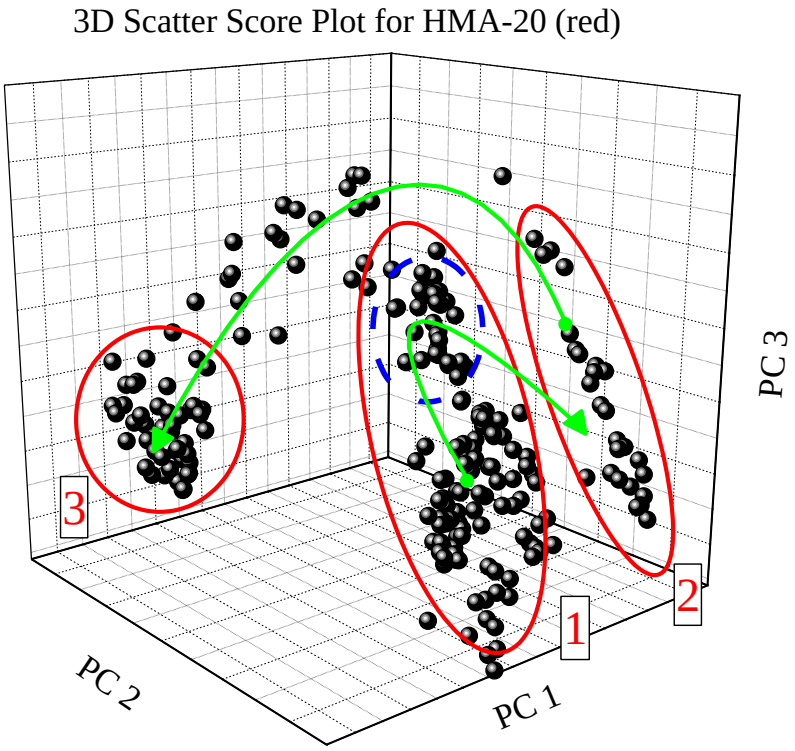

Figure VI.3 - 3D Scatter Score Plot for the TPR of the HMA-20 matrix data set. Circles indicate clusters, i.e., similarity among samples. Green arrows tell direction of the reaction. (See text)

The 3D scatter score plot (Figure VI.*3*) give us a broader view of the evolvement of the process. For reference purposes, the red circles are the same ones that are drawn in Figure VI.*2* (as a matter of fact, it is a 2D projection of the 3D figure above). By looking by the one-by-one plot, we are able to highlight two new features: a small cluster inside region 1 (blue dashed circle) and the sense of the reaction, indicated by the green arrows. It is harsh to know really if this new subgroup is actually a new species or just slight variation of the starting one. It is well known that changes in temperature may induce slight changes in XAS spectra (mainly due to the Debye-Waller parameter) without lost the main structure itself. However, it is not known how if PCA recognizes such changes as to be a new species, making so two PC's for the same structure. Since we do not have enough data to deal with this issue, it will remain as an open question.

Another feature that can be extracted from score plots is the shape of the sense of the reaction. Since the spectra of the mixture that occurs during the reaction are linear combination of pure spectra, the mixtures are found on the line connecting the pure species in PCA space. In the simplest case, an A → B reaction should give a straight line, with the pure species laying on the vertices of this line. In that sense, an arched curve suggests three species in the reaction, and each vertices of the body the data is forming (a triangle, in that case) representing a good estimate for the pure component in the reaction.

Particularly concerning the Figure VI.*3*, if we ignore the small subgroup (by the arguments presented above) we should have one component representing the cluster number 1, another component

representing the cluster number 2, the final reduced state given by the cluster number 3 and an extra component due the arched arrow linking the groups 2 and 3. Nevertheless, one must ponder if we try to extract more information than the data can deliver to us. Cluster 1 and 2 are elongated enough to doubt the nature of the arched arrow, for instance. Once again, we recall the cumulative variance explained by the PC choice (see Table 23); the first 3 components describe 98.48% of the data whereas with 5 components this value passes to 98.73%. Thereby, an increase of 0.25% does not seem to be enough to justify including two extra components. In fact, it is not that there is no exist four or five pure compounds in the reaction, it is just the fact that they are so close among them that we do not have sufficient quality information to ensure that number and to make a clear distinction among them. Eventually, even if we consider 4 or 5 PC's the resulting spectra (and concentration profile) calculated by MCR will tell us if it is a good or a bad choice, according our data quality.

A proper way to interpret PCA results involve simultaneous analysis of both score and loading plots. Figure VI.*4* shows the value of each principal component weighted by its eigenvalue. It is not hard to realize that first three PC's are responsible for the major variance for the whole data set (namely, 98.48%). Indeed, PC 1 represents the average of the whole data set, while the next principal components represent the main variances observed in the data set. For instance, PC 2 is responsible for the variance in the edge and XANES oscillations, while PC 3 is responsible mainly for the variance in pre-edge region. From fourth PC onward, the magnitude of each component becomes very low and, additionally, score plot (Figure VI.*2*) evidences their noisy aspect. Even if the fourth principal component represent something real, it accounts to just 0.11% of the variance. Probably, it is beyond the distinguishing capability of MCR for our system.

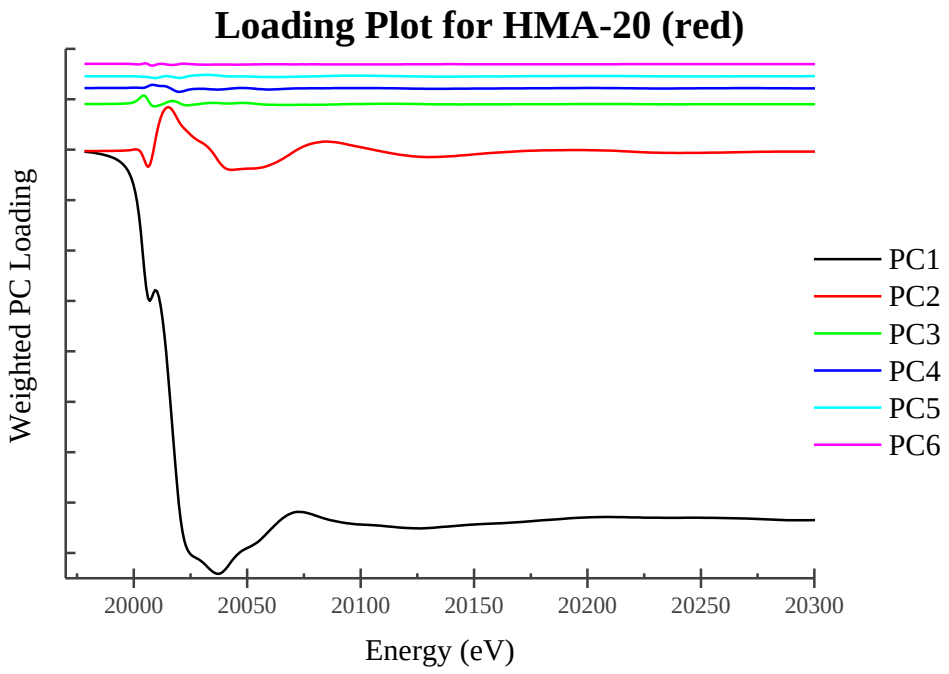

Figure VI.4 - Loading Plot for the TPR of HMA-20. Each component was weighted by its eigenvalue.

The last PCA plot we present is the residual of reconstructed experimental data, i.e., how much variation in the data remains to be explained once the current PC has been taken into account. In PCA analysis, one can reconstruct each experimental data using whatever number of principal components we judge necessary. In order to check if three PC's are enough to rebuild satisfactorily the experimental data, we proceed with this evaluation considering 2 PC's, 3 PC's, 4 PC's and 5 PC's, as shown in Figure VI.5.

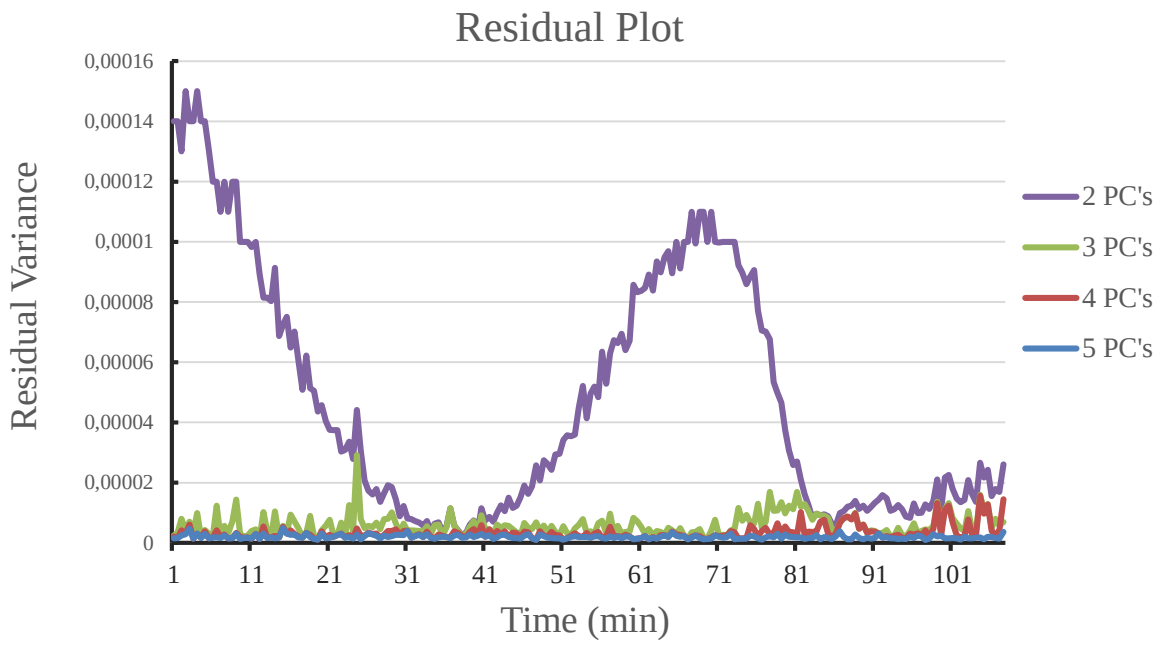

Figure VI.5 - Residual plot resulting from the reconstruction of the experimental data using two, three, four and five principal components.

It is obvious that just two principal components are not enough to reproduce the experimental data. It is also clear that the fourth and the fifth PC's do not contribute to a better description of the data; they are at the same average level of residual, about 3 x 10^{-6} (PC 3 is about 8 x 10^{-6}). Such residual plots also reveals where the third species (in that case) is most influent concerning the data, around 70 minutes of the reaction. That is because in a system with three components, the first two represent more than 98% of the total variance, thus, the higher mismatch with the experimental data appears at the time when this third species is dominant.

In conclusion, it seems that three principal components is the proper choice for the TPR HMA-20 matrix. As discussed so far, PCA analysis gives us a suitable guess for our number of pure compounds in the reaction though we have to keep in mind that is not 100% guarantee. It will be the quality of MCR results that will allow us to give the best answer.

2.1.2. Plot Analysis of the Activation of HMA-20

Since the method is well-described in the preceding section, in order to avoid exhaustive argument repetition concerning the PCA analysis, from now on we will try to condensate the explanation and results, highlighting those that best endorse our choice. We let further discussions when MCR results are on the table.

The first clue on good PC number is in Table 23, by the eigenvalue and variance explained we should say 3 or 4 components, which accounts to 98.58% and 98.70%, respectively, to the cumulative variance explained.

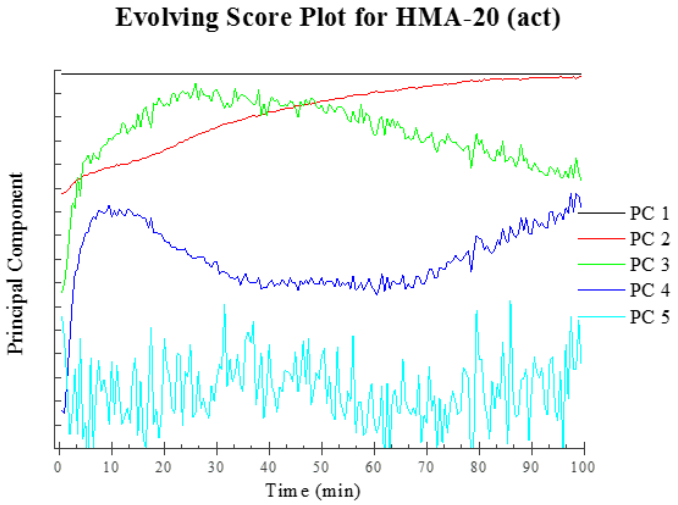

Figure VI.6 - Evolving score plot for Activation of HMA-20 showing contribution from five first principal components.

The present case of the activation of HMA-20, the choice becomes easier when one looks at score plot in Figure VI.6. The first five principal components are drawn and the drastic change in structure from well-behave PC 4 to noisy PC 5 lead us to consider four principal components for this matrix.

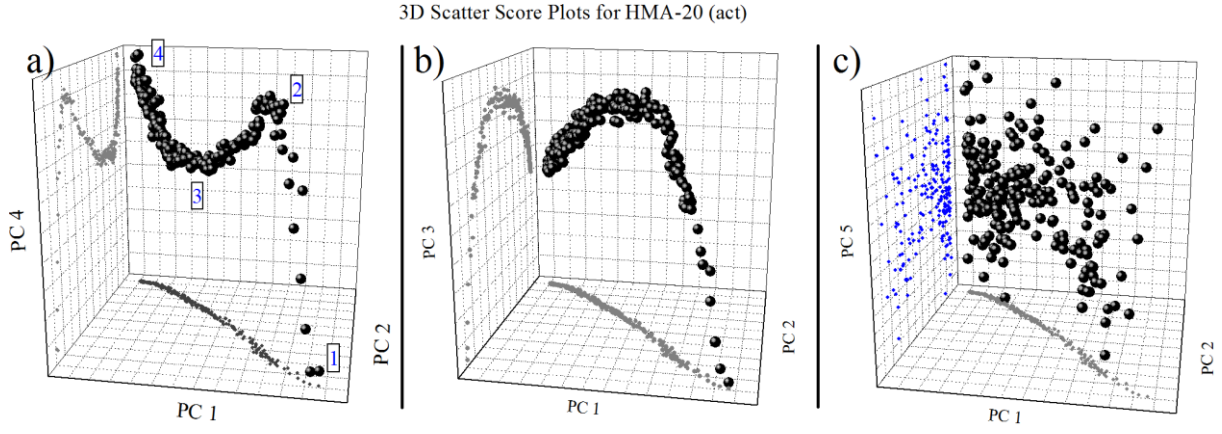

Figure VI.7 - 3D Scatter Score plots considering PC 1, PC 2 and a third distinct contribution for z-axis (see text).

We appeal to scatter score plot to ensure our choice. Figure VI.*7*a shows 3D scatter plot for HMA-20 activation matrix. Instead of use PC 1, PC 2 and PC 3 as coordination axes, we replace the latter by PC 4. Here we no longer see clusters, which means a more homogeneously progressing reaction. However, it has a well-defined shape, with a quick transformation of the start structure (each vertices is pointed by a number) until a moment where more variables (components) play into reaction. Four vertices are well detached, and allied to the score graphic of the Figure VI.*6* seem to answer unambiguously the question on the good number of principal components necessary to describe the activation of HMA-20 data set. Using different set of PC's to build 3D scatter plots do not change anything about interpretation, we still perform a projection of a 4-dimentional space into a smaller one. The only difference is by doing so the interpretation based on what was previously discuss is evident. In order to illustrate it and discuss how it interfere the interpretation, we refer to Figure VI.*7*b where the 3D scatter plot consider PC 1 x PC 2 x PC 3 as coordinate axis. While PC 1 x PC 2 projection remains the same as in Figure VI.*7*a, PC 3 do not reveals the structure that allows us to include the fourth principal component. In this case, we state that 3 PC's are not enough to describe the whole system, since in fourth one we have clear information on it. If we, now, consider PC 5 (Figure VI.*7*c) one observes a completely random behavior when such fifth component is considered, as evidenced by XZ-projection (blue dots) in the figure. It means that PC 5 represents nothing but noise for the data.

2.1.3. Plot Analysis of the Augmented Column-Wise Matrix of HMA-20

Before presenting the PCA analysis of the augmented system, we can make some consideration in what to expect from it. Foremost, we expect 3 PC's in the reduction and 4 PC's. As upper limit in the augmented system, we can expect 6 PC's, because they both share the same initial state. As lower limit, we suppose 4 PC's, since there is at least one species that exists in the activation (the final compound, MoS_2) and do not exist in the reduction.

Above, in Figure VI.*8*, we use score plots in order to take a guess on number of principal components for the augmented column-wise matrix. Joint analysis of eigenvalues (Table 23) and scree plot (Figure VI.*1*) suggest from 4 up to 7 components. We have considered a range from 4 PC's up to 6 PC's. The left score plot in Figure VI.*8*, at a first glance, may suggest that all 6 components are able to describe the system, but since the 6^{th} presents highly noisy feature, we tend to discard it.

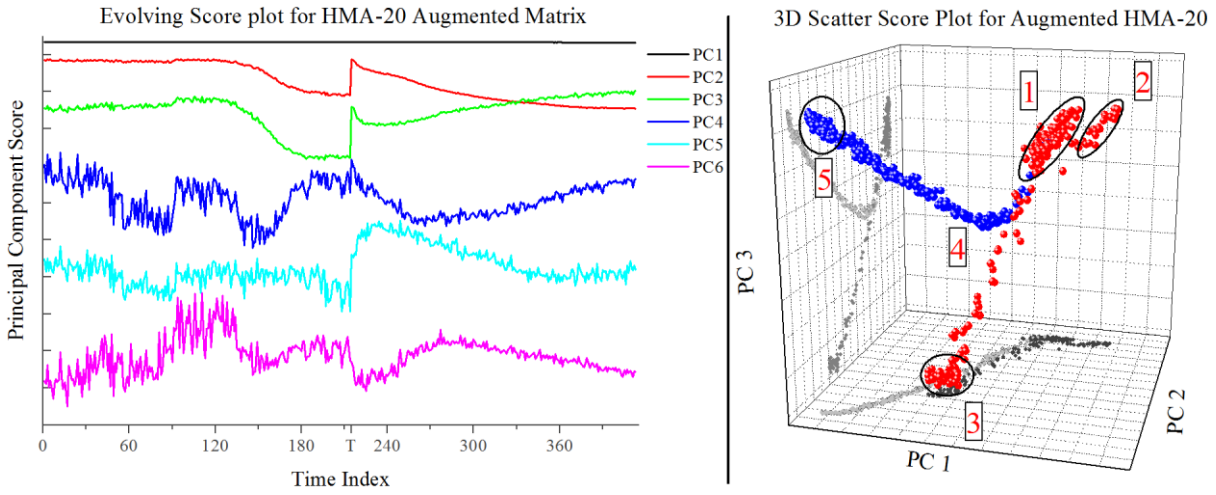

Figure VI.8 - Scores plot for the HMA-20 augmented column-wise matrix.

3D scatter score plot (Figure VI.*8*, on the right) strongly suggests 5 principal components. It is noteworthy that we can recognize features from both different processes, the TPR (red balls) and the activation (blue balls). The clusters are circled as in Figure VI.*3* in order to coincide the numeration. Thereby, cluster number 1 represents the depart of (both) reaction, whereas the cluster number 3 asserts to the reduced species at the end of the TPR and cluster 5 the end of activation. By probing point-by-point such plot, we observe that firstly the reaction takes the red balls path (TPR). As in the single matrix analysis of TPR, the formation of an extra cluster (labeled number 2) next to the first one is noted. Later, on the end of TPR the balls on scatter plot (Figure VI.*8*-right) suddenly go back to the region of cluster 1, meaning that TPR reaction is finished and it starts activation, the blue balls path). By record effects, it happens at the *time index*[13] 214 (marked with a *T* on time-axis of Figure VI.*8*-left, where the activation starts).

A remarkable feature on this 3D scatter plot is that when using augmented column-wise matrix, the TPR branch of the scatter seems to be "corrected" comparing to the TPR alone. While in Figure VI.*3* one has an arched line linking the clusters 1 and 2 to the cluster 3, in Figure VI.*8* (right panel) we have clearly a straight line with the longitudinal sense of the clusters perfectly aligned (see plane projections on 3D plot). It seems to be typical case where one gains information by using the augmented column-wise matrix (the confirmation comes with MCR analysis). We can find some examples in literature when the use of augmented matrix applied to other spectroscopy techniques than XAS (for example, [7][8][9]) were of critical help, but until the writing of this manuscript, it was not found any record in such case (the activation).

[13] This "time index" is an artifact due the fact that we must to stack both TPR and the activation matrices in order to perform the augmented column-wise matrix analysis. In that sense, we have a continuous scale of time, from 1 up to 214 for the TPR and from 215 to 413 for the activation, with each unity in this scale is equal to 30 s of the reaction.

We stress one last time that whatever the result concluded by PCA analysis on the good number of components, it will be the analysis of MCR-ALS results, namely, the concentration profile and the pure spectra, allied to our own prior knowledge for the system that must give the right (or the best) answer to the problem. Thereby, MCR-ALS test must be performed with alternative PC numbers (usually, ± 1 in respect to the initial PC guess) in order to ensure a reliable answer.

2.2. MCR-ALS on H_2S Activation of HMA-20

As largely discussed on the previous chapters, despite in MCR-ALS calculation no *a priori* information is necessary to run a matrix calculation and recover concentration profile and pure spectra, additional information must be set in order to avoid ambiguity in solution. This additional information is carried by either combining soft to hard modeling or, more commonly, by using constraints. It is noteworthy to say that MCR solution can be ambiguous and quite vague, transmitting an unnecessarily negative impression if no information on the extent and location of such ambiguity is provide. Ambiguity is a concept related to each component in the system and to each profile within a dyad (i.e., a pair of matrices concentration profile and pure spectra). An ambiguous solution of MCR can be very satisfactory if the components of interest are uniquely resolved or affected by a very low degree of ambiguity, even if the rest of the system is not perfectly defined.

To obtain satisfactory results, it is relevant to pay attention to the steps of the selection of the initial estimates and constraints. Initial estimates are the starting point of the optimization process, and sensible guesses should be the first step. Conversely, constraints are the properties that the profiles should obey. Therefore, selecting the appropriate constraints and knowing how to apply them is the most crucial point to ensure the obtention of meaningful and reliable solutions, affected by as little uncertainty as possible.

Further, in order to perform a suitable selection of constraints, we should first know which kind of profiles we expect to obtain in the MCR decomposition model. Once this is known, constraints can be applied by tuning the tolerance in the application according to some natural characteristics of the data set, such as the noise level. When in doubt about the application of a constraint, MCR models built with and without introducing this constraint can be compared. The introduction of a certain constraint should not produce a significant decrease in the variance explained in the data set. If so, the data set probably does not obey this constraint, or it has been applied in too strict a way [10].

In that sense, given the large range of possibilities, we decided to perform tests in order to compare the influence of both initial estimates and constraints to the results. Furthermore, we also checked accuracy and reliableness of the choice on the PC number, varying the number of components inside a small window (namely, ± 1) around the choice was made in previous section. The evaluation of results is based on the convergence of calculations and, fundamentally, on the spectra/concentration profile shape.

Table 24 - Summary of MCR-ALS Analysis with Different Initial Guess and Constraints.

PC'S	INITIAL GUESS[a]	CONSTR.	N° CICLES	SIGMA	LOF IN % PCA	LOF IN % EXP	VAR. EXPL.
5	SIMPLISMA	1,2	1000	0.001	0.0002	0.12	99.9998
5	EFA	1,2	562	0.001	0.0001	0.12	99.9998
5	SIMPLISMA	1,2,3	49	0.007	0.71	0.72	99.9947
5	EFA	1,2,3	71	0.001	0.14	0.19	99.9996
5	SIMPLISMA	2,(3),5	(14)/50	0.001	0.13	0.18	99.9996
5	EFA	2,(3),5	(34)/50	0.001	0.15	0.19	99.9996
4	SIMPLISMA	1,2	1000	0.001	0.0002	0.14	99.9998
4	EFA	1,2	1000	0.001	0.0001	0.14	99.9998
4	SIMPLISMA	1,2,3	13	0.009	0.97	0.98	99.9904
4	EFA	1,2,3	140	0.001	0.1	0.17	99.9997
4	SIMPLISMA	1,2,4	24	0.001	0.11	0.18	99.9997
4	SIMPLISMA/EFA	2,3,5	25/24	0.001	0.08	0.16	99.9997
3	SIMPLISMA	1,2	1000	0.001	0.0001	0.19	99.9996
3	EFA	1,2,3	121	0.002	0.11	0.22	99.9995

Constraints Code:
1 - Euclidean normalization in Spectra
2 - Non-Negativity in Concentration Profile And Spectra
3 - Unimodality in Concentration Profile (tolerance = 1.0)
4 - Selectivity in Concentration Profile (to the unity)
5 - Closure

[a] In SIMPLISMA algorithm, 5% of noise was tolerated in spectra determination.

Table 24 summarizes the results for the tests performed. There in is showed the algorithm used to determine the Initial Guess (SIMPLISMA or Evolving Factor Analysis), the constraints in each calculation, the number of iterations until convergence is achieve (red number means that either fit was not improved after 20 iterations consecutively or the number of iterations exceeded the allowed), standard deviation, fitting error (lack of fit) and the percent of variance explained.

When MCR is performed with 3 or 5 PC's, whatever the initial guess and constraints combination considered, either the concentration profile or pure spectra (or both) give not reliable shape (i.e., they do not look like physical real objects each one in its own sense), in spite of figure of merits values. When using 4 PC's, similarly to the previous cases, a wide range of dyads are obtained depending on which method was used to determine the initial guess as well as the constraints used. As before, the majority of them are not physically representative. Nevertheless, good results were obtained (the highlighted line in Table 24) under specific conditions, namely, non-negativity in concentration profile and spectra, unimodality and closure in concentration profile (Figure VI.9).

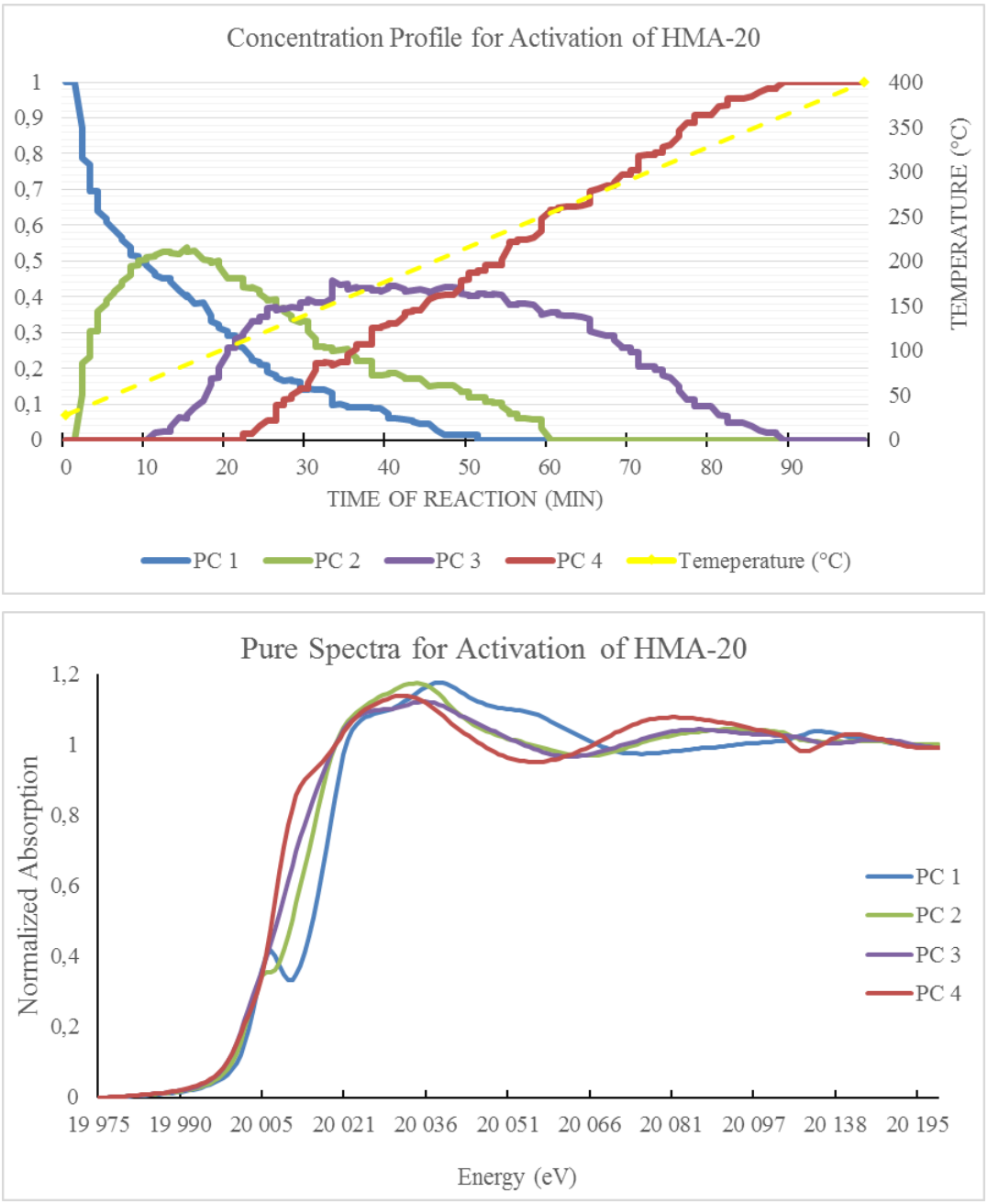

Figure VI.9 - MCR-ALS results for activation of HMA-20, (up) Concentration Profile and (down) Pure Spectra.

These results suggest that the activation of the HMA-20 catalyst obeys a kinetics given by its concentration profile (Figure VI.9, upper panel). Further, according the results, the precursor oxide transforms completely in the final state (MoS_2) passing by two intermediates pure compounds. The first one starts to rise early in very low temperature domains (about 50 °C). The second one, appears a dozen minutes after (about 100 °C), when the first intermediate achieve its maximum concentration and starts to fall in concentration. MoS_2 starts to be forged about 22 minutes along the reaction, in a temperature slightly below 150 °C. From 90 minutes on, at 350 °C, all precursor is converted into MoS_2 and the

reaction is completed. Just for record, this value (100% of active phase) is in accord with linear combination of XAS spectra with MoS_2 bulk reference, as discussed in previous chapter.

Pure spectra XANES analysis do not allow us to assure exactly which transformation occurs from oxide precursor to active phase. Latter, fine structural analysis will fulfill this lack. From a first qualitative analysis from the MCR results, by XANES (Figure *VI.9*) and EXAFS (Figure *VI.10*) We assert that the first intermediate (PC 2) is a transformation of the start structure, likely a reduced compound, since we see a shift of the edge to lower energy values and a reminiscent pre-edge feature is still observed. The second intermediate (PC 3) should be an oxysulfide compound. XANES features is closer to the final state, the MoS_2 spectra (PC 4) and is the last compound before the rising of the final MoS_2 state. Such oxysulfide as well as MoS_3 intermediates are suggested in the literature for this kind of reaction in similar systems, i.e., in supported Mo- and CoMo-based catalysts (for instance, see [11] [10] [11] [14]). It was suggested that intermediate can appears as $MoO_2S_2^{2-}$, MoO_3S^{2-}, $MoOS_3^{2-}$ [15], or commonly refereed as $\{MoOS_2\}$ [16][17]. A first glance on EXAFS extract from the MCR-calculated spectra (Figure VI.*10*) allows us to observe the significant structural changes during the activation.

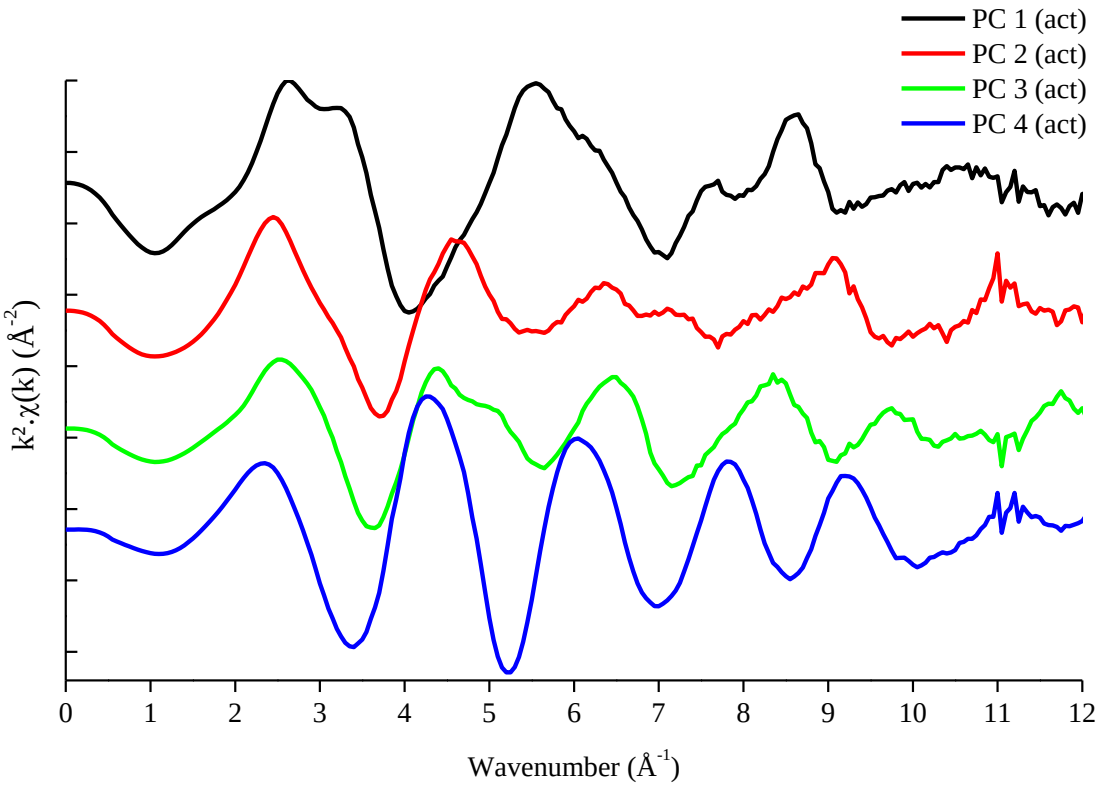

Figure VI.10 - k²-weighted EXAFS extracted from MCR-calculated spectra for the activation of HMA-20.

MCR results allows to describe all the reaction in terms of these four species. We can check how accurate is this description by looking the unexplained part of the MCR calculation in $\boldsymbol{D} = \boldsymbol{CS}^T + \boldsymbol{E}$, i.e., the residual matrix $\boldsymbol{E}$.

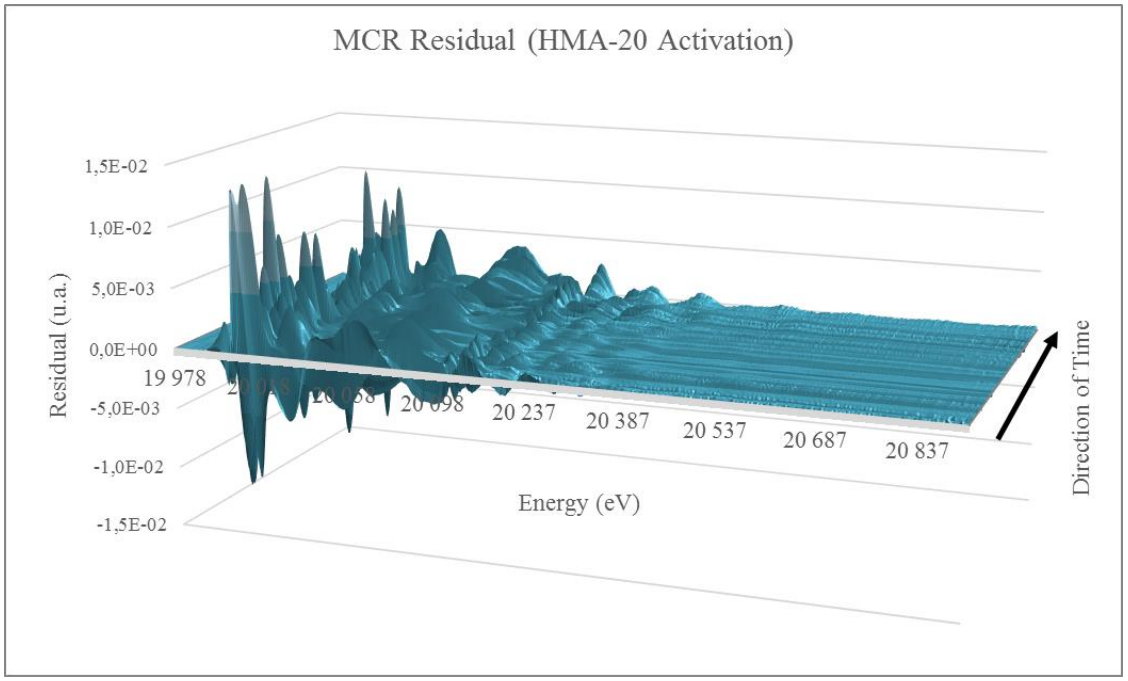

Figure VI.11 - Residual (unexplained) matrix in MCR calculation of HMA-20 activation.

Figure VI.*11* shows the graphical representation of residual after MCR calculation of HMA-20 activation matrix. For each experimental spectrum the difference between the experimental value and the calculated via $\boldsymbol{C*S^T}$ product was considered. In that sense, we have the residual evolvement for this data set. Except for few particular regions, the residual value stay below 1.0 x 10^{-2} and especially, such residual plot do not present real structure shape (i.e., a shape of a XANES spectra, for instance), which ensure a suitable description of the data by the previously proposed 4 PC's.

Once results obtained in MCR (Figure VI.*9*) look like real and feasible (concentration profiles and spectra), we are able to perform a fine structure refinement in order to well-describe it in terms of atomic order. Before doing so, however, we present a method developed in order to evaluate the ambiguity that may exist in solution. Then, we describe qualitatively MCR analysis for TPR and Augmented systems.

2.2.1. Ambiguity of the Solutions and The Bands Method

At this point, where reliable dyad seems to be obtained, it is interesting and important to check the ambiguity issue for such solution. We should recall another kind of ambiguity quite common in MCR analysis, the intensity ambiguity. In plain words, the correct reproduction of the original data matrix can be achieved by using component profiles differing in shape (rotational ambiguity) or in magnitude (intensity ambiguity) from the sought (true) ones ([18], [19]). In a hypothetical case with no rotational ambiguity, that is, in the case where the shapes of the profiles in $\boldsymbol{C}$ and $\boldsymbol{S}$ are correctly recovered, the basic resolution model could still be subject to intensity ambiguity. Consider the equation below:

$$\boldsymbol{D} = \sum_{i=1}^{n} \left(\frac{\mathbf{1}}{\boldsymbol{k_i}} \boldsymbol{c_i}\right)\left(\boldsymbol{k_i s_i^T}\right) \tag{29}$$

Here, k_i are scalars and n refers to the number of components. Each concentration profile of the new $\boldsymbol{C_{new}}$ matrix (in Equation (30)) would have the same shape as the real one, but it would be k_i times smaller, whereas the related spectra of the new $\boldsymbol{S^T_{new}}$ matrix (in Equation (30)) would be equal in shape to the real spectra, though k_i times more intense. This is why concentration values and pure response intensities are always in arbitrary units unless the reference information on real intensities is available and actively used in the resolution process. Normalization of concentration profiles or resolved spectra or use of reference concentration values within the optimization help to suppress the intensity ambiguity.

Concerning rotational ambiguity, a method was recently developed to evaluate the boundaries of the so-called feasible bands, within which should lies all the feasible solutions, named bands method [20][21][22][23]. We use the MCR-BANDS toolbox implemented on MATLAB to perform our calculations [24]. A short explanation of Bands Method is described in the following paragraphs.

Briefly, in absence of any constraint, $\boldsymbol{D} = \boldsymbol{C}*\boldsymbol{S^T} + \boldsymbol{E} = \boldsymbol{D'} + \boldsymbol{E}$ (with $\boldsymbol{D'} = \boldsymbol{CS^T}$) has an infinite number of solutions, since there are an infinite number of matrices $\boldsymbol{C}$ and $\boldsymbol{S^T}$, which when they are multiplied, they will produce the same result, the data matrix $\boldsymbol{D'}$ (apart from noise $\boldsymbol{E}$). This indeterminacy is described mathematically by the following equation:

$$\boldsymbol{D' = C_{old}\ S^T_{old} = (C_{old}\ T^{-1})\ (T\ S^T_{old}) = C_{new}\ S^T_{new}} \tag{30}$$

The evaluation of the bands are made using:

$$f_n = \frac{\left\|\boldsymbol{c_n s_n^T}\right\|}{\left\|\boldsymbol{CS^T}\right\|} \tag{31}$$

Where f_n is a scalar value that gives the relative signal contribution of a particular component to the whole signal for the mixture of N components (n = 1,…N). This relative signal contribution is measured by the quotient of two norms (Frobenious norm), one from the signal of the considered component n, $\|\boldsymbol{c_n s_n^T}\|$, and other from the whole signal considering of all components of the system together, $\|\boldsymbol{CS^T}\|$.

Eq. (30) say that the product $\boldsymbol{CS^T}$ produces the same results for any invertible matrix $\boldsymbol{T}$. Therefore, the value of $\|\boldsymbol{CS^T}\|$ in Eq. (31) is a constant value for any $\boldsymbol{T}$ value. On the contrary, for every component n = 1,…N, every $\boldsymbol{T}$ matrix will give a different set of $\boldsymbol{c_n}$ and $\boldsymbol{s_n^T}$ profiles with different shapes, and their product $\boldsymbol{c_n s_n^T}$ will be also different as well as their norm and their relative signal contribution f_n defined by Eq. (3). Therefore, the scalar value of f_n will depend on the considered $\boldsymbol{T}$ matrix. The application of constraints makes only possible some of these $\boldsymbol{T}$ matrices. It is then possible to look for those $\boldsymbol{T}$ matrices which give maximum and minimum values of the relative contribution function for each component of

the system, f_n n = 1,…N, called respectively f_n^{max} and f_n^{min} and their respective matrices $\boldsymbol{T_n^{max}}$ and $\boldsymbol{T_n^{min}}$ of a particular set of profiles $\boldsymbol{C}$ and $\boldsymbol{S^T}$. For a well-suitable constrained system, the difference between the coefficients are minimized (close to zero) and rotational ambiguities are practically extinguished. ■

Table 25 - MCR-Bands Results for HMA-20 Activation Matrix with 4 PC.

Initial Guess	f	Component 1	Component 2	Component 3	Component 4
EFA	f_{max}	0.2361	0.2843	0.296	0.5933
	f_{min}	0.2361	0.2843	0.296	0.5933
	$\boldsymbol{\Delta f}$	**2.975e^{-005}**	**1.915e^{-005}**	**0**	**1.211e^{-005}**
SIMPLISMA	f_{max}	0.2658	0.5994	0.2533	0.2759
	f_{min}	0.2657	0.5994	0.2533	0.2759
	$\boldsymbol{\Delta f}$	**1.983e^{-005}**	**1.107e^{-005}**	**0**	**0**

In our particular case, both SIMPLISMA and EFA initial guess methods give us virtually the same result in concentration profile and pure spectra. MCR-Bands calculation converges and it gives narrow bands (see Table 25) that allows us to say that such calculated profiles are reliable (and unique) solutions. A graphical output may be useful when broader bands are obtained (not showed here because the narrow bands coincides with the solution). This can be helpful in evaluating the feasibility for the solutions and the range of ambiguity, which is not the present case.

The calculation of these band boundaries allows the assessment of the effect of the constraints on the decreasing the rotational ambiguities that are naturally associated to multivariate curve resolution solutions. This open up the possibility of a sort of quantitative report associated to the non-solved ambiguities accompanying MCR results in order to systematically validate the quality of solution and assess their reliability.

2.3. MCR-ALS on Reduction of HMA-20

We proceed in the same way for HMA-20 TPR matrix. Taking into account the number of components discussed in PCA section (2.1.1) we proceed in analogue way to the activation case discussed above, when we concluded as to be 3 compounds to describe the reduction of HMA-20.

Nevertheless, when dealing with 3 or more PC's, no matter the constraints combination or the initial guess, MCR fails to retrieve result as feasible as for activation. At the best guess (not showed), 3 component associated with non-negativity in both concentration and spectra profiles, closure and local rank selectivity, we found suitable concentration profile and a low residual matrix with acceptable figure of merits. However, the PC 1 and PC 2 pure spectra were quite overlapped, and they looked like to be

almost the same one. It is noteworthy that in this particular case, unimodality seems to mess up the calculation, acting like an actual wrecker to the convergence.

We should accept, thus, that 2 PC's correctly describe the system and that, finally, we have a simple reaction where, at a given moment, the oxide precursor reduce to the final form following the typical transformation A → B. Indeed, using two components we can reasonable explain and describe the TPR of HMA-20, if we consider the figures of merit (about 98% of total variance), residual (typically, 10^{-3}) or statistical stop rules in principal component analysis [6], which is quite intriguing, given all the discussion previously made when looking at PCA of this system. We must put the question if 2 components is more appropriate to explain the data set instead of 3. Despite that, we do not believe that just two compounds are present in this particular system and we present two facts that seems to overcome this issue.

The first one is that, regardless of the PCA deeply performed in HMA-20 TPR matrix, when we did the equivalent analysis in the augmented system, the reduction part of the data seemed to be "corrected" compared to single HMA-20 TPR matrix analysis (compare Figure VI.*3* and Figure VI.*8*(right) and see discussion in the text). It very interesting because it may indicate how careful we have to be when doing such analysis in order to do not overestimate the PC number.

The second fact passes by activation HMA-20 matrix. After a closer look at MCR-PC 2 from HMA-20 activation, we realize, that this first intermediate species has a EXAFS that is not far from the oxide structure. Thus, we suspect that this component could be related to the reduction. Since we have an entire record of TPR for the same sample, the first procedure was to cross the data in order to figure out if such MCR intermediate (PC 2) belongs to this series. (Not a coincidence, it is the region where both SIMPLISMA and EFA accuse to exist a pure compound). By direct comparison (Figure VI.*12*), it is obvious that the first intermediate of activation (PC 2) has not the same features of the last spectrum of the TPR record (namely, the spectrum #214). Instead, apart slight deviations, it is somewhere around the spectrum #163 of our series. XANES (the arrow in upper panel) indicates that as we move up into the series, the pre-peak feature tends to vanish. Further, the low energy first bump (around 20022 eV) increases, whereas the second bump (20032 eV) decreases (dashed lines). In EXAFS (lower panel), we highlight the shift of the first oscillation around 2.5 $Å^{-1}$, the narrowing of the band (around 5 $Å^{-1}$) and the split peak oscillation around 7 $Å^{-1}$ (dashed lines). Deviation are predicted and it happens because PC 2 do not appear (likely) in the reaction as pure compound, instead there is contribution from other components to form experimental data.

In this scenario, we have two possibilities to consider. The first one, the MCR for HMA-20 reduction alone is correct and we have just 2 PC's in the system, the first and the last spectra, roughly. In such case, this experimental "intermediate" spectrum #165 from reduction (and the MCR-calculated PC from activation) is a linear combination of the first and the last spectrum of the reduction. The second

possibility is that such intermediate spectrum #165 represents roughly a pure compound, which for any reason MCR calculation cannot well separate it in the regular matrix system (it is quite reasonable, given the complexity of the system). As told above, the slight deviations from MCR-calculated spectrum and experimental #163 may rise by the fact it is unlike that this reduced intermediate appears as a pure compound in a given moment of the reaction. In other words, is very likely that #163 spectra is a linear combination between the oxide start compound and this intermediate, or even a linear combination among the three spectra that exist in the reduction. Anyway, this consideration states that it is in this region the maximum of concentration of such pure intermediate, if it really exists.

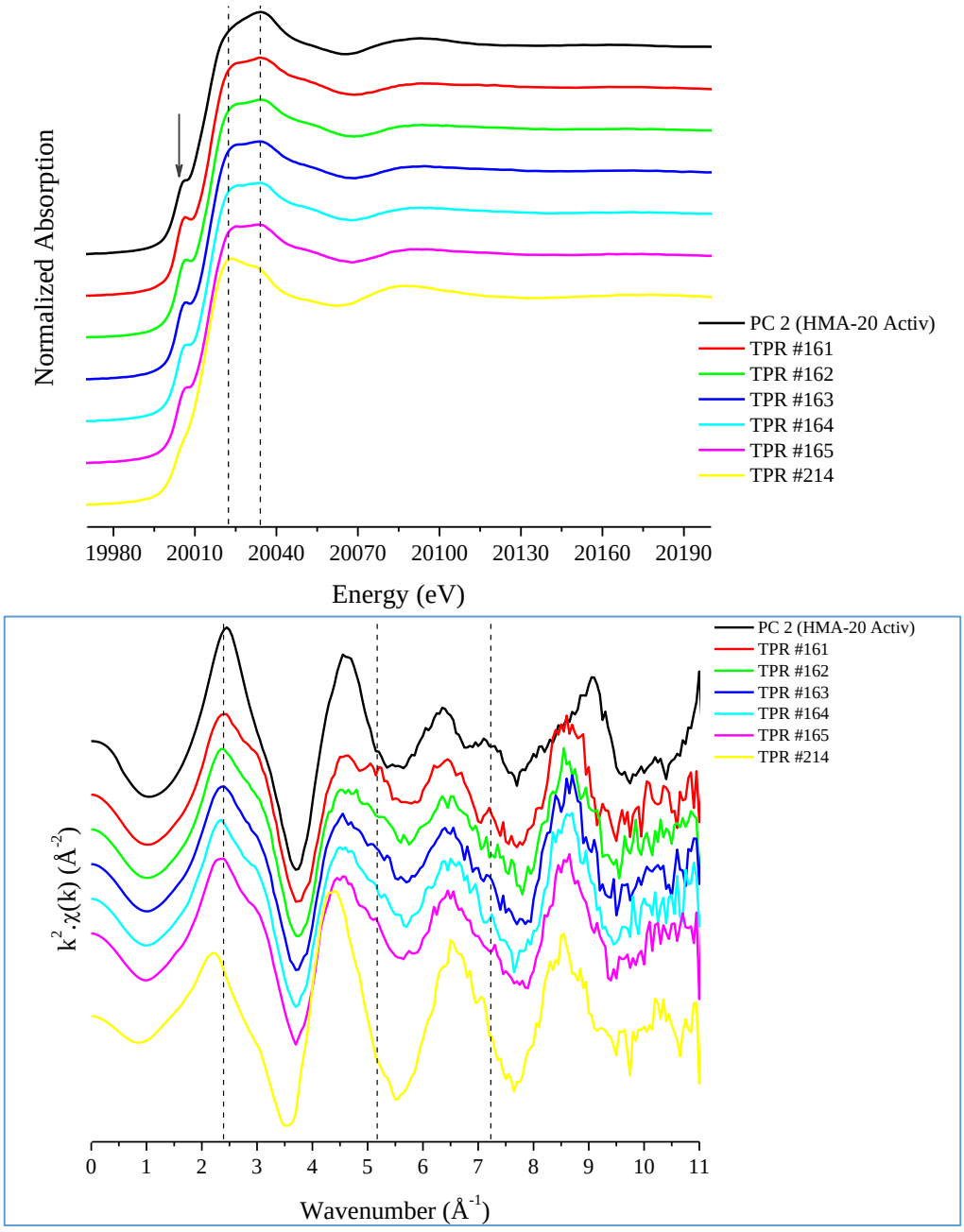

Figure VI.12 - Direct comparison (top, XANES and down, EXAFS) between MCR-calculated PC 2 (from HMA20 activation) and some selected experimental data. Arrow and dashed lines indicate remarkable features (see text).

In order to check the first hypothesis, we perform linear combination of PC 2 from HMA-20 activation (which is roughly the spectrum #163) by using as reference the first and the last spectrum of reduction data set. By doing so, we assume that both the start and the final spectra are linear independent, i.e., they are not linear combination of two other spectra (they are not mixed phases), instead, they are pure compounds. Figure VI.*13* shows the linear combination proposed. One observe an important mismatch, especially on EXAFS linear combination, which may be enough to consider that it is a failed hypothesis. It should exist a third pure component in there.

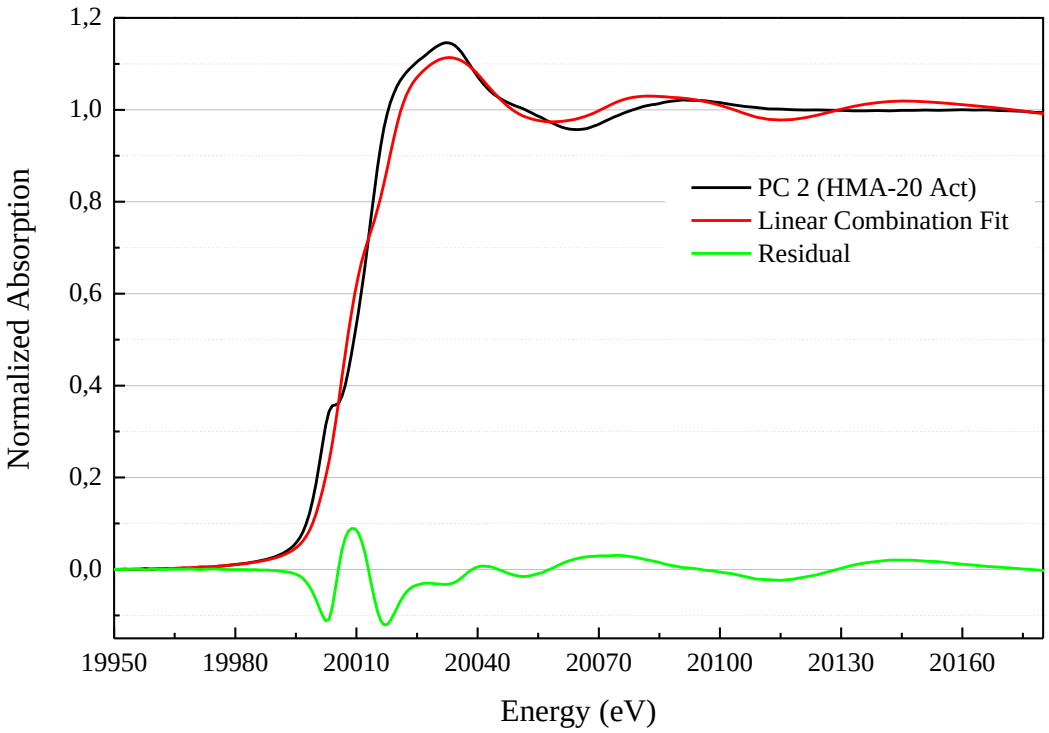

Figure VI.13 - Linear combination fitting of PC 2 (HMA-20 activation). The references used were #1 (32.6%) and #214 (67.4%) spectra of HMA-20 reduction data set. The figures of merit for this fit are: R-factor = 0.0215, χ^2 = 0.2366 and reduced χ^2 =0.0017.

For the second hypothesis, we must consider the results of the next topic. MCR calculation applied to the augmented matrix will tell us which path we should consider the best guess closer to the reality.

2.4. MCR-ALS on Augmented Column-Wise System HMA-20

As stated before, augmented matrix, and in our particular case, a column-wise augmented matrix, is set to provide additional correlated information to the system, correcting the matrix rank-deficiency of the system. Here we consider a combined “TPR + Activation” HMA-20 matrix (413,425), where the first 214 lines represent the TPR data set whereas the last 199 lines represent activation data set.

It is noteworthy to stress the importance of a particular pre-treatment concerning the data set before start MCR. Often in XAS experiments, we face the problem of some small shift in energy beam due to whatever trouble may occurs. For that reason, we use reference metallic foils in order to calibrate the energy of the beam. The big problem is that, at least in MATLAB implementation for MCR calculations, one just disregard the energy axis and all the information it carries with it, which includes energy calibration. It is no use to calibrate in energy using dedicated XAS software if this information is lost when it is imported to MATLAB. After all, it is exclusively energy grid that survives and deliver such calibration information to MCR when the data are treated in MATLAB. Thereby, as important as proceeding with such calibration using dedicated XAS software is to guarantee that the whole and each spectra in data set lies in the same energy grid.

The Principal Component Analysis for the augmented system tell us there exist about 5 pure compounds in the system. The challenge now is to find a way to correlate and cross the information of separate experiments in one MCR analysis. For that, we consider now the three-way system, but still bilinear. This proposition guarantee the cross correlation saying, for instance, that both experiments share the same initial state and, eventually, any other component.

In that sense, the strategy adopted was, given the PC number, to implement progressively the number of constraints. The optimal result was achieved using, for both matrices, non-negativity in concentration profile and pure spectra, closure (equals to the unity), three-way bilinear data and local rank selectivity in concentration profile. When using augmented matrix, initial guess cannot be built by direct EFA. Our Initial Guess matrix was constructed by looking SIMPLISMA guess combined with peak position in concentration profile when individual (TPR or activation) matrix are MCR-calculated alone. Thus, our Initial Guess Vector (***IG***) was formed by 5 experimental spectra that are placed in the region with the most probability to be find the referent pure compound, i.e., ***IG*** =⟨4|214|234|309|413⟩. In this vector, each number corresponds to a line number in the augmented matrix. Local rank selectivity was a fundamental constraint to enable calculation convergence. We have set (assume), basically, that start state is formed by one just compound (is not a mixed state) as well as final states in both reduction and activation. Further, we forbid presence of PC 4 and PC 5 in the reduction (one may consider it as a stronger rank selectivity), since they represent, respectively, oxysulfide and MoS_2 compounds.

The MCR procedure delivers us individual component spectra that can be processed as conventional XANES and EXAFS spectra. In the Mo K-edge, pure spectra and concentration profiles for the augmented HMA-20 matrix are drawn gathered in Figure VI.*14*. One sees that MCR successfully recover the same profile-type when comparing the MCR results for single activation reaction (in Figure VI.*9*).

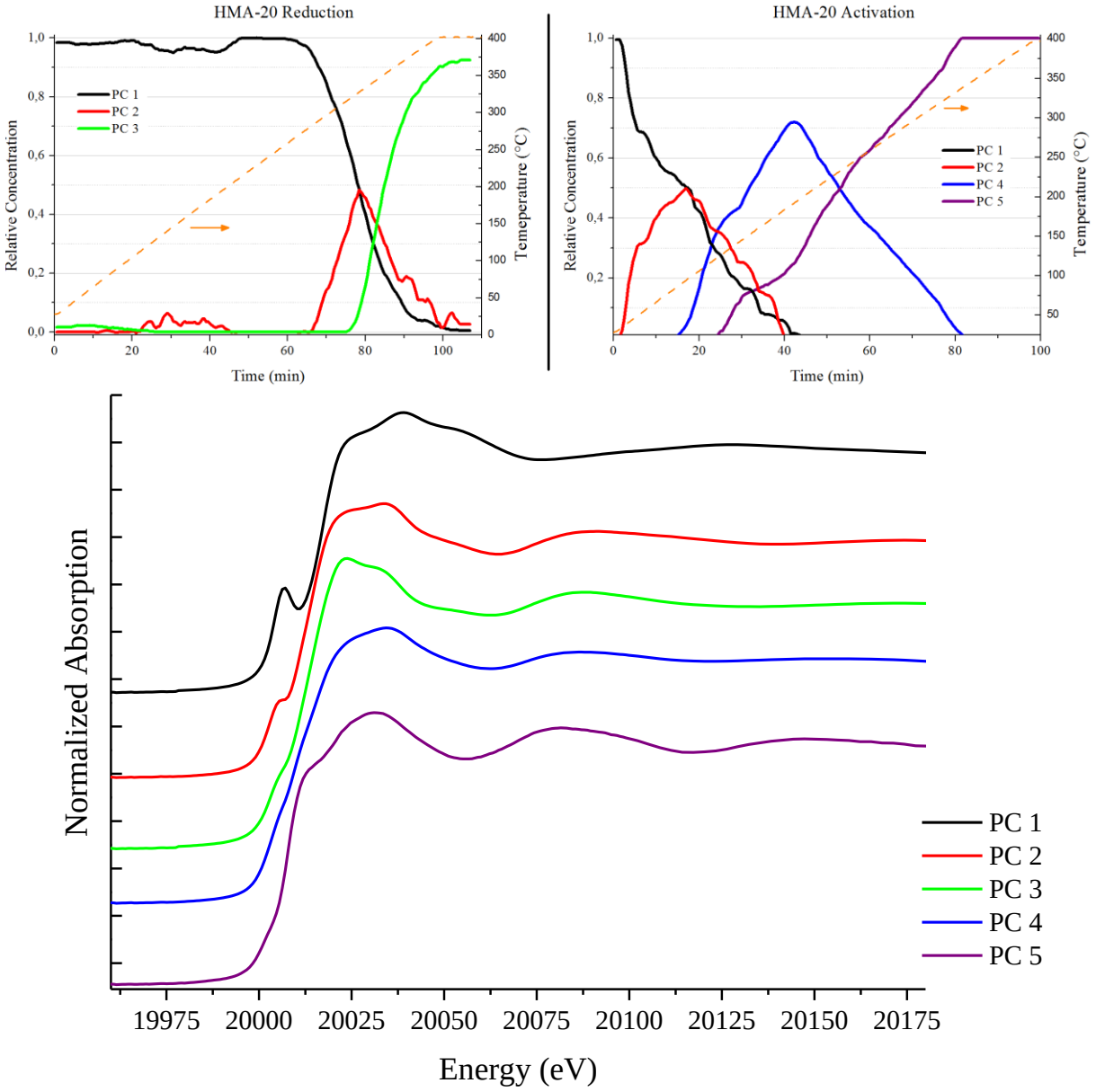

Figure VI.14 - MCR profiles for HMA-20 column-wise augmented matrix. (Upper panel) Concentration Profile of Reduction (Left) and Activation (Right), (lower panel) Pure Spectra. Figure of merits are, standard deviation (σ) = 0.028, LOF in % (PCA) = 2.94, LOF in % (exp) = 2.95 and percent of variance explained (R^2) = 99.9127.

In qualitative XANES analysis, all pure spectra are consistent with expected physic-chemical white-line shift to lower energies along the reaction. The start compound is in the same oxidation state as MoO_3 (formally, Mo^{6+}). In opposite extreme, MoS_2 (the last state) has a formal oxidation state of Mo^{4+}. Anything else may lies inside these limits, i.e., PC 3 has formal oxidation state of +4 (since its edge position is close to MoO_2), PC 2 has formal oxidation state between +4 and +6, close to +5 (since it is not a completely reduced oxide) and PC 4' formal oxidation state lies between +5 and +6. This last one it is not evident to determine because of the XANES-sulfided features, like the typical shoulder around 20020 eV. One observe this trend by looking the position of absorption edge to lower energies. The second PC is shared in both reduction and activation reaction, and is a partially reduced state, since the

final reduction is in a lower edge energy. The next step of activation is something between this so-partially reduced state and the final MoS_2 state, a supposed oxysulfide state.

Before go deeper in EXAFS analysis of the pure spectra, it is interesting to compare MCR results in activation obtained when using single matrix and augmented matrix. Figure VI.*15* shows the concentration profiles in both cases. Bold lines represent augmented-matrix concentration profile, whereas doted light lines, those results from single activation matrix. One observes that despite of some small changes in intensity and start position of some components (mainly for PC 2 end position) the global behavior remains the same.

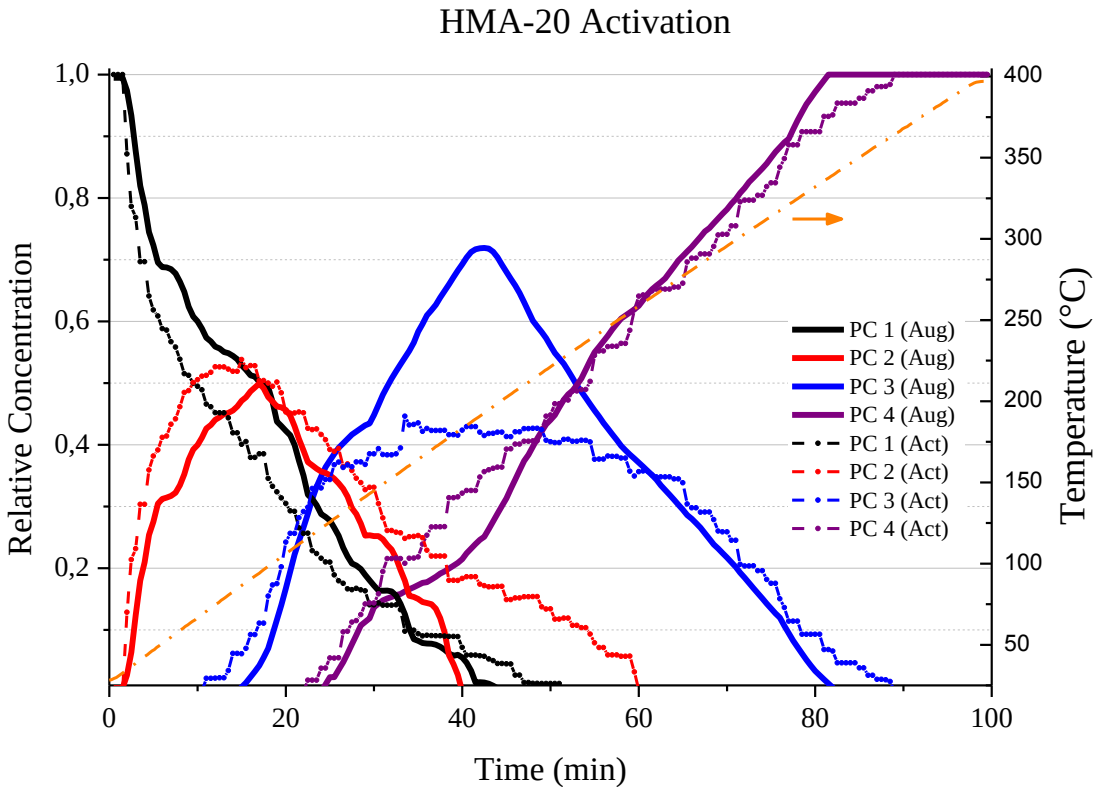

Figure VI.15 - Concentration Profile comparison for activation-MCR calculations when using single matrix and augmented matrix.

Figure VI.*16* shows the comparison among pure spectra. For the start and final components, the spectral coincidence is virtually perfect, whereas for the two intermediates components a good, but not perfect, agreement between the two results is found in XANES. Despite of small differences in some XANES bumps, the overall structural equivalence seems to be the same. For the first intermediate (upper right panel), the main difference arises from the presence of a first shoulder around 20020 eV for, whereas for the second intermediate (lower left panel) is the absence of a "shoulder" in this region. It is not surprising at all, since MCR is all about variance explanation, the major variance present in data are due XANES part of a XAS spectrum.

Looking at the EXAFS (which is the place where structural information is actually in), perfect accord between calculated and experimental spectra is found on the first (PC 1) and the last components (PC 5). Concerning intermediates, as long XANES present small mismatches, some differences in oscillations were expected. In the first intermediate (PC 2), a good coincidence is observed in low wavenumber region. The intermediary wavenumber region, namely the bump around 7 $Å^{-1}$, presents a non-split and more intense peak, but it is clear the presence of two frequencies. For the high wavenumber-values region, we keep intensity of bumps, but the peaks around 9 $Å^{-1}$ are shifted to lower values. In fact, if we consider the same comparison with experimental data as it was done in Figure VI.*12* we note that this "new" MCR spectrum for PC 2 in closer to the spectral features of the considered series, particularly, it is evident when look at bump split oscillation around 7 $Å^{-1}$. Therefore, despite of the mismatch, we still have a partially reduced structure.

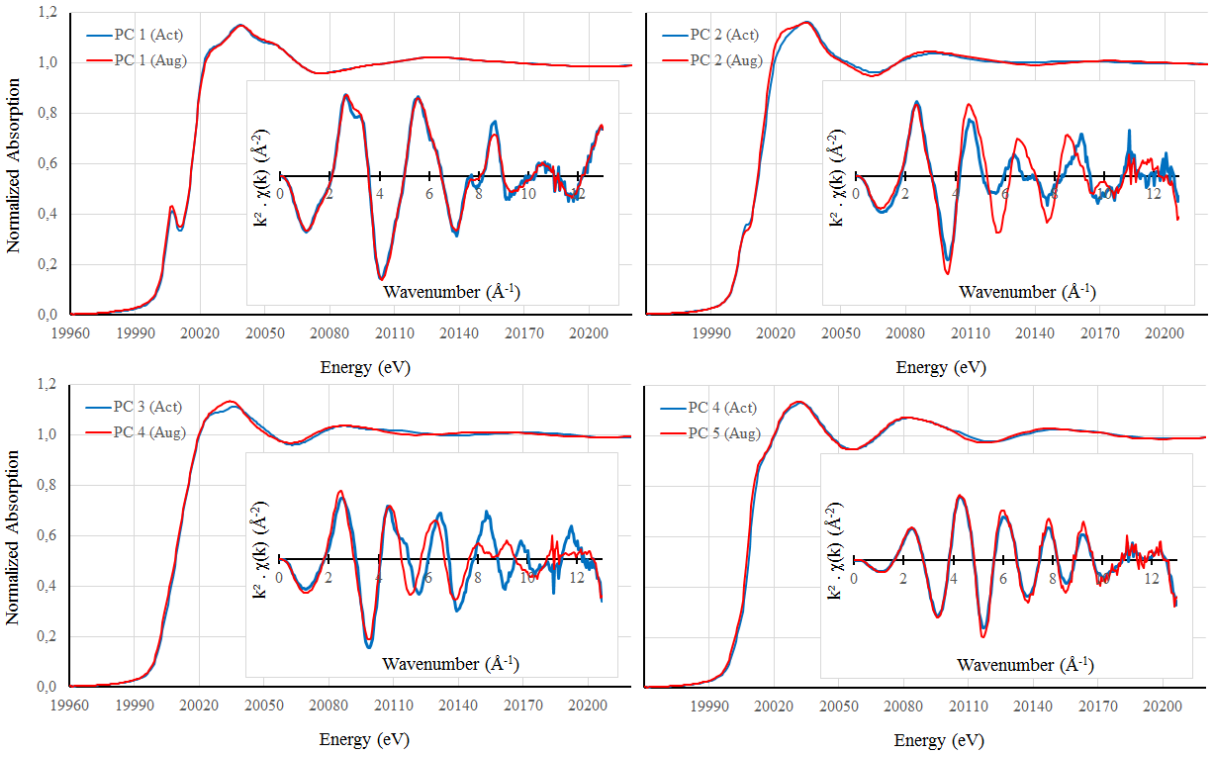

Figure VI.16 - Pure Spectra comparison (XANES and EXAFS, the inset) for activation-MCR calculations when using single matrix and augmented matrix. Note that PC 3 in single activation data set is related to PC 4 in augmented matrix as well as the last component in single activation (PC 4) corresponds to PC 5 in augmented matrix.

A similar trend concerning the mismatches is observed for the second intermediate, but more prominent difference in intensity peak and wavenumber shift is viewed. Nevertheless, in despite of such mismatches, when considering Fourier Transform of EXAFS, the main EXAFS features (namely, peak position), are preserved, i.e., we equally observe oxygen and sulfur contributions for the "new" second intermediate. Therefore, for structural analysis by EXAFS modeling both results are equivalent. This allow us to state that whatever result is considered (the one calculated by single activation matrix or the one considering augmented matrix), the description of the system will be essentially the same.

In fact, we can speculate that the increase of the amount of data (the size of the matrix) driven by augmented data set introduces more complexity to the resolution method at the same time that introduces more realistic and unambiguous information. *In situ* experiments (particularly *in situ* XAS) are by nature complex systems and maybe the price to extract fine information is having to deal with a more delicate and subtle system, in a computational-statistical-data analysis sense. Nevertheless, it is important to stress that was due to augmented data set we were able to resolve intermediate species in reduction.

2.4.1. Structural Analysis of Intermediates

We now proceed with traditional EXAFS analysis of each PC in order to determine the structural parameters of the pure compounds. MCR calculations for augmented matrix result in 5 pure compounds to be present in both TPR and activation reactions. Further, we saw that the start states are no mixed states so that PC 1 is virtually the same spectrum that was EXAFS treated in the previous chapter. Analogously, PC 3 and PC 5 describe, respectively, the final reduced state and MoS_2 final active state of the catalyst. For that reason, we just copied the values from refinement previously done for such structures. It remains PC 2 and PC 4 to be treated, respectively, the partially reduced intermediate (shared in both activation and reduction reactions) and the second intermediate of the activation, the oxisulfide state. The structural parameters are gathered in Table 26. For the partially reduced compound (PC 2), one observe a very complex structure with many distinct oxygen and molybdenum distributions. This complexity, naturally, affects the fit quality, particularly on the uncertainty of the coordination number. Besides that, one observes that such intermediate compound has actually features of an intermediary structure between an oxide and a reduced one. Concerning the oxisulfide compound (PC 4), as expected, we found Mo-O and Mo-S contributions. However, Mo-Mo distances cannot be satisfactorily simulated, suggesting that such long and weaker bonds might had be broken to give place to Mo-S and Mo-Mo from MoS_2 active phase.

Therefore, a succinct description of the activation reaction in terms of local atomic structure could be given as follow: the initial oxide state (PC 1) turns to a complex reduced state (PC 2) where oxygen distribution is distorted and Mo-Mo original bonds lengthened (we highlight the loss of the short Mo=O bond at 1.74 Å). In TPR, this structure becomes simpler (PC 3) and well-structured, one Mo-O contribution with high coordination number and two Mo-O distinct bonds, typical for a reduced Mo-species. In activation, all oxygen bonds but one (originally at 2.04 Å, then at 2.08 Å) disappears as well as Mo-Mo bonds, which give place to a weak Mo-S contribution typical of MoS_2 (PC 4). Finally, as last step of activation, the Mo-O contribution vanishes, and MoS_2-type active phase consolidates its structure, with increasing Mo-S coordination ($N_{Mo\text{-}S}$ goes from 1.0 to 5.6) and one sees arise the other

typical bonds of this structure, namely, a Mo-Mo at 3.17 Å and a second Mo-S bond at 4.10 Å. Time-evolution of each step is given by Figure VI.*21*.

Table 26 - Mo K-edge EXAFS structural parameters for components determined by MCR.

Sample	PC	Bond	N	R (Å)	σ² (Å²)	Δσ	ΔE (eV)	Parameters
HMA-20	PC 1	Mo-O	3.4	1.74	0.005	0.001	2.0	Δk = 5.1-13.6 ΔR = 1.1-3.9 N_{ind} = 16 χ^2_{Red} = 212 R_{factor} = 0.003
		Mo-O	1.6	1.96				
		Mo-Mo	1.0	3.27	0.003	0.005		
		Mo-Mo	1.0	3.41				
		Mo-Co	0.1	2.75	0.0007	0.005		
		Mo-Co	0.1	3.88				
	PC 2	Mo-O	1.4	1.93	0.001	0.004	-8.9 (5.5)	Δk = 4.8-12.7 ΔR = 1.1-3.6 N_{ind} = 12 χ^2_{Red} = 1220 R_{factor} = 0.01
		Mo-O	1.4	2.04				
		Mo-O	1.4	2.42				
		Mo-Mo	0.9	3.23	0.005	0.01		
		Mo-Mo	0.9	3.36				
		Mo-Mo	0.9	3.81				
	PC 3	Mo-O	3.6	2.03	0.004	0.001	-3.4 (3.5)	Δk = 4.5-13.6 ΔR = 1.1-3.9 N_{ind} = 16 χ^2_{Red} = 1835 R_{factor} = 0.05
		Mo-Mo	0.5	2.60	0.004	0.005		
		Mo-Mo	0.4	3.29				
	PC 4	Mo-O	2.6	2.08	0.010	0.008	-3.0	Δk = 4.6-12.7 ΔR = 1.1-3.1 N_{ind} = 10 χ^2_{Red} = 1357 R_{factor} = 0.05
		Mo-S	1.0	2.40	0.004	0.004		
	PC 5	Mo-S	5.6	2.40	0.0045	0.0005	6.5 (0.7)	Δk = 4.7-13.5 ΔR = 1-4 N_{ind} = 16 χ^2_{Red} = 436 R_{factor} = 0.005
		Mo-Mo	3.5	3.17	0.005	0.001		
		Mo-S	0.7	4.10	0.0045	0.0005		
Uncertainty:	PC 1: $N_{Mo\text{-}O}$ = 0.5; $N_{Mo\text{-}Metal}$ = 0.8/0.1 PC 2: $N_{Mo\text{-}O}$ = 0.6; $N_{Mo\text{-}Mo}$ = 0.9 PC 3: $N_{Mo\text{-}O}$ = 0.8; $N_{Mo\text{-}Mo}$ = 0.3 PC 4: $N_{Mo\text{-}O}$ = 2.0; $N_{Mo\text{-}S}$ = 0.6 PC 5: $N_{Mo\text{-}S}$ = 0.3/0.6; $N_{Mo\text{-}Mo}$ = 0.7							

At this point, it is clear the importance of augmented matrix to resolve intermediate states for some reactions. If it was not so important to solve intermediates in activation reaction, we can say that it was fundamental in order to determine correctly intermediate of reduction.

Nevertheless, up until now, we need arguments to ensure that this intermediate in reduction is really a pure new compound instead of just an early step that was found by MCR because we impose the presence of three components.

In following, we present a recent result that may help to answer unambiguously this issue. A combined study of *in situ* XANES spectroscopy and DFT calculations of TiO_2 supported Mo-based catalysts [25] revealed some particularities in the reduction of such compounds. DFT calculation have shown that in such catalytic structures the reduction is driven in steps. By this, we mean that there are sites that appear with greater probability to be reduced compared to others (Figure VI.*17*, upper panel). That mechanism would be led by the number of Mo=O bonds in each site, a great number of such bonds make it either most possible, possible, less possible or not possible to suffer reduction. Confronting calculated-EXAFS for such H_2-reduced Mo-based model catalyst with experimental reduction in methanol reveals deviations between them. However, such methanol-reduced compound matches quite well with our intermediate calculated compound (PC 2 in augmented system) (Figure VI.*17*, lower panel). Additionally, DFT calculated reduced compound have some similarities with our final HMA-20 reduced, which shows that reduction in H_2 (calculated by DFT) is different of the reduction in methanol (experimental). In fact, it supports that fact of our first intermediate actually is an intermediate reduced pure compound, not just an early-step of total reduction.

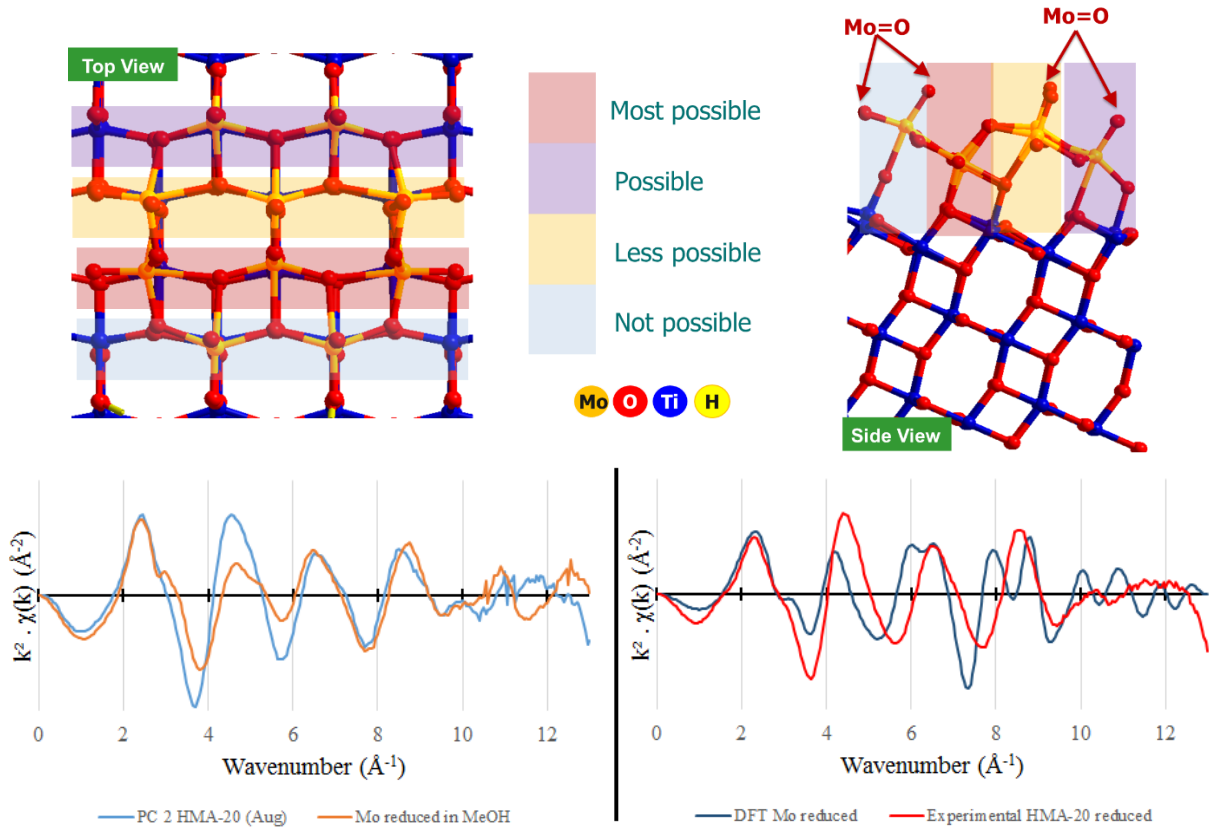

Figure VI.17 – (Upper panel) DFT calculation on Mo-polymolybdate showing different sites able to be sulfided and their distinct susceptibilities degree for it. (Lower left panel) EXAFS comparison between PC 2 and Mo-polymolybdate partially reduced in methanol, (lower right panel) totally reduced calculated Mo-polymolybdate and final HMA-20 reduced spectra.

2.5. Co K-Edge MCR-ALS of HMA-20 Activation Matrix

The main problem concerning the Co K-edge is on the quality of the data. As discussed in the previous chapter, despite of great efforts to record high quality data, we face the problem of, mainly, low signal to noise ratio (s/n) and a systematic glitch in XAS spectra. This is critical to MCR since this method is supported on the explanation of the variance and subtle changes on the data along time.

In order to minimize the influence of bad quality data, we consider just the XANES part of the spectra (in fact, about 200 eV after the absorption edge) in MCR calculations. For the same reasons, we also discard the region before the edge (as it was done also in Mo K-edge).

In terms of PCA, it seems that there is no doubt about the number of components in reaction. Figure VI.*18* shows two plots that suggest three components in the reaction. In anyway, we stress that no matter the indication of number of components given by PCA, we have adopted a protocol of testing MCR inside a small range around the number of principal components indicated by the analysis.

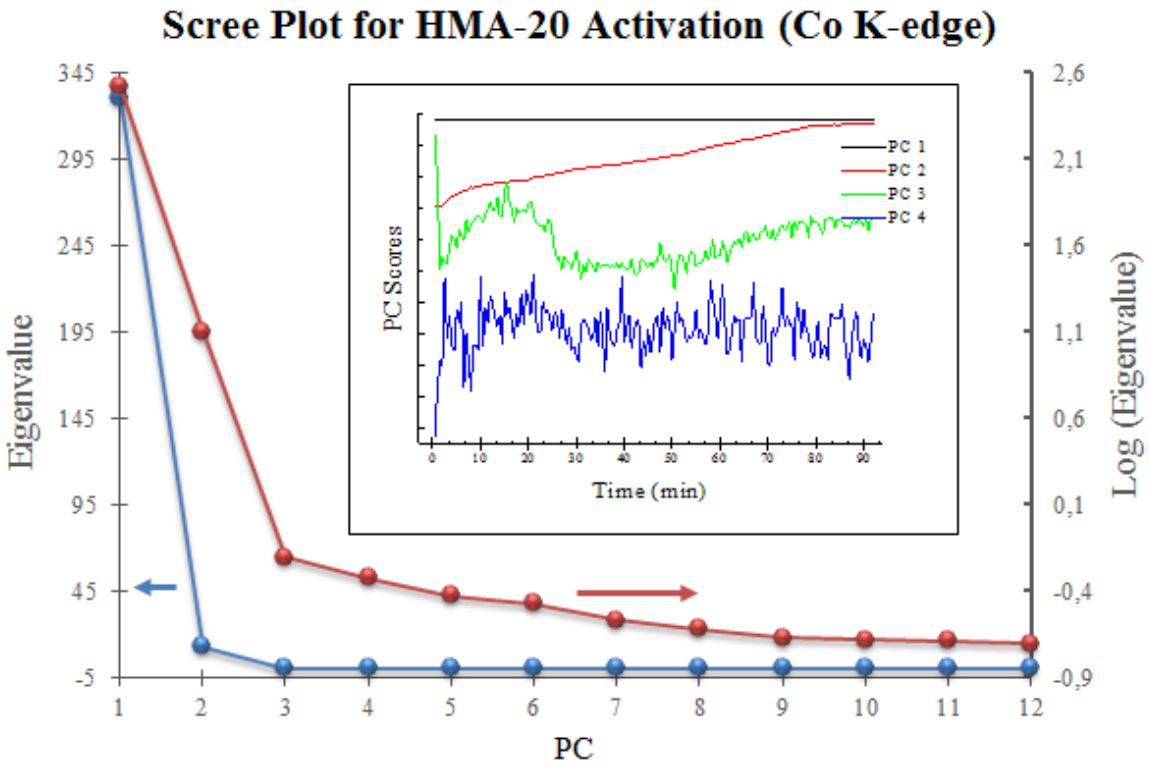

Figure VI.18 - Scree plot and the four first score contribution for HMA-20 at Co K-edge.

Particularly for this data set, we observe an uncommon situation. The inset of figure above show us the evolving scores plot for the four first components. Even though at a first glance PC 4 represent just noise contribution to the description of data, at least for the quite beginning of the reaction (precisely, for the 10 points, which corresponds to the first 3 minutes) it seems that this 4th PC has a strong influence on the data. It is certainly true that a very rapid transformation happens in the very beginning of the reaction, as it can be seen in the XANES evolution (see previous chapter) of this sample. It is also true that the

white line feature seems to decrease in intensity in a different rate in this first short time after the start of the reaction and after goes decreasing in a slowly rate. However, it do not seem to be a new pure compound. For some unknown reason, MCR results using four PC's do not converge under any combination of initial guess and constraints, which reinforces the presence of just three components. Whatever it is causing this perturbation, it was just discarding the first (20) spectra that we were able to perform MCR calculations to obtain satisfactory results. We are not neglecting the transformation that occurs in this short time scale, there is certainly something passing over the first few minutes. Instead, we just eliminate (as less as we can) the disturber, adapting the data in order to obtain reliable profiles. By doing so, MCR was able to calculate rightly the concentration profile and the spectra for the three components proposed, as is shown in Figure VI.19.

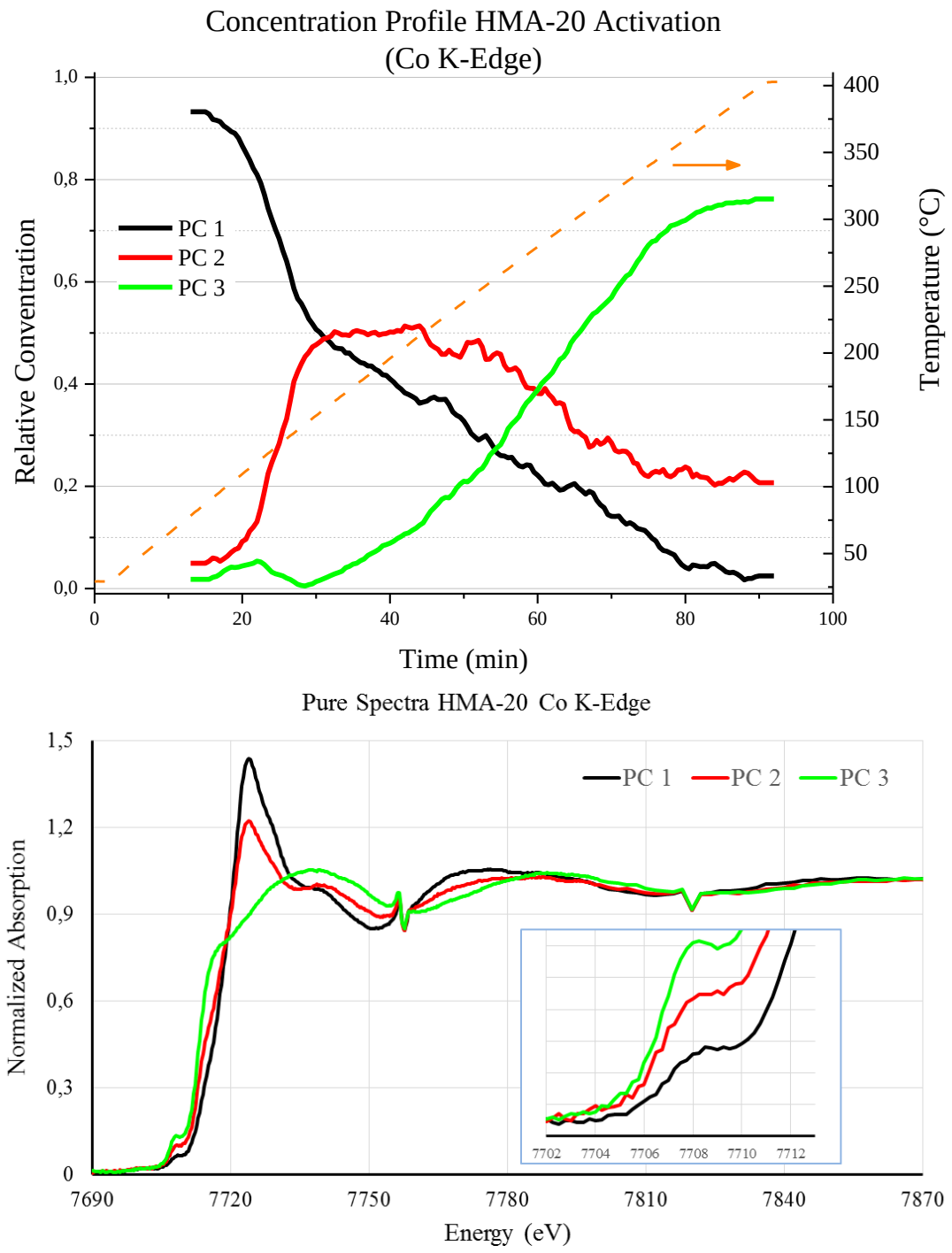

Figure VI.19 - MCR calculated profiles from HMA-20 activation at Co K-edge. Figure of merits are, σ = 0.024, LOF in % (PCA) = 2.55, LOF in % (exp) = 2.61 and percent of variance explained (R^2) = 99.9316.

PC 1 describes perfectly the oxide state. This compound was analyzed in the previous chapter. Unfortunately, it becomes a hard task to say anything about Co-intermediate state once we have available for analysis only XANES part of x-ray absorption spectra. At the same time that PC 2 XANES saves some oxide features (the white line, for instance), the pre peak region suggests sulfide formation. It is harsh to predict if such intermediate is just another form of oxide or is, indeed, a Co_xS_y compound. Different kinds of species reported in literature provide conditions to take place and to be attributed to

this intermediate, such as CoS [26][27], CoS_2 [28] or metallic phase [27]. By visual inspection, we discard metallic intermediate. Without EXAFS to a deeper analysis of oxygen and sulfur contribution, we prefer to keep it as an open question. PC 3, instead has all features of a Co_9S_8 phase, like prominent $1s \rightarrow 3d$ transition (the pre peak) and the shoulder around 7713 eV. Therefore, we attribute such compound to our third principal component. It is noteworthy to say that some studies claim that prominent pre edge structure in Co_9S_8/C is due to majority (8/9) tetrahedral species [29]. Other carbon-supported cobalt sulfide catalysts such CoS_2 are fully octahedral coordinate and weak pre peak is observed. The same argument is extrapolated by the authors to CoMo/C, i.e., CoMo species should not present the pre peak feature.

2.6. Issues on MCR-ALS calculation: Limitation in resolve profiles

At this point, it is of fundamental importance to discuss about the capability of MCR method to resolve individual profiles on each reaction. We discuss previously (see 2.2.1) situations in which ambiguity in solution could be found, but we also have to stress that there are necessary conditions to recover the real response profiles, particularly when one components (or more) has signal entirely inside the concentration window of another component in the mixture. Sometimes, we may face situations when such requirements are not fulfilled and the true solutions are not obtained. Thus, this topic serves as important complementation of the ambiguities conditions that we discussed previously.

We recall results from Co K-edge obtained above (see 2.5). One observes how MCR readily were able to find pure compound (PC 3, sulfided Co-species) even the last HMA-20-state is not purely Co-sulfided-type species shaped.

In that sense, as discussed by Tauler and de Juan (in [18]), the correct performance of any curve-resolution method depends strongly on the complexity of the multicomponent system. In particular, the ability to correctly recover dyads of pure profiles and spectra for each of the components in the system depends on the degree of overlap among the pure profiles of the different components and the specific way in which the regions of existence of these profiles (the so-called concentration or spectral windows) are distributed along the row and column directions of the data set. According to Manne [30], the necessary conditions for correct resolution of the concentration profile and spectrum of a component (at least in chromatography) must obey two theorems:

i. If all interfering compounds that appear inside the concentration window of a given analyte also appear outside this window, it is possible to calculate the concentration profile of the analyte.

ii. If for every interferent the concentration window of the analyte has a subwindow where the interferent is absent, then it is possible to calculate the spectrum of the analyte.

As a simple example of these statements, consider a hypothetical true concentration profile of a given system described as in Figure VI.*20*. The pure concentration profile of component *B* can be recovered because *A* is inside and outside *B*'s concentration window. However, *B*'s pure spectrum cannot be recovered because its concentration profile is totally embedded under the major compound, *A*. Analogously, the pure spectrum of *A* can be obtained, but not the pure concentration profile because *B* is present inside its concentration window, but not outside.

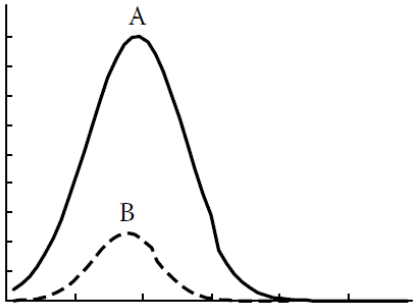

Figure VI.20 - Hypothetical concentration profile for a two-component system.

The same formulation of these two theorems holds when, instead of looking at the concentration windows in rows, the "spectral" windows in columns are considered. In this context, the theorems show that the goodness of the resolution results depends more strongly on the features of the data set than on the mathematical background of the MCR method. Therefore, a good knowledge of the properties of the data sets before carrying out a resolution calculation provides a clear idea about the quality of the results that can be expected.

As consequence, we can have linear combination of actual pure compounds forming what mathematically the method consider as a "pure component" (which is the case for rank deficient systems). For instance, suppose that the actual spectrum of a certain specie *B* can be expressed by the linear combination of two spectra (Component *A* + Component *B*) as follows:

$$\text{Spectrum B} = \alpha \cdot \text{Spectrum } A + \text{Spectrum } B'$$

In MCR analysis, it is possible that Spectrum *A* part with a certain weight of α within Spectrum *B* is included into the component that is separately identified with Spectrum *A*. Hence, Spectrum *B* will show Spectrum *B'*, representing the spectral difference from Spectrum *A* and, thus, highlighting the spectral changes.

2.7. Activation Description of the HMA-20 Catalyst

Finally, we gather all information and results in order to describe fully the activation of impregnated HMA-20 catalyst and transformations that happens during the reaction. Figure VI.*21* shows the

concentration profile of different cobalt and molybdenum species obtained during the reaction. A first transformation starts soon in the activation; at room temperature, the formation of the partially reduced Mo species rises. Regardless the very beginning of Co activation that is missing, we see that cobalt first intermediate and molybdenum second intermediate compounds start to form at the same time, after 20 min of the reaction at 100 °C. At this time, half of Mo oxide is already reduced. Co and Mo oxides have the same decreasing ratio. Co-intermediate and the Mo-oxisulfide reach their respective maximum at the same time, about 40 minutes after the beginning when temperature is 190 °C. MoS_2 and Co-sulfided phase also start their formation at the same time, after 25 min of reaction at 150 °C (strictly speaking, there is a little gap of 5 minutes between rising of the former and the latter). However, about the end of the reaction (80 min, 350 °C), while the whole molybdenum precursor turned to MoS_2 the cobalt precursor remains into a mixed state and the reaction ceases, both Co-intermediate and Co-sulfided phase tends to an asymptote. Thereby, it seems that it is not a matter of timing; we observe that final Co specie achieve a plateau at the time that MoS_2 complete its conversion, suggesting that the formation of such compound (or equivalently, the end of Mo reaction) ceases the sulfuration preventing further formation of final Co species. These results corroborates with XPS measurements, taking as reference the extrapolated XPS Mo^{+4}/Co_9S_8 ratio from HMA-15 after sulfidation

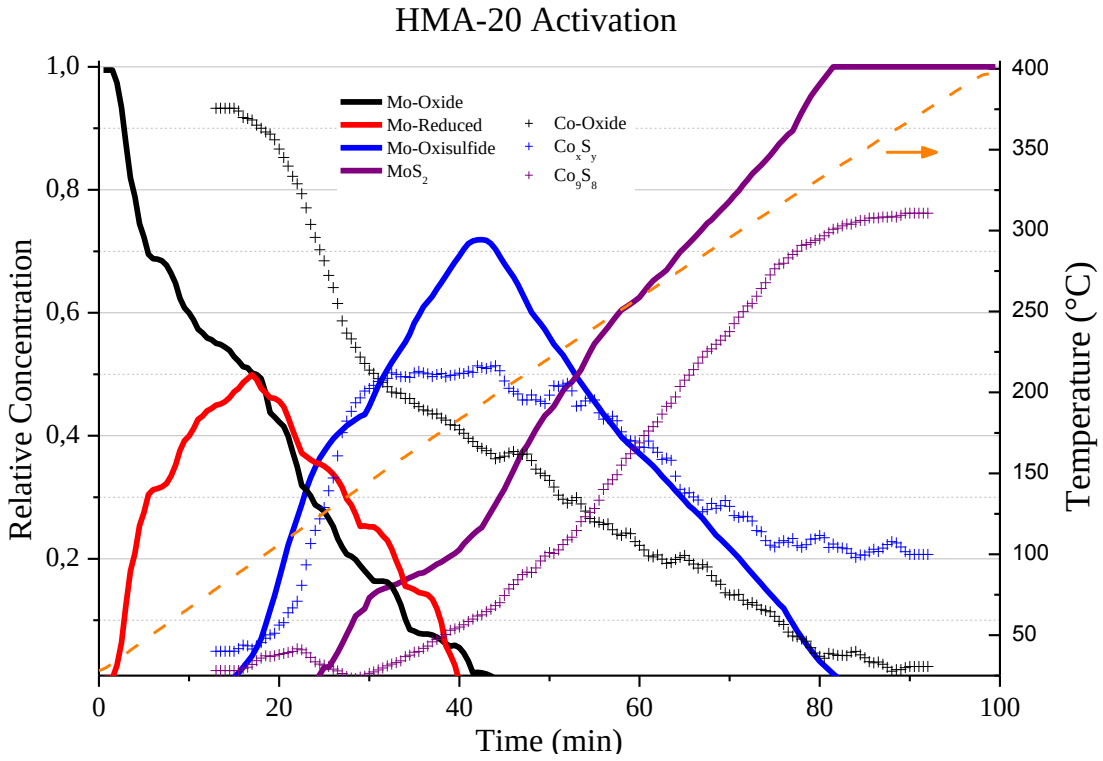

Figure VI.21 - Full description of activation process of HMA-20 catalyst.

It may be fruitful to compare differences between alumina- and anatase-supported CoMo-based catalysts in equivalent systems. *In situ* XAS study carried by Amélie Rochet [5] with promoted Mo-based

catalysts prepared by IWI resulted in concentration profile showed in Figure VI.*22*, (A) for dried and (B) for calcined $CoMo/Al_2O_3$ catalysts. The preparation method was quite similar between us, but the difference was that she used MoO_3 + $CoCO_3$ (diluted in H_2O_2) as precursor oxide and 12 h maturation in water.

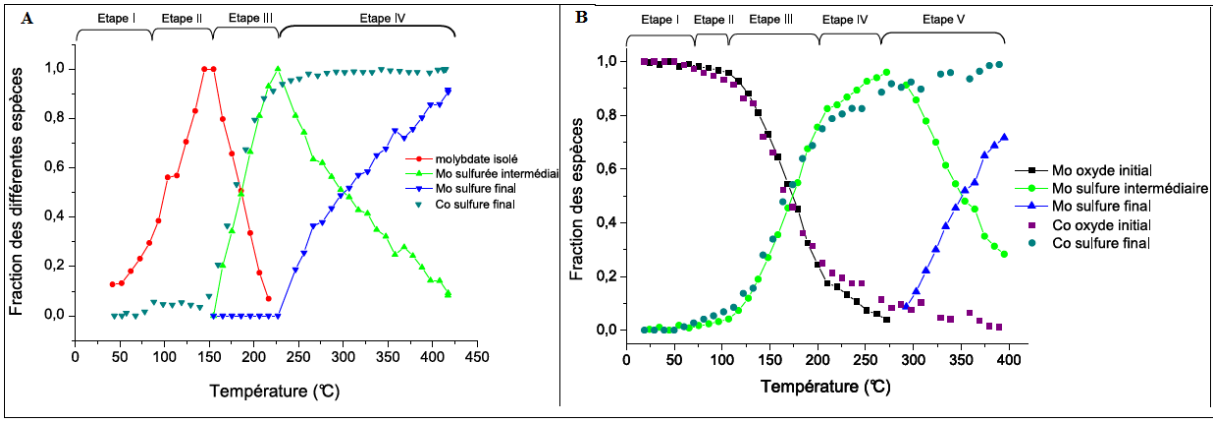

Figure VI.22 - Concentration profiles of Al-supported CoMo catalysts. Such profiles were obtained by XANES linear combination fitting of "pure" spectra. (A) Dried CoMo catalysts and (B) calcined CoMo catalyst (from [5]).

The differences are remarkable, firstly, for dried catalyst (Figure VI.*22* A) from room temperature up to 150° no big changes but a depolymerization of Mo species and slight sulfidation of Co species is observed. After this mark, formation of Co-sulfided final species starts together the Mo-sulfided intermediate ($MoOS_2$-type). When temperature is around 230 °C, MoS_2 begins to be formed and major part of Co species is already transformed into Co final sulfided compound. Calcined catalysts (Figure VI.*22* B) are stable up to 60 °C, but is just from 115 °C that kinetics begins, where one observes simultaneous formation of $MoOS_2$-type species together with final Co-sulfided specie. As in dried catalyst, MoS_2 starts formation when the Co-oxide is majority transformed into sulfided, from 270 °C onwards. It is important to stress that the identification of different species was carried by considering point were isosbestic point variation were identified. Therefore, for each intermediate, inevitably there is a point of relative concentration equals to 1, in other words, experimental spectra are assumed to be pure compounds, which is not necessarily true. Even if it is not as sophisticated as method, we consider the results as representative to describe actually the system.

Both methods are not equivalent, but we can try to compare differences in atomic structure and kinetics of the compounds during reaction in order to attribute such differences to the support interaction. On the oxide starting structure, the comparison among EXAFS parameters is displayed in Table 27.

Table 27 - Structural parameter comparison between CoMo-based catalyst supported in TiO_2 and Al_2O_3.

Mo K-edge					Co K-edge				
HMA-20			MoCo(cal)*		HMA-20			MoCo(cal)*	
N	R(Å)	Bond Type	N	R(Å)	N	R(Å)	Bond Type	N	R(Å)
3.4	1.75	Mo-O	2.6	1.72	4.4	2.03	Co-O	1.6	1.93
1.5	1.96	Mo-O	0.3	2.13	-	-	Co-O	2.6	2.08
-	-	Mo-O	0.5	2.26	0.3	3.18	Co-Mo	-	-
1.0	3.28	Mo-Mo	0.3	3.20	0.8	3.83	Co-Mo	-	-
1.0	3.41	Mo-Mo	0.8	3.34					
0.1	2.75	Mo-Co	-	-					
0.1	3.88	Mo-Co	-	-					

*(from [5])

Regarding Mo K-edge, we have a more regular oxygen distribution, with total average of 4.9 O surrounding Mo atoms (3.4 O at 1.75 Å and 1.5 O at 1.96 Å), while it was found 2.9 O in average surrounding each Mo atom (2.6 O at 1.72 Å, 0.3 O at 2.13 Å and 0.5 O at 2.26 Å) in Rochet's sample. Our structure has more elongated Mo-Mo distances and we are able to identify a small Mo-Co contribution. Concerning Co K-edge, the oxygen atoms are distributed more regularly in our structure (4.4 O atoms at 2.03 Å against 1.6 O and 2.6 O at, respectively, 1.93 Å and 2.08 Å) although in equal number, about 4 in both structures.

2.8. Partial Conclusions

PCA analysis was used in order to evaluate the number of components of our matrix systems, namely, single activation matrix, single reduction matrix and gathered reduction-activation matrix. Taking into account the different PCA methods of evaluation experienced, we considered four components into activation, three into reduction and five components into the combined system, wherein two components are shared in both systems. Column-wise augmented system is used in order to provide further information to PCA and unambiguously evaluate the data. Particularly, in HMA-20 system, reduction experience helped to get information on the intermediates of the activation system, particularly, one observed that the second component of the activation is an uncompleted reduced state observed during the reduction reaction.

We observed that in HMA-20 activation, the system passes by a sequence of steps well defined. Such steps seem be a general trend for the other samples and they are described just for the Mo K-edge; we recall that we could not fully exploit structural evolution at Co K-edge because experimental issues on

data recording. Summarily, in HMA-20 it goes like this: in the first structural transformation of the reaction (which corresponds PC 1 turning to PC 2), the oxide precursor loss the short length double Mo=O bond (1.75 Å), one observes the arising of a long Mo-O bond (2.42 Å) typical for reduced Mo-species (such MoO_2) and no more Mo-Co bonds are observed. Then, such partially reduced compound turns to an oxisulfided specie with a long Mo-O bond (2.08 Å) and the Mo-S contribution typical for the active phase, at 2.40 Å. The final step of the reaction is the consolidation of the active nano-MoS_2 phase, with a strong Mo-S contribution as well as the other typical bonds in this structure, a Mo-Mo bond at 3.17 Å and Mo-S contribution at 4.10 Å. All Mo-precursor was transformed into the active phase.

MCR results at Co K-edge allow us to make a qualitative analysis of the XANES evolution during the activation. The results were instable for the first very rapid transformation suffered by the oxide precursor and this first part of the reaction was not considered. We found 3 components, wherein the first one do not represent the starting structure, but the one just after this sudden fall of the white line feature during the first few minutes of the reaction. The second Co XANES spectrum still has oxide features, but since we do not have EXAFS data, no further conclusion can be done. The last XANES spectrum has all features of a sulfided specie. Looking experimental data at the end of the reaction, we observes clearly that Co species are not completely sulfided, since the final HMA-20 state at Co K-edge can be described as a linear combination of the Co-sulfided specie (PC 3) plus the intermediate non-sulfided specie (PC 2).

3. MCR-ALS Results for the Others Matrix System Reactions

On the previous topic, we explained in details the approaches behind the MCR issues and results. Once done that, from now on we limit in exhibiting of results succinctly, emphasizing the interpretation of the concentration profile and structural analysis.

3.1. HMA-5

3.1.1. Mo K-Edge

Regarding individually the PCA of the HMA-5 reduction matrix, one observes the same behavior when compared to individual HMA-20 reduction matrix, which suggests three components. The main

evidences come from score plots. Evolving scores plot (not showed) shows a low s/n from the fourth PC on, indicating they are related to noise and do not represent physical components. Further, as in HMA-20 reduction matrix, scatter plot indicates three clear distinguishable clusters and similar behavior between the two systems (HMA-5 and HMA-20). Finally, the SVD eigenvalues are considerably more expressive for the three first components: **273**, **4.45**, **1.38**, 0.42 and 0.28 are, respectively, eigenvalues for PC 1 to PC 5. Together, they count to 97.65% of total variance.

Conclusion on the PCA of individual HMA-5 activation matrix and HMA-5 augmented matrix is similar to corresponding matrices in HMA-20, i.e., 3 or 4 components for activation matrix and 5 components for augmented matrix, which is not surprising regarding the well-behavior aspect of the HMA series it must be not far from HMA-20. Looking at the similar features in start and final atomic structures of HMA-20 and HMA-5 described in previous chapter and the smooth growing in catalytic activity curve, we should expect they present equivalent MCR results.

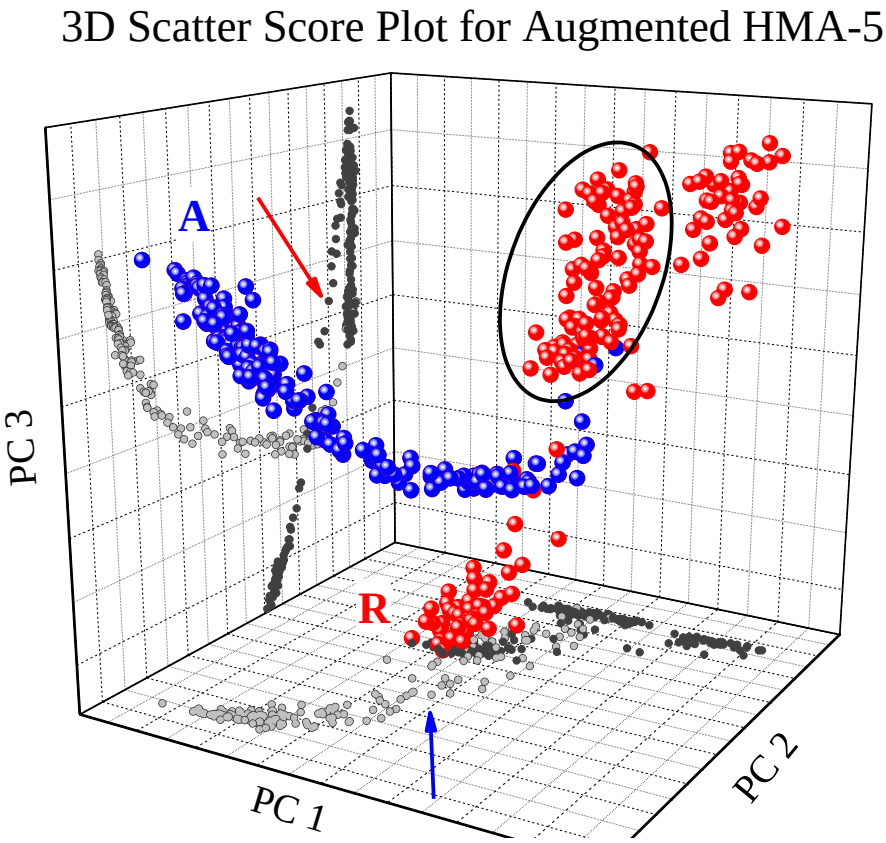

Figure VI.23 - 3D scatter plot for augmented matrix of HMA-5. Red balls are related to TPR process, blue balls are related to activation. The black circle marks the cluster of initial state (shared by both reactions). Red *R* indicates the cluster of the end of reduction and blue A, the end of activation. Arrows point to plane projection either for activation (light grey) or reduction (grey).

In 3D scatter plot of scores of augmented HMA-5 matrix (Figure VI.*23*) we can see the typical features of the assembly system, namely, the clusters (see the legend of the figure) and the branches of reduction (red balls) and activation (blue balls). It is interesting to note that besides reduction and activation

trajectory lines are close, they do not lie on the same plane (see the projections in the figure), as it happens in HMA-20 augmented system. It may suggest an absence of correlation or a certain independence degree between reduction and activation.

5-component MCR-ALS optimization was performed in augmented matrix using a concentration profile as initial guess. To build such initial guess, EFA were performed individually in reduction and activation matrices and then, they were gathered in a single column augmented matrix. Non-negativity in concentration profile and spectra, closure, three-way bilinear, local rank selectivity and spectra selectivity were the constraints used. Local rank selectivity was set to guarantee that start structure in both reactions is not mixed state and that at the end of activation a unique MoS_2-type structure is found.

Figure VI.*24* shows the profiles obtained after MCR calculations. A remarkable aspect is noted in the reduction, a well-defined 3-component system arises with a prominent and noticeable intermediate.

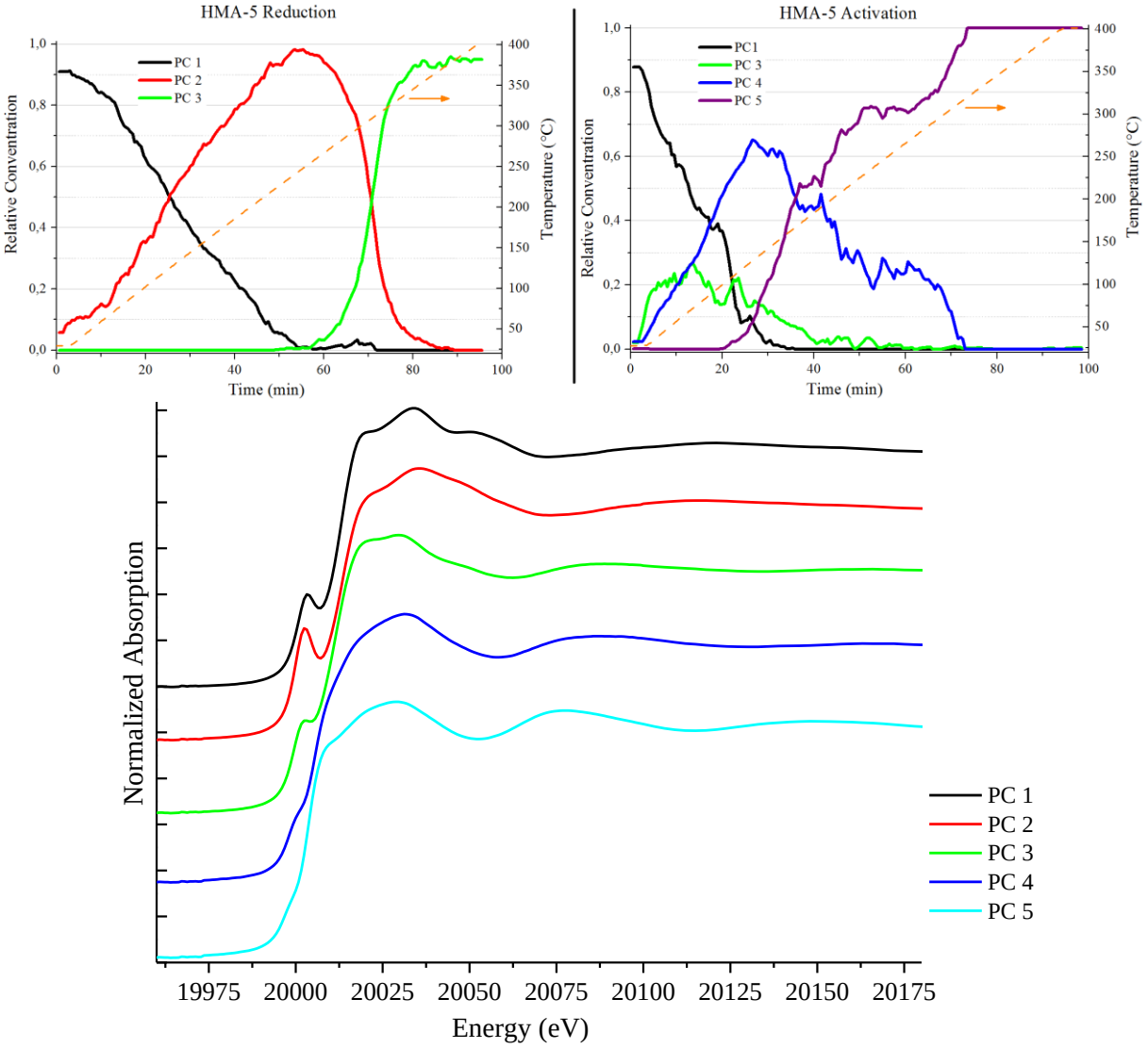

Figure VI.24 - MCR profiles for HMA-5 column-wise augmented matrix. (Upper panel) Concentration Profile of Reduction (Left) and Activation (Right), (lower panel) Pure Spectra. Figure of merits are, σ = 0.025, LOF in % (PCA) = 2.65, LOF in % (exp) = 2.67 and R^2 = 99.9286.

It was reported in literature the existence of a variant of TiO_2-supported molybdenum oxide that appears at low molybdenum loading. As reported by Hu *et al.* [31], in such situation the surface molybdenum oxide species appears as isolated tetrahedral. Similar conclusions were also obtained by Hamraoui *et al.* [32]. Further, such tetrahedral species are less susceptible to be reduced when compared to polymeric Mo-species. Besides the prominent pre peak of our PC 2 may suggest a tetrahedral species, it cannot be the case, since our specie PC 2 is clearly reducible (Figure VI.*24* upper left panel). Indeed, if we compare PC 2 XANES of HMA-5 with experimental tetrahedral molybdate, one observe that pre-peak intensity feature is not enough to attribute such symmetry to our PC (Figure VI.*25*). EXAFS (inset of Figure VI.*25*) not only confirms this assessment but also unambiguously shows that PC 2 is a variation of our initial state spectrum.

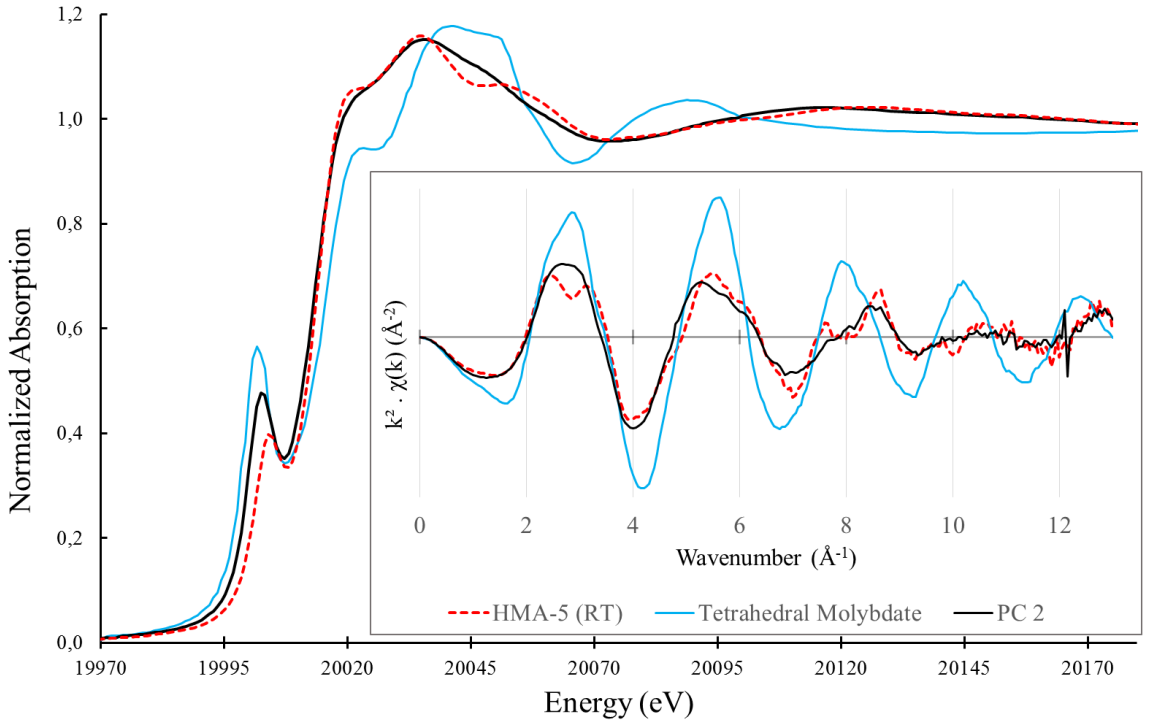

Figure VI.25 - XANES and EXAFS (inset) comparison among MCR-calculated HMA- PC 2, room temperature HMA-5 state, and tetrahedral molybdate.

We observe that in reduction of HMA-5, this species arises as soon as temperature start to increase. Such uniform growing suggest a sort of dehydration and, at least at a PCA/MCR point of view, this is indeed a new species. No matter the path taken to arrive in final state it seems not change the final reduced structure. The fact is that reduced HMA-5 (the final state) is equivalent to reduced HMA-20 in local atomic arrangement (see XAS analysis in the previous chapter), which apparently do not suffer such kind of early structural transformation.

In activation of HMA-5 (Figure VI.*24* upper right panel) one observes the presence of two intermediates arising at the same time and PC 3 is shared in both TPR and activation reactions, being attributed to the reduced state of HMA-5.

PC 4 has XANES (Figure VI.*24*) similar features to final HMA-5 sulfided state (MoS_2-type), but as long it arise early in the reaction, we must assure if such sulfided character is real or the species is just another reduced form of HMA-5 oxide. Figure VI.*26* definitively answer this question, PC 4 Fourier transformed EXAFS is compared with experimental data in particular cases, namely, the initial oxide, the reduced and final sulfided state. Peaks characteristic for Mo-O in reduced state and Mo-S sulfided are indicated. PC 4 FT is close to reduced HMA-5 but is undeniable the presence of a Mo-S contribution. Therefore, we can state that is an actually oxyulfide specie although not exactly the same of HMA-20.

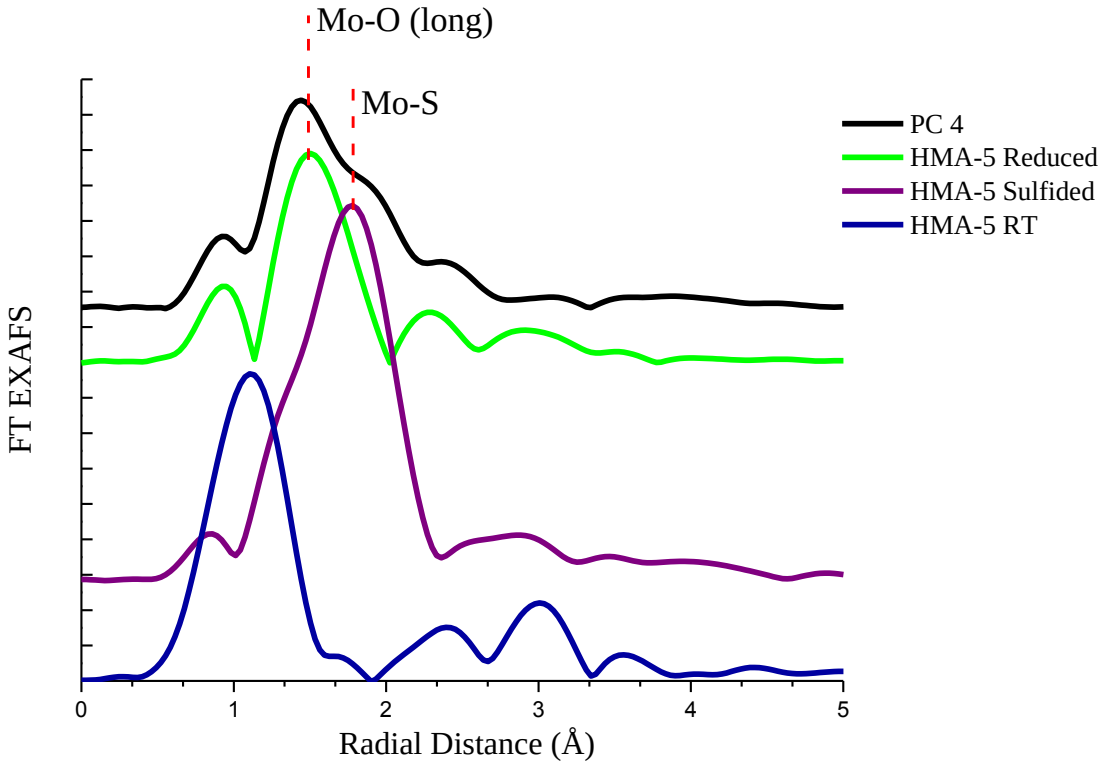

Figure VI.26 - EXAFS Fourier Transform comparison among PC 4 and experimental spectra from HMA-5 series. It is highlighted the *R* position of Mo-O (long, from reduced specie) and Mo-S bond distances (without phase correction).

Table 28 gives the structural parameters obtained from EXAFS refining of MCR-calculated components. As in HMA-20 case, PC 1 corresponds to the oxide initial structure, PC 3 to the reduced structure and PC 5 to the sulfided one. Thus, the structural parameter values were copied from EXAFS fitting previously done for these structures.

In HMA-5, contrary to HMA-20 sample, we do not have a partially reduced compound, as discussed above. PC 2 represents another oxide structure, with an oxygen radial distribution more distorted when compared to initial oxide state. Concerning next-nearest radial distribution, one observes that Mo-Mo

short bond (at 2.92 Å) typical for reduced Mo species is already present in structure. Further, the original Mo-Mo distance of oxide state (at 3.27 Å and 3.40 Å) seem to be averaged to 3.33 Å. It suggests that such bonds are weakened during the reaction to give place to Mo-Mo short length bond that we found in reduced structure (PC 3). An analogous process seems to happen when we pass from reduced compound (PC 3) to the oxisulfide one (PC 4). As in HMA-20, such Mo-Mo short bond disappears, the Mo-O distribution remains nearly the same and the typical Mo-S bond at 2.40 Å arises unobtrusively. Then, in the last step of the activation, the Mo-O bonds are broken to consolidate the formation of MoS_2-type final structure, with the increasing of N_{Mo-S} coordination number (from 0.5 to 5.3) and N_{Mo-Mo} typical in such compound (from 0.5 to 2.9). Time and thermal profile evolution is described in Figure VI.*24* (top).

Table 28 - Mo K-edge EXAFS structural parameters for components determined by MCR.

Sample	PC	Bond	N	R (Å)	σ² (Å²)	Δσ	ΔE (eV)	Parameters
HMA-5	PC 1	Mo-O	2.8	1.74	0.004	0.001	2.0	Δk = 4.1-13.4 ΔR = 1-3.7 N_{ind} = 15 χ^2_{Red} = 86 R_{factor} = 0.01
		Mo-O	1.4	1.94				
		Mo-Mo	0.9	3.27	0.003	0.006		
		Mo-Mo	0.9	3.40				
		Mo-Co	0.2	2.74	0.001	0.005		
		Mo-Co	0.2	3.83				
	PC 2	Mo-O	3.2	1.74	0.009	0.004	-6.0 (±5.6)	Δk = 3.6-12 ΔR = 0.9-3 N_{ind} = 10 χ^2_{Red} = 2429 R_{factor} = 0.01
		Mo-O	1.5	1.97				
		Mo-Mo	0.9	2.92	0.002	0.005		
		Mo-Mo	0.9	3.33				
	PC 3	Mo-O	3.6	2.01	0.004	0.003	-6.9 (±6.4)	Δk = 4.7-13.4 ΔR = 1.1-4 N_{ind} = 11 χ^2_{Red} = 237 R_{factor} = 0.09
		Mo-Mo	0.3	2.61	0.001	0.006		
	PC 4	Mo-O	3.2	2.04	0.009	0.007	0.5	Δk = 4.6-12.7 ΔR = 1.05-3.0 N_{ind} = 10 χ^2_{Red} = 359 R_{factor} = 0.06
		Mo-S	0.5	2.40	0.004	0.005		
		Mo-Mo	0.5	2.46	0.004	0.005		
	PC 5	Mo-S	5.3	2.40	0.0053	0.0006	3.2 (±0.9)	Δk = 4.6-13.7 ΔR = 1-4.1 N_{ind} = 9 χ^2_{Red} = 136 R_{factor} = 0.008
		Mo-O	0.7	4.10	0.0053	0.0006		
Uncertainty:	PC 1: N_{Mo-O} = 0.6; $N_{Mo-Metal}$ = 0.8/0.2 PC 2: N_{Mo-O} = 1.5; N_{Mo-Mo} = 0.7 PC 3: N_{Mo-O} = 1.3; N_{Mo-Mo} = 0.3 PC 4: N_{Mo-O} = 2.0; N_{Mo-S} = 0.4; N_{Mo-Mo} = 0.4 PC 5: N_{Mo-S} = 0.3/0.7; N_{Mo-Mo} = 0.9							

3.1.2. Co K-Edge

When doing PCA analysis on Co-activation HMA-5 matrix, a very similar behavior to HMA-20 concerning the first few minutes of reaction is observed. The great majority of the analysis suggest a system with 3 PC's, among these tests the representation of eigenvalues is drawn in Figure VI.*27*. Nevertheless, the presence of an odd rapid change in some features of early spectra (particularly in the white line) makes PCA accounts 4 principal components to describe the system, although this fourth PC drive a role just in the very beginning of the reaction Figure VI.*27* (inset). In that sense, three models are proposed to explain kinetics at Co K-edge, two with a spectral constraint (we impose the presence of Co_9S_8-type compound from Co-activation of HMA-20, namely, PC 3) and other free of such constraint. The idea is to keep the reason taking as reference the similarities between HMA-5 and HMA-20 at Mo K-edge.

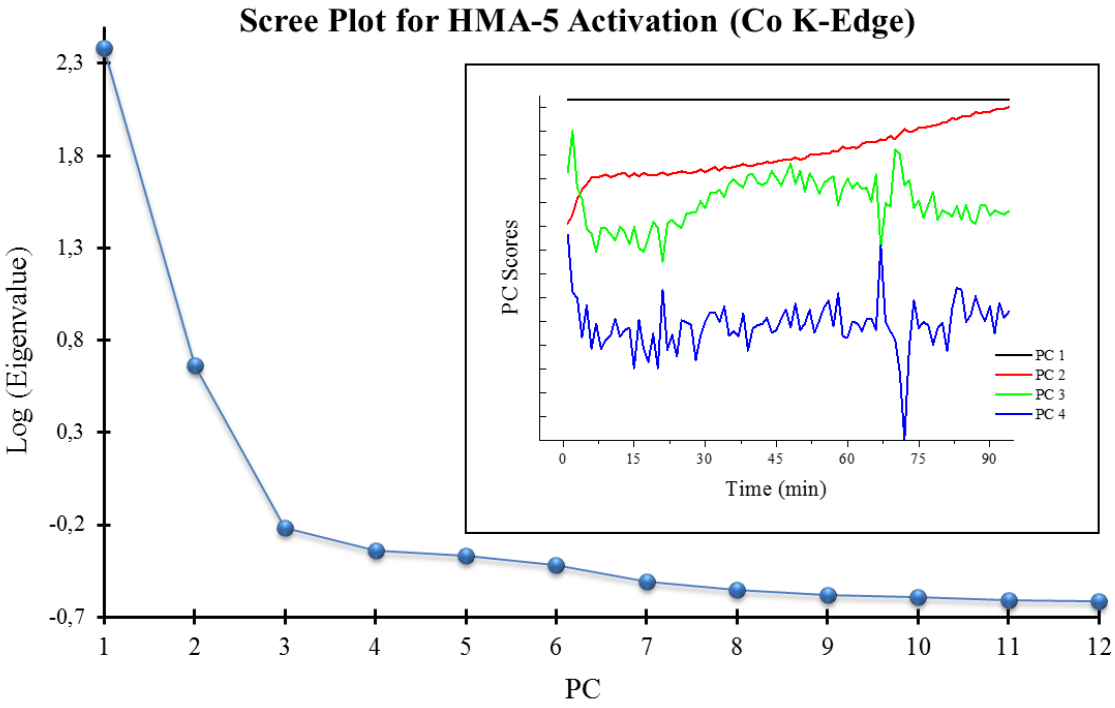

Figure VI.27 - Scree plot and Scores plot for HMA-5 activation at Co K-edge.

As in HMA-20 Co activation, this awkward evolution perturbs MCR calculations in a way that reliable results are not obtained. A practical and direct solution is to proceed in the same manner, cut off some few first spectra. Another solution was to be more rigid concerning the constraints, using selectivity and unimodality. In this way, the profiles for the three models are illustrated in Figure VI.*28*.

On the line *A*, spectra are free of constraints; just non-negativity (in concentration profile and spectra) and closure were set. However, the 5 first spectra were discarded. In that case, PC 1 virtually coincides with first spectra and PC 3 virtually coincides with the last spectra. However, the later do not coincides with PC 3 in HMA-20, which represents sulfided specie.

On the line *B*, it was used the whole matrix and an imposition on PC 3 to be Co-sulfided (a copy-paste from HMA-20 PC 3). Additionally, unimodality (with factor of tolerance equals 1.6; obtained by try and error) was added to the calculations. The concentration profile reproduces the very initial changing but with an uncommon evolution for the rest of the reaction. Regarding the pure spectra, PC 2 in model *A* and *B* are equal.

In model *C* we have the same conditions that was used in model *B*, i.e., spectral selectivity and unimodality. A fourth principal component (set as HMA-20 PC 3) was proposed. Despite of quite good convergence of MCR calculations, such fourth PC 4 (the Co-sulfided specie) do not appears in the concentration profile (in fact, its contribution is negligible and is not drawn here). Thus, PC 1 is the initial state, PC 3 is the same as model *A* and PC 2 an intermediate responsible to the rapid initial transformation.

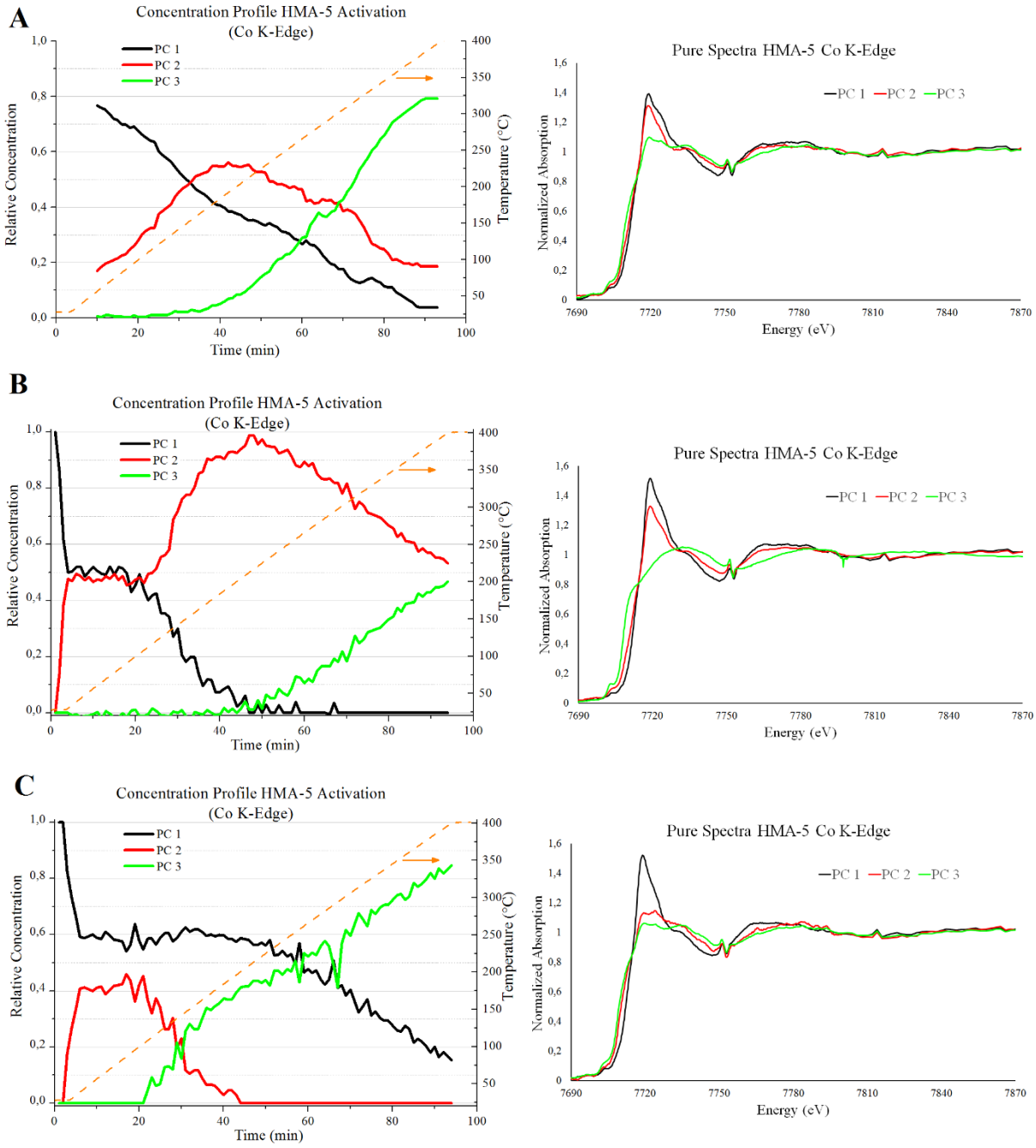

Figure VI.28 - Profiles from MCR calculation for HMA-5 activation at Co K-Edge. Three models are proposed (see text).

Judging only by XANES it should be desirable to find Co-sulfided-type species as a pure spectrum to make a good equivalence with HMA-20. No other model than *B* contains such compound. Model *A* and *C* give something very close to the final spectrum of the series as a pure compound. Judging by concentration profile, in model *A* and *C* the last species begins to be formed after 20 minutes of reaction, which corresponds to the beginning MoS_2 formation (Figure VI.*24*). This coincidence is similar on HMA-20. In model *B*, such species starts formation later, around 40 minutes of reaction. Model *A* is the closer of HMA-20 in terms of concentration profile, in shape and transformation rate of species, but again we have no information on the rapid transformation at the very beginning of the reaction.

A try of obtaining of a better profile that explain Co-evolution of HMA-5 is to consider to constrict the pure spectra profile of the model *A* and preserve its features from concentration profile. Thus, we impose selectivity in PC 3 setting it as Co-HMA-20-MCR-calculated PC 3. Results are showed in Figure VI.*29* (top).

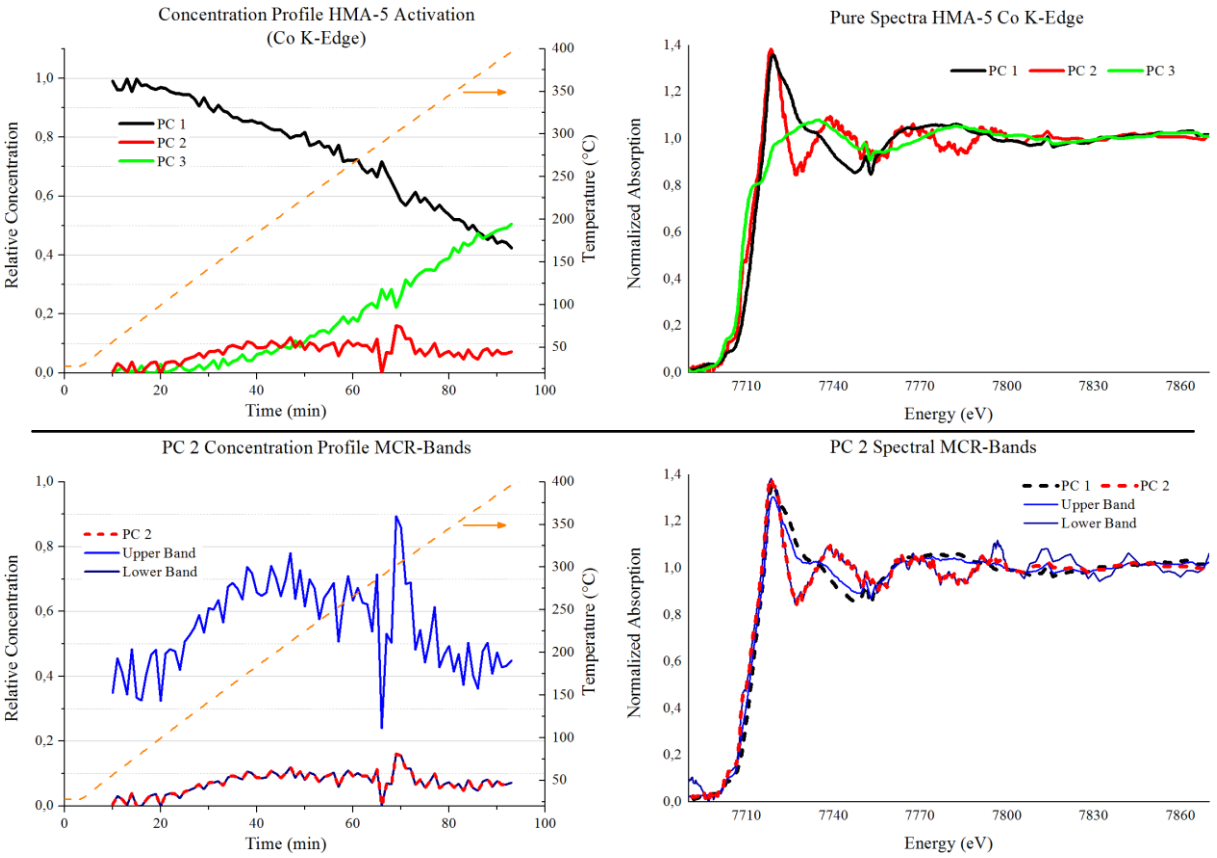

Figure VI.29 - (Top panel) Model *A* profile refining. (Low panel) MCR-Bands for PC 2. Figure of merits are, σ = 0.008, LOF in % (PCA) = 0.559, LOF in % (exp) = 0.874 and R^2 = 99.9924.

By constraining PC 3 to have a Co-sulfided species form, we obtained a satisfactory result for concentration profile, particularly concerning final concentration values (roughly, 50/50 percent ratio Co-sulfided and Co-oxide), which is in accord to XPS results discussed in the previous chapter. PC 1, the Co-oxide specie, have a smooth and continuous decreasing. Considering that such specie present a white-line feature in XANES spectrum at room temperature, we observe that such evolution of concentration profile is in agreement with the evolution (the decreasing) of its XANEs white-line during the reaction (as showed in previous chapter). Co-sulfided specie concentration profile evolves from 30 min of reaction (150 °C), increasing smoothly until the end. In this model, PC 2 do not play an important role (at least inside the reaction domain considered, i.e., excluding the very begin of the reaction), but it clearly represents an oxide specie. We observe that its spectrum is noisy, which can be explained by the MCR-Bands calculation. Figure VI.*29* (lower panel) show us just MCB-Bands calculation for PC 2 because Δ*f* values for PC 1 and PC 3 are virtually equal to zero, while $\Delta f_{PC\ 2}$ = 0.4923. On the right, solid blue lines represents the band limits for PC 2 spectral MCR-Bands. PC 2 (viewed as dashed line)

is the spectrum that minimizes the calculations and it coincides with the lower band. We can observe that the upper band almost coincides with PC 1 spectrum (black dashed line), and this wide range of possibilities is responsible for the noise in the PC 2 spectral component. The possibility window is also showed for PC 2 concentration profile (down-left). Obviously, PC 2 concentration profile lies in the lower band limit, as in pure spectra range.

No matter the considered case for the Co-evolution of HMA-5, we must to recall the discussion previously done about limitations of MCR method (2.6). It is difficult to assert if the concentration profile from Figure VI.*29* is the real one because the lack of data (in the MCR sense) prevent us to obtain the actual result. However, such refined model *A* seems to be a good choice (considering both concentration profile and pure spectra) for an explanation of the evolution of Co-species in activation of HMA-5.

3.1.3. Activation Description of the HMA-5 Catalyst

Figure VI.*30*, shows the concentration profile when regarding the whole information about the activation of HMA-5. As in HMA-20 (Figure VI.*21*) we see similar trends, the intermediary species arises approximately at the same time. Early in the first few minutes of the reaction, at room temperature, the transformation of Mo-oxide into its intermediate is followed by the first Co-intermediate. The same behavior happens for the final species, MoS_2 in HMA-5 begins to be formed after 20 minutes of reaction, at 100 °C, so it is the final Co-species. Both final structures have the same conversion rate up to 350 °C (after 80 min), when the Mo reaction is completed, ceasing also the Co reaction.

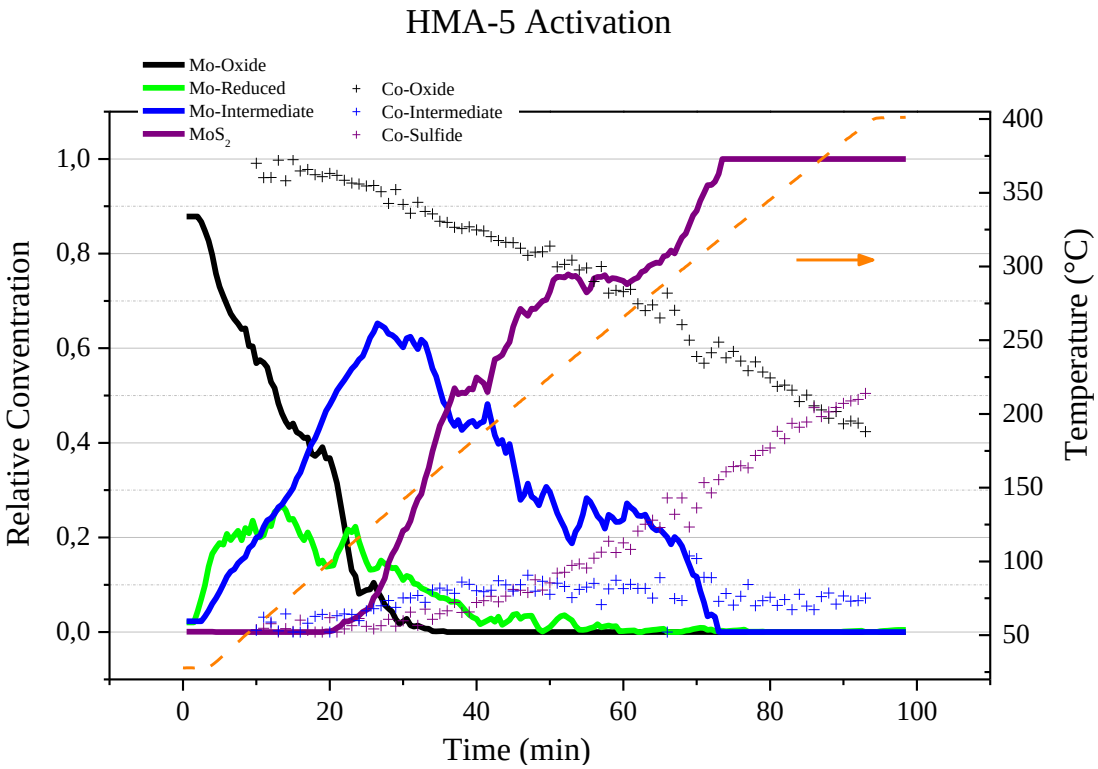

Figure VI.30 - Full description of HMA-5 catalyst activation.

Comparing with HMA-20, one observes that the general aspect of the reaction is preserved, as discussed above. However, HMA-5 has its own particularities, such as the presence of two oxidic species in reduction (and its thermal evolution during the reaction) and the presence of an intermediate compound that arise together with reduced species at the Mo-activation.

3.2. SG-20

Among the samples in sol-gel series, SG-20 is the one that shows to be the closer to the impregnated HMA series, in terms of structure and physico-chemistry properties (textural, catalytic activity, etc.). We expect to obtain a similar analysis concerning PCA and MCR.

3.2.1. Mo K-Edge

PCA in augmented SG-20 matrix suggests 4 components for the system. 3D scatter score plot (Figure VI.*31*) show a typical two-branched behavior, one representing the reduction and the other one representing activation. The arched curve for activation points to 3 components, while the straight line in reduction suggest 2. As in HMA-20 augmented system, activation and reduction lie in the same trajectory line regarding the PC 1 x PC 2 projection. The difference here is that there is no satellite cluster formation just beside the initial state cluster. However, reduction and activation paths in scatter

score plot are far from each other, seems to take independent and uncorrelated directions. Further, the reduction branch is a straight line, which suggests a typical A → B transformation.

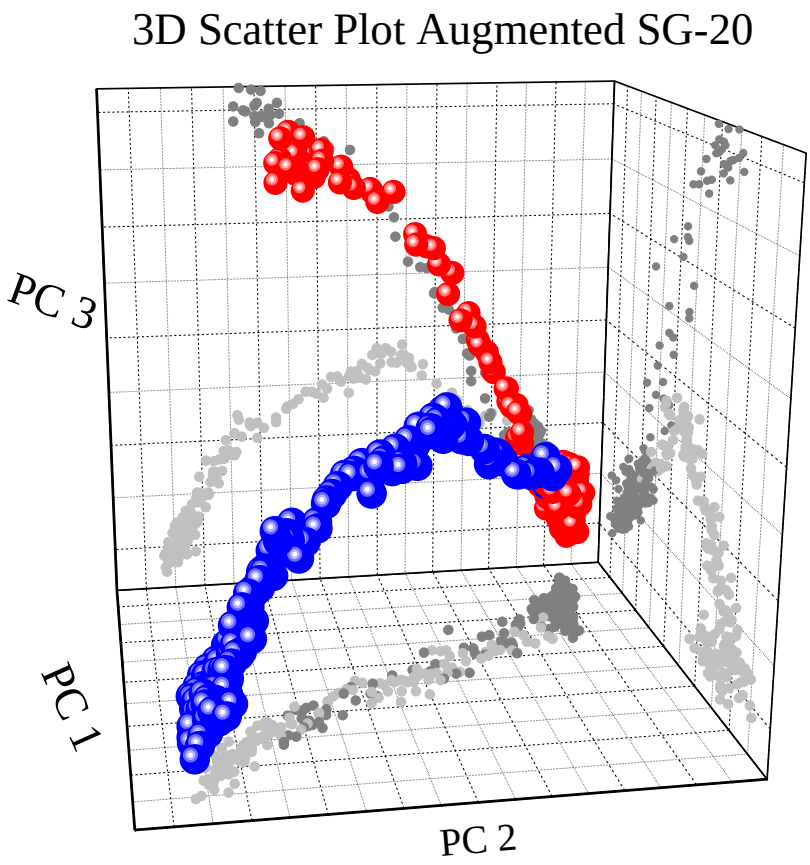

Figure VI.31 - 3D scatter plot for augmented SG-20 matrix. Red balls represent the reduction path, whereas blue balls the activation. The cluster where coincides the two paths indicates the initial state.

MCR-ALS calculations were performed with considering 4 principal components. The initial guess was determined by spectra selection, regarding SIMPLISMA algorithm and EFA information. The constraints used were, non-negativity (in concentration profile and pure spectra), closure, local rank selectivity, and spectrum selectivity. On this later, linear combination fit of SG-20 final spectrum using MoS_2, and reduced SG-20 spectra as reference points to 50% of MoS_2 in the final state, as discussed in the previous chapter. Thus, as long MCR by itself was unable to resolve MoS_2 species in SG-20 system, we impose that the last spectra must be the MoS_2. (It is important to stress that calculations also were performed considering this selectivity as an extra PC (so, 5 components), but no convergence was achieved.) The inconvenient in such statement, is that we will not be able to refine particular MoS_2 that arises from SG-20, instead, we have used (and imposed) HMA-20 PC 5 as a nanometric MoS_2 model. Thus, this is the price to be paid if we want to describe accurately the kinetics of the reaction. In the following, we present the profiles obtained by MCR-ALS to SG-20 augmented system at Mo K-edge.

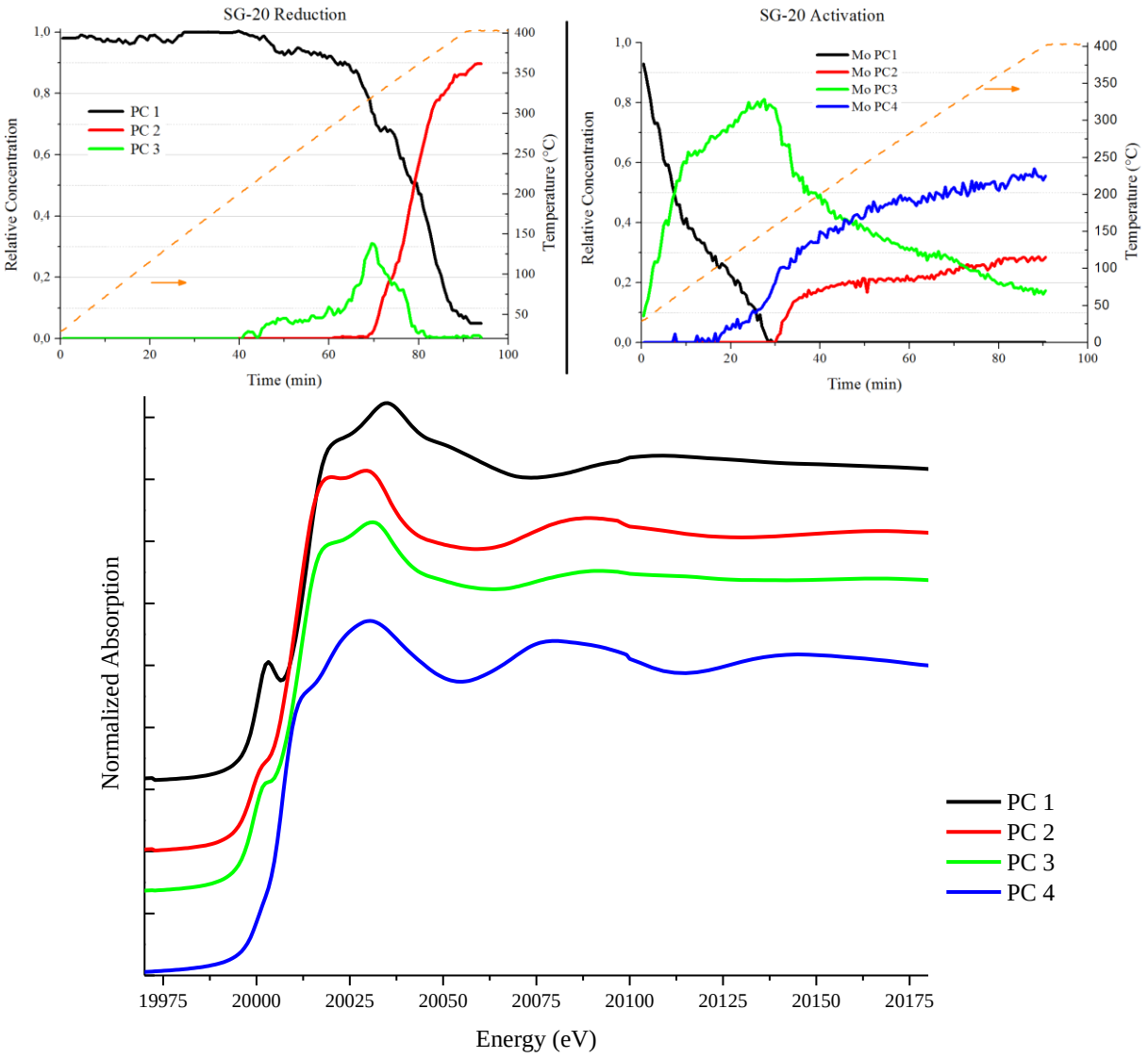

Figure VI.32 - MCR profiles for SG-20 column-wise augmented matrix. (Upper panel) Concentration Profile of Reduction (Left) and Activation (Right), (lower panel) Pure Spectra. Figure of merits are, σ = 0.035, LOF in % (PCA) = 2.07, LOF in % (exp) = 2.08 and R^2 = 99.9565.

Figure VI.*32* shows the MCR profiles obtained for SG-20 augmented matrix. On the reduction, as in HMA-20, we found an intermediary species before complete (or deep) reduction. However, in SG-20 its importance is more unobtrusive, seen by smaller area under the curve. Besides that, one observes that as in HMA series, that "final" reduction is started in high temperatures (above 300 °C), around 330 °C.

On activation, we found a profile that is closer to HMA-5 than HMA-20, i.e., just one intermediate before the formation of MoS_2. This first intermediate starts to be formed still in room temperature and grows fast as the oxide precursor downs with about the inverse rate. Less than 10 minutes of reaction and under in a temperature of 50 °C a half of oxide turns into this intermediate. However, unlike HMA-5, where a reduced specie with a small Mo-S contribution, here no sulfur contribution is seen. As in HMA series, MoS_2 also arise in relatively low temperatures, about 100 °C (in fact, it is close to HMA-5, but in HMA-20 this temperature is slightly higher, 130 °C). Nevertheless, we also see formation of

final reduced species when the temperature passes up 150 °C, which coincides with a change in kinetics of the species. This trend is kept until the end of the reaction and no single phase is achieved.

Table 29 shows us the structural parameters obtained from classical EXAFS analysis. As discussed, PC 1 corresponds to the oxide initial structure, PC 2 to the reduced structure and PC 4 was imposed to be MoS_2 in order to follow results from final state linear combination fit of XANES (see the previous chapter). Therefore, PC 1 and PC 2 were already largely discussed in the previous chapter.

PC 3 is a reduced species with some features from oxide structure. Oxygen radial distribution is simple, with one Mo-O bond length at 2.02 Å typical of a reduced Mo species. Mo-Mo radial distribution has three distinct contributions that keeps similarities of both oxidic and reduced species.

Describing local structural evolution in terms of chemical bonds is not as evident as in impregnated series. Even so we can draw the following picture: the start oxide structure (PC 1) takes two different paths depending on the reaction, under TPR (PC 2) the oxygen bonds are lengthened and become more balanced (one has equal coordination numbers for both Mo-O contributions), while Mo-Mo distribution is completely distorted. Under activation, the reduced species (PC 3) has weak Mo-O contribution (coordination number goes down to 1.9), the original Mo-Mo bonds are lengthened (goes from 3.20 Å and 3.33 Å to, respectively, 3.26 Å and 3.36 Å) and a new Mo-Mo contribution appears at 3.17 Å. It is difficult to assert if such one is the same of Mo-Mo typical contribution from MoS_2, which could suggest an influence of H_2S atmosphere, because we do not see Mo-S contribution. Such Mo-Mo bonds are weak (low coordinated) and in the last step of the reaction, we see arising the typical MoS_2 structure. The lengthening behavior of Mo-Mo bonds are in agreement with the trend observed in impregnated solids during activation, such bonds are gradually lengthened and weakened to give place to other contributions in the structural evolution of activation. By “structural evolution of activation” we mean that seemingly there is a sequence of steps that are followed during the reaction, firstly the loss of the short Mo = O bond (1.75 Å), then, the arising of a longer Mo-O bond, etc., as previously discussed for HMA-20 (see 2.4.1). We recall that SG-20(sulf) discussed in the last chapter presents Mo-O, Mo-S and Mo-Mo bond lengths consistent with PC 3 + PC 4 formation, its EXAFS structural parameters are recalled in Table 29. Lifetime of each compound in reaction can be checked in Figure VI.*32*.

Table 29 - Mo K-edge EXAFS structural parameters for components determined by MCR.

Sample	PC	Bond	N	R (Å)	σ² (Å²)	Δσ	ΔE (eV)	Parameters
SG-20	PC 1	Mo-O	3.8	1.75	0.008	0.002	-4.8 (3.3)	Δk = 4.0-12.8 ΔR = 1.1-3.6 N_{ind} = 14 χ^2_{Red} = *397* R_{factor} = 0.01
		Mo-O	1.6	1.96				
		Mo-Co	1.0	3.10	0.005	0.004		
		Mo-Co	1.0	3.84				
		Mo-Mo	0.9	3.20	0.003	0.005		
		Mo-Mo	0.9	3.33				
	PC 2	Mo-O	2.1	1.96	0.0007	0.003	-2.1 (4.1)	Δk = 4.5-13.6 ΔR = 1.1-3.5 N_{ind} = 13 χ^2_{Red} = 2049 R_{factor} = 0.03
		Mo-O	2.1	2.09				
		Mo-Mo	1.5	2.63	0.009	0.005		
		Mo-Mo	1.5	2.88				
		Mo-Mo	1.5	3.31				
	PC 3	Mo-O	1.9	2.02	0.004	0.003	-9.5	Δk = 4.8-12.7 ΔR = 1.1-3.6 N_{ind} = 12 χ^2_{Red} = 1126 R_{factor} = 0.09
		Mo-Mo	0.8	3.17	0.002	0.006		
		Mo-Mo	0.8	3.26				
		Mo-Mo	0.8	3.36				
	PC 4*	Mo-S	5.6	2.40	0.0045	0.0005	6.5 (0.7)	Δk = 4.7-13.5 ΔR = 1-4 N_{ind} = 16 χ^2_{Red} = 436 R_{factor} = 0.005
		Mo-Mo	3.5	3.17	0.005	0.001		
		Mo-S	0.7	4.10	0.0045	0.0005		
	SG-20 (sulf)	Mo-O	2.0	1.97	0.005	0.005	-5.3 (3.0)	Δk = 4.3-13.2 ΔR = 1-4.2 N_{ind} = 12 χ^2_{Red} = 606 R_{factor} = 0.03
		Mo-S	2.7	2.40	0.004	0.002		
		Mo-Mo	2.1	3.19	0.006	0.002		
		Mo-Mo	1.1	3.68	0.006	0.002		
Uncertainty:	PC 1: $N_{Mo\text{-}O}$ = 1.0; $N_{Mo\text{-}Metal}$ = 0.7 PC 2: $N_{Mo\text{-}O}$ = 0.6; $N_{Mo\text{-}Mo}$ = 1.2 PC 3: $N_{Mo\text{-}O}$ = 0.8; $N_{Mo\text{-}Mo}$ = 0.7 PC 4: $N_{Mo\text{-}S}$ = 0.3/0.6; $N_{Mo\text{-}Mo}$ = 0.7							

3.2.2. Co K-Edge

Co K-edge of SG-20 activation is not clear in PCA determination of components. Eigenvalues relevance (scree plot, not showed) suggests 3 or 4 principal components. At a first glance, evolving scores suggests 4 PC's (Figure VI.*33* right), but the fourth one presents low s/n ratio although some visual structure evolution. The origin of such ambiguous behavior may be explained looking at 3D scatter plot of scores (Figure VI.*33* left), we should account one component for each vertices of the curve, thus 3 PC's. However, the final state clearly is split into two clusters (the circle in the figure, also, see the plane projections), which can cause the ambiguity in determining the number of principal components. In this

picture, after performing MCR calculations using 3 and 4 components, we chose just 3 PC's to describe the system.

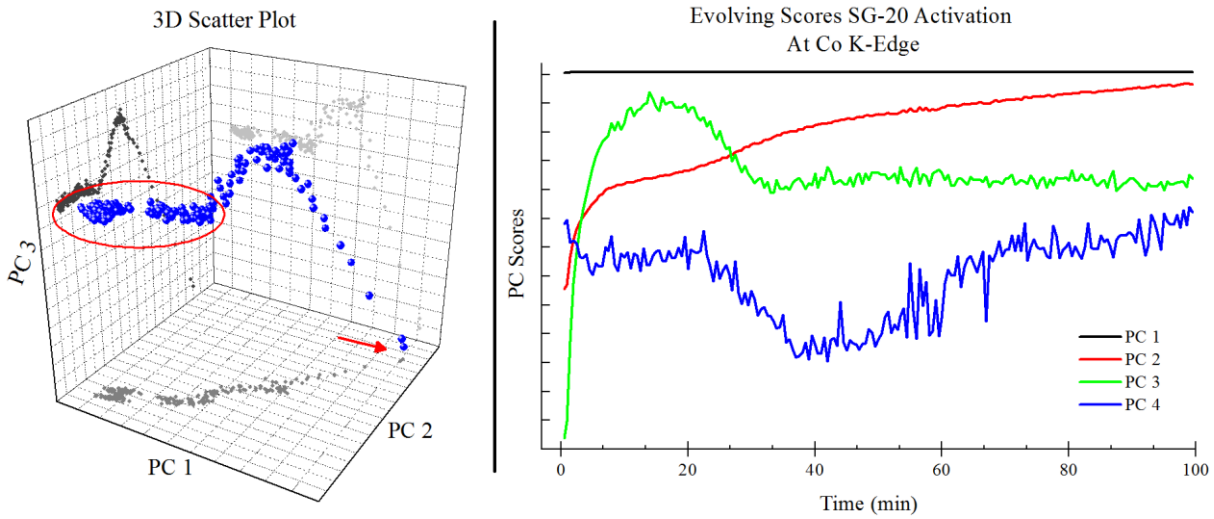

Figure VI.33 - (Left) 3D scatter plot of Scores and (right) evolving scores. Red arrow indicate the beginning of the reaction, the split final state is circled.

Initial guess was determined by EFA and constraints such as non-negativity (in both profiles), unimodality, closure, local rank selectivity and spectral selectivity were selected. The selectivity in spectra was taken to consider the third PC as Co-sulfided species (PC 3 from HMA-20) in order to be coherent with XPS results. The profiles obtained after MCR are in Figure VI.*34*.

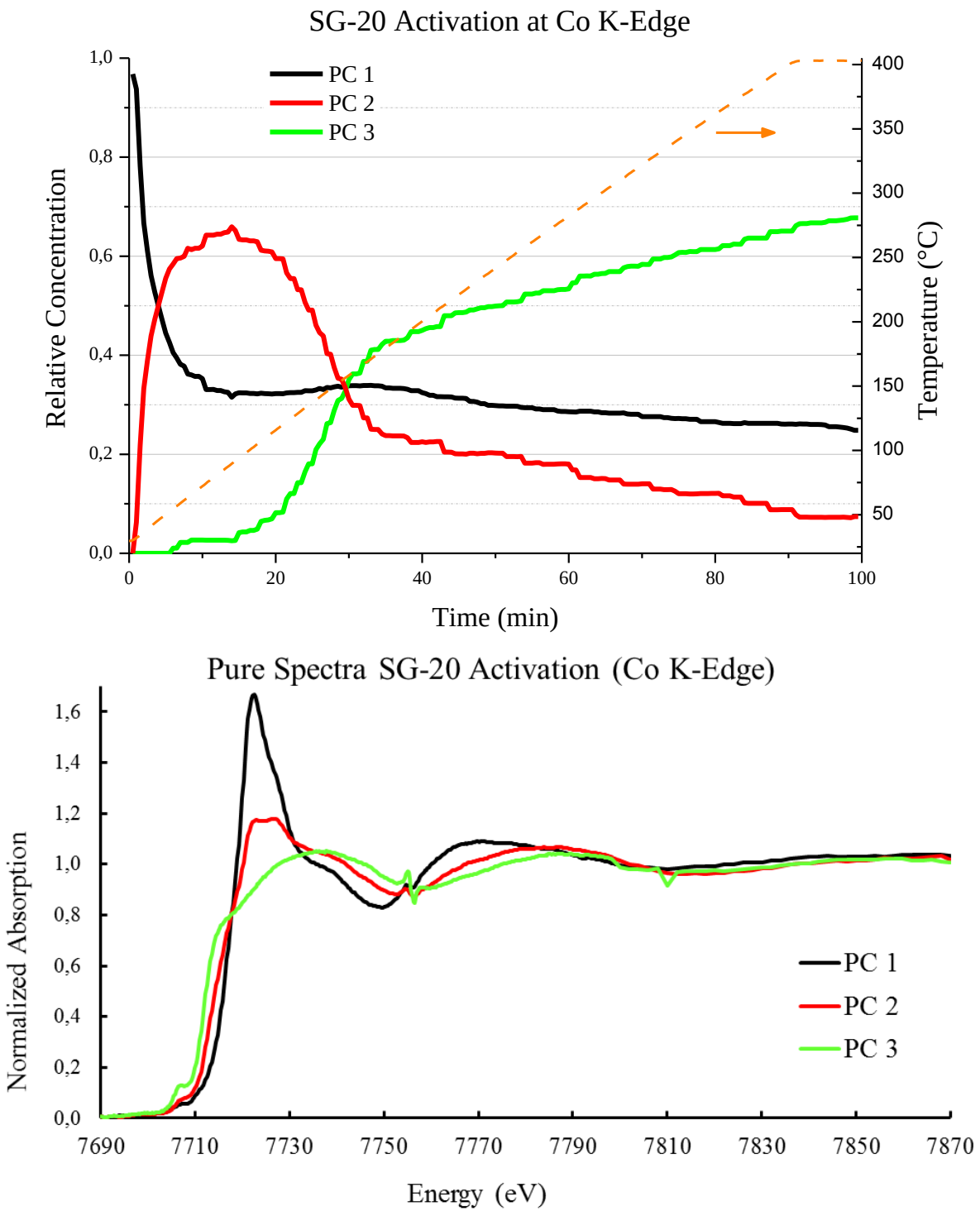

Figure VI.34 - Profiles from MCR calculation for SG-20 activation at Co K-Edge. Figure of merits are, σ = 0.071, LOF in % (PCA) = 0.69, LOF in % (exp) = 0.76 and R^2 = 99.9942.

As stated above, PC 3 is a fixed spectrum that is attributed to a Co-sulfided specie (indeed a copy of PC 3 of Co-component from HMA-20), whereas PC 1 is virtually the start compound. PC 2 at HMA series had an aspect close to an oxide, while here PC 2 has its white line very low compared to those from HMA series.

It may be fruitful to make some qualitative comparisons between results found by MCR of SG-20 and HMA-20. Both final XANES states (not necessarily equals to the final PC-component) are very similar, but HMA-20 seems to be closer to a sulfided state. In HMA-20, MCR was able to recover a pure final Co-sulfided spectrum, which was not the case fort SG-20. That was the reason from which we decided to put such Co-sulfided-type spectra as a selectivity constraint in MCR calculations for sol-gel sample. This assumption was similar that one followed for the MCR treatment used in SG-20 Mo K-edge activation.

3.2.3. Activation Description of the SG-20 Catalyst

We are now able to describe fully the activation reaction of the SG-20 catalyst. Figure VI.*35* shows concentration profile of different molybdenum and cobalt species formed during the reaction. One note that no matter the "considered point of view" (either molybdenum or cobalt) the initial structure quickly transform with the same rate. After about five minutes (at 50 °C), a half of molybdenum oxide and a half of cobalt oxide are turned to an intermediate species. Next, while Mo oxide keep falling in concentration until the vanishing (about 30 min and 150 °C), Co oxide stabilizes at 33% of initial concentration. Then, the moment that intermediates achieve a maximum, the formation of MoS_2 and Co-sulfide species start almost at the same time, 15 minutes after starting of reaction (95 °C). Strictly, the delay is about 5 minutes, wherein the Co conversion starts first. Both Mo and Co conversion into active form goes with the same ratio. Few minutes later (35 min), many trends happens around this moment: a slow-down in MoS_2 and Co_9S_8 increase rate, a slow-down in Co-intermediate decrease rate, Co-oxide concentration restarts to decrease slowly and constantly, and it starts the formation of Mo-reduced specie. The scenario does not change until the plateau of 400 °C. In fact, such slow-down conversion seems to carry on even in the stabilized temperature of the plateau. Additionally, MoS_2 and reduced SG-20 seems to compete between them along the reaction.

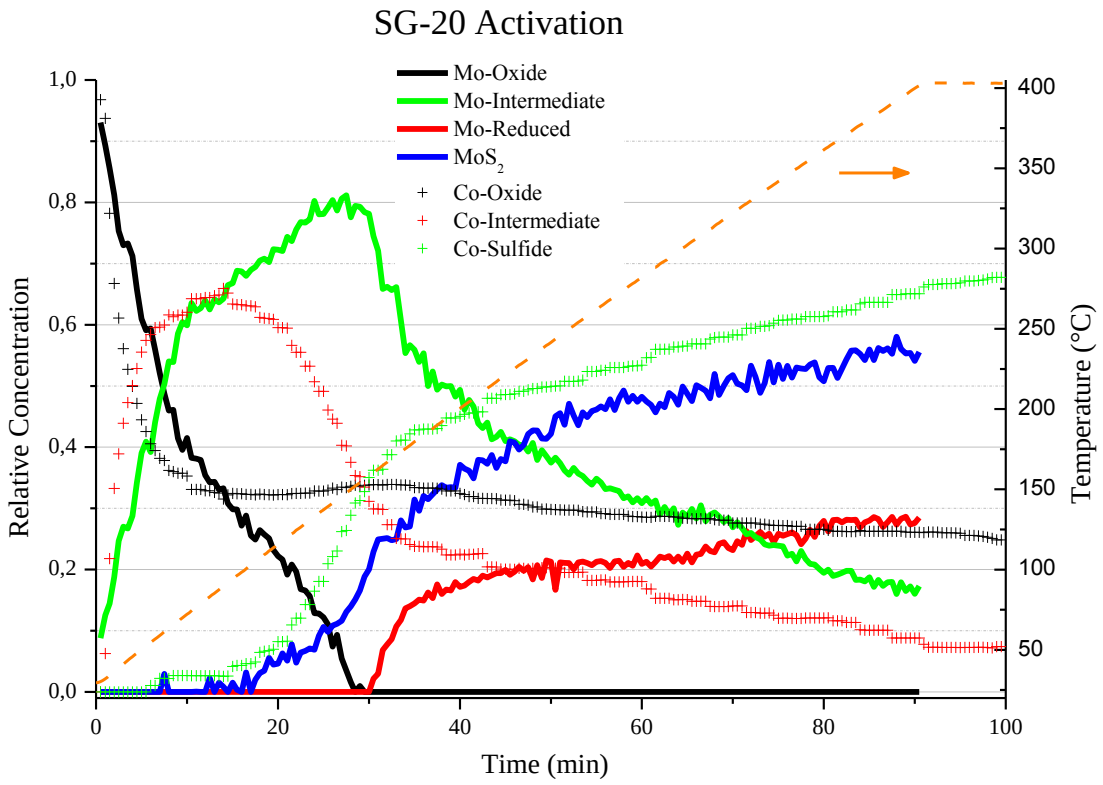

Figure VI.35 - Full description of SG-20 catalyst activation.

Another kind of "competition" seems to exist early in Co-species formation. As soon as the reaction begins, all the H_2S available is used to convert Co-oxide into its Co-intermediate. However, Co_9S_8-type specie (as well as MoS_2) formation also starts soon and now Co-intermediate uses this feedstock to convert to final Co specie. It seems to prevent further Co-oxide to Co-intermediate conversion. It is clear that the whole system is very susceptible to change easily and rapidly, but is intrigue that it do not arrive in a real "end of reaction", where MoS_2 formation is finally completed, as seen in HMA series.

At this point, it may be fruitful to compare these results with a similar system, the HMA-5. Table 30 show differences between these two samples concern structural parameters obtained by EXAFS fitting. The main remarkable contrast between them, whatever the K-edge considered (Mo or Co), is that in SG-20 structure the both metallic sites are equally present, i.e., in Mo K-edge we observe other molybdenum neighbors as intense as cobalt neighbors. In numbers, each molybdenum in SG-20 structure sees on average, 2 other molybdenum atoms and 2 cobalt atoms around it.

Table 30 - Structural parameter comparison between HMA and SG series.

Mo K-edge					Co K-edge				
HMA-5			SG-20		HMA-5			SG-20	
N	R(Å)	Bond Type	N	R(Å)	N	R(Å)	Bond Type	N	R(Å)
2.8	1.74	Mo-O	3.8	1.75	4.2	2.02	Co-O	3.8	2.01
1.4	1.94	Mo-O	1.6	1.97	0.7	3.15	Co-Mo	3.1	3.10
0.9	3.27	Mo-Mo	0.9	3.21	-	-	Co-Mo	-	-
0.9	3.40	Mo-Mo	0.9	3.33					
0.2	2.74	Mo-Co	1.0	3.10					
0.2	3.83	Mo-Co	1.0	3.85					

* *R* values without phase correction.

Despite of some variances in bond distances, the greatest difference between both structures is concerning how they look Co neighbors. In Mo K-edge of HMA-20, the presence of cobalt neighbors is on limit of uncertainty, while in SG-20 it is proportional to the molybdenum neighbors (virtually, 1:1). This difference is important also in Co K-edge, SG-20 cobalt atoms sees, in average, 3.1 Mo atoms surrounding them, whereas in HMA-20 this number falls to 0.3.

In order to check our results, we can compare MCR calculated concentrations at the end of the reaction with independent analysis previously done, namely, XPS measurements. Considering the concentration profile for Co species at the end of the reaction, they are in accord in agreement with XPS modeling proposed for sulfided SG-20 (Figure V.13). XPS gives us about 76% of total cobalt after sulfidation attribute to the Co-sulfided-type oxidation state (32% of the so-called CoMoS and 44% of the so-called Co_9S_8) and 23% due to Co^{+2}-oxide species. MCR calculated-concentration are, 65% attributed to Co-sulfided specie, 10% to first intermediate and 25% attributed to oxide-Co^{2+}.

Analogously, for the Mo XPS case, our results are, 46% of total Mo after sulfidation are in Mo^{+4} form (i.e., MoS_2), while 27% is attributed to Mo^{6+} (namely, oxide) and 27% to Mo^{+5} species. MCR gives us 55% of MoS_2, 28% of SG-20 reduced and 17% of Mo-intermediate species. We also showed in the last chapter that the linear combination of final SG-20 spectra accuse an amount of about 50% of MoS_2.

It is not evident to make direct comparison between two different techniques with different approaches (XPS and XAS) and caution must be considered when interpreting the results. For instance, comparing Co results, one notes that XPS resolves two distinct Co-sulfided species (CoMoS and Co_9S_8), while we have attributed just one in XAS MCR-calculated spectra. Keeping in mind the discussion on the limitations of MCR profiles depending on the system consider (see sections 2.2.1 and 2.6) and the different approaches of these two techniques we will considered the comparison of the two paragraphs above just an evaluation of "good direction of interpretation".

3.3. SG-5, SG-10 and SG-15: Qualitative Analysis

For the lower loadings of the sol-gel series, the MCR result is twofold. SG-15 has clean data so *a priori* we should be able to explore it. However, as seen up to here, augmented matrix gives us additional critical information to resolve correctly the system. For this sample, just single activation matrix is available. SG-5 and SG-10 belong to the same "family" of samples. They are not quite susceptible to suffer greater transformation and/or the quality of data is compromised because the low loading. In anyway, we discuss separately the cases with a certain degree of skepticism.

3.3.1.SG-15

SG-15 catalyst belongs to the same "family" that we have attributed SG-20. The similarities that justify this group are discussed in the previous chapter. However, whatever the method used in principal component analysis to determine PC number one obtains just three components (Figure VI.*36*). In scatter plot, one sees the typical shape (a triangle) suggesting a two steps transformation (3 principal components).

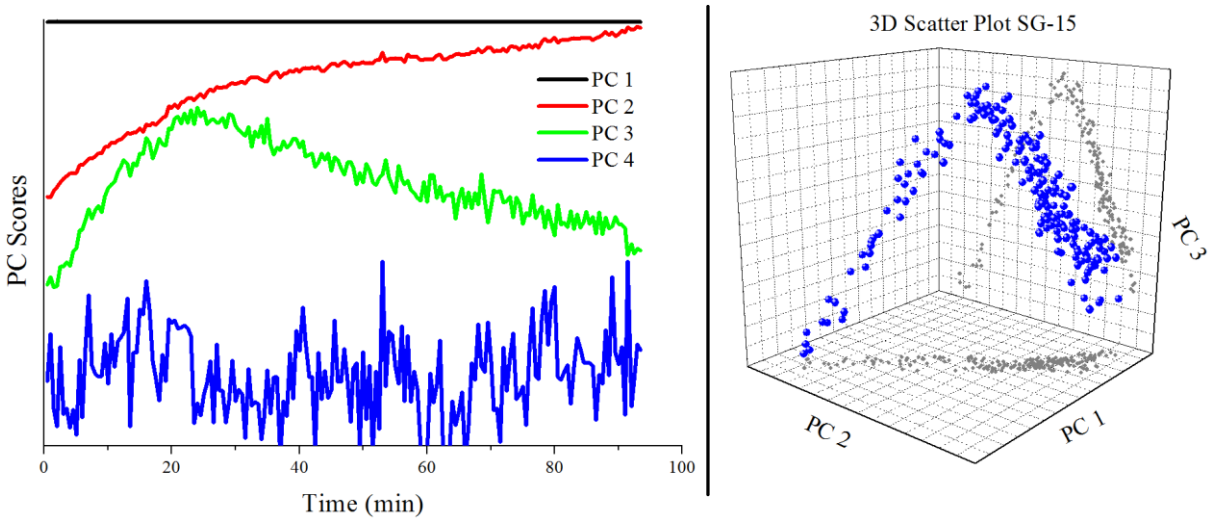

Figure VI.36 - Plot of scores (left) and 3D scatter score plot (right) for SG-15.

MCR calculation were performed using non-negativity, closure and selectivity in spectra (following the same reasoning used in SG-20, the linear combination fit of the XANES). Thus, selectivity in spectra takes into account that the last PC corresponds to MoS_2 and Co_9S_8-type, respectively, in Mo and Co K-edge calculations. In this case, we try MCR calculations considering 3 and 4 PC's in Mo-activation. Both results are equivalent, but we prefer 4 components because it follows the reasoning as predicted by reference studies (namely, HMA-20). The fact that the principal component analysis indicates just three PC's do not prevent us at all to give additional information to the system in order to resolve it. We

stress that this interpretation itself is ambiguous (even the calculations via MCR-Bands are not) and carefully attention and prudence must be considered by doing so. The activation description and the calculated pure spectra are shown in (Figure VI.*37*).

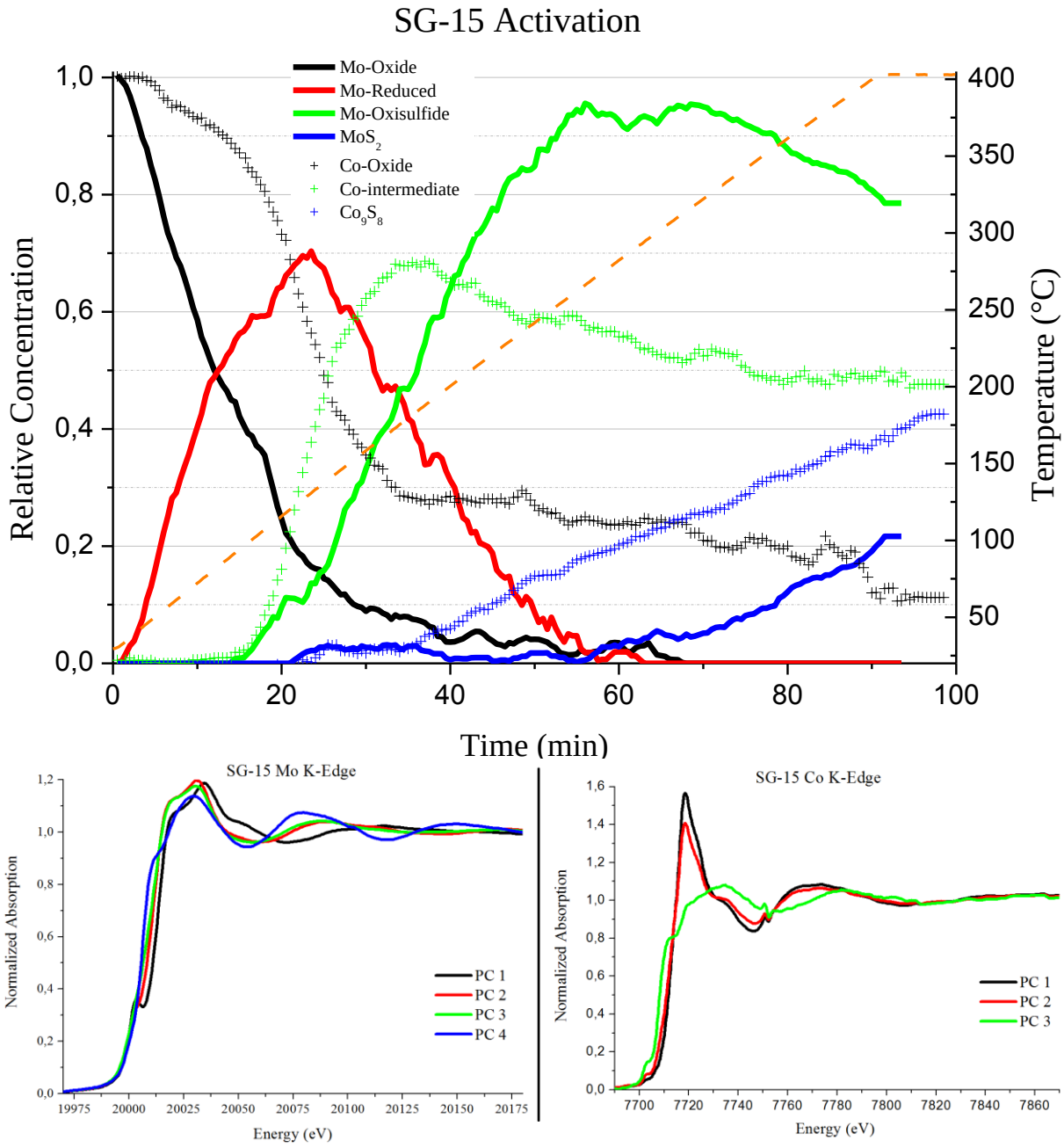

Figure VI.37 - Description of the Activation of SG-15 (upper panel) and pure spectra for Mo (lower left panel) and Co (lower right panel) K-edges. The figures of merit for Mo-activation are σ = 0.0038, LOF in % (PCA) = 0.31, LOF in % (exp) = 0.34 and R^2 = 99.9988. For Co-activation are σ = 0.0039, LOF in % (PCA) = 0.17, LOF in % (exp) = 0.41 and R^2 = 99.9983.

Concerning the Mo K-edge components, we expect PC 2 as a reduced compound, whereas PC 3 should be an oxysulfide one. However, XANES of PC 2 and PC 3 are quite similar (Figure VI.*37* lower left panel). To ensure of PC 3 nature, we appeal to Fourier transform of EXAFS (Figure VI.*38*). Comparing PC 2 and PC 3, and considering HMA-20 as Mo-S gauge, one observes a slight enlargement of first

radial distribution exactly where it should be the Mo-S contribution for the later. It seems PC 3 is a form of an oxysulfide. Since it is a subtle feature, one may wonder eventually to be just an artifice of MCR since we impose 4 components and, in addition, we fixed it to be a particular spectrum. Furthermore, it is harsh give an unambiguous answer in this case, because no other data (TRP, for instance, as we had in SG-20 case) is available. Since such behavior (4 intermediates, among which one reduced and other an oxisulfide) goes on the good sense (considering HMA-20 as reference), we keep, thus, the interpretation of a weak-oxisulfide specie.

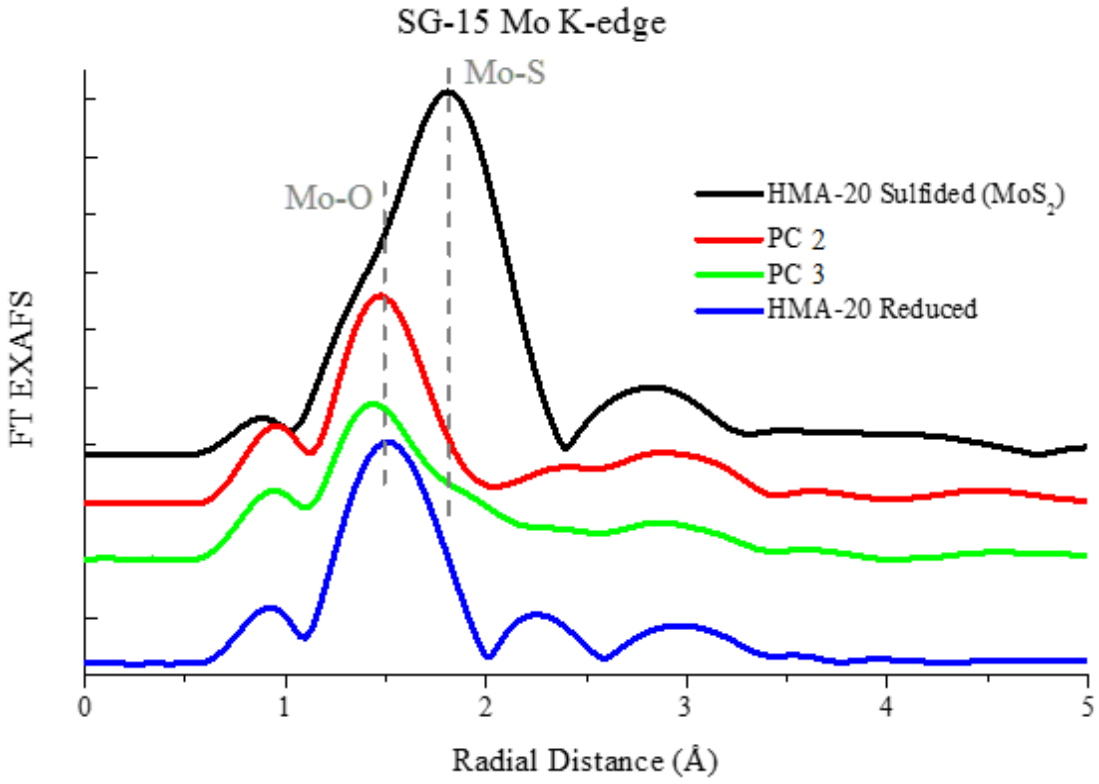

Figure VI.38 - EXAFS Fourier Transform comparison among PC 4, PC 3 and experimental spectra from HMA-20 series (used as reference). It is highlighted the *R* position of Mo-O (long, from reduced specie) and Mo-S bond distances (without phase correction).

On the description of the whole process of activation (Figure VI.37 upper panel), one observes a good correspondence between the two K-edge calculations. The Mo-oxide slowly turns to a reduced specie although the transformation starts early, at room temperature after 5 minutes of reaction. Ten minutes later, 50% of the Mo-oxide is already reduced. The Co-intermediate starts to be formed around 100 °C at the same time that the second Mo-intermediate. Both final states has very low formation rate, which starts at the same time, around 150 °C. At the end of reaction, about 1/4 of Mo species are in form of MoS_2 and the rest is in a "weak-oxisulfide" state. The Co conversion is a slightly better and, at the end, a little less than 50% of Co specie are in Co_9S_8-type form.

In Table 31 we present structural parameters obtained from EXAFS modeling fit of pure spectra calculated by MCR. For this sample, we have not data from TPR, thus we are only able to associate PC

1 to oxide initial state (and copy the previous fit from this structure). As discussed above and following the reasoning of the others solids, PC 2 is associated to a reduced specie, PC 3 to an oxysulfide and, as for SG-20, we have imposed MoS_2 structure for this component.

Structural parameters allow us to describe the structural evolution of the solid during activation. The initial oxide compound (PC 1) is reduced to a structure with just one Mo-O contribution and Mo-Mo distribution slightly complex compared to the initial state (PC 2). Throughout the reaction (from PC 1 to PC 3), oxygen bond at 1.98 Å seems do not move (although such bond length in PC 1 and PC 2 are not connected), only weakening. Mo-Mo contributions at 3.26 Å and 3.39 Å are also present for the three first principal components (with slight length changes). Therefore, the structure evolution do not follow the behavior observed in impregnated catalysts where lengthening in Mo-Mo bonds were gradually taking place.

Table 31 – SG-15 Mo K-edge EXAFS structural parameters for components determined by MCR.

Sample	PC	Bond	N	R (Å)	σ² (Å²)	Δσ	ΔE (eV)	Parameters
SG-15	PC 1	Mo-O	3.9	1.76	0.009	0.003	-2.1 (3.8)	Δk = 4.0-12.4 ΔR = 1.1-3.8 N_{ind} = 14 χ^2_{Red} =580 R_{factor} = 0.02
		Mo-O	2.4	1.97				
		Mo-Co	1.4	3.11	0.007	0.006		
		Mo-Co	1.4	3.84				
		Mo-Mo	1.4	3.26	0.01	0.01		
		Mo-Mo	1.4	3.41				
	PC 2	Mo-O	2.8	1.98	0.003	0.002	-7.2 (5.2)	Δk = 4.8-12.7 ΔR = 1.1-3.6 N_{ind} = 12 χ^2_{Red} = 491 R_{factor} = 0.05
		Mo-Mo	1.9	3.16	0.006	0.007		
		Mo-Mo	1.9	3.26				
		Mo-Mo	1.9	3.37				
	PC 3	Mo-O	1.1	1.98	0.002	0.003	-5.1 (3.0)	Δk = 4.3-13.2 ΔR = 1-4.2 N_{ind} = 11 χ^2_{Red} = 998 R_{factor} = 0.08
		Mo-S	1.6	2.38	0.01	0.01		
		Mo-Mo	1.7	3.21	0.008	0.004		
		Mo-Mo	1.7	3.39				
	PC 4*	Mo-S	5.6	2.40	0.0045	0.0005	6.5 (0.7)	Δk = 4.7-13.5 ΔR = 1-4 N_{ind} = 16 χ^2_{Red} = 436 R_{factor} = 0.005
		Mo-Mo	3.5	3.17	0.005	0.001		
		Mo-S	0.7	4.10	0.0045	0.0005		
	SG-15 (sulf)	Mo-O	1.5	1.97	0.005	0.005	-5.4 (2.6)	Δk = 4.3-13.4 ΔR = 1-3.8 N_{ind} = 15 χ^2_{Red} = 1800 R_{factor} = 0.04
		Mo-S	2.0	2.40	0.007	0.004		
		Mo-Mo	1.5	3.23	0.009	0.005		
		Mo-Mo	1.5	3.62	0.009	0.005		
Uncertainty:	PC 1: N_{Mo-O} = 1.1; $N_{Mo-Metal}$ = 0.8 PC 2: N_{Mo-O} = 0.9; N_{Mo-Mo} = 1.7 PC 3: N_{Mo-O} = 0.8; N_{Mo-S} = 1.6; N_{Mo-Mo} = 1.0 PC 4: N_{Mo-S} = 0.3/0.6; N_{Mo-Mo} = 0.7							

One last remark, since we have not complementary data that provide additional information, as in SG-20, we observe that PC 3 structure is not far from SG-15(sulf) discussed in the previous chapter (and presented again here in Table 31). Consequently, PC 3 is also close to SG-20(sulf) (see Table 29) and we must take into account the limitations of MCR method in such case, as discussed in 2.7.

3.3.2. SG-5 and SG-10

The lowest loadings, SG-5 and SG-10, are certainly special cases. For SG-5 at Mo K-edge, no difference between activation and reduction is observed, in fact, the activation itself is just a reduction, and the final state of activation is equal to the final state of reduction. As if for any unknown reason, the catalyst is available just for the very first part of the activation reaction. At Co K-edge, no change at all is observed during activation, for both SG-5 and SG-10. At this situation, it is not too much attributing any difference between initial and final spectra to temperature variation. The structure seems to be not accessible to the reaction and the final spectrum coincides with the start spectrum.

PCA performed in individual reaction (for SG-5) and activation (for both SG-5 and SG-10) matrices give nothing but two components each. In any cases, score from the third component has low s/n and counts just for noise, so that, besides initial and final states in both edges, no additional spectral information can be extracted. Unfortunately, such low Mo loading system allied to technical experimental troubles in data acquisition prevent further quantitative analysis. In that sense, sadly we cannot extract reliable information of the evolving process.

3.4. Partial Conclusions

Chemometrics have been applied to study activation step of HDS catalysts. In HMA-5, Mo K-edge augmented matrix suggested that reduction and activation of this sample do not seem to be interconnected. Reduction reaction do not follow the same steps as in HMA-20, indicating that reactions are very sensitive to Mo loading. Particularly, in reduction of HMA-5, the oxide precursor evolves readily to another oxide species and then is reduced without an intermediate. Such behavior is completely distinct of one observed in the reduction HMA-20. Nevertheless, such particularity do not seem to play an important role for activation, since one observes the formation of an oxysulfide specie as intermediate and we have the totally formation of a nano-MoS_2-type active phase, just like in HMA-20 activation. At Co K-edge, HMA-5 presents also particularities in MCR calculations that prevent us to give a satisfactory answer for the activation reaction. Nevertheless, we found a profile that corroborates (at least at the end of activation) with the results previously presented, i.e., a mixed phase with 50/50% ratio of a sulfided and an oxide species.

Concerning sol-gel solids, SG-20 and SG-15 could be nicely exploited, although the lack of reduction data for SG-15 prevent better results for this sample.

Principal component analysis (PCA) for Mo K-edge SG-20 augmented system is very similar to HMA-20. However, the description of SG-20 activation did not provide true profiles for this sample. Good results for concentration profile were achieved when constraining in spectra was done, which spoiled the fully description of the system. In this particular case, reduction did not provide fruitful information. Nevertheless, MCR was able to provide profiles that seems to represent accurately the SG-20 activation. In this solid, no complete sulfidation of the species was achieved. At the end of the reaction, about 60% of the oxide precursor has turned to a MoS_2-type species, the active phase. In a full description of the activation, i.e., gathering information from Co and Mo K-edges, we observed that intermediate species as well as final sulfided species arise at the same time in the reaction, suggesting a stronger synergy in sol-gel solids when compared to HMA catalysts.

It is interesting to correlate these results with the catalytic performance in thiophene HDS. Even though SG-20 solid was not completely sulfided at the end of the activation, its efficiency (slightly superior to 20%) is higher than impregnated catalysts with lower SSA (100 m^2/g, with a plateau of conversion around 14%) and comparable to impregnated catalysts with higher SSA (200 m^2/g, with 24% of conversion). It seems to indicate that SG-20 active phase can be more reactive than the one obtained in impregnated solids. We reported that MCR was not able to determine precisely the active phase of SG-20 (due to the constraint in spectra), but, structural information on actual SG-20 active phase can be extract from *ex situ* analysis of final activation state. Clearly, the Mo-S bond at 2.39 Å and the Mo-Mo bond at 3.19 Å come from the SG-20 active phase. The coordination number of such bonds, respectively, 2.7 and 2.1, suggests a well-defined MoS_2-type structure that obeys the same atomic local arrangement observed in bulk MoS_2 (where $N = 6$ for both Mo-S bond at 2.40 Å as well as for the Mo-Mo bond at 3.17 Å). We recall that in the active phase of HMA-20 such coordination numbers are, respectively, 5.6 and 3.5. Such slight difference in the active phase can be driven by the influence of the promoter, the Co atoms. While in HMA-20 the final Co-sulfided specie starts to be formed after MoS_2, in SG-20 they arise virtually at the same time in the activation. This synergy between Co and Mo atoms for sol-gel preparation method seems to play an important role in active phase formation.

For SG-15, we were able to obtain good profiles from MCR results, but as for SG-20 information on the Mo-final active phase structure were spoiled by constraints imposed in spectral selectivity. Just a small part of the oxide precursor were transformed into MoS_2-type phase (about 20%). The remaining is found in an oxisulfide phase. The description of Co-species evolution follows the trend observed at SG-20.

Finally, for the other solids, SG-5 and SG-10, no fruitful information could be obtained from MCR calculations. Previous analysis by TEM or XPS showed that a minimum amount of active phase is formed after activation. As also discussed, it seems that such behavior is strongly related to insertion of

oxide species into the titanium matrix. Thus, the structural transformation experienced by these solids are not sufficient to MCR method resolve the reaction mechanism and, roughly, we observe a single (one step) reaction from the oxide precursor to reduced oxide.

4. Conclusion

Principal component analysis offers us a wide way to treat data in order to obtain qualitative information. As it was demonstrated, eigenvalues, percentage of explained variance, scores and loading values obtained from singular value decomposition can be used in order to evaluate the number of relevant components in the system. However, usually, in not possible to find an incontrovertible value for such number of components. In complex reaction systems as the one studied in this work, usually are rank-deficient and single matrix evaluation leads to ambiguous or ill-defined profiles. Many of the limitations associated with the resolution of a single matrix are partially or completely overcome when several matrices, the so-called three-way data sets, are treated together [33]. Three-way resolution methods always introduce a significant improvement in the recovery of the true response profiles and have the additional benefit of providing quantitative information. Column-wise augmented matrix is insert in three-way data set context and helps to resolve unambiguously the profiles.

Particularly, in our study, we have used such systems to resolve kinetics of HDS catalytic activation and molecular atomic structure evolution. We have showed that the method resolves accurately the mechanism of active phase formation for impregnated and sol-gel catalysts. *In situ* data from XAS evolution during the TPR and activation of Mo and Co K-edges were used to propose a mechanism of structural evolution of HDS catalysts from oxide precursors to the active phase. Concerning Mo-species, a 3 steps reaction with two intermediates is proposed taking as reference the transformation observed on HMA-20. As a first step, the oxide precursor (Mo^{VI}) is reduced partially at the beginning of the reaction. Then, such partially reduced oxide (Mo^{V}) is partially sulfided via substitution of Mo-O bonds to Mo-S. The last step of the activation is the consolidation of the active phase, where a MoS_2-type structure is observed. Co-species evolve in a single 2 step reactions (thus, just one intermediate), and at the end of activation the whole amount of Co-oxide precursors do not transform into sulfided Co-species.

Depending on the method of preparation and the Mo loading of the solid, slightly different profiles are obtained, but it seems that the general mechanism discussed in the last paragraph is followed. For instance, in impregnated catalysts with low Mo loading, the mechanism of activation is strongly influenced by the first step of the reaction, the reduction. A quite distinct profile is observed for such solid compared to higher Mo loading, which reflects in the profile of transformation observed in the activation although the final active phase are quite similar.

One-pot sol-gel method seems to be suitable for tailored HDS catalytic synthesis, but a greatest issue seems to be linked to insertion of Mo-species into the titania matrix, which prevents the whole activation of the catalytic promoted species. Particularly, for lower Mo loadings (namely SG-5 and SG-10), this phenomenon becomes so relevant at the point that no significant sulfidation is observed. Thus, for these two samples, no evolving steps-reaction is obtained via MCR calculations. For higher Mo loadings, the previously mentioned 3-steps activation mechanism is observed, although the profile evolution of species inside SG-20 prevents the resolution with a free-constrained model. SG-20 catalyst presents great HDS conversion and we showed that local structure is closely connected to this feature; the active phase of such catalysts contains structural features similar to HMA-20. The high efficiency of this particular sol-gel solid seems to be linked to the preparation method, where a stronger synergy with the promoter leads to the formation of well-tailored active phase with good dispersion on the support.

Activation of supported HDS catalysts is a complex reaction, and quite sensible to different factors, mainly the preparation method and oxide precursor solutions used to synthesize the solids. Thus, different profile evolutions can be found, and this effect is particularly true depending on the Mo loading, as it was observed in our results. Depending on the particular evolution of the species, MCR fails in correctly resolve concentration profiles for a particular reaction. This is a major issue when dealing with this combined XAS-MCR method.

For this reason, it is of fundamental importance to consider performing coupled technique measurements when recording data from a reaction and alternative experiments that can reveal a particular component of the reaction. For instance, in our particular case where we studied the activation of the catalyst, we have performed the reduction reaction under H_2 atmosphere, which provided fruitful information to resolve the system. Nevertheless, it should be considered to perform a thermal evolution of the spectra without any reagent in order to separate any spectral changes due temperature of the spectral evolution from the reaction itself. As it was also observed, in some systems, particularly HMA-5, reaction and activation were at certain point of view, disconnected. In such system, the gathering of experiments did not bring novel information. It means that, despite column-wise augmented system, one has observed that in many cases MCR calculations are not able to provide real profiles.

References

[1] E. R. Malinowski, Factor Analysis in Chemistry, 3rd ed. New York: Wiley, 2002.

[2] M. Amrhein, B. Srinivasan, D. Bonvin, and M. M. Schumacher, "On the rank deficiency and rank augmentation of the spectral measurement matrix," Chemometrics and Intelligent Laboratory Systems, vol. 33, no. 1, pp. 17–33, May 1996.

[3] H. Shen, J. Wang, Y. Liang, K. Pettersson, M. Josefson, J. Gottfries, and F. Lee, "Chemical rank estimation by multiresolution analysis for two-way data in the presence of background," Chemometrics and Intelligent Laboratory Systems, vol. 37, no. 2, pp. 261–269, Jun. 1997.

[4] S. Navea, A. de Juan, and R. Tauler, "Modeling Temperature-Dependent Protein Structural Transitions by Combined Near-IR and Mid-IR Spectroscopies and Multivariate Curve Resolution," Analytical Chemistry, vol. 75, no. 20, pp. 5592–5601, Oct. 2003.

[5] A. Rochet, "Caractérisation Structurale de Catalyserus Hétérogènes en Condition de Fonctionnement par Spectroscopie d'Absorption des Rayons X Résolue dans le Temp," Paris Sud, 2011.

[6] P. R. Peres-Neto, D. A. Jackson, and K. M. Somers, "How many principal components? stopping rules for determining the number of non-trivial axes revisited," Computational Statistics & Data Analysis, vol. 49, no. 4, pp. 974–997, Jun. 2005.

[7] C. Ruckebusch, A. De Juan, L. Duponchel, and J. P. Huvenne, "Matrix augmentation for breaking rank-deficiency: A case study," Chemometrics and Intelligent Laboratory Systems, vol. 80, no. 2, pp. 209–214, Feb. 2006.

[8] M. Garrido, I. Lázaro, M. S. Larrechi, and F. X. Rius, "Multivariate resolution of rank-deficient near-infrared spectroscopy data from the reaction of curing epoxy resins using the rank augmentation strategy and multivariate curve resolution alternating least squares approach," Analytica Chimica Acta, vol. 515, no. 1, pp. 65–73, Jul. 2004.

[9] M. Garrido, F. X. Rius, and M. S. Larrechi, "Multivariate curve resolution-alternating least squares (MCR-ALS) applied to spectroscopic data from monitoring chemical reactions processes.," Analytical and bioanalytical chemistry, vol. 390, no. 8, pp. 2059–66, Apr. 2008.

[10] A. de Juan, J. Jaumot, and R. Tauler, "Multivariate Curve Resolution (MCR). Solving the mixture analysis problem," Analytical Methods, vol. 6, no. 14, p. 4964, Jun. 2014.

[11] E. Payen, S. Kasztelan, S. Houssenbay, R. Szymanski, and J. Grimblot, "Genesis and characterization by laser Raman spectroscopy and high-resolution electron microscopy of supported molybdenum disulfide crystallites," Journal of Physical Chemistry, vol. 93, pp. 6501–6506, 1989.

[12] R. Leliveld and A. Van Dillen, "The sulfidation of γ-alumina and titania supported (cobalt) molybdenum oxide catalysts monitored by EXAFS," Journal of catalysis, vol. 129, pp. 115–129, 1997.

[13] R. Leliveld and A. Van Dillen, "A Mo–K Edge XAFS Study of the Metal Sulfide-Support Interaction in (Co) Mo Supported Alumina and Titania Catalysts," Journal of catalysis, vol. 196, pp. 184–196, 1997.

[14] A. V. Pashigreva, G. A. Bukhtiyarova, O. V. Klimov, Y. A. Chesalov, G. S. Litvak, and A. S. Noskov, "Activity and sulfidation behavior of the CoMo/Al2O3 hydrotreating catalyst: The effect of drying conditions," Catalysis Today, vol. 149, no. 1–2, pp. 19–27, Jan. 2010.

[15] P. ARNOLDY, "Temperature-programmed sulfiding of MoO3/Al2O3 catalysts," Journal of Catalysis, vol. 92, no. 1, pp. 35–55, Mar. 1985.

[16] T. Weber, J. C. Muijsers, J. H. M. C. Van Wolput, C. P. J. Verhagen, and J. W. Niemantsverdriet, "Basic Reaction Steps in the Sulfidation of Crystalline MoO 3 to MoS 2 , As Studied by X-ray Photoelectron and Infrared Emission Spectroscopy," vol. 3654, no. 96, pp. 14144–14150, 1996.

[17] D. Genuit, I. Bezverkhyy, and P. Afanasiev, "Solution preparation of the amorphous molybdenum oxysulfide MoOS2 and its use for catalysis," Journal of Solid State Chemistry, vol. 178, no. 9, pp. 2759–2765, Sep. 2005.

[18] P. Gemperline, Practical Guide To Chemometrics, 2nd ed. Boca Raton: CRC Press, 2006.

[19] E. Spjøtvoll, H. Martens, and R. Volden, "Restricted Least Squares Estimation of the Spectra and Concentration of Two Unknown Constituents Available in Mixtures," Technometrics, vol. 24, no. 3, pp. 173–180, Mar. 2012.

[20] P. J. Gemperline, "Computation of the range of feasible solutions in self-modeling curve resolution algorithms.," Analytical chemistry, vol. 71, no. 23, pp. 5398–404, Dec. 1999.

[21] R. Tauler, "Calculation of maximum and minimum band boundaries of feasible solutions for species profiles obtained by multivariate curve resolution," Journal of Chemometrics, vol. 15, no. 8, pp. 627–646, Sep. 2001.

[22] M. Garrido, M. S. Larrechi, F. X. Rius, and R. Tauler, "Calculation of band boundaries of feasible solutions obtained by Multivariate Curve Resolution–Alternating Least Squares of multiple runs of a reaction monitored by NIR spectroscopy," Chemometrics and Intelligent Laboratory Systems, vol. 76, no. 2, pp. 111–120, Apr. 2005.

[23] H. Abdollahi and R. Tauler, "Uniqueness and rotation ambiguities in Multivariate Curve Resolution methods," Chemometrics and Intelligent Laboratory Systems, vol. 108, no. 2, pp. 100–111, Oct. 2011.

[24] J. Jaumot and R. Tauler, "MCR-BANDS: A user friendly MATLAB program for the evaluation of rotation ambiguities in Multivariate Curve Resolution," Chemometrics and Intelligent Laboratory Systems, vol. 103, no. 2, pp. 96–107, Oct. 2010.

[25] H. HU, A. TOUGERTI, J.-C. MORIN, B. Lassalle, D. VANTELON, V. BRIOIS, and S. CRISTOL, "Study of the Reduction of TiO2 Supported Molybdenum Oxyde Catalysts by Combining in situ XANES spectroscopy at L2,3, K edge and DFT Calculations," 2014, p. SOLEIL User's Meeting (Poster).

[26] T. KADONO, T. KUBOTA, I. HIROMITSU, and Y. OKAMOTO, "Characterization of highly dispersed cobalt sulfide catalysts by X-ray absorption fine structure and magnetic properties," Applied Catalysis A: General, vol. 312, pp. 125–133, Sep. 2006.

[27] K. INAMURA, "Temperature-programmed sulfiding of precursor cobalt oxide genesis of highly active sites on sulfided cobalt catalyst for hydrogenation and isomerization," Journal of Catalysis, vol. 133, no. 2, pp. 498–514, Feb. 1992.

[28] S. M. A. M. Bouwens, D. C. Koningsberger, V. H. J. de Beer, and R. Prins, "The structure of the cobalt sulfide phase in carbon-supported Co and Co-Mo sulfide catalysts as studied by exafs and xanes," Catalysis Letters, vol. 1, no. 1–3, pp. 55–59, Jan. 1988.

[29] M. J. Ledoux, "On the structure of cobalt sulfide catalysts," Catalysis Letters, vol. 1, no. 12, pp. 429–431, 1988.

[30] R. Manne, "On the resolution problem in hyphenated chromatography," Chemometrics and Intelligent Laboratory Systems, vol. 27, no. 1, pp. 89–94, Jan. 1995.

[31] H. Hu, I. E. Wachs, and S. R. Bare, "Surface Structures of Supported Molybdenum Oxide Catalysts: Characterization by Raman and Mo L3-Edge XANES," The Journal of Physical Chemistry, vol. 99, no. 27, pp. 10897–10910, Jul. 1995.

[32] K. Hamraoui, S. Cristol, E. Payen, and J.-F. Paul, "Computational Investigation of TiO2-Supported Isolated Oxomolybdenum Species," Journal of Physical Chemistry C, vol. 111, no. 10, pp. 3963–3972, Mar. 2007.

[33] R. Tauler, "Multivariate curve resolution applied to second order data," Chemometrics and Intelligent Laboratory Systems, vol. 30, no. 1, pp. 133–146, Nov. 1995.

General Conclusion

Fossil fuels still represent the principal source of energy in the world nowadays, mainly on the transportation sector. Governmental policies concerning environmental controlling of pollutants have boosted researches in clean fuel production area. One of the most important processes used in industry to control undesirable species in oil feedstock is hydrotreating, wherein hydrodesulfurization (HDS) is the particular hydrotreating procedure used to remove sulfur from petroleum product. Researches for catalysts with increased efficiency in HDS reaction through improvement of the knowledge concerning the activation of precursors that leads to the active phase formation as well as for the reaction itself are still very active. Seeking for tailored solids with enhanced catalytic properties, new supports and routes of preparations have been proposed.

In parallel, third generation synchrotron facilities provide suitable conditions to perform *in situ* experiments, which are fundamental for a better comprehension of the catalytic process (the mechanism and kinetics). Indeed, novel *in situ* apparatus (time-resolved data collection systems, reaction cells, etc.) have been further and further developed being readily available for users, particularly in spectroscopy, which is able to reveal molecular fine structure of the materials. In this picture, the goal of this work was to provide contributions on the understanding of HDS catalytic reactions by adapting chemometrics methods such as PCA and MCR to treat spectroscopy data from time-resolved *in situ* synchrotron-based techniques, particularly X-ray absorption spectroscopy. We have applied chemometrics to resolve activation reaction of two particular series of TiO_2-supported CoMo-based HDS catalysts, one from classical impregnation and another via one-pot sol-gel method.

One-pot sol-gel method has been used to produce $CoMo/TiO_2$ catalysts. As it is the first time such a preparation is reported for anatase-supported catalysts, we performed a wide physicochemical characterization of these solids. A series from 5 up to 40 wt.% of MoO_3 loading was prepared and analysis from different techniques points to an optimal loading of 20 wt.% of MoO_3. This solid present enhanced textural properties, which allows good dispersion of molybdenum and cobalt species with increased Mo loading, which provides enhanced efficiency. It has a catalytic activity peak for thiophene HDS superior to the highest conversion obtained on reference catalysts prepared by impregnation supported on commercial titania. Nevertheless, the analysis suggests that part of Mo-species is retained into the titania matrix. Although this effect does not affect too much the catalytic properties of the SG20 catalysts, it is very important for the low loading catalysts resulting in a very poor sulfidation and hence, a very low catalytic activity.

Principal component analysis (PCA) offers us a wide way to treat huge amount of data (such records from *in situ* experiments) in order to obtain qualitative information on an evolving system. This analysis has been applied recently to treat time-resolved XAS-based experiments. Information such as number of relevant components necessary to describe suitably the data is commonly extracted from a usual analysis. PCA also offers deeper possibilities in data analysis by studying *scores* and *loadings* via factor

analysis. An important issue on this subject concerns the interpretation of PCA results. Depending on the complexity of the evolving reaction, it can be a tough task to extract suitable information. Furthermore, PCA does not offer an easy systematic protocol to treat, interpret and exploit data, particularly in accurate determination of the actual number of relevant components in the reaction. Multivariate Curve Resolution (MCR) is a further step on *in situ* data treatment with the advantage of return as result easier exploitable results, such as concentration profile and pure spectra. Another advantage is that no *a priori* information is necessary in order to build a model for the evolving system. Such qualities gave rise a growing interest in its application to *in situ* catalytic reaction studies. We have tested different tools in PCA to evaluate the applicability in determining the number of the suitable components necessary to describe the system. Further, we used such information to perform MCR-ALS analysis in order to obtain profiles that serves to describe the kinetics of the reaction and resolve molecular structural changes from oxide precursor to the formation of the active phase. Generally, we are not able find incontrovertibly the actual value for such PCA number of relevant components. Complex reaction systems as the one studied in this work usually are rank-deficient and single matrix evaluation leads to ambiguous or ill-defined profiles. In such cases, many of the limitations associated with the resolution of a single matrix are overcome partially or completely when several matrices are treated together, the so-called three-way data sets. Three-way resolution methods actually introduce a significant improvement in the recovery of the true response profiles and have the additional benefit of providing quantitative information. Column-wise augmented matrix is insert in three-way data set context and helps to resolve unambiguously the profiles. In our study, we have built column-wise augmented systems performing temperature programmed (TPR) reduction for the studied samples. The complexity of such chemical systems requires caution in modeling and interpretation of results. Thus, suitable XAFS analysis (i.e., XANES and EXAFS treatment) were crucial in order to evaluate the goodness of molecular structures obtained from MCR calculation and prior chemical knowledge of the reaction balanced the evaluation of concentration profile.

In situ time-resolved XAS experiments were performed at SAMBA beamline at Synchrotron SOLEIL. Thanks to the Quick-EXAFS monochromator we were able to record both Mo and Co K-edge spectra during activation of the proposed solids. The good performance of the beamline and suitable quality of data allowed us to propose a sulfidation mechanism related to the oxide precursors in the catalysts via MCR calculation results. For Mo-species in impregnated catalyst, a 3-steps mechanism of sulfidation is observed, although differences in the kinetics are observed depending on the Mo loading. For highest Mo loading, a clear and well-separated mechanism was obtained by MCR. The oxide precursor turns to a partially reduced structure. Such compound turns to an oxisulfide compound and, then, transforms in the active nanosized MoS_2 phase. For lowest Mo loading impregnated catalyst, a similar behavior is observed. However, the MCR-calculated concentration profile of intermediate compounds are slightly different, particularly, an earlier formation of the oxisulfided phase. The main difference is observed in

TPR, where clearly different mechanisms are observed with different final products. Sol-gel reaction mechanisms are far more complex than impregnated reactions. Firstly, it is highly sensitive to the Mo loading. Lowest Mo loading sol-gel catalyst present virtually null sulfidation and at the end of the reaction, its final state is very similar to the final reduced state. The highest Mo loading presents a mechanism of activation with some similarities concerning impregnated series mechanism. One observes the formation of an intermediate, partially reduced, but even using an augmented-matrix system, we were not able to resolve totally the activation mechanism. The active phase profile remained hidden, probably because it arises together (or inside) another component, and truly profile separation in that case is impossible without further information. The solution adopted was to constraint the active phase spectrum (expected to be MoS_2) to reveal the concentration profile.

In that sense, it is crucial when dealing with such complex systems to plan experiments that may serve to construct three-way data sets, namely, column- and row-wise augmented systems. The attention paid in data quality recording (fundamental in XAS-based experiments) must be not only associated to the amount of data, but also in its variety. As precious as record good data with suitable time resolution is to diversify experiments in order to reveal single or isolated individual compounds of the whole reaction. One great advantage in synchrotron beamlines nowadays is the possibility to perform coupled technique measurements for a same experiment. Certainly, the use of such facilities must be considered when planning studies involving complex reactional systems in which subtle structural transformations are involved. The perspectives of application of MCR to the resolution of evolving systems are anyway quite broad, no matter the kind of spectroscopy, no matter the evolving system. Based on the exposed above, we can state that MCR applied in data treatment of time-resolved *in situ* XAS-based experiments are a promising and powerful tool to resolve molecular structural kinetics of reactions.

As far as the HDS catalysis is concerned, we presented a new route of preparation of efficient HDS catalyst. This new sol-gel route presents a major issue: part of the molybdenum is trapped within the support matrix and seems to be reducible but not sulfidable. As a consequence, part of the potential active phase remains inactive. On the other hand, analyzing the results of the high loaded catalysts (20 wt.% MoO_3), even if some of the molybdenum is lost within the titania, the activity remains quite high. This high activity might be related to the activation process. Indeed Co and Mo do evolve in a very similar way. The higher activity per sulfide molybdenum atom could be related to a better promotion of MoS_2 phase arising from this similar time evolution. It would be desirable to enhance the amount of the accessible active phase while keeping its peculiarity. Whether it is possible or not is out of the scope of the present work but it might be a track for further investigation and improvements of this sol-gel route for the preparation of HDS catalysts.